Experimental study of turbulent heat transport in Alcator C-Mod

by

Choongki Sung

B.S., Seoul National University (2008)
M.S., Seoul National University (2010)

Submitted to the Department of Nuclear Science and Engineering
in partial fulfillment of the requirements for the degree of

Doctor of Philosophy in Nuclear Science and Engineering

at the

MASSACHUSETTS INSTITUTE OF TECHNOLOGY

June 2015

Author ..... Signature redacted .....
Choongki Sung
Department of Nuclear Science and Engineering
Jan 29, 2015

Certified by... Signature redacted .....
Anne E. White
Associate Professor of Nuclear Science and Engineering
Thesis Supervisor

Certified by. Signature redacted .....
Dr. Martin Greenwald
Senior Research Scientist
Thesis Reader

Accepted by... Signature redacted .....
Mujid S. Kazimi
TEPCO Professor of Nuclear Engineering
Chair, Department Committee on Graduate Students

Experimental study of turbulent heat transport in Alcator C-Mod

by

Choongki Sung

Submitted to the Department of Nuclear Science and Engineering
on Jan 29, 2015, in partial fulfillment of the
requirements for the degree of
Doctor of Philosophy in Nuclear Science and Engineering

Abstract

The comprehensive analysis was performed to study turbulent transport in Alcator C-Mod plasmas in this thesis. A new Correlation Electron Cyclotron Emission (CECE) diagnostic was designed and installed as a part of this thesis work. Using this diagnostic, we measured local T_e fluctuations in $r/a \gtrsim 0.75$ in C-Mod for the first time. This thesis work provided new information about the Ohmic confinement transition, from the linear to the saturated confinement regime with the increase in average density. It was found that T_e fluctuations near the edge (r/a$\sim$0.85) tend to decrease across the Ohmic confinement transition. Although the Ohmic confinement transition has been considered predominantly as a result of the linear turbulence mode transition, we found no changes in the dominant turbulence mode across this transition via gyrokinetic analysis using the code, GYRO. The GYRO simulations performed near the edge reproduce experimental ion heat flux and T_e fluctuations, but electron heat flux was under-predicted. Considering that both ion heat flux and the T_e fluctuations mainly come from ion scale turbulence, the under-prediction of electron heat flux suggests the importance of electron scale turbulence. Intrinsic rotation reversals in C-Mod plasmas were studied in this thesis. Similar changes in electron temperature fluctuations, the reduction of T_e fluctuations near the edge, were observed across RF rotation reversals and Ohmic rotation reversals. The gyrokinetic and self-similarity analyses also showed similarities between rotation reversals in Ohmic and RF heated discharges. These observations suggest that the physics of Ohmic confinement transition and the rotation reversal can be applied to the physics of rotation reversal in RF heated discharges. This thesis also found the reduction of T_e fluctuations inside pedestal region with the transition from low to high energy confinement regime, which indicates the changes in core turbulence are correlated with the global energy confinement.

Thesis Supervisor: Anne E. White
Title: Associate Professor of Nuclear Science and Engineering

Acknowledgments

Even at this moment that I am writing "Acknowledgments" section, it is hard to believe that I am finishing this thesis project. I cannot imagine completing this thesis project without the help of many others. I would like to acknowledge some of them here.

I would first like to thank my supervisor, Prof. Anne White. She always encourages me and provides useful advices every time I am stuck in difficult problems. She also tried to improve my English skill. I learned a lot from her not only about turbulent transport in fusion plasma but also English and how to make a progress. I also appreciate her patience about my slow progress.

I would also like to thank my thesis reader, Dr. Martin Greenwald. His kind but acute advices and comments were helpful to finish this thesis project. I also sincerely thank my thesis committee members, Dr. David Mikkelsen and Prof. Ian Hutchinson. Dr. David Mikkelsen gave me a practical guidance about running GYRO and how to interpret the simulation results. The questions I got from Prof. Ian Hutchinson in every semester in the committee meeting were very useful and helpful to build my own logic about this thesis project. I also thank Prof. Felix Parra, who was my thesis reader, before he moved to Oxford. I would also like to thank Dr. Nathan Howard. He gave me his tool used to interpret GYRO outputs. I also learned how to run GYRO and TRANSP from him. His feedback was really essential in my thesis project. Dr. Olivier Sauter guided me the self-similarity analysis, and Dr. Jeff Candy helped me to run GYRO. Dr. Chris Holland's help was essential to perform a GYRO validation study. I would like thank them for their helps. I also thank Alexander Creely. He edited my awkward grammar in this thesis. Without his help, many people would have a difficulty in reading this thesis.

I hope to thank C-Mod team. All members in C-Mod team are great. I would like to thank C-Mod Engineering team, especially Rick Leccacorvi, Rui Vieira, Samuel Pierson, and Jim Irby. Without their knowledge and insights, CECE diagnostic could not be built. I also appreciate the technical support of C-Mod team, especially, Ed Fitzgerald, Joseph Bosco, William Parkin, Josh Stillerman, Mark Iverson, Paul Lienard, Brandon Savage, and Lee Berkowitz. I hope to highlight the contribution of Curran Oi to the CECE diagnostic. I also recognize the help of scientists and students in C-Mod, especially Dr. Amanda Hubbard, Dr. John Rice, Dr. Matthew Reinke, Chi Gao, Paul Ennever, Dr. John Walk, Dr. Jerry Hughes,

Dr. R. Michael Churchill, and Dr. Christian Theiler. They helped me get the data that I need for this thesis. I also would like to thank Mark Chilenski and Franco Mangiarotti. Studying together for the qual exam was helpful. I appreciate the help of Jungpyo Lee and Seung-Gyou Baek for their help and advice.

I also would like to thank my parents and family. My parents always trust and support me. I deeply thank their support and trust over more than 30 years. I also thank my sister. She also always cheers me up and helps me. I love all of you. I also would like to thank my mother in law for her support when my son, Shian, is born. Without her help, it was hard to finish this thesis. Finally, I would like to thank my wife, Hyoji, for her endless support and love. You make me better person, every day. Without you, I might not even start this thesis project. I love you. I also thank my son, Shian. Your smile gives me power.

Contents

List of Figures

List of Tables

Chapter 1

Introduction

Nuclear fusion has been considered as an attractive possible energy source for over 50 years. However, more research is required in both physics and engineering before a commercial power plant based on fusion reactions can be built. Anomalous transport in fusion plasmas is one of the main problems on the path to fusion, and must be solved in order to realize a fusion power plant. In this thesis, the turbulent heat transport in Alcator C-Mod Tokamak plasmas was studied via new turbulence measurements, transport analysis, and gyrokinetic simulations.

This chapter will be used to define the terms related to turbulent transport research in Tokamaks and to introduce the research topics covered in this thesis.

1.1 Nuclear Fusion

In this section, we will first introduce nuclear fusion as an energy source including its advantages over other energy sources and the requirements for obtaining fusion in the laboratory. After the basic explanation about nuclear fusion, the fusion experiment facility, the Alcator C-Mod Tokamak, will be introduced.

1.1.1 Nuclear fusion as an energy source

Nuclear fusion is a term used to indicate the kind of nuclear reaction in which two light nuclei are combined to produce heavier nuclei. In nuclear reactions (either fission or fusion), energy is produced due to mass deficit. While nuclear fission obtains its energy through the

separation of a heavy nucleus, which is heavier than iron, nuclear fusion attains its energy from the merging of two light nuclei, which are lighter than iron. For energy production, the following nuclear fusion reactions are of interest because of their high fusion reaction rates in the relatively low temperature range which is used in laboratory fusion experiments (~10-30keV).

$$\begin{aligned} D + D &\rightarrow He^3 + n + 3.27MeV \\ D + D &\rightarrow T + p + 4.03MeV \\ D + T &\rightarrow \alpha + n + 17.6MeV \end{aligned} \tag{1.1}$$

where D is a deuterium nucleus ($_1H^2$), T is a tritium nucleus ($_1H^3$), p indicates a proton or a hydrogen nucleus ($_1H^1$), and n is a neutron ($_0n^1$). He^3 and α indicate the helium nuclei, which are $_2He^3$ and $_2He^4$, respectively. The energy in units of MeV in Eq. 1.1 is the energy produced by each fusion reaction.

Nuclear fusion power using the reactions in Eq. 1.1 is a promising energy source for the following reasons. First, we will obtain tremendous energy from the reactions in Eq. 1.1, from small amounts of fuel. The energy produced by 0.14 tonnes of deuterium via fusion reaction is equivalent to 10^6 tonnes of oil [53]. Second, the fuel resources for fusion energy are almost unlimited. Deuterium can be easily obtained from sea water [53]. Although tritium is a radioactive nucleus with a half-life of about 12 years, we can obtain it from lithium isotopes (Li^6, Li^7) in the following reactions.

$$\begin{aligned} Li^6 + n &\rightarrow T + He^4 + 4.8MeV \\ Li^7 + n &\rightarrow T + He^4 + n - 2.3MeV \end{aligned} \tag{1.2}$$

Since the quantity of lithium isotopes are also sufficient to fuel fusion [53], we could breed as much tritium as we need once the relevant engineering issues are resolved. Third, fusion energy is clean compared to fossil fuels and nuclear fission. Unlike fossil fuels, there will be no pollution and greenhouse gases from fusion energy. Radioactive waste will be produced when the structural materials in a fusion power plant are activated by high energy neutrons generated in fusion reactions. However, this waste has a relatively short half-life, requiring

relatively short storage time ($\lesssim$100yrs) [53] compared to the radioactive waste from nuclear fission power, which must be stored for up to 300-400yrs. Fourth, Fusion energy is safe compared to fission energy. Fission energy uses a chain reaction. That is, one nuclear fission reaction induces another nuclear fission reaction. This chain reaction makes that the large amounts of fuel that are stored in the core of fission reactors may be dangerous in the event of an uncontrollable accident. Fusion energy does not use chain reactions the way fission energy does. The fuel is fed into the chamber from the outside in a fusion power plant. Thus, severe accidents like the accident in Fukushima cannot occur in a fusion power plant.

1.1.2 Fusion ignition condition

In order to realize a commercial fusion power plant, a positive energy balance must first be achieved via a sufficient number of fusion reactions to compensate for any power loss. In a fusion reaction, the Coulomb repulsive force exists between the two nuclei that have positive charges. These nuclei must have energy sufficient to overcome this Coulomb barrier for a fusion reaction. Thus, heating to high temperatures is required to produce fusion energy. Even with a high temperature, the fusion reaction is not a dominant reaction when two fuel nuclei (D or T) interact. They are usually scattered, since the cross section of Coulomb scattering is more than an order of magnitude larger than the cross section of a fusion reaction [171]. Thus, simple beam-beam fusion or beam-target fusion will not work. Instead, it is required to confine a sufficient number of fuel particles with high enough temperature for sufficiently long time. This fusion scheme is called thermonuclear fusion. The required temperature in thermonuclear fusion using the reactions in Eq. 1.1 is around 10keV. At this temperature, all fuel particles will be ionized. Consequently, the fusion reactions will occur when fuel is in the plasma state. The confinement of a sufficient number of plasma ions for a long time will ensure enough fusion reactions to generate energy and heat the plasma, maintaining fusion temperatures. In other words, the plasma will be self-heated by the energy produced by fusion reactions through this confinement. Fusion ignition refers to this state.

The most promising approach to achieve ignition is magnetic confinement. The fundamental fact that charged particles will follow a helical trajectory in a background magnetic field is used in magnetic confinement. In other words, the charged particles are confined

by the magnetic field in the direction perpendicular to the field. The ignition condition can be quantified as a function of plasma density, n [m^{-3}], temperature, T [keV], and the confinement time, τ_E [sec]. For a D-T plasma, which has the same amount of deuterium and tritium as plasma ions ($n_D = n_T = n_e/2 = n/2$, with deuterium density, n_D, tritium density, n_T, and electron density, n_e), and confined by magnetic fields, the ignition condition is given by [97],

$$n\tau_E > \frac{12}{<\sigma v>}\frac{T}{E_\alpha} \tag{1.3}$$

where $<\sigma v>$ is the rate coefficient for the D-T reaction [m^3/s], T is the thermal temperature of the plasma, and E_α is the energy of the alpha particle produced by the D-T reaction (~3.5MeV).

It is noteworthy that the D-D reactions in Eq. 1.1 also occur in D-T plasmas. However, their reaction rates are much smaller than the D-T reaction in the relevant temperature range (10-20keV), so only the D-T reaction is considered in Eq. 1.3. The neutron produced by the same fusion reaction will not be confined by the magnetic field. Thus, under magnetic confinement, only the alpha particle produced by the D-T reaction will heat the plasma. The reaction rate coefficient, $<\sigma v>$ for the D-T reaction in T=10-20keV is given by [171],

$$<\sigma v> = 1.1 \times 10^{-24} T^2 m^3 s^{-1} \tag{1.4}$$

where T is in keV.

Applying Eq. 1.4 to Eq. 1.3 with E_α=3.5MeV, the ignition condition is obtained as a product of density, temperature and energy confinement time, as follows.

$$nT\tau_E > 3 \times 10^{21} m^{-3} keV s \tag{1.5}$$

Although remarkable progress has been made so far, as shown in Fig. 1-1, experiments have not yet achieved the ignition condition. Since the pressure of the plasma in a reactor, p(=2nT), is determined by the desired power and engineering constraints related to the allowable wall loading power [53], energy confinement time, τ_E, is the parameter we should improve to satisfy the ignition condition. Plasma particles will move along the magnetic field, and by confined well perpendicular to the magnetic field. However, these particles

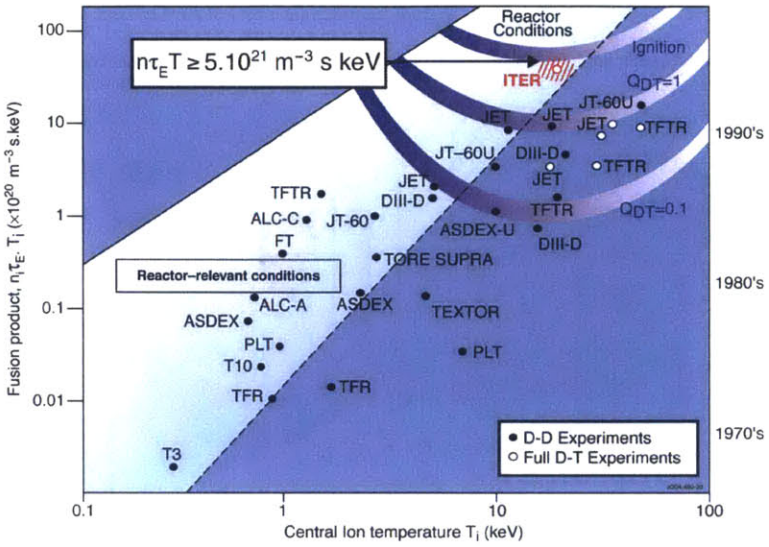

Figure 1-1: Progress in fusion in terms of triple product of ion density, ion temperature, and energy confinement time, as explained in Eq. 1.5. This figure is adapted from the EUROfusion website (https://www.euro-fusion.org).

deviate from their trajectories along the magnetic field due to various mechanisms, such as collisions, drift motions and turbulent eddies, which cause transport across the magnetic field. In order to increase the τ_E value in the plasmas, we must minimize this cross field heat transport. This is the main motivation of transport research in fusion plasmas, including this thesis. More details about the transport in fusion plasmas will be discussed in section 1.2.

1.1.3 Alcator C-Mod Tokamak

The most promising fusion reactor concept based on the magnetic confinement of a plasma is the Tokamak. The Tokamak is a toroidal device which has both toroidal and poloidal magnetic fields to confine the plasma. The geometry of the magnetic field in a Tokamak is shown in Fig. 1-2. The dominant magnetic field used for the confinement is the toroidal magnetic field, which is applied by external coils. The poloidal magnetic field is required to get a balance between the plasma pressure and magnetic pressure in the toroidal geometry (or, to get an equilibrium). The poloidal magnetic field in the Tokamak is generated by a current in the plasma flowing in the toroidal direction. This plasma current is induced by the central solenoid (or the inner poloidal field coils in Fig. 1-2). Helical field lines are thus generated in the Tokamak, and a high temperature plasma will be confined by this helical

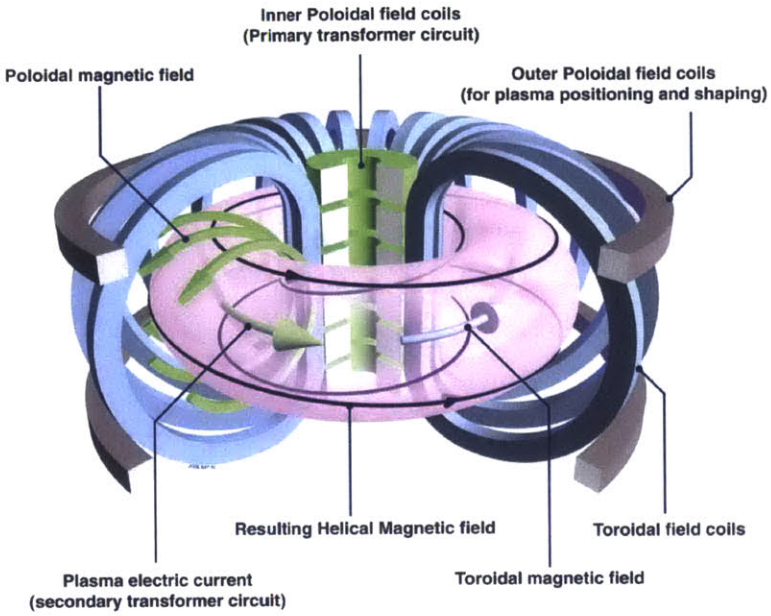

Figure 1-2: Magnetic field coils and the magnetic field lines produced by these coils in Tokamak. This figure is adapted from the EUROfusion website (https://www.euro-fusion.org).

field structure.

Alcator C-Mod is a Tokamak located at the Plasma Science and Fusion Center (PSFC), at MIT. Although C-Mod is a compact device with major radius, R=0.67-0.68m, and minor radius, a=0.22m, its high toroidal magnetic field (nominal 5.4T, but max. 8T on axis) makes this Tokamak unique. Since fusion power is proportional to $\beta^2 B^4$, where β is the ratio of plasma pressure to magnetic field pressure ($\beta = \frac{p_e + p_i}{B^2/2\mu_o}$, with electron pressure, $p_e (= 2n_e T_e)$, and ion pressure, $p_i (= 2n_i T_i)$.), fusion experiments with high magnetic field are desirable. This high magnetic field also relieves the operational limit on density and plasma current due to instabilities, which allows C-Mod to have high plasma current (nominal 0.6-1.0MA, max. 2MA) and high density (max. $5 \times 10^{20} m^{-3}$) compared to other Tokamaks in the world. The heating schemes used in C-Mod plasmas include Ohmic heating and ion cyclotron resonance heating (ICRH). Unlike other Tokamaks, neutral beam heating is not used on C-Mod for heating. C-Mod does not have any external momentum sources. In addition, C-Mod is a diverted Tokamak, which can be operated in either upper/lower single null or double null configurations. Table 1.1 shows the operational parameters of the Alcator C-Mod Tokamak.

All of the data studied in this thesis are obtained from the Alcator C-Mod Tokamak. The extensive diagnostic suite in C-Mod allows us to comprehensively investigate the trans-

Major radius [m]	0.67-0.68
Minor radius [m]	0.22
Toroidal magnetic field [T]	3-8
Plasma current [MA]	0.4-2.0
Line averaged density $[m^{-3}]$	0.2-5.0
Ion Cyclotron Resonance Heating [MW]	Max. 5.5
Plasma duration [s]	2.0

Table 1.1: Alcator C-Mod operational parameters

port behavior in C-Mod plasmas. A Thomson scattering diagnostic [84, 14] provides the electron density and temperature profiles, and Electron Cyclotron Emission (ECE) diagnostics [14, 115] also measure the electron temperature profile. High resolution imaging x-ray spectroscopy (HiRex) [87, 122] is used to measure the core profiles of toroidal velocity and ion temperature. Edge profiles of toroidal velocity and ion temperature are measured by charge exchange spectroscopy (CXRS) [103]. The robust profile measurements by these diagnostics in C-Mod allow for detailed transport research through profile analysis, power balance transport analysis, and gyrokinetic analysis, which will be explained in section 3.3 and 3.4. Since small-scale micro-turbulence induced by drift wave instabilities leads to anomalous transport in fusion plasmas, turbulence (fluctuation) measurements are required for transport research. In C-Mod, various fluctuation diagnostics have been installed. Line averaged electron density fluctuations are measured by Phase Contrast Imaging (PCI) diagnostic [98, 121]. Local density fluctuations can be measured by reflectometry [46], but the signal is not calibrated. We used reflectometry to measure the edge density fluctuations. It is possible to measure large amplitude ($\gtrsim 2\%$) electron temperature fluctuations in the core region using the ECE diagnostic. However, one must apply the correlation technique to the signal measured by the ECE radiometer to measure the electron temperature fluctuations relevant to turbulent transport. In the past, attempts were made to measure core electron temperature fluctuations in C-Mod, but it was difficult to measure the T_e fluctuations above the noise level [168]. One of main works in this thesis is to explore the core electron temperature fluctuations in C-Mod via a newly developed ECE diagnostic, which is optimized for the correlation technique. Details about this diagnostic will be explained in Chapter 2, and the measurement results are studied in Chapter 4-6.

1.2 Anomalous transport in fusion plasmas

The heat transport levels in fusion plasmas are much higher than those expected from collisional transport considering the toroidal magnetic field topology, such as trapped particles in Tokamaks, i.e., neoclassical transport theory. This anomalous transport is one of the important problems hindering fusion energy development and must be understood to realize a fusion power plant. It has been widely accepted that turbulence in the plasma, induced by drift wave instabilities, is responsible for this anomalous transport in fusion plasmas. The plasma turbulence and the induced transport have been studied extensively, but predictive models are still elusive, and more work is needed. The reader can find a review of relevant works in [74, 40, 159, 55]. In this section, we will briefly introduce electrostatic turbulent transport, and the relevant drift instabilities. Electromagnetic turbulence will not be relevant in this study due to the low β value in C-Mod plasmas ($\beta \lesssim 1\%$) studied in this thesis. However, it is noteworthy that electromagnetic turbulence will be important in fusion plasma in the future, with β value of a few percent or more.

1.2.1 Turbulent electrostatic particle and heat transport

We first introduce the simple relation between the cross-field (radial) transport and turbulent fluctuations in the electrostatic limit. When magnetic field fluctuations are ignored, fluctuating $E \times B$ drifts induce turbulent particle and heat fluxes across the magnetic field. With electric field fluctuations, $\tilde{E} \simeq \nabla\tilde{\phi}$, the radial velocity due to the fluctuating $E \times B$ drift, $\tilde{v}_r$ is,

$$\tilde{v}_r \simeq \frac{\nabla_\theta \tilde{\phi} \times \vec{B}_t}{B^2} \simeq \frac{\tilde{E}_\theta}{B} \tag{1.6}$$

where B_t is the equilibrium magnetic field in the toroidal direction, the dominant magnetic field in Tokamak plasmas. The contribution from the cross product of toroidal electric field and poloidal magnetic field is ignored in here because $k_{||} << k_\perp$ in the drift waves we are interested in this study.

The time-averaged particle flux due to the electrostatic turbulence, $\tilde{\Gamma}$ will be the product of the density fluctuations and the fluctuating radial velocity as follows:

$$\tilde{\Gamma}_j =< \tilde{n}_j \tilde{v}_r >=< \frac{\tilde{n}_j \tilde{E}_\theta}{B} > \tag{1.7}$$

where <> indicates a time average or ensemble average, and j denotes the species of particle (main ion, electron or impurity).

In the same manner, the time averaged heat flux due to the electrostatic turbulence, $\tilde{Q}$, is given as the products of energy fluctuations and fluctuating radial velocity.

$$\tilde{Q}_j =< \tilde{E}_j \tilde{v}_r > \tag{1.8}$$

Energy fluctuations, $\tilde{E}$, is defined as,

$$\tilde{E}_j = \frac{3}{2}\tilde{p}_j \simeq \frac{3}{2}[\tilde{n}_j T_j + \tilde{T}_j n_j] \tag{1.9}$$

where n and T are equilibrium density and temperature.

We then obtain the turbulent heat flux as a function of three fluctuating quantities: density fluctuations, temperature fluctuations and potential fluctuations (or poloidal electric field fluctuations).

$$\begin{aligned} \tilde{Q}_j &\simeq \frac{3}{2} < [\tilde{n}_j T_j + \tilde{T}_j n_j]\tilde{v}_r > \\ &= \frac{3}{2}[\frac{< \tilde{n}_j \tilde{E}_\theta > T_J}{B} + \frac{< \tilde{T}_J \tilde{E}_\theta > n_j}{B}] \\ &= \frac{3}{2}[\tilde{\Gamma}_j T_j + \frac{< \tilde{T}_j \tilde{E}_\theta > n_j}{B}] \end{aligned} \tag{1.10}$$

It is noteworthy that fluctuation quantities in Eq. 1.7-1.10 are fluctuations at each position, although position dependency is neglected in the equations. In other words, these fluctuations are local fluctuations. It follows that the turbulent particle and heat fluxes are also defined at each location. We notice that turbulent particle flux is a function of density fluctuations, potential fluctuations and the phase between them, and that turbulent heat flux is a function of density fluctuations, temperature fluctuations, potential fluctuations, the phase between density and potential fluctuations, and the phase between temperature and potential fluctuations from Eq. 1.7 and 1.10. Thus, one must measure these fluctuations and phase relations in the experiment and calculate the unmeasured quantities via simulations to understand the turbulent transport. In this thesis, we use, for the first time in C-Mod, local T_e fluctuations measured with CECE to study turbulent transport, as will be explained in Chapter 2. Other local fluctuating quantities and turbulent heat flux values in

the core can be obtained from gyrokinetic simulations, which will be explained in section 3.4.

1.2.2 Drift wave instabilities

In this section, drift wave instabilities, responsible for the turbulent fluctuations in the last section, will be briefly explained. We first introduce what the drift wave is and how the drift wave is converted to the instabilities. Three important drift wave instabilities will then be introduced, which are ion temperature gradient (ITG) modes, trapped electron modes (TEMs), and electron temperature gradient (ETG) modes.

Drift wave

The simplest form of a drift wave is a pure oscillatory wave propagating with the electron diamagnetic velocity along the diamagnetic drift direction, perpendicular to both the background magnetic field and pressure gradient. With the 1-D slab geometry shown in Fig 1-3, the dispersion relation of this wave is given by,

$$\frac{\omega}{k_y} = v_{*,e} \tag{1.11}$$

where y is the direction of diamagnetic drift direction when the density gradient is along x direction and the background B field is applied on z direction. $v_{*,e}$ is an electron diamagnetic velocity, which defined as,

$$v_{*,e} = -\frac{1}{n}\frac{\partial n}{\partial x}\frac{T_e}{eB} \tag{1.12}$$

where T_e is in the energy unit such as eV.

The derivation of Eq. 1.11 can be found in [170, 32, 74], but it is worth noting the assumptions used in this derivation. First, electron inertia terms are neglected ($m_e \rightarrow 0$). Second, only weak perturbations of density and potential, within a few percent of the equilibrium quantities so that a first-order Taylor series approximation is enough, were considered with the density gradient. Any other gradients and perturbations, such as from temperature, were not considered. Third, any dissipation of energy (e.g., by collisions) is not included. Fourth, the propagating velocity of this wave along the magnetic field is much smaller than the electron thermal velocity. The simple physical picture of this wave is shown

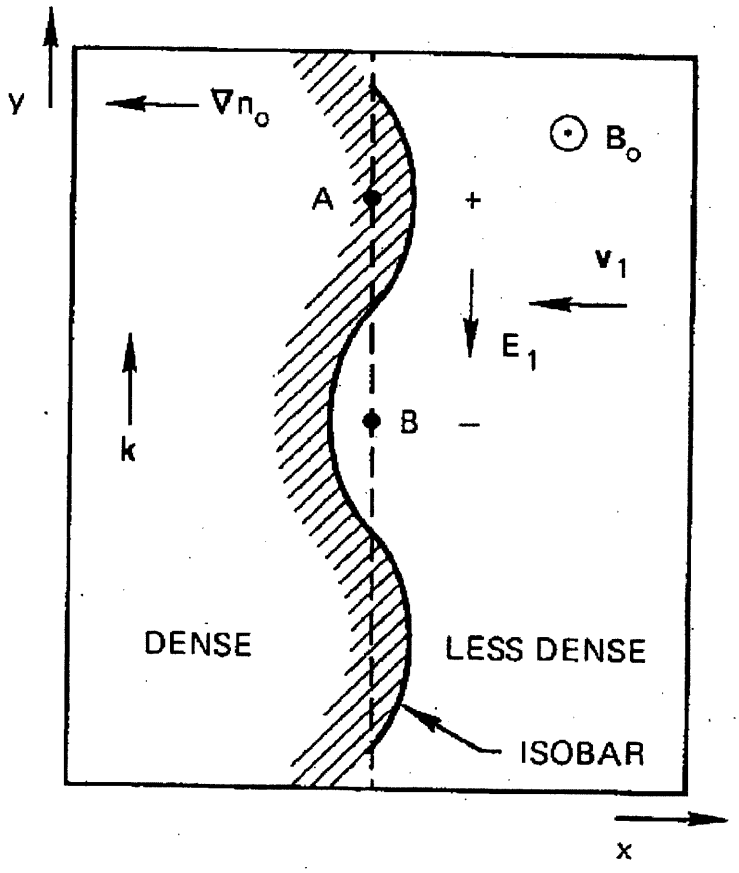

Figure 1-3: A plasma drift wave in a slab geometry. This figure is adapted from F. F. Chen, 1984, *Introduction to Plasma Physics and Controlled Fusion.*

in Fig. 1-3. There is an initial ion density perturbation varying sinusoidally along y direction with the background density gradient in the x direction and the background magnetic field in the z direction. The density imbalance due to the initial perturbation induces a potential, and an electric field in the y direction. This electric field results in $E \times B$ drift in the x direction. This drift and density gradient make this perturbation propagate along the y direction. The small electron inertia and the thermal motion of electrons, which are faster than the phase velocity of the wave parallel to the external magnetic field, yields the Boltzmann relation of the electron [170, 74].

$$\frac{\tilde{n}_e}{n} = \exp e\tilde{\phi}/T_e - 1 \simeq \frac{e\tilde{\phi}}{T_e} \tag{1.13}$$

The approximation in the equation is valid when the potential perturbation is weak ($e\tilde{\phi} << T_E$).

Eq. 1.13 shows that electron density perturbations are in phase with the potential perturbations. In other words, electrons respond rapidly to a potential perturbation to keep the Boltzmann relation, or to compensate the ion perturbation. It is noteworthy that the density perturbation is 90° out of phase with the electric field perturbation. There will thus be no cross-field flux due to these perturbations. This can be easily seen from Eq. 1.7. As shown in Appendix G, no electron temperature fluctuations will be induced when electrons are in the Boltzmann relation. It is then noticeable from Eq. 1.10 that there is no energy flux generated by this wave. As implied by Eq. 1.11, these perturbations are just oscillating. Since there is no energy loss due to the fast electron response, this response is adiabatic.

However, if there is a dissipation of parallel electron motion by some mechanism such as collisions or wave-particle interactions, there will be time (or phase) delay between perturbation of electron density and potential, inducing cross field flux. In other words, the electron response becomes non-adiabatic. One simple model used to show this non-adiabatic response is i-δ model (Terry-Horton model) [157]. In this model, the Boltzmann relation is modified in the following way,

$$\frac{\tilde{n}_e}{n} = \frac{e\tilde{\phi}}{T_e}(1 - i\delta) \tag{1.14}$$

Consequently, the modified dispersion relation due to the phase shift in Eq. 1.14 is given by [170],

$$\omega = \frac{k_y v_{*,e}}{1 - i\delta} \simeq k_y v_{*,e}(1 + i\delta) \tag{1.15}$$

The approximation is satisfied when $\delta << 1$.

An instability will occur when $\delta > 0$ since the amplitude of the wave is proportional to $\exp(-i\omega t)$. We must note that a non-adiabatic electron response is not a necessary condition to make the drift wave unstable. Even with an adiabatic electron response, the drift wave can be generated by other mechanisms, such as ion dynamics which induce a phase shift of ion density perturbations with respect to potential perturbations. The typical example of this type of drift wave instability is the Ion Temperature Gradient (ITG) modes, which will be introduced in the next section.

Ion Temperature Gradient (ITG) modes

The ion temperature gradient (ITG) modes refer to the drift wave instabilities driven by ion temperature gradient or η_i, defined as $\eta_i = |\nabla \ln T_i|/|\nabla \ln n_i|$. The ITG modes have been thought to be responsible for the anomalous ion transport in magnetic fusion plasmas with low β, and an extensive study of this mode was performed in the past ([40, 74] and references therein). There are several different ITG modes, depending on the geometry, collisionality, magnetic shearing and so on. A summary of different ITG modes can be found in Table A1 in [40] and Table 3 in [75]. We will note the common features of ITG modes.

The spatial scale of the ITG modes are ion scale ($k_y \rho_s \sim 0.1 - 1.0$, where ρ_s is the sound gyroradius of the main ion, defined as $\rho_s = c_s/\Omega_{ci}$ with $c_s = \sqrt{T_e/m_i}$ and $\Omega_{ci} = eB/m_i c$). There is a stability threshold (critical ITG or η_i value) in the ITG modes. This property can be linked to the stiffness and self-similarity argument, introduced in section 1.3. The diffusivity of the ITG modes are also proportional to η_i. Thus, the important mode characteristics are determined by the η_i value. In this reason, the ITG modes are also called as η_i modes. However, when the density profile is flat ($\eta_i \to 0$), the modes are characterized by the ITG value [40]. It is noteworthy that the diffusivity of the ITG modes follows the gyro-Bohm scaling ($\chi_{gB} = \frac{\rho_s}{L_n}\frac{cT_e}{eB} \sim \rho_s^2 c_s/L_n$ with the density gradient length, $1/L_n = -\partial \ln n$). The Gyro-Bohm scaling of the ITG mode can be derived by simply assuming the characteristic length of the ITG mode is about the ion (or sound) gyroradius and the characteristic time is $1/\omega_{*,i}$ with ion diamagnetic frequency, $\omega_{*,i}$. As mentioned in

the last section, a non-adiabatic electron response is not necessary for ITG modes. However, non-adiabatic electrons increase the growth rate of the ITG mode [136] and even generate another type of instability, the so-called hybrid trapped electron ITG mode [13]. It is also noteworthy that the ITG modes with adiabatic electrons do not cause any electron transport. In the more realistic picture with non-adiabatic electrons, the ITG modes are also linked to the electron transport.

Two types of ITG modes are thought to be important. They are the slab ITG mode and toroidal ITG mode [40, 74]. The slab ITG, or slab η_i, mode is generated by the interaction between the drift wave driven by ion temperature gradient and the ion acoustic wave. The phase shift is caused by the effect of parallel compression from the ion acoustic wave on the ion density response. When a toroidal geometry is considered, another ITG mode is found. A toroidal ITG mode is caused by the magnetic curvature drift coupled with a drift wave due to the ion temperature gradient.

Trapped Electron Mode (TEM)

Trapped electron modes (TEMs) refer to the drift wave instabilities driven by the non-adiabatic electron response due to trapped electrons. We must note that the non-adiabatic electron response will mainly come from trapped electrons since the thermal velocity of passing electrons is much higher than the parallel phase velocity of the drift wave. In a Tokamak, trapped particles occur due to the 1/R dependence of the toroidal magnetic field and helical field lines, and most of them will stay in the bad (or unfavorable) curvature region. TEMs are driven by electron pressure gradients (or electron density gradients [8] or electron temperature gradients [93]). A threshold condition for stability (or the critical gradient of n_e and T_e) exists in TEM as well [8, 50, 70]. TEM can be classified by either the driving gradient ($\nabla T_e/\nabla n_e$) or the destabilizing mechanism (collisionless/dissipative), but the common features of TEMs are as follows. The TEM induces ion scale turbulence like the ITG modes, but these modes are responsible for electron heat transport rather than ion heat transport. The growth rate of TEMs increases with the increase of the inverse aspect ratio, ϵ. This is because the fraction of trapped electrons is proportional to $\epsilon^{0.5}$. For the same reason, the growth rate of TEMs tends to decrease with increased collision frequency due to collisional de-trapping of the trapped electrons. However, we should note that the dependency of the dissipative TEM on the collision is more complicated. As will

be explained in the next paragraph, dissipation through collisions destabilizes this mode. Thus, the growth rate of this mode initially increases with higher collision frequency, but after a certain point, the growth rate will be reduced as collisionality increases due to the de-trapping of the trapped electrons [92].

Depending on the destabilizing mechanism, there are two types of TEM [92, 93]. One is collisionless TEM and the other is dissipative TEM. The collisionless TEM will occur when the effective collision frequency for the trapped electrons, $\nu_{eff} = \nu_e/\epsilon$ with electron collision frequency, ν_e, is smaller than the bounce frequency of the trapped electrons, $\omega_{b,e} = \epsilon^{1/2}\frac{v_e}{qR}$. This mode is driven by wave-particle interactions between the magnetic drift of the trapped electrons and the parallel velocity of the drift wave [159]. We must note that this collisionless mode is due to the curvature of the magnetic field (bad curvature), and is localized in the bad-curvature region. The dissipative TEM occurs when ν_{eff} is comparable to $\omega_{b,e}$. This mode is due to Coulomb collisions between trapped and passing electrons. These collisions will limit the mobility of electrons along the field line. This dissipative mode is also localized in the trapped region, mainly bad curvature region, but the reason for localization is different than that for the collisionless mode. The dissipative mode is localized in the trapped region due to the large population of the trapped electrons in bad curvature region, while the collisionless mode is localized due to the sign of curvature of the magnetic field.

Electron Temperature Gradient (ETG) modes

Electron temperature gradient (ETG) modes may be considered as the electron version of ITG modes. By switching the roles of ions and electrons, we can study the ETG modes from the known ITG results when non-adiabatic effects and electromagnetic effects are excluded. ETG modes also have the slab and toroidal modes depending on the geometry [170], and a threshold condition for the stability (a critical $\eta_e(= |\nabla \ln T_e|/|\nabla \ln n_e|$ or ETG value) also exists [89]. The growth rates are also proportional to η_e (or ETG value). However, electron scale turbulence is generated by the ETG modes $k_y\rho_e \sim 0.1 - 1.0$ with the electron gyroraidus, ρ_e. The spatial scale of ETG modes ($k_y\rho_s >> 1$) makes the ion dynamics almost adiabatic. It follows that ETG modes contribute mainly to electron transport and little to ion transport. Electromagnetic effects can be important to electron scale turbulence such as ETG, because the collisionless skip depth, $\delta_s = c/\omega_{p,e}$ with plasma frequency, ω_{p_e}, can be comparable to the spatial scale of electron turbulence ($\sim \rho_e$) [89]. When ρ_e is smaller than

the Debye length, λ_{De}, the Debye shielding effect can stabilize the ETG mode. The Debye shielding effect will be important near the edge of plasma where the density is low [89, 86].

The diffusivity of the ETG mode can be estimated from its characteristic spatial scale, ρ_e, and its characteristic time, $1/\omega*, e$. We can then obtain that $\chi_{ETG} \sim \rho_e^2 v_{te}/L_n \sim (m_e/m_i)^{0.5}\chi_{ITG}$. This simple estimate indicates that the transport induced by the ETG modes is much less than the transport due to the ITG modes. However, previous studies have shown that the contribution of the ETG modes can be significant through radially elongated vortices (streamers) [90, 47] and through the interaction with ion scale turbulence [77]. However, the contribution of the ETG modes to transport is still an open question, and this area is being studied actively.

1.2.3 The gyrokinetic model

In the previous section, the drift wave instabilities and three important modes, ITG, TEM, and ETG, are introduced. Turbulent transport in the fusion plasmas will occur via not only the drift wave instabilities but also their non-linear interactions. Thus, instead of studying each instability, we need a "first principles" physical model which can describe the realistic nonlinear physics of the turbulent transport. The gyrokinetic model is widely used in the fusion community to study turbulent transport [55]. The derivation of the gyrokinetic model is beyond of the scope of this thesis, but the origin of this model will be briefly introduced in this section. The readers can find the detailed derivation of various versions of the gyrokinetic model in [30, 54, 66, 150, 24, 55, 7] and references therein.

The kinetic approach, which uses a particle distribution function in six dimensional phase space (3 in physical space and 3 in velocity space), $f(\vec{r}, \vec{v}, t)$, is appropriate to describe plasma dynamics because of the large number of particles in the plasma. In fusion plasmas, where the kinetic energy of particles is higher than their potential energy, particles are weakly coupled. Consequently, binary collision events are important, and the correlations of multiple particles (≥ 3) will be ignorable. The Boltzmann equation is appropriate in this condition (where binary collisions are dominant), as given by,

$$\frac{Df_s}{Dt} = \frac{\partial f_s}{\partial t} + \vec{v} \cdot \nabla f_s + \vec{a} \cdot \nabla_v f_s = C(f_s, f_{s'}) \tag{1.16}$$

where, $C(f_s, f_{s'})$ is a collision operator for the binary collisions.

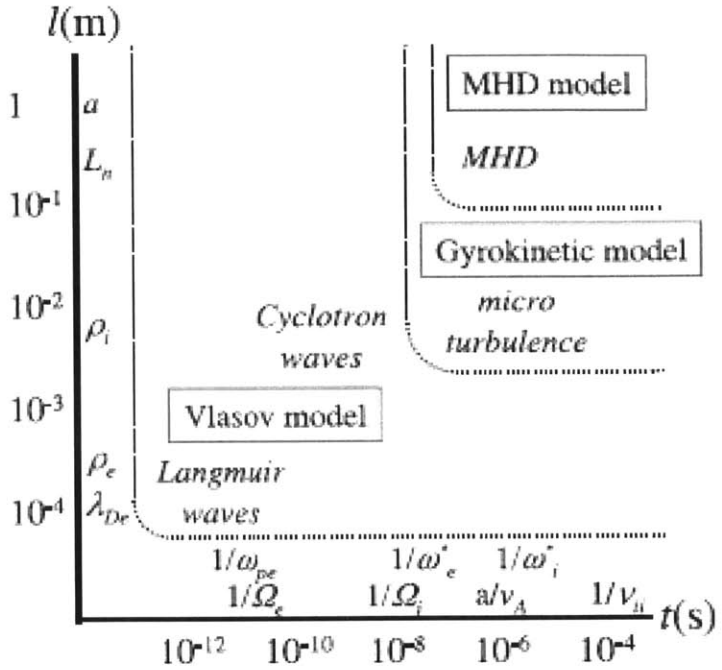

Figure 1-4: Wide ranges of spatio-temporal scales of physical events in fusion plasmas. The figure is adapted from X. Garbet et al, 2010, *Nuclear Fusion*, *50*, 043002, copyright 2014 IOP publishing.

In fusion plasmas, small angle Coulomb scattering is a dominant collisional process, and the series of small angle Coulomb scatterings between two particles can be modeled by the Fokker-Planck collision operator. The Fokker-Plank equation is obtained by replacing the collision operator in Eq. 1.16 with the Fokker-Planck collision operator. The Fokker-Plank equation for fusion plasmas is thus given by,

$$\frac{Df_s}{Dt} = \frac{\partial f_s}{\partial t} + \vec{v} \cdot \nabla f_s + \vec{a} \cdot \nabla_v f_s = \Sigma_{s'} C_{ss'}(f_s, f_{s'}) \tag{1.17}$$

with Fokker-Planck collision operator, $C_{ss'}(f_s, f_{s'})$.

The exact form of the Fokker-Planck collision operator and its derivation can be found in [69]. The Fokker-Plank equation coupled with Maxwell's equations are used to study plasma dynamics.

The physical events such as transport and ideal MHD (Magnetohydrodynamics) type instabilities occur in a wide range of temporal and spatial scales in fusion plasmas, as shown in Fig. 1-4. We notice that the temporal scale of micro-turbulence (or drift wave type instabilities) is much longer than the cyclotron motion of the electrons and ions. The

gyrokinetic model is a tool to treat physical events which occur on a time scale much slower than the gyromotion of the particles, such as turbulence induced by drift wave instabilities. Since many gyro motions will be completed within a time scale of the turbulent fluctuations, these motions will not be well coupled (or not relevant) with these fluctuations. These gyro motions are eliminated through the transform of the particle orbit coordinate to gyro-center coordinate in the gyrokinetic model. This transform reduces the six dimensional phase space to five dimensional phase space, which saves significant computing time to solve the equation. The reduced Fokker-Planck equation is then given by [55],

$$\frac{D\bar{f}_s}{Dt} = \frac{\partial \bar{f}_s}{\partial t} + \frac{d\vec{R}}{dt} \cdot \frac{\partial \bar{f}_s}{\partial \vec{R}} + \frac{d\vec{u}}{dt}\frac{\partial \bar{f}_s}{\partial \vec{u}} = < \Sigma_{s'} C_{ss'}(f_s, f_{s'}) > \tag{1.18}$$

where $\bar{f}_s$ is a distribution on gyro-center coordinates, $\vec{R}$ is the gyrocenter position vector, $\vec{u}$ is the gyrocenter velocity, and $< \Sigma_{s'} C_{ss'}(f_s, f_{s'}) >$ is the gyro-averaged Fokker-Planck collision operator.

It is noteworthy that the gyrokinetic model also separates the spatial scales, and that gyroaveraging is applied after the spatial scales are separated. Although the fast time scale ($\sim \Omega_s$) is removed in the reduced Fokker-Planck equation through gyro-averaging, the distribution function in this equation still cover a wide range of spatial scales from the ion gyroradius to machine size ($\sim$ a). In order to separate the spatial scales, the distribution function is separated into two parts, a long wavelength (ensemble averaged) part (f_s^{lw}) and a fluctuating (turbulence) part (f_s^{tb}), as follows:

$$f_s = f_s^{lw} + f_s^{tb} \tag{1.19}$$

The spatial scale of the long wavelength part is around the gradient scale length of the density or temperature profiles, and the fluctuating part has a spatial scale comparable to the gyroradius of a particle. In this ordering, the basic assumption is that the gradient scale length of the profiles (L) are much longer than the gyroradius (ρ). In other words, the dimensionless parameter, $\rho* = \rho/a \sim \rho/L << 1$ in the gyrokinetic model. The gyrokinetic ordering, which is the basic assumption in the gyrokinetic model is given by,

$$\frac{\omega}{\Omega_s} \sim \frac{k_\parallel}{k_\perp} \sim \frac{v_E}{v_{th,s}} \sim \rho* << 1 \tag{1.20}$$

with the characteristic frequency of turbulence, ω, and the wave number of turbulence in the parallel and perpendicular to the background magnetic field, $k_{||}$ and $k_{\perp}$.

Using the same ordering, the electric field and magnetic field, which will be used in the third term of the left hand side of the Fokker-Planck equation, are also separated in spatial scale. We can then separate the Fokker-Planck equation into two spatial scales, long wavelength and turbulence scales.

In order to solve the each equation order by order, both the long wavelength and fluctuating parts of the distribution function (f), electric field ($\vec{E}$) and magnetic field ($\vec{B}$) are expanded in $\rho*$. For example, the long wavelength and fluctuating part of f will be expanded in the following way.

$$\begin{aligned} f_s^{lw} &= f_{s,0}^{lw} + f_{s,1}^{lw} + f_{s,2}^{lw} + \cdots \\ f_s^{tb} &= f_{s,1}^{tb} + f_{s,2}^{tb} + \cdots \end{aligned} \tag{1.21}$$

The zeroth order of the long wavelength part will be the equilibrium distribution ($f_{s,0}^{lw} \sim f_{M,s}$, with the maxwellian distribution, f_{M_s}), and then $f_{s,1}^{lw} \sim \rho * f_{M,s}$, $f_{s,2}^{lw} \sim \rho *^2 f_{M,s}$, $f_{s,1}^{tb} \sim \rho * f_{M,s}$, and $f_{s,2}^{tb} \sim \rho *^2 f_{M,s}$. A similar expansion can be applied to the electric field and the magnetic field.

The information about the equilibrium is obtained from the lowest order and/or the zeroth order of gyro-averaged equation for the long wavelength part. The first order gyro-averaged equation for the long wavelength part is called the drift-kinetic equation. A gyrophase independent part of $f_{s,1}^{lw}$ can be determined from this equation. The first order gyro-averaged equation for the fluctuating part is called the gyrokientic equation. We can obtain information about $f_{s,1}^{tb}$ from this equation. A detailed explanation of the gyrokinetic model can be found in [55, 150, 3] and references therein.

The gyrokinetic equation which includes electromagnetic turbulence and large mean flow, V_o, on the same order of the thermal velocity, V_{ts}, is given by [150],

$$
\begin{aligned}
&[\frac{\partial}{\partial t} + (\vec{V}_o + v'_{\|}\vec{b} + \vec{v}_{ds} - \frac{c}{B}\nabla\psi^{tb}_{s,1}(\vec{R}) \times \vec{b}) \cdot \nabla]h^{tb}_{s,1}(\vec{R}) - < \Sigma_{s'} C_{ss'}(f_s, f_{s'}) > \\
&= \frac{c}{B}\nabla\psi^{tb}_{s,1}(\vec{R}) \times \vec{b} \cdot [\nabla + \{\frac{e_s}{T_s}\frac{\partial < \phi^{lw}_1 >}{\partial\Psi} + \frac{m_s}{T_s}(R^2 V^{\xi} + \frac{I}{B}v'_{\|})\frac{\partial V^{\xi}}{\partial\Psi}\}\nabla\Psi]f^{lw}_{s,o} \qquad (1.22) \\
&+ \frac{e_s}{T_s}[(\frac{\partial}{\partial t} + V_o \cdot \nabla)\psi^{tb}_{s,1}(\vec{R})]f^{lw}_{s,o}
\end{aligned}
$$

where $h^{tb}_{s,1}(\vec{R})$ is the non-adiabatic part of the first order fluctuation distribution, defined as, $h^{tb}_{s,1}(\vec{R}) = f^{tb}_{s,1}(\vec{r}) + \frac{e_s}{T_s}(\phi^{tb}_1 - \frac{1}{c}\vec{V}_o \cdot \vec{A}^{tb}_1(\vec{r}))f^{lw}_{s,o}$ with particle position, $\vec{r}(= \vec{R} + \vec{\rho}_s)$. $v'_{\|}$ is the parallel velocity in the moving frame, $v'_{\|} = v'\vec{b}$, with $v' = v - V_o$. V_{ds} is the first order guiding center drift velocity of the long wavelength part. $\psi^{tb}_{s,1}(\vec{R})$ is given as $\psi^{tb}_{s,1}(\vec{R}) =< \phi^{tb}_1(\vec{r}) - \frac{1}{c}\vec{v}\cdot A^{tb}_1(\vec{r}) >$, with the first order fluctuating vector potential, A^{tb}_1. Psi is the poloidal flux, and I is the covariant toroidal component of the magnetic field, $I = RB_t$ with major radius, R. Here, $\vec{R}$ is the position vector of the guiding center, while the scalar quantity, R, denotes major radius. V^{ξ} represents the toroidal angular velocity, defined as, $V^{\xi} = -c\frac{\partial\Phi^{lw}_o}{\partial\Psi}$, with the lowest order long wavelength electrostatic potential, Φ^{lw}_o. Φ^{lw}_1 denotes the first order long wavelength electrostatic potential. $f^{lw}_{s,o}$ is the lowest order long wavelength distribution, which is a Maxwellian distribution.

In Eq. 1.22, the first term on the left hand side indicates the changes in the first order non-adiabatic fluctuating distribution ($h^{tb}_{s,1}(\vec{R})$) with time. The second and third terms indicate the changes in $h^{tb}_{s,1}(\vec{R})$ due to the plasma flow, and parallel motion along the magnetic field, respectively. The fourth term indicates the changes in $h^{tb}_{s,1}(\vec{R})$ due to drift motions including ∇ B drift, curvature drift, Coriolis drift, and the equilibrium (lowest order) $E \times B$ drift. It is noteworthy that the mean plasma flow affects $h^{tb}_{s,1}(\vec{R})$ through the Coriolis drift, and the $E \times B$ shearing effect [26] is included in the equilibrium $E \times B$ drift. The nonlinear interaction between turbulent $E \times B$ drift with $h^{tb}_{s,1}(\vec{R})$ is considered via the fifth term. The last term on the left hand side is a collision term. Since the Fokker-Plank collision operator is used in the gyrokinetic equation, small angle Coulomb scattering events between particles are included with this term. The first term on the right hand side represents the effect of turbulent motion. With some algebra, it can be shown that this term is a function of density and temperature scale lengths of the equilibrium profiles [3], which destabilize the linear turbulence modes introduced in section 1.2.2. This term is therefore responsible for destabilizing turbulence modes with higher gradient scale lengths. Last, the effects of

fluctuating electrostatic potential are included via the second term on the right hand side.

It is noteworthy that we can obtain realistic turbulent transport, which is saturated and self-regulated via non-linear interactions among unstable modes, through this gyrokientic equation. We must note that the gyrokinetic model can vary depending on the purpose of the study or the assumptions used in the study. For example, if we want to ignore the electromagnetic effects, it can be done by neglecting the fluctuating magnetic field in the gyrokinetic equation. We will also have different results if we assume an adiabatic electron response or study the electron response from the drift kinetic equation or the gyrokientic equation. Thus, we should clarify what type of the gyrokinetic model, such as a particle treatment (adiabatic, drift/gyrokinetic) and physics included in the model, is used when we perform gyrokientic analysis.

Although the gyrokinetic model is an approximate kinetic approach, solving the equations in this model is quite challenging due to both numerical issues and the required computing time. The gyrokinetic simulation, which will be introduced in section 3.4, is a numerical tool which can solve the set of equations in the gyrokinetic model. A review of gyrokientic simulation itself can be found in [55]. In this thesis, the gyrokinetic simulation code GYRO is used to analyze the turbulent transport. This code (GYRO) will be introduced in section 3.4.

1.3 Research topics in this thesis

This section will introduce the research topics and define the terms used frequently in this thesis.

1.3.1 Ohmic confinement transition

One of the oldest unsolved problems in Tokamak transport research is the change of confinement regime in Ohmic plasmas. It has been observed in several Tokamaks spanning a wide range of parameters that energy confinement time increases linearly with the average electron density, before saturating above a critical density value [116, 21, 57, 19, 163, 125, 51, 98, 129, 128, 131]. These confinement regimes are referred to as the Linear and Saturated Ohmic Confinement (LOC and SOC) regimes, respectively. An example from Alcator C-Mod is shown in Figure 1-5. One hypothesis that has long been considered is that a

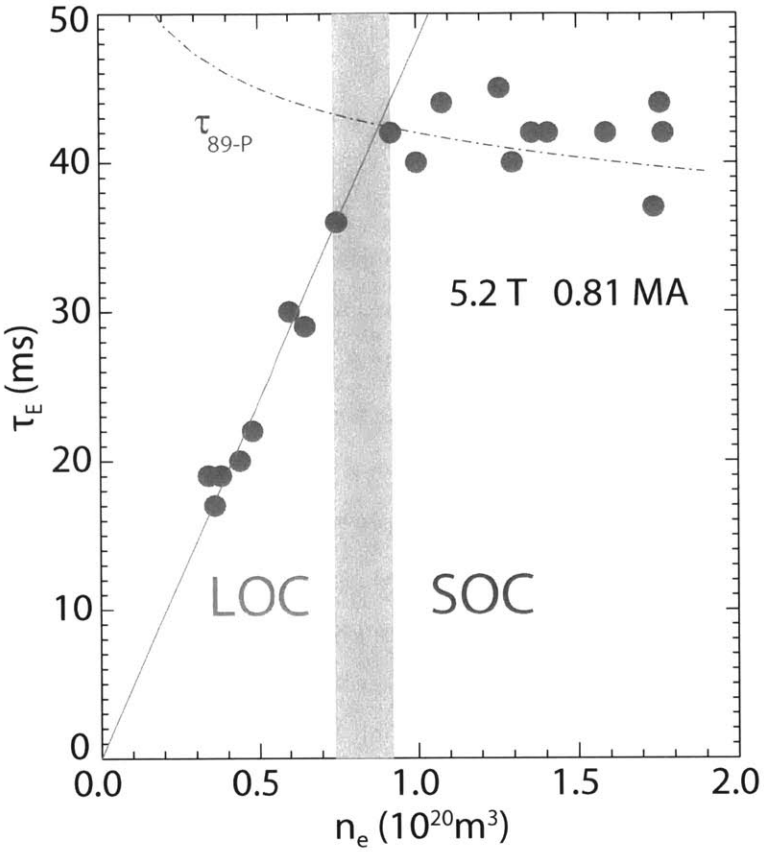

Figure 1-5: An example of the Ohmic confinement transition in Alcator C-Mod discharges ($B_t = 5.2T, I_p = 0.81MA$). The vertical axis is the energy confinement time [ms] and the horizontal axis is the line averaged electron density [$10^{20}m^{-3}$]. The energy confinement time saturates as density increases above shaded transition region. The solid green line is fit to the data in the LOC regime, and the purple dash-dot line is the ITER 89P L-mode scaling. The figure is adapted from J. E. Rice et al, 2012, *Physics of Plasmas*, *19*, 056106, copyright 2014 American Institute of Physics.

change in the dominant type of turbulence, from TEM in the LOC to ITG in the SOC, is related to the change of confinement regime [163, 125, 11].

Numerous investigations of the LOC to SOC transitions have been performed on Tokamaks around the world. In Alcator C, it was observed that the propagation of the density fluctuations measured by CO_2 laser scattering and correlation techniques changed from the electron to the ion diamagnetic direction across the LOC/SOC transition [165]. In ASDEX-U, it was found that density profiles in the LOC regime were flattened when Electron Cyclotron Heating (ECH) is applied, consistent with quasi-linear predictions in TEM dominated plasmas [11]. In FTU, power balance analysis indicates that electron heat dif-

fusivity decreases and ion heat diffusivity increases as density increases in Ohmic plasmas, implying a change of turbulence from TEM to ITG as density increases [51]. In DIII-D, using coherent Thomson scattering, it was observed that there is a sudden increase in line integrated density fluctuations in the low frequency range near the boundary between LOC and SOC. Linear gyrokinetic simulation with adiabatic electrons suggests the observed turbulence in the SOC regime is consistent with ITG modes [125]. Using a similar scattering system, ion mode turbulence in the SOC regime was also observed in TEXT, and found to be also consistent with ITG modes [25]. However, in Tore-Supra, a decrease in the relative density fluctuation level was observed as density increases in Ohmic plasmas. Power balance analysis of these plasmas found that the electron heat diffusivity was reduced as density increases without a significant change in ion heat transport, opposing the hypothesis that the Ohmic confinement regime is linked to a change in ITG/TEM dominance [57]. In Alcator C-Mod, using Phase Contrast Imaging (PCI) [98, 121] ion mode turbulence was observed in the SOC regime, and through gyrokinetic simulations, it was concluded that ITG modes are dominant in the SOC regime in the past. However, in the LOC regime, electron and ion heat diffusivities from experimental profiles were not consistent with the values from nonlinear gyrokinetic simulations [99].

Despite extensive previous work, the cause of the different Ohmic confinement regimes is still not well understood, and experiments aimed at correlating the change in Ohmic confinement regime with changes in measured turbulence have been restricted to line integrated density fluctuations. Local measurements of the turbulence, along with measurements of different fluctuating quantities (e.g. temperature), can help to test the hypothesis that the Ohmic confinement transition is related to changes in the dominant turbulent mode.

1.3.2 Validation study of gyrokinetic simulations

Validation is defined as, "a physical process which attempts to ascertain the extent to which the model used by a code correctly represents reality within some domain of applicability, to some specified level of accuracy" [61]. As implied from its definition, validation is one of the processes performed to test a conceptual model and a code (or computational model) used to implement the conceptual model. Other processes in this testing procedure are qualification and verification [61]. In order to understand a certain phenomenon, we need experiments

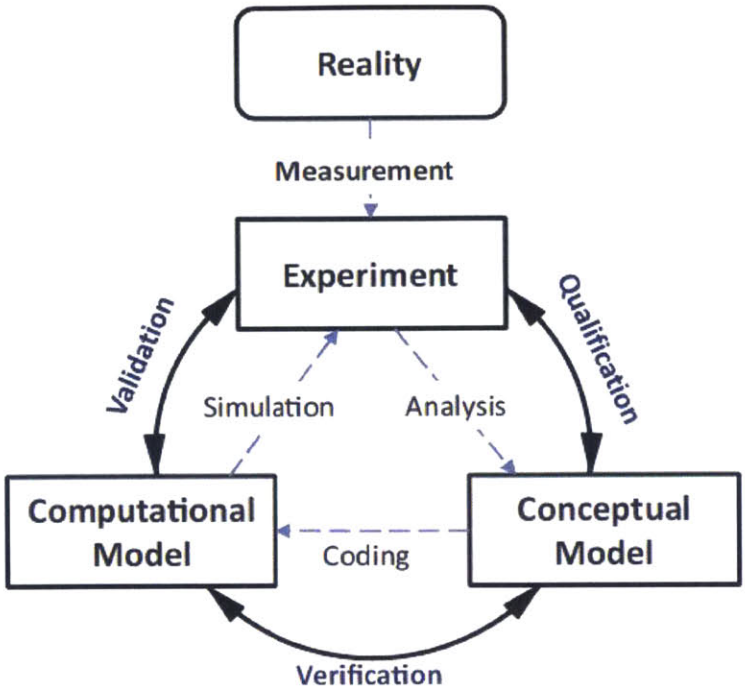

Figure 1-6: The verification and validtion procedure of the model and the relations between models and experiments. This figure is adapted from M. Greenwald, 2010, *Nuclear Fusion*, *17*, 058101, copyright 2014 AIP Publishing.

to quantify this phenomenon and a model, which can show the essential aspects of this phenomenon, to understand this phenomenon and interpret the measurements. To use a certain model, we first need to determine whether or not the existing model is applicable for the phenomenon of interest. This activity is called as "Qualification." The computational model (code) will be built based on the qualified model. The activity to test whether or not the code implements the conceptual model correctly refers to "verification." Once the code is verified, we should then validate this model. That is, we must see whether the conceptual model has enough physics to describe the essential part of the phenomenon in which we are interested. If the validation activity is done successfully, we will then have a proper model, which can describe a certain phenomenon that we want to study, and the simulation based on this model can be used to predict the changes in this phenomenon inside or outside the validated domain with the estimated error obtained from the validation process. Figure 1-6 shows these processes. As mentioned in [61], these processes can be cyclic with improvements in both experiments and models until the model is validated. Details on the standard procedure of verification and validation activities can be found in [61, 156].

The validation procedure explained in the last paragraph can be applied in fusion transport research. In section 1.2, anomalous transport in fusion plasmas is introduced. Although it is believed that drift wave instabilities are the main reason for this anomalous transport, it is difficult to tell whether or not the transport in fusion plasmas is sufficiently understood to predict the performance of future device unless we have a prediction tool based on first principle of fusion plasma transport. This prediction tool will be essential in the design of a fusion power reactor in the future. The gyrokinetic model introduced in section 1.2.3 has been thought to have enough physics to describe turbulent transport. Thus, the gyrokeintic model is a conceptual model for the turbulent transport in fusion plasmas. As explained in section 1.2.3, this model already considered the spatio-temporal scales of turbulent transport, implying that this model is quantified. The gyrokinetic simulation will be the computational model for the gyrokinetc model. The verification activity of the gyrokinetic simulations was performed successfully by cross-comparing different gyrokinetic simulation codes [45, 28, 29, 109].

However, the validation study of gyrokinetic simulations is quite challenging. In DIII-D, the electron and ion heat fluxes and fluctuations simulated by the gyrokinetic simulation codes, GYRO [28] and GEM [33], are much smaller than the experimental levels in the region where normalized radius, $\rho \gtrsim 0.7$, in NBI heated L-mode discharges, while these quantities are matched with the experimental levels within the uncertainties in $\rho \lesssim 0.7$ [73, 72, 126]. The under-prediction of heat fluxes and turbulent fluctuations outside the $\rho \sim 0.7$ region by the gyrokinetic simulations is called "shortfall." In C-Mod, a validation study using GYRO was performed in Ohmic and RF heated L-mode discharges inside $r/a < 0.8$. In the Ohmic discharges, GYRO simulations including only ion scale electrostatic turbulence over-predict the ion heat diffusivity and under-predict the electron heat diffusivity in the linear Ohmic confinement (LOC) regime. Nonetheless, the line-integrated electron density fluctuations measured by Phase Contrast Imaging(PCI) agreed with the synthetic fluctuations. The synthetic fluctuations are the post-processed quantities obtained from the simulation to consider to the experimental condition. The discrepancy in the core heat transport is still being investigated. In RF heated L-mode discharges, it was found that the GYRO simulations including only ion scale electrostatic turbulence can reproduce the experimental levels of electron and ion heat fluxes in $r/a < 0.8$ when TEM activity is significant. However, the electron flux is under-predicted in the GYRO simulations when

the TEM activity is small [78]. From these results, we notice that there is no "shortfall" in C-Mod. In this thesis, validation study of GYRO including electrostatic ion scale turbulence will be performed for C-Mod Ohmic discharges near the edge (r/a~0.85) by comparing the simulated heat fluxes and the synthetic T_e fluctuations with the measurements.

1.3.3 Intrinsic toroidal rotation in Tokamak plasmas

Plasma rotation is important in plasma stability and transport. A high rotation can be used to suppress the resistive wall mode (RWM) [183], one of the large scale MHD instabilities that should be avoided for plasma operation. It is also known that a moderate rotation shear ($E \times B$ shear) can reduce turbulent transport levels [26]. External momentum input using neutral beam injection causes plasma rotation in most existing Tokamak experiments. The plasma also rotates toroidally without any external momentum inputs, a phenomenon called intrinsic toroidal rotation. Intrinsic rotation has been observed in several Tokamak experiments ([133] and references therein). It is expected that the intrinsic toroidal rotation will provide a significant amount of toroidal momentum in future generations of Tokamaks, which can be used to suppress RWM. Since it will be hard to provide the external momentum in large scale high performance Tokamaks in the future due to their high density levels, intrinsic rotation is a very important research topic.

Changes in intrinsic rotation are also correlated with changes in plasma transport, such as the transition from low to high confinement regime [134, 133, 132], the Ohmic confinement transition [129], and stiffness [101]. High confinement regime and stiffness will be introduced in the following section. As mentioned in section 1.1.3, there is no external momentum input in Alcator C-Mod Tokamak. Thus, all observed rotation in C-Mod is self-generated by the plasma. The origin of this self-generated flow is still unknown, and study its origin is not in the scope of this thesis. Nevertheless, we will investigate more deeply the correlation between changes in the intrinsic rotation and transport relevant quantities in this thesis.

1.3.4 Self-similarity analysis and profile stiffness

Understanding transport phenomena and improved confinement of energy in fusion plasmas is important for the development of fusion energy. The shape and height of density and temperature profiles indicate the quality of confinement and transport in the plasmas. We

must therefore investigate the change in the shape and height of profiles, if any, with different discharge conditions. In this context, the so-called "stiffness" property has been studied, along with the related critical gradient model ([56, 105] and references therein).

As pointed out in [56], the definition of "stiffness" is ambiguous. It sometimes refers to the resistance of the change in profile shape with external heating [56, 105, 142], while the degree of stiffness (or even stiffness itself) is defined as the ratio of diffusivity (or heat flux) to the difference between the temperature gradient scale length and its critical gradient scale length [56, 39, 38], or the change of diffusivity of heat pulses compared to the value from power balance in power modulation experiments [139, 100]. In other words, stiffness refers to a global change in some cases, while it refers to a local change in other cases. Following critical gradient arguments, if the gradients of a profile are near the critical gradient value in the region where a profile keeps its shape, then the profile in this region will be stiff and keep its gradient scale length even with a change in input heating power. In this case, the stiffness used for a local change will be connected to a global change. However, the similar shape of profiles with different discharge conditions is not a necessary condition for this assumption, but it is a sufficient condition. It is also noteworthy that the property of keeping the shape of profiles with changes in experimental conditions is also referred to with several different terms such as self-similarity [63, 62], profile consistency [41], profile resilience [137, 138] and profile stiffness [56, 142, 105]. In order to prevent any confusion arising from different terms, "self-similarity" will be used to refer to "the similar shape of core profiles with different discharge conditions" in this thesis and using the term "stiffness" will be avoided. We quantify the self-similarity of n_e and T_e profiles and explore the correlation between the changes in the shape of profiles and the transport phenomena in which we are interested, such as the Ohmic confinement transition, core rotation reversal, and the transition from low to high confinement regime.

1.3.5 I-mode and H-mode : high confinement regimes

It was found in the 1980's that the energy confinement time can be improved almost a factor of two by increasing the external heating power above a certain threshold value in the ASDEX Tokamak [162]. This improved confinement regime is called the high confinement regime (H-mode) and the regime before confinement is improved is called the low confinement

regime (L-mode). After H-mode was discovered in ASDEX, H-mode was obtained universally in most fusion experiments using toroidal plasmas including C-Mod ([161] and reference therein). The threshold power for H-mode depends on several discharge conditions such as wall condition, density, and equilibrium configuration [161, 147]. For example, in single null plasmas, the magnetic configuration which has ion ∇B drift motion toward the active X-point has lower threshold power than the opposite magnetic configuration with ion ∇B drift away from the X-point, with the former configuration known as a "favorable" configuration [147, 180]. H-mode reduces not only energy transport, but also transport of particles, including impurities, and momentum, simultaneously [161].

The most evident change in H-mode plasmas compared to L-mode plasmas is the formation of a pedestal in the edge radial pressure profiles. In Fig. 1-7, the change in the electron density and temperature profiles in H-mode compared to L-mode is shown, which is the high edge gradient in the H-mode profiles. This steep-gradient region is called the pedestal. In H-mode, both density and temperature profiles have a pedestal structure, which indicates that H-mode is a high particle confinement regime as well as a high energy confinement regime. The self-generated poloidal flow (zonal flow) is thought to be responsible for the pedestal formation and the L/H transition [91]. It is noteworthy that the increase in external heating is not the only way to access H-mode. H-mode can be achieved in Ohmic heated discharges as well by applying high Ohmic power with low density and magnetic field [114, 148] or by applying external electric field [155]. Although H-mode has been considered as the operating regime for a future fusion reactor, there are several problems that should be solved or improved. These problems include high particle confinement, which is unnecessary and undesirable, and the edge localized mode (ELM), the burst of heat and particles at the edge of the plasma due to MHD instability, and an unfavorable scaling of energy confinement time with external heating power [180]. These issues motivated the search for an alternative high confinement regime.

In C-Mod, a new high confinement regime, which is favorable for future devices, has been found. This regime is called I-mode. I-mode is a steady state high energy confinement regime with H-mode energy confinement and L-mode particle confinement [180]. As shown in Fig. 1-7, I-mode has a pedestal in the temperature profile, not in the density profile. I-mode has desirable characteristics as an operating regime in ITER and future devices. For fusion energy production, high energy confinement is required, but high particle con-

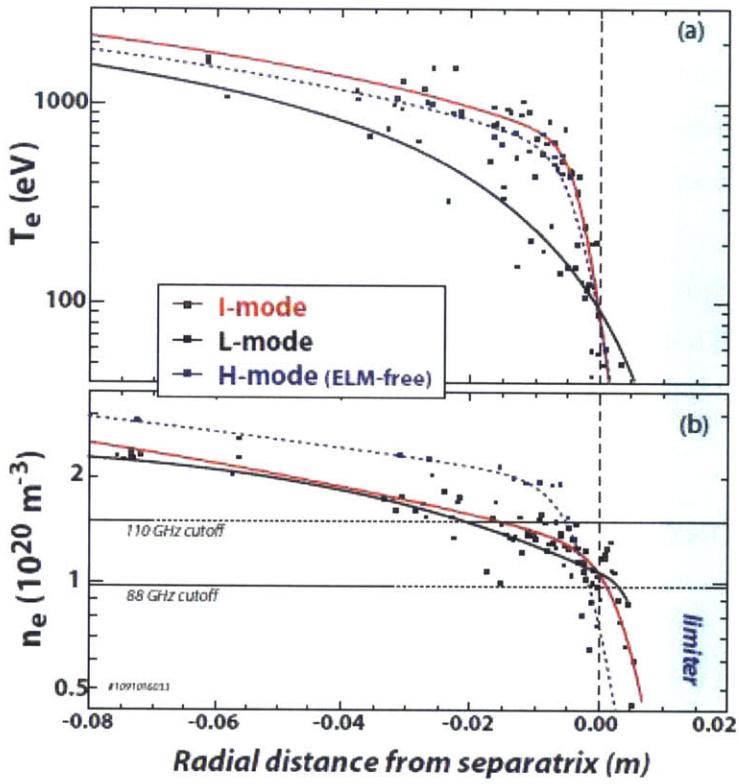

Figure 1-7: Examples of the edge (a) electron temperature and (b) electron density profiles with different confinement regimes; L-mode, I-mode and H-mode. This figure is adapted from D. G. Whyte et al, 2010, *Nuclear Fusion*, *50*, 105005, copyright 2014 IOP Publishing.

finement is undesirable in high performance plasmas (burning plasmas) due to helium ash accumulation[180]. I-mode has only a thermal transport barrier, without a particle transport barrier. Large ELMs are also naturally suppressed in the I-mode plasmas, which makes I-mode a good candidate for burning plasmas in the future. I-mode also has little degradation of energy confinement with input heating power, while H-mode has a relatively strong degradation in energy confinement with input heating power ($\tau_E \propto P_{in}^{-0.7}$) [180].

Here, however, we are interested in studying the natural separation of energy and particle transport in I-mode from a basic physics perspective, and the correlation between turbulence and the confinement transition. Although the most evident change in the transition from low to high confinement regimes is observed in the edge region (edge pedestal), previous studies show a correlation between core turbulence and the transition from low to high confinement regimes [146, 173]. This thesis will investigate the correlation between the changes in turbulence and confinement regime. We will compare the changes in local T_e fluctuations, simulated turbulence, and the self-similarity property across the transition from L-mode to I-mode and L-mode to H-mode.

1.4 Summary of physics results in the thesis

This thesis studies anomalous heat transport in the Alcator C-Mod Tokamak through new T_e fluctuation measurements, profile analysis including self-similarity analysis, experimental power balance transport analysis, and linear and nonlinear gyrokinetic analysis. To be specific, we investigate the physics of important topics in fusion transport research, such as the Ohmic confinement transition, intrinsic rotation reversal, and the transition from low to high confinement regimes, via these four analysis methods.

We will first introduce a new Correlation Electron Cyclotron Emission (CECE) diagnostic in C-Mod built for this thesis, which can measure small amplitude ($\sim 1\%$) T_e fluctuations in the core region. The CECE diagnostic was designed and built in C-Mod to study turbulent transport behavior in C-Mod plasmas [154, 79]. This thesis will show core T_e fluctuation measurements ($0.7<r/a<0.96$) in C-Mod, and the correlation of these measurements with the transport phenomena studied in this thesis. This thesis presents the first core T_e fluctuation measurements in C-Mod, and can prove the existence of measurable core T_e fluctuations in C-Mod plasmas, which was an open question after a past trial showing

no T_e fluctuations above the background noise level [168]. The correlation of T_e fluctuations with macroscopic transport phenomena also suggests that the measured T_e fluctuations are induced by drift wave instabilities, thought to be responsible for anomalous transport behavior in fusion plasmas. It is also noteworthy that the self-similarity property of radial pressure profiles in C-Mod was quantified by adopting the analysis technique applied in the TCV Tokamak [142]. Although profile self-similarity was observed in C-Mod plasmas in the past [63], this study provides the first quantitative information about profile self-similarity in C-Mod plasmas [151].

As explained in section 1.3.1, the Ohmic confinement transition (LOC/SOC transition) remains an old mystery in fusion transport research. The predominant hypothesis for this transition is that the dominant turbulence mode change from TEM to ITG is responsible for the Ohmic confinement transition. We found that T_e fluctuations near the edge region (r/a$\sim$0.85) tend to decrease across the LOC/SOC transition in C-Mod plasmas [153], which is the first local T_e fluctuation measurements in LOC and SOC plasmas, and superficially indicates changes in TEM activity across the LOC/SOC transition. Self-similarity analysis shows the core radial pressure profiles keep a similar shape across the LOC/SOC transition, but that the edge profile shape changes are correlated with the transition [142, 151]. However, both linear and non-linear gyrokinetic analysis show no dominant mode change across the LOC/SOC transition, inconsistent with this hypothesis. All these results indicate that the hypothesis about the LOC/SOC transition should be revised. First, the results from T_e fluctuation measurements and self-similarity analysis indicate that the changes in the edge region are related to the Ohmic confinement transition. Instead of the crude statement about the dominant mode change across the transition, we should investigate which radial region is responsible for the LOC/SOC transition. Gyrokinetic analysis results suggest no simple linear mode transition across the transition. A more realistic picture including non-linear interaction of turbulence modes should be considered to understand the LOC/SOC transition physics.

The validation study of the gyrokinetic model that considers electrostatic ion-scale turbulence (using GYRO) was performed near the edge region (r/a$\sim$0.85) in the C-Mod Ohmic discharges. Previous validation work at C-Mod was performed only in $r/a \leq 0.8$ region [99, 78]. This study is therefore the first attempt to validate the gyrokinetic model outside of the r/a=0.8 region at C-Mod. We found that GYRO can reproduce the experimental ion

heat flux and the measured T_e fluctuations and their spectral shapes within the uncertainty of input parameters. However, the simulated electron heat flux was underestimated compared to the experimental level. Matching T_e fluctuations which come from the ion scale turbulence with the underestimation of electron heat flux, which will come from both ion and electron scale turbulence, suggests that the contribution of electron scale turbulence (ETG) is a strong candidate for this disagreement. However, further study is required in the future. The validation study results also imply that electron scale turbulence may be important in C-Mod Ohmic discharges and the LOC/SOC transition, which is not considered in the traditional hypothesis for the LOC/SOC transition.

As mentioned in section 1.3.3, intrinsic rotation reversals are correlated with the LOC/SOC transition, which may suggest a correlation between the changes in T_e fluctuations at r/a$\sim$0.85 and the intrinsic rotation reversal in the core region. A reduction of T_e fluctuations near the edge (r/a$\sim$0.85) was found between two RF heated discharges rotating in opposite directions with different average density levels ($\sim$ 50% difference) [175, 152]. However, no changes outside the uncertainty in T_e fluctuations were found in the rotation reversal discharge, in which rotation reversal occurs with smaller changes in the average electron density ($<$ 5%). A similar trend is also observed in the self-similarity analysis. This analysis shows changes in edge profile shape between two RF heated discharges with rotation reversals due to large difference in the average density ($\sim$ 50%), while no significant changes across rotation reversal were found in the rotation reversal discharge where rotation is reversed with smaller changes in the average density ($<$ 5%) [151]. Gyrokinetic analysis results also indicate no linear mode transition (ITG/TEM transition) across the rotation reversal [175]. From these results, we first notice that T_e fluctuations are not directly correlated with the rotation reversal. T_e fluctuations will be linked to the changes in the density level or the gradient scale length values associated with different density levels. We also obtained a similar trend in the RF heated discharges which have different density levels from T_e fluctuation measurements, gyrokinetic analysis and self-similarity analysis. This may indicate that the same physics, which is responsible for the LOC/SOC transition and rotation reversals in Ohmic plasmas, can be applied to the RF heated discharges.

We also investigate the changes associated with the transition from low to high confinement regimes such as I-mode and H-mode. It is found that T_e fluctuations are reduced across the transition from L-mode to I-mode [173]. We show that this reduction is correlated

with the confinement regime, not the changes in the external heating power used to induce the L/I transition [152]. These measurement results are consistent with the previous study in the DIII-D Tokamak [146]. However, the estimated $E \times B$ shearing rate is similar across the L/I transition, and we found no significant changes in the dominant turbulence mode obtained from linear stability analysis across the L/I transition. Nonlinear gyrokinetic analysis suggests changes in $E \times B$ shear and stiffness across the L-mode to I-mode transition [172].

Self-similarity analysis shows that the changes in the edge radial pressure profiles associated with the pedestal are correlated with the improvement in energy/particle confinement. It is also found that the pedestal region can be fit by a linear fit as well as the modified tanh fit [65], usually applied to the pedestal region. This new finding can be used to improve the pedestal modeling in the future. For the core profiles, we notice that the shape of the core electron temperature profiles remains similar across L/I/H transition, but the core density profile tends to be flatter in H-mode as compared to L- and I-modes. We also observe that the self-similar region, where a similar profile shape is maintained and the exponential fit is valid, is extended in T_e profiles in the high energy confinement regime (I- and H-modes) [151]. Thus, we identify the changes that are correlated with the transition from low to high confinement regime, the reduction of T_e fluctuations and changes in profile self-similarity in this study. In the future, we must investigate the relations among the changes in turbulence (T_e fluctuations), profile self-similarity, and the low to high confinement transition.

1.5 Thesis outline

There are seven chapters and eleven appendices in this thesis.

Chapter 1 gives background information about fusion transport research. The terms that will be used in this thesis are also defined in this chapter. A summary of physics results in this study and outline are provided in this chapter as well.

Chapter 2 explains the Correlation Electron Cyclotron Emission (CECE) diagnostic in C-Mod. A brief introduction of the ECE and CECE diagnostics is first provided. We then explain the CECE diagnostic in C-Mod from its design process to the specification in the hardware. The laboratory test performed for the CECE diagnostic is also described in this chapter.

Chapter 3 introduces the analysis methods used in this study. Four related analysis methods are applied. They are CECE signal analysis, profile analysis, experimental transport analysis, and gyrokinetic analysis. Each analysis method is described in a sub-section of this chapter.

Chapter 4 presents the results for the Ohmic confinement transition. This chapter will provide new information about the changes in T_e fluctuations near the edge across the Ohmic confinement transition, and will prove that the old picture of the Ohmic confinement transition is not valid and thus should be revised.

Chapter 5 studies the correlation between turbulent transport and core rotation reversal. We will show similarities between the analysis results found in the Ohmic discharges with the rotation reversals in Chapter 4 and the findings from RF heated discharges that rotate in opposite directions. The results in this chapter suggest that Ohmic confinement transition physics is not limited to the Ohmic discharges, and can be expanded into RF heated discharges as well.

Chapter 6 studies the changes in turbulence across the low to high confinement regime transition. We will show the correlation of T_e fluctuations and the shape of radial pressure profiles with the confinement regime.

Chapter 7 contains the summary and conclusions of this thesis and future work.

Appendix A describes the procedure for the in-vessel mirror alignment for the CECE diagnostic.

Appendix B explains the noise issues in the CECE measurements.

Appendix C introduces the Y-factor method used to estimate the system temperature of the CECE receiver.

Appendix D explains how the calibration factor of the CECE diagnostic is estimated in the laboratory.

Appendix E shows the derivation of the T_e fluctuation levels from the CECE measurements.

Appendix F describes the details of the profile analysis performed to prepare GYRO input profiles for C-Mod Ohmic discharges.

Appendix G shows the importance of non-adiabatic electron response in T_e fluctuations.

Appendix H describes error analysis for experimental heat flux values obtained from TRANSP.

Appendix I describes the details of analyses performed to obtain a GYRO base run for C-Mod Ohmic discharges and error analysis for synthetic T_e fluctuation levels, rotation relevant parameters (rotation frequency, $E \times B$ shearing rate), and collision frequency used in GYRO.

Appendix J shows the global gyrokinetic simulation results for C-Mod Ohmic discharges near the edge.

Appendix K provides a list of C-Mod discharges and a list of analysis codes used in this thesis.

Chapter 2

Correlation Electron Cyclotron Emission (CECE) diagnostic in Alcator C-Mod

In order to measure turbulent T_e fluctuations, a new Correlation Electron Cyclotron Emission (CECE) diagnostic was designed and constructed in C-Mod as a part of this thesis work. This chapter will introduce a CECE diagnostic and describe the CECE diagnostic in C-Mod. We first need to understand Electron Cyclotron Emission (ECE) diagnostics is to understand CECE diagnostic. As will be explained in section **??**, ECE diagnostics have been commonly used to measure electron temperature (T_e) in fusion plasmas. It is natural to consider using an ECE diagnostic to measure electron temperature fluctuations and to study the turbulent transport in fusion plasmas, discussed in section 1.2. However, an ECE diagnostic is limited in its ability to measure small amplitude ($\sim$ 1%) electron temperature fluctuations, and a cross correlation technique is required to resolve electron temperature fluctuations from ECE signals. The CECE diagnostic is an ECE radiometer which is modified for electron temperature fluctuation measurements through the cross correlation technique. In Alcator C-Mod, the CECE diagnostic was designed and installed in the 2012 campaign. In this chapter, we first briefly review the principle of ECE and its limitations as a fluctuation diagnostic. More details about ECE diagnostic can be found in [15, 18, 85]. Then, Correlation ECE (CECE) will be introduced, and details of the CECE diagnostic in C-Mod will be explained.

2.1 Principle of CECE

2.1.1 ECE diagnostic

A ECE diagnostic uses Electron Cyclotron (EC) radiation emitted due to the gyromotion of a electron in fusion plasmas using the magnetic confinement. If the relativistic effect is ignored, electrons in an external magnetic field will rotate along the magnetic field with the cyclotron frequency, ω_{ce}, defined as,

$$\omega_{ce} = \frac{eB}{m_e} \tag{2.1}$$

where e is the elementary charge, B is the total magnetic field, and m_e is the mass of the electron. In addition, the cyclic cyclotron frequency, f_{ce}, is $\omega_{ce}/2\pi$.

The electromagnetic radiation emitted by the rotating charged particles along the magnetic field is called the cyclotron radiation. For electrons, it is electron cyclotron (EC) radiation. The frequencies of the EC radiation are ω_{ce} and its harmonics, $n\omega_{ce}$ with harmonic number, n. Thus, the electrons in a plasma with an external magnetic field, such as tokamak plasmas, emit EC radiation. If the emission layer of the cyclotron radiation (or the cyclotron resonance layer) is optically thick for this radiation, this radiation will be absorbed by the emission layer. In other words, an optically thick emission (or resonance) layer will act like a black body, and this absorbed radiation and the particles will be in the local thermal equilibrium. Thus, the intensity of the radiation emitted in this layer with the same frequency as the absorbed cyclotron radiation is determined by the local particle temperature. The intensity of the emitted radiation is given as the intensity of the black body radiation with frequency, f, $B(f)$, is given by[119, 15],

$$B(f) = \frac{f^2}{c^2}\frac{hf}{e^{hf/T}-1} \simeq \frac{f^2 T}{c^2}\ [W/m^2/sr/Hz] \tag{2.2}$$

where c is the speed of light, h is Planck's constant, and T is the temperature of the medium in terms of energy units such as joules [J] or electron volts [eV]. The approximation used in $B(f) \simeq \frac{f^2 T}{c^2}$ is called the Rayleigh-Jeans approximation, which is valid when $hf << kT$. This approximaion is valid in most fusion plasmas since $hf \lesssim 1$meV, while $T > 1$eV in most fusion plasmas.

It is noteworthy that the intensity of the black body radiation is proportional to the

temperature in Eq. 2.2. This indicates that once the plasma is optically thick for the EC radiation, we can measure the temperature of medium, the perpendicular temperature of electrons for the EC radiation, by measuring the intensity of the EC radiation. This measurement is useful in magnetic confined plasmas in which the toroidal magnetic field is dominant such as tokamak. This is because the toroidal magnetic field is well defined with the major radius, R, as follows.

$$B_t(R) = \frac{B_o R_o}{R} \tag{2.3}$$

where, B_o is the magnetic field on axis, R=R_o.

Since the frequency of EC radiation is defined as the magnitude of the magnetic field as given by Eq. 2.1, the emission position of the EC radiation with a certain frequency, f, is well defined in terms of major radius, R, in tokamak plasmas.

In order to use EC radiation for the diagnostic (ECE), we first need to determine whether or not the plasma is optically thick for the EC radiation with frequency, f. In the tenuous plasma limit, we can derive the equation for the intensity of the EC radiation with its frequency, f_o, and the well defined emission position, s_o. Using Kirchoff's law and the radiation transport equation in the slab geometry, the intensitiy of the EC radiation, I, can be derived as given by [85],

$$I(f_o) = \frac{f_o^2 T_e(s_o)}{c^2}(1 - e^{-\tau}) \tag{2.4}$$

where optical depth, τ(s), is defined as,

$$\tau \equiv \int^s \alpha \, \mathrm{d}s \tag{2.5}$$

with absorption coefficient $[m^{-1}]$, α, defined as $\frac{1}{I}\frac{dI}{ds}$, and path of the radiation in the slab geometry, s.

As shown in Eq. 2.4, optical depth, τ, is the parameter used to determine whether or not the plasma is optically thick. Only if τ is enough to approximate $1 - e^{-\tau} \simeq 1$, we can obtain the tempeature from the measured intensity of EC radiation. Thus, higher τ values are desirable, and $\tau > 2$ is a sufficient condition, and $\tau > 1$ is a somewhat marginal condition, that we can use EC radiation for electron temperature measurements [15, 166]. It is noteworthy that electron temperature fluctuation measurements require higher τ value than the temperature measurements. This is because τ is the function of electron density and

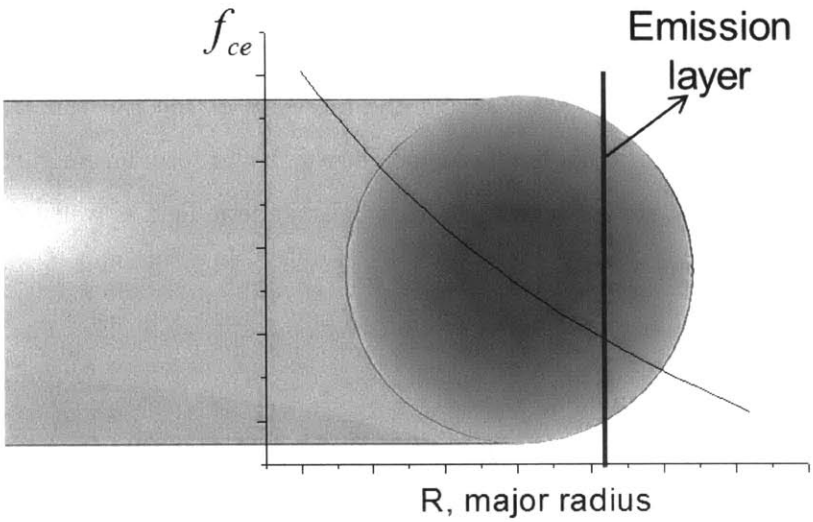

Figure 2-1: Example of electron cyclotron frequency in the tokamak plasma. The emission layer of the EC radiation with a certain f_{ce} is well defined with major radius, R.

temperature, and the fluctuations in the electron density can contribute to the fluctuations in the measured intensity of the EC radiation in Eq. 2.4. More details will be discussed in section 3.1. Assuming a Maxwellian distribution in the electron velocity perpendicular to magnetic field, we can calculate the values of optical depth, τ, and absorption coefficient, α, for EC radiations with different harmonics (n=1,2,3...) and polarizations (ordinary mode, O-mode (polarization parallel to the external magnetic field) and extraordinary mode, X-mode (polarization parallel to the external magnetic field)). The formulas for these parameters can be found in [18, 85]. In tokamak plasmas, fundamental O- and X-modes and second harmonic X-modes are usually optically thick in most regions except for the edge region. However, due to the accessibility of EC radiation from the measurement position, fundamental O-mode or second harmonic X-mode is commonly used for the ECE diagnostic.

The ECE diagnostic is one of the most useful diagnostics in fusion plasma experiments. This is because we can measure the electron temperature profile from the well defined emission layer of EC radiation as shown in Fig. 2-1. In addition, ECE is a passive diagnostic, which means that we do nothing actively to the plasma to know the plasma status. All we need to do is to detect the EC radiation emitted from the plasma. However, ECE has two limitations as a diagnostic. First, ECE can measure electron temperature only if the plasma

is in thermal equilibrium or has a Maxwellian distribution. Thus, if the plasma has non-thermal electrons due to external RF wave launching (lower hybrid or EC wave) or other reasons, it is difficult to measure the correct electron temperature from ECE. Second, it is hard to measure the turbulent electron temperature fluctuations from the ECE diagnostic. As will be explained in the next section, the heterodyne radiometer is the appropriate ECE measurement technique for fluctuation measurements (Details about each ECE measurement techniques is out of the scope, and review about various ECE measurements techniques can be found in [80]). However, the ECE radiometer has a limitation in the turbulent electron fluctuation measurements because of thermal noise in the ECE signal. It is known that the expected thermal noise level ($> 1\%$) in the signal measured by the ECE radiometers is higher than the real electron temperature fluctuation level ($\sim 1\%$ in the core region). Thus, we cannot resolve electron temperature fluctuations directly from the ECE radiometer. In the next section, the limitation of the ECE radiometer as a fluctuation diagnostic will be further discussed.

2.1.2 Correlation ECE

Radiometer

A heterodyne radiometer is used for the CECE diagnostic in C-Mod. Thus, it is required to introduce a heterodyne radiometer first to describe the CECE diagnostic in C-Mod. A radiometer is an instrument that measures the power of radiation in a well-defined frequency range. The ECE diagnostic detects the power of the EC radiation in a certain frequency range to measure the electron tempeature in a certain region in space. Thus, a radiometer is the proper survey instrument for the ECE diagnostic, and the heterodyne radiometer is widely used for the ECE diagnostic because of its good spectral and temporal resolutions [80]. The main components of the heterodyne radiometer are shown in Fig. 2-2. First, the radiation emitted from a certain object will be received by the antenna. In the heterodyne detector, the EC radiation from the plasma, which is a millimeter wave, is down-shifted to intermediate frequency (IF) signals ($f \lesssim$20GHz) by a mixer and a local oscillator. The frequency range of the measured EC radiation is determined from the band pass filter with bandwidth, B_{IF}. In other words, the radiation outside the frequency range we want to detect will be filtered out. The power of the radiation measured by the single-mode antenna

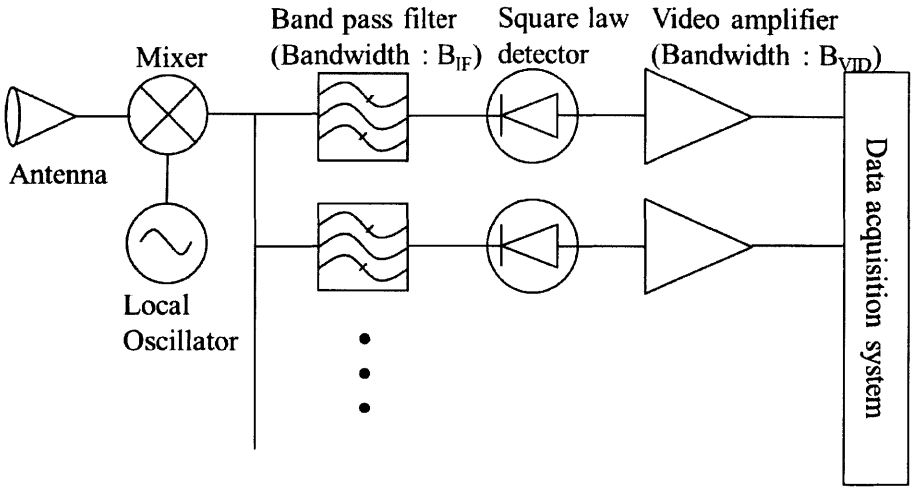

Figure 2-2: The block diagram of the main components of the heterodyne radiometer.

in the radiometer, $\bar{P}$ [W], with IF bandiwidth,B_{IF}=B is given by [111, 44, 36]

$$\bar{P} = TB \tag{2.6}$$

where T is the temperature of the medium in units of energy. For the ECE radiometer, T will be the electron temperature, T_e, if the plasma is optically thick. Thus, the detected power by radiometer is independent of the frequency, f. One may think that this contradicts Eq. 2.2, which shows that the blackbody intensity is proportional to f^2. The average effective cross section of the antenna is proportional to $1/f^2$ as shown in [94]. Since the detected power is proportional to the product of the intensity of the radiation and the cross section of the antenna, the frequency dependency will be cancelled out, then the detected power will be independent of the frequency as shown in Eq. 2.6.

Then, the power of this radiation is measured by a square-law detector whose output voltage is proportional to the square of the amplitude of the input signal, that is, the power of the input signal. The output of the square-law detector is smoothed by an integrator. This process can be also considered as low pass filtering. In the ECE radiometer, the video amplifier with its bandwidth, B_{vid}, is used to smooth the signal as an integrator as well as to amplify the signal. Then, the voltage of the smoothed signal will be measured and stored by the data acquisition system. More details about radiometers and the heterodyne detection can be found in [15] and [67].

The sensitivity of the ECE radiometer

The limitation of the ECE radiometer as a fluctuation diagnostic comes from its sensitivity limit. The sensitivity limit of the ECE radiometer, that is, the lowest temperature that the ECE radiometer can measure, is determined by the background noise level from the system noise temperature and the thermal (or statistical) noise level. In most fusion experiments, the background noise temperature ($\lesssim$10eV) is not a barrier to the electron temperature ($\geq$100eV) measurements. The root mean square (RMS) fluctuation level of thermal noise is determined by the radiometer formula, which is given by[15, 166],

$$\frac{\tilde{T}_{RMS}}{\bar{T}} = \sqrt{\frac{2B_{vid}}{B_{IF}}} \tag{2.7}$$

The thermal noise level given by Eq. 2.7 is less than 10% in most experiments, and the sensitivity of the ECE radiometer will be sufficient to measure the electron temperature. However, this thermal noise level limits the fluctuation measurements by the ECE radiometer since the thermal noise level given by Eq. 2.7 in the typical ECE radiometer exceeds the small amplitude turbulent fluctuation level ($\sim$ 1%). For example, the thermal noise level of the ECE heterodyne radiometer in Alcator C-Mod (FRCECE) is about 4% with B_{IF}=1.5GHz and B_{vid}=1MHz[31]. Thus, it is not possible to measure the turbulent fluctuations directly from a single ECE channel in the typical ECE measurements. We may increase the sensitivity by decreasing B_{vid} or increasing B_{IF}. However, decreasing B_{vid} will be limited by the required temporal resolution and increasing B_{IF} will be limited by the required radial resolution for the fluctuation measurements. More details will be mentioned in Section 2.2

Cross correlation technique to resolve T_e fluctuations

In order to measure electron temperature fluctuations in the presence of thermal noise, we use a Correlation ECE (CECE). CECE is a diagnostic technique used to extract small amplitude electron temperature fluctuations through standard cross-correlation analysis methods by removing incoherent thermal noise in the ECE radiometer. Let us suppose that the fluctuating parts of two ECE signals ($\tilde{T}_{e,1,2}$) have the incoherent thermal noise ($N_{1,2}$) and

common turbulent temperature fluctuations ($\tilde{T}_e$).

$$\tilde{T}_{e,1} = N_1 + \tilde{T}_e \tag{2.8}$$

$$\tilde{T}_{e,2} = N_2 + \tilde{T}_e \tag{2.9}$$

Then, cross-correlating two signals will be done as follows.

$$R_{1,2} =< \tilde{T}_{e,1}\tilde{T}_{e,2} >=< N_1N_2 > + < N_1\tilde{T}_e > + < N_2\tilde{T}_e > + < \tilde{T}_e^2 > \tag{2.10}$$

Assuming that the thermal noise for each signal is not correlated and the physical electron temperature fluctuations are not correlated to this thermal noise, then averaging the cross-correlating for enough time will give $< N_1N_2 > \simeq < N_1\tilde{T}_e > \simeq < N_2\tilde{T}_e > \simeq 0$, and only physical electron temperature fluctuations will remain.

$$R_{1,2} \simeq < \tilde{T}_e^2 > \tag{2.11}$$

Consequently, the sensitivity of the fluctuation measurement through cross correlation analysis is given as follows,

$$\frac{\tilde{T}_{RMS}}{\bar{T}} \geq \sqrt{\frac{1}{N^{1/2}}\frac{2B_{vid}}{B_{IF}}} \tag{2.12}$$

where N is the number of independent samples used in the correlation, given by N=$2B_{vid}\Delta$t, and Δt is the time used to correlate two signals. When Δt is 0.5 sec with B_{IF}=1.5GHz and B_{vid}=1MHz, the sensitivity level from Eq. 2.12 is about 0.1%. Then the sensitivity is enough to measure the small amplitude ($\sim$ 1%) turbulent fluctuations.

Required conditions for T_e fluctuation measurements through correlation analysis

From Eq. 2.8-2.11, we find three conditions required to resolve electron temperature fluctuations through the cross correlation technique. First, there should not be any coherent noise whose level is comparable to the electron temperature fluctuations. In Eq. 2.8-2.11, no coherent noise was assumed. Since the coherent noise cannot be removed by cross-correlating two signals, it should be minimized and be negligible compared to the real electron temperature fluctuations. Second, two signals should have common or coherent physical fluctuations.

This requirement can be fulfilled by adjusting emission volumes of two signals separately within the correlation length of turbulence in both the radial and poloidal directions.

The third requirement is the uncorrelated thermal noise. There are two popular ways to obtain the uncorrelated thermal noise in two ECE signals. The first method is called "spatial decorrelation." [140] In this method, two radiometers are used, and they detect the radiations from almost the same emission volume, but through different sightlines with the separation angle larger than the given decorrelation angle, to obtain the incoherent thermal noise. Then, thermal noise will be eliminated and temperature fluctuation will remain through cross-correlation analysis of two signals. Another method is called "spectral decorrelation." [37] In this method, only one radiometer is used, and two channels measure EC radiation from two separate frequency ranges which correspond to different emission volumes, but two volumes that overlap in physical space due to the line broadening of the EC radiation. The main broadening mechanisms are relativistic effect and Doppler effect. Although the broadening of the EC radiation will be explained in section 2.2.2, it is noteworthy that the emission volume of EC radiation will be broadened when we measure a certain frequency range of the radiation due to this broadening. If we measure a radiation emitted from a certain spatial region, then we will observe the spectral broadening. Since we measure a certain frequency of the EC radiation using radiometer, there will be a spatial broadening of the measured radiation, then it is possible to measure two EC signals with disjoint frequency band, but with partially overlapped emission volume. line broadening Since thermal noise from disjoint frequency ranges are uncorrelated, signals from these two ECE channels will have incoherent thermal noise and coherent electron temperature fluctations from the overlapped emission volume (or the emission volume separated within a radial correlation length of the turbulence). Thus, the result obtained through this scheme after cross-correlation analysis of two signals is the same as the result obtained through the spatial decorrelation scheme. The spatial decorrelation scheme has better radial resolution than the single sightline method, and is able to measure poloidal correlation length of the temperature fluctuations[167]. However, this method has poorer poloidal resolution than the spectral decorrelation scheme, and is hard to implement since two radiometers are required and the accurate alignment of the two sightlines is critical.

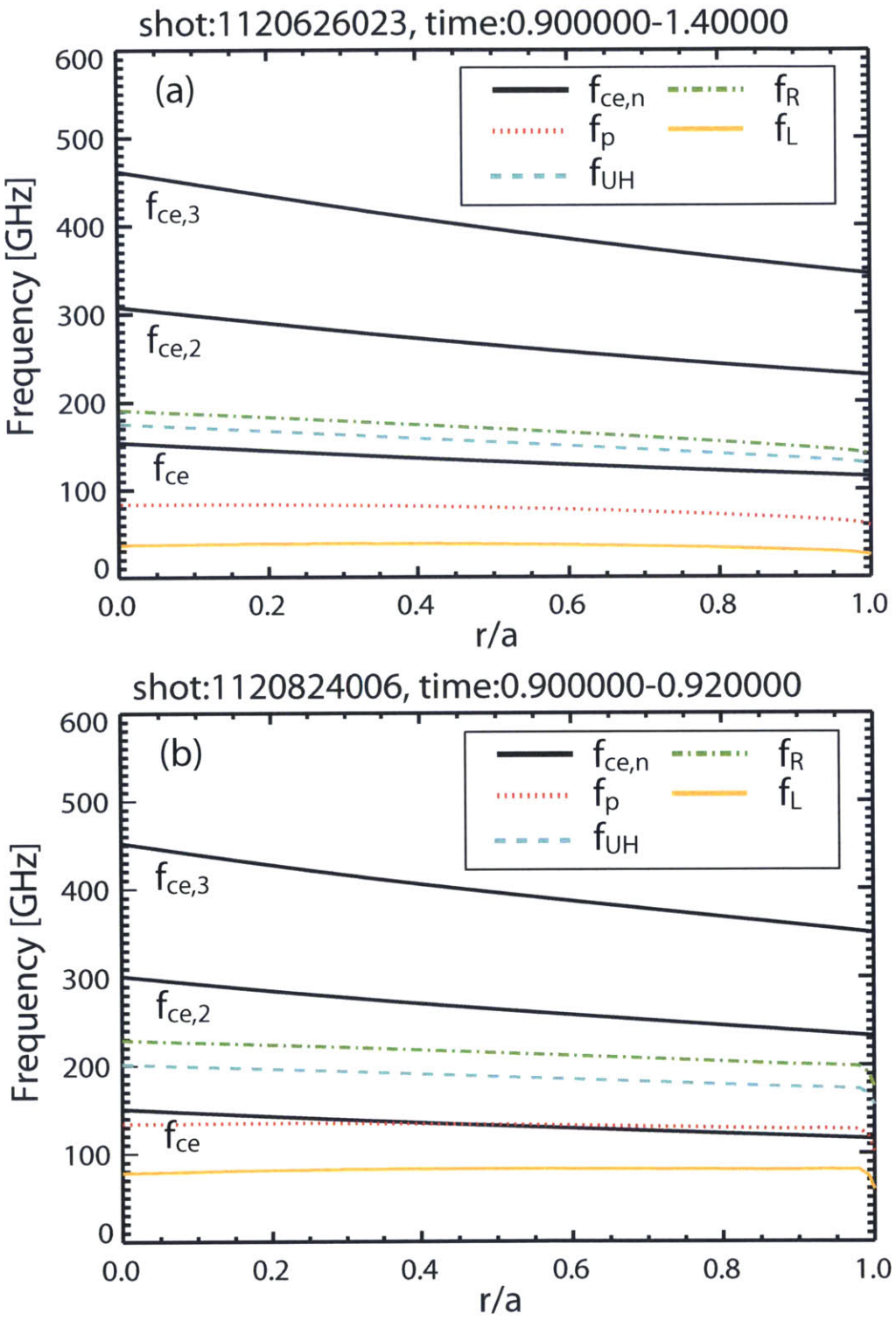

Figure 2-3: Electron cyclortron frequencies with resonance and cutoff frequencies for EC emission in (a) an Ohmicdischarge (shot : 1120626023, t:0.9-1.4s) and (b) H-mode discharge (shot : 1120824006, t:0.9-0.92s). $f_{ce,n}$ is the nth harmonic of the electron cyclotron frequency. In the figure, fundamental to third harmonic are presented. f_p is a plasma frequency, f_{UH} is an upper hybrid resonance frequency, $f_{R,L}$ are right/left hand cutoff frequencies, respectively.

2.2 Design of CECE in C-Mod

This section will explain how the CECE diagnostic in C-Mod was designed. In the design process for the CECE diagnostic in C-Mod, we need to consider several contraints from the characteristics of turbulence and the fundamental physics of EC radiation, which will be introduced in the following subsections.

2.2.1 Accessibility

We first consider the contraint from the physcis of EC radiation, which is the accessability of EC radiation. It is evident that we can measure EC radiation which can propagate from the inside of plasma to the receiver outside the plasma. This constraint will be applied generally to the ECE diagnostics as well as the CECE diagnostics. The cutoff frequency of the O-mode polarized radiation is the plasma frequency, f_p. That is, the O-mode radiation can propagate only when $f > f_p$. The cutoff regions for the X-mode radiation with frequency, f, are $f_{UH} < f < f_R$ and $f < f_L$, where f_{UH} is upper hybrid resonance frequency, and $f_{L,R}$ are the left/right-hand cutoff frequencies. These frequencies are given as follows.

$$f_p = \sqrt{\frac{n_e e^2}{m_e \epsilon_o}} \tag{2.13}$$

where ϵ_o is a vacuum permittivity.

$$f_{UH} = \sqrt{f_c e^2 + f_p^2} \tag{2.14}$$

$$f_{R,L} = f_{ce}[\pm 1 + \sqrt{1 + 4f_p^2/f_{ce}^2}]/2 \tag{2.15}$$

As shown in Eq. 2.13-2.15, cutoff frequencies depend on f_p and f_{ce}. f_p and f_{ce} are the functions of density and total magnetic field, respectively. Thus, these two factors will determine the accessibility of the EC radiation. It is noteworthy that the cutoff frequencies are proportional to density (or f_p). Thus, high density will limit the ECE measurements. Figure 2-3(a) and (b) show the harmonics (n=1,2,3) of EC frequency with the cutoff and resonance frequencies in the low-field side in the Ohmic(shot : 1120626023) and H-mode (shot : 1120824006) discharges, respectively. In Fig. 2-3(a), we can see that the fundamental X-mode is not accessible since there is a cutoff region where $f_{UH} < f_{ce} < f_R$ along the

beam path to outside the plasma. Thus, among optically thick EC emissions mentioned in Section 2.1.1, which are fundamental O- and X-modes and second harmonic X-mode, fundamental X-mode is not appropriate for the ECE diagnostic due to the limited accessibility. We also note that $2f_{ce}$ is higher than f_R in Fig. 2-3(a), which is typical in most ECE measurements in fusion experiments. Thus, the cutoff frequency for the second harmonic X-mode will be f_R in the ECE measurements. The cutoff densities of fundamental O-mode and second harmonic X-mode can be calculated from $f_{ce} = f_p$ and $2f_{ce} = f_R$, respectively. The cutoff density for the fundamental O-mode is $n_{cutoff,O1} = f_{ce} m_e \epsilon_o / e^2$, and the cutoff density for the second harmonic X-mode is $n_{cutoff,X2} = 2 f_{ce} m_e \epsilon_o / e^2$. Thus, second harmonic X-mode has two times higher cutoff density. For this reason, between fundamental O-mode and second harmonic X-mode, second harmonic X-mode has a wider density range for the ECE measurements. Figure. 2-3(b) is the relevant example. In the H-mode discharge which has high density, you can see that the fundamental O-mode is not accessible in r/a>0.4 , while the second harmonic X-mode is still accessible in the whole radial region. Because of better accessibility, second harmonic X-mode is widely used in the ECE measurements in present fusion experiments, and the CECE diagnostic in Alcator C-Mod will also detect the second harmonic X-mode in the low-field side.

2.2.2 Resolution of the ECE diagnostic

The CECE diagnostic should have enough temporal and spatial resolution to measure turbulent electron temperature fluctuations. Temporal resolution of the ECE radiometer is determined by the video bandwidth, B_{vid}, and we can measure the fluctuations whose frequency, f, is $0 < f < B_{vid}$. Thus, B_{vid} should be sufficiently higher than the typical frequency of the turbulent fluctuations.

The finite sample volume of the measurements limits the fluctuation measurements. This is because the fluctuations whose wavelength (or correlation length) is shorter than the dimension of the sample volume in each direction (poloidal, radial and toroidal) will be averaged out [23]. The spatial resolution for the turbulence measurements with the dimension of the sample volume in a certain direction, d, is given by[166],

$$k \lesssim 2\pi/d \tag{2.16}$$

where k is the wavenumber of the turbulence sensitive to the measurements.

Thus, each dimension of the emission volume should be shorter than the correlation length of the turbulent fluctuations in each direction. The poloidal and toroidal spatial resolutions of the ECE diagnostic are determined by the optical system, including the antenna and lens or other focusing components and collimating components. The beam pattern determined by the optical system defines the dimension of emission volume in the poloidal and toroidal directions, and the determined poloidal and toroidal dimensions of the emission volume limit the poloidal and toroidal resolutions for turbulence measurements.

Radial resolution of the ECE diagnostic is determined by the spectral broadening of EC radiation, reabsorption and IF bandwidth, B_{IF}. It is known that relativistic and Doppler broadenings are the main mechanisms for the spectral broadening of EC radiation and other broadening mechanisms such as natural broadening and collision broadening are negligible in fusion plasmas [85]. The relativistic broadening comes from the decrease of the frequency of EC emission due to the relativistic mass increase with the total velocity of each particle, and Doppler broadening is due to the change of the detected frequency by Doppler effect. These effects can be observed in the equation for EC frequency with the consideration of relativistic mass increase and the emission angle (detection angle) to the magnetic field, θ, as follows.

$$\omega_{ce} = \frac{eB(1-\beta)^{1/2}}{m_e(1-\beta_{\|}\cos\theta)} \tag{2.17}$$

where $\beta = v/c$, $\beta_{\|} = v_{\|}/c$, c is the speed of light, v is the velocity of the electron, $v_{\|}$ is the velocity of the electron parallel to the magnetic field.

As shown in Eq. 2.17, the relativistic broadening with mass increase by $(1-\beta)^{-1/2}$ decreases $f_{ce}(=\omega_{ce}/2\pi)$ by $(1-\beta)^{1/2}$, and Doppler broadening decreases or increases f_{ce} by $(1-\beta_{\|}\cos\theta)$. We also notice that the Doppler broadeing effect can be minimized by detecting EC radiation with emission angle, $\theta \simeq 90°$ although relativistic mass increase cannot be avoided. Within the emission layer of the EC radiation with f_{ce} determined by these broadening mechanism, this EC radiation will be absorbed and re-emitted at the black body level if the emission layer is optically thick [158]. This reaborption effect will increase the radial resolution limited by the radial broadening. Last, the ECE diagnostic will measure EC radiation with the finite frequency range, B_{IF}, not one specific frequeny value, f_{ce}. Thus, larger B_{IF} will increase the radial dimension of the emission volume, though

it will improve the sensitivity of the radiometer for fluctuation measurements as shown in Eq. 2.7. In order to calculate the radial width of EC emission layer, these effects should be considered, and the detailed calculation will be shown in section 2.3.3.

2.2.3 Design constraints due to the characteristics of turbulence

The design of the CECE diagnostic in C-Mod was also contrained by the characteristics of the turbulence simulated by a gyrokinetic simulation (GYRO). In the past, attempts to measure electron temperature fluctuations in Alcator C-Mod using the ECE heterodyne radiometer (FRCECE) [31] did not resolve broadband fluctuations above the sensitivity limit [168]. Three possible explanations for this null result were given in [168]. First, there are no turbulent electron temperature fluctuations, above the sensitivity limit, in Alcator C-Mod plasmas. Second, large spot size ($\sim 4cm$) in the measurements do not give enough poloidal resolution to measure the electron temperature fluctuations. Third, off-axis view (below the midplane) might affect the measurements. Nonlinear gyrokinetic simulations using the GYRO code [28] were used to reexamine these explanations [176]. GYRO is a code used to find the perturbed distribution function, δf, by solving the non-linear gyrokinetic equation. Characteristics of turbulence in the plasmas can be studied through GYRO simultaiton. More details about GYRO will be given in Chapter 3. The gyrokinetic simulation (GYRO) results in [176] show that turbulent electron temperature fluctuations should exist in Alcator C-Mod plasmas and that variation of electron temperature fluctuation levels with the different poloidal angles is small, which suggests that the first and third explanations are not valid.

These simulation results first suggest the decorrelation scheme used for the CECE diagnostic in C-Mod. It was shown by these simulations that the large beam diameter as used in past measurements [168] results in filtering out of most turbulent fluctuations. Thus, a small beam diameter will be the first constraint obtained from the gyrokinetic simulations. Figure 6 in [176] shows that beam diameter should be equal to or smaller than about 1cm to measure core electron temperature fluctuations. As discussed in section 2.1.2, the spectral decorrelation scheme is more appropriate than the spatial decorrelation scheme when high poloidal resolution is required. Thus, the spectral decorrelation scheme is more proper for

the CECE diagnostic in C-Mod. Besides, due to the spatial contraints, it is hard to find the space for two radiometers, which are required for spatial decorrelation scheme, in Alcator C-Mod. Thus, we will use the spectral decorrelation scheme for the CECE diagnostic in C-Mod.

Second, the gyrokinetic simulations predict that the radial correlation length of the turbulence is less than 1cm (0.4-0.8cm) at $\rho \sim 0.5$, where ρ is normalized square root of toroidal flux. This gives a constraint in the IF (Intermediate Frequency) bandwidth and on the spacing of neighboring IF filters. As mentioned in section 2.1.2, in order to obtain electron temperature fluctuations through correlation technique (single sightline correlation method), two channels should be separated in frequency space, but they should have the coherent temperature fluctuations. For these conditions, the two channel separation should be smaller than the radial correlation length. For the second harmonic EC radiation, 0.4 cm radial distance corresponds to about 1GHz separation in the frequency space. At least two channels should be totally separate within 1GHz, and it will limit the IF bandwidth, $B_{IF} \leq$ 250MHz with the consideration of the margin from the fact that the bandwidth of the filter is usually 3dB bandwidth.

Third, the receiver should be able to measure high frequency fluctuations, which can extend to about 0.3 MHz in the core of C-Mod plasmas, due to the effects of ExB flow that Doppler shift the measured laboratory-frame fluctuation power spectrum. This sets the lower limit on the video bandwidth, $B_{vid} \geq 0.5 - 1.0MHz$. Last, the sensitivity of CECE diagnostic, given by Eq. 2.12, should be less than 0.5%, since fluctuations are predicted to be between 0.5-2.0% in the core region. With B_{IF}=100MHz and B_{vid}=1MHz, we need 0.32 sec averaging time to obtain 0.5% sensitivity level given by Eq. 2.12. However, as mentioned in [140], we need to note that a lower sensitivity level than the fluctuation level that we are trying to measure is required to resolve the fluctuations clearly. Thus, increasing the averaging time, reducing the video bandwidth or increasing the IF filter bandwidth will be required to reduce the sensitivity level and measure 0.5% fluctuation level in the experiments. The design constraints obtained from gyrokinetic simulations are summerized in table 2.1.

It is noteworthy that the design constraints obtained in this section is different then requirements for a profile radiometer. For the profile radiometer, we do not have to consider the thermal noise level, since the important value in the measurements using the profile radiometer will be a DC level, not its fluctuations. In the same reason, we also do not have

the lower limit for the video bandwidth. The dimensions of the emission volume should be determined from the correlation length of the turbulence in the CECE design. In contrast, the profile radiometer does not have a serious constraint for the size of the emission volume. For the radial dimension, we may want to find the optimum IF bandwidth (B_{IF}) due to the tradeoff between the sensitivity limit and the radial resolution in the CECE design. In the profile measurements, we do not have to use the small value of B_{IF} much smaller than the radial broadening width of the EC radiation. Depending on the radial broadening width and the number of points in the profile, B_{IF} will be determined in the profile radiometer. In the poloidal direction, we may want to have a flat beam pattern over the plasma for the profile measurements. In the CECE design, higher poloidal resoluton will be required for the region which has smaller correlation lengh than the other regions.

Findings from the gyrokinetic simulation	Design constraint
Large spot size filters T_e fluctuations	New optical system should be designed for small spot size($\sim$1cm)
Radial correlation length is less than 1cm	$B_{IF} \leq$250MHz
The frequency of fluctuations is up to 300kHz	$B_{vid} \geq$0.5MHz
$0.5 \leq \frac{\tilde{T}_e}{T_e}(\%)$	Sensitivity level of CECE should be lower than 0.5%

Table 2.1: Design constraints for CECE diagnsotic in Alcator C-Mod given from gyrokinetic simulation (GYRO)[176].

2.3 Overview of CECE system

Following the constraints in section 2.2.3, a CECE diagnostic for C-Mod was designed and built. This section will describe the details of the CECE diagnostic in C-Mod. This CECE diagnostic consists of two parts. The first part is the optical system, which determines the CECE beam pattern in the plasmas and collects the emission. The second part of the diagnostic is the receiver. Each part will be described first in this section. We will also estimate the radial broadening width of the CECE diagnostic in this section. This estimation is required to develop a synthetic diagnostic for the CECE diagnostic in C-Mod.

A synthetic diagnostic is a computational model used to consider experimental conditions in the simulated quantities to compare simulation results with measurements. A synthetic diagnostic for the CECE diagnostic in C-Mod will be introduced in section 3.4.4, and the comparison of a synthetic T_e fluctuations with the CECE measurements measurements will be performed in Chapter 4.

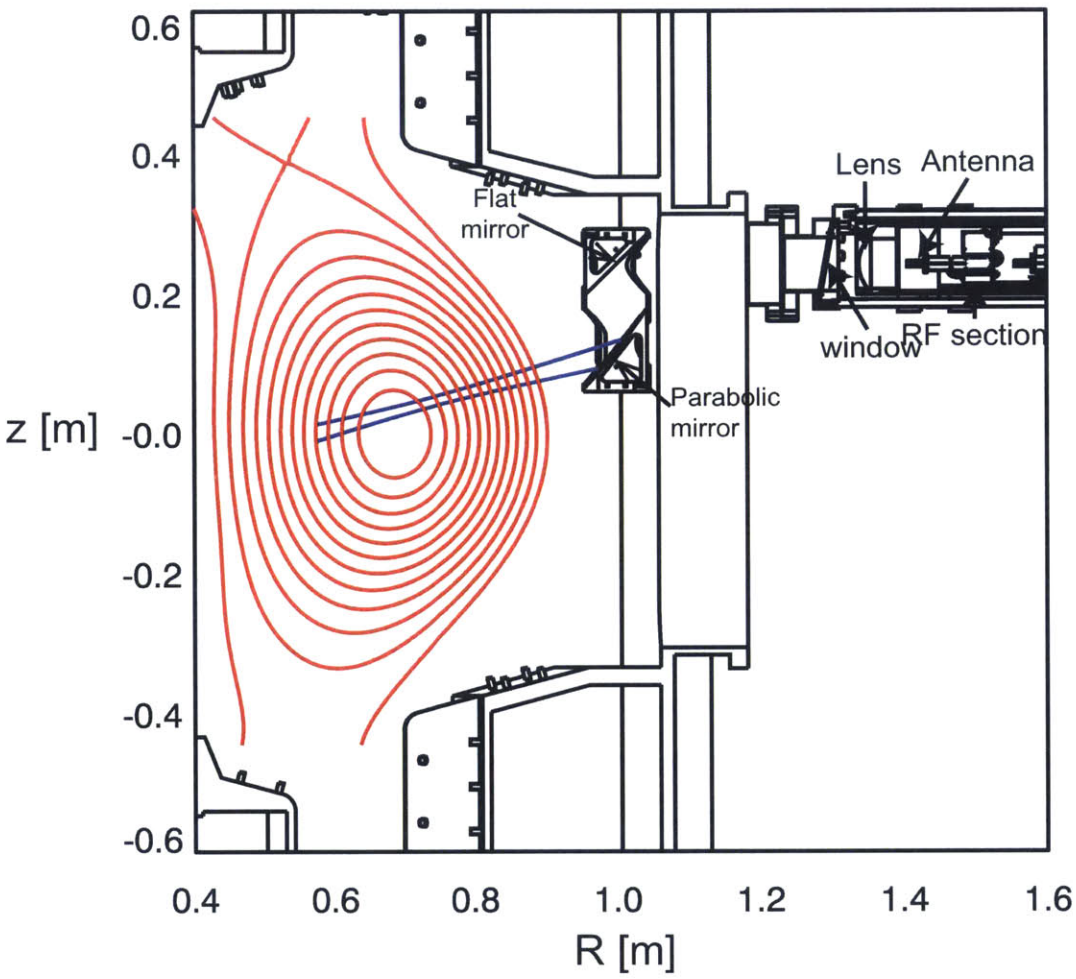

Figure 2-4: CECE diagnostic with C-Mod plasma (shot 1120221014, t=1.0 sec). The 1/e beam width along the line of sight is shown as blue curve.

2.3.1 Optical system for the CECE diagnostic

We will first describe the optical system for the CECE diagnostic in C-Mod. The CECE radiometer collects 2nd harmonic X-mode electron cyclotron emission (230-248GHz), viewing the plasma from the low field side approximately 7 cm above the midplane in the region, $\rho \sim 0.8$, where ρ is normalized square root of toroidal flux. Due to the limited space in

C-Mod, the upper port in A-port is used for the new CECE diagnostic in C-Mod. The antenna pattern from the initial optical design overlaid on a contour plot of flux surfaces for a typical C-Mod plasma with the CECE optical system is shown in Fig. 2-4. The optical system (drawn to scale) consists of two in-vessel stainless steel mirrors (flat and off-axis parabolic mirror), and outside the vessel an aspherical HDPE (High Density Polyethylene) collimating lens and corrugated, high gain scalar horn antenna (230-270GHz). In this system, the antenna beam pattern is determined by the in-vessel parabolic mirror. The flat mirror is used to change the direction of beam path, and the ex-vessel HDPE lens focuses the beam onto the antenna.

Design of the optical system

As shown as Table 2.1, small beam size is required for the T_e fluctuation measurements in C-Mod. In order to design the optical system with small beam diameter, Gaussian beam calculations were used. The beam radius of a Gaussian beam, w, which is 1/e electric field radius, is given by [58]

$$w = w_o[1 + (\frac{\lambda z}{\pi w_o^2})^2]^{0.5} \tag{2.18}$$

where, w_o is the beam waist radius, λ is the wavelength of the beam, and z is the distance from the focal position of the beam, where $w = w_o$.

Since the flat mirror does not contribute to the beam pattern and the parabolic mirror is used as the focusing lens, we can consider this optical system as a 1D system with the antenna and two lenses. Although the beam is emitted from the plasma, we can also think of the EC radiation as starting from the antenna to the plasma from the general law of reciprocity[119]. Thus, we can consider the Gaussian beam with the beam waist, w_o, propagating from the antenna. The beam will be collimated by an ex-veseel lens by setting the distance between the antenna and the ex-vessel lens to the same as the focal length of the lens. Then, the collimated beam will be focused in the plasma by the in-vessel lens (parabolic mirror). In the 1-D system, the parabolic mirror can be considered as the lens whose focal length is the effective focal length (EFL) of the parabolic mirror. EFL is defined as the distance from the center of the surface of the off-axis parabolic mirror to the focal point. In order to calculate the transformed Gaussian beam by the lens, the thin lens approximation is used as shown in Eq. 3.31a and 3.31b in [58]. In addition, a z-cut crystal quartz window was used at

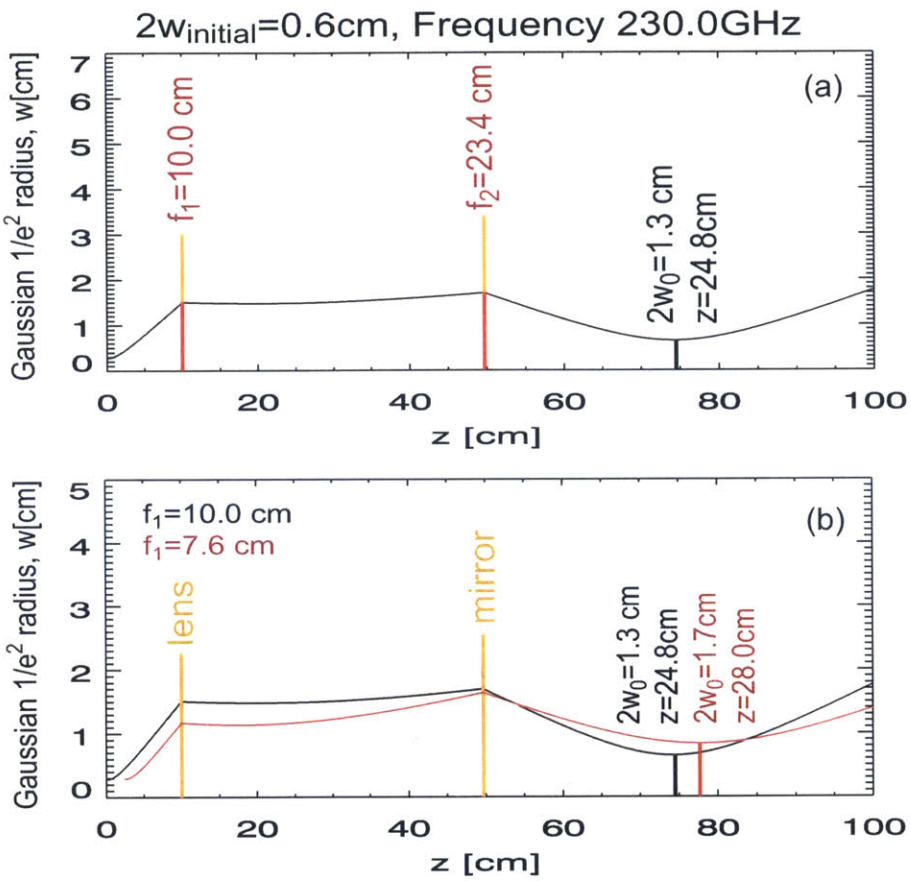

Figure 2-5: Gaussian beam calculation for optical system design. (a) The calculation of Gaussian beam propagation in the designed optical system. (b) The change of focal point depending on the different collimating lenses.

the viewing port. Because of its thin thickness ($\simeq$0.3cm), the window was not considered in this calculation. This calculation method was verified experimentally for similar optical arrangements at DIII-D [127].

The initial beam waist is 0.12cm in the CECE optical system, and this value was determined by the scalar horn antenna (SFH-04-R0390), manufactured by Millitech. With the given initial beam waist, the parabolic mirror and the focal length of the collimating lens were adjusted to obtain the small beam diameter ($\sim$1cm) in the plasma. The initial design result with EFL of parabolic mirror=23.4cm and focal length of ex-vessel lens=10.0cm is shown in Fig. 2-5(a). The final beam diameter is about 2w=1.3cm at $\rho = 0.2$ (2w = 1.5cm at $\rho = 0.5$), where w is the 1/e electric field radius. In the calculation, it was also found that we can change the focal point of the Gaussian beam by changing the collimating lens. Depending on the focal length of the collimating lens, beam spreading on the parabolic mir-

ror can be varied. When the beam size on the parabolic mirror is increased, the focal point moves radially deeper into the plasma. Thus, we can adjust the focusing point by changing the ex-vessel lens without changing the in-vessel components. One possible configuration is shown in Fig. 2-5(b). By changing the focal length of collimating lens from 10cm to 7.6cm, the focal point moves 3.2cm further into the plasma.

Installation of the optical system

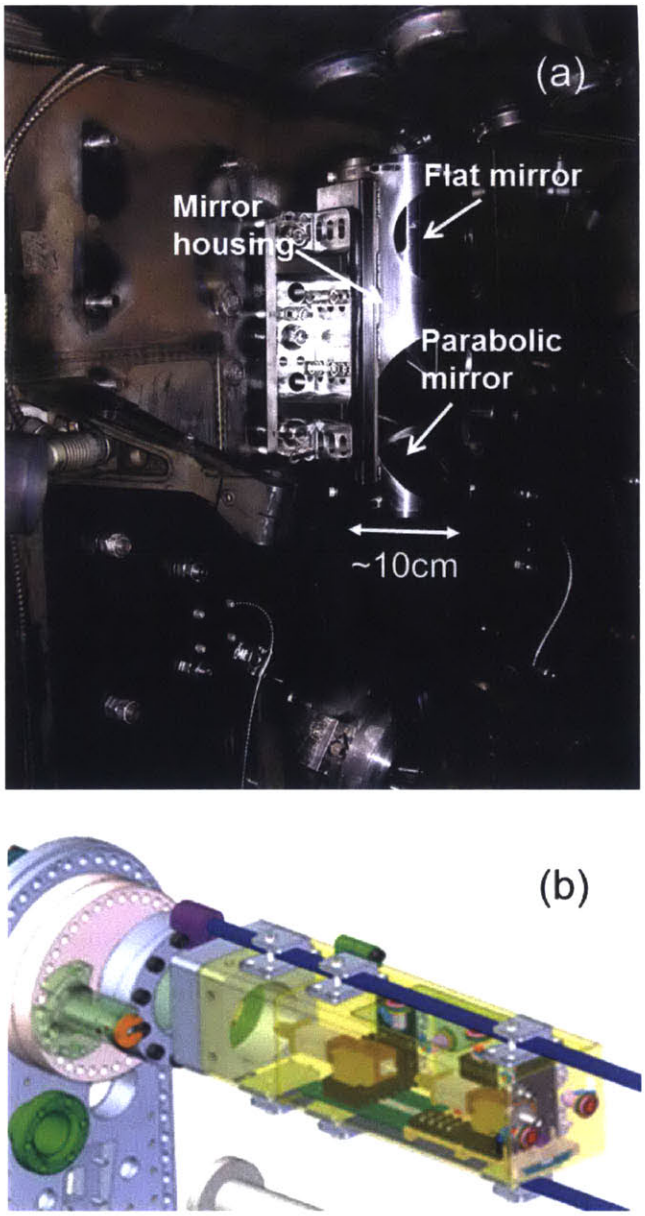

Figure 2-6: (a) In-vessel optical system for CECE diagnostic in C-Mod (b) front-end components for selecting 2^{nd} harmonic EC emission (232-248 GHz)

Following the initial design parameters, the parabolic and flat mirrors and their housings were fabricated and installed in the veseel as shown in Fig. 2-6(a). It is noteworthy that the width of the in-vessel mirrors was set to 8.6cm, which is more than 4 times larger than the estimated beam diameter at the mirror, to prevent the loss of beam power due to the small area of the mirrors. In the installation of mirrors, laser pointers are used to align the mirrors since the housing for the mirrors can be tilted toroidally and radially. The position of mirrors and housing was aligned by iterating the position of the housing until the beams from four laser points hit the co-centric inner wall target located at the expected position of the beams when the mirrors are correctly installed. This alignment process was performed every time the optical system was upgraded by replacing the parabolic mirror. More details about the alignment process will be explained in appendix A. As shown in Fig. 2-6(b), the ex-vessel lens and antenna were installed in front of the diagnostic port with the RF section of the CECE receiver, which will be discussed in section 2.3.2. Fig. 2-6(b) also shows that the distance from the collimating lens to the antenna with RF section components can be adjusted to modify the antenna beam pattern by replacing the ex-vessel collimating lens as discussed in the last paragraph.

Upgrades in the optical system

With the initial optics, which set the poloidal resolution of CECE to $k_\theta \leq 4.8cm^{-1}$, no electron temperature fluctuations were measured. This may indicate that the initial beam pattern was not enough to resolve the fluctuations in Alcator C-Mod. A new parabolic mirror was designed with smaller beam width ($< 1cm$) near the focal point. The upgraded system was also optimized for the measurements near the edge ($\rho \sim 0.8$) since the fluctuation level is larger at outer radii, as shown by the previous experiments in other devices[37, 178]. Fig. 2-7 shows the upgraded beam pattern with the initial beam pattern. With the upgraded optics (EFL of parabolic mirror=14.5cm, focal length of collimating lens=7.5cm), the EC radiation beam was focused near $\rho \sim 0.8$ with the beam diameter, d$\sim$0.6cm. The poloidal resolution of CECE is improved as $k_\theta \leq 9.8cm^{-1}$ ($k_\theta \rho_s \leq 0.3$, where ρ_s is the sound gyroradius, which is defined by $\rho_s = c_s/\Omega_{ci}$, where $c_s = \sqrt{T_e/m_i}$ and $\Omega_{ci} = eB/m_i c$). With the improved poloidal resolution, the electron temperature fluctuations near the edge ($\rho \sim 0.8$) were resolved. By replacing the collimating lens with a shorter focal length, f=5cm, we expand the measurement region to $\rho \sim 0.7$ region. This indicates that high poloidal resolution with

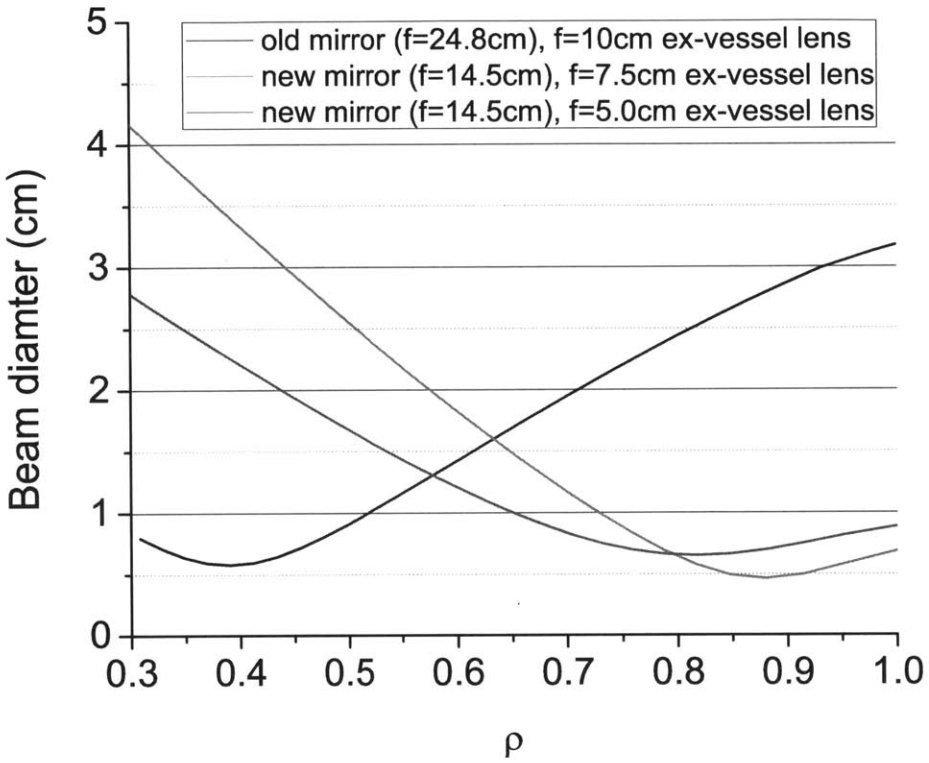

Figure 2-7: Change of the CECE beam pattern in the plasma depending on the focal length of in-vessel parabolic mirror and ex-vessel lens. The vertical axis is a 1/e electric field diameter, and the horizontal axis is the normalized square root of the toroidal flux calculated from EFIT for the one C-Mod discharge (shot 1120626023, t:1.0s). CECE optical system was upgraded from black to red, and then to blue curve. The old mirror (f=24.8cm) with f=10cm ex-vessel lens was used in the initial stage of the CECE diagnostic before May 2012. The new mirror (f=14.5cm) had been used from run day 1120501 in 2012 campaign. The f=10cm ex-vessel lens was replaced with f=7.5cm ex-vessel lens on run day 1120605, and this lens was replaced with f=5cm lens on run day 1120710.

small beam diameter is critical in the electron temperature fluctuation measurements in Alcator C-Mod.

2.3.2 CECE receiver

This section will describe the details of the CECE receiver. As shown in Fig. 2-8, the CECE receiver consists of an RF and an IF section. The RF section accepts high frequency signals (230-248 GHz) and downshifts these signals to the intermediate frequency (IF) range (2-18 GHz). The components in the RF section include a band pass filter, a local oscillator (LO), an active multiplier chain, a sub-harmonic mixer and a first amplifier for IF frequency signals.

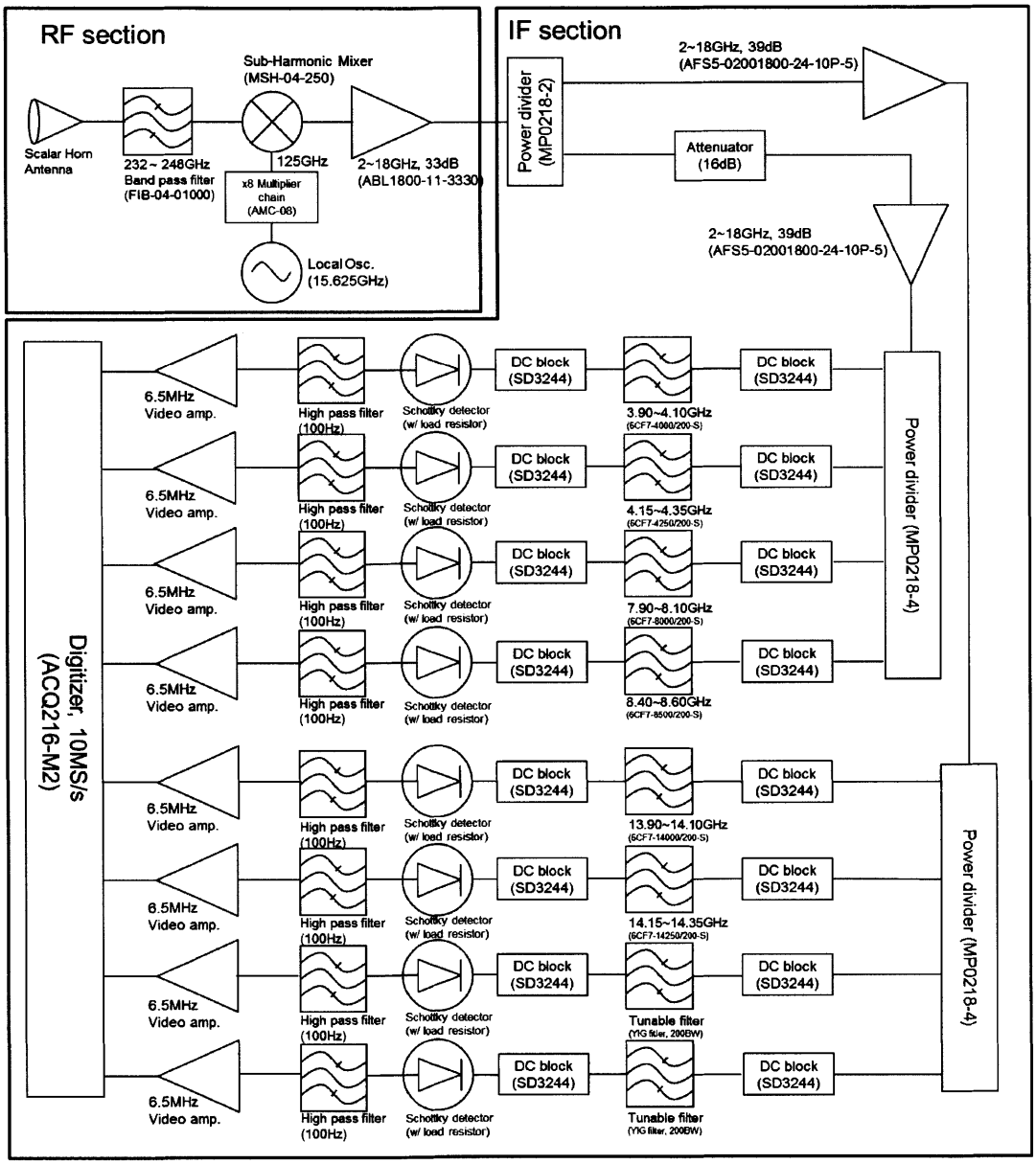

Figure 2-8: The block diagram of CECE receiver

After the scalar horn antenna, the input RF frequency range is chosen to be 232-248GHz by a band pass filter (FIB-04-01000 by Millitech), then these signals are down-shifted by the sub-harmonic mixer (second harmonic operation, MSH-04-250 by Millitech). The other signal (f=15.625GHz) for the mixer is generated by an LO (TGM1610AC by TelGaAs Inc.). The active multiplier chain (AMC-08 by Millitech) multiplies the frequency of the signal 8 times. Thus, the frequency of the other signal in the mixer is 125GHz. The frequency of the output signal through the second harmonic operation in the sub-harmonic mixer, which is mixing the 232-248GHz signal from plasma with the 250GHz (125×2 GHz) signal from LO and the multiplier chain, will be 2-18GHz. Last, the output signal is amplifed 33dB by the first low noise amplifier for IF signals (ABL1800-11-3330 by Wenteq Microwave Corp.). In order to prevent any negative effects on the electronics due to the stray magnetic field, RF components were shielded by mu-metal (thin nickel foil, thickness$\sim$0.01 inch). The RF components with the RF box is shown in Fig. 2-9(a).

The signal is then transmitted to the relatively low frequency components (IF section) through a 6.1m low loss SMA cable (SCF651410-300, loss rate : 0.45dB/FT at 10GHz, manufactured by Fairview Microwave). The IF section consists of two boxes. At the initial operation, only one IF box which consisted of 4 channels with fixed frequency IF filters was in the IF section. Later, the IF section was ungraded by adding another IF box with another 4 channels including 2 tunable frequency channels [79]. The signal is divided in each IF section by a power divider (MP0218-2 by Fairview Microwave). In each IF box, the signal is attenuated by the attenuator (SA18E-XX, XX : attenuation level [dB], (ex) SA18E-03 indicates 3dB attenuator.) before being amplified 39dB by a second low noise amplifier (AFS5-02001800-24-10P-5 by MITEQ). The attenuation can be varied, but usually 10-16dB attenuation was used for the first box and no attenuation was applied to the second box.

In each box, the signal is split into four channels by power divider, and in each channel the signal is filtered by IF band pass filter (MP0218-4 by Fairview Microwave). As mentioned above, all four of the filters have the fixed center frequency whose range is 4-14GHz and 3dB bandwidth B_{IF}=200MHz (6CF7-XXXX/YYY-S, XXXX : center frequency [MHz], YYY : 3dB bandwidth, by Lorch Microwave. (ex) 6CF7-8500/200-S for the filter whose center frequency is 8.5GHz and 200MHz bandwidth.) in the first IF box. In the second IF box, two of them are the same kind of filters used in the first IF box and the other two filters are

Yttrium Iron Garnet (YIG) bandpass filters (MLFP-1629PA by Micro Lambda Wireless). The YIG filters are shielded by a magnetic housing made of quarter inch, low-nickel stainless steel to avoid the effect from stray magnetic field [79]. The center frequencies of these filters are remotely tunable between 6-18GHz by external voltage (0-10V) with a 3dB bandwidth, B_{IF}=200MHz. It is worth noting that IF bandwidth, B_{IF}, was conservatively selected as 100MHz in order to ensure that the two filters can measure emission in disjoint frequency bands within a radial correlation length (<1cm) of the turbulence. However, it was hard to resolve the electron temperature fluctuations clearly with 100MHz filters in the experiments. This may indicate that the sensitivity level of the CECE radiometer was not enough. Once 100MHz filters were replaced by 200MHz filters, the fluctuations were resolved more clearly, and 200MHz filters were used in most measurements from the discharge 1120626023. (That is, for the shot number higher than 1120626023, 200MHz filters were used. Before this discharge, both 100MHz and 200MHz filters were used to test them.)

Inner DC blocks (SD 3244) were added before and after IF filtering to prevent the noise due to ground loops. The power of these signals is measured by a square-law detector (Schottky diode detector, 8472B by Agilent). The output of this detector has negative polarity. The pairs of the detectors whose responses with the input power are matched are used for each of the two CECE channels, which will be used in the correlation analysis. We note that the responses of all channels are adjusted to be similar as will be shown in section 2.4.1. The load resistor was added after the square law detector to extend the square law region (from $\sim$-18 dBm to $\sim$ -10 dBm from the data sheet[9]) where the output voltage signal of the detector is proportional to the square of the amplitude of the input signal, i.e., power of the input signal. Since the amplification in the IF section is limited by the input power range of square law region in the detector, adding the load resister is desirable in most measurements. Extending the square law region of the detector will broaden the range of the temperature, including its fluctuations which can be measured by the CECE diagnostic with fixed amplification. If the signal amplitude from the highest temperature plasma is still far below the saturated region of the square law detector, then we can amplify the signal more to improve signal to noise ratio.

The output signal from the detector is passively high pass filtered at around 10kHz before amplification by a video amplifier to remove the direct current (DC) signal which is proportional to electron temperature. This high pass filtering allows us to amplify fluctuation

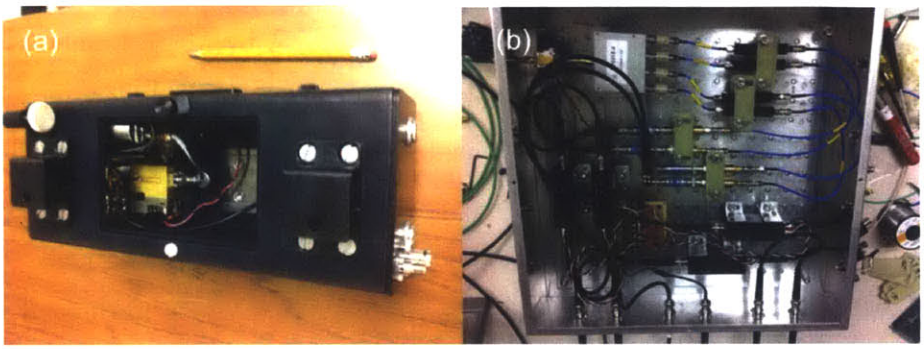

Figure 2-9: The (a) RF section (b) First IF box of CECE diagnostic in the laboratory

signals to obtain higher signal to noise ratio. In other words, eliminating the DC signal by high pass filtering allows us to use the full dynamic range of the video amplifier and digitizer for the fluctaution measurements. With the DC signal, the amplification will be limited by the dynamic range of video amplfier ($16V_{pp}$) and the voltage range of digitizer ($|V| \leq$10V). As will be shown in section 2.4, the passive high pass filters were added after we checked CECE radiometer functioned as an ECE radiometer.

The high pass filtered signal is amplifed by a video amplifier (351A-2-4.7-NI, by Analog Modules, INC.) with video bandwidth, B_{vid}=6.5MHz and the varied voltage ratio gain, G=100-1000. B_{vid}=6.5MHz is too large to obtain enough sensitivity to measure the small amplitude fluctuations (0.5-1.0%). Digital low pass filtering was used to decrease B_{vid} in post processing, improving the sensitivity of the CECE radiometer. In the measurements, B_{vid} is usually set to 0.5-1MHz. Last, the amplified signal in each channel which is proportional to the power of the EC radiation, i.e., electron temperature for the optically thick plasmas, is transmitted to the digitizer (ACQ216CPCI-16-50 by D-Tacq) by BNC cables. The 50 ohm termination is added at the output of the video amplifier to eliminate the noise due to the impedeance mismatchng with the digitizer whose input impendance is high (5k ohm). The details about noise due to the impedance mismatching with the digitizer is discussed in Appendix B. The sampling rate of digitizer can be chosen between 6 and 10Ms/s. We observed the electron temperature fluctuations with both 6 and 10 Ms/s, and most fluctuation measurements were performed with 6Ms/s. Figure 2-9(b) shows the first IF box in the laboratory.

2.3.3 Estimation of radial broadening width of CECE

The radial broadening width of the CECE diagnostic was estimated with the consideration of Doppler and relativistic broadening, as described in this section. Doppler and relativistic broadening are the main broadening mechanisms of the EC radiation as mentioned in section 2.2.2. The Doppler broadening effect can be ignored when the observation angle is close to 90 degree from the magnetic field. In this case, including most ECE measurements in fusion experiments, the radial broadening is determined mainly by relativistic broadening. However, toroidal beam spreading on the surface of the in-vessel mirror makes the Doppler broadening effect comparable to the relativistic effect in Correlation ECE (CECE) measurements in C-Mod. Assuming that the plasma is tenuous, which means the refractive index of the plasma, N_p, is equal to 1, the radiation intensity of a certain frequency, f, at a certain point, s_2, $I(f, s_2)$ is given by [18],

$$I(f, s_2) \simeq \int^{s_2} \alpha(f, s) B(f, s) exp(-\tau(f, s))\, \mathrm{d}s \tag{2.19}$$

where α is the absorption coefficient, τ is the optical depth, and B(f,s) is the black body radiation intensity. The definitions of each variable are given as follows [85].

$$\alpha(f, s) = \frac{\pi}{2c} \frac{e^2 n_e}{m_e \epsilon_o} \frac{m^{2m-1}}{(m-1)!} \left(\frac{T_e}{2 m_e c^2} \right)^{m-1} (\sin\theta)^{2(m-1)} (1 + \cos^2\theta) \frac{\phi(f, \theta)}{2\pi} \tag{2.20}$$

with harmonic of cyclotron radiation, m, observation angle from magnetic field, θ, shape function of the radiation with frequency, f, $\phi(f, \theta)$.

When the plasma is optically thick, radiation intensity, $I(f, s_2)$, can be approximated as $I(f, s_2) \simeq \alpha(f, s_2) B(f, s_2) exp(-\tau(f, s_2))$, and this approximated form will be used to calculate the radiation intensity at each position. For this calculation, the shape function,$\phi(f, \theta)$ should be calculated, which is defined as,

$$\phi(f, \theta) = \frac{j_m(f, \theta)}{j_m(\theta)} \tag{2.21}$$

where, $j_m(\theta)$ is a total emissivity for a single harmonic, m, and $j_m(f, \theta)$ is a emissivity of a certain frequency, f, for a single harmonic, m. Thus, $\int \phi(f, \theta)\, \mathrm{d}f = 1$.

Assuming a Maxwellian distribution, $j_m(\theta)$ and $j_m(f, \theta)$ are given as follows [85].

$$j_m(\theta) = \frac{e^2\omega_m^2 n_e}{8\pi\epsilon_o c}\frac{m^{2(m-1)}}{(m-1)!}(\sin\theta)^{2(m-1)}(1+\cos^2\theta)\left(\frac{T_e}{2m_e c^2}\right)^m \tag{2.22}$$

$$\begin{aligned} j_m(f,\theta) &= \frac{e^2\omega_m^2}{4\pi\epsilon_o c}\frac{m^{2(m-1)}}{(m-1)!^2}(\sin\theta)^{2(m-1)}(1+\cos^2\theta)\times \\ c^3\iint\delta(\{1-\beta_\parallel\cos\theta\}\omega - m\omega_c) & f_M(\beta_\perp,\beta_\parallel)\left(\frac{\beta_\perp}{2}\right)^{2m} 2\pi\beta_\perp\,\mathrm{d}\beta_\perp\mathrm{d}\beta_\parallel \end{aligned} \tag{2.23}$$

where $\beta = \frac{v}{c}$, ω_c is the electron cyclotron frequency, $\omega_c = \frac{\Omega}{\gamma}$ with $\Omega = \frac{eB}{m_e}$ and $\gamma = (1-\beta^2)^{-1/2}$. Also, ω_m=mΩ, ω=$2\pi\nu$ and f_M is the Maxwellian distribution.

As indicated in Eq. 2.23, it is hard to obtain analytic expression for $j_m(f,\theta)$ (and $\phi(f,\theta)$) due to the integral in $j_m(f,\theta)$ unless $\theta = \frac{\pi}{2}$. However, we may be able to calculate Eq. 2.23 numerically for any θ value. For numerical integration, we first change variables $(\beta_\perp,\beta_\parallel)$ as follows.

$$\begin{gathered} (\beta_\perp,\beta_\parallel)\rightarrow(\beta,\psi)\ \text{ with } \beta_\parallel = \beta\cos\psi, \beta_\perp = \beta\sin\psi \\ \beta_\perp\colon[0,1], \beta_\parallel\colon[-1,1]\rightarrow\beta\colon[0,1], \psi\colon[0,\pi] \end{gathered} \tag{2.24}$$

Then, Eq. 2.23 will be,

$$\begin{aligned} j_m(f,\theta) &= \frac{e^2\omega_m^2}{4\pi\epsilon_o c}\frac{m^{2(m-1)}}{(m-1)!^2}(\sin\theta)^{2(m-1)}(1+\cos^2\theta)\times \\ c^3\iint\delta(\{1-\beta\cos\psi\cos\theta\}\omega - m\omega_c) & f_M(\beta,\psi)\left(\frac{\beta\sin\psi}{2}\right)^{2m} 2\pi\beta^2\sin\psi\,\mathrm{d}\beta\mathrm{d}\psi \end{aligned} \tag{2.25}$$

Let $g(\beta) = (1-\beta\cos\psi\cos\theta)\omega - m(1-\beta^2)^{1/2}\Omega$, and θ is considered as the give value. Then, using the property of the delta function, i.e., $\delta(g(\beta)) = \frac{1}{|g'(\beta_o)|}\delta(\beta-\beta_o)$ with $g(\beta_o) = 0$ and $g'(\beta) = \frac{dg}{d\beta}$, the integrand in Eq. 2.25 can be written as Eq. 2.26.

$$\begin{aligned} j_m(f,\theta) &= \frac{e^2\omega_m^2}{4\pi\epsilon_o c}\frac{m^{2(m-1)}}{(m-1)!^2}(\sin\theta)^{2(m-1)}(1+\cos^2\theta)\times \\ c^3\int\frac{1}{|g'(\beta_o(\theta,\psi))|} & f_M(\beta_o(\theta,\psi),\psi)\left(\frac{\beta_o(\theta,\psi)\sin\psi}{2}\right)^{2m} 2\pi\beta_o(\theta,\psi)^2\sin\psi\,\mathrm{d}\psi \end{aligned} \tag{2.26}$$

where $|g'(\beta)| = |-\cos\psi\cos\theta\omega + \beta(1-\beta^2)^{-1/2}\omega_m|$, and $\beta_o(\theta,\psi)$ value is as follows.

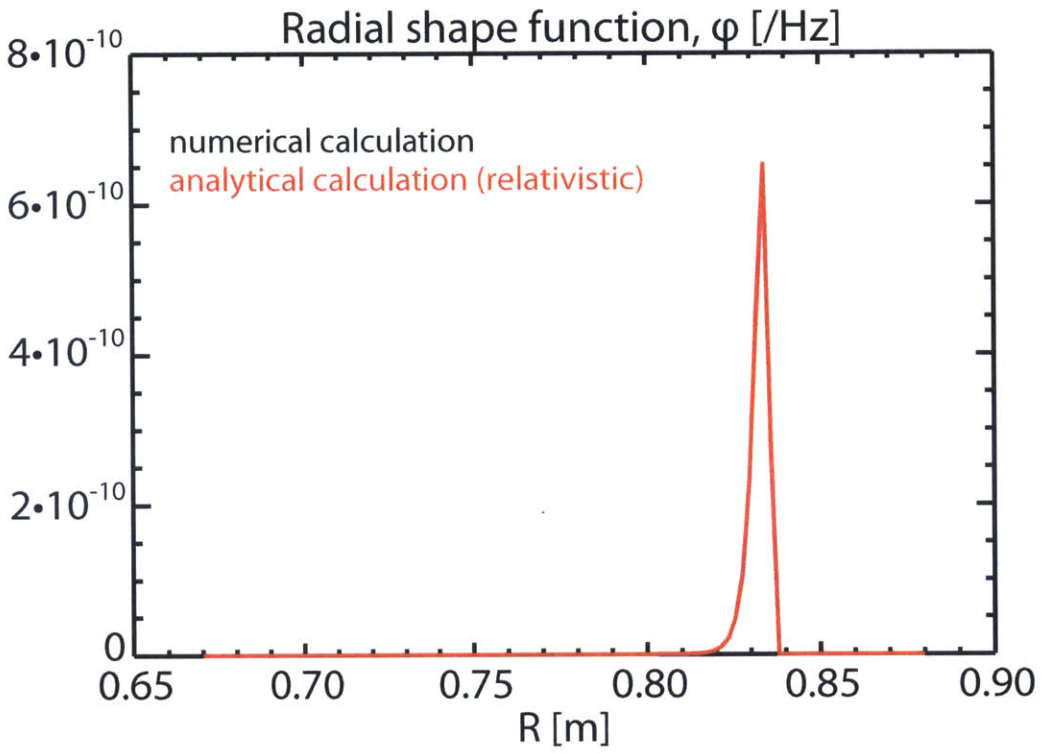

Figure 2-10: The radiation shape function of 242GHz beam when $T_e(0)$=2keV, $n_e(0) = 10^{20}m^{-3}$, observation angle, $\theta = 90\circ$, black : numerical calculation from Eq. 2.28, red : the result from analysis expression for the relativistic broadening, Eq. 2.29

$$\beta_o(\theta,\psi) = \frac{\omega^2\cos\psi\cos\theta \pm \sqrt{\omega^4\cos^2\psi\cos^2\theta - (\omega^2-\omega_m^2)(\omega^2\cos^2\psi\cos^2\theta+\omega_m^2)}}{\omega^2\cos^2\psi\cos^2\theta+\omega_m^2}. \quad (2.27)$$

Thus, at each ψ value, we can calculate $\beta_o(\theta,\psi)$ values and the integrand value in Eq 2.26 for each $\beta_o(\theta,\psi)$ value. Then, by summing whole integrand values, the $j_m(f,\theta)$ value is easily obtained. It is possible that β_o value in Eq. 2.27 is complex or this value is not between 0 and 1 even when it is real. These cases should be excluded in the calculation because they are not physically possible solutions. From Eq. 2.21,2.22 and 2.26, the shape function, $\phi(f,\theta)$ can be obtained from the following equation.

$$\phi(f,\theta) = \frac{2\pi}{m}c^3\left(\frac{2m_ec^2}{T_e}\right)^m \int \frac{1}{|g'(\beta_o(\theta,\psi))|}\frac{f_M(\beta_o(\theta,\psi),\psi)}{n_e}\left(\frac{\beta_o(\theta,\psi)\sin\psi}{2}\right)^{2m} 2\pi\beta_o(\theta,\psi)^2\sin\psi\,\mathrm{d}\psi \quad (2.28)$$

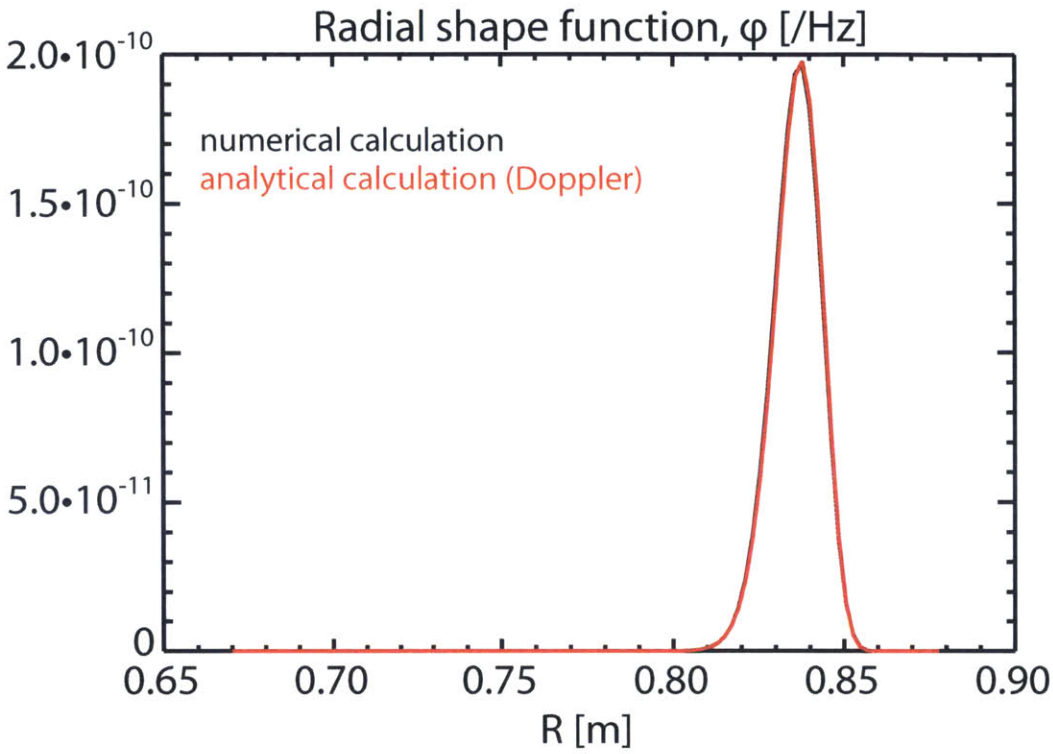

Figure 2-11: The radiation shape function of 242GHz beam when $T_e(0)$=0.1keV, $n_e(0) = 10^{19}m^{-3}$, observation angle, $\theta = 10\circ$, black : numerical calculation from Eq. 2.28, red : the result from analysis expression for Doppler broadening, Eq. 2.30

In order to check whether the result of the shape function, ϕ, from numerical integration is correct or not, the results from Eq. 2.28 were compared with the analytic expressions in the extreme cases, in which either relativistic or Doppler broadening is dominant. When relativistic broadening is dominant ($\theta = \pi/2$), the shape function, ϕ is given by as follows [85].

$$\phi(f,\pi/2) = \frac{\pi^{1/2}\omega}{(m\Omega)^2}\left(\frac{2m_ec^2}{T_e}\right)^{m+\frac{3}{2}}\frac{m!}{(2m+1)!}\left(1-\left(\frac{1}{m}\frac{\omega}{\Omega}\right)^2\right)^{m+\frac{1}{2}}\exp\left(-\frac{m_ec^2}{2T_e}\left(1-\left(\frac{1}{m}\frac{\omega}{\Omega}\right)^2\right)\right) \tag{2.29}$$

When Doppler broadening is dominant ($\cos\theta \gg \beta, 1-\beta^2 \sim 1$), the shape function, ϕ is given as below [85].

$$\phi(f,\theta) = \left(\frac{m_ec^2}{2\pi T_e}\right)^{\frac{1}{2}}\frac{1}{f_m\cos\theta}\exp\left(-\frac{m_ec^2}{2T_e}\left(\frac{f-f_m}{f_m\cos\theta}\right)^2\right) \tag{2.30}$$

First, we compared the result from Eq. 2.28 with Eq. 2.29. Electron density, n_e, and tem-

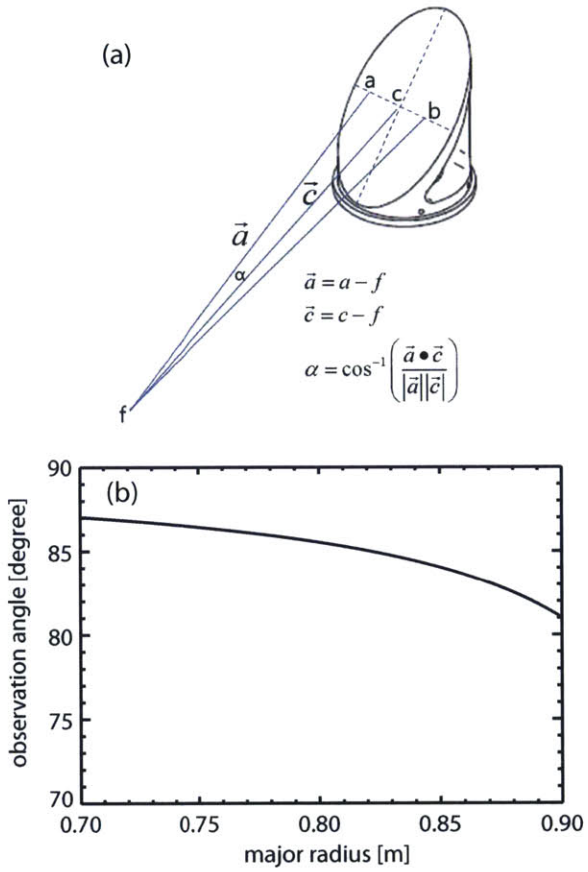

Figure 2-12: (a) Description of toroidal deviation angle, α. Positions a and b indicate the edge of the region where the half of the beam is deposited on the mirror's surface. The positions a and b are calculated as 0.67w, where w is the beam radius from Gaussaian beam calculation. (b) The observation angle, θ, with the major radius along the CECE beam path.

perature, T_e, profiles are assumed as $f(r) = f(0)(1-(r/a)^2)$, $T_e(0)$=2keV, $n_e(0)$=$10^{20}m^{-3}$. Only toroidal B field was considered in this comparison. Then, $B(r) = B_o R_o/(R_o + r)$, and B_o was set to 5.4T. Last, the observation angle, θ, was set to $\pi/2$, and f was set to 242GHz, which is usually used in the CECE measurements. As shown in Fig. 2-10, the result obtained numerically from Eq. 2.28 is exactly same as the result from analytic expression from Eq. 2.29. To compare the result from Eq. 2.28 with Eq. 2.30, we set $T_e(0)$=0.1keV, $n_e(0)$=$10^{19}m^{-3}$, and θ=$\frac{\pi}{18}$(= 10°) with B_o=5.4T and f=242GHz to satisfy $\cos\theta \gg \beta$. Figure. 2-11 shows that the calculated shape function from Eq. 2.28 agrees perfectly with the analytic expression from Eq. 2.30. These comparisons show that the numerical calculation for the shape function is correct.

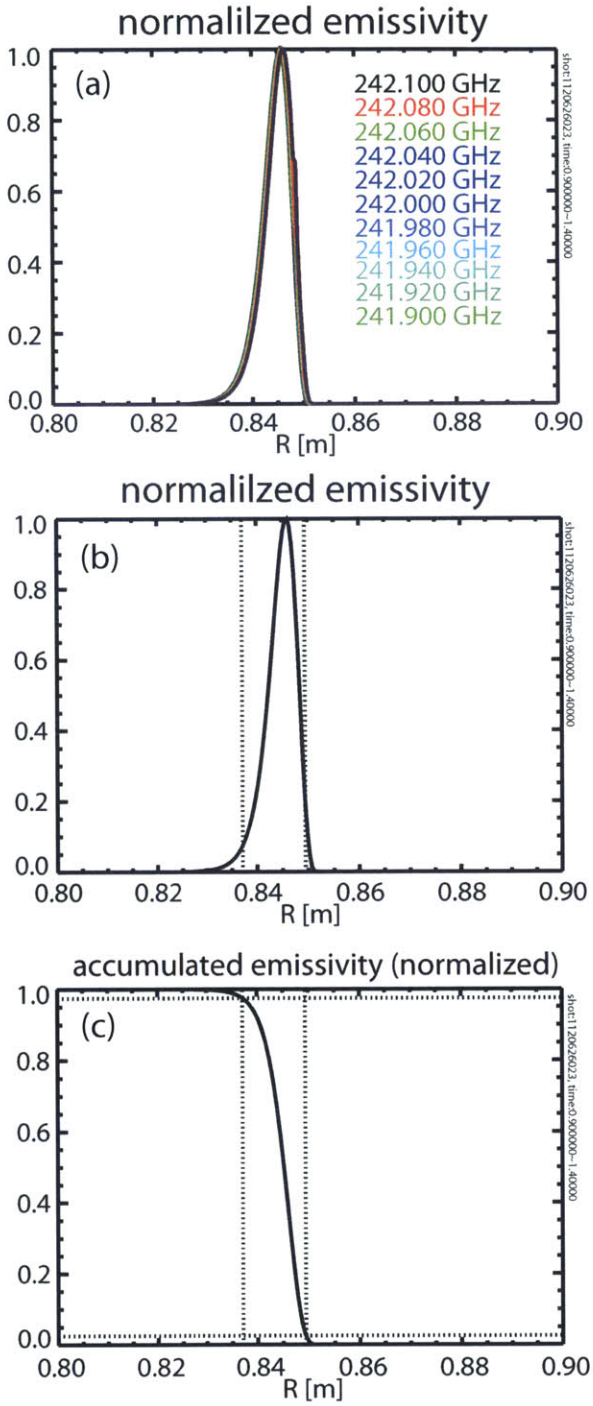

Figure 2-13: (a) Emissivity curves of 11 frequencies in 241-243GHz range for the shot 1120626023, t:0.9-1.4s. (b) The emissivity curve of the channel whose center frequency is 242GHz with 200MHz bandwidth, this curve is obtained by summing emissivity curves of 11 frequencies shown in (a). (c) Accumulated emissivity curve of the channels used in (b). Vertical dot lines in (b) and (c) show the position where accumulated emissivity is 2.5% and 97.5%, respectively.

Before applying Eq. 2.28 to the CECE measurements, the observation angle should be decided. In the CECE measurements, the in-vessel parabolic mirror is used for beam focusing, and after the parabolic mirror, the beam is collimated. If the toroidal deviation angle is set to the angle between the line from the beam's center at a certain position in the plasma to the mirror's center and the line from beam's center to mirror's edge, the angle might be too large compared to the real measurements. This is because the beam will have a Gaussian distribution in both poloidal and toroidal directions, and the whole surface of the mirror will not be used in the measurements. One way to estimate the proper toroidal deviation angle will be as the angle between the line from the beam's center in the plasma at a certain position to the mirror's center and the line from the beam's center to the edge on the toroidal direction of the region where 50% of beam power is in, as shown fig. 2-12(a). In fig. 2-12(a), positions a and b are the edge on the toroidal direction where the half of beam's power is deposited, and this point can be calculated as ~0.67w, where w is beam's radius on the mirror's surface. Then, the observation angle, $\theta = \pi/2 - \alpha$, where α is the toroidal deviation angle shown in Fig. 2-12(a). Fig. 2-12(b) shows the observation angle with the major radius. It is worth noting that CECE measurements are not on the midplane, and the major radius in Fig 2-12(b) is the major radius along the beam path, not the major radius on the midplane.

Using the estimated observation angle in Fig. 2-12(b), the intensity of radiation measured by CECE was calculated. Each CECE channel measures EC radiation in a certain frequency range, determined by the bandwidth of the filter in the IF section (~200MHz). To consider this, the radiation intensities of 11 frequencies in the measured frequency range were calculated and summed, with the summed emissivity representing the emissivity of one CECE channel. As an example, the emissivity curves of 11 frequencies in the measured frequency range (241-243GHz) for one C-Mod discharge (shot 1120626023) and the summed emissivity curve are shown in Fig. 2-13(a) and (b). In this calculation, time-averaged n_e and T_e profiles during stationary period (t:0.9-1.4s) were used. Fig. 2-13(c) shows the accumulated intensity of the CECE channel used in Fig. 2-13(b). All intensity values in Fig. 2-13 are normalized by its maximum value.

The radial broadening width of EC radiation measured in one CECE channel was calculated as the radial distance between the radii where the accumulated intensity is 2.5% and 97.5%, comparable to $1/e^2$ diameter from the Gaussian beam calculation. Since the

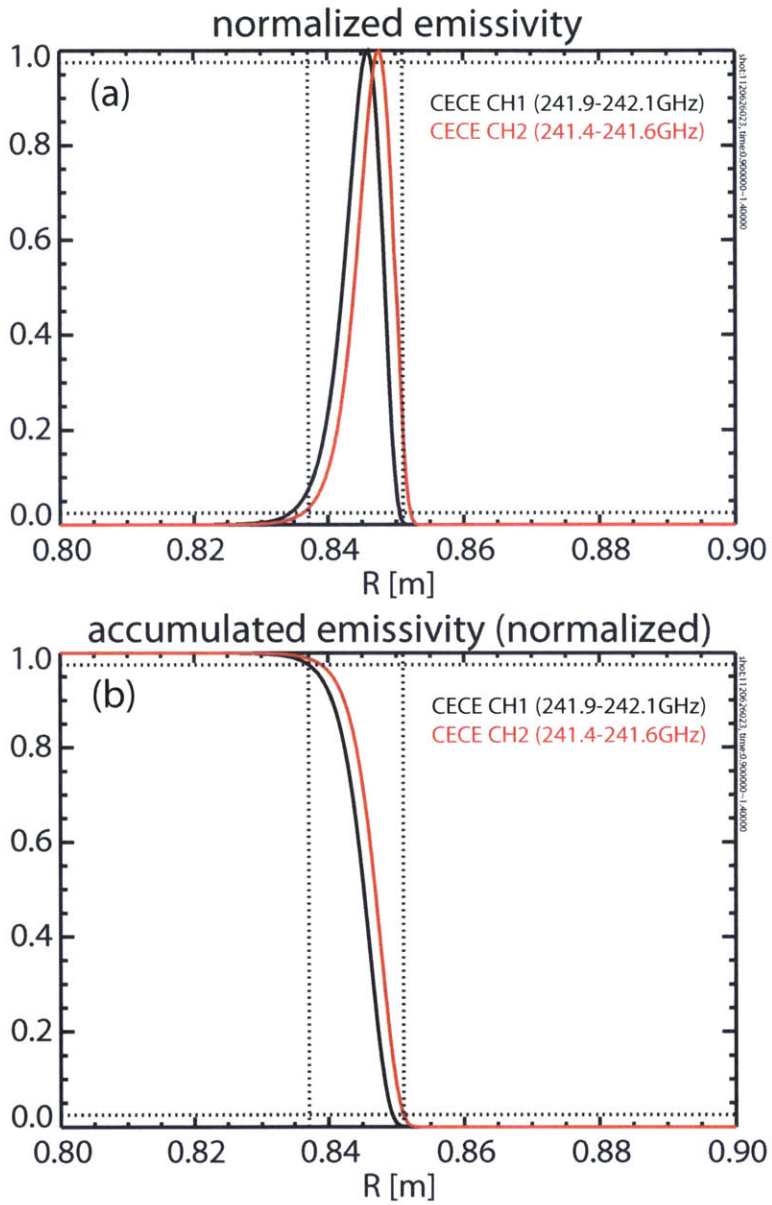

Figure 2-14: (a) Emissivity curves of 2 channels whose center frequencies are 241.5GHz and 242GHz, respectively, with 200MHz bandwidth for the shot 1120626023, t:0.9-1.4s. (b) Accumulated emissivity curve of these two channels. Vertical dot lines in (b) and (c) shows the position where accumulated emissivity of 241.5/242GHz channel is 97.5/2.5%, respectively.

	Radial width [cm] (both relativistic & Doppler from Eq. 2.28)	Radial width [cm] (only relativistic broadening from Eq. 2.29)
CECE CH1 (241-243GHz)	1.22	0.64
CECE CH2 (240.5-242.5GHz)	1.20	0.61
CECE measurements	1.39	0.81

Table 2.2: Radial broadening width of CECE ch1 (241-243GHz) and ch2 (240.5-242.5GHz) in shot 1120626023, t:0.9-1.4sec.

cross-correlation technique is required in the CECE measurements, two channels are used in these measurements. As an example, in the same discharge used in Fig. 2-13 and 2-14 (shot 1120626023), two channels whose center frequencies are 241.5GHz and 242GHz, respectively, are used for the CECE measurements. B_{IF}=200MHz for both channels, and they are about 0.2cm apart. The emissivity curves of these two channels in the shot 1120626023, t:0.9-1.4s are shown in Fig. 2-14(a). Then, the radial resolution of the CECE measurements can be calculated as the difference between radii where the accumulated intensity of the inner channel is 97.5% and the accumulated intensity of the outer channel is 2.5%, as shown in Fig. 2-14(b). Table 2.2 shows the radial broadening width of the two CECE channels used in the 1120626023, and the radial broadening width of the CECE measurements when these two channels are used. We can also see the radial broadening width when only relativistic broadening was considered. As you can see, the small deviation of observation angle from $\pi/2$ increases the radial broadening width almost 2 times compared to the case when observation angle is exactly $\pi/2$. Last, the radial wave number range for the CECE measurements in this example will be $k_r < 2\pi/d \simeq 4.5cm^{-1}$ with d=1.39cm. It is noteworthy that radial broadening width is a function of electron density and temperature. Thus, the width will vary with plasma conditions.

2.4 Tests for CECE diagnsotic

Before attempting to measure electron temperature fluctuations, we performed tests to see whether or not the CECE diagnostic works as a fluctuation diagnostic. The performed tests indicate that we can measure turbulent T_e fluctuations using this diagnostic, as shown in this section. It is first required to confirm that the CECE diagnostic is working as an ECE radiometer and that thermal noise will be decorrelated through the cross-correlation analysis since these conditions are necessary for the electron temperature fluctuation measurements. Several tests should be performed to confirm this. First, we need to check whether the receiver of the CECE diagnostic is working or not. The tests using the noise source in the laboratory was performed to verify the performance of the receiver. Second, if the receiver is working properly, the whole diagnostic system should be tested to verify the ability to measure the electron temperature as an ECE radiometer through the calibration of the CECE signal. We also need to verify the spectral decorrelation scheme with various filters

with different center frequencies. Last, it is possible that the crosstalk within the channels in the digitizer, i.e., interference between channels in the digitizer, results in coherent electronic noise between the CECE channels. Thus, the channels vulnerable to crosstalk or the pairs of channels interfering with each other should be found in a crosstalk test, and they should be avoided in the measurements. These tests were performed at the initial stage of the CECE diagnostic before the CECE receiver was upgraded to the 8ch receiver, so 4 channels with fixed frequency filters (B_{IF}=100MHz) were used for the tests in section 2.4.1-2.4.3. The tests in this section were performed without plasmas except for the calibration discussed in section 2.4.2. The plasmas used in the calibration test are the discharges performed on the run day 1120210, 1120214, 1120216 and 1120217.

2.4.1 IF section test in the laboratory

We first test the response of the IF section in the receiver using a noise source (346B by HP) whose noise temperature is about 0.86eV at 8GHz (from the given Excess Noise Ratio (ENR) = 15.26 at 8GHz). From Eq. 2.6, the power of the noise source at 8GHz is about 78.5dBm with B_{IF}=100MHz. This noise source is connected to the first amplifier instead of the antenna module including the mixer shown in Fig. 2-2. The IF filters used in each channel in this test are as follows: center frequency, f_c (GHz) : 8.0 (Ch1), 8.08 (Ch2), 8.5 (Ch3), 8.05 (Ch4), the center frequency of the detected second harmonic EC radiation, $f_{ce,2}$ [GHz]= 250-f_c. The block diagram of the test setup is shown in Fig. 2-15. It is noteworthy that the high pass filter discussed in section 2.3.2 was not added in this test setup since we measured the mean value of output voltage to check the response of the IF section using the oscilloscpe (TDS 2004B by Techtronics) in this test. To be specific, the response of the receiver with the noise source in this test refers to the change of the voltage signal in each channel by turning on/off the noise source using the oscilloscope.

We first check the response of each channel with the noise source, and then adjust the response of each channel to be similar by changing the gain of the video amplifier in each channel. The response of each channel after the adjustment is shown in Table 2.3. It is shown that the responses of the four channels are similar to within 10%. We also note that V_{off} is not zero, ~-80mV. In this test, V_{off} is the mean amplitude when the amplifiers including both video and IF amplifiers for 2-18GHz are on. From the V_{off} values, we can

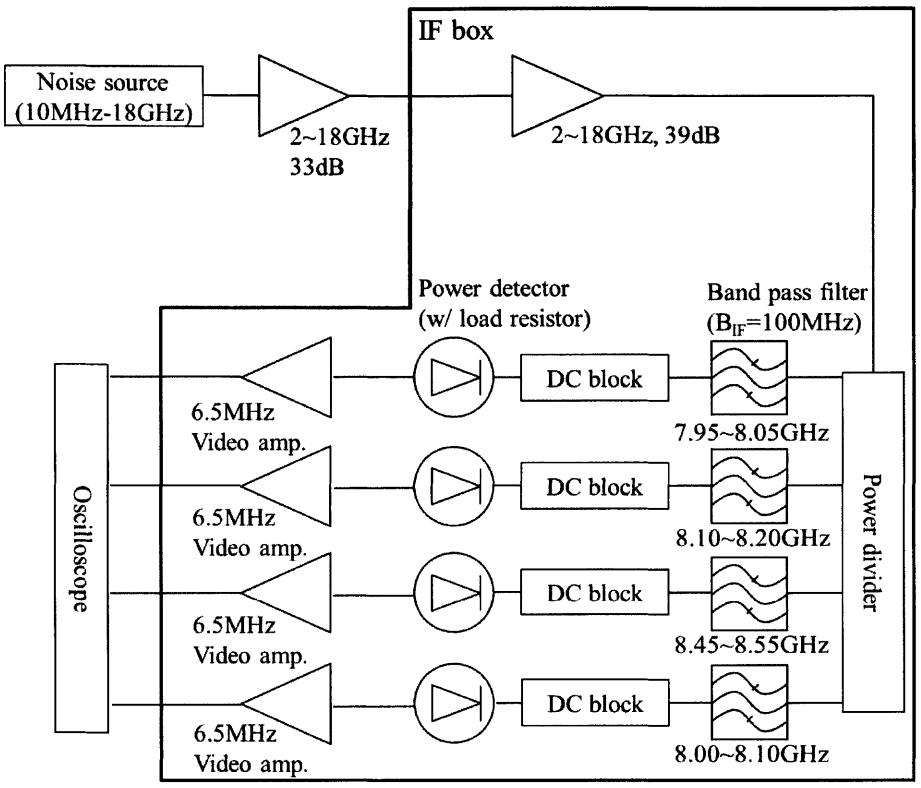

Figure 2-15: Block diagram of the receiver response test set-up

estimate the system noise temperature mentioned in section 2.1.2 using Y-factor method as shown in appendix C. The estimated noise temperature of the IF section in this test is less than 1eV. The estimated value can be varied with different responses by adding the attenuator, but the estimated values were at most 10eV in the various set-ups with different combinations of attenuator and amplifiers.

However, checking only the response of the receiver may not be sufficient to say that the receiver is working. Another critical part that should be checked is the linear response of the square-law detector. This test can be performed by adding an attenuator between two amplifiers in the set-up for the response test shown in Fig. 2-15. In this test, we used 3, 6 and 10dB attenuators. The changes in response of each channel, which are the voltage difference of each channel with different attenuations, are shown in Fig. 2-16. We can see that the response curves with different attenuators are linear for all 4 channels and that they are similar, which confirms the performance of the square-law detector.

Since the C-Mod experiments are usually performed for 8 hours (from 9:00 am to 5:00 pm) on normal runday, we need to check that the response of the receiver is stable with

	Ch1	Ch2	Ch3	Ch4
V_{off} [mV]	-82	-81	-85	-84
V_{on} [mV]	-1120	-1040	-1080	-1000
ΔV [mV]	1038	959	995	916

Table 2.3: The response of CECE channels with the noise source. V_{off} [mV] is the mean amplitude of each channel when the amplifiers including both amplifiers for 2-18GHz and video amplifiers are on, but the noise source is off. V_{on} [mV] is the mean amplitude of each channel when both amplifiers and the noise source are on. When both the amplifiers and the noise source are off, the mean amplitude was zero for all four channels. ΔV [mV] is the absolute value of the difference between V_{on} and V_{off}, $|V_{on} - V_{off}|$. The mean amplitude level in this test is the mean value from 128 samples measured by the oscilloscope.

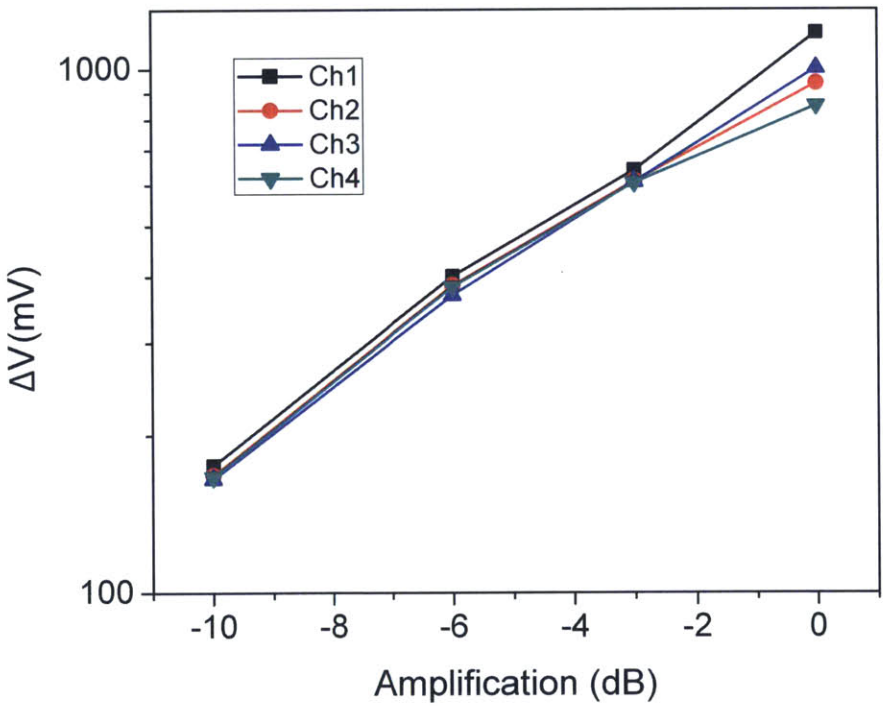

Figure 2-16: Detector response, ΔV [mV], defined in Fig. 2-15, with the various attenuations. In the figure, the horizontal axis is the amplification since the reference case is the test set-up without the attenuator. Then, the attenuator (3, 6 and 10dB) was used in each case. Thus, the amplification is -3, -6 and -10dB. Since the horizontal axis in Fig. 2-16 is in dB, the vertical axis is in log scale to observe the linear response.

operation time. If it is unstable, the main cause is likely to be insufficient cooling for the amplifiers. Although a heat sink is attached to the amplifier to prevent over-heating of the amplifier, it is possible that the heat sink used in the laboratory test is not enough for the amplifiers in real measurements for long operation times. If this is the case, the performance of the amplifier will keep degrading with time. Then, we will not obtain a meaningful signal, and we will need to find a more efficient cooling method for the amplifiers. In the laboratory, we checked the response of the IF section with noise source during 5 hours. Figure 2-17 shows the change of response with the operation time compared to the initial response. We can see that the response degrades for approximately the first thirty minutes, but after thirty minutes, the response is saturated around 75-80% level of the initial response in all four channels. This test result indicates the performance of the IF section will be stable once the CECE receiver is turned on about 30 minutes before the C-Mod experiment is started.

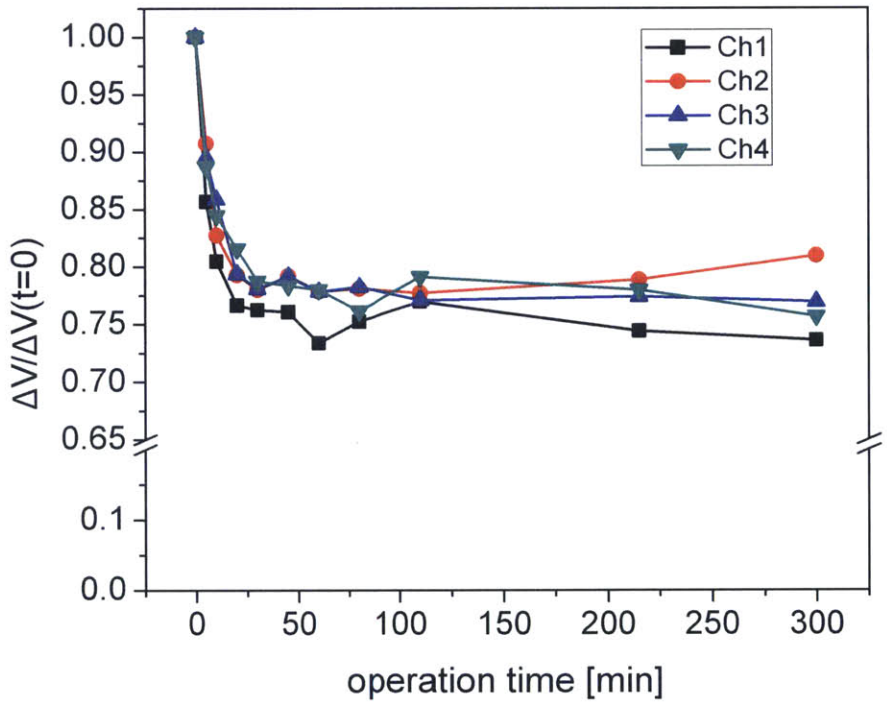

Figure 2-17: The ratio of detector response, ΔV [mV], defined in Fig. 2-15, to the initial ΔV [mV] (t=0) with the operation time (from 0 to 300 minutes)

So far, this section has verified the performance of the IF section of the receiver, including the response with input power, linear output resoponse with changes in input, and stable

response with operation time. It is noteworthy that the performance of the high pass filter was not verified in these tests. The passive high pass filter was initially designed with cutoff frequency, f_{cutoff}=100Hz with a 1M ohm resistor and a 1.5nF capacitor [112]. The response of the high pass filter with frequency was checked using a function generator (33210A by Agilent). As shown in Fig. 4-8 in [112], the response curve of high pass filters used in the measurements are almost identical, and the response of one of them is shown in Fig. 2-18(a). We can see that the cutoff frequency is near 100Hz as designed.

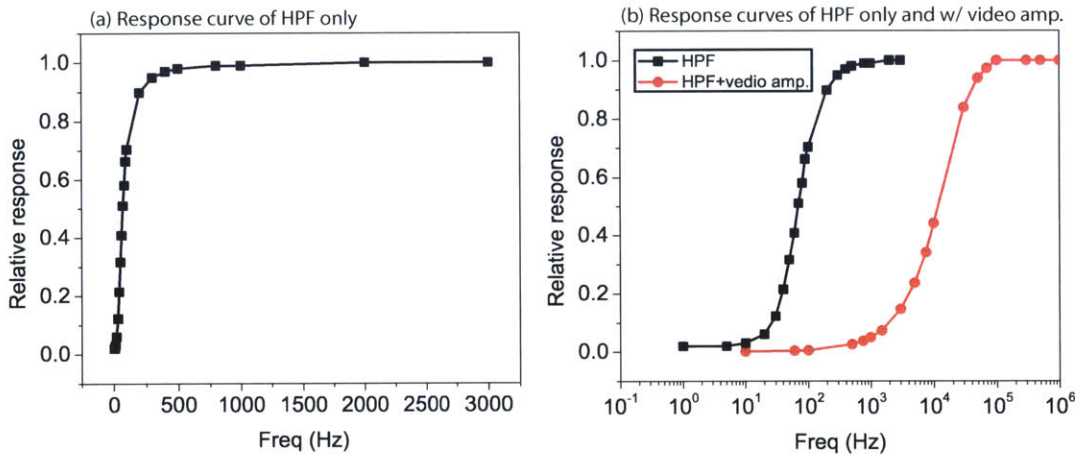

Figure 2-18: The relative response curve of a high pass filter used in the IF section. Vertical axis indicates the relative response normalized to the maximum value of outputs with frequency. (a) The relative response curve of the high pass filter only (b) The comparison of the relative response curves between the case using the high pass filter only (black line with the square points) and the case using the high pass filter connected to the video amplifiers (red line with the circle points)

However, the high pass filter is added before the video amplifier to use the given dynamic range of the video amplifier. Thus, the actual response of high pass filtering should be checked from the high pass filter connected with the video amplifier. To be specific, the output of video amplifier whose input is connected to the high pass filter should be measured for the actual response. The red line in Fig. 2-18(b) shows the response curve from the high pass filter connected with the video amplifier. It is shown that the cutoff frequency increases significantly from ~100Hz to ~10kHz. The impedance coupling with the video amplifier, whose input impedance is 4.7k ohm, may result in the increase of cutoff frequency of filtering. Although fluctuation measurements in this study, which are usually spread higher than 10kHz due to the Doppler effect, were not limited by the high pass filtering shown as the red

curve in Fig. 2-18(b), it should be improved in the future to study relatively low frequency fluctuations ($f < 10kHz$).

2.4.2 Calibration of CECE

In section 2.4.1, the IF section of the receiver was tested. The integrated system including the IF and RF section and the optical system should be tested to confirm that the CECE diagnostic is working properly as an ECE radiometer for electron temperature measurements before turbulence measurements are attempted. This verification was obtained through the calibration of CECE signals using other ECE diagnostics in Alcator C-Mod. In this section, the data from CECE in C-Mod was cross-calibrated to the independent profile ECE radiometer diagnostic in C-Mod (FRCECE), which has 32 channels [31].

The IF filters used in the calibration test are identical to the filters used in the test in section 2.4.1 (center frequency, f_c (GHz) : 8.0 (Ch1), 8.08 (Ch2), 8.5 (Ch3), 8.05 (Ch4), the center frequency of the detected second harmonic EC radiation, $f_{ce,2}$ [GHz]= 250-f_c). For the calibration, C-Mod discharges from four run days (1120210, 1120214, 1120216, 1120217) were used for Ch2-4. The digitizer for O-mode reflectometry [46] (sampling rate : 2Ms/s) was used in this calibration. At that time, the digitizer for the CECE diagnostic was still being tested and not used for the CECE signals. Three run days all, except for 1120216, were used for the calibration of Ch1 because Ch1 was not connected to reflectometry's digitizer on run day 1120216 to test the digitizer for the CECE diagnostic. In the calibration, the amplitudes of the signals in the CECE diagnostic were compared with the amplitude of Ch4 in FRCECE (f_c=241.5GHz, B_{IF}=1.5GHz). From the spectral range of the detected radiation in Ch4 in the FRCECE diagnostic (f:240.75-242.25 GHz), which includes the spectral range of all four channels in the CECE (f:241.45GHz-242.05GHz), we think the measured temperature should be the same. In each run day, we obtained the amplitude of all CECE channels and FRCECE ch4 at t=1.0 sec. Figure 2-19 shows that the amplitude of the CECE signal is linearly proportional to the amplitude of FRCECE Ch4 in all CECE channels (Ch1-4). From the linear fitting line, we obtained a calibration factor, mainly the slope of the linear fitting line with a small offset. Although most data points in Fig. 2-19 are T_e <1keV measured by FRCECE Ch4, Fig. 2-19(b)-(d) shows that the point near 4keV is still near the linear fitting line for the calibration, indicating the calibration is valid up to 4keV for Ch2-4.

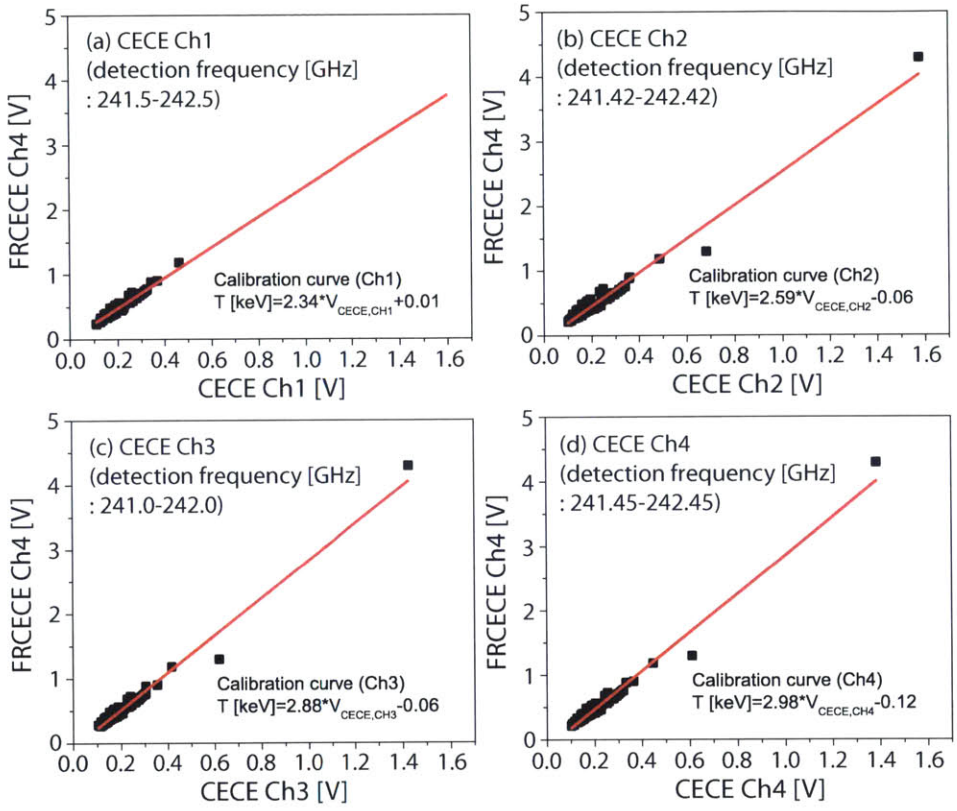

Figure 2-19: Amplitude of FRCECE Ch4 (dectected frequency of EC radiation, f, : 240.75-242.25GHz) with the amplitude of CECE channels (a) Ch1 (f : 241.5-242.5GHz) (b) Ch2 (f : 241.42-242.42GHz) (c) Ch3 (f : 241.0-242.0GHz) (d) Ch4 (f : 241.45-242.45GHz). The red solid line in each figure is the calibration curve obtained by the linear fit.

Considering the similar response of Ch1, the calibration will be also valid up to T_e ~4keV in Ch1 as well. As shown in Fig. 2-19, the calibration factor of 2-3keV/V for each channel was obtained. This value are close to the independently estimated calibration factors obtained in laboratory tests in Appendix D.

The cross-calibrated CECE data were compared to other temperature measurements (Grating Polychromator (GPC)[115] and Thomson Scattering[84] diagnostics). Figure 2-20 shows the comparison of the cross-calibrated temperature measured by CECE channels (Ch1-4) with other diagnostics for one C-Mod discharge (shot : 1120221014). For a clear comparison, all CECE signanls are digitally low pass filtered up to 10kHz. As shown in Fig. 2-20, the electron temperature of CECE diagnostic agrees well with the other temperature

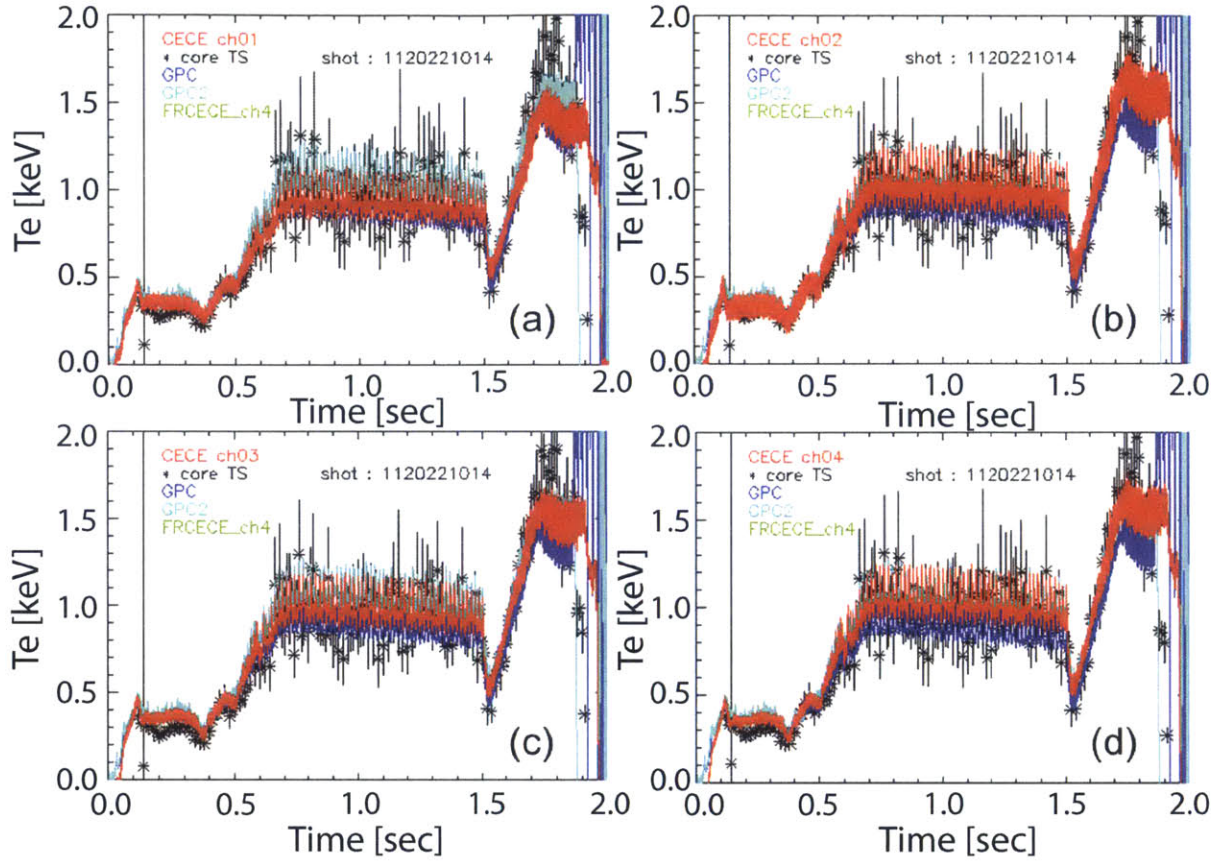

Figure 2-20: Comparison of the cross-calibrated CECE channels with other diagnostics (GPC, GPC2, FRC-ECE and core Thomson scattering) in the C-Mod discharge (shot : 1120221014). CECE signals are low pass fitler up to10kHz.

diagnostics in C-Mod within the uncertainties, which verifies the CECE diagnostic is working properly as an ECE radiometer.

2.4.3 Decorrelation test

The spectral decorrelation can be verified in the laboratory from the test using the noise source. We first use four CECE channels with the following IF filters : center frequency, f_c (GHz) : 8.0 (Ch1), 8.05 (Ch2), 8.08 (Ch3), 8.15 (Ch4) with B_{IF}=100MHz. In this test, we will compare the correlation curve (cross correlation coefficient, C_{xy} with lag time) for the three different pairs of channels as shown in Fig. 2-21. It is shown that the measured frequency bands in the first pair (8.0GHz and 8.05GHz or Ch1 and Ch2) and the second pair (8.0GHz and 8.08GHz or Ch1 and Ch3) are partially overlapped. Thus, the thermal noise

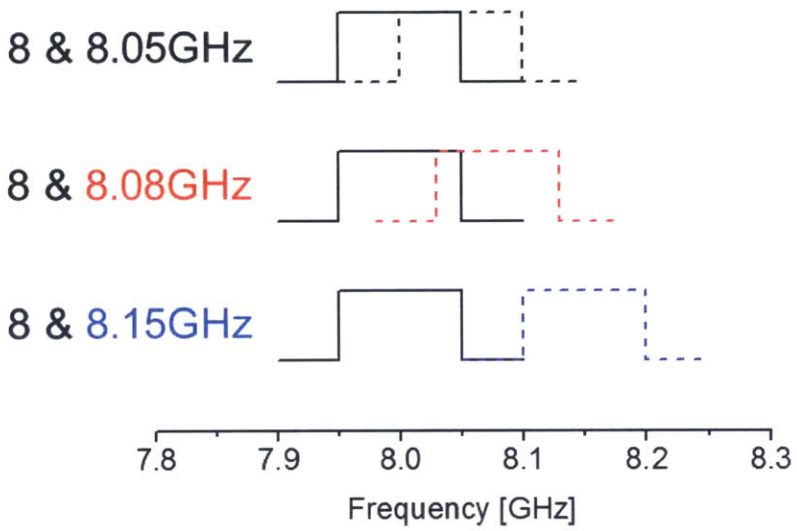

Figure 2-21: The pairs of filters used in the decorrelation test.

will be partially coherent in these two pairs. In the third pair (8.0GHz and 8.15GHz or Ch1 and Ch4), the two channels are separate in the frequency space. Thus, the thermal noise in the two channels in the third pair will be incoherent, and it will be possible to eliminate them through cross correlation analysis.

As expected, the $C_{xy}(0)$ value decreases as the overlapped frequency band is reduced, and is near zero when the two channels are separate in the frequency space as shown in Fig. 2-22(a). We also notice that the width of the correlation curve does not change. The width of the correlation curve indicates the correlation time of the noise. In this test, the correlation time of the coherent thermal noise is determined by the video bandwidth, B_{vid}, which is the same among the pairs used in this test.

In order to see the change of $C_{xy}(0)$ with the changes in the seperation of filters in the frequency space more deeply, we added other pairs of filters with different seperations in terms of the difference in the center frequencies between two filters, Δf such as Δf=0.03, 0.08, 0.1, 0.35, 0.42 and 0.5 GHz. The result is shown in Fig. 2-22(b). It is shown that $C_{xy}(0)$ decreases with an increase of Δf, and $C_{xy}(0)$ reaches around the statistical limit when $\Delta f > 100$MHz, which is the 3dB bandwidth of the filters used in this test. The results in Fig. 2-22 indicate that thermal noise in EC emission signal from CECE receiver can be

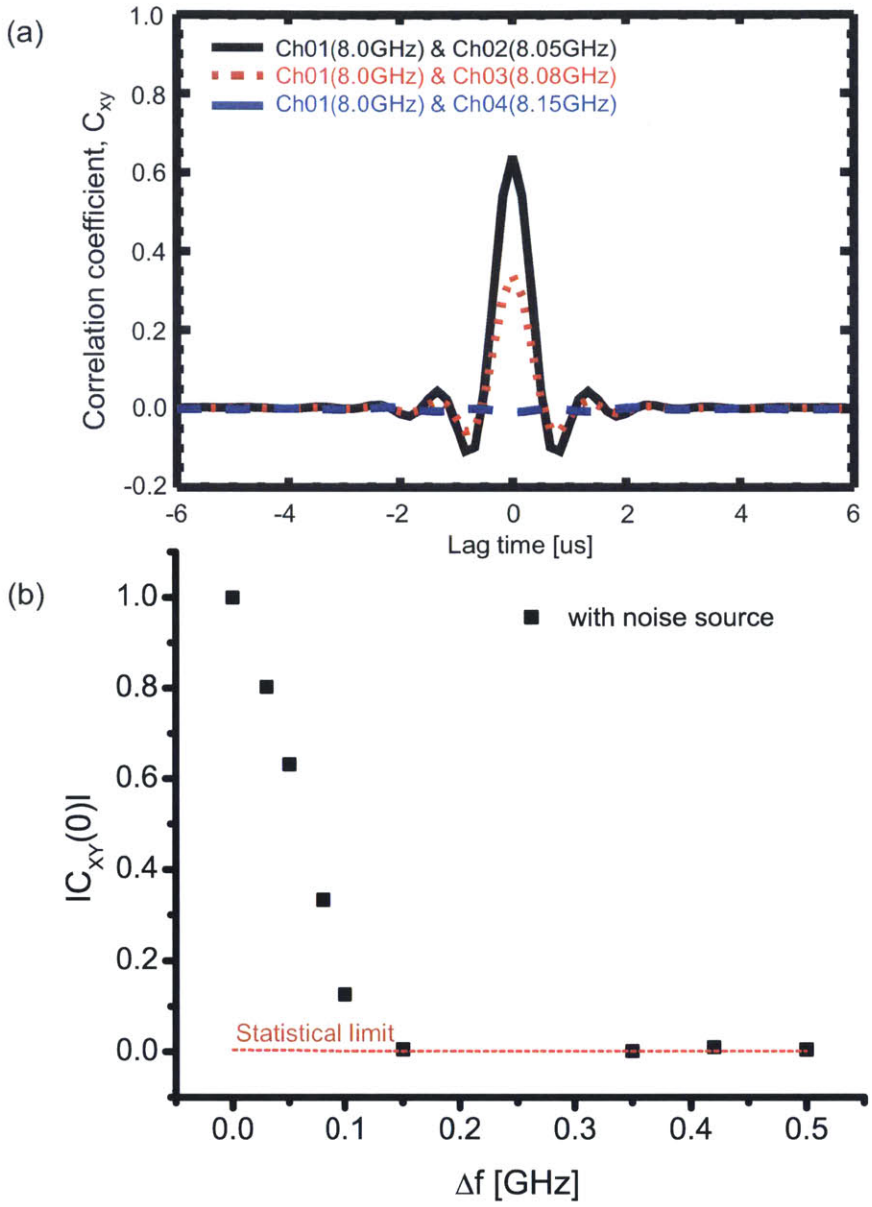

Figure 2-22: (a) Cross correlation coefficient, C_{xy} from CECE channels with noise source. Channel 01-04 have different IF filters (8-8.15GHz, BW=100MHz) (b) Absolute value of cross correlation coefficient at lag time=0 for different IF filter separations with statistical level. The uncertainty of $C_{xy}(0)$ given in [17] was used as the statistical limit.

removed by using spectral decorrelation techniques.

2.4.4 Crosstalk test

A crosstalk test was performed to identify any pairs of channels that we should be cautious to apply the correlation technique to due to the interference between them. The test procedure is as follows. A sine wave with a specific frequency, f_{in}, generated by a Function generator (33210A by Agilent), is connected to only one channel in the digitizer, and other channels are not connected to any devices. Then, the amplitude of the signal in the connected channel at $f = f_c$ is compared with the amplitude of other channels. From the ratio of the magnitude of the un-connected channel to the magnitude of the connected channel at $f = f_{in}$, we determine the interference from the connected channel to the unconnected channel. The magnitude of each channel at $f = f_{in}$ was calculated from the ensemble-averaged FFT with the number of data points in one FFT, nfft, =16384 and the number of time slice used in the averaging =124. The criteria for the weak interference set in this test was set to the amplitude ratio larger than 0.01% , the criteria for the strong interference is 0.025%. When the electron temperature fluctuation level is about 0.5%, the weak interference (0.01-0.025%) will affect more than 2 % in the fluctuation measurements, and strong interference (>0.025%) will affect more than 5%. The peak to peak voltage of input signal was set to $1V_{pp}$ and, 10kHz and 500kHz were used as the input frequencies in the test. Table 2.4 and 2.5 show the vulnerable channels to crosstalk from each input channel when f_{in}=10kHz and 500kHz, respectively.

From Table 2.4 and 2.5, we first notice that crosstalk is frequency dependent. It gets stronger as the frequency increases, which indicates capacitive coupling between channels as expected. From the gyrokinetic simulations in section 2.2.3, the frequency of interest in most experiments will be up to near 500kHz. Thus, 500kHz will be proper as the input frequency, f_{in} to determine the crosstalk and bad channels from this test. Table 2.5 shows Ch8 interfered with several channels (Ch4, 7, 10, 12, 13, 14), Thus, we may need to avoid using Ch8 in the measurements. We also note that Ch1 and Ch7 are cross-talked. Thus, these two channels should not be used at the same time. The channels which are not interfered with or interfered with less than the criteria when Ch7 and 8 are not used are Ch1, 2, 3, 4, 5, 6, 11, 12, 15, 16. In the measurements, we used these 10 channels for the

Input channel	vulnerable channels to crosstalk		
	1^{st} trial	2^{nd} trial	3^{rd} trial
1	none	none	none
2	none	none	none
3	none	none	none
4	8 (0.014%)	8 (0.014%)	8 (0.014%)
5	none	none	none
6	none	none	none
7	8 (0.01%)	8 (0.01%)	8 (0.01%)
8	none	none	none
9	none	none	none
10	8 (0.014%)	8 (0.014%)	8 (0.014%)
11	none	none	none
12	8 (0.019%)	8 (0.018%)	8 (0.019%)
13	8 (0.012%)	8 (0.012%)	8 (0.013%)
14	8 (0.013%)	8 (0.013%)	8 (0.014%)
15	none	none	none
16	none	none	none

Table 2.4: The vulnerable channels to crosstalk (the channels whose output signals are affected by the output of the input channel connected to the function generator) at f_{in}=10kHz. For the interference channel, the ratio of amplitude of the interference channel with the input channel at $f = f_{in}$ was shown in parenthesis.

Input channel	The vulnerable channels to crosstalk		
	1^{st} trial	2^{nd} trial	3^{rd} trial
1	**7 (0.025%)**	7 (0.024%)	**7 (0.025%)**
2	none	none	none
3	9 (0.019%)	9 (0.018%)	9 (0.018%)
4	8 (0.015%) 13 (0.015%)	8 (0.015%) 13 (0.015%)	8 (0.014%) 13 (0.015%)
5	10 (0.015%)	10 (0.015%)	10 (0.015%)
6	14 (0.017%)	14 (0.017%)	14 (0.017%)
7	**1 (0.026%)** 8 (0.01%)	**1 (0.026%)** 8 (0.011%)	**1 (0.026%)** 8 (0.011%)
8	2 (0.011%)	2 (0.011%)	2 (0.011%)
9	3 (0.022%)	3 (0.022%)	3 (0.022%)
10	5 (0.019%) 8 (0.013%)	5 (0.019%) 8 (0.013%)	5 (0.020%) 8 (0.013%)
11	none	none	none
12	8 (0.018%)	8 (0.018%)	8 (0.018%)
13	4 (0.019%) 8 (0.013%)	4 (0.019%) 8 (0.012%)	4 (0.020%) 8 (0.013%)
14	6 (0.016%) 8 (0.013%)	6 (0.017%) 8 (0.013%)	6 (0.016%) 8 (0.014%)
15	none	none	none
16	none	none	none

Table 2.5: The vulnerable channels to crosstalk (the channel whose output signals are affected by the output of the input channel connected to the function generator) at f_{in}=500kHz. For the interference channel, the ratio of amplitude of the interference channel with the input channel at $f = f_{in}$ was shown in parenthesis. The strong interference case is shown as bold.

8 ch CECE diagnostic with 2 channels to store the voltage signal used to control the YIG filters remotely.

2.5 Summary

In this chapter, we discussed the CECE diagnostic in C-Mod. An ECE diagnostic is a useful diagnostic for electron temperature measurements because of the well-defined emission position of the EC radiation and its passiveness in the measurements. However, the sensitivity level of the ECE radiometer mainly due to the intrinsic thermal noise is not enough to measure the small amplitude electron temperature fluctuations induced by turbulence. Cross correlation analysis of two ECE channels can be used to resolve the electron temperature fluctuations by eliminating incoherent thermal noise in these two channels. The ECE radiometer which is optimized for the cross correlation technique used to resolve the electron temperature fluctuations is the Correlation ECE diagnostic. In the past, the cross correlation technique was applied to resolve the temperature fluctuations in the ECE radiometer in C-Mod, but no fluctuations above the statistical limit were resolved [168]. Gyrokinetic analysis using GYRO suggested the poloidal resolution was not enough to resolve the fluctuations in C-Mod.

A new CECE diagnostic was designed and built based on the constraints obtained from the gyrokinetic simulations. This diagnostic has two main parts, the optical system and the receiver. The optical system detects the second harmonic X-mode EC radiation on the low-field side because of the accessibility. In order to achieve the high poloidal resolution, the optical system was designed to have the beam diameter close to or less than 1cm. The optical system was also designed to modify the beam pattern by changing the ex-vessel module with the same in-vessel optics. Because of the required high poloidal resolution and spatial constraints, the spectral decorrelation scheme was used. The sensitivity level given in Eq. 2.12 should be as low as possible, but decreasing the sensitivity level by increasing the IF bandwidth, B_{IF}, or decreasing the video bandwidth, B_{vid}, is limited by the required resolution and condition for the turbulence measurements. From gyrokinetic analysis results, these parameters were limited as B_{IF} $\leq$250MHz and B_{vid} $\geq$0.5MHz for the turbulence measurements.

Before attempting the turbulence measurements, we verified the performance of the

receiver and the spectral decorrelation scheme from a laboratory test. We also checked the crosstalk in the digitizer and found proper pairs of channels we can used for the CECE diagnostic. After the diagnostic was installed, the CECE signals were cross-calibrated by the ECE radiometer [31]. Through the calibration, we confirmed that the CECE diagnostic is working as an ECE radiometer for electron temperature measurements.

After we confirmed that this diagnostic works properly as an ECE radiometer, we upgraded the system for turbulence measurements. The optical system is optimized for measurements near the edge region (ρ ~0.8), and a high pass filter was added to remove the DC signal and use the full dynamic range of the video amplifier and digitizer. In order to obtain the low sensitivity level, B_{IF} was set to 200MHz and B_{vid} was set to 0.5MHz in most measurements. After upgrades, the poloidal resolution of the CECE diagnostic was $k_\theta \leq 9.8cm^{-1}$ and the sensitivity level was about 0.3% with the averaging time, Δt=0.5 sec. As a result, the electron temperature fluctuations near the edge ($\rho \sim 0.8$) were resolved in Alcator C-Mod plasmas. The optical system was modified to extend the measurement region deeper into the core. It was successful, but the measurement region was limited to $\rho > 0.7$. Nevertheless, this result, extending the measurement region with the modified optics, indicates that the high poloidal resolution is critical in the electron temperature fluctuation measurements in Alcator C-Mod as predicted by the gyrokinetic simulation. In the following sections, it will be discussed how the measured fluctuations are analyzed (Chapter 3) and the physics results obtained from the measurements (Chapter 4-6).

Chapter 3

Transport analysis method

This chapter introduces the transport analysis methods used in this study. They are the turbulence measurements mainly by CECE (section 3.1), profile analysis (section 3.2), experimental transport analysis (section 3.3) and gyrokinetic analysis (section 3.4). Each method will be explained in a section of this chapter. However, we need to note that these four approaches are connected, not independent of one another.

The first approach is to observe microscopic changes in turbulence, mainly electron temperature fluctuations measured by the CECE introduced in Chapter 2. As explained in Chapter 1, turbulence is a strong candidate for anomalous transport, and studying the changes in turbulence with different discharge conditions will elucidate the physics related to anomalous transport. The analysis used to study changes in electron temperature fluctuations using CECE is discussed in section 3.1.

The second approach we used is to study changes of macroscopic profiles such as temperature, density and rotation. The change of profiles are the result of confinement and transport in the plasma. External heating and particle flux will also affect the profiles. At the same time, as shown in Chapter 1, the characteristics of profiles such as the gradient scale length and collision frequency affect turbulence and transport. In order to study how the profiles affect the turbulence, we first need to analyze the profiles and to estimate the parameters relevant to turbulence such as gradient scale length, the ratio of electron and ion temperatures and collision frequency. Using the results from this analysis, we may predict the characteristics of turbulence in the plasma. However, this prediction will not be accurate since various parameters can affect the turbulent transport. More sophisticated prediction

can be performed by using gyrokinetic simulations with experimental profiles as input, which is the fourth approach which will be discussed in section 3.4. The gyrokinetic simulation code, GYRO [28] was used in this study. As preparation for the simulation, profile analysis, including fitting the profile and the estimation of the uncertainty, should be performed on the experimental data. The profile analysis for this purpose is explained in section 3.2.1. We also performed the self-similarity analysis by applying the method used in TCV [142] to see how the turbulence affects the profiles. This analysis method is explained in section 3.2.2.

Characteristics of transport such as heat flux and diffusivity can be obtained from power balance analysis using the experimental profiles and the measured quantities required for the power balance analysis, such as total heating power, plasma current and so on. Power balance analysis was performed by using the code TRANSP [4]. TRANSP is an experimental transport code which solves not only power and particle balance equations, but also the quantities or profiles which are not measured feasibly in the experiments such as RF and Ohmic heating profiles. The profile analyzed in section 3.2.1 is also used as the input profile for TRANSP. It is noteworthy that TRANSP is also used to prepare the GYRO input profiles that are not directly measured in the experiment, such as the ExB velocity and the ExB shearing rate. The experimental transport analysis using TRANSP including the prepartion of GYRO input profiles is explained in section 3.3.

Lastly, section 3.4 will describe gyrokinetic simulations using the GYRO code, including the code itself and the simulation set-up used in this study. Gyrokinetic simulations including GYRO are sophisticated prediction tools for the transport induced by turbulence. Thus, we can use it as an interpretation tool for the observed or analyzed fluctuations or transport behavior in the experiments. However, the validation studies for these gyrokinetic simulations are still in progress as mentioned in Chapter 1. Thus, we need to not only study the characteristics of turbulence given by GYRO but also validate the results from GYRO by comparing them with the measured fluctuations explained in section 3.1 and the experimental transport parameters explained in section 3.3. For the comparison of the electron temperature fluctuations between the simulation and the measurements, the post processing is required to consider the experimental conditions related to the measurements [22, 73]. The model used in the post processing is called the synthetic diagnostic. The synthetic CECE diagnostic used for the comparison of the CECE measurements with the GYRO results is

explained in section 3.4.4.

3.1 CECE signal analysis

3.1.1 T_e fluctuation level calculation

This subsection will explain how T_e fluctuation level is calculated from the CECE measurements in this study. We can calculate the electron temperature fluctuation level from either the correlation coefficient, C_{xy}, as performed in [141], or the cross power spectrum, $G_{xy}(f)$, as performed in [37].

The cross correlation coefficient (C_{xy}) is defined as [17],

$$C_{xy}(\tau) = \frac{R_{xy}(\tau)}{\sqrt{R_{xx}(0)R_{yy}(0)}} \tag{3.1}$$

where τ is the lag time, $R_{xx}(0)$ and $R_{yy}(0)$ are the auto correlation functions of each signal when lag time, τ, is equal to 0, and $R_{xy}(\tau)$ is a cross correlation function of the two signals, and are written as follows [17].

$$R_{xx}(\tau) = \frac{1}{T}\int_0^T x(t)x(t+\tau)\mathrm{d}t \tag{3.2}$$

$$R_{yy}(\tau) = \frac{1}{T}\int_0^T y(t)y(t+\tau)\mathrm{d}t \tag{3.3}$$

$$R_{xy}(\tau) = \frac{1}{T}\int_0^T x(t)y(t+\tau)\mathrm{d}t \tag{3.4}$$

If two CECE signals have coherent temperature fluctuations and incoherent thermal (random) noise, $R_{xy}(0)$ will be proportional to the amplitude of time-averaged electron temperature fluctuations, and we can obtain the relative temperature fluctuation level ($\tilde{T_e}/T_e$) from the $C_{xy}(0)$ value (see Appendix E).

We can also observe electron temperature fluctuations using the cross spectral density function ($G_{xy}(f)$) or the coherence ($\gamma_{xy}(f)$) spectrum. The coherence (γ_{xy}) is defined as [17],

$$\gamma_{xy}(f) = \sqrt{\frac{|G_{xy}(f)|^2}{G_{xx}(f)G_{yy}(f)}} \tag{3.5}$$

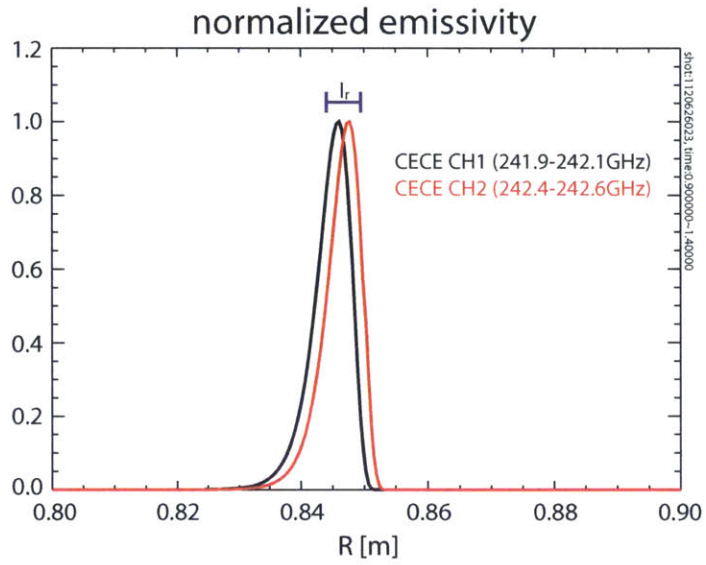

Figure 3-1: Normalized emissivity curves of 2 channels whose center frequencies are 241.5GHz and 242GHz, respectively, with 200MHz bandwidth for one C-Mod discharge (shot 1120626023, t:0.9-1.4s). The purple horizontal line above the emissivity curve indicates the typical radial correlation length of turbulence, l_r, estimated in Chapter 2 via gyrokinetic simulations (GYRO).

where the $G_{xx}(f)$ and $G_{yy}(f)$ are auto spectral density functions for signals x(t) and y(t), and $G_{xy}(f)$ is a cross spectral density function of the two signals.

The meaningful turbulence features will be coherent, and will be larger than the statistical limit of coherence, which is taken to be the standard deviation of the coherence [17]. We can determine the amplitude of the coherent fluctuations by integrating the cross spectral density function ($G_{xy}(f)$) in the frequency range where we observe fluctuations above the statistical limit. Since parasitic noise can also lead to coherent fluctuations above the statistical limit, we need another tool to determine whether or not the coherent fluctuations are real turbulent fluctuations. The cross phase angle (θ_{xy}) can be a tool for this. The cross phase angle (θ_{xy}) is defined as [17],

$$\theta_{xy}(f) = \tan^{-1} \frac{Q_{xy}(f)}{C_{xy}(f)} \tag{3.6}$$

where $G_{xy}(f) = C_{xy}(f) - jQ_{xy}(f)$.

In the CECE measurements in C-Mod, two channels are usually separated by 0.3-0.5GHz, which corresponds to 0.1-0.2cm, but the radial linewidth of the EC emission is about 1cm as

estimated in section 2.3.3. As shown in Fig. 3-1, this implies that the emission volumes of the two channels are significantly overlapped in physical space. Since the emission volumes of the two CECE signals used for cross-correlation in C-Mod are mostly overlapped, real turbulent fluctuations from the two signals are likely to be in phase and will not have a random phase relation. In contrast, parasitic noise from two signals does not necessarily have a fixed phase relation. That is, the cross phase between parasitic noise from two signals will vary randomly. Figure 3-2 shows an example. We can see the evident broadband fluctuations in f$\lesssim$170kHz in Fig. 3-2(a), but small peaks are also observed in f>200kHz. However, we can see the evident difference in cross phase spectrum in f$\lesssim$170kHz and the other region. The cross phase in f>200kHz varies randomly, which indicates the peaks in this region result from the coherent noise between the two signals, not from the coherent turbulent fluctuations in the plasma.

Thus, we can distinguish the real physical fluctuations from noise with more confidence by using both the coherence and cross phase spectrum. Once the frequency range is decided, then the temperature fluctuation, $\tilde{T}_e$, is,

$$\tilde{T}_e{}^2 = c_x c_y \int_{f_1}^{f_2} G_{xy}(f)\mathrm{d}f \tag{3.7}$$

where C_x and C_y are calibration factors for the two CECE signals, x(t) and y(t).

The T_e value will be proportional to the mean value of the signal. That is, $T_e = c_x\bar{x} \simeq c_y\bar{y}$, where $\bar{x}$ indicates the mean value of the signal, x(t). The second equality comes from the assumption that the electron temperatures from the two signals are almost same. As mentioned earlier in this section, the emission volumes of the two channels used in the CECE measurements separate radially much less than the radial broadening width of the measured EC emission. Thus, the two channels have almost same electron temperature. Then, the relative fluctuation level will be,

$$\frac{\tilde{T}_e}{T_e} = \sqrt{\frac{\int_{f_1}^{f_2} G_{xy}(f)\mathrm{d}f}{\bar{x}\bar{y}}} \tag{3.8}$$

It is noteworthy that the calibration factors, c_x and c_y, are cancelled out. Thus, we do not need to calibrate the CECE diagnostic for fluctuation measurements. In most measurements, CECE signals are high pass filtered as mentioned in section 2.3.2. Thus, it is not possible to

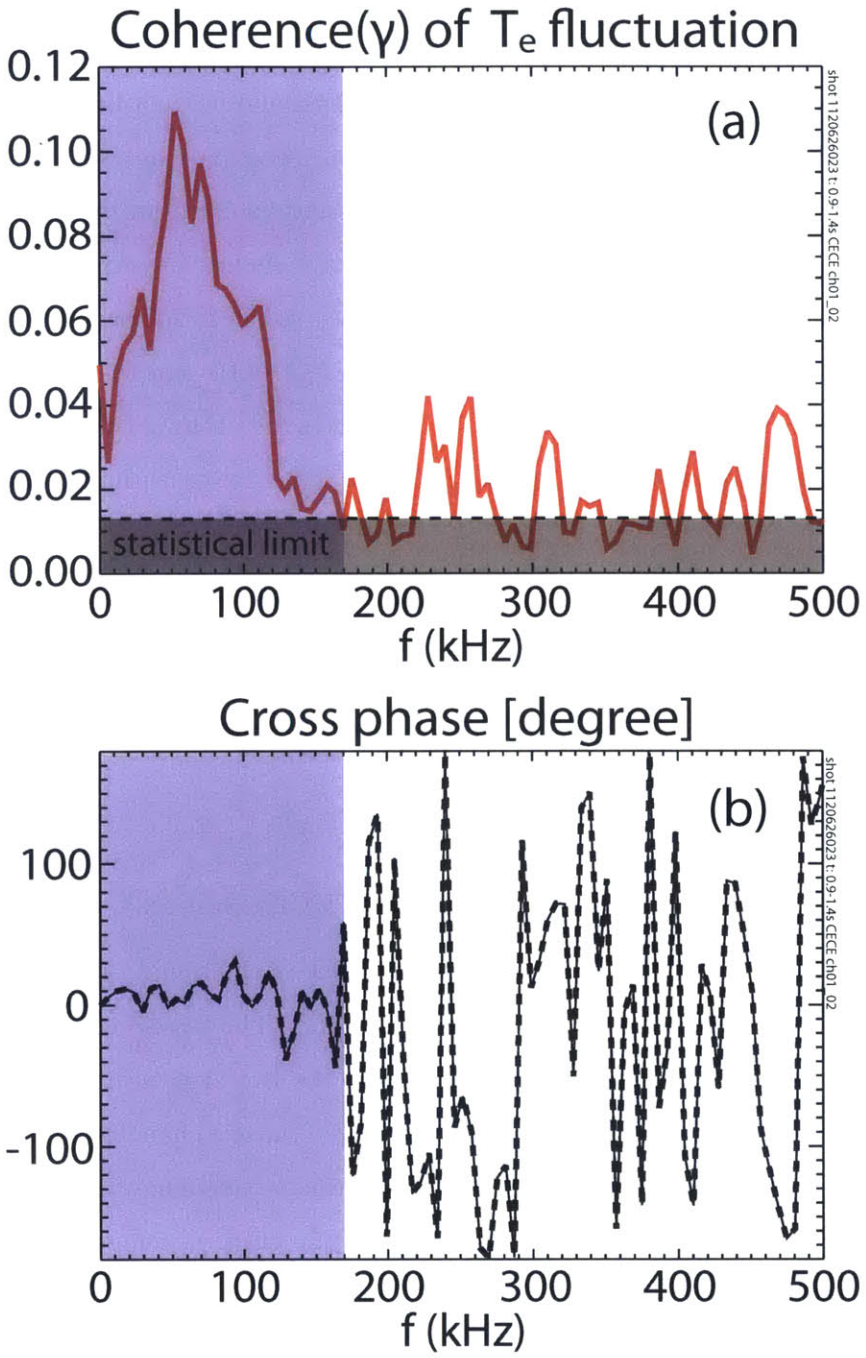

Figure 3-2: (a) Coherence (γ) and (b) cross phase spectrum of two CECE signals in one C-Mod discharge (shot:1120626023, t:0.9-1.4sec). Horizontal dotted line in (a) indicates the statistical limit of coherence, and the shaded area indicates the frequency range for the real turbulent electron temperature fluctuations.

measure the mean value of the signal directly. Instead, the radiometer formula (Eq. 2.7) can be used to estimate the mean value of the signal. The radiometer formula can be rewritten as follows.

$$\frac{\tilde{T}_{RMS}}{\bar{T}} = \frac{s.d.[x]}{\bar{x}} = \sqrt{\frac{2B_{vid}}{B_{IF}}} \tag{3.9}$$

where s.d.[x] is the standard deviation of x(t), which is the RMS deviation from the mean value.

We can then estimate the mean value of the signal from its standard deviaton if thermal (random) noise is dominant in the signal. Then, using Parseval's theorem [85], we can easily derive the relative electron temperature fluctuation level given as Eq. 3.10.

$$\frac{\tilde{T}_e}{T_e} = \sqrt{\frac{2B_{vid}T\int_{f_1}^{f_2}|G_{xy}(f)|\mathrm{d}f}{2B_{IF}[\int_0^\infty|X_T(f)|^2\mathrm{d}f\int_0^\infty|Y_T(f)|^2\mathrm{d}f]^{0.5}}} \tag{3.10}$$

where $[f_1, f_2]$ is the frequency range for cross spectral density integration, and $X_T(f)$ and $Y_T(f)$ are the Fourier transformed quantities during time length, T. The derivation of Eq. 3.10 is given in Appendix E.

In this study, we calculate the relative electron temperature fluctuation level from the coherence and the cross phase spectrum rather than from the cross correlation coefficient. This is because we can minimize the effect of the noise in the calculation of electron temperature fluctuations from coherence and cross phase spectrum by excluding them in the integration, while it is hard to exclude the effect of parasitic noise when the fluctuation level is calculated from $C_{xy}(0)$ as shown in Appendix B. However, we need to note that it is hard to resolve the turbulent fluctuations from noise in the cross power (or coherence) spectrum when the fluctuations are spread out in a wide frequency range with small amplitude, as discussed in [141]. There is also a subtlety in determining the frequency range of the turbulent fluctuations. The frequency range of the turbulent fluctuations is defined in this study as the region where the coherence values are larger than their uncertainty and the absolute value of the cross phase is smaller than $\pi/2$ without random fluctuations in the cross phase spectrum. However, the criteria for phase, smaller than $\pi/2$, is conservatively correct for the coherent fluctuations. A more rigorous approach should be used in the future.

Two error sources are considered to estimate the uncertainty of the fluctuation level

calculation, the random error from CECE radiometer's signal and the uncertainty of the IF bandwidth. The random error comes from the uncertainty of each point in G_{xy}, calculated from the given formula in [17]. In order to evaluate the uncertainty of the integrated value based on the uncertainty of each point, we first generated 100 G_{xy} spectra from the measured G_{xy} spectrum by varying points in G_{xy} randomly, but weighted by the uncertainty given in [17]. The fluctuation level of each randomly generated profile was then calculated, and the standard deviation of these fluctuation levels was considered to be the random error. The uncertainty of the IF bandwidth is set to 20%. The total error is calculated from error propagation of the two errors.

3.1.2 Caveats in CECE signal analysis

The contribution of density fluctuations

As briefly mentioned in section 2.1.1, density fluctuations can contribute to the measured fluctuations of the intensity of EC radiation. It is known that fluctuation signals in the CECE diagnostic can be contaminated by density fluctuations when the optical depth, τ, is low($\tau < 2$) for the second harmonic X-mode case, like in the CECE measurements in this study [124]. In order to avoid this density fluctuation effect, CECE signals whose optical depth, $\tau < 2$ at their cold resonance positions are excluded in this study. The contribution of density fluctuations to the fluctuations in CECE signals can be estimated from the equations given by [124],

$$\frac{< \tilde{I}_1 \tilde{I}_2^* >}{I^2} = (1+A)^2 \frac{\tilde{T}_e^2}{T_e^2} + A^2 \frac{\tilde{n}_e^2}{n_e^2} + 2A(1+A) \frac{Re < \tilde{T}_e \tilde{n}_e >}{T_e n_e} \tag{3.11}$$

where $A = \frac{\tau \exp(-\tau)}{1-\exp(-\tau)}(1 - \chi \frac{1-\exp(-\tau)}{1-\chi \exp(-\tau)})$, $I_{1,2}$ is the intensity of each CECE signal used in the correlation technique, and χ is the wall reflectivity with a typical value of ~ 0.8 for a metal wall facility like C-Mod.

From Eq. 3.11, it is required to know the relative density fluctuation level and phase between density and temperature fluctuations to estimate the contribution of density fluctuations to the measured radiation intensity fluctuations. When density fluctuations and temperature fluctuations are in phase or out of phase, the contribution of density fluctuations is maximum. In other words, the range of electron temperature fluctuations with a

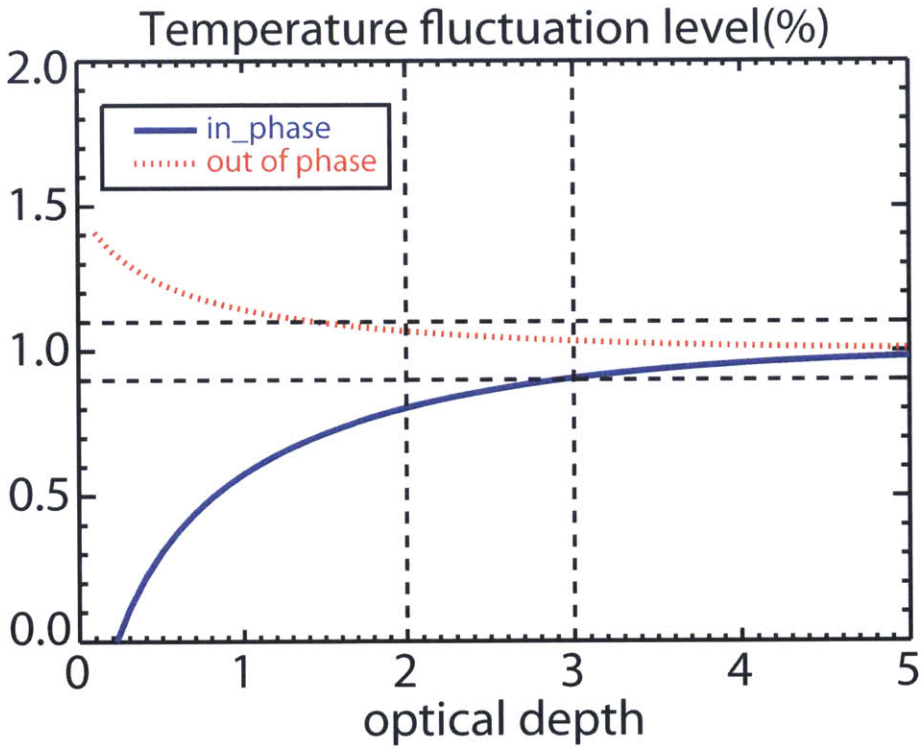

Figure 3-3: The upper and lower range of T_e fluctuations with the optical depth values when the measured fluctuation level of radiation's intensity is 1% and n_e fluctuation level is 2%. The horizontal dashed line indicates 10% boundary of the measured fluctuations, i.e., 0.9% and 1.1%.

given density fluctuation level will be as follows.

$$\frac{1}{1+A}[\frac{\tilde{I}}{I} - A\frac{\tilde{n}_e}{n_e}] \leq \frac{\tilde{T}_e^2}{T_e^2} \leq \frac{1}{1+A}[\frac{\tilde{I}}{I} + A\frac{\tilde{n}_e}{n_e}] \tag{3.12}$$

Figure 3-3 shows the upper and lower range of electron temperature fluctuations when the measured fluctuation level of the radiation's intensity is 1% and the electron density fluctuation level is 2%. The horizontal dashed lines indicate the 10% boundary of the measured fluctuation level. We can see that the contribution of density fluctuations is less than 10% when $\tau \geq 3$, and will be less than 20% when $\tau \geq 2$. Thus, $\tau \geq 3$ may be sufficient to approximate the fluctuations of the measured intensity as due to the temperature fluctuations, but $\tau \geq 2$ is somewhat marginal in the case shown in Fig. 3-3. It is noteworthy that the density fluctuation effect will be larger when the temperature fluctuation level is smaller or the density fluctuation level is larger. Although we do not measure the local density fluctuation level, it has been observed that the density fluctuation levels are comparable to the temperature fluctuation levels in tokamak plasmas [179]. We used this information to estimate the maximum contribution of density fluctuations. Since the maximum electron temperature fluctuation level observed in the 2012 C-Mod campaign was less than 2.0%, it is reasonable to assume the density fluctuation level is 2% to estimate the contributions of density fluctuations to the CECE measurements. The contribution of density fluctuations to the measured fluctuations should be considered in the signals from the $\tau = 2 - 3$ region, such as the measurements in Ohmic plasmas in Chapter 4.

Spectral analysis set-up

The standard spectral analysis technique described in [17] was used in the CECE signal analysis. In order to reduce the random error in auto and cross power spectral density functions (G_{xx} and G_{xy}), ensemble averaging is required, and it is desirable to use more sub-data sets in the averaging to reduce the random error. Thus, increasing total time length or decreasing the time length of each sub data set (or the number of points in each sub data set) will be helpful to reduce the random error. Increasing the total time length is limited by the steady time period of each discharge. In most C-Mod plasmas, it is less than 0.6 sec. If we decrease the time length of each sub data set, then the spectral resolution of the analysis will be worse since $\Delta f = 1/\Delta t_{ens}$, where Δt_{ens} is the time length of one sub data

set. Thus, decreasing the time length of each sub data set will be limited by the required spectral resolution. In the measurements, the spectral width of the measured broadband fluctuations was around 50-200kHz. Thus, a spectral resolution Δf of less than 10kHz will be desirable. In the measurements, Δf was set at around 6kHz (Δt_{ens} ~0.2 ms when the sampling rate is 6Ms/s) because most fluctuations in the coherence spectrum were resolved more clearly when $\Delta f \sim$ 6kHz rather than ~3kHz as shown Fig. 3-4. It is hard to resolve the broadband fluctuations in Fig. 3-4(a), where Δf ~3kHz, while the broadband fluctuations (70-170kHz) can be resolved as shown in Fig. 3-4(b), where Δf ~6kHz and the number of sub data sets used in the averaging is two times higher than (a), though the fluctuations are weak. This difference is mainly due to the lower coherence level of random or thermal noise achieved by increasing number of sub data sets used in the averaging. It is noteworthy that the structure around 300kHz in Fig. 3-4(b) is not considered to be the coherent fluctuations from the cross phase spectrum, not shown here, but which will be shown in Chapter 4.

As mentioned in section 2.3.2, a low pass filter (Butterworth filter with order, n=5 [27] was applied in the analysis to improve the sensitivity level given as Eq. 2.12. Using the low pass filter, we checked whether or not Eq. 3.9 is valid in these measurements in one C-Mod discharge (shot 1120502021,t=1.0-1.3 sec). We compared the ratio of standard deviation of the CECE signal to its mean value with the expected thermal noise level given by Eq. 3.9 as we varied the cutoff frequency of the low pass filter. In this discharge, the IF bandwidth was, B_{IF}=200MHz for Ch1 and 2, and B_{IF}=100MHz for Ch3 and 4. Without low pass filtering in post processing, B_{vid} is determined by the sampling rate of the digitizer (=10Ms/s), since the Nyquist frequency (5MHz) is smaller than the bandwidth of video amplifier (=6.5MHz). As shown in Table 3.1, the measured values are matched within 10% with the expected values from Eq. 3.9. This indicates two things. First, thermal noise is dominant in the CECE signals. Thus, we can estimate the mean value of the CECE signal from its variance or the sum of its Fourier transformed quantity (from Parseval's theorem). Second, the low pass filter used in this signal analysis works appropriately. In the spectral analysis for CECE signals, we also applied the notch filter and high pass filter to remove the parasitic noise when they are required as shown in Appendix B.

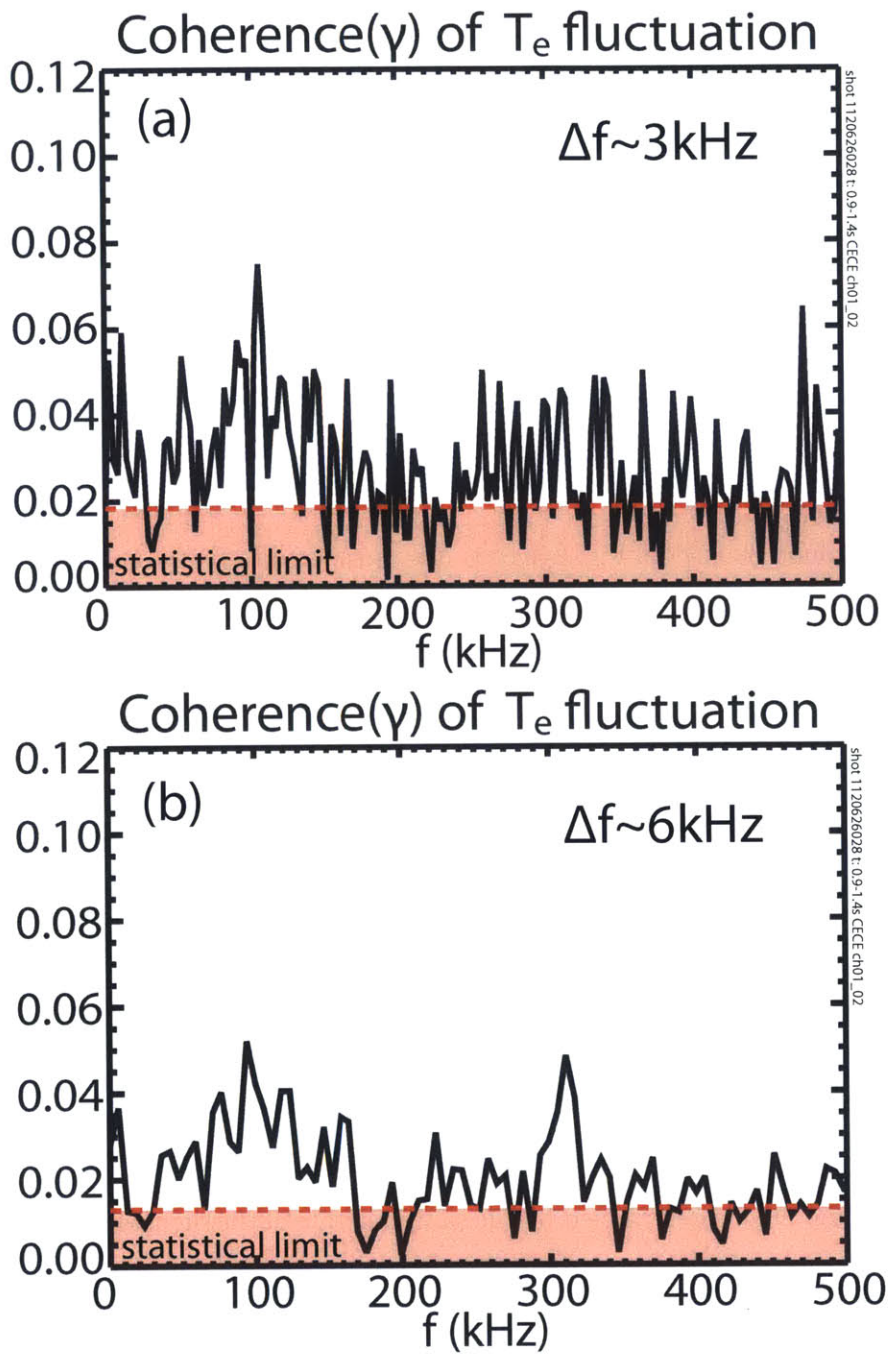

Figure 3-4: Coherence(γ) spectrum of two CECE signals in one C-Mod discharge (shot:1120626028, t:0.9-1.4sec) with different time lengths of one sub data set. (a) The time length of one sub data set, Δt_{ens} ~1ms, spectral resolution, Δf ~3kHz and the number points in one sub data set, n_{ens}=2048 (b) Δt_{ens} ~2ms, Δf ~6kHz and n_{ens}=1024

Channel (B_{IF})	B_{vid}	The mesured noise level	The expected noise level
Ch 1 (200MHz)	5MHz	0.22	0.22
	1MHz	0.096	0.10
	0.5MHz	0.070	0.071
Ch 2 (200MHz)	5MHz	0.21	0.22
	1MHz	0.092	0.10
	0.5MHz	0.067	0.071
Ch 3 (100MHz)	5MHz	0.30	0.32
	1MHz	0.13	0.14
	0.5MHz	0.094	0.10
Ch 4 (100MHz)	5MHz	0.31	0.32
	1MHz	0.13	0.14
	0.5MHz	0.096	0.10

Table 3.1: Comparison of the measured noise level, ratio of the standard deviation of the signal to its mean value, with the expected thermal noise level given Eq. 3.9 in one C-Mod discharge (shot 1120502021, t: 1.0-1.3sec)

3.2 Profile analysis

Although the data points and their uncertainties in the experimental profiles such as density and temperature are measured, not only the raw data values themselves but also radial gradients in the profiles are important to study turbulent transport as shown in Chapter 1. The profile gradient and its uncertainty should be estimated through profile analysis. We will introduce two different profile analysis methods in this section. The analysis method explained in section 3.2.1 is mainly used to prepare the input profiles for the codes used to interpret the transport (TRANSP, GYRO). In this analysis, the gradient was determined mostly by B-spline fitting. The analysis method introduced in section 3.2.2 is to see whether the gradient scale lengths of electron density and temperature profiles in the core region keep similar among discharges with different discharge conditions. In other words, this analysis method is to see the self-similarity explained in Chapter 1. The details of these two analysis methods will be explained in following two sub-sections.

3.2.1 Profile analysis for input profile preparation for GYRO and TRANSP

This section will describe the profile analysis performed to prepare input profiles for GYRO and TRANSP, such as electron density (n_e), electron temperature (T_e), ion temperature

(T_i), and toroidal rotation (V_t) profiles. We first see important profiles (or parameters) for the analysis using GYRO and TRANSP. As explained in Chapter 1, the gradient scale length of temperature and density such as a/L_n, a/L_{T_e}, and a/L_{T_i} are important parameters in turbulent transport models. These parameters will be calculated from the radial profiles of n_e, T_e, and T_i, and these radial profiles are input profiles for the transport analysis codes used in this study, TRANSP and GYRO. Toroidal rotation is also crucial in the transport analysis. The radial gradient of the toroidal rotation profile affects the ExB shearing rate, which stabilizes the turbulence [26]. The rotation velocity itself also affects the spectrum shape of turbulence measurements due to the Doppler effect. In addition, the parameters related to the impurity such as Z_{eff} and the fraction of main ion (n_D/n_e) should be specified in the transport analysis. Z_{eff} is defined as follows.

$$Z_{eff} = \frac{\Sigma n_i Z_i^2}{\Sigma n_i Z_i} \tag{3.13}$$

where n_i is the density of each impurity in the plasma, and Z_i is the charge of each impurity.

Z_{eff} affects the transport by decreasing the non-adiabatic electron response, in which the trapped particle is dominant. This is because the collisionality, which determines the trapped particle's effect, is a function of Z_{eff}. The lower n_D/n_e will decrease the transport due to the ITG mode by a dilution of the main ion and the modification of the mode-particle resonance [104]. Although we are not capable of measuring the radial profile of Z_{eff} and n_D/n_e, their average values can be estimated from the analyzed profiles, the equilibrium reconstruction [96] constrained by magnetic diagnostics [14], and the spectroscopic measurements [14].

The measurements used for the profile analysis are in the following. The Thomson scattering diagnostic [84, 14] was used to measure the n_e and T_e data, and the ECE grating polychrometer diagnostic [14, 115] was also used to measure T_e. T_i and V_t data were measured with high resolution imaging x-ray spectroscopy (HIREX) [87, 122] for the core region (r/a$\leq$0.8-0.85). T_i measurements by HIREX have the known instrumental offset issue (100-200eV). This will be not a critical problem for the core T_i profile, but this issue can be critical if we are interested the transport near the edge region (r/a$\sim$0.85) as in the analysis performed in Chapter 4. In order to avoid the large uncertainty because of the offset issue, charge exchange spectroscopy (CXRS) [103] was used for the edge T_i profile (r/a$\geq$0.85). V_t measurements by HIREX also have a large uncertainty near the edge region. CXRS was

also used for edge V_t data where CXRS measurements are reliable ($0.85 \leq r/a \leq 0.9$ for the discharges in Chapter 4). HIREX measures the temperature and velocity of Argon (Ar) from the line emission of Ar^{16+} and/or Ar^{17+} depending on the discharge condition, while CXRS measures the temperature and velocity of Boron (B) from the radiation generated by the charge exchange reaction of B^{5+}. Because of high collisionality in the near edge region, the temperature and toroidal velocity of two impurities will be well-coupled [182]. Figure 3-5 shows the T_i and V_t data measured by HIREX and CXRS for the Ohmic discharge used in transport analysis in Chapter 4 (shot 1120626023, t:0.9-1.4sec). It is noticeable that the data from the two different diagnostics are matched within their uncertainties near the edge region ($r/a > 0.85$), which suggests that T_i and V_t of the two impurities (Ar and B) are well coupled near edge region. However, it is noteworthy that the poloidal velocity of these two impurities will not be coupled in the near edge region because of magnetic pumping of both species [182].

We then obtain the radial profiles through the proper fitting and adjustments on the measured data. For n_e and T_e profiles, the fitting tool commonly used in C-Mod (fiTS) was applied to the measured n_e and T_e data. This fitting tool (fiTS) applies B-spline fitting in the core region, and the modified tanh fit [65] in the edge region. The two fitting lines are connected by applying cubic interpolation in the joint region between the core and edge regions. The core and edge regions in fiTS vary with the discharge conditions and the measurement position of edge Thomson scattering. More details about fiTS can be found in [1]. The time-averaged n_e and T_e profiles of each time slice fitted by fiTS in the stationary time period in the discharge were used in the study, and their uncertainty was estimated from the standard deviation of each time slice in the stationary period. These time-averaged profiles were also used as input profiles for TRANSP and GYRO. The uncertainty of a/L_{T_e} and a/L_{n_e} were estimated from the uncertainty of n_e and T_e and the uncertainty of their gradients, which was also estimated from time averaging, through error propagation technique. In order to obtain the T_i profile, we first need to estimate the instrumental offset in the measured T_i data by HIREX. This offset value was estimated by the measured neutron rate with the estimated n_D/n_e value from spectroscopic measurements (an example can be found in [120] or Appendix F.). The T_i profile in each time slice was then obtained by B-spline fitting on the T_i data from HIREX with the estimated offset when only the core profile is of interest. When the T_i profile near the edge region is important, which is the case

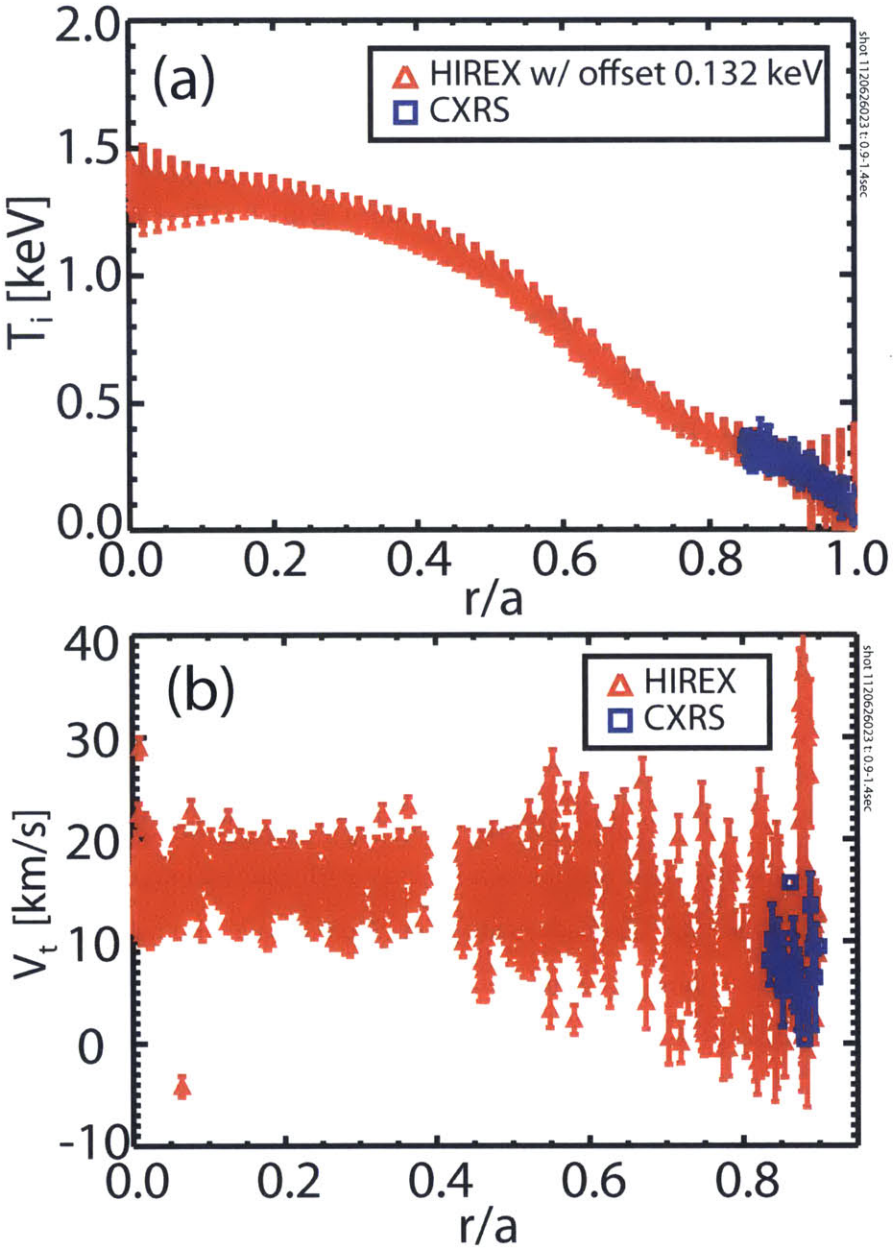

Figure 3-5: The comparison of T_i and V_t data measured by two diagnostics (HIREX and CXRS) in one Ohmic discharge (shot: 1120626023, time :0.9-1.4sec (a) T_i [keV] data measured by HIREX(red triangle) and CXRS (blue square) (b) V_t [km/s] data measured by HIREX(red triangle) and CXRS (blue square).

in Chapter 4, the core T_i data from HIREX with the estimated offset and the edge T_i data by CXRS were used in B-spline fitting. As used in the n_e and T_e profiles, time averaging in the stationary time period was applied to the T_i profile, and this profile is used in the transport analysis. In the error analysis, we included the uncertainty of the instrumental offset, photon statistics, profile asymmetries and time variation for T_i data by HIREX, and we considered the uncertainty of the data and the time variation for T_i data from CXRS. The error propagation technique was then used to estimate the uncertainty of the T_i and a/L_{T_i} profiles. Similar to the T_i profile analysis, the combined V_t data from HIREX and CXRS were used when the V_t profile near the edge region is important, and the core HIREX data were used when only the core profile is included in the analysis. The Bspline fitting is also used to obtain the V_t profile for each time slice during the stationary time period, and the average profile of all fitting profiles is used for the input rotation profile. The standard deviation of all fitting profiles is considered as the error of the toroidal rotation profile. The Z_{eff} value is estimated from the neoclassical resistivity calculation [143]. The details of the profile analysis for T_i, V_t and the estimation of Z_{eff} and n_D/n_e values for Ohmic discharges used in Chapter are explained in Appendix F.

3.2.2 Self-similarity analysis

As mentioned earlier, self-similarity analysis was performed in this thesis to study the changes in profile self-similarity (the shape of the profiles) with different discharge conditions or with transport phenomena by adopting the analysis technique applied in TCV [142]. A recent study in TCV showed two interesting features in profile changes with different discharge conditions such as external heating power, plasma current, plasma shaping (triangularity) and average electron density in L-mode discharges [142]: the correlation between the changes in the profiles in the edge region ($\rho \gtrsim 0.8$, where ρ_v is the square root of the normalized plasma volume) and confinement improvement (or L-mode pedestal) and maintaining a similar shape of core n_e and T_e profiles ($\rho_{inv} < \rho_v \lesssim 0.8$, where ρ_{inv} is the sawtooth inversion radius) [142]. The core T_e profiles in TCV were represented by an exponential function, and the power of the exponential function for core T_e profiles remains similar in spite of the change in the discharge conditions, maintaining a similar shape of the profiles. The same tendency was also observed in the core n_e profiles in the same study.

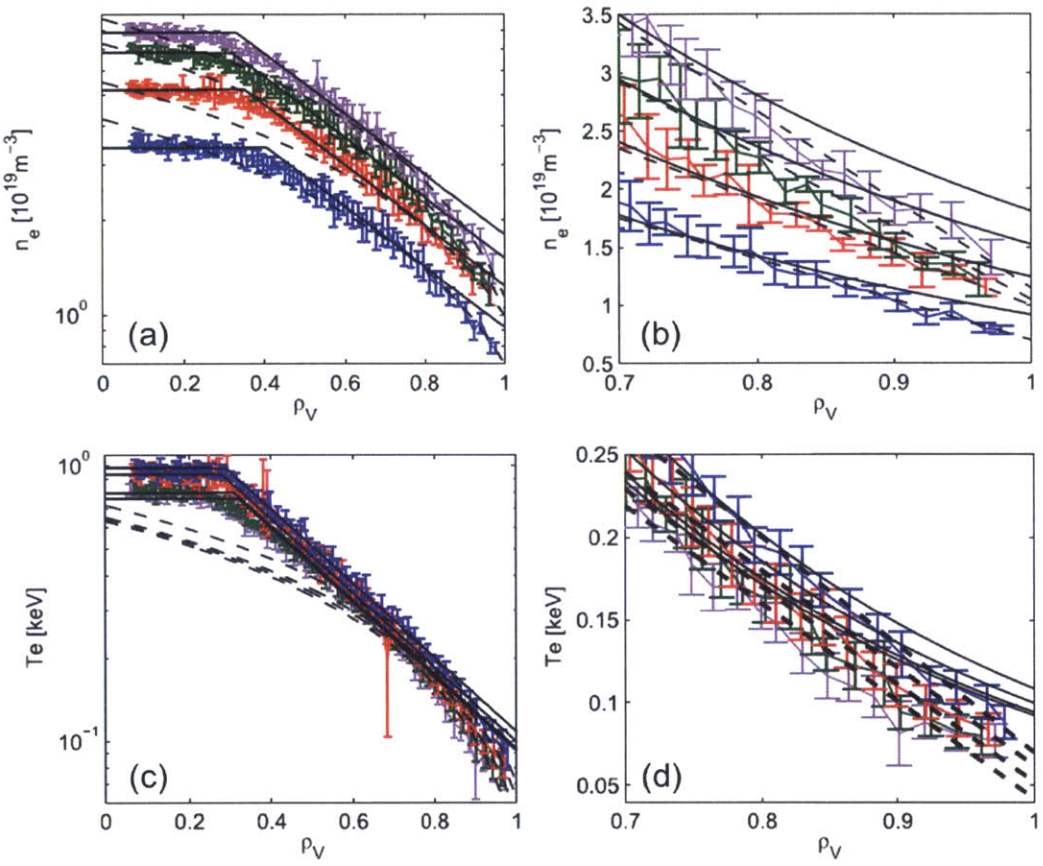

Figure 3-6: An example of self-similarity analysis results in TCV. The analysis performed for four ohmic dischasrge in TCV with different average density levels. A solid line indiates an exponential fitting line for the core profiles, and a dashed line denotes a linear fitting line in the edge profiles. (a) n_e profiles in the whole radial region (b) edge n_e profiles (c) T_e profiles in the whole radial region (d) edge T_e profiles. Adapted from O. Sauter et al, 2014, *Physics of Plasmas*, *21*, 055906, copyright 2014 American Institute of Physics.

Previous studies in C-Mod and other tokamaks also showed a similar shape of core T_e profiles [137, 63, 62] and the importance of the edge region in improvements of confinement in H-mode discharges [63, 62, 42, 118]. A study in TCV [142] quantified the similar shape of core profiles by applying an exponential fit. This study also extends the importance of the edge region to L-mode discharges, and the shape of edge profiles is quantified by a linear fit.

Figure 3-6 shows an example of the analysis results performed in TCV. In this figure, four ohmic discharges in the linear ohmic confinement (LOC) regime with the scan of average density were analyzed. As explained in section 1.3.1, the energy confinement time increases with average density in the LOC regime. It is shown that both n_e and T_e profiles of ohmic

discharges with different average density levels can be fit by the exponential fitting line (solid) line with the same exponential power, while the edge region is not fitted well by the exponential function. This figure also shows that the linear fit works in the edge n_e and T_e profiles in these Ohmic discharges, but the slope and the value of the linear fitting line at ρ_v=1.0 vary with the average density value, which indicates the correlation between the edge profiles and the global confinement. It is interesting to investigate whether or not the findings in TCV, profile self-similarity quantified by an exponential fit and the importance of the edge region ($\rho_v > 0.8$) in L-mode discharges, are universal by analyzing profiles in Tokamaks other than TCV.

In this study, we will apply the same analysis method used in TCV [142] to the n_e and T_e profiles in the Alcator C-Mod tokamak [102]. That is, we will first apply the exponential fit to the core n_e and T_e profiles, and apply the linear fit to the edge n_e and T_e profiles in C-Mod Ohmic discharges in different Ohmic confinement regions. The change of fitting parameters for the core and edge profiles across the Ohmic confinement transition will then be studied to see if the results in C-Mod are consistent with the findings in TCV. We will also extend these analyses to the high energy confinement regimes, i.e., H-mode and I-mode. While both particle and energy confinement is improved in H-mode, only energy confinement is improved in I-mode. In other words, I-mode has H-mode like T_e profiles and L-mode like n_e profiles [180, 164]. Comparing the fitting parameters for n_e and T_e profiles with the changes of confinement regime (L/I/H-modes) will be not only interesting for understanding I-mode and H-mode, but is also helpful to understand both energy and particle transport generally.

In order to analyze the self-similarity and the change of profile shapes in the edge in Alcator C-Mod, the Thomson scattering diagnostic [84] (for n_e and T_e) and the ECE diagnostic [115] (for T_e) were used. In the same way as described in [142], a flat profile shape was used to fit inside the sawtooth inversion radius ($\rho_v < \rho_{inv}$), and exponential and linear fits were applied in the core ($\rho_{inv} < \rho_v \leq \rho_{ped}$) and edge regions ($\rho_V \geq \rho_{ped}$), respectively. ρ_{ped} is the outer boundary of the core region, where the exponential fit is valid. That is, the T_e profile on outboard side was fitted with the following three equations.

$$\begin{aligned} T_e(\rho_v) &= T_{e,o} \quad \text{for } \rho_v < \rho_{inv} \\ T_e(\rho_v) &= T_{e,o} e^{-\lambda_{Te}(\rho_v - \rho_{inv})} \quad \text{for } \rho_{inv} < \rho_v \leq \rho_{ped,Te} \\ T_e(\rho_V) &= T_{e,edge} + \mu_{T_e}(1-\rho_v) \text{for } \rho_v \geq \rho_{ped,Te} \end{aligned} \tag{3.14}$$

Here, $T_{e,o}$ is the averaged T_e value in $\rho_v < \rho_{inv}$, and λ_{T_e} is an exponential fitting parameter. This parameter is approximately a normalized gradient scale length, a/L_{T_e} in the core region, where $a/L_X = \frac{a}{X}|\frac{dX}{dr}|$, and a is the minor radius. That is, $\lambda_{T_e} = \frac{1}{T_e}\frac{dT_e}{d\rho_v} = a/L_{T_e}|\frac{1}{a}\frac{dr}{d\rho_v}|$. It may be possible to resolve the variation of the gradient scale length in the core region using another fitting method such as bspline fitting. Nevertheless, if an exponential fit works well within the uncertainty of the data, the variation of λ_{T_e} in the fitting region will be small enough to consider λ_{T_e} as a good parameter which can represent a characteristic of the profile in the fitting region, which is the average gradient scale length. The fitting parameter in the edge region, μ_{T_e}, is the slope of the linear fit, and $T_{e,edge}$ is the T_e value at ρ_v=1.0, determined by the linear fit. μ_{T_e} and $T_{e,edge}$ have the same units as T_e. In this analysis, we define the pedestal position of the T_e profile, $\rho_{ped,Te}$ as the radial location which has the minimum difference between the two fitting lines (exponential function and linear function) at $\rho_v > \rho_{inv}$. The same equations and definitions are used for the n_e profile.

In order to mitigate a scatter in the data, we used the data within one standard deviation from time averaging in each confinement regime when the time length of the confinement regime is longer than 0.1 sec. When the time length of the confinement regime is less than 0.1 sec, all raw data were included in the analysis since there were less than 5 data points at each radial location, which is not enough to use any statistical techniques. Equilibrium reconstruction (EFIT)[96] constrained by magnetic diagnostics [14] was used to map the measurement locations of Thomson scattering and ECE diagnostics to the normalized axis, the square root of normalized plasma volume, in this study. Although we use the square root of normalized plasma volume as the horizontal axis to compare results between C-Mod and TCV, it is noteworthy that the analysis results are not different when the square root of normalized toroidal flux is used as the horizontal axis.

3.3 Experimental transport analysis using TRANSP

In the last two sections, we discussed the analysis methods for the measured fluctuations and profiles. In this section, we will discuss how to obtain the transport coefficients and the transport relevant quantities which are not measured in the experiments. It is noteworthy that heat fluxes are most important quantity obtained via this analysis, since the experimental heat flux levels obtained in this analysis will be used to not only study the changes in the experimental heat transport but also to validate the simulated heat transport by gyrokinetic simulation code, GYRO, which will be explained in section 3.4. It is possible to obtain these quantities by solving transport equations such as the energy and particle conservation equations. Since several transport equations are coupled, it is impossible to solve them analytically. In this study, we use the transport analysis code, TRANSP [4] to obtain the important transport quantities which were not measured, such as heat flux. TRANSP is also used to prepare the input profiles for gyrokinetic simulation, GYRO. A detailed this code is out of the scope of this study, and can be found in [4, 59, 68, 113]. In the following sub-sections, we will explain how we use TRANSP for this study.

3.3.1 Estimation of experimental heat flux using TRANSP

The procedure of heat flux estimation in the TRANSP is briefly reviewed in this section. We will first see the form of the transport equation that TRANSP solves. Since charged particles move along the magnetic field, diffusion along the magnetic surface in a magnetically confined plasma is much faster than the cross-field diffusion, which makes the transport quantities almost constant on the magnetic surface. In a tokamak plasma, we can also make use of toroidal symmetry. Then the transport equations should be solved only along the radial direction. In order to map the transport quantities correctly to the magnetic surface, we must consider the 2D plasma equilibrium due to a non-circular plasma cross section in most experiments. The term 1.5D is used to describe a 1D (poloidally averaged) transport solution, in a 2D magnetic geometry [113]. The measured quantities are usually not enough to solve

these 1.5D transport equations, so some quantities must be estimated by modelling. For this reason, TRANSP is coupled with other models for plasma equilibrium, wave heating and so on. The basic structure of TRANSP can be found in [68, 113]. The main reason for using TRANSP in this study is to estimate the experimental electron/ion heat fluxes and diffusivities. These quantities are obtained through solving the electron and ion energy conservation equations. When the viscosity terms are neglected, the electron energy conservation equation is given as follows.

$$\frac{3}{2}\frac{\partial}{\partial t}(n_e T_e) + \nabla \cdot \vec{q}_{e,cond} + \nabla \cdot (\frac{5}{2} n_e T_e \vec{v}_e) - \vec{v}_e \cdot \nabla(n_e T_e) = P_{OH} + P_{ext,e} - P_{ion} - P_{rad} - q_{ie} \tag{3.15}$$

where electron heat flux by conduction, $q_{e,cond}$, is defined as $q_{e,cond} = n_e \chi_e \frac{\partial T_e}{\partial r}$ with electron heat diffusivity, χ_e. P_{OH} is the Ohmic power, defined as $P_{OH}(r) = j^2(r)/\sigma(r)$ where j(r) is the current density profile and $\sigma(r)$ is the conductivity. $P_{ext,e}$ is the external heating power absorbed by electrons, and P_{ion} is the power loss due to ionization of a neutral. P_{rad} is the radiation power loss and q_{ie} is the power loss by transfer to ions through coulomb collisions, defined as $q_{ie} = \frac{3m_e}{m_i}\frac{n_e}{\tau_e}[Z](T_e - T_i)$ with electron collision time, τ_e and $[Z] = \frac{1}{n_e}\Sigma_j \frac{n_j Z_j^2}{A_j}$ where Z_j and A_j are the charge and atomic weight of ion species j.

The notation for the radial and temporal dependence of each term is ignored for the simplified notation, but it is noteworthy that Eq. 3.15 is solved in each radial location at each time slice. The first term on the left side of Eq. 3.15 represents the rate of change of electron energy, and the second term indicates the conduction power loss. The third and fourth terms indicate the convective power loss and the work done by electrons against the pressure gradient. These two terms can be expressed differently through simple algebra as below.

$$\nabla \cdot (\frac{5}{2} n_e T_e \vec{v}_e) - \vec{v}_e \cdot \nabla(n_e T_e) = \nabla \cdot (\frac{3}{2} n_e T_e \vec{v}_e) + n_e T_e \nabla \cdot (\vec{v}_e)). \tag{3.16}$$

In this case, these two terms will represent the convective power loss and compression power loss. It is noteworthy that convective power loss can be represented differently from the theoritical model for the flux, used in the analysis, as shown in [68].

Neglecting viscosity terms, the ion energy balance equation is given similarly as follows.

$$\frac{3}{2}\frac{\partial}{\partial t}(n_i T_i) + \nabla \cdot \vec{q}_{i,cond} + \nabla \cdot (\frac{5}{2} n_i T_i \vec{v}_i) - \vec{v}_i \cdot \nabla(n_i T_i) = P_{ext,i} - P_{CX} + q_{ie} \tag{3.17}$$

The left hand side of Eq. 3.17 is almost identical. On the right hand side, similarly to $q_{e,cond}$, ion heat flux by conduction, $q_{i,cond} = n_i \chi_i \frac{\partial T_i}{\partial r}$, with ion heat diffusivity, χ_i. $P_{ext,i}$ is the external heating power absorbed by ions, and P_{CX} is the power loss due to charge exchange with neutrals.

In TRANSP, the heat flux and diffusivity of electrons and ions are obtained by estimating all terms except for the conduction power loss term. The rate of energy change (first term on the left hand side in Eq. 3.15 and 3.17) can be calculated from the measured density and temperature profiles. For the third and fourth terms in Eq. 3.15 and 3.17, the radial flow velocity must be known, and can be estimated from the particle conservation equation given as follows.

$$\frac{\partial n_\alpha}{\partial t} + \nabla \cdot \vec{\Gamma}_\alpha = S_{vol,\alpha} + S_{wall,\alpha} \tag{3.18}$$

where α can be electrons or any ion species, Γ is particle flux, S_{vol} and S_{wall} are volume and wall sources of the particle, calculated by modelling.

For the Ohmic power calculation, conductivity ($\sigma(r)$) can be calculated from one of the neoclassical models, and current density profile (j(r)) can be either measured or estimated from the poloidal magnetic field diffusion equation, given as,

$$\frac{\partial B_\theta}{\partial t} = \frac{\partial}{\partial r}(\frac{1}{r\mu_o \sigma(r)} \frac{\partial}{\partial r} r B_\theta) \tag{3.19}$$

External heating power for electrons and ions, $P_{ext,e}$ and $P_{ext,i}$, should be obtained from another model depending on the external heating method used in the experiment. For example, the TORIC model [20, 181] is used to calculate the Ion Cyclotron Resonance Heating (ICRH) power deposition in C-Mod. Neutral transport modelling is required to estimate P_{ion} and P_{cx}. Last, q_{ie} can be estimated from the measured density and temperature profiles with the assumption that the ion density profile shape is the same as the shape of electron density profile.

Once all terms except for the conduction power loss term, $\nabla \cdot \overrightarrow{q}_{e,cond}$ and $\nabla \cdot \overrightarrow{q}_{i,cond}$ will be simply obatined from Eq. 3.15 and 3.17. Then, using the Divergence theorem, we can calculate the total heat flux from both conduction and convection as shown in Eq. 3.20, and heat diffusivity will be simply estimated from its definition, $\chi = q_{cond}/n\partial T/\partial r$.

$$q(r_o, t_o) = \frac{1}{A(r_o, t_o)} \int_0^{V(r_o,t_o)} \nabla \cdot (\overrightarrow{q}_{cond}(r,t) + \overrightarrow{q}_{conv}(r,t))\, dV \qquad (3.20)$$

where $A(r_o, t_o)$ and $V(r_o, t_o)$ are the area and volume of the flux surface at $r = r_o$ and $t = t_o$, and $\overrightarrow{q}_{conv}(r,t))$ is the heat flux due to convection.

3.3.2 TRANSP code set-up in this study

As shown in the previous section, one must use various models and measurements to obtain each term in Eq. 3.15 and 3.17. Depending on the model or the measurements used in the code, the heat flux value estimated from TRANSP will vary. Thus, we must clarify the TRANSP set-up used in this study. First, the inputs used in TRANSP were as follows: the n_e, T_e, T_i, and V_t profiles and Z_{eff} value, analyzed in section 3.2, the total plasma current, I_p, measured by the Rogowski coil [14], P_{rad} measured by bolometry [14], neutron rate measured by the neutron detector [14], and external heating power (Ion Cyclotron Resonance Heating (ICRH) for C-Mod). The input profiles are mapped on r/a coordinates in this study. We used the "pretransp", GUI (Graphical User Interface) developed by IDL, to provide the prepared inputs to TRANSP. The input profiles are re-mapped onto the flux coordinates (onto the

normalized square root of toroidal flux) in TRANSP. For this mapping and equilibrium calculation, the fixed boundary solver, TEQ [4] was used in TRANSP. For the current density profile, the poloidal magnetic field diffusion equation (Eq. 3.19) was used. Conductivity ($\sigma(r)$) was estimated using the NCLASS module [76]. NCLASS solves the fluid force balance equations for multiple species to determine the neoclassical transport quantities. This code is also used to estimate the bootstrap current. The profile of ICRH power was determined by the TORIC code, which calculates the wave propagation and absorption in the plasma [20, 181]. Last, the convective power loss, q_{conv} is defined in TRANSP as follows.

$$q_{conv} = \nabla \cdot (\alpha \frac{5}{2} nT\vec{v}). \tag{3.21}$$

where α is a free parameter.

In this study, α is set to 2/3, which means the convective power loss term in Eq. 3.16 is used instead of the third term on the left hand side of Eq. 3.15 and 3.17.

The uncertainty of the experimental heat fluxes can be estimated in two ways. We can estimate it from the uncertainty of each term in the power balance through the error propagation technique such that $\sigma_Z^2 = \sigma_X^2 + \sigma_Y^2$ with an uncertainty, σ, and the sum of X and Y, Z(=X+Y), under the assumption that X and Y are uncorrelated. Figure 3-7 shows the profiles of each term in the electron and ion energy balance equations (Eq. 3.15 and 3.17) for one C-Mod discharge. It is shown that P_{OH}, P_{rad} and q_{ie} are dominant in the electron power balance and q_{ie} is dominant in the ion power balance equation. We can then estimate the uncertainty of q_i and q_e from the uncertainty of P_{OH}, P_{rad} and q_{ie}. More details are shown in Appendix H. We can also estimate the uncertainty of heat fluxes from a group of runs with different input parameters within their uncertainties. In this method, we will obtain a range of the heat flux values within the uncertainty of input parameters. Assuming the heat flux values of each run are not correlated, it is possible to convert the obtained range of the heat flux to its standard deviation [108].

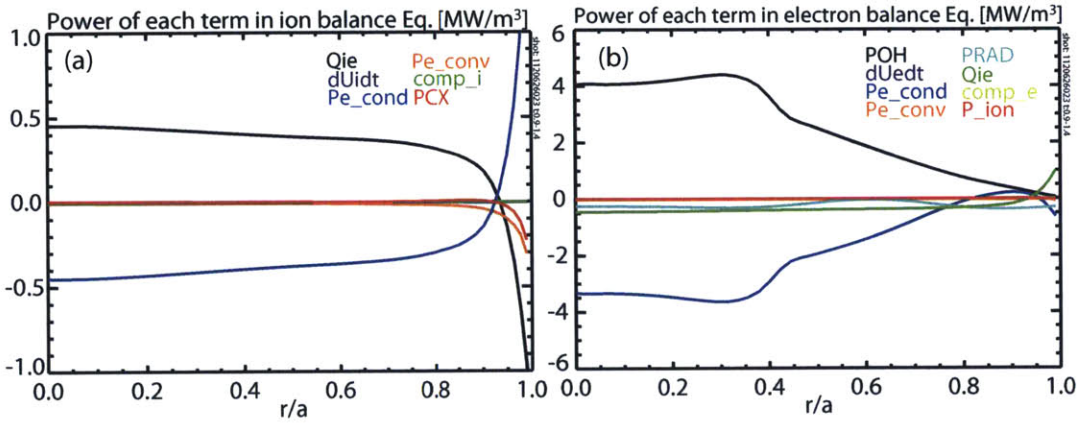

Figure 3-7: The power of each term $[MW/m^3]$ in the (a) ion power balance equation and (b) electron power balance equation in one C-Mod discharge (shot : 1120626023, t: 0.9-1.4s). Energy gain has a positive sign and loss is presented by a negative sign. In (a), black : the power transferred from electrons to ions by collisions, q_{ie}, purple : the rate of change of ion energy, blue : ion conduction power loss, orange : ion convective power loss, green : ion compressional power, red : power loss due to charge exchange. In (b), black : Ohmic heating power, purple : the rate of change of electron energy, blue : electron conduction power loss, red : electron convective power less, light blue : power loss due to radiation, green : q_{ie}, yellow : electron compression power, red : power loss due to ionization

3.3.3 Prepration of input files for the gyrokinetic simulation (GYRO)

The analysis using TRANSP is deeply related to the gyrokinetic analysis, which will be explained in the next section. The experimental heat fluxes estimated from TRANSP will be compared with the simulated heat fluxes by the gyrokinetic simulation (GYRO) to validate the gyrokinetic model. TRANSP is also used to prepare the input profiles for the gyrokinetic simulation (GYRO). In the GYRO input preparations, we use TRANSP for two purposes. First, we obtain the unknown quantity required to run GYRO from TRANSP, which is the radial electric field, E_r, profile. NCLASS, mentioned in section 3.3.2, was used to estimate the E_r profile. In this study, we used the toroidal velocity of impurity (Ar) as input, and NCLASS calculates the E_r profile using the input toroidal velocity profile and the estimated poloidal velocity from the neoclassical calculation. The E_r value itself affects the rotation frequency in GYRO inputs, and its gradient determines the $E \times B$ shearing rate, which

are important to the stabilization of turbulence. However, the agreement of the neoclassical poloidal velocity with the experimental value is questionable [64, 149, 35], and this can be an issue in the comparison of GYRO outputs with the experiments as will be shown in Chapter 4. Second, we use the TRANSP output files to generate GYRO input profiles. To generate GYRO input profiles, a plasma state netCDF file is first generated using TRANSP outputs through the TRXPL software [6]. This plasma state file is used to generate GYRO input profiles through profiles_gen utility [5]. It is noteworthy that the time-averaged profiles are used in GYRO, and averaging was performed using TRXPL after the TRANSP run is done. Thus, the TRANSP input profiles are not time-averaged profiles, they are profiles at each time slice, and heat fluxes and diffusivities are also a function of time and space. The presented heat flux and diffusivity in this study are averaged in the post processing in the time range we used for the analysis.

3.4 Gyrokinetic analysis using GYRO

The last analysis method introduced in this chapter is gyrokinetic turbulence simulation using GYRO [28]. Gyrokinetic simulations were performed to understand the physics related to transport phenomena we observed and to interpret the measured fluctuations. As mentioned in Chapter 1, the validation of gyrokinetic simulation is also an important task that should be performed. In this section, we first explain the simulation setup used in this study, after a brief introduction of GYRO. More details about GYRO can be found in [28, 3]. The procedure of gyrokinetic analysis performed in this thesis is then discussed. Last, we introduce the synthetic CECE diagnostic model used in this study, required for the validation study using the CECE measurements.

3.4.1 Overview of GYRO

GYRO is a numerical solver for the non-linear gyrokinetic equation using the initial value Eulerian scheme. The explanation of the Eulerian scheme can be found in [55].

This code solves the perturbed part of distribution function, δf from the equilibrium distribution function, assumed as Maxwellian, from the gyrokinetic equation. GYRO is capable of solving the gyrokinetic equation with a realistic plasma geometry and shape, impurities (up to 5), collisions, profile variations (global effects), electromagnetic effects and rotation relevant effects such as rotation/$E \times B$ shearing effects. The particles (electrons and ions) can be treated as adiabatic, drift-kinetic or gyrokinetic. Depending on the purpose of the simulations, these terms can be included or not. GYRO uses the shifted velocity frame, the frame rotating with the plasma with $E \times B$ velocity at the reference location in the simulation. Thus, there will be Doppler shift in the simulated fluctuations when we convert this shift velocity frame to the lab frame. This effect should be considered in the comparison of the fluctuations from GYRO with the experiments. The fluctuating quantities in GYRO are decomposed in the toroidal direction (or represented by a Fourier series of toroidal modes). For example, potential fluctuation, $\tilde{\phi}$, is represented as follows.

$$\tilde{\phi}(r, \theta, \alpha) = \Sigma_{j=-N_n+1}^{N_n+1} \tilde{\phi}_n(r, \theta) e^{-in\alpha} e^{in\omega_o t} \tag{3.22}$$

where θ is the poloidal angle, α is the Clebsch angle in a flux coordinate [95], and n is the toroidal mode number, defined as $n = j\Delta n$ with toroidal mode spacing, Δn. N_n indicates the number of toroidal grid points, and ω_o is the $E \times B$ rotation frequency of the reference radius, defined as $\omega_o = cE_r/RB_p$ with the speed of light, c, radial electric field, E_r, major radius, R, the poloidal magnetic field, B_p.

Each toroidal mode number, n, can be linked to a poloidal wave number, k_y, with the relation given as follows.

$$k_y = \frac{nq}{r} \tag{3.23}$$

with safety factor, q.

GYRO solves each toroidal mode from the gyrokinetic equation. However, the gyrokinetic equation for one toroidal mode has the non-linear term coupled with the equations for other toroidal modes. If GYRO solves the linearized gyrokinetic

equation by neglecting the non-linear term, we are able to obtain the real frequency and the growth rate of the unstable modes in the plasma. The unstable mode in this linear simulation has the form (Potential fluctuation is used in the example).

$$\tilde{\phi}_n(r,\theta,t) = \tilde{\phi}_n(r,\theta)e^{-i\omega_R t+\gamma t} \tag{3.24}$$

with the real frequency of the mode, ω_R and its growth rate, γ.

Through the linear simulations, we see clearly the characteristics of the unstable mode, which can exists in the plasma condition used as input, for each toroidal mode or poloidal wavenumber, k_y, in the range of interest of k_y or $k_y\rho_s$, with the sound gyroradius of the main ion, ρ_s, defined as $\rho_s = c_s/\Omega_{ci}$ with $c_s = \sqrt{T_e/m_i}$ and $\Omega_{ci} = eB/m_ic$. The propagating direction of the mode is determined from the sign of real frequency. In GYRO, negative real frequency indicates the ion diamagnetic direction and positive real frequency indicates the electron diamagnetic direction. The sensitivity analysis for the growth rate about input parameters will identify the mode, such as TEM or ITG mode. In GYRO, we can use either an initial value solver or eigenvalue solver for the linear simulation. An initial value solver finds the dominant mode, which has the highest growth rate, but we do not know the sub-dominant mode. Using an eigenvalue solver, we are able to obtain sub-dominant unstable modes. Depending on the purpose of the simulations, either one of them can be used.

Although linear simulations are useful, we need nonlinear simulations to obtain a more realistic picture. As shown in Eq. 3.24, the linear unstable mode increases exponentially, and will go to infinity eventually, which is not true in the real experiments. In these linear simulations, the nonlinear interaction between the linear modes at different toroidal (or poloidal) wavenumbers is not considered. This nonlinear coupling provides the dissipation mechanism of the unstable mode, by transferring the linear free energy to the stable modes at other wavenumbers, and the amplitude of the unstable mode will be saturated when its linear free energy is balanced with the nonlinear energy transfer to other modes. The nonlinear interaction is generated due

to the convective derivative term in the gyrokinetic equation [159]. Including the non-linear term, we can obtain more realistic quantities relevant to turbulence, such as heat flux due to turbulent transport and turbulent fluctuations. These realistic fluctuating quantities can be compared to the experimental quantities analyzed in section 3.1 and 3.3. In other words, we will get a realistic picture about the transport in the plasma from the non-linear simulations. However, the required computational time for each non-linear run is quite demanding. To reduce the cost of the run, we need to find the minimal resolutions (in time, velocity and real space) and the minimal domain size that can be used in the study. This can be found by checking the convergence of the simulated outputs with changes in the resolutions and domain size.

Among the simulated outputs from the non-linear runs, this thesis uses the electron and ion heat fluxes and the electron temperature fluctuations. The heat flux values are given as output, but the temperature fluctuation value is not directly given by GYRO. Instead, the simulated density and energy fluctuations are given. The temperature fluctuations are calculated from the first order approximation as follows.

$$\frac{\tilde{T}}{T} \simeq \frac{2}{3}\frac{\tilde{E}}{nT} - \frac{\tilde{n}}{n} \tag{3.25}$$

The simple algebra related to Eq. 3.25 is shown in Appendix G. Fluctuations from GYRO are already normalized by the corresponding equilibrium values. The density fluctuations are normalized by the equilibrium density value, and the energy fluctuations are normalized by the product of equilibrium density and temperature. Thus, temperature fluctuations can be calculated easily using density and energy fluctuations from GYRO via Eq. 3.25.

GYRO can be run either at a local flux surface or globally with profile variations in the simulation domain. In the local simulation, the values of input profiles are constant across the simulation domain. Running the local simulation corresponds to solving the gyrokinetic equation with the limit of $\rho_* \to 0$, where $\rho_* = \rho_s/a$ with minor radius, a. The periodic boundary condition is usually used in the local flux-

tube simulations. However, a non-periodic boundary condition is used in this study to include rotation relevant effects in the local simulation. The global simulation uses the input profile itself including its variation in the simulation domain. The boundary condition is thus naturally non-periodic. It is known that local simulation results agree with the global simulation results when the ρ_* value is small enough ($1/\rho_* \gtrsim 400$) [29].

3.4.2 GYRO simulation set-up

In this study, both linear and non-linear simulations were performed using GYRO. In most cases, local simulations were performed, but the results will be similar to global simulations because of the small ρ_* values as shown in Appendix I, and previous gyrokinetic analysis performed in C-Mod [78]. Due to the low β values of plasmas used in this study ($\beta_t \lesssim 1\%$), it is expected that electromagnetic effects are negligable. Thus, only electrostatic turbulence modes were considered in this analysis. As explained in section 3.3.3, GYRO input profiles are obtained from the experimental profiles of n_e, T_e and T_i and the profiles estimated by TRANSP, such as safety factor, q, and rotation frequency, ω_o. A realistic plasma shape is considered in the simulations through the Miller type equilibrium model [106] based on the equilibrium information obtained from TRANSP. Electron collisions are modeled by using pitch angle scattering, and ion-ion collisions are not included in the simulations. One impurity species (Boron, B) is used with the estimated main ion fraction (n_D/n_e). It was assumed that the main ion density profile has the same radial gradient as the electron density profile, but with the different amplitude, determined by the main ion fraction. Although impurities can affect the main ion density gradient, we assumed that the main ion density gradient was not changed by including impurities in the simulations. The treatment of impurity in the gyrokinetic analysis should be improved in the future to investigate the effect of impurity to the turbulent transport.

Although it is known that we cannot always ignore the contribution of electron scale turbulence, as shown in [90, 47] in the past and in [77] recently in C-Mod, the simulations include only ion scale turbulence ($k_y\rho_s \lesssim 1.2 - 1.7$) in this analysis

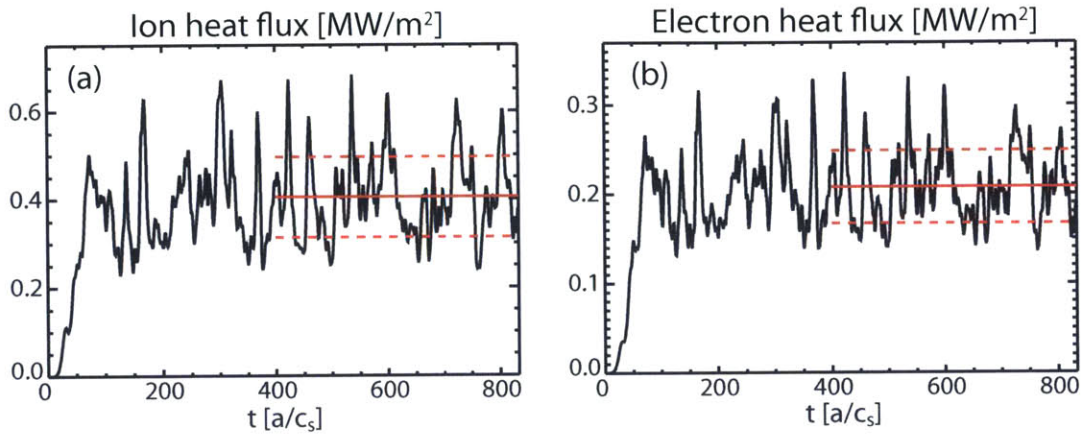

Figure 3-8: The simulated heat flux $[MW/m^2]$ of (a) ions and (b) electrons for one C-Mod discharge (shot 1120626028, t:0.9-1.4 s) at r/a=0.6. The stationary time period is set to t: 400-833 $[a/c_s]$. The red solid line is the average value, and the red dotted line indicates the uncertatiny of the mean value, the standard deviation of the time averaging.

because of the enormous time required for the simulations including both electron and ion scale turbulence (this does not mean that ion scale simulations are cheap). This can be a caveat in this analysis. For the ion scale simulations, gyrokinetic ions and drift-kinetic electrons are used. All simulated quantities in this study were averaged in the stationary time period for more than $300[a/c_s]$, where the spatially averaged ion heat flux, Q_i, electron heat flux, Q_e and potential fluctuations of each toroidal modes are saturated. Figure 3-8 shows the example of saturated Q_i and Q_e from GYRO for one C-Mod discharge (shot : 1120626028, t : 0.9-1.4s). The red solid line in this figure indicates the averaged heat flux in the stationary time range, and the red dotted lines indicate the uncertainty of this mean value estimated from the standard deviation from the time-averaging. The uncertainties of the other fluctuating quantities, which are spatially averaged and are functions of only time, are also estimated from the standard deviation of the time averaging in the stationary time period.

In order to find the proper domain size and resolution of the simulation, a convergence study of simulated ouputs for the simulation setup parameters is required. For example, the domain size should be large enough to include many turbulent eddies for accurate simulation results. In order to know whether or not the present domain

size is sufficient, a run with a domain larger than the present domain is needed. If the simulation results from the run with the larger domain are simlar to the the present run within the uncertainty (in other words, the simulation results converge with the domain size), then it is concluded the present domain size is sufficient. We also want to include all relevant ion turbulence modes in the simulation for accurate results. This is related to the range of $k_y\rho_s$ in the simulation. Similar to the domain size, we should perform a convergence test about the range of $k_y\rho_s$ to check whether or not the simulation results are saturated with $k_y\rho_s$ values than the present value. The same kind of convergence tests can be done for the setup in velocity space such as the resolution of velocity space and the maximum energy included for the δf calculation. An example of the convergence study for the Ohmic discharges in Chapter 4 can be found in Appendix I. However, we need to note that each non-linear run is expensive, and it is hard to perform the convergence study for each run used in the analysis. Instead, once we have the proper resolutions and domain size for one run, then the same resolution and domain size were used for the other runs used to simulate plasmas which have similar discharge conditions. The domain size used in this analysis is $L_x, L_y \sim 60 - 130\rho_s$ with radial domain size, L_x, and poloidal domain size, L_y. The radial grid spacing, $\Delta x/\rho_s$ is set to 0.25-0.35. The maximum $k_y\rho_s$ value is set to 1.2-1.7. In velocity space, 128 grid points were set with 8 energies, 8 pitch angles and 2 signs of velocity.

It is noteworthy that there are observable symptoms if domain size is not sufficient or if the $k_y\rho_s$ range is not sufficient. One typical symptom that can be observed due to an insufficient domain size is the peak at the longest wavelength mode or at the lowest $k_y\rho_s$ mode in the distribution of flux among toroidal modes, that is, the $Q(k_y\rho_s)$ spectrum. It is usually observed in the $Q_i(k_y\rho_s)$ spectrum. If this is the case, we need to increase the poloidal box size by decreasing the toroidal grid spacing, Δn. In this study, we had a run with a large accumulation in $k_y\rho_s < 0.1$ in the $Q_i(k_y\rho_s)$ spectrum, and this accumulation was not consistent with the experimental observations. In this case, we tried to suppress the mode in $k_y\rho_s < 0.1$ within the uncertainty of input parameters. The details about this run can be found in Appendix I. If the $k_y\rho_s$ range

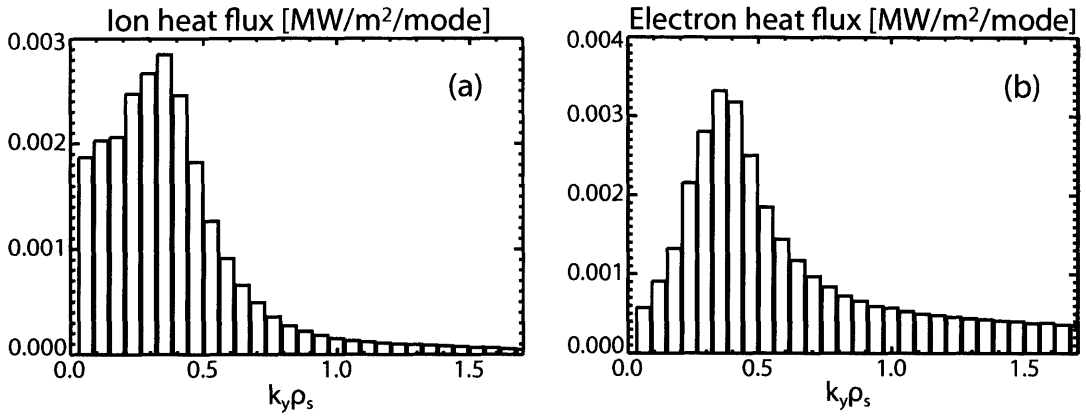

Figure 3-9: The distribution of simulated heat flux [MW/m^2/mode] on toroidal modes, The spectrum of Q($k_y\rho_s$) for one C-Mod discharge (shot 1120626023, t: 0.9-1.4s) at r/a$\sim$0.85. The stationary time period is set to t: 430-860 [a/c_s]. (a) $Q_i(k_y\rho_s)$ (b) $Q_e(k_y\rho_s)$ spectrum.

is not sufficient, the $Q(k_y\rho_s)$ spectrum will have the high amplitude tail. It is usually observed in the $Q_e(k_y\rho_s)$ spectrum. In this case, we need to increase the maximum $k_y\rho_s$ value by increasing the number of toroidal modes. Then, the $Q(k_y\rho_s)$ spectrum from the run with the proper setup will have the bell-like shape as shown in Fig. 3-9. Although the convergence study was not performed in detail for each simulation in this study, all GYRO runs used here do not have any issues in the $Q(k_y\rho_s)$ spectra.

3.4.3 Gyrokinetic anaylsis procedure

We performed both linear and nonlinear gyrokinetic analyses in Chapter 4 and 5, and only the linear analysis was done in Chapter 6. In linear gyrokinetic analysis, we first find the dominant mode in the plasma using an initial value solver with experimental input profiles. From the sign of the real frequency, we are able to determine the propagation direction of the dominant mode (positive : electron, negative : ion, where ion/electron direction refers to the direction of ion/electron diamagnetic velocity, respectively). In ion scale simulations, we usually connect the mode propagating in the ion direction (ion mode) to the ITG mode, and the opposite case (electron mode) to TEM. The sensitivity analysis of the growth rate of the dominant mode about the input gradient scale lengths is the second step in the linear gyrokinetic

analysis in this study. For the sensitivity analysis in this thesis, a/L_{T_i} and a/L_{T_e} are varied to study whether the dominant mode is ITG- or TEM-like turbulence. This sensitivity study identifies the characteristics of the dominant turbulence mode more clearly. Last, an eigenvalue solver (field eigenvalue solver) is used to identify and study the sub dominant mode if necessary. The details about the eigenvalue solver used in this analysis can be found in [3]. The eigenvalue solver is required when the sensitivity analysis shows that the dominant mode is near the ITG/TEM boundary, which indicates that the sub-dominant mode is not ignorable. It is noteworthy that we cannot know how the dominant and sub-dominant modes, studied in the linear gyrokinetic analysis, affect the turbulent transport. A more realistic picture should be investigated using non-linear gyrokinetic analysis.

The first step in non-linear gyrokinetic analysis is to find the base case with the proper resolution and domain size as explained in the previous section. The next step is to obtain the heat flux matched simulation. The simulated heat flux values with the experimental profile or the profile from the base case usually do not match with the experimental values since heat flux values from turbulent transport are sensitive to the gradient scale lengths due to the stiffness property explained in Chapter 1. Changing gradient scale lengths or other input parameters within the uncertainty, we check whether or not the non-linear run can reproduce the experimental heat flux values, obtained from TRANSP. If the run with the modified inputs can reproduce one or both of the electron and ion heat fluxes, we use this run as the "physical" base case since this run simulates the transport in the plasma closer to the real experiment than the "numerical" base case obtained in the first step. We then analyze the results of the heat flux-matched simulations by comparing the trend of heat fluxes with the experiments or by comparing the simulated heat fluxes and fluctuations from various heat flux-matched runs used to analyze different discharges. Similar to the linear analysis, it is also possible to identify the dominant mode in the non-linear run from the power spectrum of the simulated fluctuations. The last step is the sensitivity analysis. In this analysis, we varied input parameters from the heat flux matched simulation, and investigated the sensitivity of the simulated outputs about input

parameters. From this analysis, we can determine what kind of turbulence mode is dominant or responsible for the turbulent transport in the discharge used in the simulation.

The validation study introduced in Chapter 1 was performed for the C-Mod Ohmic discharges studied in Chapter 4. In order to validate the gyrokinetic model used in this study, electrostatic ion-scale turbulence, we first compared the outputs from the heat flux-matched simulations with the experiments. The robustness of this comparison was then checked via the sensitivity analysis. The experimental heat flux and the electron temperature fluctuations measured by the CECE diagnostic were used in the comparison for the validation study. The simulated electron temperature fluctuations cannot be compared directly with the measured fluctuations. We must consider the experimental conditions in the measurements in the post-processing through a synthetic diagnostic model, which will be explained in the next section.

3.4.4 Synthetic CECE diagnostic

The overview of the existing synthetic diagnostic model for the CECE diagnostic

In order to compare quantitatively the simulated outputs with the measured quantities, we need a computational model which can convert the simulated "raw" outputs into simulated diagnostic signals by considering the measurement conditions such as resolutions, Doppler effects and any limitations in the measurements. This computational model is called a synthetic diagnostic [22, 73]. For the comparison of T_e fluctuations simulated by GYRO with the T_e fluctuations measured by the CECE diagnostic, a synthetic CECE diagnostic model was developed by Holland et al [73]. This existing model was used in this study with improvements for the CECE diagnostic in C-Mod. We will first briefly review how the existing model [73] (Holland's model) considers the CECE measurement conditions. Readers can find more details about the synthetic CECE model in [73].

GYRO uses the coordinates co-rotating with the plasma as shown in Eq. 3.22. It

is therefore necessary to convert the signal in the co-rotating frame to the laboratory frame. This was done by a mode number-dependent transform in [73] as follows:

$$X_{lab}(r,\theta,n,t) = X_{sim}(r,\theta,n,t)e^{-in\omega_o t} \tag{3.26}$$

with the simulated output in the GYRO coordinate, X_{sim}, and the simulated output in the laboratory coordinate, X_{lab}.

As explained in Chapter 2 and [23], the finite sample volume will attenuate the short wavelength signals. In Holland's model, this effect is accounted for by convolving a two dimensional point spread function (PSF) in the radial and poloidal directions with the simulated raw signal at each time slice as shown by,

$$X_{syn}(R_o,Z_o,t) = \frac{\iint dRdZ\psi(R-R_o,Z-Z_o)X_{lab}(R,Z,t)}{\iint dRdZ\psi(R-R_o,Z-Z_o)} \tag{3.27}$$

with the center of measurement position, (R_o, Z_o), point spread function (PSF), ψ, and the synthetic signal, X_{syn}.

In Holland's model, a Gaussian form was used given by,

$$\psi(R-R_o,Z-Z_o) = e^{-\frac{1}{2}[\frac{R-R_o}{l_R}]^2 S} e^{-\frac{1}{2}[\frac{Z-Z_o}{l_Z}]^2} \tag{3.28}$$

with the $1/e^2$ diameters in radial direction, l_R and poloidal direction, l_Z.

An example of synthetic T_e fluctuations using Holland's model is shown in Fig. 3-10. The attenuation of fluctuations by the finite sample or PSF is shown. We also see the spread of spectrum when higher rotation frequency is applied.

Improvements in synthetic CECE model

In this study, we improved the model for the CECE diagnostic in C-Mod in three aspects. First, more a realistic radial broadening shape, which is determined by both the relativistic and Doppler effects, is considered in this analysis. As shown in Eq. 3.28, Holland's model assumed the sample volume has a Gaussian shape in both radial and poloidal directions, which are symmetric. As shown in Chapter

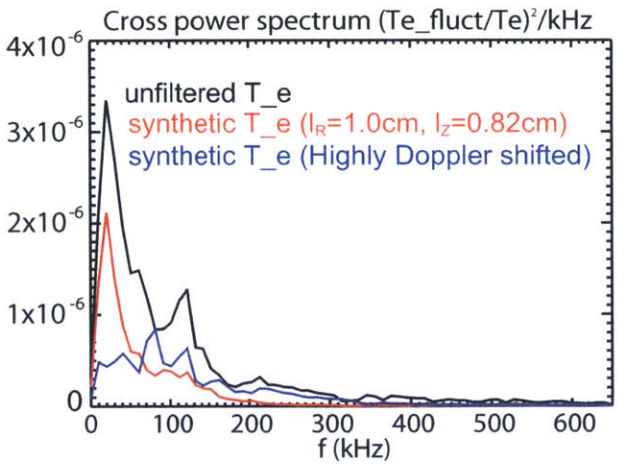

Figure 3-10: The power spectra of the unfiltered (raw) T_e fluctuations (black), synthetic T_e fluctuations using Holland's model (red, with $1/e^2$ diameter in Gaussians in radial and poloidal directions, l_Z=0.82cm and l_R=1.0cm) and synthetic T_e fluctuations with higher rotation frequency (blue, ω_o with the same l_R and l_Z values used in the red line) for one C-Mod discharge (shot 1120626023, t:0.9-1.4s). ω_o ~-0.0025 $[a/c_s]$ for the black and red lines, ~-0.025 for the blue line.

2, Gaussian optics can be applied in the CECE optical system. Thus, a Gaussian shape is appropriate in the poloidal direction. However, the radial shape estimated in Chapter 2 shows that the Gaussian shape is not proper in the radial direction. Instead of a Gaussian shape, the estimated emissivity curves in the radial direction for each CECE channel shown in Fig. 2-14(a) are used in this study. Figure. 3-11(a) shows the PSF used in Holland's model, which is symmetric in both radial and poloidal directions. The improved PSF is shown in Fig. 3-11(b). It is noticeable that the PSF is asymmetric in the radial direction due to the relativistic effect, explained in Chapter 2.

Synthetic T_e fluctuations using the calculated radial shape are compared with the synthetic fluctuations using the Gaussian PSF in the radial direction. The $1/e^2$ diameter, l_R for the synthetic fluctuations using the Gaussian PSF in the radial direction was estimated from the radial broadening width including 95% emissivity in the calculated emissivity curve. Other conditions used for the synthetic fluctuations are identical between them. Figure 3-12 shows that the synthetic fluctuations obtained from the calculated broadening shape are almost identical to the synthetic fluctua-

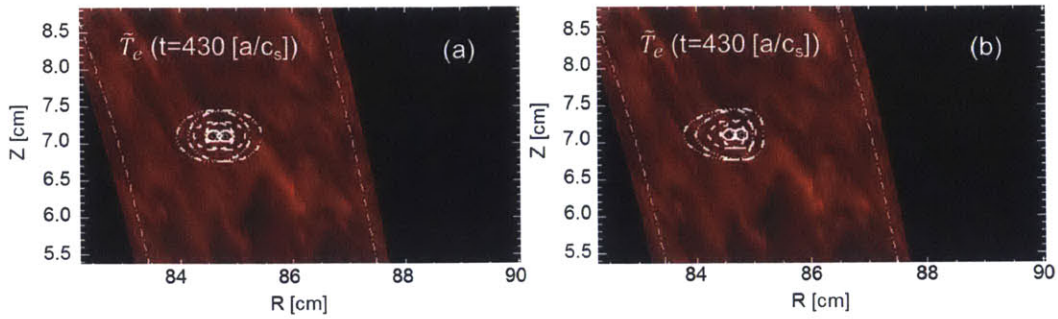

Figure 3-11: The comparison of the point spread function (PSF) applied in the synthetic CECE diagnostic for one C-Mod discharge (shot 1120626023, t:0.9-1.4s). The background fluctuations are simulated T_e fluctuations at t=430 $[a/c_s]$. (a) PSF from Holland's model, two Gaussian in both poloidal and radial direction with $1/e^2$ diameter, l_Z=0.64cm l_R=1.2cm. (b) The modified PSF with the more realistic radial shape estimated in Chapter 2 and Gaussian in poloidal direction with l_Z=0.64cm. The white lines indicate the 10, 50, 90% level of the power from the center of the PSF.

tions obtained from the Gaussian. This may indicate that the width of sample volume is more important than the shape of the sample volume. Although the difference is not significant, the more realistic shape in the radial direction was used for PSF in the synthetic diagnostic in this study.

The contribution of n_e fluctuations to the measured fluctuatons considered in section 3.1.2 should be included in the synthetic diagnostic as well. The measured intensity fluctuations in each CECE channel considering the contribution of n_e fluctuations is given by [124],

$$\frac{\tilde{I}}{I} = (1+A)\frac{\tilde{T}_e}{T_e} + A\frac{\tilde{n}_e}{n_e} \tag{3.29}$$

where $A = \frac{\tau \exp(-\tau)}{1-\exp(-\tau)}(1 - \chi\frac{1-\exp(-\tau)}{1-\chi\exp(-\tau)})$, I is the intensity of each CECE signal used in the correlation technique, and χ is the wall reflectivity, with a typical value of ~ 0.8 for a metal wall facility like C-Mod.

The contribution of n_e fluctuations in the CECE measurements is considered in the following steps. First, both n_e and T_e fluctuations are loaded, and the A value in Eq. 3.29 is calculated from the n_e and T_e values used in the simulation. The wall reflectivity, χ was assumed as 0.8 in this calculation. Then, the intensity fluctuation

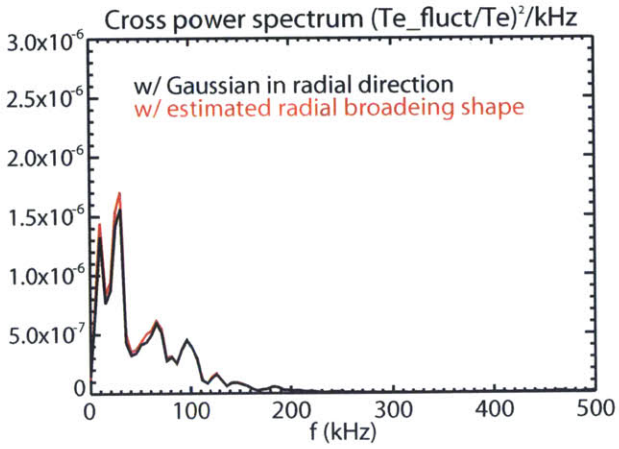

Figure 3-12: The power spectra of the synthetic T_e fluctuations for one C-Mod discharge (shot : 1120626023, t:0.9-1.4s) with the different PSF in the radial direction. A Gaussian function is used for the black curve, and the estimated radial shape is used for the red curve. Other input parameters between the two curves are identical.

signal in each channel considering the n_e fluctuation effect was generated through Eq. 3.29 using the simulated n_e and T_e fluctuations and the calculated A value. Once the intensity fluctuation signals are obtained, the rest of analysis is the same as the case using only T_e fluctuations. It is noteworthy that the phase angle between the n_e and T_e fluctuations, which should be known for an accurate estimation of n_e fluctuations from Eq. 3.11, will be naturally considered in the spectral analysis (cross power spectrum) of the simulated intensity fluctuation signals. The example is shown in Fig. 3-13(a). It is shown that the contribution of density fluctuations are not significant in this case. Nevertheless, the contribution of n_e fluctuations can be more important in other runs than the case in Fig. 3-13(a) due to the changes in the phase between n_e and T_e fluctuations or the decrease of the optical depth, τ, value.

In chapter 2, it was mentioned that high pass filters were used in the measurements to use the full dynamic range of the video amplifiers and digitizer. This high pass filter should also be considered in the synthetic CECE diagnostic. In order to consider the high pass filter, a digital filter using the measured response curve in Fig. 2-18(b) is applied to the synthetic signal before applying the standard spectral analysis technique. The example of the synthetic fluctuation with a high pass filter is shown in Fig. 3-13(b).

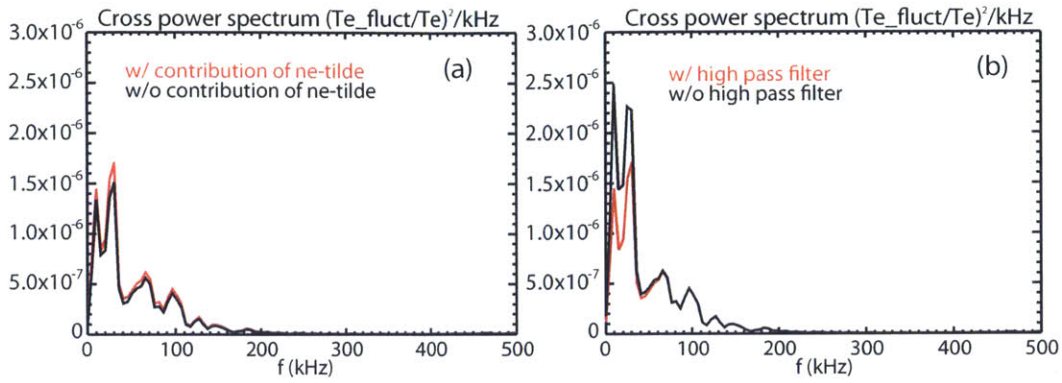

Figure 3-13: The comparison of power spectra of the synthetic T_e fluctuations for one C-Mod discharge (shot : 1120626023, t:0.9-1.4s) (a) w/ and w/o considering the contribution of n_e fluctuations (b) w/ and w/o considering the high pass filter used in the measurements.

Implementation of the synthetic CECE diagnsotic in C-Mod

In order to implement the synthetic diagnostic, we need to consider the temporal and spatial resolution of GYRO outputs. The temporal resolution of the GYRO output (c_s/a ~600kHz) is increased by a factor of two through the linear interpolation of data in the time domain before applying the transform from the plasma to the lab frame to prevent aliasing in the synthetic spectra and to have a sufficient sampling rate for Doppler-shifted spectra. The radial and poloidal resolution of the CECE diagnostic estimated in Chapter 2 is about 1cm and less than 1cm, respectively. In the GYRO runs for C-Mod Ohmic discharges used in Chapter 4, the radial spacing was set to $0.25\rho_s$. Since $0.25\rho_s$ <0.1cm, the radial spacing of the GYRO output is enough for the synthetic CECE diagnostic. In the poloidal direction, 3200 grid points are set to have a sufficient resolution (~0.05cm). Since the vertical measurement position of the CECE was about 7cm above midplane, the simulated fluctuations at 7cm above midplane were used for synthetic signals.

In order to match the spectral shape, it is required to modify the rotation frequency, ω_o. In GYRO, it is possible to apply the mode number-dependent transform shown in Eq. 3.26 with the modified ω_o in the post-processing. Another way is to modify the rotation frequency in the input profiles. Since the former method will

generate synthetic signals which are not consistent with the simulation, the latter method was used in this study. It is noteworthy that only the amplitude of the rotation frequency was modified with the fixed gradient, so that the same rotation and $E \times B$ shearing rates are used in the simulation with the modified ω_o.

In the local simulations, which use flat profiles, all points in the simulation domain use the same input parameters. Six pairs of signals with different radial points in the simulation domain, which are not correlated, were used to increase the number of sub-data sets in the averaging, decreasing the statistical error in the synthetic cross power spectrum. The spectral analysis technique used for the synthetic fluctuations is almost identical to that used for the measured fluctuations as explained in section 3.1. The synthetic fluctuation level was calculated by integrating the cross power spectrum with the same frequency range used for the measured fluctuations. One difference is the normalization. The measured T_e fluctuations were not calibrated, and the relative T_e fluctuation level was obtained using the radiometer formula (Eq. 3.9), while all fluctuations from GYRO are already normalized properly. Thus, we do not have to apply any normalization to obtain the relative T_e fluctuation level. The spectral frequency for the synthetic spectrum was set to ~5kHz, which is similar to the value used for the measured spectrum. The uncertainty of the synthetic fluctuation level was estimated from the random error of the cross power spectrum and the systematic error from the estimation of radial broadening shape and the distance between two CECE channels. Using the error propagation technique, the uncertainty of the synthetic fluctuation level was then calculated. More details can be found in Appendix I.

3.5 Summary

In this chapter, four transport analysis methods or tools used in this thesis were introduced. They are CECE signal analysis, profile analysis, experimental transport analysis using TRANSP and gyrokinetic analysis using GYRO. In order to investigate the transport research topic in each chapter, these four analysis methods will be used.

One main work flow introduced in this chapter is the preparation of the gyrokinetic simulation, GYRO and the use of GYRO results to interpret the turbulence measurements and study the research topic of interest. In addition, the synthetic T_e fluctuations are compared with the T_e fluctuations measured by the CECE diagnostic. Profile analysis is first performed to prepare the input profiles for TRANSP. These input profiles are used in TRANSP via pretransp. TRANSP is then run, and the outputs from TRANSP are converted to GYRO input profiles through TRXPL and profiles_gen. Last, we run GYRO, and obtain the heat flux-matched simulation by modifying the input parameters within the uncertainty. In the heat flux-matched simulation, synthetic T_e fluctuation signals are generated in the post-processing using the synthetic CECE diagnostic for C-Mod. These signals are finally compared with the measured T_e fluctuations. However, it is worth noting that the outputs of each stage in this workflow can be used to study the transport research topic in each chapter. From the profile analysis, the transport relevant parameters such as gradient scale lengths will be obtained, and we are able to explore the correlation among these parameters with the changes in the transport phenomenon of interest. From TRANSP, the experimental heat flux levels are obtained. These experimental heat flux values will indicate the changes in heat transport behavior with the changes in the transport property that we want to investigate. Last, the correlation between turbulence changes with the transport property of interest is studied using the measured and simulated turbulence from the CECE diagnostic and GYRO, respectively.

The analysis procedure using these four analysis methods is as follows. We will first analyze the measured fluctuations in C-Mod plasmas, which have different/similar behaviors related to the research topic studied in each chapter. We will determine the correlation between turbulence and the transport property we want to investigate at this stage. The second step is profile analysis to prepare the inputs for TRANSP and GYRO. Before running TRANSP or GYRO, we can compare transport relevant terms to investigate the observed relation between the turbulence and the transport property in the first step. The third step is running TRANSP. From TRANSP, the experimental heat flux and diffusivity will be obtained. We can then see the relation

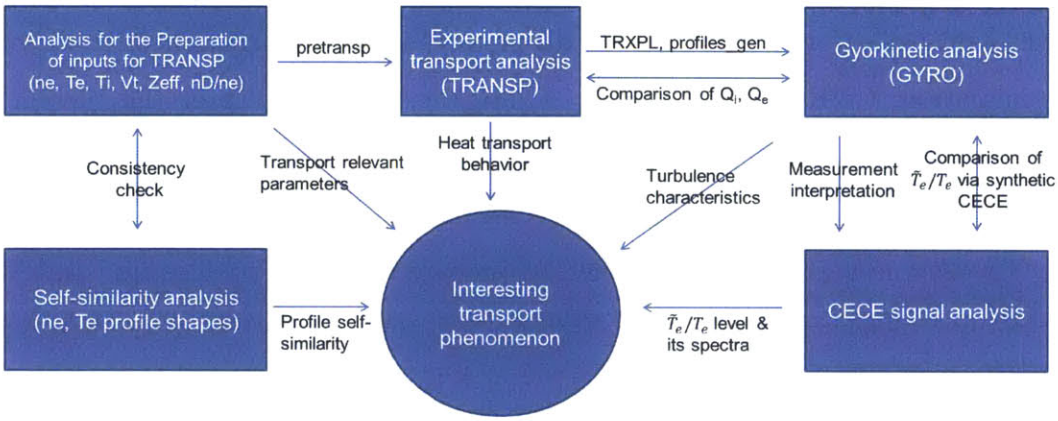

Figure 3-14: The simplified analysis procedure used in this study using the analysis methods introduced in this chapter.

among the changes in the measured turbulence, macroscopic heat transport behavior and the transport property of interest. The next step is gyrokinetic analysis using GYRO. GYRO will show the characteristics of turbulence in the plasmas in which we are interested. We are then able to interpret the measured turbulence using GYRO. In addition, self-similarity analysis is performed to determine the relation between the self-similarity property of the n_e and T_e profiles with the transport property of interest in this study. This analysis will show the relation between two macroscopic changes, changes in the profile shape and the transport phenomenon of interest. Using this additional profile analysis, we can check whether or not the results from two different profile analyses are consistent. The simplified analysis procedure is shown in Fig. 3-14.

In the following chapters, we investigate the following interesting transport phenamena, the Ohmic confinement transition, and core rotation reversal, transition from low to high energy confinement regime, using these four analysis methods.

Chapter 4

Study of Ohmic confinement transition physics and GYRO validation study for C-Mod Ohmic discharges near the edge

As explained in Section 1.3.1, the Ohmic confinement transition is an old mystery in fusion transport research. One reason why we still do not understand this transition may be the lack of turbulence measurements. In section 4.1, we present measurements of electron temperature fluctuations obtained using the CECE system on Alcator C-Mod explained in Chapter 2. These measurements are both the first local core turbulence measurements and the first measurements of electron temperature fluctuations ever to be performed in LOC and SOC regimes. In order to interpret fluctuation measurements in section 4.1, we performed profile analysis (introduced in section 3.2.1), power balance analysis (introduced in section 3.3) and gyrokinetic analysis (introduced in section 3.4) for the LOC/SOC plasmas. The self-similarity analysis (introduced in section 3.2.2) was also performed to explore macroscopic changes related to the LOC/SOC transition.

4.1 Fluctuation measurements in Ohmic L-mode plasmas

In this section, we first describe the changes in local electron temperature fluctuations near the edge (r/a$\sim$0.85) across the LOC/SOC transition. Then, using a phase contrast imaging (PCI) diagnostic [98, 121], the changes in line integrated density fluctuations are presented. Then, we will compare the trends of the two fluctuating quantities across the Ohmic confinement transition.

4.1.1 The reduction of electron temperature fluctuations in the SOC discharge compared to the LOC discharge

We first compared T_e fluctuations over the long stationary periods of two Ohmic plasma discharges (t=0.9-1.4 sec, i.e., Δt=0.5sec, during the plasma discharge); one in the LOC regime and one in the SOC regime. These discharges operated with a toroidal magnetic field of B_t=5.4 T in the co-current direction, Ohmic input power, P_{OH}=1MW, and plasma current, I_p=0.9 MA in Lower Single Null (LSN) configuration with R=0.67m, a=0.22m, elongation, κ=1.6, lower triangularity, δ_l=0.5 and upper triangularity, δ_u=0.3. They differ only in their densities (line averaged density measured by a two color interferometer [14, 88], $\bar{n}_e = 0.8 \times 10^{20} m^{-3}$ for LOC and $\bar{n}_e = 1.3 \times 10^{20} m^{-3}$ for SOC). It has been observed robustly that the direction of toroidal rotation is reversed at the LOC/SOC transition [129]. In C-Mod, LOC plasmas have core toroidal rotation in the co-current direction and it changes to counter-current direction in the SOC regime. We used the change in the core toroidal rotation direction to distinguish between Ohmic confinement regimes since it is the most sensitive indicator [129, 128, 131].

In order to verify stationary plasma conditions, which are required for the CECE measurements, we consider macroscopic plasma parameters such as plasma current and central line averaged electron density. Figure 4-1 shows the time series data for a typical LOC plasma (shot 1120626023) and a SOC plasma (shot 1120626028) in C-

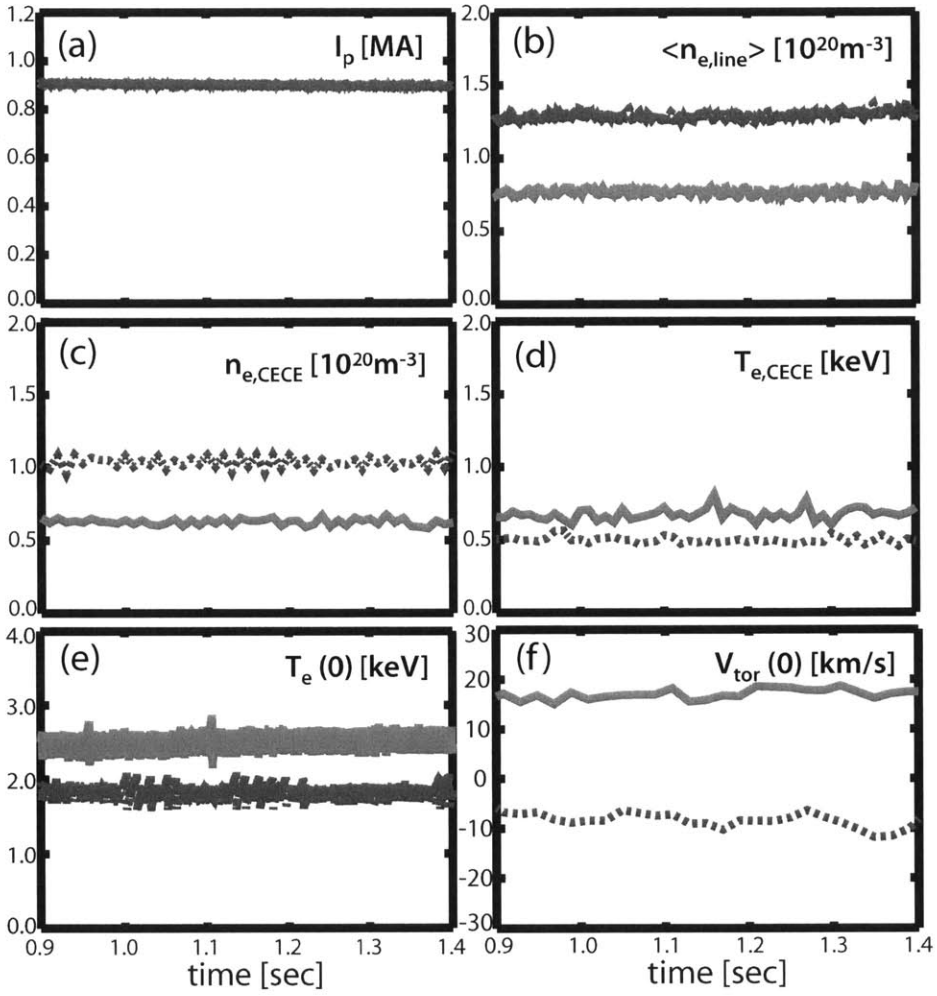

Figure 4-1: Time series data during CECE measurement time for LOC (shot:1120626023, red solid line) and SOC (shot:1120626028, blue dotted line) plasma. (a) Plasma current [MA], (b) central chord line averaged density [$10^{20}m^{-3}$], (c) electron density [$10^{20}m^{-3}$] at CECE measurement position (r/a$\sim$ 0.85), (d) electron temperature [keV] at CECE measurement position (r/a$\sim$0.85), (e) electron temperature [keV] at plasma center, (f) central toroidal velocity [km/s].

Mod during the measurement time (0.9-1.4s). Figure 4-1(a) shows the plasma current of the two plasmas, which is almost constant in this time range. C-Mod also has a very steady toroidal magnetic field (varies less than 1% of the mean value during measurement time), which ensures the position of CECE channels will also be steady. Figure 4-1(b) shows the central chord line averaged density. As shown in the figure, this quantity was steady, and fluctuated less than 5% of the mean value during the averaging time range (0.9-1.4s). We also checked electron density and temperature at the CECE measurement position (r/a$\sim$0.85) in this time range, shown in Fig. 4-1(c) and (d). The electron density and temperature at the CECE measurement position did not vary outside the error of each measurement. Figure 4-1(e) shows the electron temperature at the plasma center, where the presence of sawtooth activity results in perturbations of the electron temperature. However, the CECE measurement region (r/a$\sim$0.85) is well outside of the sawtooth inversion radius (r/a$\sim$0.35), and is not significantly affected by this perturbation. Figure 4-1(f) shows the core toroidal velocity. As expected, the LOC plasma (shot 1120626023) has toroidal rotation in the co-current direction, and the SOC plasma (shot 1120626028) rotates toroidally in the counter-current direction.

We notice the changes in T_e fluctuations between the LOC and SOC discharges. Figure 4-2 shows the coherence (γ_{xy}) and cross phase angle (θ_{xy}) of two adjacent CECE channels, which are separated radially by about 2mm along the CECE beam path and located at r/a$\sim$0.85 for typical LOC (shot 1120626023) and SOC (shot 1120626028) plasmas shown in Fig. 4-1. The dotted line in the coherence spectrum indicates the statistical limit of coherence. The spectrum in Fig. 4-2 was averaged over 0.5 sec (0.9-1.4 sec) to reveal electron temperature fluctuations and reduce random thermal noise. Figure 4-2(a) shows the spectrum in the LOC (shot 1120626023) regime. We can see broadband fluctuations above the statistical limit up to $\sim$170kHz in this spectrum. Figure 4-2(b) shows the coherence of two CECE signals in a SOC plasma. We can see that fluctuations up to 170kHz were reduced in the SOC regime compared to the LOC regime. We can also see that the cross phase spectra in Fig. 4-2(c) and (d) are correlated with the broadband fluctuations, indicating that the observed fluctuations

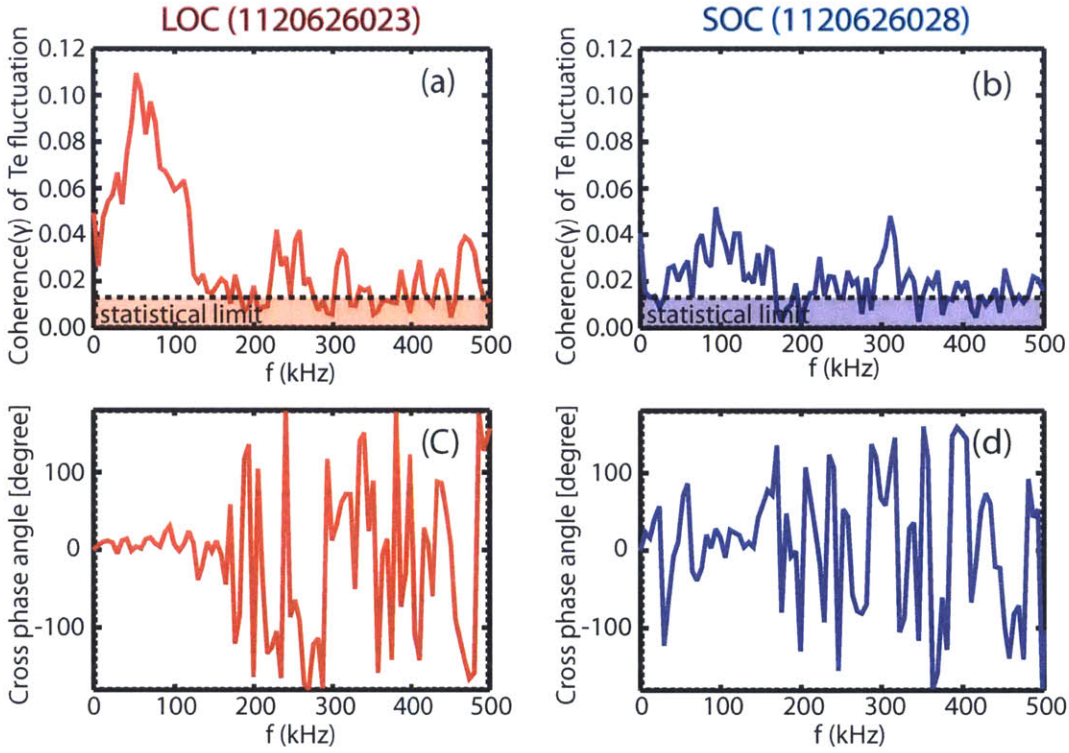

Figure 4-2: (a) Coherence (γ) of two CECE signals in the LOC plasma (shot:1120626023), horizontal dotted line indicates the statistical limit of coherence (b) Coherence (γ) of two CECE signals in the SOC plasma (shot:1120626028) (c) the cross phase spectrum of two CECE signals in the LOC plasma (d) the cross phase spectrum of two CECE signals in the SOC plasma.

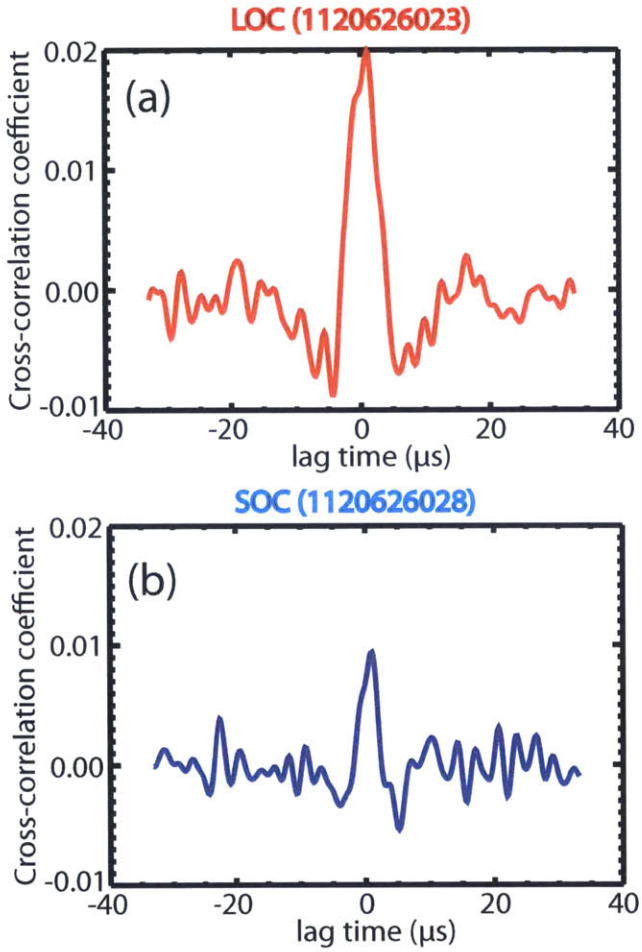

Figure 4-3: (a) Cross correlation coefficient (C_{xy}) depending on lag time [μs] of two CECE signals in LOC plasma (shot:1120626023) (b) C_{xy} depending on lag time of two CECE signals in SOC plasma (shot:1120626028).

in Fig. 4-2 (a) and (b) are real physical fluctuations. The reduction of fluctuations can be also observed in Fig. 4-3. Figure 4-3(a) and (b) shows the cross correlation coefficient(C_{xy}) curve of the same LOC and SOC plasmas during 0.5sec (0.9-1.4sec) respectively. As shown in Fig. 4-3, we can see that the correlation peak at lag time=0 ($C_{xy}(0)$) decreases in the SOC regime compared to the LOC regime. As explained in section 3.1, $C_{xy}(0)$ is proportional to the fluctuation level. Thus, the decrease of $C_{xy}(0)$ implies the reduction of the relative electron temperature fluctuation level across the LOC/SOC transition.

Using Eq. 3.10 in section 3.1.1, the relative fluctuation level ($\tilde{T}_e/T_e$) was calculated. The proper frequency range for cross spectral density integration was determined

from coherence and cross phase spectrum, and was 0-170kHz and 70-170kHz for the LOC and SOC plasma, respectively. The calculated T_e fluctuation level was reduced from 1.0% in the LOC regime to 0.6% in the SOC regime, a 40% reduction. It can be pointed out that the reduction is related to the smaller frequency range for the fluctuations in the SOC regime compared to the LOC regime. When we set the same frequency range as 0-170kHz, the fluctuation level in the SOC regime is 0.7%, and we still see a 30% reduction of electron temperature fluctuations.

4.1.2 The observation of changes in line-integrated density fluctuations in the SOC discharge compared to the LOC discharge

Using the PCI system on Alcator C-Mod [98, 121], line integrated density fluctuations are measured in the same LOC and SOC plasmas where CECE measurements are made. Figure 4-4(a) and (b) show the normalized frequency/wavenumber spectra of PCI measurements, which is defined as the frequency/wavenumber spectra, $S(k_R, f)$ divided by the square of the line averaged density in the LOC and SOC plasmas, respectively. Thus, the relative line integrated density fluctuation level, $|\int \tilde{n}_e \mathrm{d}l|/n_e l$, can be calculated by integrating this spectrum. The positive wave number in this spectrum indicates that the turbulence moves radially to the lower field side, and the negative wave number represents turbulence that propagates to the higher field side radially in PCI measurements [99]. From these figures, we can observe that the SOC plasma has larger fluctuations than the LOC plasma. The relative line integrated fluctuation level ($|\int \tilde{n}_e \mathrm{d}l|/n_e l$) was increased $\sim$10% in the SOC plasma compared to the LOC plasma from 0.049% to 0.054% when whole k_R values are included and the frequency range is set to 50kHz<f<1000kHz.

In the past, there has been an observed "wing" structure in the frequency/wavenumber spectra, $S(k_R, f)$ of PCI measurements of electron density fluctuations in LOC plasmas [128, 129]. This structure disappears abruptly after the transition from LOC to the SOC regime, as shown in Figure 22 in [129]. However, in our experiments, we

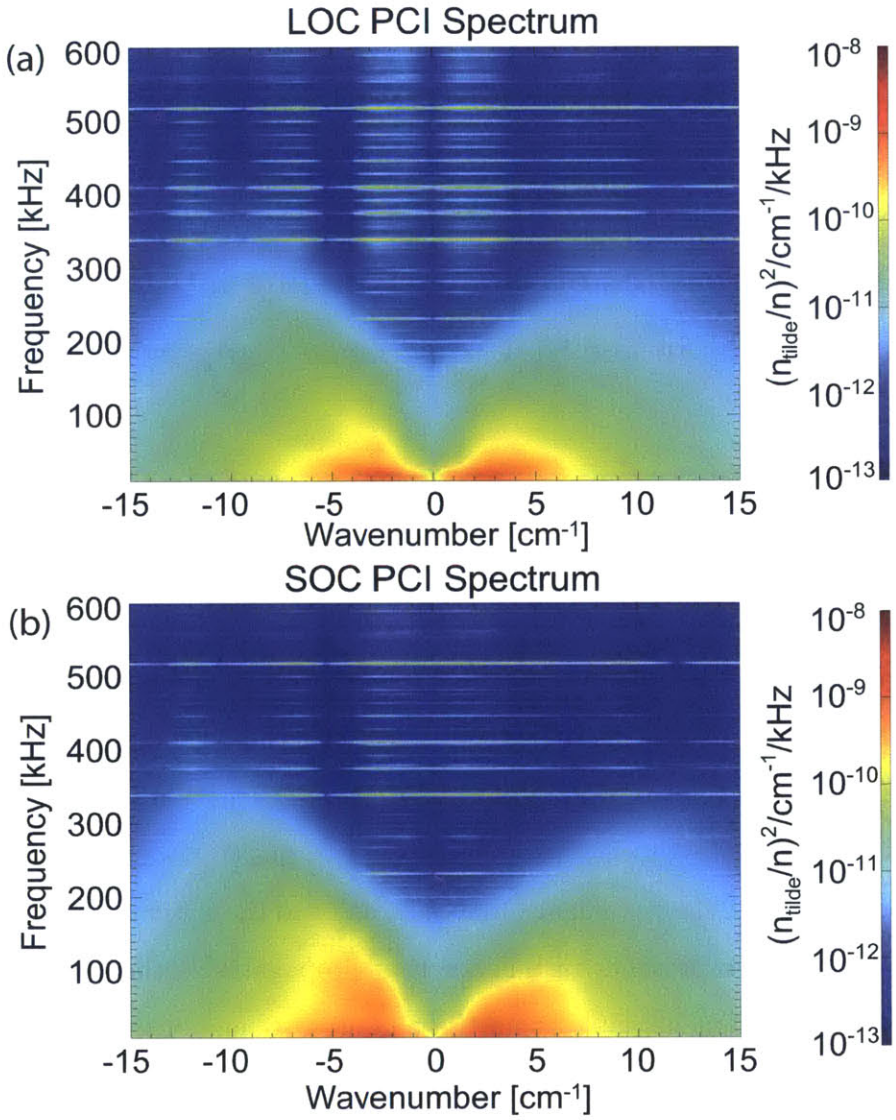

Figure 4-4: Normalized frequency/wavenumber spectra ($S(k_R, f)/n_e$) of PCI measurements (a) in LOC (shot:1120626023) and (b) in SOC (shot:1120626028) plasmas.

could not observe any distinct structure in the PCI $S(k_R, f)$ spectrum for the LOC plasma compared to the SOC plasma as shown in Figure 4-4. Since the rotation reversal at the LOC/SOC transition occurs inside in a q=3/2 surface [129], the plasma current may be related to whether or not this feature appears in the PCI spectra. Moreover, it was only in a high plasma current LOC discharge ($I_p \geq 1$ MA) that the wing structure was observed in the past and the plasma in Figure 4-4 has lower plasma current ($I_p \sim 0.9$ MA). Thus, low plasma current might be responsible for the lack of wing structure in Figure 4-4. However, it is unclear whether the plasma current is directly related to the wing structure or other relevant parameters that scale with plasma current. The relation between the wing structure to the LOC/SOC transition is still inconclusive and is being investigated. It is noteworthy that this feature in the PCI spectra has been localized by past analysis to a radial region farther inside of the plasma ($r/a \lesssim 0.65$, inside of the reversal radius) [128, 129] than the CECE measurement position ($r/a \sim 0.85$) in this work. It is also noteworthy that the contribution of the wing structure to the relative line integrated fluctuation level ($|\int \tilde{n}_e dl|/n_e l$) is negligible.

4.1.3 Variations of electron temperature fluctuations and density fluctuations across the LOC/SOC transition

In order to explore possible causes for the observed differences in how electron temperature and density fluctuations change in Ohmic plasmas across the LOC/SOC transition, we studied the dependence of the T_e and n_e fluctuation levels on the normalized average electron density (n_e/n_{crit}). The critical density for the rotation reversal in C-Mod Ohmic discharges, $n_{crit} = 2.8 I_p/B^{0.6}$ with n_{crit} in $10^{20} m^{-3}$, on axis toroidal magnetic field, B, in T and I_p in MA, and, is indicative of the transition from the LOC/SOC according to [129]. Since this critical density comes from an empirical scaling, it is hard to say whether a plasma with an average density value near the critical density is in the LOC or SOC regime. However, considering errors in the scaling, we can robustly say that if this normalized density value is less than

1 ($n_e/n_{crit} \lesssim 0.85$), the plasma is in the LOC regime, and for the opposite case ($n_e/n_{crit} \gtrsim 1.15$), the plasma is in the SOC regime.

In this analysis, we included most Ohmic discharges conducted in the 2012 campaign (2012.06-09) which satisfy the following three criteria. First, the discharges whose stationary time period is longer than 0.3 sec were chosen to have enough sensitivity level ($\geq 0.3\%$ from Eq. 2.12 with IF bandwidth, $B_{IF} = 200$MHz, video bandwidth, $B_{vid} = 0.5$MHz). Second, discharges should be optically thick at the measurement position. Since the CECE measurement position in this study is near the edge, it is possible that the optical depth is not high enough to ignore the effect of the density fluctuations. As discussed in section 3.1.2, fluctuations of radiation intensity measured by the CECE diagnostic can be contaminated by density fluctuations when optical depth, τ, is low ($\tau < 2$) [124]. Thus, the discharges whose optical depth is less than 2.0 were excluded. Last, the signals which have the noise issue, described in Appendix B, were excluded.

Figure 4-5 shows the changes in T_e fluctuations near the edge (r/a=0.83-0.87) across the LOC/SOC transition. We found that T_e fluctuations tend to decrease as plasma moves from the LOC regime to the SOC regime or as the normalized density by critical density for rotation reversal (n_e/n_{crit}) value increases as shown in Fig. 4-5(a). It is also noticeable that the average value of T_e fluctuation levels in the LOC region ($n_e/n_{crit} \lesssim 0.85$) is higher than the average value in the SOC region ($n_e/n_{crit} \gtrsim 1.15$). However, as discussed in section 3.1.2, we should be cautious about the electron temperature fluctuation data from the discharges whose optical depth is 2-3 at the measurement position due to the density fluctuations. The red and blue points in Fig. 4-5(b) are the maximum and minimum values when the relative density fluctuation level is 2%. As mentioned in section 3.1.2, electron density fluctuation level was conservatively set to 2% in this analysis from the past measurements in DIII-D, which showed that relative density fluctuation levels are comparable to the temperature fluctuation levels [179], and the maximum electron temperature fluctuation level in C-Mod is less than 2%. As shown in Fig. 4-5(b), red and blue points still tend to decrease with the normalized density (n_e/n_{crit}). Thus, even assuming the

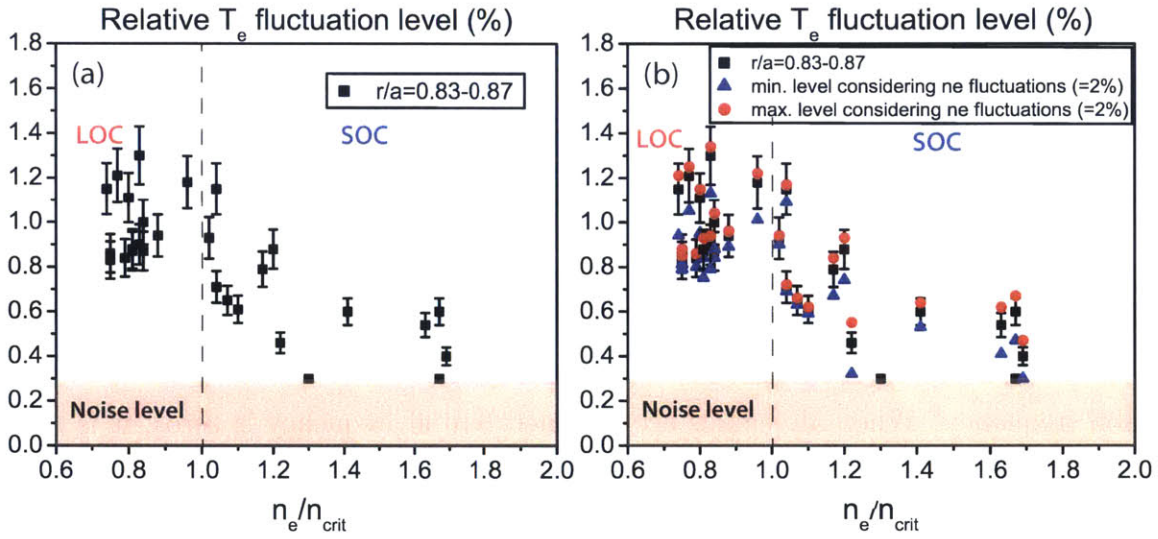

Figure 4-5: Time averaged relative T_e fluctuation levels with $n_{e,avg}/n_{crit}$ at r/a=0.83-0.87 in the C-Mod Ohmic discharges. (a) The relative fluctuation level without considering density fluctuations (only black points) (b) The relative fluctuation levels with considring density fluctuations. Red/blue points are minimum/maximum values of the relative electron temperature fluctuation level when the relative density fluctuation level is 2%. n_{crit} is the critical density for toroidal rotation reversal in the core region, defined as $n_{crit} = 2.8I_p/B^{0.6}$ with n_{crit} in $10^{20}m^{-3}$, on axis toroidal magnetic field, B, in T and I_p in MA, and. The toroidal rotation reversal in the core region is indicative of the transition from the LOC/SOC according to [129].

maximum contamination by large density fluctuations ($\sim 2\%$) does not eliminate the observed trend in the CECE measurements. Furthermore, since electron temperature decreases as density increases, there must also be a reduction in *absolute* temperature fluctuation levels, given the measured decrease in *relative* temperature fluctuation levels near the edge.

However, the trend in the relative line integrated electron density fluctuation level with the normalized density (n_e/n_{crit}) was not clear. Figure 4-6 shows the relative line integrated electron density fluctuation level ($|\int \tilde{n}_e dl|/n_e l$) for the same plasmas. The error bar in Fig. 4-6 was estimated from time averaging. It is known that the low frequency fluctuations from PCI measurements propagate in both the ion and electron diamagnetic directions. This indicates that low frequency PCI signals come from the edge [99], and therefore to estimate the core density fluctuation level, we only consider the higher frequency fluctuations. However, it is not clear what the proper cutoff frequency should be to isolate the core density fluctuations, so we varied the cutoff frequency. When all signals are included (cutoff frequency is zero), it is hard to identify any trend in the relative line integrated electron density fluctuation level with n_e/n_{crit} as shown in Fig. 4-6(a). When cutoff frequency is 50-200kHz, Fig. 4-6(b)-(d) shows that the density fluctuation level tends to increase with n_e/n_{crit} in the SOC regime ($n_e/n_{crit} \gtrsim 1.15$). However, the variations in amplitude of the density fluctuation level in $n_e/n_{crit} \gtrsim 1.15$ are comparable to the variations in $n_e/n_{crit} \lesssim 1.15$. Thus, the trend in $n_e/n_{crit} \gtrsim 1.15$ is not clear at this point. Although it is inconclusive whether the line integrated density fluctuations in the core region (filtered by high pass filter) has a trend with n_e/n_{crit} or not, we can say that the trend is not as clear as observed in electron temperature fluctuations. Even if there is a trend, it is valid only in the SOC regime, and the tendency of core line integrated density fluctuations is opposite to the tendency of electron temperature fluctuations near the edge region.

These two different trends in T_e and n_e fluctuations can be interpreted from two different points of view. First, we can think of it as the different trends between local and global fluctuations. We see a clearer trend in local fluctuation changes near the edge than the global, line integrated fluctuations. This may suggest that the local

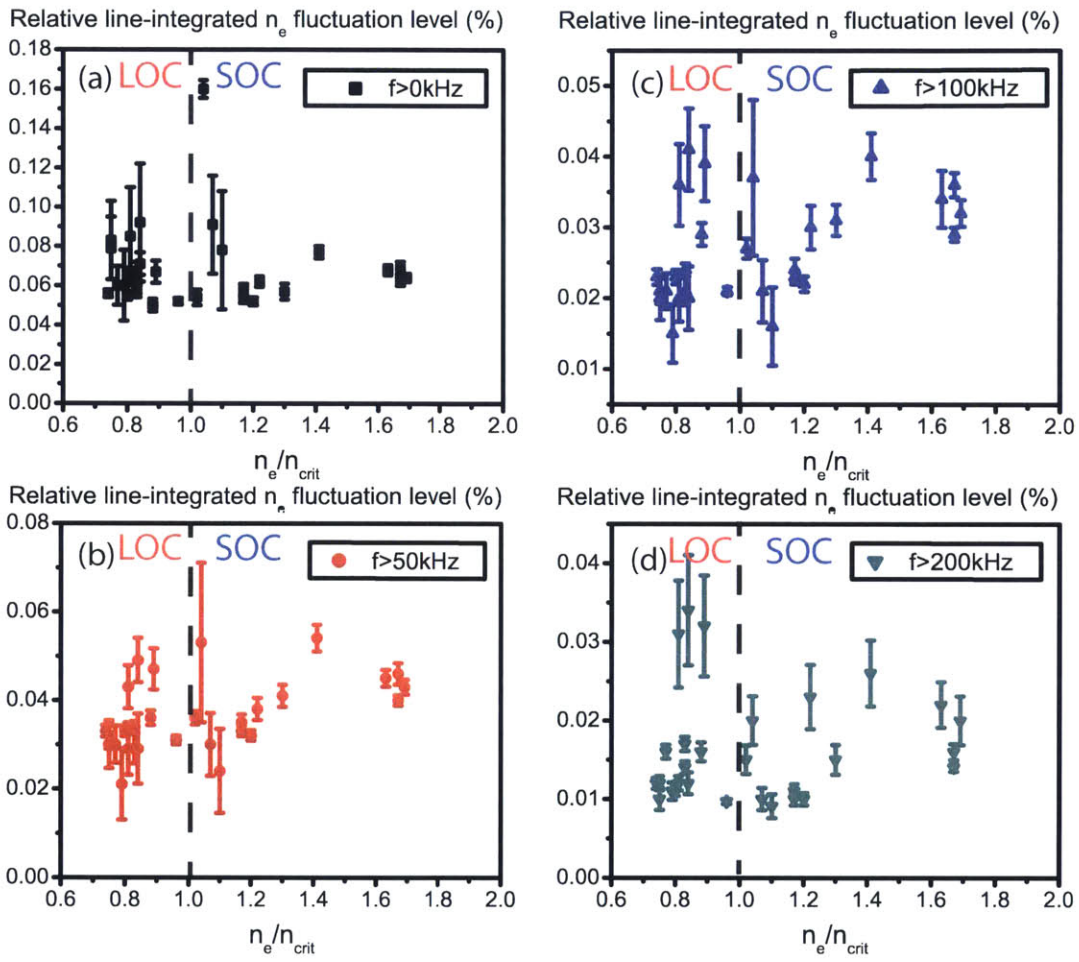

Figure 4-6: Relative line-integrated n_e fluctuation levels with $n_{e,avg}/n_{crit}$ in the C-Mod Ohmic discharges. n_{crit} is the critical density for toroidal rotation reversal in the core region, defined as $n_{crit} = 2.8I_p/B^{0.6}$ with n_{crit} in $10^{20}m^{-3}$, on axis toroidal magnetic field, B, in T and I_p in MA, and. The toroidal rotation reversal in the core region is indicative of the transition from the LOC/SOC according to [129]. In order to observe n_e fluctuations in the core region, low frequency signals are filtered (a) f>0kHz (b) f>50kHz (c) f>100kHz (d) f>200kHz.

changes in fluctuations correlate with the global confinement changes. However, local turbulence measurements deeper in core region are required to verify this speculation. It is also possible to see the difference in the two fluctuation measurements as the difference between electron temperature and density fluctuations. Following the arguments in [179], the ratio of electron temperature and density fluctuations is proportional to the ratio of the linear growth rates of the TEM and ITG mode. Although the density fluctuations observed in this section are not local fluctuations, assuming local density fluctuations near the edge region follow the trend in line integrated fluctuations, the decrease of electron temperature fluctuations with no or weak increase of electron density fluctuations can be linked to the *ansatz* about LOC/SOC transition, that TEM is dominant in the LOC regime and ITG is dominant in the SOC regime, as explained in Chapter 1. In order to verify this interpretation, we need local density fluctuation measurements in the future and gyrokinetic analysis to see the changes in turbulence across the LOC/SOC transition as shown in section 4.3 and 4.4.

4.2 Profile analysis & power balance analysis for the LOC/SOC plasmas : Preparation of input profiles for gyrokinetic analysis

In this section, we performed profile analysis and power balance analysis using TRANSP for the LOC/SOC discharges used in section 4.1.1 and 4.1.2. As explained in Chapter 3, these analyses are required to prepare the input profiles for the gyrokinetic simulation (GYRO). It is noteworthy that we can also predict the changes in turbulence, such as the changes in dominant turbulence mode, across the LOC/SOC transition by comparing the turbulence relevant parameters between the LOC and SOC discharges such as gradient scale lengths obtained from the profile analysis before running the expensive gyrokinetic simulations. In order to interpret the fluctuation measurements in section 2.1 and their connection to the global confinement transition, the turbu-

lence relevant profiles are compared between LOC/SOC discharges. We also study the changes in electron and ion heat transport behaviors from power balance analysis using TRANSP.

4.2.1 Comparison of turbulence relevant profiles between LOC and SOC plasmas

We first compared the turbulence relevant profiles between the LOC and SOC discharges in section 4.1.1 and 4.1.2 to interpret the fluctuation measurements in section 4.1. Since the measured fluctuations in section 4.1 were time-averaged (t=0.9-1.4sec for these two discharges), we used the time averaged profiles in the same time range. Figure 4-7 shows the time-averaged profiles relevant to turbulence for LOC and SOC plasmas. The solid line in this figure shows the experimental value and the dotted line represents the uncertainty in the measured profiles. The green vertical line indicates the CECE measurement position (cold resonance position of the measured EC radiation). The profile analysis explained in section 3.2.1 and Appendix F was performed to obtain profiles and their uncertainties shown Fig. 4-7(a)-(h) (the profiles of electron density (n_e), temperature (T_e), ion temperature (T_i), their gradient scale lengths (a/L_{n_e}, a/L_{T_e}, a/L_{T_i}, where $a/L_x = a|d(lnx)/dr|$) and toroidal rotation velocity, V_t). Electron collisionality, ν_e^*, shown in Fig. 4-7(i), is defined as $\nu_e^* = \frac{\nu_e}{\omega_{b,e}}$, where ν_e is the electron ion collision frequency, defined as $\nu_e = 2.91 \times 10^{-6} n_e[cm^{-3}] \ln\Lambda T_e[eV]^{-3/2}$ [Hz] with the Coulomb logarithm, $\ln\Lambda$, and $\omega_{b,e}$ is the electron bounce frequency, defined as $\omega_{b,e} = \epsilon^{1/2}\frac{v_e}{qR}$ with the inverse aspect ratio, ϵ, the velocity of electron, v_e, and the safety factor, q [144]. The collisionality was calculated from TRANSP [4] and its uncertainty was obtained from the standard deviation of time-averaged profiles. The safety factor, q, profile (Fig. 4-7(j)) was obtained from the equilibrium reconstruction constrained by magnetic diagnostics via the equilibrium code (EFIT) [96].

As shown in Fig. 4-7, the SOC discharge has higher electron density and lower electron temperature in the whole radial region except for the edge region (r/a>0.9) where the T_e values in the SOC plasma are similar to the values in the LOC within the

uncertainty. The higher n_e and lower T_e make the SOC discharge more collisional than the LOC discharge in the core region as shown in Fig. 4-7(h). Ion temperature is similar between LOC/SOC plasmas in the whole radial region. Consequently, the ratio of T_e to T_i (T_e/T_i) is lower in the SOC discharge compared to the LOC discharge. Last, there was no significant difference outside, errors, between the LOC/SOC discharges in gradient scale lengths and safety factor, q. They have the opposite direction of core toroidal rotation from the toroidal rotation velocity (V_t) profile. The V_t value itself does not affect the turbulence, but does affect the fluctuation measurements. This is because the measured fluctuations will be spread more with the higher toroidal velocity due to the Doppler effect. The radial gradient of V_t will affect the ExB shearing rate ($\gamma_{E\times B}$), and thus affect the turbulence. The V_t profile shown in Fig. 4-7 are used to estimate the rotation frequency, ω_o, and $\gamma_{E\times B}$ for the gyrokinetic analysis in section 4.3 and 4.4. It is noteworthy that all parameters shown in Fig. 4-7 except for collisionality are similar within the uncertainty at the CECE measurement position. Higher collisionality in the SOC regime will reduce the response of non-adiabatic electrons, which are mostly trapped electrons. Higher collisionality can be a reason of reduction of electron temperature fluctuations near the edge because temperature fluctuations come from the non-adiabatic electrons' response as shown in Appendix G. However, CECE measurements do not necessarily imply a change of dominant turbulent mode across the LOC/SOC transition, as suggested by past authors [163, 125, 131]. This is because non-adiabatic electrons destabilize the ITG mode as well [136, 40]. It is also noteworthy that the LOC plasma is more diluted by impurities than the SOC plasma. The estimated main ion fraction (n_D/n_e) for the LOC/SOC discharges is 0.82($\pm$0.09) for the LOC and 0.95($\pm$0.03) for the SOC discharges. More details about this estimation are explained in Appendix F. Since higher n_D/n_e destabilize ITG turbulence more [104], the ITG mode will be less stable in the SOC discharge. In the core region, deeper than the CECE measurement region, an additional difference was observed. T_e/T_i decreases across the LOC/SOC transition. It is known that higher T_e/T_i is favorable for the ITG mode, while the TEM is not affected by this ratio [117, 169]. Then, the decrease of T_e/T_i makes the LOC more ITG favorable,

which is conflicted with the old hypothesis about the LOC/SOC transition. It will be interesting to observe how the increase of collisionality and n_D/n_e and the decrease of T_e/T_i across the LOC/SOC transition affect the changes in turbulence across the LOC/SOC transition in the core region through gyrokinetic analysis.

4.2.2 Power balance analysis using TRANSP

Changes in the experimental heat transport behavior between the LOC/SOC plasmas were studied from the electron/ion heat diffusivities and fluxes obtained through power balance analysis using TRANSP, as explained in section 3.3. The profiles shown in Fig. 4-8 are time-averaged during the steady periods of interest (t=0.9-1.4sec), and their uncertainties are estimated by considering the uncertainties of the dominant terms in the power balance analysis through error propagation. More details can be found in Appendix H. As shown in Fig. 4-8, the SOC plasma has lower electron thermal heat diffusivity and flux than the LOC plasma, while ion heat diffusivity and heat flux in the SOC plasma are higher in the whole radial region outside the sawtooth inversion radius (~0.4) although their differences are within the uncertainty except for the ion heat flux. This result is consistent with similar analysis performed in the past in FTU [51] and C-Mod [99], but inconsistent with the result in Tore Supra [57].

4.2.3 Input parameters of gyrokinetic simulations for the LOC/SOC plasmas

Table 4.1 shows the input parameters used in the local gyrokinetic simulations, performed at two locations, r/a=0.6 and ~0.85 (cold resonance position of the CECE measurements for the LOC/SOC plasmas). In the last two sections, we observed the changes in the measured fluctuations and experimental ion/electron transport across the LOC/SOC transition. In the next section, we will study the changes in turbulence and transport through gyrokinetic analysis using GYRO for the same LOC/SOC plasmas analyzed in the last section (LOC : 1120626023, SOC : 1120626028, t:0.9-1.4sec).

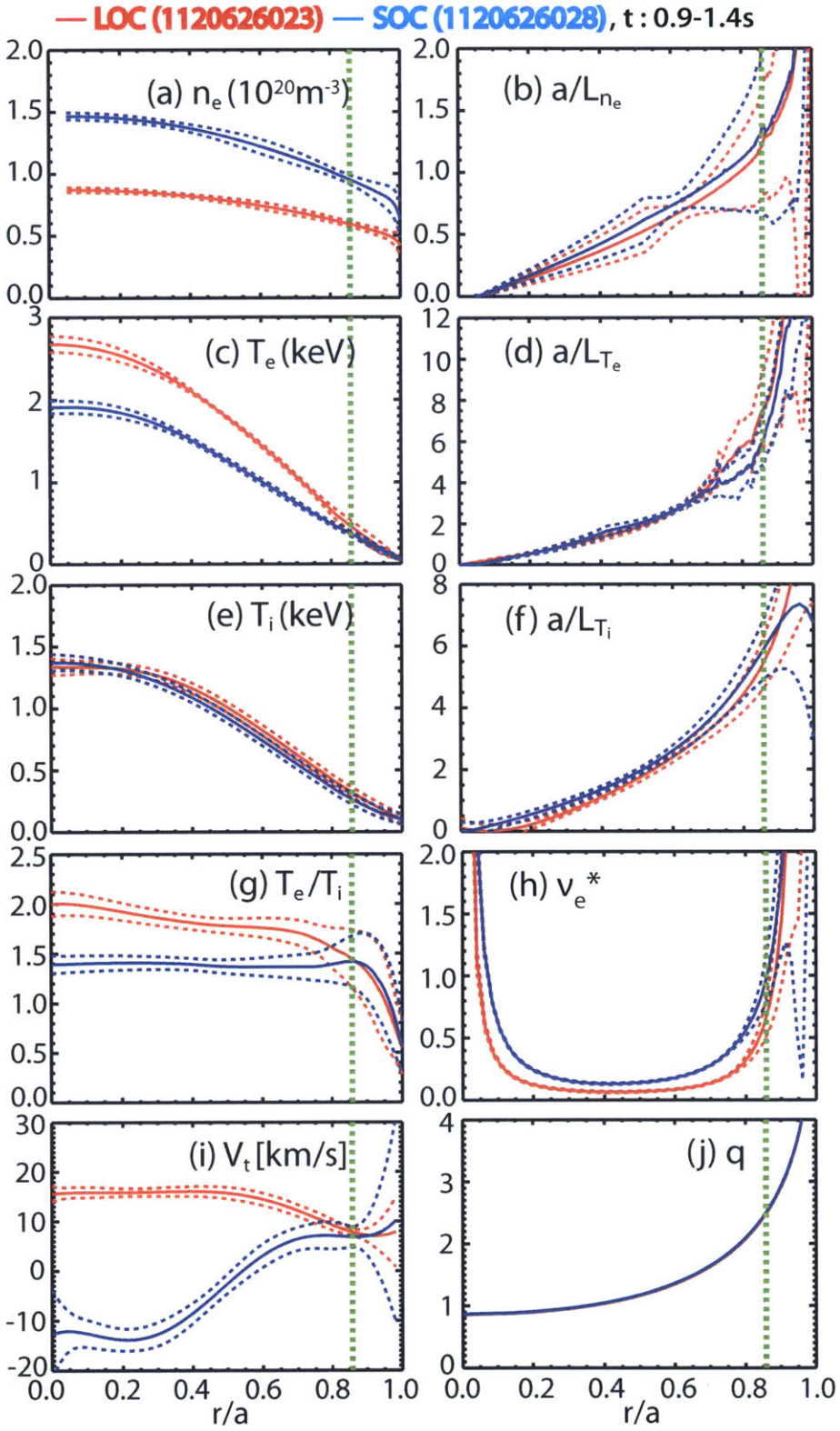

Figure 4-7: Profiles relevant to turbulence and CECE measurements in the LOC/SOC discharges (red : LOC discharge, blue : SOC discharge). The solid line shows the experimental value and the dotted line indicates the uncertainty. The vertical green line shows the CECE measurement position.

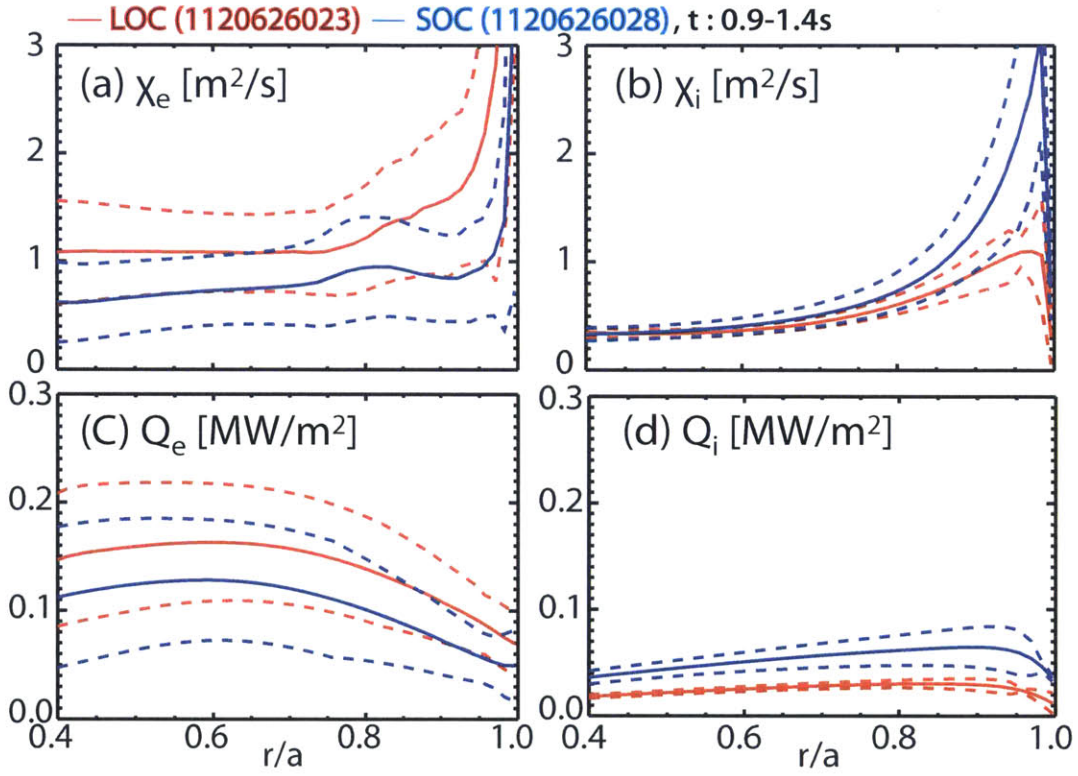

Figure 4-8: Heat diffusivity and flux for LOC/SOC plasmas (red : LOC discharge, blue : SOC discharge) (a) Electron heat diffusivity (χ_e $[m^2/s]$) (b) Ion heat diffusivity (χ_i $[m^2/s]$) (c) Electron heat flux (Q_e $[MW/m^2]$), (d) Ion heat flux (Q_i $[MW/m^2]$). The solid line shows the experimental value and the dotted line indicates the uncertainty.

	LOC		SOC	
r/a	0.6	~0.85	0.6	~0.85
ρ_*	3.4×10^{-3}	1.5×10^{-3}	2.8×10^{-3}	1.4×10^{-3}
c_s/a [MHz]	1.17	0.65	0.98	0.59
$n_e[10^{20}m^{-3}]$	0.74 (±0.030)	0.58 (±0.022)	1.20 (±0.059)	0.94 (±0.036)
a/L_{n_e}	0.65 (±0.085)	1.25 (±0.45)	0.74 (±0.071)	1.30 (±0.57)
T_e [keV]	1.40 (±0.027)	0.43 (±0.068)	0.97 (±0.037)	0.35 (±0.030)
a/L_{T_e}	2.65 (±0.11)	7.48 (±1.84)	2.70 (±0.13)	6.28 (±1.16)
T_i [keV]	0.80 (±0.044)	0.31 (±0.040)	0.71 (±0.042)	0.25 (±0.039)
a/L_{T_i}	2.47 (±0.17)	5.54 (±0.84)	2.70 (±0.18)	5.86 (±0.95)
T_e/T_i	1.75 (±0.010)	1.39 (±0.28)	1.37 (±0.096)	1.40 (±0.25)
Z_{eff}	2.53 (±0.47)	2.53 (±0.47)	1.48 (±0.25)	1.48 (±0.25)
n_D/n_e	0.82 (±0.09)	0.82 (±0.09)	0.95 (±0.03)	0.95 (±0.03)
n_B/n_e	0.036 (±0.018)	0.036 (±0.018)	0.01 (±0.006)	0.01 (±0.006)
$\nu_{ei}[c_s/a]$	0.071 (±0.013)	0.56 (±0.11)	0.23(±0.039)	1.28 (±0.22)
$\omega_o[c_s/a]$	0.0080 (±0.0014)	-0.0025 (±0.0016)	-0.0045 (±0.0027)	-0.0037 (±0.0045)
$\gamma_{E\times B}[c_s/a]$	0.011 (±0.0029)	0.017 (±0.016)	-0.021 (±0.0071)	0.0015 (±0.022)
$\gamma_P[c_s/a]$	0.084 (±0.014)	0.16 (±0.014)	-0.17 (±0.028)	0.015 (±0.22)
q	1.50	2.78	1.61	2.83
s	1.10	2.74	1.05	2.48

Table 4.1: Input experimental values for GYRO runs for LOC (shot 1120626023) and SOC (shot 1120626028) at r/a=0.6 and CECE measurement position (~0.85). The values are time averaged over 0.5s (0.9-1.4s). The definition of parameters are as follows. $\rho_* = \rho_s/a$ with sound gyroradius of main ion, ρ_s and minor radius, a. ν_{ei} is the electron-ion collision frequency, ω_0 is the ExB toroial rotation frequency, $\gamma_{E\times B}$ is the ExB shearing rate, and γ_P is a rotation shearing rate. q is the safety factor, and s is the magnetic shear defined as $s = r/q|dq/dr|$.

As explained in section 3.4, electrostatic, ion scale fluctuations were considered. In these ion scale simulations, the electron and ion modes can be connected to the TEM and ITG mode. Then, we can investigate an old hypothesis about the LOC/SOC transition (TEM-LOC, ITG-SOC) through gyrokinetic analysis. The experimental profiles shown in Fig. 4-7 were used as inputs. Also in the simulations, one impurity species (Boron, B) was used with the estimated main ion fraction (n_D/n_e). It was assumed that the main ion density gradient was not changed by including impurities in the simulations.

4.3 Gyrokinetic anaylsis in the core region for the LOC/SOC plasmas

We will first look at the changes in turbulence deeper in core (r/a=0.6). Since toroidal rotation reversal across the LOC/SOC transition occurs further inside, near the q = 3/2 surface (r/a~0.65 for the LOC/SOC discharges of interest) in C-Mod [129], it will be interesting to see the changes in turbulence where toroidal rotation reversal occurs.

4.3.1 Local linear gyrokinetic analysis

We first studied the changes in the dominant turbulence mode between the LOC/SOC plasmas in the core (r/a = 0.6) through linear stability analysis with the experimental parameters shown in Table. 4.1 without modification. In these simulations, the dominant modes, which have the highest growth rates, were found using an initial value solver in the ion scale turbulence ($k_y\rho_s \leq 1.2$, k_y is the poloidal wave number and ρ_s is the sound gyroradius of main ion, defined as $\rho_s = c_s/\Omega_{ci}$ with $c_s = \sqrt{T_e/m_i}$ and $\Omega_{ci} = eB/m_ic$). As explained in section 3.4, electron/ion modes refer to modes that propagate in the electron/ion diamagnetic directions. The sign of the real frequency is used to determine whether the mode is electron or ion mode. In GYRO, negative real frequency indicates the ion diamagnetic direction, and positive frequency indicates the electron direction. As shown in Fig. 4-9, the ion mode is dominant in the whole $k_y\rho_s$ region in both LOC and SOC discharges. In both discharges, the E×B shearing rate is less than 10% of the highest growth rate of the dominant mode in Fig. 4-9.

In order to verify the dominant turbulence mode at r/a=0.6, we performed sensitivity analysis of the most unstable mode with scans of a/L_{T_e} and a/L_{T_i}. Figure 4-10(a) and (b) show the results of this analysis where the contours of the growth rate of the most unstable linear mode in the $k_y\rho_s \leq 0.7$ are plotted. The horizontal and vertical axes indicate the values of a/L_{T_i} and a/L_{T_e} used in each simulation, respectively,

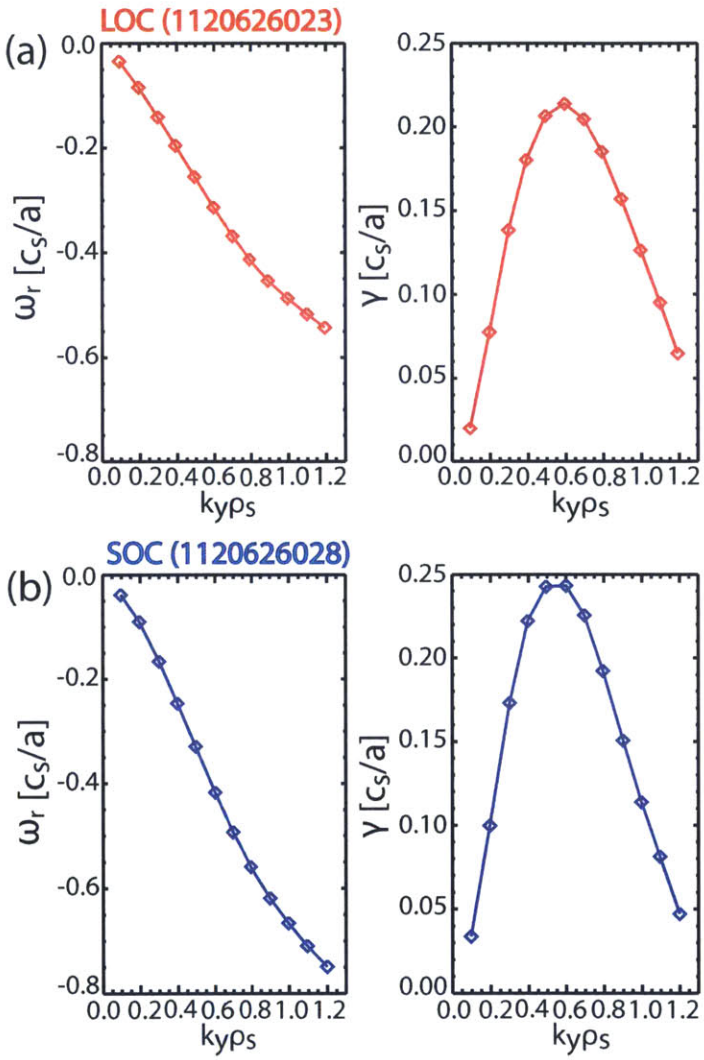

Figure 4-9: Linear stability analysis of (a) the LOC discharge and (b) SOC discharge. The left figures show the real frequency of the most unstable mode and the right figures show the growth rate of the unstable mode. The positive real frequency indicates the mode propagating in the electron diamagnetic direction, and negative real frequency indicates the opposite case. The unit of both real frequency and growth rate is c_s/a with $c_s = \sqrt{T_e/m_i}$ and minor radius, a. ($c_s/a = 1.17 \times 10^6$ /s (LOC) and 9.75×10^5 /s (SOC))

and the thick black line in the contour indicates the boundary between electron and ion modes from the sign of the real frequency. The location of the a/L_{T_i} and a/L_{T_e} values from the experiment is marked by a + sign, and the extended + sign by the dotted line indicates the experimental region within the errors. Since the ITG mode is sensitive to a/L_{T_i}, the change of growth rate will be sensitive to a/L_{T_i}, not a/L_{T_e}, if the ITG mode is dominant in the simulation. The same thing can be expected for the TEM, which is sensitive to a/L_{T_e}. We can see that the growth rate in the upper left region is sensitive to the a/L_{T_e} value. Consequently, the dominant turbulence mode in this region is driven by the electron temperature gradient, indicating TEM-type turbulence. In contrast, the growth rate of the lower right region of the contour is sensitive to the a/L_{T_i} value, so that the dominant mode in this region is driven by ITG, indicating the ITG mode.

Through this sensitivity analysis, we found that the ITG mode is dominant at r/a=0.6 in the both LOC and SOC discharges. As shown in Fig. 4-10, both LOC/SOC discharges are in the ITG dominant region at r/a=0.6. The uncertainties of a/L_{T_i} and a/L_{T_e} from Table 4.1 are about 4−8%. The typical uncertainty of T_e and T_i measurements is about 5-10%. Since a radial gradient of the profile is less constrained than the amplitude of the profile, and the uncertainty of the gradient scale length is obtained by propagating the uncertainties of the amplitude of profile and its gradient, it is expected that a gradient scale length has the larger uncertainty than the uncertainty of the profile itself, at least more than 5-10% in this case. Thus, it is hard to believe the estimated uncertainties of gradient scale lengths, comparable to the uncertainty in the profile measurements. It is possible that the core T_e and T_i profiles are over-constrained by the fitting for these profiles, we will then small uncertainties from the amplitude of the profile and its gradient. In the future, alternative analysis for the core profiles could be performed [34]. In this study, 20% uncertainty is used instead of the estimated uncertainty as shown in Fig. 4-10. Even with this generous uncertainty, both plasmas are still in the ITG dominant region. We also attempted to find the sub-dominant mode using the eigenvalue solver explained in section 3.4. However, no sub-dominant mode was found in either discharges. Thus, the ITG mode

is dominant at r/a=0.6 in both LOC and SOC discharges, and no changes in turbulence mode between the LOC and SOC plasmas were observed at this location from linear gyrokinetic analysis, consistent with the previous study in C-Mod [99].

4.3.2 Investigation of turbulence characteristics in the LOC/SOC plasmas through gyrokinetic simulations using experimental values.

We performed the non-linear gyrokinetic analysis for the LOC/SOC plasmas at r/a=0.6. The basic set-up for non-linear simulations in this section, such as velocity grid, rotation effects and particle treatments (gyro kinetic ion & drift kinetic electron) is the same as explained in section 3.4. For both LOC and SOC discharges, toroidal grid spacing Δn=12 and 16 toroidal modes are used. Then, ion scale turbulence modes ($k_y\rho_s$ <1.4-1.5) were considered in the simulations. Domain size was set to $L_x \sim 70 - 80\rho_s$ by $L_y \sim 60 - 70\rho_s$ with radial spacing, $\Delta r \sim 0.3 - 0.35\rho_s$. As shown in Fig. 4-11, GYRO over-estimated Q_i significantly (more than 8 times) in both LOC and SOC discharhges, while electron heat fluxes are matched within the uncertainties. This is consistent with previous studies [99, 120]. [120] shows that modifying the n_D/n_e value can be a way to solve this disagreement, but the study is in progress. Investigation of the over-predicted Q_i will be out of the scope of this study. Instead of matching Q_i by varying input parameters, we will study the turbulence characteristics and difference between the LOC and SOC discharges from the simulations using the experimental profiles without modification, as shown in Fig. 4-11. It is noteworthy that the over-prediction of ion heat flux in the ITG dominated region may suggest the overall turbulence levels are wrong. Thus, matching electron heat flux might not be meaningful. In this study, we just note the changes in the simulated turbulence by GYRO across the LOC/SOC transition.

It was found that the ion mode is dominant at r/a=0.6 in both LOC and SOC discharge from the nonlinear simulations. The dominant turbulence mode in the nonlinear runs can be observed from the power spectrum of fluctuating quantities

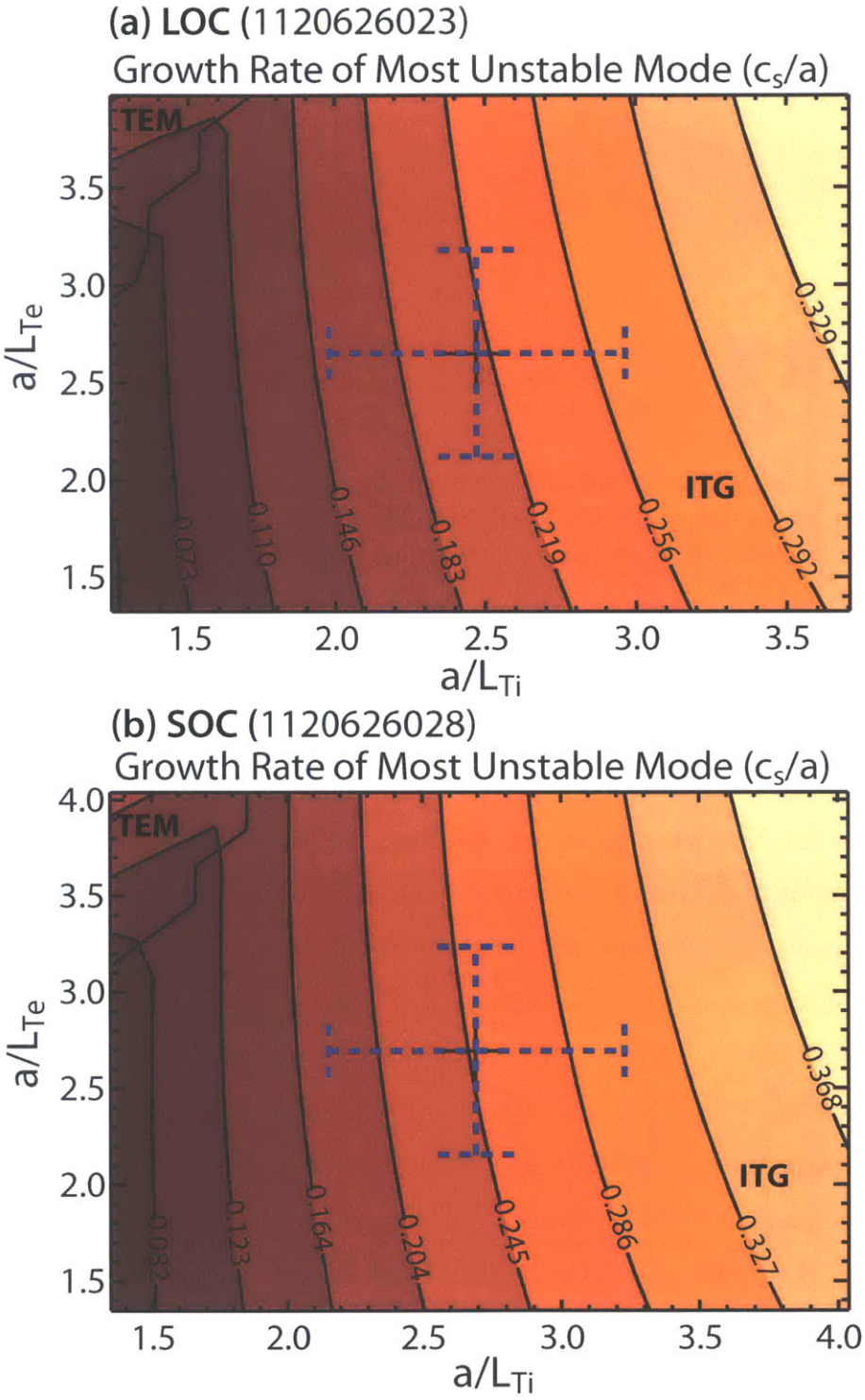

Figure 4-10: Contour of growth rate of most unstable mode with the change of a/L_{T_e} and a/L_{T_i} in the $k_y\rho_s$ range [0.1-0.7] in (a) the LOC discharge and (b) the SOC discharge. The uncertainties of a/L_{T_e} and a/L_{T_i} were set to 20%.

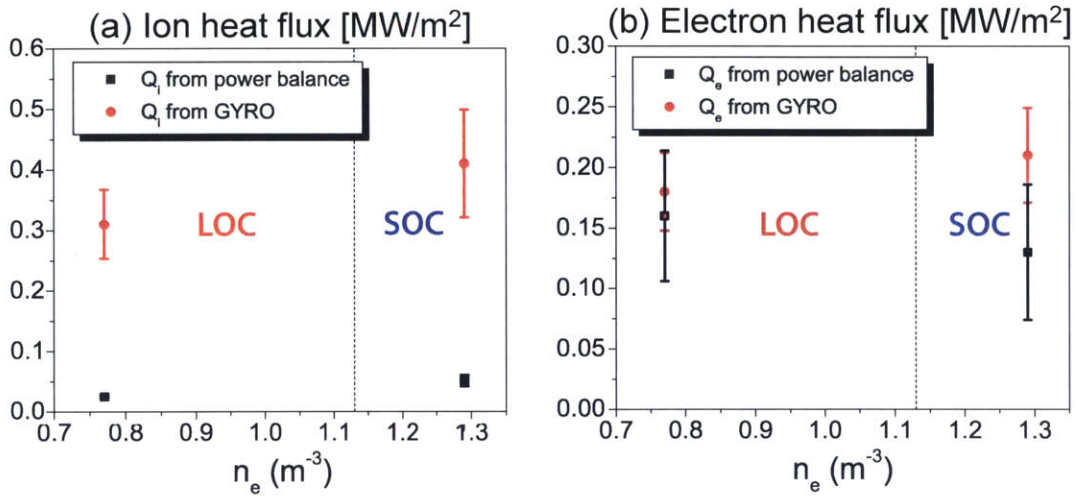

Figure 4-11: Comparison of simulated heat fluxes with the experimental heat flux obtained from power balance in the LOC/SOC discharges at r/a=0.6 (shot : 1120626023 (LOC), 1120626028 (SOC)) (a) Ion heat flux, $Q_i[MW/m^2]$ (b) Electron heat flux, $Q_e[MW/m^2]$. Vertical dash line indicates the rotation reversal density, obtained from the average electron density of rotation reversal discharge (shot 1120626028) on the same run day with the LOC/SOC discharges

per toroidal number, n. As explained in the last section, the electron and ion modes are determined from the sign of the real frequency (positive-ion, negative-electron). If the ion mode is dominant, we will see the mode propagating in the negative real frequency space. For the electron mode, it will be the opposite. Figure 4-12 shows the power spectrum of potential fluctuations on the midplane from the base cases for the LOC and SOC discharges. The fluctuations are averaged radially. It is shown that the potential fluctuations in the ion diamagnetic direction are stronger than in the electron direction in both LOC and SOC discharges, implying that the ion mode is dominant in both discharges. Although other fluctuating quantities are not shown here, the power spectrum of other fluctuations also have similar results, that is, stronger in the ion mode than in the electron mode.

Although we found that both LOC and SOC discharges are ion mode dominant, this does not indicate that the turbulence in both discharges is identical. To investigate the difference in turbulence between the LOC and SOC discharges, heat fluxes and RMS fluctuation levels of fluctuating quantities on the midplane were compared

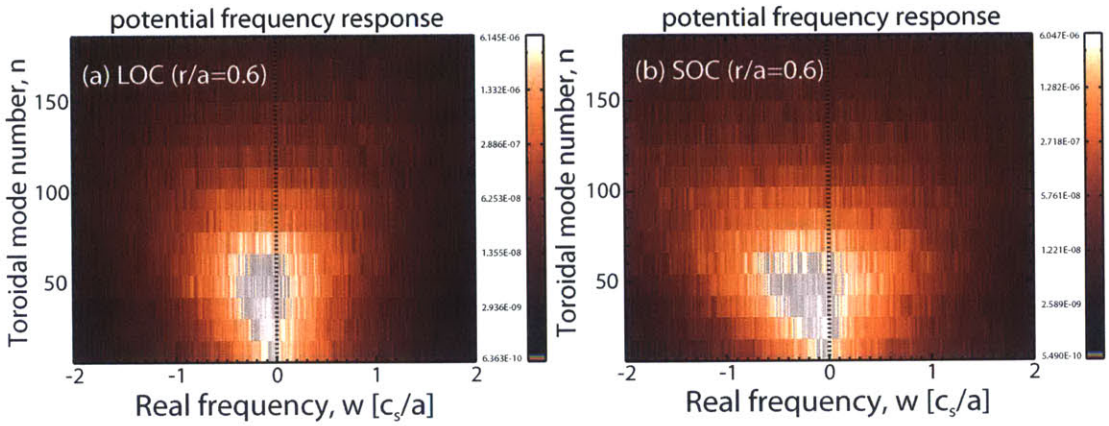

Figure 4-12: Power spectrum of simulated potential fluctuations on the midplane from the local nonlinear simulations at r/a=0.6 for (a) the LOC discharge (shot:1120626023) and (b) the SOC discharge (shot: 1120626028) with experimental input values. The simulated potential fluctuations are averaged radially. This figure was made by modifying GYRO analysis tool, "vugyro".

as shown in Table 4.2. In Table 4.2, heat fluxes are averaged in space and time, and midplane fluctuations are averaged radially and in time. The uncertainty is estimated from the standard deviation of the time averaging.

Table 4.2 shows that both ion and electron heat transport is enhanced in the SOC discharge compared to the LOC discharge. We also note that the increase of ion heat flux ($\sim 30\%$) is relatively larger than the increase of electron heat flux ($\sim 15\%$) between the LOC and SOC discharges. The enhancement of the ion heat transport is consistent with the power balance analysis results in section 4.2.2. In the fluctuating quantities on the midplane, the RMS fluctuation level of all fluctuations except for the electron temperature fluctuations increase in the SOC discharge compared to the LOC discharge. To be specific, potential fluctuations, electron density and ion temperature fluctuations increase by about 15-20% in the SOC discharge, while electron temperature fluctuations decrease slightly less than 5%. Ion density fluctuations also increase by about 10% in the SOC discharge. The increase of both density and temperature fluctuations of the ion may enhance ion transport in the SOC discharge, and the increase of only electron density fluctuations can explain the weaker increase of electron transport compared to ion transport across the LOC/SOC transition in these simulations. However, we must note that all changes in fluctuations and heat

	LOC	SOC
$Q_i[MW/m^2]$	0.31 ($\pm$0.057)	0.41 ($\pm$0.089)
$Q_e[MW/m^2]$	0.18 ($\pm$0.032)	0.21 ($\pm$0.039)
$e\tilde{\phi}/T_e[\%]$	3.06 ($\pm$0.46)	3.54 ($\pm$0.68)
$\tilde{n}_i/n_i[\%]$	1.72 ($\pm$0.13)	1.89 ($\pm$0.18)
$\tilde{n}_e/n_e[\%]$	1.46 ($\pm$0.11)	1.79 ($\pm$0.17)
$\tilde{T}_i/T_i[\%]$	2.56 ($\pm$0.28)	3.18 ($\pm$0.36)
$\tilde{T}_e/T_e[\%]$	1.65 ($\pm$0.14)	1.59 ($\pm$0.14)

Table 4.2: The non-linear simulation results, which are electron/ion heat fluxes and fluctuations, for the LOC and SOC plasmas with experimental profiles without modification. Heat fluxes are averaged in space and time. Fluctuations are the values on the midplane, and averaged radially and time. The uncertainty comes from the standard deviation in time averaging.

fluxes are within the uncertainties and these values can be varied significantly with the changes in input parameters within the uncertainty. If the trend in heat fluxes or fluctuating quantities is reversed by changing input parameters within their uncertainties, it is difficult to say that this trend is meaningful. Thus, we should check the variations of heat fluxes and fluctuating quantities with the changes in input parameters by their uncertainties to see whether or not the trends observed in this section are meaningful.

4.3.3 Sensitivity analysis of the simulated outputs of the runs using experimental values in the LOC/SOC discharges

We performed sensitivity analysis of the simulated outputs of the nonlinear runs for the LOC/SOC discharges at r/a=0.6 by changing input parameters by their uncertainties. Through this analysis, we will know the turbulence characteristics from the sensitivity of heat transport about input parameters. For example, from the sensitivity of heat transport about a/L_{T_i}, we will see whether or not the simulated turbulence has ITG-like characteristics. Observing the variations of heat fluxes and fluctuating quantities with the changes in input parameters by their uncertainties, we will also check whether or not the variations of heat fluxes and fluctuating quantities between

the LOC and SOC discharges, observed in the last section, are meaningful. In this analysis, we varied the gradient scale lengths (a/L_{T_i}, a/L_{T_e} and a/L_n) by $\pm 20\%$, and electron-ion collision frequency (ν_{ei}) by $\pm 30\%$. ν_{ei} was varied more than the gradient scale lengths since it is the most evident difference among input parameters. The main ion fraction (n_D/n_e) was varied by the estimated uncertainty shown in Table 4.1.

Figure 4-13 shows the changes in ion/electron heat flux with input parameter changes. Considering the uncertainty of simulated heat fluxes ($\sim 20\%$), more than 20% changes will be meaningful. We first notice that a/L_{T_i} is the most sensitive parameters for ion heat fluxes, implying ITG-like turbulence is dominant in both the LOC and SOC discharges. This is consistent with the linear simulation results which show that the ITG mode is dominant in both discharges. The changes in a/L_{T_e} result in the significant changes in Q_e in the LOC discharge, while Q_i changes by less than 10%. It is noteworthy that Q_e is also sensitive to the changes in a/L_{T_i} in both LOC and SOC discharges. The increase of n_D/n_e also affects both ion and electron heat transport significantly in the LOC discharge. In spite of 30% changes in ν_{ei}, the fractional changes in both Q_i and Q_e with ν_{ei} are less than 20%. The fractional changes in Q_i and Q_e with a/L_n are also not significant.

From the sensitivity analysis, it follows that a/L_{T_i} and n_D/n_e are important parameters for Q_i and a/L_{T_i}, a/L_{T_e} and n_D/n_e are important for Q_e. From the dependency of Q_i on a/L_{T_i}, we found that the dominant ion mode observed in non-linear simulations has ITG mode characteristics in both LOC/SOC discharges. Thus, we do not see any significant differences in turbulence characteristics in the core region between LOC/SOC from gyrokinetic analysis.

Concerning the trend in simulation outputs found in section 4.3.2, we observed that heat fluxes varied more than 30% with $\pm$ 20% changes of input parameters. Although it was not shown here, midplane fluctuations varied by 20% in this sensitivity analysis. Thus, it is hard to say whether or not the tendency observed in section 4.3.2, the enhancement of ion transport across the LOC/SOC transition with about 30% increase of ion heat flux and about 15-20% increase of potential and ion temperature fluctuations on the midplane in the SOC discharge, is meaningful at this point. In

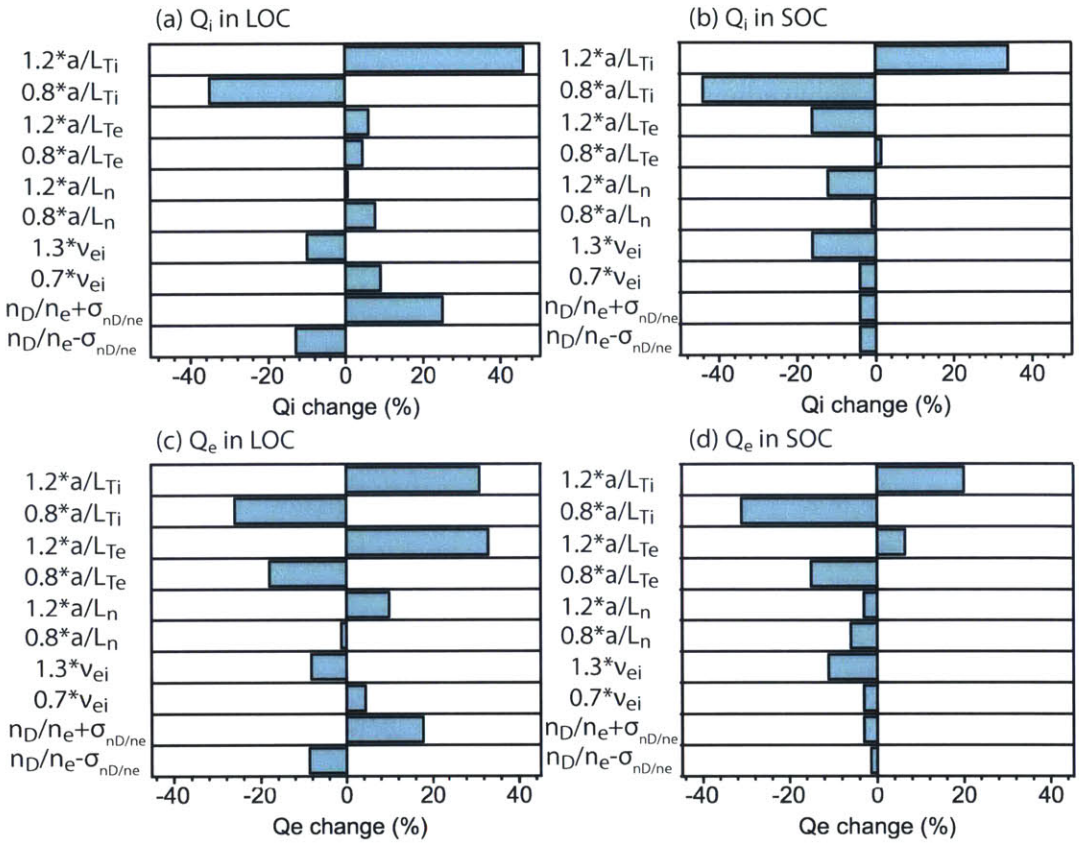

Figure 4-13: Sensitivity of ion and electron heat fluxes to input parameters for the LOC and SOC discharges (a) Ion heat flux (Q_i) in the LOC (b) Q_i in the SOC (c) Electron heat flux (Q_e) in the LOC (d) Q_e in the SOC.

the future, we may need to obtain the correct uncertainty of the input parameters in this section to draw a solid conclusion about this tendency. Considering uncertainties of output parameters in the simulation, making a database of simulation outputs by running more simulations from other LOC/SOC discharges will be helpful to analyze this tendency in spite of large uncertainty.

4.4 Gyrokinetic analysis near the edge region for the LOC/SOC plasmas

From both linear and non-linear gyrokinetic analyses, no significant changes in the turbulence characteristics, including dominant mode, across the LOC/SOC transition were found at r/a=0.6. In this section, we will compare the gyrokinetic analysis

results between the LOC and SOC discharges near the edge region (r/a$\sim$0.85) where we observed the reduction of electron temperature fluctuations across the LOC/SOC transition. Comparing simulated heat fluxes and synthetic electron temperature fluctuations from GYRO with the experiments, we will also try to validate the gyrokinetic model, which considers only local electrostatic and ion scale turbulence. Regardless of the plasma conditions, the validation study near the edge region will be interesting, but quite challenging. In DIII-D, "the transport shortfall", under-prediction of both ion and electron heat fluxes and fluctuations, for RF heated L-mode plasmas was observed at $\rho > 0.55$ [73, 126]. In C-Mod, GYRO under-predicted only electron heat flux at r/a=0.6-0.8 for the C-Mod RF heated L-mode discharge, which tends to be ITG dominant [78]. However, it is noteworthy that near the edge region ($r/a > 0.8$) has not been investigated using gyrokinetic simulations in C-Mod. Thus, the validation study near the edge region ($r/a > 0.8$) will bring meaningful information for not only transport research related to the LOC/SOC transition but also for the validation study in C-Mod.

4.4.1 Linear stability analysis using experimental input parameters

We first studied the changes in the dominant turbulence mode at the CECE measurement position between the LOC and SOC discharges via the linear stability analysis with experimental input profiles shown in Table 4.1 without modification. In these simulations, the dominant modes, which have the highest growth rates, were found using an initial value solver with the ion scale turbulence ($k_\theta \rho_s = [0, 1.2]$). We can see that electron and ion modes are mixed in the LOC discharge and an ion mode seems to be dominant in the SOC discharge in $k_y \rho_s < 1.0$. In the CECE relevant region ($k_y \rho_s < 0.3$), the electron mode is dominant in both LOC and SOC discharges. However, it is not evident whether the dominant mode in $k_y \rho_s < 0.3$ in the SOC discharge is ITG or TEM since the real frequency is close to zero. The electron mode is dominant in the both discharges in $k_y \rho_s > 1.0$.

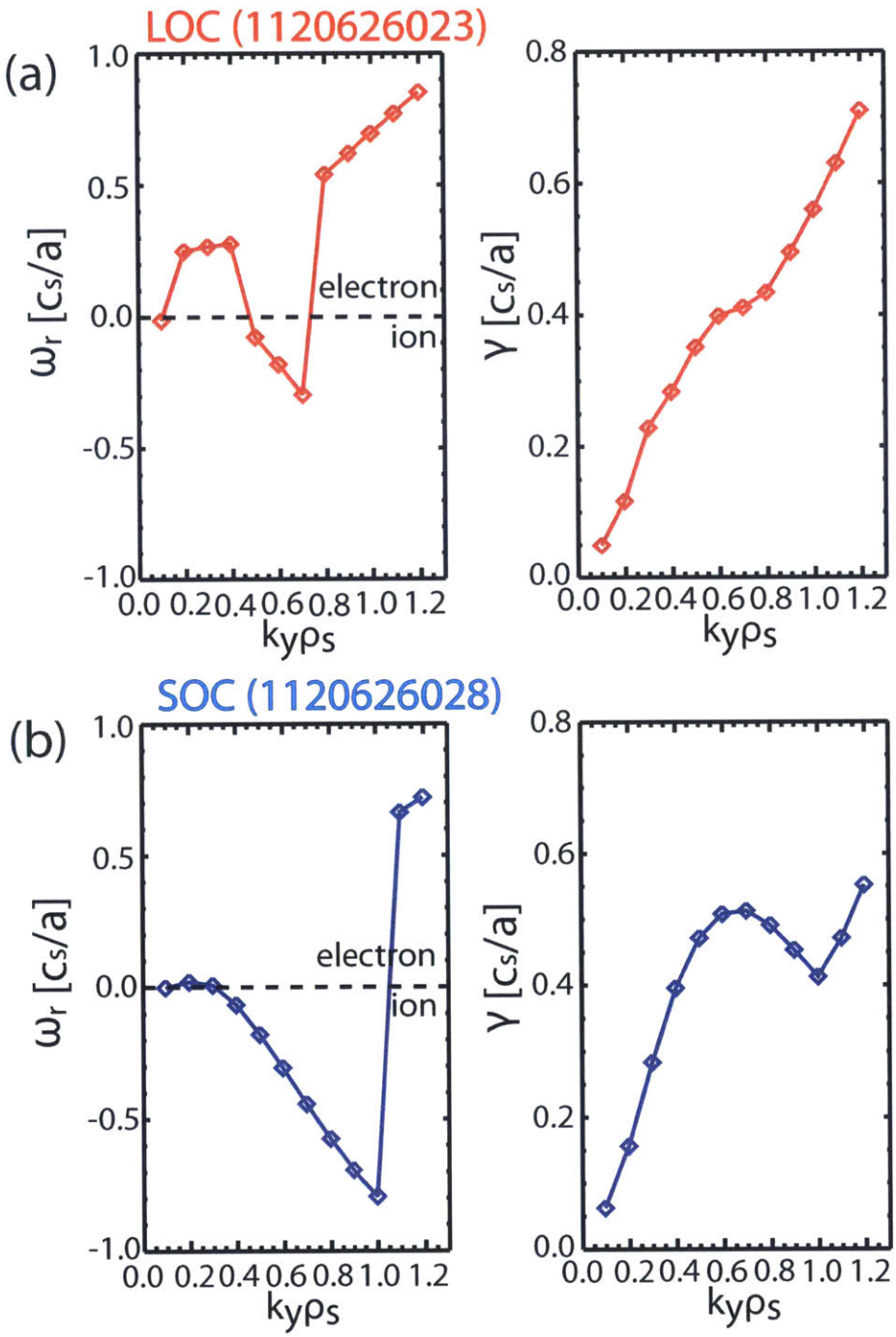

Figure 4-14: Linear stabiliy analysis of (a) the LOC discharge and (b) SOC discharge. The left figures show the real frequency of most unstable mode and right figures show the growth rate of the unstable mode. The positive real frequency indicates the mode propagrating in the electron diamagnetic direction, and negative real frequency indicates the opposite case. The units of both real frequency and growth rate is c_s/a ($c_s/a = 6.50 \times 10^5$ /s (LOC), 5.90×10^5 /s (SOC)).

In the same manner as explained in section 4.3, sensitivity analysis was performed by varying a/L_{T_e} and a/L_{T_i} in the LOC/SOC discharges to study the characteristics of the dominant turbulence mode. We first plot the analysis results where the contours of the growth rate of the most unstable linear mode in the $k_y\rho_s \leq 0.3$ in Fig. 4-15(a) and (b). These figures show the changes in the sensitivity of the dominant turbulence mode in the CECE relevant region. From Fig. 4-15(a) and (b), we first notice that the response of the growth rate provides a different view of the identity of the instability compared to the sign of the real frequency. As shown in Fig. 4-14, the dominant modes in $k_y\rho_s < 0.3$ are electron modes from the sign of real frequency in both discharges. However, the most dominant mode in the LOC discharge is more sensitive to the electron temperature gradient, while the mode in the SOC discharge is more sensitive to the ion temperature gradient. It is noteworthy that the dominant modes in both discharges are near the boundary of ITG/TEM, and we cannot resolve the changes of the dominant mode between the LOC and SOC discharges from these two contours within the estimated uncertainties of a/L_{T_i} and a/L_{T_e}. Figure 4-15(c) and (d) are the maximum growth rate contours in the $k_y\rho_s$ range [0.1-0.7]. This region was chosen because the dominant mode in the LOC changes to the electron mode from the ion mode around $k_y\rho_s \sim 0.7$ and the maximum growth rate of the dominant ion mode in the SOC discharge is within this range as shown in Fig. 4-14. It is shown that the dominant mode in the LOC discharge is near the ITG/TEM boundary. The dominant mode in the SOC discharge is in the ITG dominant region, sensitive to the ion temperature gradient. However, considering the uncertainty of input parameters, the SOC discharge can also be near ITG/TEM boundary. Thus, it will be proper to say that both LOC and SOC plasmas are near the ITG/TEM boundary within the uncertainty of these input parameters at the CECE measurement position.

Since neither the ITG mode nor TEM is dominant in both LOC/SOC discharges, it will be interesting to observe the sub-dominant modes. Figure 4-16 shows the sub-dominant electron/ion modes from eigen value solver for the LOC and SOC discharges. We first need to compare the eigenvalue solver results with the initial value solver results. As shown Fig. 4-16, the eigenvalue solver results are consistent

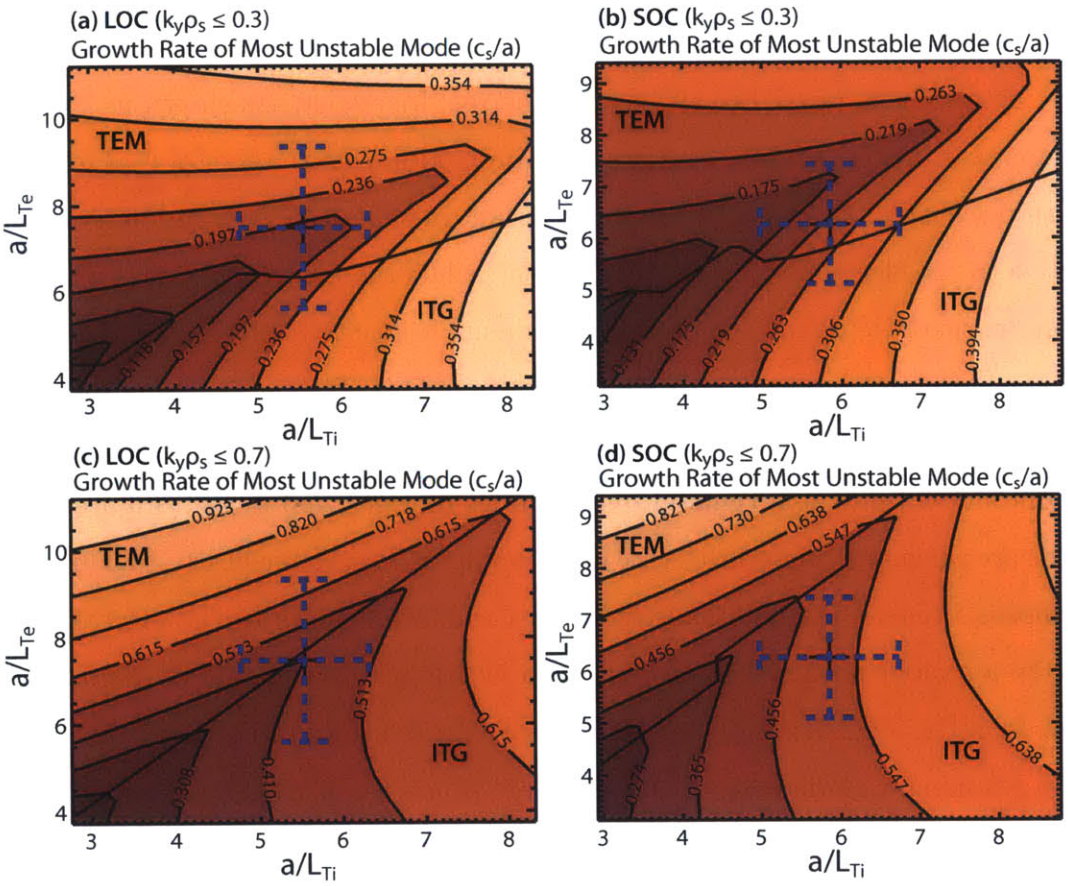

Figure 4-15: Contour of growth rate of most unstable mode with the change of a/L_{T_e} and a/L_{T_i} in the $k_y\rho_s$ range [0.1-0.3] in (a) the LOC discharge and (b) the SOC discharge, in the $k_y\rho_s$ range [0.1-0.7] in (c) the LOC discharge and (d) the SOC discharge

with the initial value solver results in both discharges. In the CECE relevant region ($k_y\rho_s < 0.3$), it is noticeable that the additional electron mode, closer to the TEM turbulence from Fig. 4-15(a), exists in the LOC discharge with the common electron mode which has very low real frequency and is closer to the ITG-like turbulence from Fig. 4-15(b). The most unstable ion modes in each discharge are similar. Although the LOC discharge has additional unstable ion modes, their growth rate is less than half of the most unstable ion mode in the LOC discharge. It is possible that a TEM-like electron mode in the LOC discharge correlates with the larger electron temperature fluctuations. In $k_y\rho_s > 0.3$, the growth rates of the most unstable ion modes in each discharge are comparable. In contrast, the electron mode in the LOC discharge has a higher growth rate than the electron mode in the SOC discharge.

From these results, we may be able to say that the LOC discharge has a more unstable electron mode, but we should be cautious to draw a definite conclusion because the type of mode (electron/ion or TEM/ITG) can be varied within the experimental uncertainty. It is also noteworthy that we can find at least two unstable ion modes in the whole $k_y\rho_s$ region. Since all these unstable electron/ion modes will be coupled in the real experiments, it is unknown whether the stronger electron mode in the LOC discharge is more important than the unstable ion modes in the real experiment. In order to investigate this, we need to perform non-linear gyrokinetic analysis.

4.4.2 Local non-linear gyrokinetic simulation setup for the base run

Local, non-linear gyrokinetic simulations were performed for the LOC and SOC discharges at the CECE measurement position (r/a$\sim$0.85). Similar to non-linear runs at r/a=0.6, the basic set-up for runs at r/a$\sim$0.85 in this section, including velocity grid, rotation effects and particle treatments (gyro/drift kinetic ion/electron) is the same as explained in section 3.4. Ion scale turbulence modes ($k_\theta\rho_s \lesssim 1.7$ with toroidal grid spacing, Δn=12 and 30-32 toroidal modes) were considered in these simulations with the assumption that electron scale turbulence is ignorable, but it is noteworthy

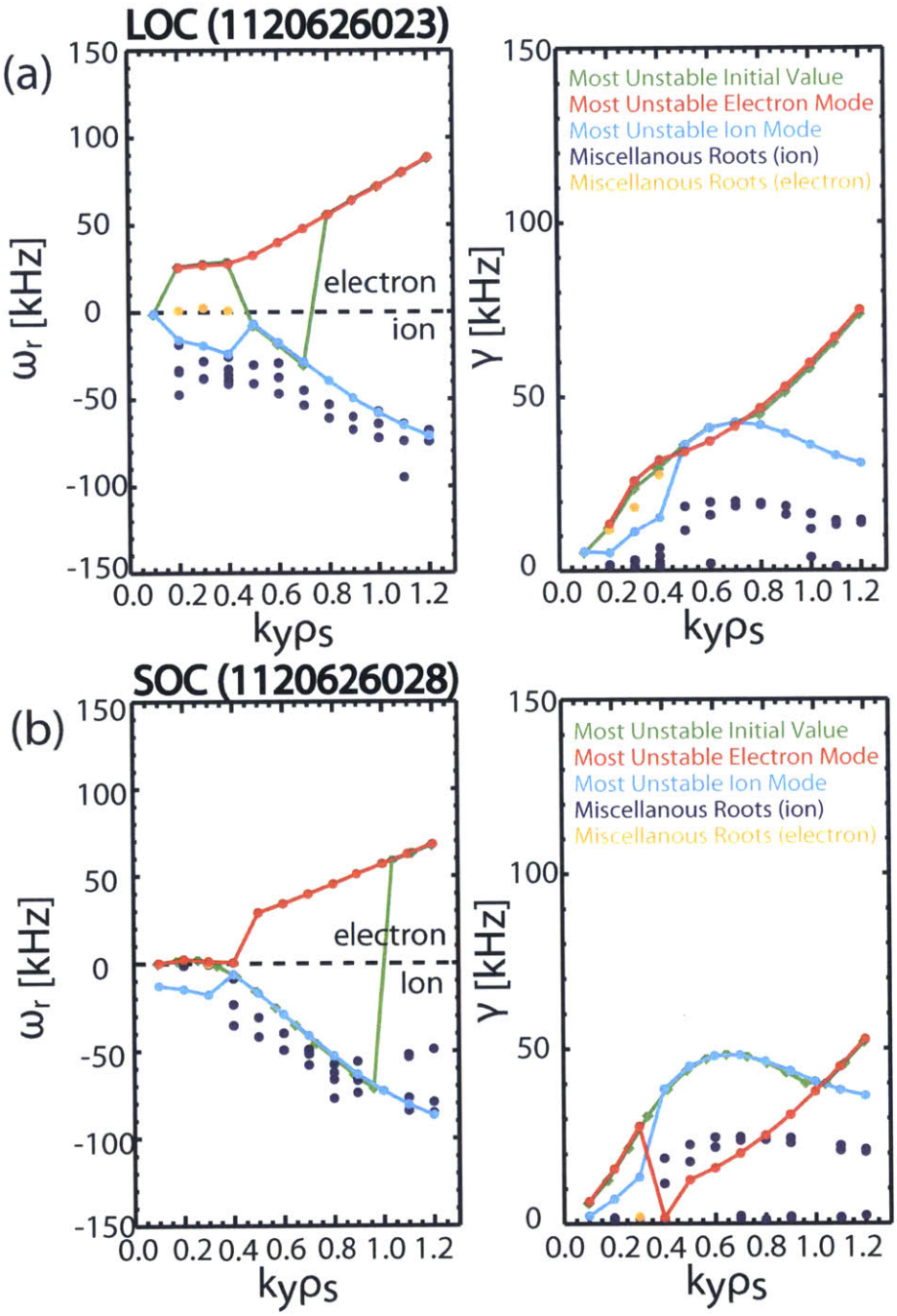

Figure 4-16: Linear stability analysis using eigenvalue solver with experimental values for (a) the LOC dischare (shot 1120626023) and (b) the SOC discharge. Color codes are used in this figure as follows. Green : Most unstable mode from initial value solver. Red : Most unstable electron mode, Blue : Most unstable ion mode, Purple : Sub-dominant ion modes, Orange : Sub-dominant electron modes

that the contribution of electron scale turbulence to heat transport is unknown in this case. The domain size was set to $L_x \sim 130\rho_s$ by $L_y \sim 110\rho_s$ with a radial grid spacing $\Delta x/\rho_s \sim 0.25$.

In non-linear simulations near the edge (r/a$\sim$0.85), the strong mode was observed in the low k_y region ($k_y\rho_s < 0.1$). As explained in section 3.4, the peak in the lowest k_y region should be resolved by increasing the poloidal domain size, L_y, since this peak indicates the domain size may not be large enough considering the size of turbulence or turbulent eddies in the simulation. It was found that a large domain size ($L_y > 200\rho_s$) was required to resolve the peak in the lowest k_y region in these simulations. The simulations with this large domain are not only intractable in terms of both computational and wall clock time but also physically not meaningful since the basic gyrokinetic ordering will be threatened by this large domain size, as explained in Appendix I.

However, the observed peak in the lowest k_y region will not be a real physical turbulence, which can be observed in the experiment, for the following three reasons. First, this peak is mitigated by changing the order of the radial basis function of the collision operator, corresponds to the ORD_RBF parameter in GYRO input, especially in the SOC discharge, indicating a numerical issue is related to this peak. Second, through sensitivity analysis of the low k_y peak, we found that this peak is sensitive to $\gamma_{E\times B}$ and a/L_n. The experimental $\gamma_{E\times B}$ value is small compared to the nominal value ($\sim 0.05[c_s/a]$) and has large uncertainty as shown in Table 4.1. It is possible that a value of $\gamma_{E\times B}$ much smaller than the real value in the experiment causes the strong turbulence in the low k_y region ($k_y\rho_s < 0.1$). Third, in the real experiments, the high poloidal resolution was one of the important considerations in the CECE measurements as explained in Chapter 2. If this low k_y peak, which has a long poloidal wavelength (3-4cm), existed in the C-Mod experiments, this peak will be dominant in the CECE measurements due to the sensitivity of the CECE ($k_y\rho_s < 0.3$), and poloidal resolution would be less important in the measurements. Consequently, T_e fluctuations could be obtained in the past attempts in 2004 [167]. Although the origin of this low k_y peak is unknown, it is concluded that this peak will not be

a real turbulence which exists in the experiments. We found that this mode can be suppressed with small changes in the modes at other wavenumbers from the sensitivity study of this peak in Appendix I, which suggest the nonlinear coupling of this spurious mode to other modes is small. However, the contribution of this spurious peak, which may not be real, to the synthetic T_e fluctuations will not be ignorable. Thus, this peak should be suppressed by changing the input parameters within uncertainty. The LOC base run with the suppressed low k_y peak was obtained by increasing $\gamma_{E\times B}$ to the maximum value under its uncertainty. In the SOC discharge, both the ExB shearing rate and a/L_n were increased to the maximum value within their uncertainties to obtain the base run. More details about the investigation of the low k_y peak and the set-up for the base runs are discussed in Appendix I.

4.4.3 Ion heat flux, Q_i, matched simulation and comparison with experiments

As explained in section 3.4, we should obtain the "physical" base runs from the base runs (or "numerical" base runs) by matching heat flux values within the uncertainty of the input parameters. The base runs under-predict both Q_i and Q_e compared to the experimental values from power balance analysis ($Q_i[MW/m^2] = 0.030 \pm 0.005$ (LOC), 0.064 ± 0.017 (SOC), and $Q_e[MW/m^2] = 0.12 \pm 0.043$ (LOC), 0.087 ± 0.039 (SOC)) at the CECE measurement position in both LOC and SOC discharges. Unlike the r/a=0.6 runs, it was found that Q_i can be matched with the experimental Q_i by increasing a/L_{T_i} within the uncertainty in both discharges. The heat flux values of the base and Q_i matched runs are shown in Fig. 4-17. However, Q_e is still under-predicted in the Q_i matched runs in both discharges. From power balance analysis, we observed an increase of Q_i and the decrease of Q_e across the LOC/SOC transition. From simulations, it was observed that both Q_i and Q_e increase in the SOC discharge although the increase of Q_e is within the uncertainty as shown in Fig. 4-18

We also compare synthetic T_e fluctuations with the fluctuations measured by CECE. Figure 4-19 shows the comparison of synthetic T_e fluctuation levels and $\tilde{T}_e/T_e$

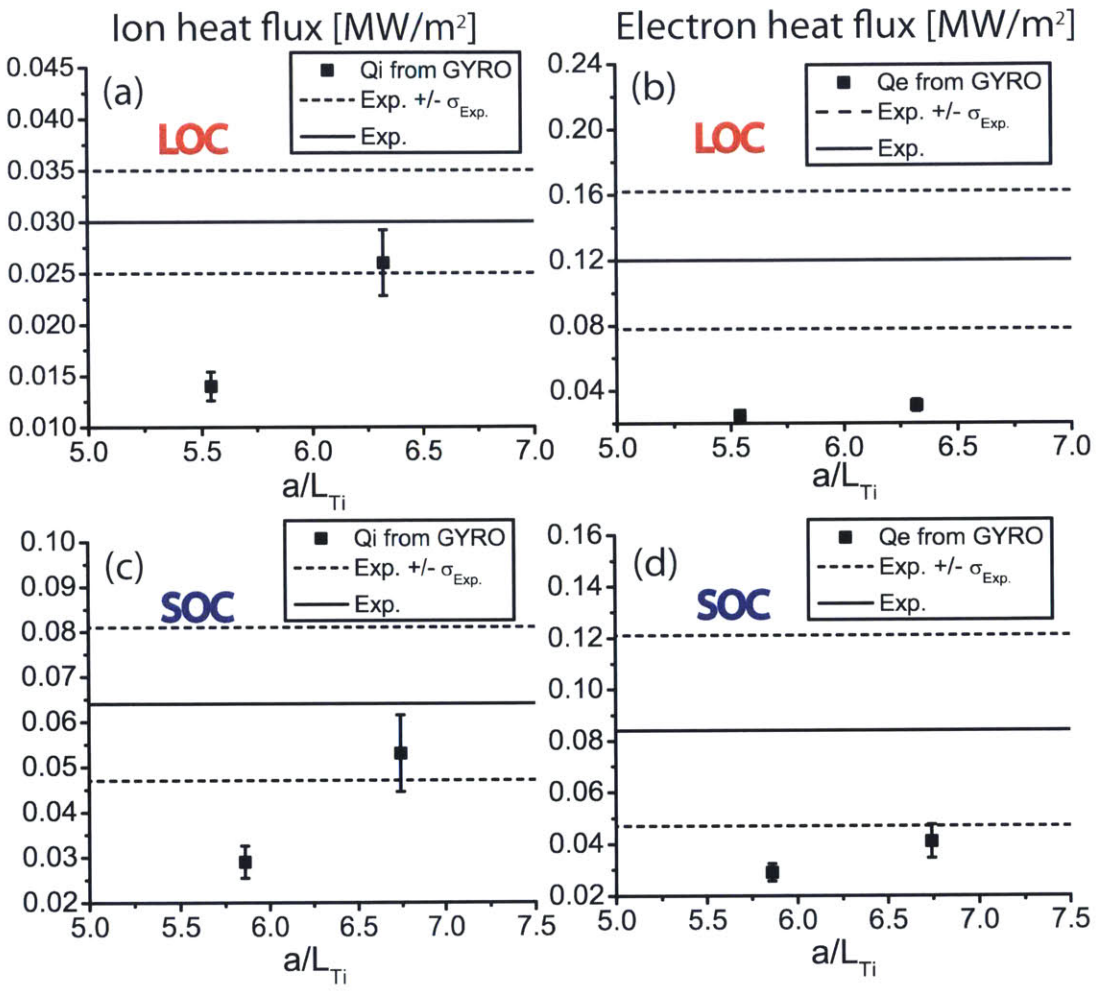

Figure 4-17: Comparison of simulated heat fluxes from the base and Q_i matched runs with the experimental heat fluxes from power balance analysis. (a) Ion heat flux, $Q_i[MW/m^2]$ in the LOC plasma (b) Electron heat flux, $Q_e[MW/m^2]$ in the LOC plasma (c) $Q_i[MW/m^2]$ in the SOC plasma (d) $Q_e[MW/m^2]$ in the SOC plasma

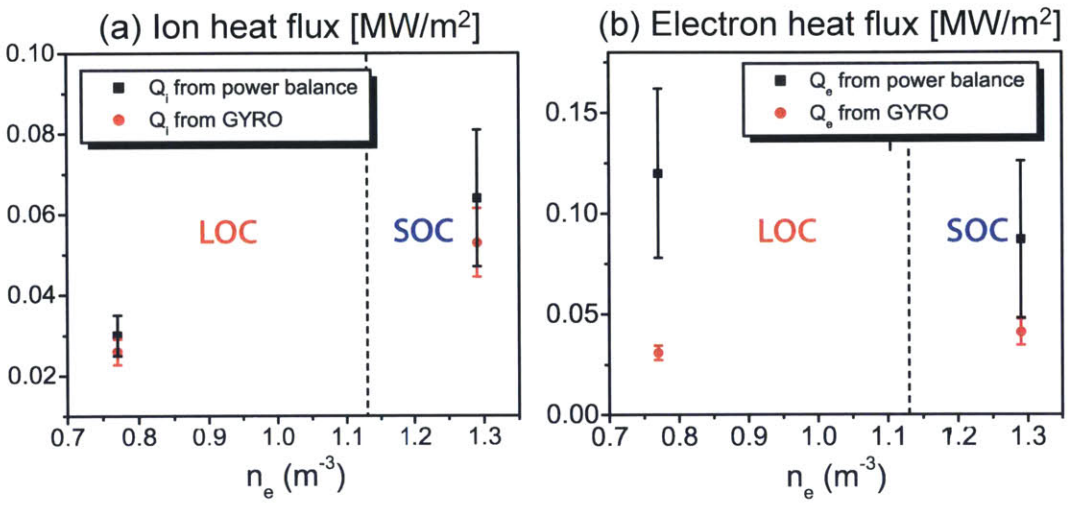

Figure 4-18: Comparison of simulated heat fluxes with the experimental heat fluxes obtained from power balance in the LOC/SOC discharges at the CECE measurement position (r/a$\sim$0.85) (shot : 1120626023 (LOC), 1120626028 (SOC)) (a) Ion heat flux, $Q_i[MW/m^2]$ (b) Electron heat flux, $Q_e[MW/m^2]$. Vertical dash line indicates the rotation reversal density, obtained from the average electron density of rotation reversal discharge (shot 1120626028) on the same run day with the LOC/SOC discharges

spectrum in these Q_i matched runs with the CECE measurements. In both discharges, the synthetic T_e fluctuation levels are matched with the measured T_e fluctuation levels and the trend in the synthetic T_e fluctuation levels agrees qualitatively with the measurements, although the change in synthetic electron temperature fluctuation levels across the LOC/SOC transition is smaller than the observed change. However, synthetic $\tilde{T}_e/T_e$ spectra are not matched with the measured spectrum in both LOC and SOC plasmas. The measured spectra are broader than the synthetic spectra. Within the estimated uncertainty of rotation frequency, ω_o and radial electric field, E_r, shown in Table 4.1, we were not able to reproduce the shape of the experimental spectrum in both discharges.

In the comparison of T_e fluctuations, an identical analysis process was applied to both synthetic and measured fluctuations. The frequency range for fluctuation level calculation was set to 0-170kHz. 170kHz is the highest frequency of the physical fluctuations in the measurement for both LOC and SOC discharges as shown in section 4.1.1. For the SOC discharge, the proper frequency range in the measurement

was 60-170kHz. This range is not appropriate for the synthetic spectra, which are narrower than the measured spectra and most fluctuations have $f < 60$kHz as shown in Fig. 4-19(b) and (c). Instead of using the exact frequency range obtained in the measurements, the broad frequency range which can include both measured and synthetic fluctuations were used in this analysis.

4.4.4 Investigation of changes in turbulence characteristics between Q_i matched simulations in the LOC and SOC discharges

In the previous section, we observed that Q_i matched runs also can match the measured T_e fluctuation level within the uncertainty, but Q_e and the synthetic spectrum shape were not matched with the experiments. In this section, we investigate the changes in turbulence in these Q_i matched simulations from both linear and nonlinear simulation results. Figure 4-20 shows the changes in linear unstable modes between two discharges. In both LOC/SOC discharges, the electron mode is dominant in the CECE relevant region ($k_y\rho_s \leq 0.3$), and the ion mode is dominant in $0.3 < k_y\rho_s < 0.8$. In the ion modes, no evident difference can be found. In both discharges, three or four unstable ion modes exist, and their growth rates are comparable between the two discharges. The SOC discharge has two unstable electron modes in $k_y\rho_s \leq 0.3$, while the LOC discharge has one unstable electron mode in the CECE relevant region. However, the growth rate of the sub-dominant electron mode in $k_y\rho_s \leq 0.3$ in the SOC discharge is not significant, less than the $E \times B$ shearing rate used in this simulation ($\sim$15kHz), and also less than half of the growth rate of the dominant electron mode. The growth rates of the dominant electron mode in $k_y\rho_s \leq 0.3$ are comparable between the LOC and SOC discharges. In $k_y\rho_s > 0.3$, the electron mode in the LOC discharge has the higher growth rate compared to the SOC discharge.

Linear simulations show no significant changes in the electron mode in $k_y\rho_s \leq 0.3$ and the ion mode in the whole $k_y\rho_s$ range in these simulations, but the electron mode

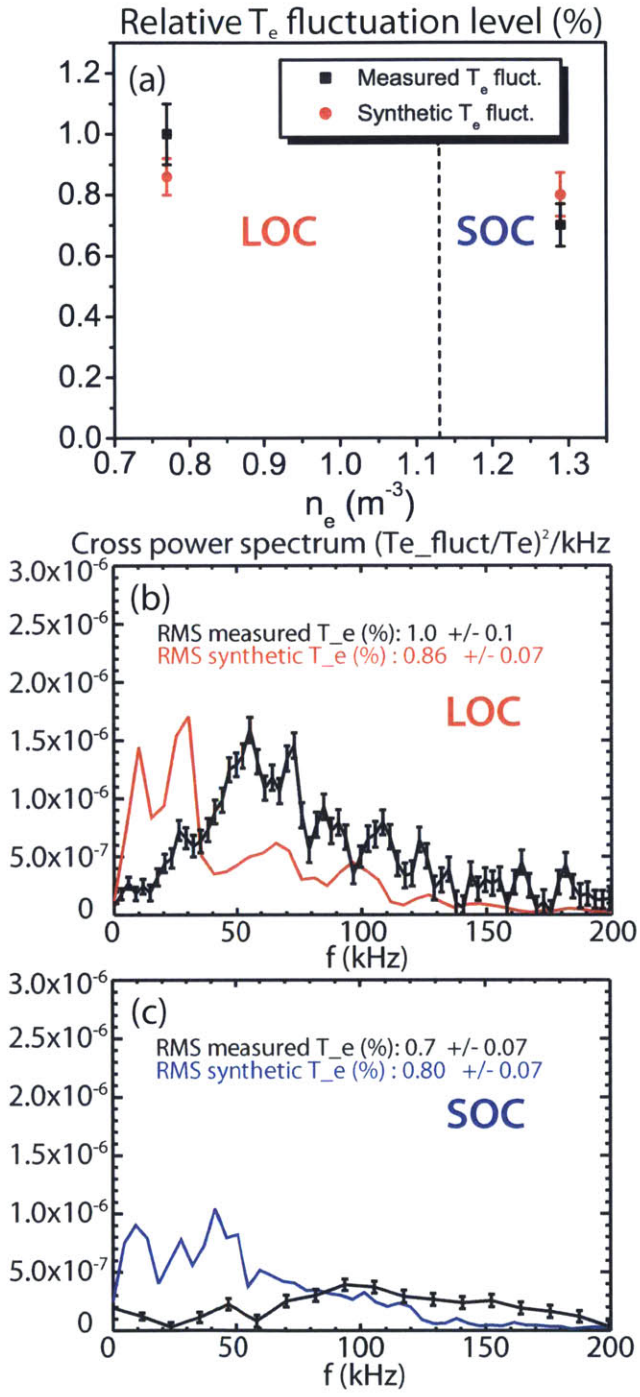

Figure 4-19: Comparison of synthetic T_e fluctuations with the measurements in the LOC and SOC plasmas (a) relative T_e fluctuation level in both the LOC/SOC plasmas (b) cross power spectrum in the LOC (c) cross power spectrum in the SOC. The dotted lines in (b) and (c) indicates the error in the synthetic spectrum.

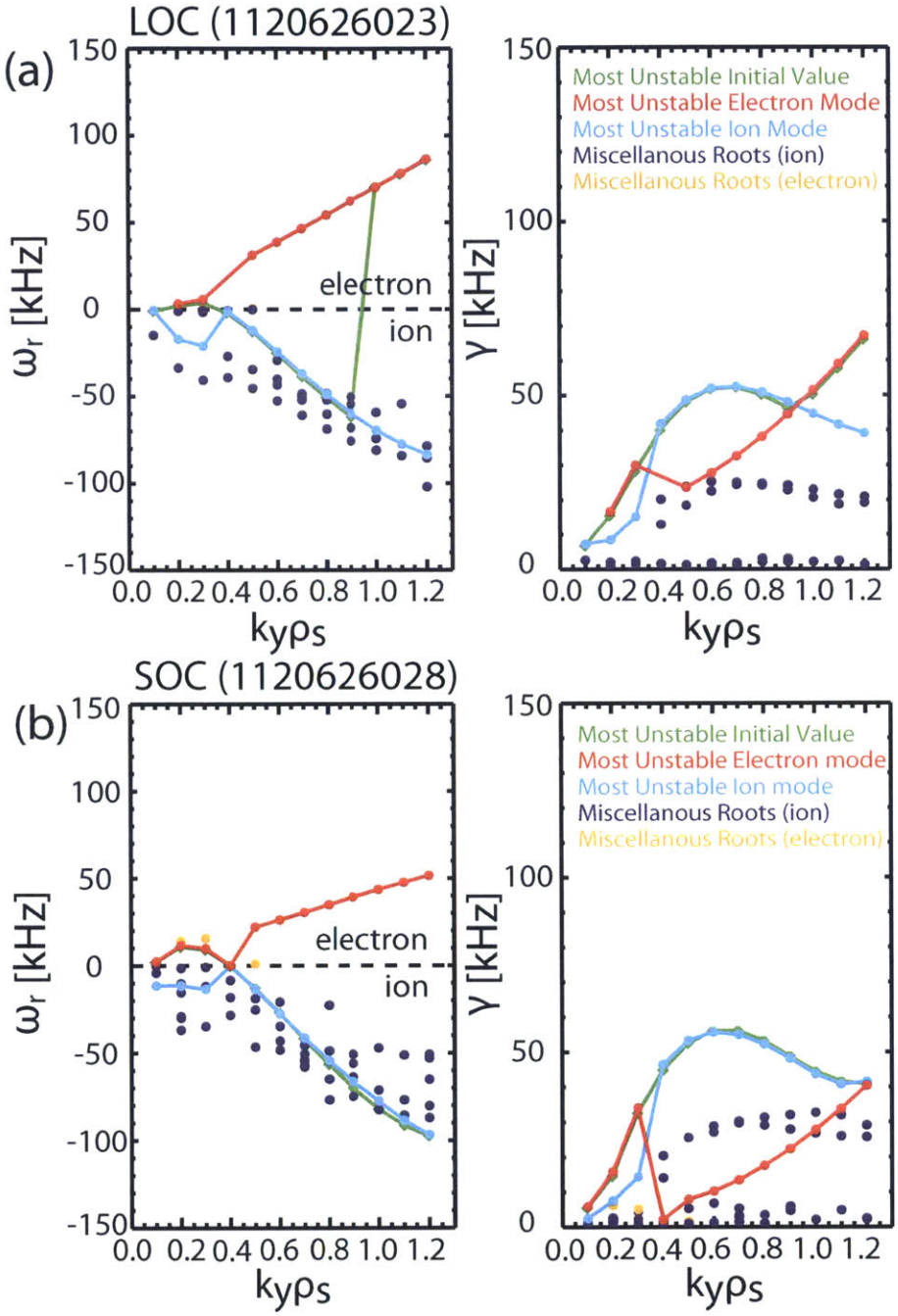

Figure 4-20: Linear stability analysis using eigenvalue solver with the input parameters used in the Q_i matched simulations for (a) the LOC dischare (shot 1120626023) and (b) the SOC discharge. Color codes are used in this figure as follows. Green : Most unstable mode from initial value solver. Red : Most unstable electron mode, Blue : Most unstable ion mode, Purple : Sub-dominant ion modes, Orange : Sub-dominant electron modes

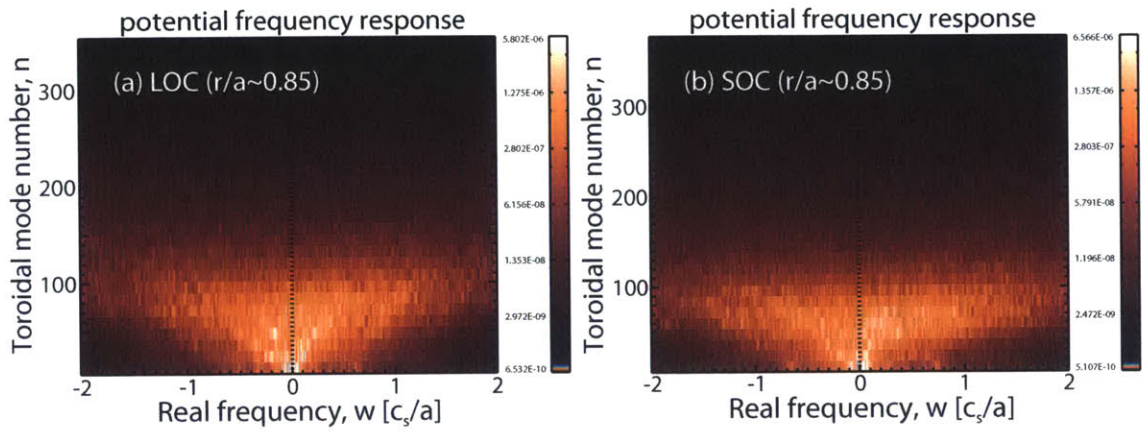

Figure 4-21: Power spectrum of simulated potential fluctuations on the midplane from Q_i matched simulations at the CECE measurement position for (a) the LOC discharge (shot:1120626023) and (b) the SOC discharhge (shot: 1120626028) with experimental input values. The simulated potential fluctuations are averaged radially.

in the LOC discharge is more unstable than in the SOC discharge in $k_y\rho_s > 0.3$. From the linear runs, it is unknown whether or not this difference is meaningful. Thus, we need to see whether a more unstable electron mode in the LOC discharge makes a meaningful difference in the simulated transport or turbulence between the LOC/SOC discharges through non-linear simulations. As performed in the analysis at r/a=0.6, we observed the changes in turbulence from the power spectrum of fluctuations per toroidal number, n, as shown in Fig. 4-21. For both LOC and SOC discharges, it is hard to identify the dominant turbulence mode or propagation direction from this figure. This result indicates that neither electron nor ion modes are dominant in the both discharges; they are both comparable. It also implies that there are no changes in the dominant turbulence mode between the LOC and SOC discharges near the edge region, which is consistent with the tendency observed in the runs at r/a=0.6.

We also investigated the changes in ion and electron heat transport at the CECE measurement position between the LOC/SOC discharges. Table 4.3 shows the heat flux values and synthetic and RMS fluctuation levels of fluctuating quantities on the midplane in the Q_i matched runs for the LOC and SOC discharges. We first observed more than a 30% increase of potential fluctuations in the SOC discharge. Ion temperature fluctuations also increase in the SOC discharge about 10-20% compared

	LOC	SOC
$Q_i[MW/m^2]$	0.026 ($\pm$0.0032)	0.053 ($\pm$0.0085)
$Q_e[MW/m^2]$	0.031 ($\pm$0.0036)	0.041 ($\pm$0.0065)
Syn. $\tilde{T}_e/T_e[\%]$	0.86 ($\pm$0.06)	0.80 ($\pm$0.07)
$e\tilde{\phi}/T_e[\%]$	4.03 ($\pm$1.07)	5.54 ($\pm$1.72)
$\tilde{n}_i/n_i[\%]$	1.97 ($\pm$0.12)	1.84 ($\pm$0.12)
$\tilde{n}_e/n_e[\%]$	1.64 ($\pm$0.09)	1.68 ($\pm$0.11)
$\tilde{T}_i/T_i[\%]$	3.62 ($\pm$0.27)	4.07 ($\pm$0.41)
$\tilde{T}_e/T_e[\%]$	2.70 ($\pm$0.15)	2.26 ($\pm$0.18)

Table 4.3: The simulation results of the base and Q_i matched cases for the LOC/SOC discharges at the CECE measurement position. Heat fluxes are averaged in space and time. Fluctuations are the values on the midplane, and are averaged radially and in time. The uncertainties of midplane fluctuations and heat fluxes come from the standard deviation in time averaging.

to the LOC discharge, while electron temperature fluctuations decrease about 15% in the SOC discharge. Both electron and ion density fluctuations vary within 10% between the LOC and SOC plasmas. The increase of potential and ion temperature fluctuations can be linked to the higher ion heat flux in the SOC discharge. The increase of electron heat flux can also be explained by the increase of potential fluctuations. The decrease of electron temperature fluctuations may mitigate the increase of electron heat flux in the SOC discharge. We should note that all changes except for the electron temperature fluctuations are within the uncertainty. Nevertheless, the increases in potential and ion temperature fluctuations within their uncertainty result in an increase in Q_i by a factor of two. It is also noteworthy that the increase of the potential and ion temperature fluctuations with the decrease of electron temperature fluctuations were consistently observed in the non-linear runs at r/a=0.6.

Since we observed the decrease of electron temperature fluctuations in both synthetic and simulated quantities on the midplane, we may be able to say that the trends of electron temperature and density fluctuations are consistent with the measurements. However, it is noteworthy that the decrease of synthetic fluctuations is

within the uncertainty and the synthetic diagnostic is not applied to the electron density fluctuations. Moreover, these quantities can be varied significantly within the uncertainties of input parameters. Thus, we perform sensitivity analysis to draw a solid conclusion.

4.4.5 Sensitivity of simulation results about input parameters

We studied whether or not the agreement of Q_i and synthetic $\tilde{T}_e$ level with experiments and the under-prediction of Q_e are robust via the sensitivity analysis. It is worth noting that the characteristics of simulated turbulence in the LOC and SOC discharges will also be studied in the sensitivity analysis. Input parameters not used for the base and Q_i matched runs were varied in this sensitivity analysis. Unlike the runs at r/a=0.6, we varied input parameters by their uncertainties, that is, $X \pm \sigma_X$ was used for the sensitivity analysis, where X is a certain input parameter and σ_X is its uncertainty. Then, we observed the variation of the simulated outputs within the experimental uncertainties of input parameters for the validation study. Since $\gamma_{E\times B}$ and a/L_{T_i} were used to establish the base and Q_i matched runs for the LOC discharge, we varied a/L_{T_e}, a/L_n, ν_{ei}, and n_D/n_e by their uncertainties for the sensitivity study of the LOC discharge. In the same manner, a/L_{T_e}, ν_{ei}, and n_D/n_e were varied by their uncertainties for the sensitivity analysis for the SOC discharge. Since $\gamma_{E\times B}$, a/L_n and a/L_{T_i} were used to obtain the base run for the SOC discharge, these parameters were fixed in the sensitivity analysis for the SOC discharge. The rotation frequency was not varied in the sensitivity analysis. The synthetic spectral shape did not vary significantly with the changes of the other input parameters, only its amplitude varied.

We first observed the variations of amplitudes of Q_i and synthetic T_e fluctuation levels in the sensitivity analysis. Figure 4-22(a) shows the highest and lowest Q_i values obtained from the sensitivity analysis. From the Q_i matched simulations, GYRO reproduces both Q_i values and their trend between the LOC/SOC discharges. However, it is shown that Q_i values vary too much to say anything conclusive about the trend of Q_i values between two discharges. Although Q_i increases in the SOC

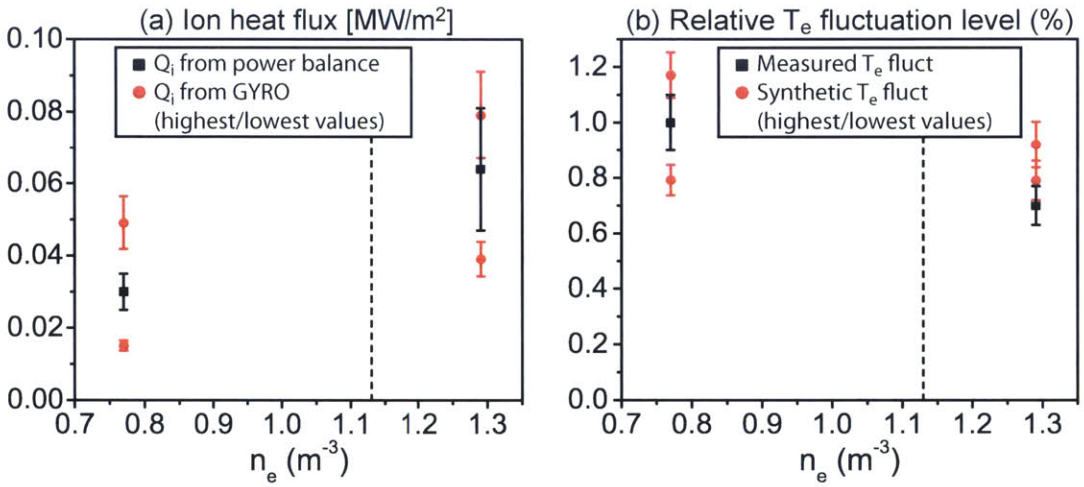

Figure 4-22: Comparison of highest and lowest value of simulated ion heat flux and synthetic electron temperature fluctuation level obtained from the sensitivity analysis for the LOC/SOC discharges at the CECE measurement position (r/a$\sim$0.85) (shot : 1120626023 (LOC), 1120626028 (SOC)) with the experiments. (a) Ion heat flux, $Q_i[MW/m^2]$ (b) Electron temperature fluctuation level [%]. Vertical dashed line indicates the rotation reversal density, obtained from the average electron density of rotation reversal discharge (shot 1120626028) on the same run day with the LOC and SOC discharges

compared to the LOC in the Q_i matched simulations, it is possible to obtain the opposite trend, smaller Q_i in the SOC discharge, within the uncertainty of input parameters by choosing the highest Q_i value among Q_i values obtained from the sensitivity analysis in the LOC and the lowest Q_i value in the SOC. Nevertheless, we are still able to say that GYRO can reproduce Q_i within the uncertainty of input parameters. Synthetic T_e fluctuation levels also vary in a large range as shown in Fig. 4-22(b), which indicates that the approximately 10% decrease of synthetic T_e fluctuation levels in the SOC discharge observed in the Q_i matched runs is not robust, and it is also possible to obtain the opposite trend. Thus, it is hard to reproduce the reduction of T_e fluctuation level observed in the experiments within the uncertainty of input parameters, although GYRO can reproduce the measured fluctuation level. The large uncertainty in the input parameters or the large variations in T_e fluctuations with the changes in input parameters by the uncertainty will be one reason for this result. However, we must note that T_e fluctuation levels in the Q_i matched runs for the LOC and SOC discharges are different only about 10%, while we observed the reduction of T_e fluctuations by 30% in the SOC discharge compared to the LOC discharge in the experiments. In this sensitivity analysis, we varied the input parameters from the Q_i matched simulations. Since T_e fluctuations are more closely related to Q_e than Q_i, the results could be different if sensitivity analysis is performed from the Q_e matched simulations or the simulations which reproduce both Q_i and Q_e. As will be shown later in this chapter, the nonlinear runs in this study, which includes only ion-scale turbulence, cannot reproduce the experimental Q_e level. We should therefore consider this different approach as the future work. In the future, it is also worth trying to have the simulations which can reproduce the measured T_e fluctuations first, sensitivity analysis is then performed from the fluctuation matched runs to see how these simulations match the heat flux.

Figure 4-23 shows the fractional changes in Q_i and synthetic T_e fluctuation levels with the changes in each input parameter. The changes in Q_i and synthetic T_e fluctuations by increasing a/L_{T_i} to match Q_i from the base run are also included in the figure. We investigated the characteristics of the simulated turbulence at the

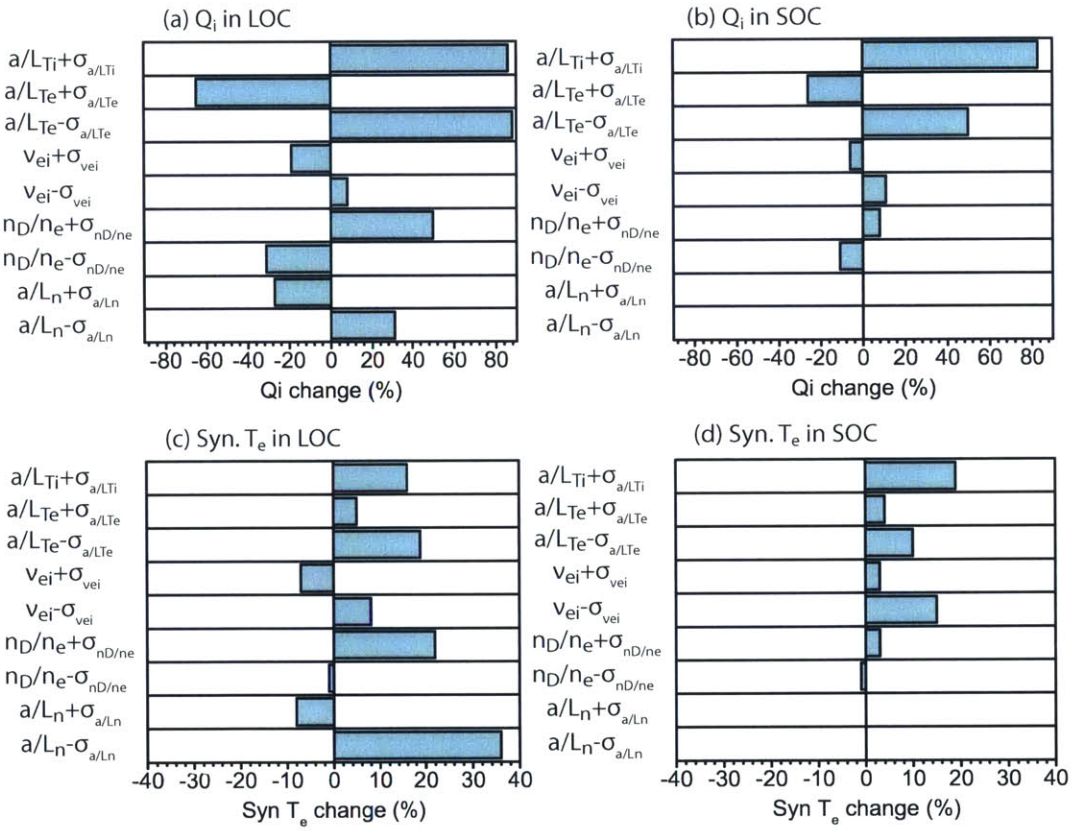

Figure 4-23: Fractional changes in the simulated ion heat flux and synthetic electron temperature fluctuation level with input parameter changes at the CECE measurement position (r/a$\sim$0.85) for the LOC and SOC discharges (shot : 1120626023 (LOC), 1120626028 (SOC)). (a) Ion heat flux, Q_i, in the LOC discharge (b) Q_i in the SOC discharge (c) Synthetic T_e fluctuation level in the LOC discharge (d) Synthetic T_e fluctuation level in the SOC discharge. a/L_n was fixed in the SOC discharge, then the fractional change due to a/L_n was represented as zero in the SOC discharge.

CECE measurement position in the LOC and SOC discharge from the sensitivity of Q_i and synthetic T_e fluctuations about input parameters shown in Fig. 4-23. From Fig. 4-23(a) and (b), we first notice that a/L_{T_i} and a/L_{T_e} are the most sensitive parameters for Q_i in both discharges. Increasing a/L_{T_i} by its uncertainty ($\sim$ 15%) results in an approximately 80% increase in Q_i. The sharp increase in Q_i with the increase of a/L_{T_i} will indicate that ITG mode is important in these simulations. It is also shown that Q_i increases with other ITG favorable changes such as increasing n_D/n_e and a/L_n. Unlike a/L_{T_i}, the decrease of a/L_{T_e} by its uncertainty ($\sim$ 20 – 25%) increases Q_i by more than 50%. The increase of a/L_{T_e} also affects Q_i significantly by decreasing it by more than 20%, although the variation in Q_i is smaller than the decrease of a/L_{T_e}. It is noteworthy that the simulated Q_i at r/a=0.6 was not as sensitive to a/L_{T_e} compared to Q_i at r/a$\sim$0.85, as shown in Fig. 4-13. This may indicate TEM turbulence is also important at r/a$\sim$0.85 in both discharges. The stabilization of TEM turbulence by increasing a/L_{T_e} is also favorable for ITG turbulence in these "mixed mode" simulations. Increasing the electron-ion collision frequency, ν_{ei}, will decrease the activity of trapped electrons, that is, the non-adiabatic electron response. Since non-adiabatic electrons destabilize the ITG mode as well as TEM, although ITG mode can be destabilized without non-adiabatic electrons, it is hard to connect the changes in Q_i with ν_{ei} to a specific turbulence mode, either ITG or TEM. It will be more appropriate to leave it as the effect of the response of non-adiabatic electrons rather than a certain turbulence mode. It is shown that Q_i decreases with the increase in ν_{ei} (or the reduction of non-adiabatic electron response) in both LOC and SOC discharges. However, Q_i changes within 20% by increasing/decreasing ν_{ei} by its uncertainty ($\sim$ 20%). This 20% variation indicates that Q_i is less sensitive to ν_{ei} than to gradient scale lengths. In the LOC discharge, dilution or main ion fraction, n_D/n_e also changes Q_i by more than 20%, which is consistent with the previous study in C-Mod [99, 120].

Figure 4-23(c) and (d) show the changes in synthetic T_e fluctuation levels with input parameters. Similar to Q_i, synthetic fluctuation levels increase with ITG favorable changes such as the increase of a/L_{T_i} and n_D/n_e and the decrease of a/L_n.

It is noteworthy that the largest variation in synthetic T_e fluctuation levels is obtained from the decrease of a/L_n by its uncertainty($\sim$ 40%), not from the increase of a/L_{T_i}. Even the increase of n_D/n_e changes the synthetic T_e fluctuation levels by more than the increase of a/L_{T_i} in the LOC discharge. The dependency of synthetic T_e fluctuation levels on a/L_{T_e} is also interesting. The decrease in a/L_{T_e} increases the synthetic level in both LOC and SOC discharges. This can be interpreted as the result of a more destabilized ITG mode, consistent with the sensitivity of Q_i. However, the increase in a/L_{T_e} also increases the synthetic T_e fluctuation level. More destabilized TEM turbulence due to the increase of a/L_{T_e} may cause the increase of T_e fluctuation level. This indicates that synthetic T_e fluctuation levels respond to both ITG and TEM relevant changes. Thus, we should be careful when connecting the changes in T_e fluctuations with the changes in the specific turbulence mode. Dependency of synthetic T_e fluctuations on ν_{ei} is similar to the observation in Q_i, but synthetic level increases not only with the increase in ν_{ei} but also with its decrease in the SOC discharge. An approximately 3% increase in synthetic T_e fluctuation levels with the increase of ν_{ei} might not be meaningful. If the ν_{ei} value in the SOC discharge is already high enough to suppress most of the response of non-adiabatic electrons, then the synthetic T_e fluctuation levels with the ν_{ei} above this level will be saturated and fluctuate within the uncertainty. If this is the case, we may need to think of the 3% increase of the fluctuation level with the increase in ν_{ei} as the saturation rather than the increase. In order to verify this possibility, a run with higher ν_{ei} outside experimental uncertainty is required. This should be performed in the future.

From Table 4.1, we notice two evident differences in input parameters at the CECE measurement position between LOC and SOC discharges. They are ν_{ei} and n_D/n_e. n_D/n_e in the SOC discharge is larger than in the LOC. The increase of n_D/n_e makes synthetic T_e fluctuation levels higher. Thus, sensitivity of the synthetic level on n_D/n_e is not consistent with the experimental observation, the reduction of T_e fluctuations across the LOC/SOC transition. ν_{ei} is also higher in the SOC discharge compared to the LOC discharge. The increase of ν_{ei} tends to decrease of synthetic T_e fluctuation level, consistent with the measurements. Although the

variation in the synthetic T_e fluctuation level is about $10 - 20\%$ with varying ν_{ei} within its uncertainty ($\sim 20\%$), Table 4.1 shows that ν_{ei} in the SOC discharge is two times higher than the LOC discharge. Thus, the increase of ν_{ei} can be a reason for the reduction of T_e fluctuations. However, it is also possible that the changes in gradient scale lengths are the main reason for the reduction of T_e fluctuations. This is because we observe the large variations of synthetic T_e fluctuation level with the changes in the gradient scale lengths by its uncertainty. At this point, it is inconclusive, since the changes in gradient scale lengths between the LOC and SOC discharges are within the uncertainties.

Figure 4-24(a) shows that the highest Q_e values obtained from the sensitivity analysis runs are still under-predicted from the experimental level in both LOC and SOC discharges. Thus, GYRO cannot reproduce the experimental Q_e value within the uncertainty of input parameters.

The variations of Q_e with the changes in input parameters are shown in Fig. 4-24(b) and (c). The increase in a/L_{T_i} causes the largest variation in Q_e in both discharges. We also note that there was no change in Q_e with the increase of a/L_{T_e} in the SOC discharge, while Q_e increases about 15% with the increase of a/L_{T_e} in the LOC discharge. Since the increase of a/L_{T_e} is favorable for TEM, this may indicate that TEM is more important in the LOC discharge than the SOC discharge. However, the variation of Q_e with a/L_{T_e} changes is less than 20%, less than the uncertainty of Q_e. Thus, it is hard to draw any solid conclusions from this observation. Instead, we are able to say that the variations of Q_e with a/L_{T_e} are smaller than the variations with a/L_{T_i}. This may indicate that ITG turbulence is stronger than TEM turbulence although neither type of turbulence is dominant.

In the LOC discharge, Q_e is sensitive to n_D/n_e and the increase of ν_{ei}. In the same discharge, Q_e increases about 10% with the decrease of a/L_n in the LOC discharge, although synthetic T_e fluctuation levels increase by about 40%. In the SOC discharge, Q_e does not vary significantly (less than 10%) with input parameter changes except for the increase of a/L_{T_i}, while synthetic T_e fluctuations are sensitive to the decrease of ν_{ei} as well as a/L_{T_i} in the same discharge. As explained in Chapter 1, Q_e is a function of

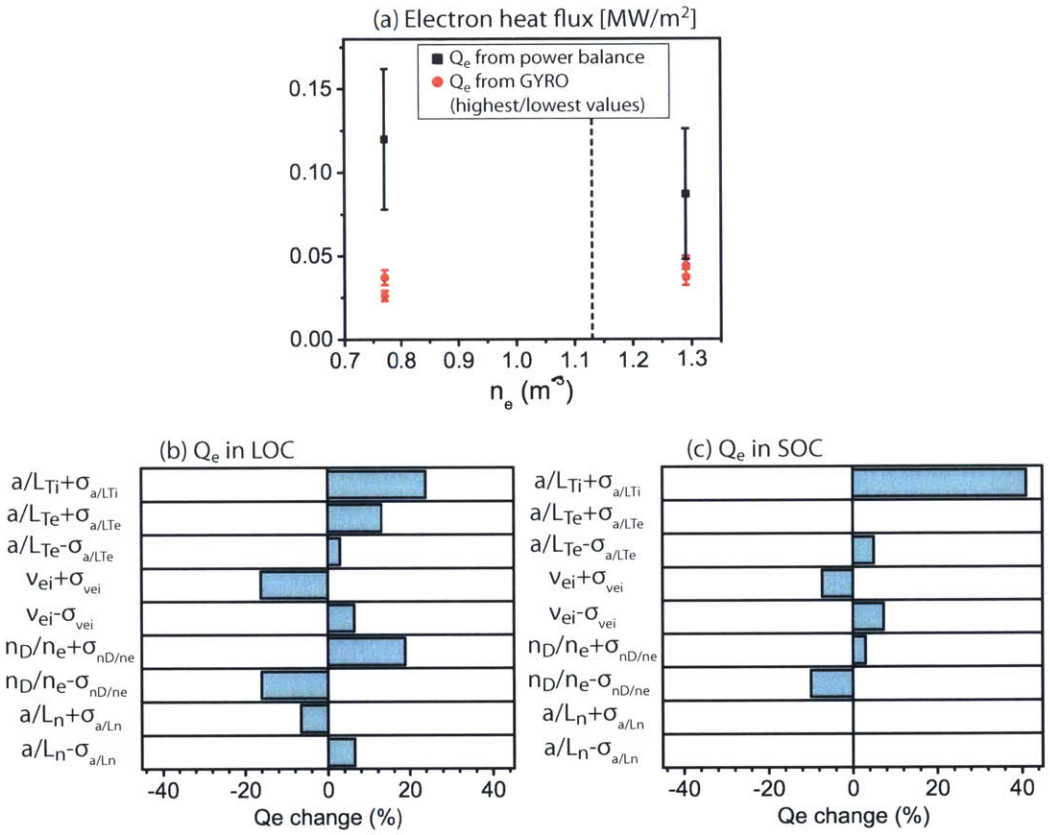

Figure 4-24: (a) Comparison of the highest and lowest values of simulated electron heat flux obtained from the sensitivity analysis for the LOC/SOC discharges at the CECE measurement position (r/a$\sim$0.85) (shot : 1120626023 (LOC), 1120626028 (SOC)) with the experiments. Fractional changes in the simulated electron heat flux with input parameter changes in the same sensitivity analysis for (b) the LOC discharge and (c) the SOC discharge. a/L_n was fixed in the SOC discharge, and the fractional change due to a/L_n was represented as zero in the SOC discharge.

three fluctuating quantities (potential fluctuations, n_e and T_e fluctuations) and their phase relations. Synthetic T_e fluctuation level is a function of T_e fluctuations and will be affected by n_e fluctuations and the phase between T_e and n_e fluctuations if optical depth is low as explained in Chapter 3. Thus, the sensitivity of Q_e to the changes in the inputs is not necessarily identical to the sensitivity of synthetic T_e fluctuations. Moreover, synthetic T_e fluctuations are sensitive to very low k_y turbulence, $k_y\rho_s < 0.3$. Further analysis is required to investigate the physics behind different sensitivities of Q_e and synthetic T_e fluctuations.

From the sensitivity analysis, we observed large variations in Q_i and synthetic T_e fluctuations with the changes of input parameters within the uncertainty. The variations are too large to reproduce their trends, including the reduction of T_e fluctuations across the LOC/SOC transition. All Q_e values from the sensitivity analysis are still under-predicted compared to the experimental level. Thus, GYRO cannot reproduce experimental Q_e within the uncertainties of input parameters. It was also found that a/L_{T_i} is one of the most sensitive parameters for Q_i, Q_e and synthetic T_e fluctuation levels in both LOC and SOC discharges. a/L_{T_e} is also important for Q_i and synthetic T_e fluctuation levels, while Q_e varies less than 20% with the changes in a/L_{T_e} in both discharges. This result may indicate that the contribution of ITG to the heat transport is larger than that of TEM in both discharges although TEM is not ignorable in these simulations. It was observed that n_D/n_e is important in the LOC discharge, consistent with previous studies [99, 120]. a/L_n is also an important parameter for Q_i and synthetic T_e fluctuations in the LOC discharge. Although variations of ν_{ei} by its uncertainty do not result in significant changes in synthetic T_e fluctuation levels, the consistent trend of synthetic T_e fluctuation levels with ν_{ei} in the experiments was observed, while the trend of T_e fluctuation levels with n_D/n_e was opposite to the experiments.

4.4.6 Investigation of discrepancies between GYRO and experiments

Two discrepancies between GYRO and experiments were found in the last two sections: the shape of the T_e fluctuation spectrum and the electron heat flux level. In this section, possible reasons for these discrepancies are investigated.

The shape of the synthetic electron temperature fluctuation spectrum

We first checked whether or not GYRO can reproduce the measured T_e fluctuation spectral shape by varying the rotation frequency, ω_o within its uncertainty. In these simulations, GYRO used the rotation frequency calculated from the radial electric field, E_r. This E_r value is estimated from TRANSP in this study. E_r can be estimated from the force balance equation as follows [103]:

$$E_r = \frac{1}{n_i Z_i e}\frac{dP_i}{dr} - V_{p,i}B_t + V_{t,i}B_p \tag{4.1}$$

where n_i, Z_i and P_i are the density, charge and pressure of the ion used in the E_r calculation. $V_{p,i}$ and $V_{t,i}$ are the poloidal and toroidal velocities of the ion, respectively, and B_t and B_p are the toroidal and poloidal magnetic field respectively.

As explained in section 3.3, TRANSP uses the experimental toroidal velocity and pressure gradient to estimate the first and second terms, and the neoclassical calculation is used to estimate the poloidal velocity through the NCLASS module [76] for the third term in Eq. 4.1. It was found that the neoclassical rotation values in both toroidal and poloidal directions are not always consistent with measurements, which indicates that a rotation can be induced by other mechanisms such as turbulence [149, 35, 64]. Using the neoclassical poloidal velocity can be an issue in these simulations since the contribution of the poloidal velocity term to total E_r value is not negligible. As shown in Fig. 4-25, the contribution of the poloidal velocity term is comparable to the contribution of the toroidal velocity term at r/a$\sim$ 0.85, and the pressure gradient term is small compared to the other two terms. We also see that the sign of the toroidal and poloidal velocity terms are opposite. Then, cancelling out two terms

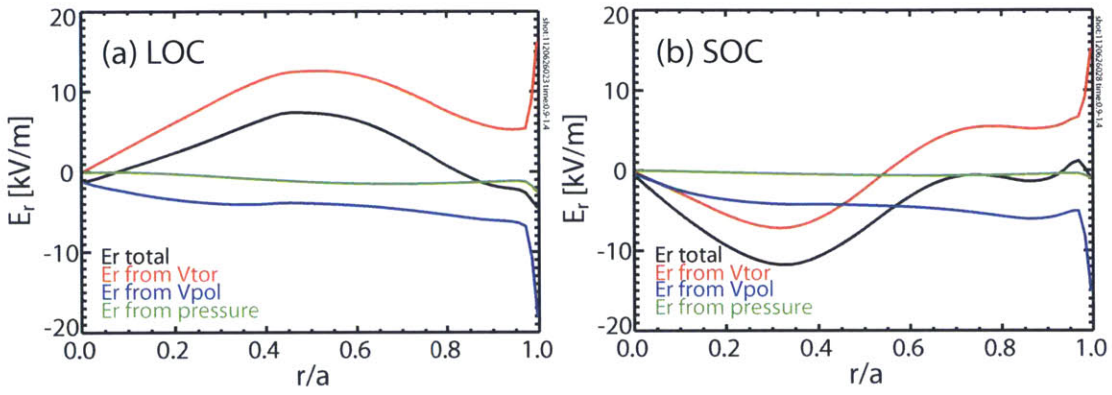

Figure 4-25: Total E_r value with the contribution of each components (Toroidal velocity, V_{tor}, poloidal velocity, V_{pol} and pressure gradient) estimated from TRANSP in (a) the LOC discharge and (b) the SOC discharge

results in a small E_r value near to zero. If the real poloidal velocity has the opposite sign to the estimated neoclassical value, it will change the E_r value significantly in this case. It is therefore possible that the neoclassical rotation profile, not consistent with the real experiments, causes narrower spectra in the simulations.

In order to check this possibility, we use the charge exchange spectroscopy (CXRS) diagnostic to estimate the E_r value with the measured toroidal/poloidal velocity and pressure gradient. It is noteworthy that we should not combine x-ray spectroscopy (HIREX) and CXRS to obtain the measured poloidal velocity as performed for toroidal velocity profile in section 3.2.1 due to magnetic pumping of each species [182]. The measured E_r by CXRS at r/a$\sim$0.85 is 3 ± 12kV/m for both the LOC and SOC discharges. The estimated E_r value from TRANSP is ~ -1kV/m, which agrees with the measurements within the uncertainty. For the comparison of fluctuation spectra, we used the Q_i matched run for the LOC discharge and the low n_D/n_e run ($n_D/n_e = (n_D/n_e)_{exp} - \sigma_{nD/ne}$) for the SOC discharge. It was found that the synthetic spectral shape can be similar to the measured spectrum over a broad frequency range when $E_r \sim 9$kV/m, which is within the uncertainty of the measured E_r value, as shown in Fig. 4-26.

However, the peak near 30kHz was observed in the synthetic spectra with $E_r \sim$

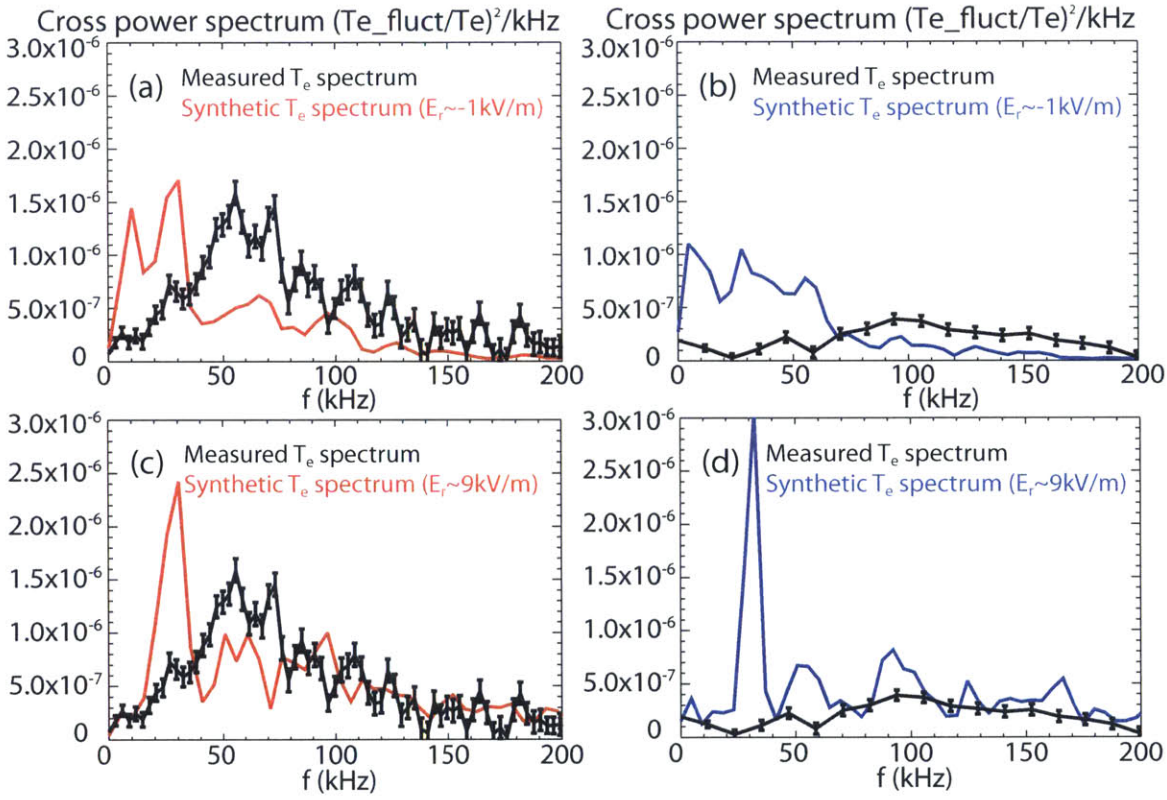

Figure 4-26: Comparison of the synthetic T_e fluctuation spectrum with the measured spectrum when the E_r value estimated from TRANSP ($\sim -1kV/m$) was used for (a) the LOC discharge and (b) the SOC discharge. The synthetic spectral with E_r ~9kV/m for (c) the LOC discharge and (d) the SOC discharge are also compared with the measurements.

$9kV/m$ in both LOC and SOC discharges. It is hard to consider that this peak comes from real physical fluctuations. In order to see that this mode is related to a numerical issue, another simulation with a different order of radial basis functions of the collision operator (ORD_RBF) was tried for the SOC discharge. As mentioned in section 4.4.2 and Appendix I, the mode in low k_y region, which was an issue in the base case setup, was mitigated by increasing ORD_RBF from 3 to 5. If this mode is related to a numerical issue, we may see changes in the peak. Figure 4-27 shows the synthetic spectra in the SOC discharge with the same E_r value as ~9kV/m but with different ORD_RBF values, 3 in Fig. 4-27(a) and 5 in Fig. 4-27(b). It is shown that increasing ORD_RBF suppresses the peak significantly, and that the synthetic spectrum with ORD_RBF=5 becomes more similar to the measured spectrum. We have not yet performed the run with ORD_RBF=5 for the LOC discharge, and it should be performed in the future. However, for a similar reason, we can also expect the suppression of the peak with ORD_RBF=5 in the LOC discharge.

Regardless of the peak near 30kHz, it is evident that GYRO can reproduce the measured spectral shape in a broad frequency range in both LOC and SOC discharges within the uncertainty of the measured E_r values by CXRS. This suggests the inaccurate estimation of poloidal velocity from neoclassical calculation is the reason for the narrower synthetic T_e fluctuation spectra compared to the experiments. However, we should note that the uncertainty in the E_r measurements for the LOC/SOC discharge is about 400%. In the future, we need a dedicated experiment for more accurate E_r measurements in Ohmic discharges to see whether or not the neoclassical poloidal velocity used in GYRO is responsible for the discrepancy of the T_e fluctuation spectral shape.

The under-prediction of electron heat flux

So far, we have observed that GYRO can reproduce experimental Q_i, T_e fluctuation levels, and T_e fluctuation spectral shape by modifying the E_r value within the uncertainty of the measurements. However, Q_e is under-predicted in these simulations. Since both Q_e and synthetic T_e fluctuations are related to electron transport, some-

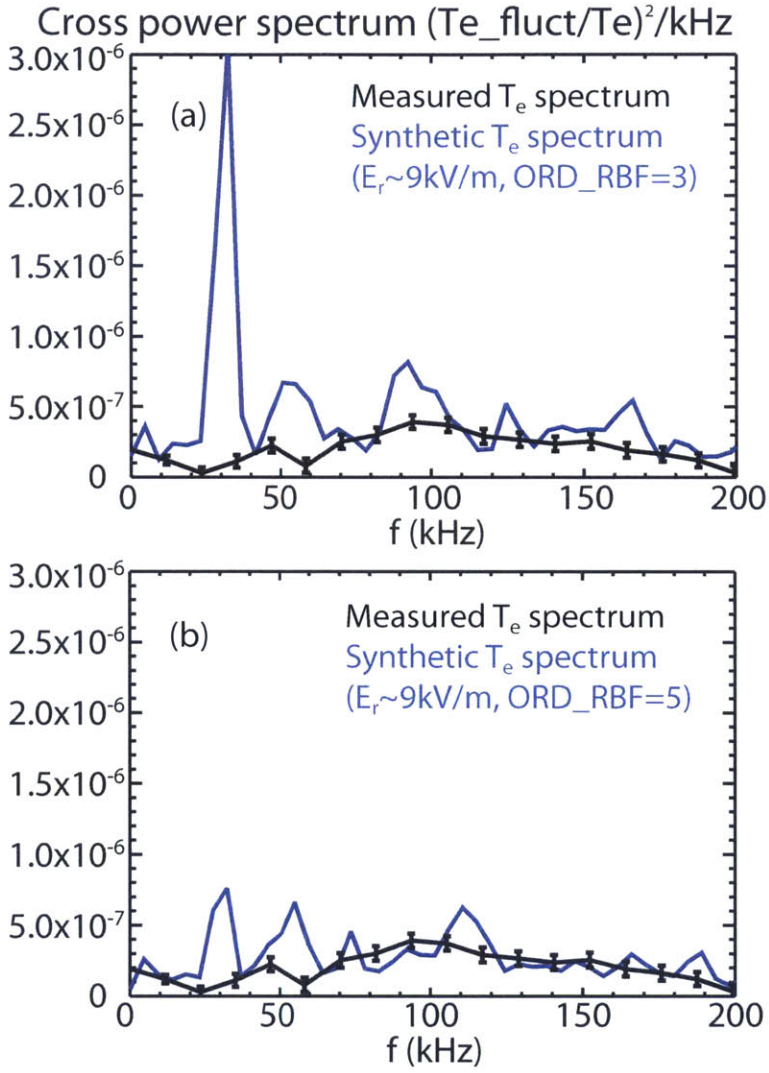

Figure 4-27: Comparison of the synthetic T_e fluctuation spectrum with the measured spectrum with E_r ~9kV/m for the SOC discharge with different ORD_RBF value. (a) ORD_RBF=3.0 (b) ORD_RBF=5.0.

one can think that these different agreement levels are incompatible. However, it is noteworthy that the measured T_e fluctuations come from low k_y, ion scale, turbulence ($k_y\rho_s < 0.3$), and that we considered the poloidal resolution of the measurements in the synthetic T_e fluctuations. In contrast, the simulated Q_e comes from only ion scale turbulence ($k_y\rho_s \lesssim 1.7$), while both electron and ion scale turbulence will affect the experimental Q_e from power balance analysis. Both electron and ion scale turbulence also affect the experimental Q_i, but Q_i will be affected mostly by ion scale turbulence. In the last sections, we have the agreements within the uncertainty in Q_i and synthetic T_e fluctuations, and the disagreements in Q_e with the experiments. In other words, the quantities from the simulations agree with the experimental quantities which mainly come from ion scale turbulence. This suggests that the electron scale turbulence (ETG turbulence), not included in the simulation in this study, could be responsible for the disagreement in Q_e. According to a simple mixing length estimate, which shows diffusivity induced by turbulence which has a growth rate, γ, and wavenumber, k, $\chi \sim \gamma/k^2$, the contribution of electron scale turbulence to the transport will be ignorable due to its short wavelength. However, previous non-linear simulation works show that electron transport, above the estimated level from a mixing length estimate, can be induced by electron scale turbulence [90, 47].

In order to check this possibility, linear stability analysis for electron scale turbulence was performed for the Q_i matched cases in the LOC and SOC discharges. Only electron scale turbulence ($k_y\rho_s = [2.0, 65.0]$ or $k_y\rho_e = [0.0, 1.0]$ where ρ_e is an electron gyroradius, defined as $\rho_e = v_e/\Omega_{ce}$ with $v_e = \sqrt{T_e/m_e}$ and $\Omega_{ce} = eB/m_ec$) was included in these simulations. Ions and electrons are treated as gyrokinetic ions and electrons, and the Debye shielding effect, which can be important for ETG turbulence due to its small spatial scale [89, 86], is included in the simulation. Boron was used as an impurity with the estimated dilution fraction, and initial value solver was used.

As shown in Fig. 4-28, the unstable electron modes are found in both discharges. We then varied a/L_{T_e} to confirm that these unstable modes are ETG turbulence. It was found that the growth rate of this mode increases with the increase in a/L_{T_e},

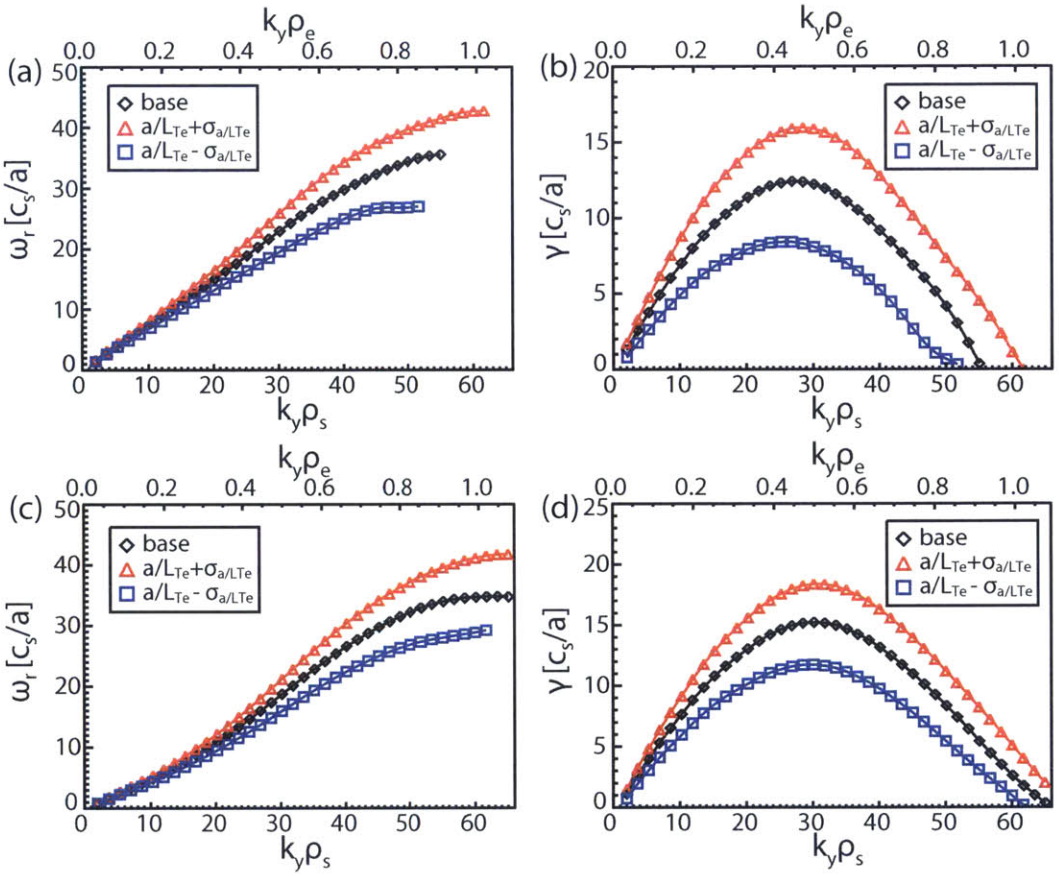

Figure 4-28: Linear stability analysis of electron scale turbulence (ETG) for the Q_i matched cases in the LOC/SOC discharges with changes in a/L_{T_e} by its uncertainty. (a) Real frequency, ω_r $[c_s/a]$ and Growth rate, γ $[c_s/a]$ in the LOC discharge (b) ω_r $[c_s/a]$ and γ $[c_s/a]$ in the SOC discharge.

	1^{st} set		2^{nd} set		
	LOC	SOC	LOC	Intermediate	SOC
magnetic configuration	LSN	LSN	LSN	LSN	LSN
$B_t(0)$ [T]	5.6	5.4	5.4	5.4	5.4
I_p [MA]	1.1	1.1	0.9	0.9	0.9
$n_{e,avg}$ $[10^{20}m^{-3}]$	0.9	1.7	0.8	1.1	1.3
κ	1.6	1.6	1.6	1.6	1.6
δ_u	0.3	0.3	0.3	0.3	0.3
δ_l	0.5	0.5	0.5	0.5	0.5

Table 4.4: Discharge conditions of the two sets of Ohmic discharges (1^{st} set : LOC and SOC, 2^{nd} set : LOC, Intermediate and SOC). Discharge conditions shown in this table are magnetic configuration (whether Lower Single Null (LSN), Upper Single Null (USN), double null configuration), magnetic field on the axis, $B_t(0)$ in Tesla, plasma current, I_p, in MA, average electron density, $n_{e,avg}$, in $10^{20}m^{-3}$, elongation, κ, upper triangularity, δ_u, and lower triangularity, δ_l. All shaping parameters (κ,δ_u and δ_l) are the values estimated at the separatrix.

which is consistent with the characteristics of the ETG turbulence. Although the unstable ETG-like turbulence was found in the linear simulations, the contribution of this unstable mode to electron transport is unknown until multi-scale simulations [77], which include both ion and electron scale simulations, are performed. This will be future work.

4.5 Profile shape variations across Ohmic confinement transition

As shown in Fig. 4-7, changes of a/L_{n_e}, a/L_{T_e} and a/L_{T_i} profiles across the LOC/SOC transition were small and within their uncertainties in the core region (r/a<0.7-0.8) in Alcator C-Mod [153]. This is also consistent with the study in TCV [142]. In TCV, it was found that the changes in the edge region correlated with the increase of Ohmic confinement time in the LOC regime. In this section, we will investigate the consistency of these observations with the profile analysis results in [142] by applying the self-similarity analysis introduced in section 3.2.2 for two sets of C-Mod Ohmic discharges.

We first analyze two Ohmic discharges (shot : 1120620027, 112062028) which have similar discharge conditions, such as Ohmic power (~1.5MW), plasma current (~1.1MA) and equilibrium parameters (Lower Single Null (LSN) configuration, elongation, $\kappa, \sim 1.6$, upper triangularity, δ_u, ~0.3 and lower triangularity, δ_l, ~0.5) except for the average electron density as shown in the "1^{st} set" column of Table 4.4. The average electron density, $n_{e,avg}$ was varied more than 40% between two Ohmic discharges (from $0.9\times10^{20}m^{-3}$ to $1.7\times10^{20}m^{-3}$) by intentionally changing the edge gas puff fueling. Toroidal magnetic field on axis is slightly different between these two discharges ($B_t(0)$=5.4 and 5.6T), but this level of difference (< 5%) is ignorable in the comparison. As used in section 4.1, the direction of core toroidal rotation was used to determine the confinement regime of each discharge.

Figure 4-29 shows the plasma parameters of these two discharges with time. One can see that the two discharges have the same plasma current and Ohmic input power (~1.5MW). It can also be seen that the increase of average electron density between two discharges correlates with the rotation reversal in the discharge with the higher density. According to the toroidal rotation direction, the lower density discharge (shot 1120620027) is in the LOC regime, and the higher density discharge (shot 1120620028) is in the SOC regime. In addition, these two discharges have discharge conditions similar to the discharges in Fig. 13 in [130], and the energy confinement time in Fig. 13 in [130] was saturated near $n_{e,avg} \sim 1.1\times10^{20}m^{-3}$. This result also supports the conclusion that the lower density discharge in this study ($n_{e,avg}$ ~$0.9\times10^{20}m^{-3}$) is in the LOC regime, and the higher density discharge ($n_{e,avg}$ ~$1.7\times10^{20}m^{-3}$) is in the SOC regime. The data in the shaded area in Fig. 4-29, which indicates the stationary period in these discharges, were used in the profile analysis.

We first studied the changes in the shape of T_e profiles between the LOC and SOC discharges. As shown in Fig. 4-30(a), the exponential function in Eq. 3.14 matches T_e data in the core region ($\rho \leq \rho_{ped,T_e}$) well for the two Ohmic discharges. Self-similarity of core T_e profiles can also be seen in Fig. 4-30(b) and (c). T_e data and the fitting lines are normalized by the T_e value at 0.8 calculated from the fitting line, $T_e(0.8)$, in Fig. 4-30(b). We can see that the normalized data in these two discharges are

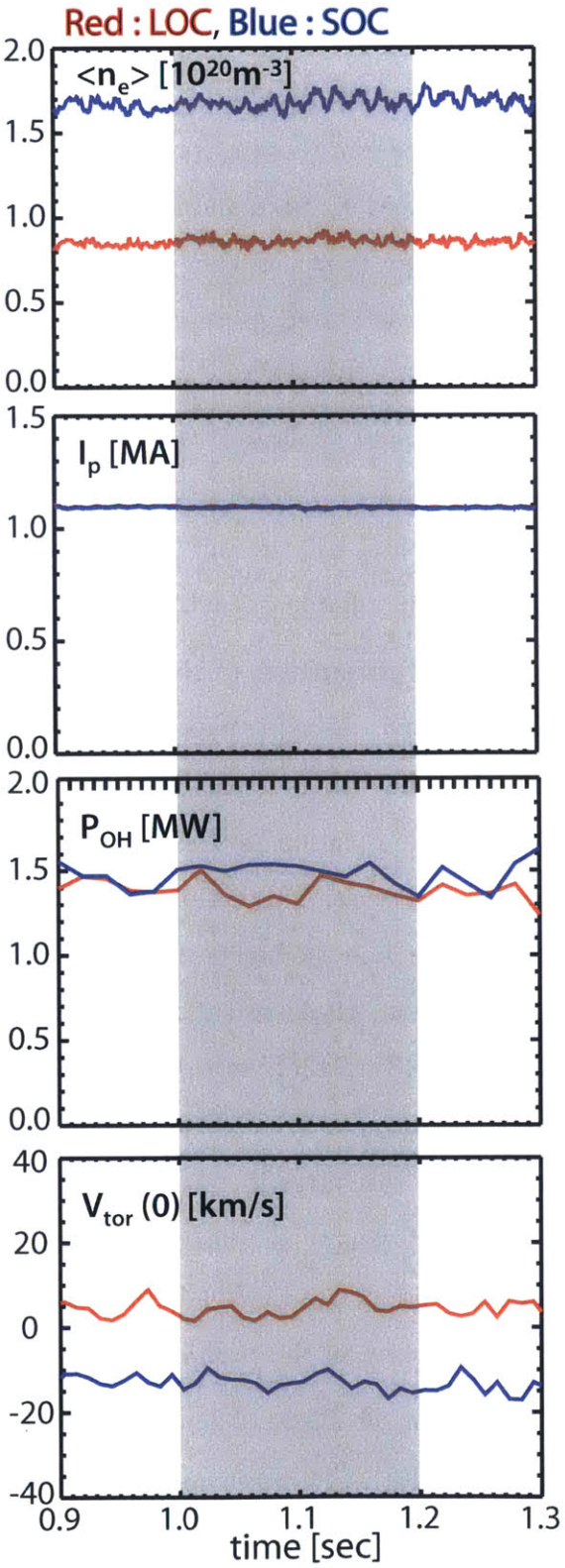

Figure 4-29: Plasma parameters with time for two Ohmic discharges with different average electron density, and different confinement regimes. Red : LOC, blue : SOC. The shaded region is the stationary period used in profile analysis.

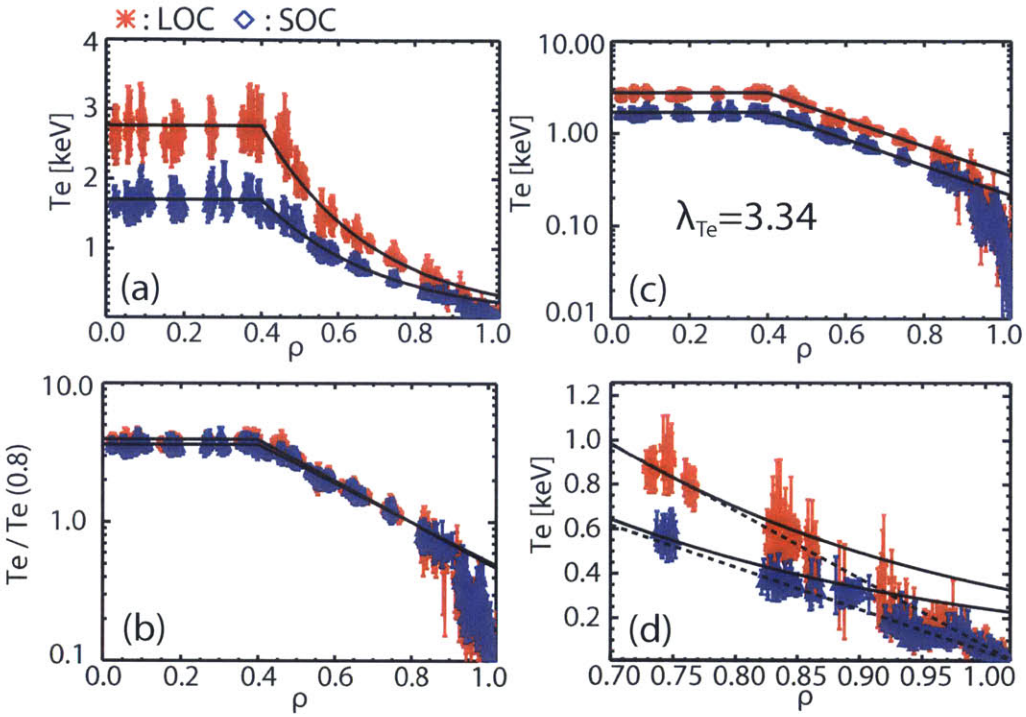

Figure 4-30: T_e profiles in two Ohmic discharges (red : LOC, blue : SOC) with the fitting lines (solid line : exponential fitting line for the core profile, dashed line : linear fitting line for the edge profile) (a) T_e Profiles with the fitting lines in linear scale (b) The T_e profiles normalized by $T_e(0.8)$ with the exponential fitting line, which is also normalized, in log scale (c) T_e profile with the fitting line with fixed λ_{T_e}(=3.34) in log scale. (d) Edge T_e profiles with the fitting lines.

well overlapped in the $\rho \lesssim 0.8$ region, which indicates that the $T_e(0.8)$ value may determine the T_e profile for $\rho \leq \rho_{ped,T_e}$. Figure 4-30(b) also shows that the fitting lines normalized by $T_e(0.8)$ are close to each other, implying that the exponential fitting parameter, λ_{T_e}, values are similar, and the T_e profiles are self-similar in the core region. In Fig. 4-30(c), the same λ_{T_e} value, which is the mean value between the two discharges, is applied to these discharges. As shown in Fig. 4-30(c), the fit with single λ_{T_e} value (=3.34) works well for both discharges. Figure 4-30(a)-(c) indicates that the T_e profiles inside $\rho \leq \rho_{ped,T_e}$ are self-similar and this property can be quantified by the exponential function. Figure 4-30(d) shows the edge temperature profiles ($\rho \geq \rho_{ped,T_e}$) of the two Ohmic discharges with the lines fit by the linear function in Eq. 3.14. Although there is a scatter in the edge T_e data, we can see that the edge data are not well fit by the exponential function used for the core T_e data, and that a linear fit is more appropriate in the edge region. It is also shown that the slope of the linear fit, μ_{T_e}, decreases with the increase of the average density.

The variations of n_e profiles between the two Ohmic discharges were also investigated as shown in Fig. 4-31. Like the core T_e profiles, exponential fitting works well for core n_e data. We can also see the self-similarity of the core n_e profiles from the fact that a single λ_{n_e} value (=0.87) can be used to fit n_e data in the core region for both Ohmic discharges, and that the data normalized by $n_e(0.8)$ are well overlapped. Figure 4-31(d) shows that linear fitting works better than exponential fitting for the edge n_e profiles ($\rho \geq \rho_{ped,n_e}$) and that both the slope of fitting line, μ_{n_e}, and the n_e value at $\rho = 1.0$ in the linear fit, $n_{e,edge}$, increase with the average electron density.

The change of the profile shape with the average density between the two Ohmic discharges is quantified by the linear and exponential fitting parameters, as shown in the "1^{st} set" column of Table 4.5. Both n_e and T_e profiles between LOC and SOC discharges have the similar exponential fitting parameters (λ_{T_e} and λ_{n_e}) within 20% in the core region regardless of the change of average electron density, which indicates that both the n_e and T_e profiles are self-similar. It is also worth noting that these fitting parameters can be considered as average gradient scale lengths, which are important for driving turbulence. These parameters do not change with electron

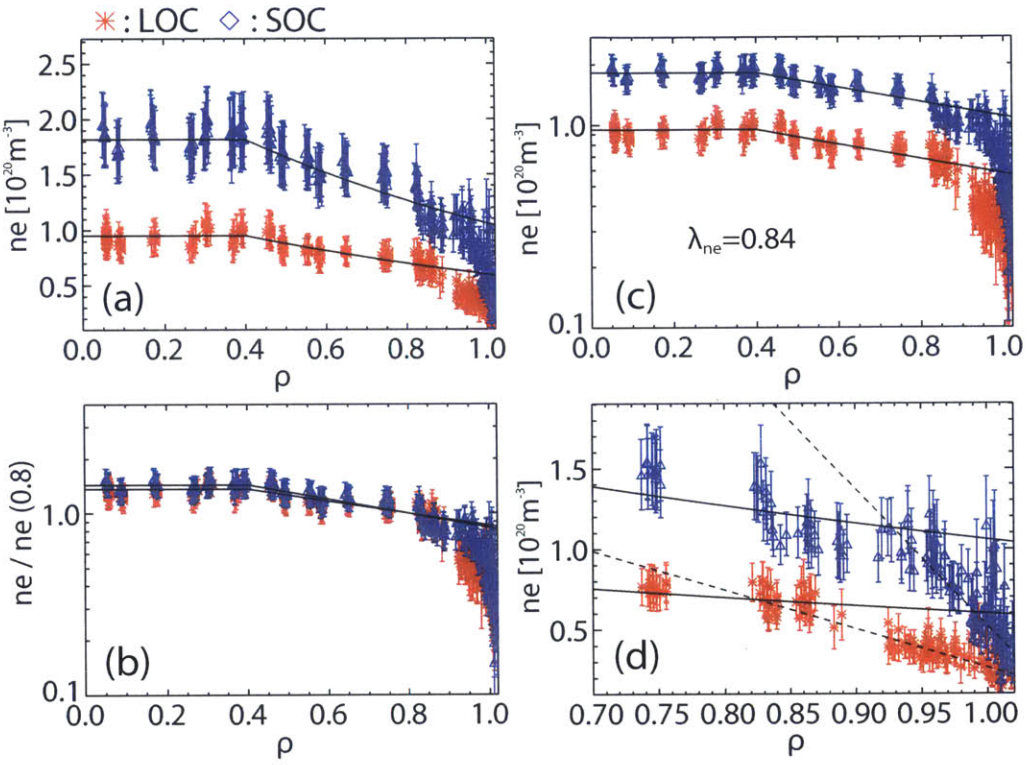

Figure 4-31: n_e profiles in two Ohmic discharges (red : LOC, blue : SOC) with the fitting lines (solid line : exponential fitting line for the core profile, dashed line : linear fitting line for the edge profile) (a) n_e Profiles with the fitting lines in linear scale (b) The n_e profiles normalized by $n_e(0.8)$ with the fitting line, which is also normalized, in log scale (c) n_e profile with the fitting line with fixed $\lambda_{n_e}(=0.84)$ in log scale. (d) Edge n_e profiles with the fitting lines.

density, while the Ohmic confinement regime changes with the density. However, we did observe changes of fitting parameters for the edge n_e profiles (μ_{n_e} and $n_{e,edge}$). μ_{n_e} increases by more than a factor of three with the average density, and $n_{e,edge}$ also increases by a factor of two. We also note that $\rho_{ped,ne}$ increases from 0.82 to 0.93 in the SOC discharge. The increase of both μ_{n_e} and $n_{e,edge}$ makes $n_e(0.8)$ higher. With the increase of the average electron density, the $T_e(0.8)$ value decreases. However, μ_{T_e} and $T_{e,edge}$ decrease by about 40%, decreasing $T_e(0.8)$ by a relatively smaller values as compared to the increase of $n_e(0.8)$ between the two discharges. A relatively larger increase of $n_e(0.8)$ results in a larger electron pressure at ρ=0.8, $p_e(0.8)$, in the higher density discharge, which indicates higher plasma energy or pressure in the core region, where the profiles exhibit self-similarity. It follows that the changes in the edge n_e profile, which are the increases of gradient and edge values, are responsible for the increase of energy confinement in C-Mod Ohmic discharges with average electron density. These results are consistent with the findings in TCV [142], which also shows that the changes in edge n_e profile are related to the increase of Ohmic confinement time with density in the LOC regime. Since the analysis results suggest the correlation between the changes outside the core region ($\rho \gtrsim 0.8$) and global confinement changes, we can also connect the results to the results shown in section 4.1., which show the correlation between the changes in T_e fluctuations near the edge and the Ohmic confinement transition, and the changes in the turbulence right inside the last closed flux surface across the Ohmic confinement transition, observed in C-Mod [130].

We also study the n_e and T_e profiles in the LOC and SOC discharges analyzed in section 4.2-4.4 (shot 1120626023 (LOC) 1120626028 (SOC)). We added the discharge which has rotation reversal in this analysis (shot 1120626027), which will be near the boundary between LOC and SOC. We refer to this discharge as "intermediate" in this study. The intermediate discharge also has the same toroidal magnetic field ($B_t(0)$~5.4T), plasma current (~0.9MA), Ohmic power (~1.0MW) and equilibrium parameters (LSN, $\kappa \sim 1.6$, δ_u ~0.3 and δ_l ~0.5) as the LOC and SOC discharges as shown in Fig. 4-32 and the "2^{nd} set" column of Table 4.4. Since we observed the correlation between core rotation reversal and T_e fluctuations near the edge, as will be

		1^{st} set		2^{nd} set		
	Parameters	LOC	SOC	LOC	Intermediate	SOC
core T_e	λ_{T_e}	3.44	3.24	3.33	3.29	3.39
($\rho \leq \rho_{ped,T_e}$)	$T_e(0.8)$ [keV]	0.70	0.47	0.59	0.47	0.41
edge T_e	μ_{T_e} [keV]	3.02	1.88	2.61	1.95	1.77
($\rho \geq \rho_{ped,T_e}$)	$T_{e,edge}$ [keV]	0.08	0.05	0.03	0.03	0.03
	ρ_{ped,T_e}	0.71	0.73	0.71	0.73	0.73
core n_e	λ_{n_e}	0.77	0.90	0.76	0.93	0.92
($\rho \leq \rho_{ped,n_e}$)	$n_e(0.8)$ [$10^{20}m^{-3}$]	0.70	1.27	0.60	0.85	0.95
edge n_e	μ_{n_e} [$10^{20}m^{-3}$]	2.41	8.51	1.27	2.48	2.59
($\rho \geq \rho_{ped,n_e}$)	$n_{e,edge}$ [$10^{20}m^{-3}$]	0.26	0.52	0.41	0.56	0.61
	ρ_{ped,n_e}	0.82	0.93	0.87	0.92	0.90
	$P_e(0.8)$ [kPa]	7.84	9.55	5.66	6.39	6.23

Table 4.5: Parameters calculated from fitting with different Ohmic confinement regimes in the two sets of Ohmic discharges (1^{st} set : LOC and SOC, 2^{nd} set : LOC, Intermediate and SOC). λ_{T_e} is an exponential fitting parameter for the core T_e profile, and μ_{T_e} is the slope of the linear fitting line applied to the edge T_e profile. $T_{e,edge}$ indicates the T_e value at $\rho = 1.0$ from the linear fitting line applied to the edge T_e profile. $\rho_{ped,Te}$ is the radial location which has the minimum difference between the exponential and linear fitting line. The same definitions are applied to λ_{n_e}, μ_{n_e}, $n_{e,edge}$ and $\rho_{ped,ne}$ for n_e profiles.

shown in Chapter 5, the stationary time period was set to shorter than the time range used in section 4.1-4-4 for the LOC and SOC discharges. It was set to t=1.15-1.4 sec, which is shown as the shaded area in Fig. 4-32, and this range was used in the analysis in this section.

We can see the self-similarity property in the core region for both T_e and n_e profiles in these discharges as observed in the first set of Ohmic discharges. Figure 4-33(a) and (c) show that core T_e data are well fit by an exponential function, and a single λ_{T_e}(=3.34) can be used for all three discharges. It is also shown that T_e data normalized by $T_e(0.8)$ overlap each other in Fig. 4-33(b). Figure 4-33(d)-(f) show that core n_e data have the same self-similar property as the core T_e data. We also notice that the exponential fitting parameter in the core region varies within 20% with the average density or across the LOC/SOC transition from the "2^{nd} set" column of Table 4.5.

Figure 4-34 shows the edge T_e and n_e profiles for these three discharges. μ_{T_e}

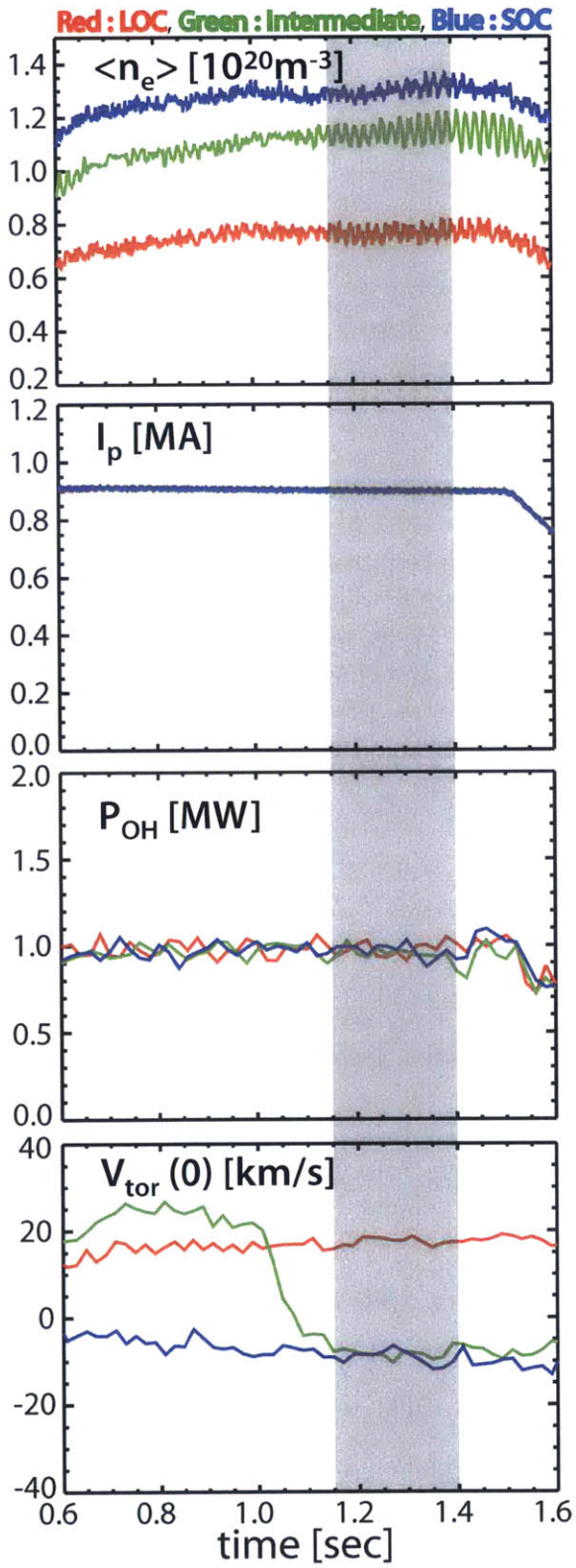

Figure 4-32: Plasma parameters with time for three Ohmic discharges with different average electron density, and different confinement regimes. Red : LOC, green : Intermediate, blue : SOC. The shaded region is the stationary period used in profile analysis.

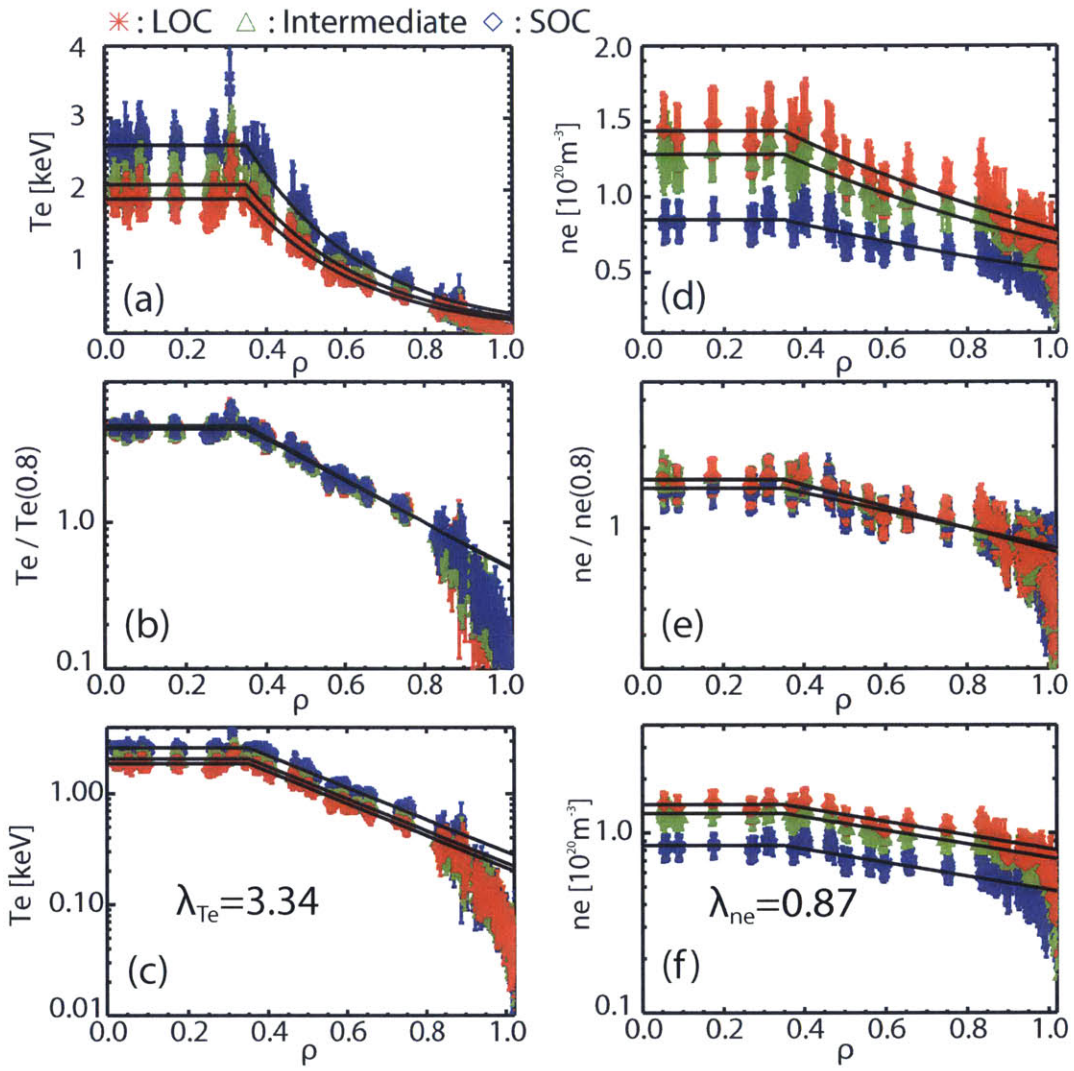

Figure 4-33: Core T_e and n_e profiles of three Ohmic discharges (red : LOC, green : Intermediate, blue : SOC) with the exponential fitting line for the core profile (solid line). (a) T_e profiles with the fitting lines in linear scale (b) The T_e profiles normalized by $T_e(0.8)$ with the fitting line, which is also normalized, in log scale (c) T_e profile with the fitting line with fixed λ_{T_e}(=3.34) in log scale. (d) T_e profiles with the fitting lines in linear scale (e) The n_e profiles normalized by $n_e(0.8)$ with the fitting line, which is also normalized, in log scale (f) n_e profile with the fitting line with fixed λ_{T_e}(=0.87) in log scale.

decreases by about 30% with almost the same $T_{e,edge}$ values, while μ_{n_e} and $n_{e,edge}$ increase by about 90% and 50%, respectively, in the intermediate and SOC discharges compared to the LOC discharge. These observations are consistent with the first set of Ohmic discharges. It is shown that the $n_e(0.8)$ value increases by about 40%, while the $T_e(0.8)$ value decreases by about 20% from the LOC to the intermediate discharge, increasing the $p_e(0.8)$ value in the intermediate discharge. Considering self-similar core n_e profiles, the 40% increase of $n_e(0.8)$ may come from the increase of μ_{n_e} and $n_{e,edge}$. Between the intermediate and the SOC discharge, edge fitting parameters in both n_e and T_e profiles vary within 10%, and $n_e(0.8)$ increases by about 15%, and $T_e(0.8)$ also decreases by about 15%, which makes $p_e(0.8)$ comparable within 5%. Considering the same input power and self-similar core n_e and T_e profiles, it indicates the saturation of Ohmic confinement time, expected in the SOC regime.

Since the LOC/SOC transition was universally observed in several tokamaks as explained in Chapter 1, and the feature obtained through self-similarity analysis in this section is consistent with the findings in TCV, it will be interesting to compare the fitting parameters in C-Mod with the parameters in TCV. The parameters in the edge region change with the discharge conditions such as plasma current, total power and average electron density, as shown in Fig. 24, 25 and 26(a) in [142]. In contrast, Fig. 26(b) in [142] shows that the exponential fitting parameters (λ_{T_e} and λ_{n_e}) in the core region do not vary with the discharge conditions. Thus, λ_{T_e} and λ_{n_e} will be appropriate for the comparison between the two machines, which have different discharge conditions. Table 4.5 shows that λ_{T_e} ~3.0-3.4 and λ_{n_e} ~0.7-1.0 in the two sets of C-Mod Ohmic discharges used in this study. From the appendix in [142], the λ_{T_e} for discharges used in [142] is ~3.0-3.5, and the values of λ_{n_e} are ~2.0-2.5. It is noteworthy that the values of λ_{T_e} are similar between C-Mod and TCV, while λ_{n_e} values in TCV are about two times higher than in C-Mod, indicating that the shape of the core n_e profile is more sensitive to discharge conditions than the shape of the core T_e profile.

The self-similarity analysis shows the correlation between the improvement of Ohmic confinement and the increase in μ_{n_e} and $n_{e,edge}$. In other words, the changes

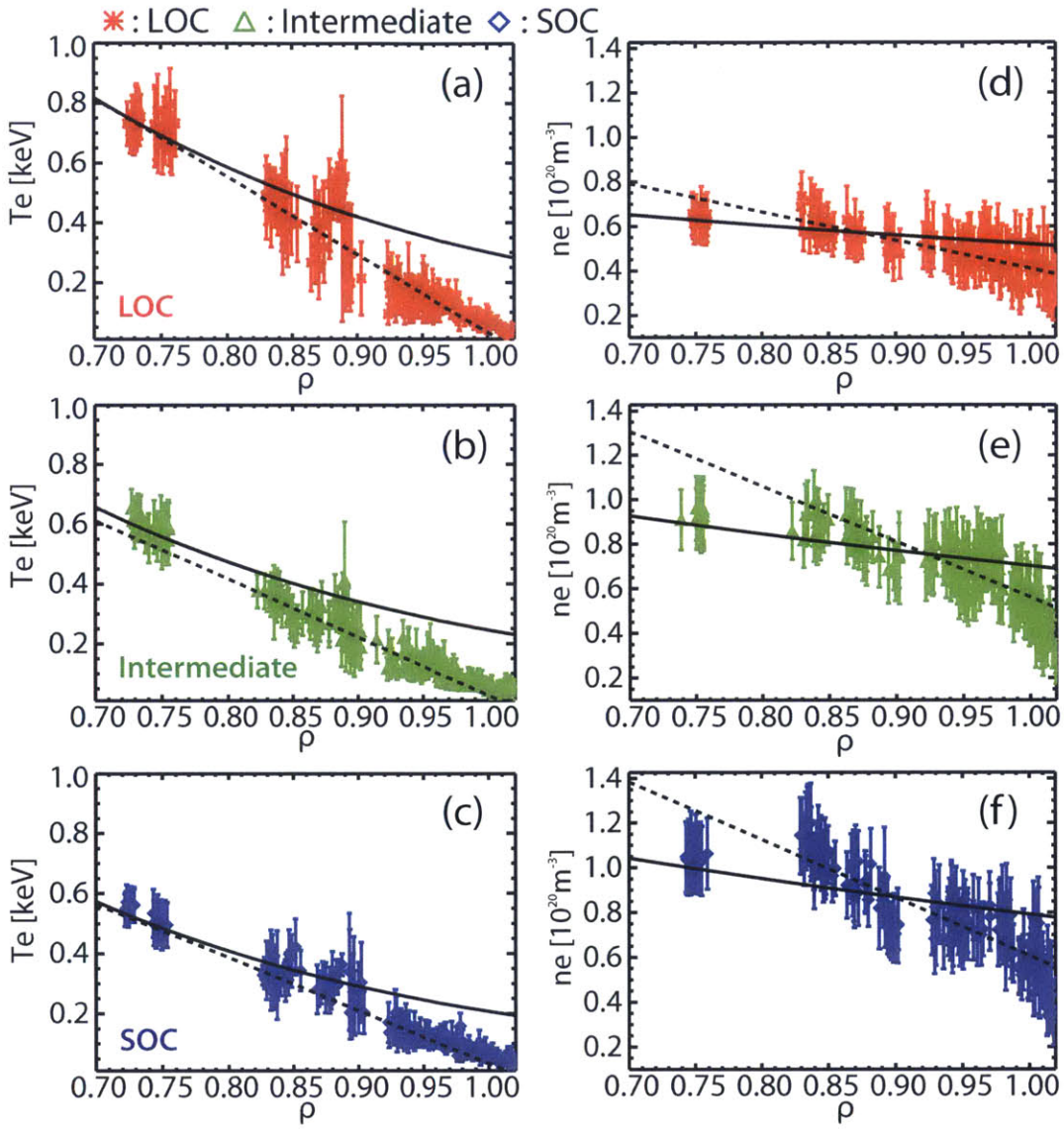

Figure 4-34: Edge T_e and n_e profiles of three Ohmic discharges (red : LOC, green : Intermediate, blue : SOC) with the exponential fitting lines (solid line : exponential fitting line for the core profile, dashed line : linear fitting line for the edge profile) (a) Edge T_e profile in the LOC regime, (b) Edge T_e profile in the "intermediate" regime, (c) Edge T_e profile in the SOC regime, (d) Edge n_e profile in the LOC regime, (e) Edge n_e profile in the "intermediate" regime, (f) Edge n_e profile in the SOC regime.

in the shape of edge profiles are correlated with the Ohmic confinement transition. We also note that similar features were observed in other Ohmic discharges, not shown in this study.

4.6 Discussion & Summary

In this chapter, we investigated the LOC/SOC transition using fluctuation measurements, power balance analysis, gyrokinetic analysis and profile analysis including self-similarity analysis. Although we do not obtain the big picture which can explain the results from these different analyses, we may have discovered some hints concerning the LOC/SOC transition through this study.

In the measurements, we observed a reduction of electron temperature fluctuations, measured by CECE, near the edge region (r/a$\sim$0.85) across the LOC/SOC transition with no clear change in relative line-integrated electron density fluctuation level, measured by PCI. The CECE measurements have been predicted to be sensitive to TEM turbulence [158], and the increase of ratio of T_e fluctuations to n_e fluctuations may indicate an increase of linear growth rate of TEM compared to that of ITG [179]. As a plasma moves from LOC to SOC with the increase of n_e and the same input Ohmic power, there is a decrease of electron temperature, reducing electron collisionality. The decrease of collisionality will reduce the effect of the trapped electrons, thus stabilizing TEM turbulence. It is therefore possible to interpret the reduction of measured temperature fluctuations with n_e fluctuations which has an unclear trend across the LOC/SOC transition as being due to a reduction of TEM turbulence due to the increase of collisionality. This result would support the hypothesis about the LOC/SOC transition, which is, a change in dominant mode from TEM to ITG mode is responsible for the LOC/SOC transition (LOC-TEM, SOC-ITG). However, these measurements do not necessarily imply a change of dominant turbulent mode, and the change of turbulence across the LOC/SOC transition should be studied through nonlinear gyrokinetic analysis.

We performed gyrokinetic analysis using the code, GYRO. The simulations use

the local value of the input profiles (excluding the profile variation) and consider electrostatic ion scale turbulence. The results from both linear and nonlinear gyrokinetic simulations show no dominant mode change across the LOC/SOC transition both in the core and near the edge regions within the uncertainty of input parameters. In the core region (r/a=0.6), the ITG mode is dominant in both the LOC and the SOC discharges, and the ITG mode and TEM are comparable in both discharges near the edge region (r/a$\sim$0.85). This suggests that the LOC/SOC transition is not as simple as a linear mode transition from the TEM to the ITG mode.

The reason for the reduction of T_e fluctuations in the SOC regime is still unclear. However, gyrokinetic analysis shows that the synthetic T_e fluctuation levels increase with not only changes in input parameters to make TEM more unstable, such as the increase of a/L_{T_e}, but also with changes making ITG more unstable, such as the increase of a/L_{T_i}, implying that the reduction of T_e fluctuations is not always connected to the reduction of TEM turbulence. We also observed the increase of synthetic T_e fluctuation level with the increase of main ion fraction. Since the main ion fraction increases across the LOC/SOC transition, the increase of main ion fraction will not be a reason for the reduction of T_e fluctuations. The decrease of collisionality increases the synthetic T_e fluctuation levels, but synthetic T_e fluctuations were less sensitive to the collisionality compared to the gradient scale lengths. Thus, it is inconclusive whether either collisionality or one of gradient scale lengths ($a/L_{T_i}, a/L_{T_e}, a/L_n$), or a combination of them is the reason for the reduction of T_e fluctuations. Dedicated experiments to reduce the edge gradient scale length will be helpful to identify the reason in the future.

Power balance analysis using TRANSP shows that ion heat transport is enhanced in the SOC discharge compared to the LOC discharge, and this consistent trend was observed in the non-linear gyrokinetic simulations. In both power balance and gyrokinetic analyses, electron heat flux changes are within the uncertainty. This may suggest that the increase of ion transport correlates with the LOC/SOC transition. It was observed that the simulated potential and the ion temperature fluctuations increase in the SOC discharge at both r/a=0.6 and $\sim$0.85. Fluctuation measurements

of potential and ion temperature may shed light on the changes in turbulent ion transport across the LOC/SOC transition.

Through self-similarity analysis, radial variations in n_e and T_e profile shapes with different Ohmic confinement regimes, as recently observed in TCV [142], were investigated in Alcator C-Mod to study self-similarity and related stiffness properties. With the increase of average density or the change of Ohmic confinement regime from LOC to SOC in two sets of Ohmic discharges, it was found that an exponential fit can be applied in the core region ($\rho_{inv} < \rho \leq \rho_{ped,Te}$) with a similar gradient scale length in both n_e and T_e profiles, regardless of the Ohmic confinement regime, consistent with the similar gradient scale lengths obtained from profile analysis in section 4.2.1. It follows that both n_e and T_e profiles in this region are self-similar across the Ohmic confinement transition. However, differences between the n_e and T_e profiles were found in the edge region, and changes in the linear fitting parameters for the edge n_e profiles, the increase of the slope of the linear fitting line for the edge n_e profile, μ_{n_e}, and the n_e value at $\rho = 1.0$ from the linear fit, $n_{e,edge}$, values, in the SOC regime compared to the LOC regime correlate with the improvement in energy confinement. These observations are consistent with the findings in TCV.

In this chapter, we also performed a validation study for the local, electrostatic gyrokinetic model including only ion scale turbulence, which is used in this study, at r/a$\sim$0.85 in the C-Mod Ohmic discharges. For the validation, the simulated heat fluxes and synthetic T_e fluctuations from the non-linear simulations at the CECE measurement position were compared with the experiments. It was found that GYRO can reproduce Q_i and the synthetic T_e fluctuation levels within the uncertainty of input parameters, and the T_e fluctuation spectral shape can also be reproduced within the uncertainty of the measured radial electric field, E_r. However, Q_e is under-predicted. Matching the T_e fluctuation level, which comes from low k turbulence ($k_y\rho_s$ <0.3), with the under-prediction of Q_e suggests that the electron scale turbulence could be a reason for the under-prediction of Q_e. In other words, electron scale turbulence could be important in C-Mod Ohmic discharges.

All these analysis results indicate that the old hypothesis about the LOC/SOC

transition should be modified. First, the simple linear ITG/TEM transition picture is not appropriate for the LOC/SOC transition. Gyrokinetic analysis performed in this chapter suggests that the LOC/SOC transition is not simply due to the changes in the dominant turbulence mode. We must also note that there will be no pure ITG or TEM turbulence in real experiments. The non-linear picture should be considered to investigate the LOC/SOC transition. Moreover, the GYRO validation study suggests that electron scale turbulence could be important in electron transport in both LOC and SOC discharges. Thus, we need to study the changes in electron scale turbulence across the LOC/SOC transition in the future. The complete picture can be found through gyrokinetic analysis including both electron and ion scale turbulence and their interactions. Second, we do not know whether the changes in turbulence across the LOC/SOC transition occur locally or globally. T_e fluctuation measurements near the edge region indicate that the local turbulence changes can be correlated with the global confinement transition. However, we note that T_e fluctuation measurements in the core region should be performed to prove this possibility. Nevertheless, self-similarity analysis also shows that the changes in the edge profiles are correlated with the LOC/SOC transition. These results may suggest that the changes near the edge region are responsible for the LOC/SOC transition, but this should be studied in the future. This study at least raises the possibility the correlation between local changes in the profile or turbulence and global confinement in the Ohmic discharges.

Chapter 5

Investigation of changes in turbulence associated with rotation reversal in Alcator C-Mod

Since the change of the direction of core toroidal rotation correlates with the Ohmic confinement transition, it will be of interest to explore the changes in turbulence across the rotation reversal. In addition to the Ohmic LOC/SOC experiments, we have used the CECE system to study changes in turbulence occurring across spontaneous rotation reversals (when the rotation profile changes from peaked to hollow) in RF heated L-mode plasmas. Like Ohmic plasmas, there is a critical density at which the intrinsic toroidal rotation reverses direction in RF heated L-mode plasmas [123, 175]. Interestingly, there are similarities between the turbulence changes in RF heated L-mode plasmas and Ohmic plasmas when the rotation reversal occurs. In this chapter, we will show T_e fluctuation measurement results in these RF heated L-mode plasmas. Turbulence changes across the rotation reversal will then be studied through the analysis methods explained in Chapter 3.

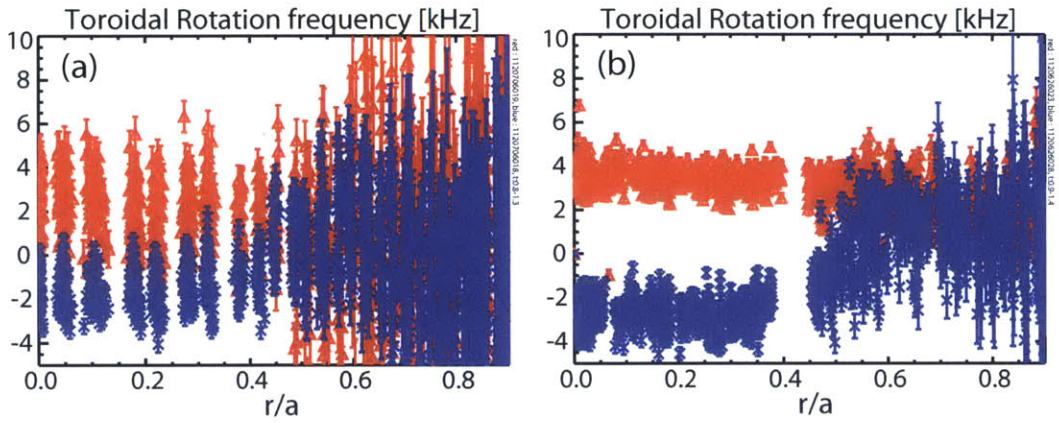

Figure 5-1: Toroidal rotation frequency profile of a pair of discharges with different average densities (Red : lower density discharge, blue : higher density discharge). (a) Two RF heated discharges (shot : 1120706018 (t: 0.8-1.3 sec, blue), 1120706019 (t: 0.8-1.3 sec, red)) (b) Two Ohmic discharges (shot : 1120626023 (t: 0.9-1.4 sec, red), 1120626028 (t: 0.9-1.4 sec, blue))

5.1 Changes in T_e fluctuations associated with rotation reversal

We first show the changes in T_e fluctuations between two RF heated discharges rotating in opposite directions due to different density levels. Although small changes in the line averaged density ($< 5\%$) can induce the core rotation reversal, the line averaged density varies about 50% in these two discharges. In order to exclude the effect on the T_e fluctuations due to changes in the density, we also investigated the changes in T_e fluctuations across the rotation reversal with small changes, less than 5%, in the density.

5.1.1 Observation of T_e fluctuation changes between RF heated L-mode discharges rotating in opposite directions due to different average densities

We first investigated two RF heated discharges (shot 1120706018, 1120706019, t:0.8-1.3 s) with similar discharge conditions except for the line averaged density. Their discharge conditions are similar as follows: toroidal magnetic field, B_t=5.4T in co-current

direction, total heating power, P_{tot}=2MW (Ohmic heating power, P_{OH} ~0.8MW, ICRF heating power, P_{RF} ~1.2MW), plasma current, I_p=0.8MA in Upper Single Null (USN) configuration with R=0.67m, a=0.22m, elongation, κ=1.7, lower triangularity, δ_l=0.3, upper triangularity, δ_u=0.6. However, their average density values, $\bar{n}_e$ are different: $\bar{n}_e = 1.4 \times 10^{20} m^{-3}$ (shot 112070618) and $0.9 \times 10^{20} m^{-3}$ (shot 112070619). These different density values result in opposite directions of core toroidal rotation; co-current direction in the lower density discharge and counter-current direction in the higher density discharge, as shown in Fig. 5-1(a). In this study, the positive sign of the rotation frequency indicates the co-current direction, and the negative sign indicates the counter-current direction. It is known that the change of rotation reversal occurs in the region where the safety factor, q, is less than 3/2 [129]. For these discharges, q=3/2 at r/a~0.6, and the change in the rotation profile occurs in the r/a< 0.6 region as shown in Fig. 5-1(a). Figure. 5-1(b) shows the rotation profile changes for the LOC and SOC discharges analyzed in Chapter 4. For both Ohmic and RF heated discharges, the direction of core toroidal rotation changes from the co- to the counter-current direction as the average density increases.

The observed changes in rotation profile are consistent with previous analyses in C-Mod [123, 175]. These studies define the changes in rotation profiles with density as the changes from "peaked" to "hollow" profiles. However, it is ambiguous whether the rotation profile changes from peaked to hollow due to the quality of data in $r/a > 0.5$ for the RF heated discharges in all C-Mod plasmas, including those with CECE data. Nevertheless, we can see clearly that the sign of the rotation frequency changes. In this study, rotation reversal refers to changes in either the direction of the core toroidal rotation or the shape of the rotation profile from peaked to hollow.

Using the CECE diagnostic, T_e fluctuations were measured near the edge ($r/a \sim 0.85$) for these two RF heated discharges in a stationary time period (t:0.8-1.3s). Figure 5-2 shows the time series data for these RF heated discharges during the stationary time period. The position of the CECE measurements was steady because of the steady toroidal magnetic field and the plasma current. Total heating power was also steady in both discharges. Although the line averaged density tends to

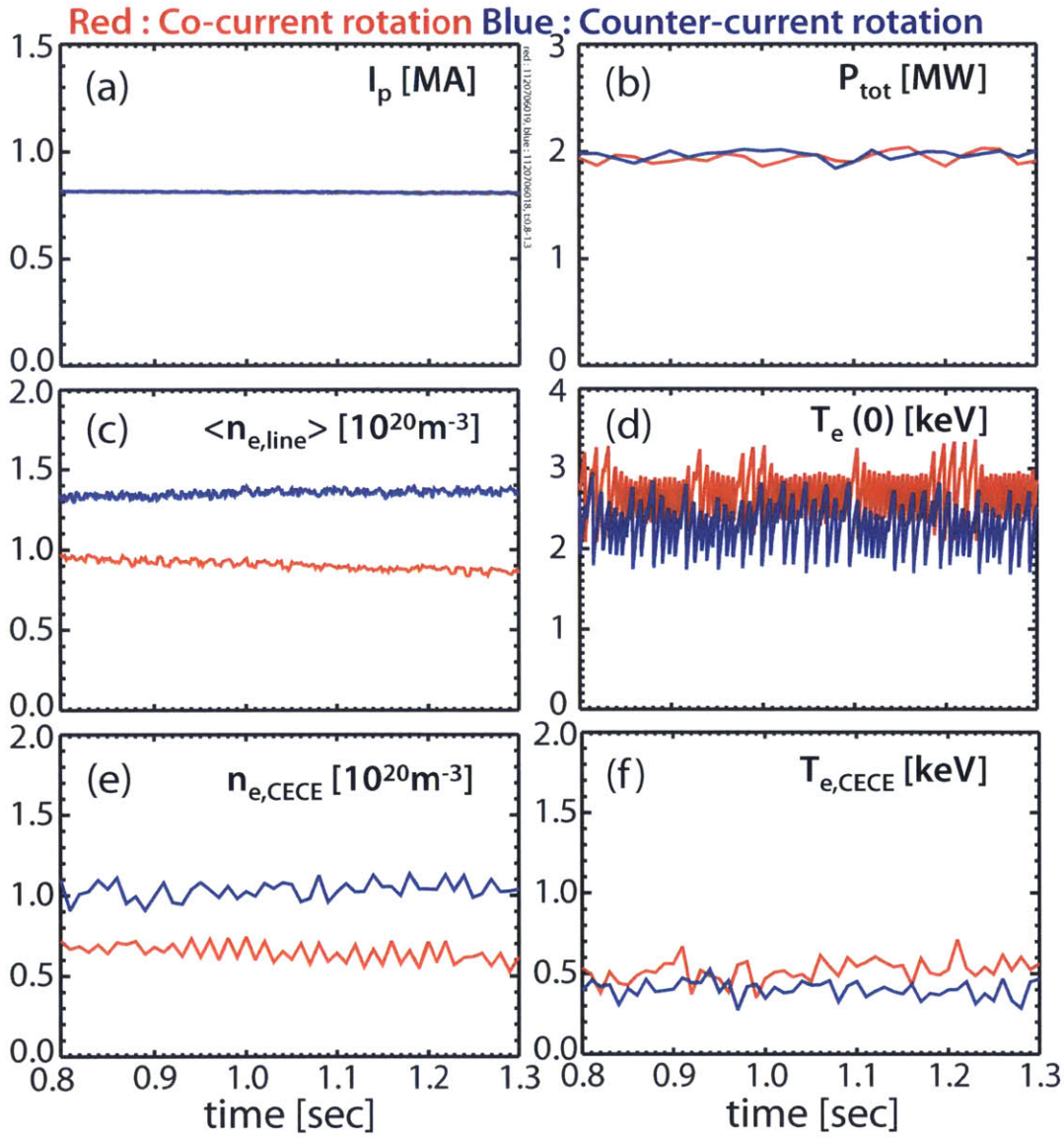

Figure 5-2: Time series data during CECE measurement time for two RF discharges (shot:1120706018 (blue) and shot:1120706019 (red)). (a) Plasma current [MA], (b) central chord line averaged density [$10^{20}m^{-3}$], (c) electron density [$10^{20}m^{-3}$] at CECE measurement position (r/a$\sim$ 0.85), (d) electron temperature [keV] at CECE measurement position (r/a$\sim$0.85), (e) electron temperature [keV] at plasma center, (f) central toroidal velocity [km/s].

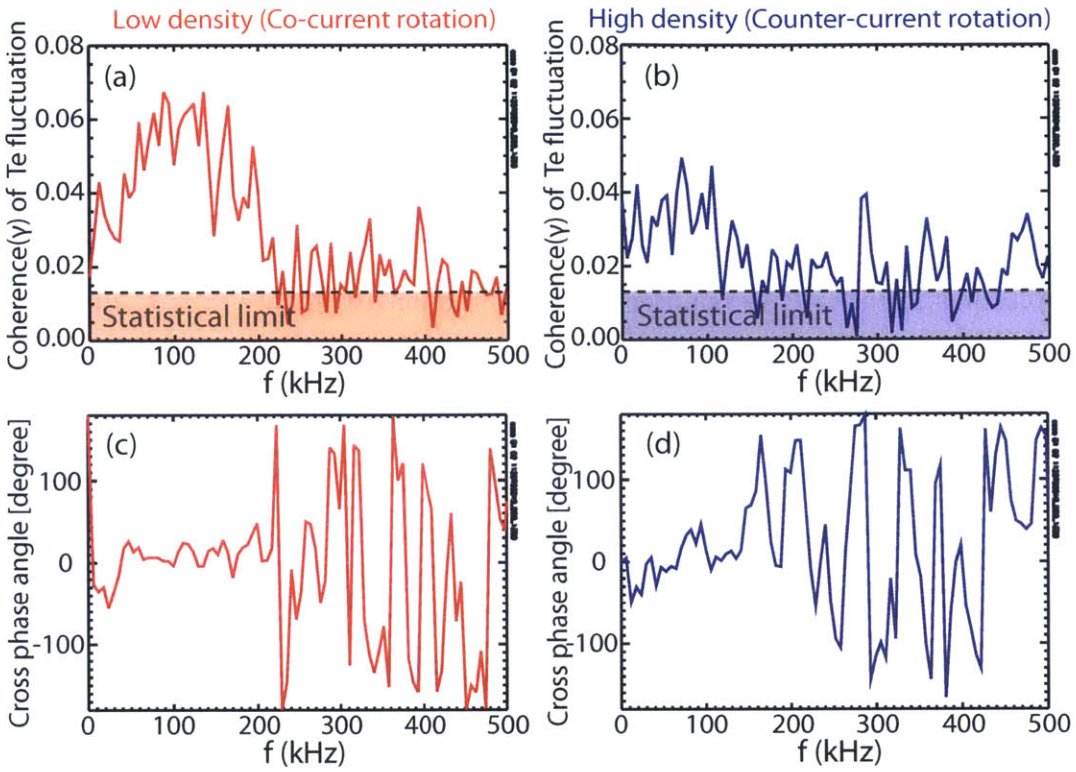

Figure 5-3: (a) Coherence (γ) of two CECE signals in a RF discharge (shot:1120706019) which rotates in the co-current direction, horizontal dotted line indicates the statistical limit of coherence (b) Coherence (γ) of two CECE signals in another RF heated discharge (shot:1120706018) which rotates in the counter-current direction (c) the cross phase spectrum of two CECE signals in the discharge rotating in the co-current direction (d) the cross phase spectrum of two CECE signals in the discharge rotating in the counter-current direction.

slightly decrease in the lower density discharge, it varied less than the uncertainty of the measurements. Both discharges have sawtooth activity, but it will not affect the CECE measurements, which are near the edge. The electron density and electron temperature at the CECE measurement position varied only within the uncertainty of each measurement.

Figure 5-3 shows the reduction of T_e fluctuations across the core rotation reversal from the co-current to the counter-current direction. In this analysis, the low frequency signals ($f < 10$kHz) were filtered out to avoid the parasitic noise issues described in Appendix B. In the discharge that has lower density and rotates in the co-current direction in the core region, the relative T_e fluctuation level is 1.0%

(10-210kHz), while the fluctuation level is 0.6% (10-110kHz) in the discharge which has the higher density and counter-current rotation. It is noteworthy that the same conditions exist in LOC/SOC data sets. In the LOC/SOC case, we observed the reduction of T_e fluctuations across the LOC/SOC transition and that LOC plasmas rotate in the co-current direction, while SOC plasmas, which have higher density than LOC plasmas, rotate in the counter-current direction. It follows that T_e fluctuations are reduced across the rotation reversal from the co- to the counter-current direction in both Ohmic and RF heated discharges. This may indicate that the physics related to the reduction of T_e fluctuations across the Ohmic confinement transition is similar to the reduction observed in the RF heated plasmas.

5.1.2 T_e fluctuation changes with different rotation phases in the rotation reversal discharge

The observation of changes in T_e fluctuations across rotation reversals in section 5.1.1 suggests that the change in T_e fluctuations are related to changes in the momentum transport corresponding to rotation reversal. However, it is noteworthy that the average density value varies by about 50% between the two RF discharges used in section 5.1.1, and that rotation reversal can occur with smaller changes in the average density near the critical value for the reversal as shown in [129] and Fig. 4-32. It will then be of interest to see whether or not T_e fluctuations are reduced with the different rotation directions in the core region even with small changes in the average density.

We observed the changes in T_e fluctuations near the edge (r/a$\sim$0.85) in the rotation reversal discharge used in section 4.5. As shown in Fig. 4-32, core toroidal rotation was reversed from the co- to the counter-current direction after t=1.0s with the slight increase in average density in this discharge. Figure 5-4(a) shows the changes in core rotation profiles before and after rotation reversal occurs (t:0.75-1.0s (before rotation reversal occurs), t:1.15-1.4s (after rotation reversal occurs)). Although the direction of core rotation and the shape of the profile change abruptly, there are no changes in the density and temperature at the CECE measurement position across

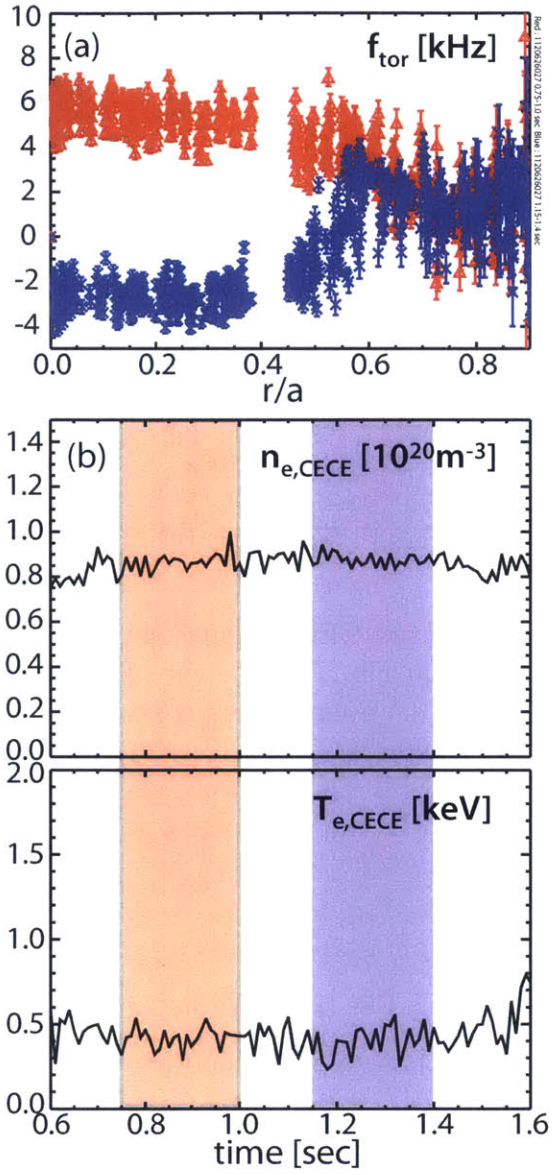

Figure 5-4: (a) Toroidal rotation frequency profile in two different time ranges (red : t:0.75-1.0s, blue : t:1.15-1.4s) in a rotation reversal discharge (shot:1120626027) (b) electron density [$10^{20}m^{-3}$] at CECE measurement position (r/a$\sim$0.85), (c) electron temperature [keV] at CECE measurement position (r/a$\sim$0.85). The shaded area indicates the time range used for (a) and CECE signal analysis.

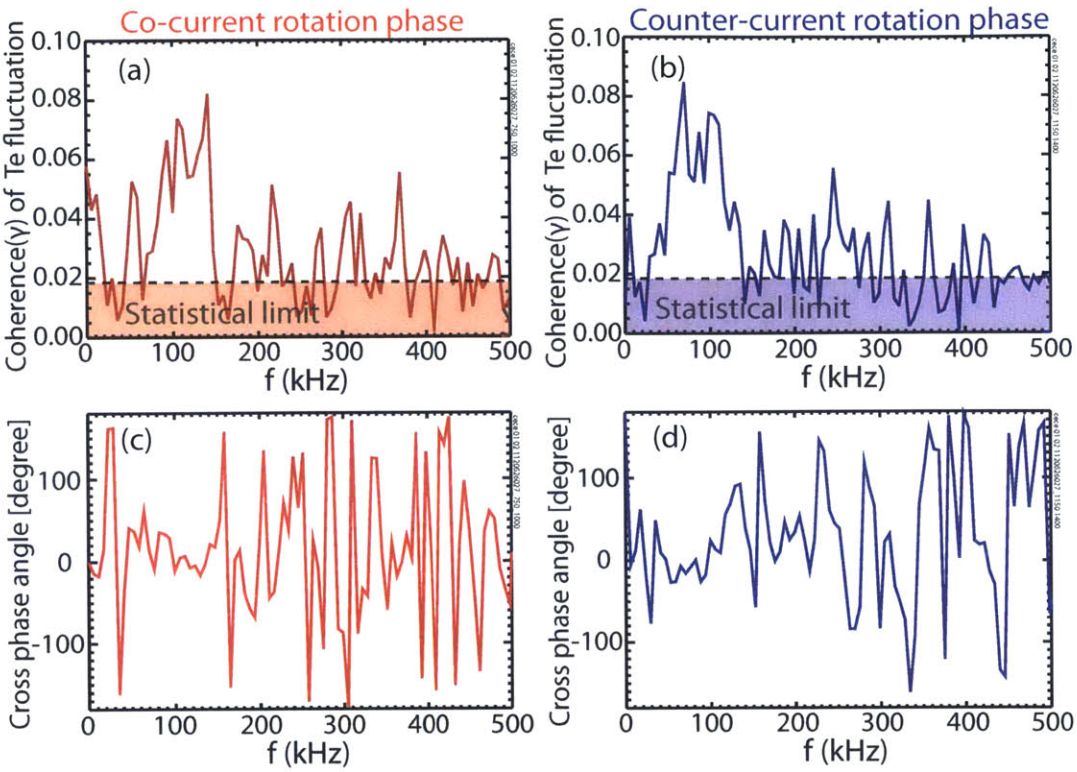

Figure 5-5: (a) Coherence (γ) of two CECE signals in the co-current rotation phase in one C-Mod discharge (shot:1120626027, t:0.75-1.0s). Horizontal dotted line indicates the statistical limit of coherence (b) Coherence (γ) of two CECE signals in the counter-current rotation phase (shot:1120626027, t:1.15-1.4s) in the same discharge (c) the cross phase spectrum of two CECE signals in the co-current rotation phase (d) the cross phase spectrum of two CECE signals in the counter-current rotation phase.

the rotation reversal, as shown in Fig. 5-4(b) and (c). The T_e fluctuations in opposite rotation phases are compared in Fig. 5-5. We notice no significant changes in the two coherence spectra in spite of the evident changes in toroidal rotation in the core region. The relative T_e fluctuation levels are 0.8% in both co- and counter-current rotation phases (40-150kHz (co-current rotation phase), 30-140kHz (counter-current rotation phase)).

This result indicates that T_e fluctuations near the edge are not directly correlated with the direction of core toroidal rotation. Instead of direct causality, it is possible that the changes in the average density affect both the core toroidal rotation and T_e fluctuations near the edge. In the following sections, we will investigate the possible causal relations among fluctuation levels, rotation reversal, and average density using

the approach explained in section 3.2-3.4.

5.2 Observations of changes in profiles and experimental transport across rotation reversal

In this section, we investigate the changes in the profiles and experimental heat transport across rotation reversal in both Ohmic and RF heated discharges.

5.2.1 Changes in sawtooth activity across rotation reversal

It was found that sawtooth activity is related to rotation reversal [49] and also to the Ohmic confinement transition in [142] in TCV. Thus, it is of interest to observe the sawtooth activity changes across the rotation reversal, including the Ohmic confinement transition, in C-Mod. Figure 5-6 shows the comparison of sawtooth activity measured by the ECE diagnostic near the magnetic axis. The changes in sawtooth activity in the two sets of Ohmic discharges analyzed in section 4.5 are shown in Fig. 5-6(a) and (b). It is shown that the sawtooth period tends to be longer and irregular in the SOC discharge as the toroidal rotation reverses from the co- to the counter-current direction with the increase in density in both sets of Ohmic discharges. A similar trend is observed in the pair of RF heated discharges studied in section 5.1.1. The higher density discharge rotating in the counter-current direction has wider and more irregular sawtooth periods than the lower density discharge rotating in the co-current direction. This observation is similar to the findings in TCV. In order to see whether or not the sawtooth activity changes rapidly with the rotation reversal, we observed the changes in sawtooth activity with different rotation phases (co-current/reversal/counter-current) in the rotation reversal discharge analyzed in section 5.1.2. As shown in Fig. 5-6(d)-(f), sawtooth activity barely changes with the different rotation phases. This may indicate that sawtooth activity does not change abruptly as the core rotation direction changes in the reversal discharge. This result is also consistent with the study in TCV as shown in Fig. 10 in [49]. We must note

that changes in T_e fluctuations were observed in the discharges used in Fig. 5-6(b) and (c), while no significant changes were found in the rotation reversal discharge used in Fig. 5-6(d)-(f).

5.2.2 Profile analysis & power balance analysis for the RF heated discharges rotating in opposite directions due to different density values

We investigated the changes in the the experimental heat transport and the profiles of n_e, T_e, and T_i, and their gradient scale lengths across RF rotation reversals in this section. Instead of the two RF heated discharges analyzed in section 5.1.1, another pair of RF heated discharges (shot 1120221011, 1120221012, t:0.9-1.2s) were anlayzed in this section, and used in power balance analysis and gyrokinetic analysis. These two discharges have similar discharge conditions to the discharges studied in section 5.1.1 except for the average density; $\bar{n}_e = 1.2 \times 10^{20} m^{-3}$ (shot 1120221011) and $1.0 \times 10^{20} m^{-3}$ (shot 1120221012).

The different average density values result in opposite toroidal rotations between these two discharges as shown in Fig. 5-7. The profiles of n_e, T_e, and T_i and their gradient scale lengths are shown in Fig. 5-8. We found that the changes in the profiles between these two RF heated discharges are similar to the changes observed between the LOC and SOC discharges in section 4.2. The discharge that rotates in the co-current direction has lower n_e and higher T_e than the discharge rotating in the counter-current direction. Thus, the discharge rotating in the co-current direction (or lower density discharge) is less collisional than the discharge rotating in the counter-current direction (or higher density discharge). However, the gradient scale lengths, which are important in driving turbulence, are almost identical between the two discharges within the uncertainty. The LOC discharge rotating in the co-current direction is less collisional than the SOC discharge rotating in the counter-current direction, but their gradient lengths are not different, within the uncertainty.

Using the profiles in Fig. 5-8, the experimental heat fluxes were obtained for these

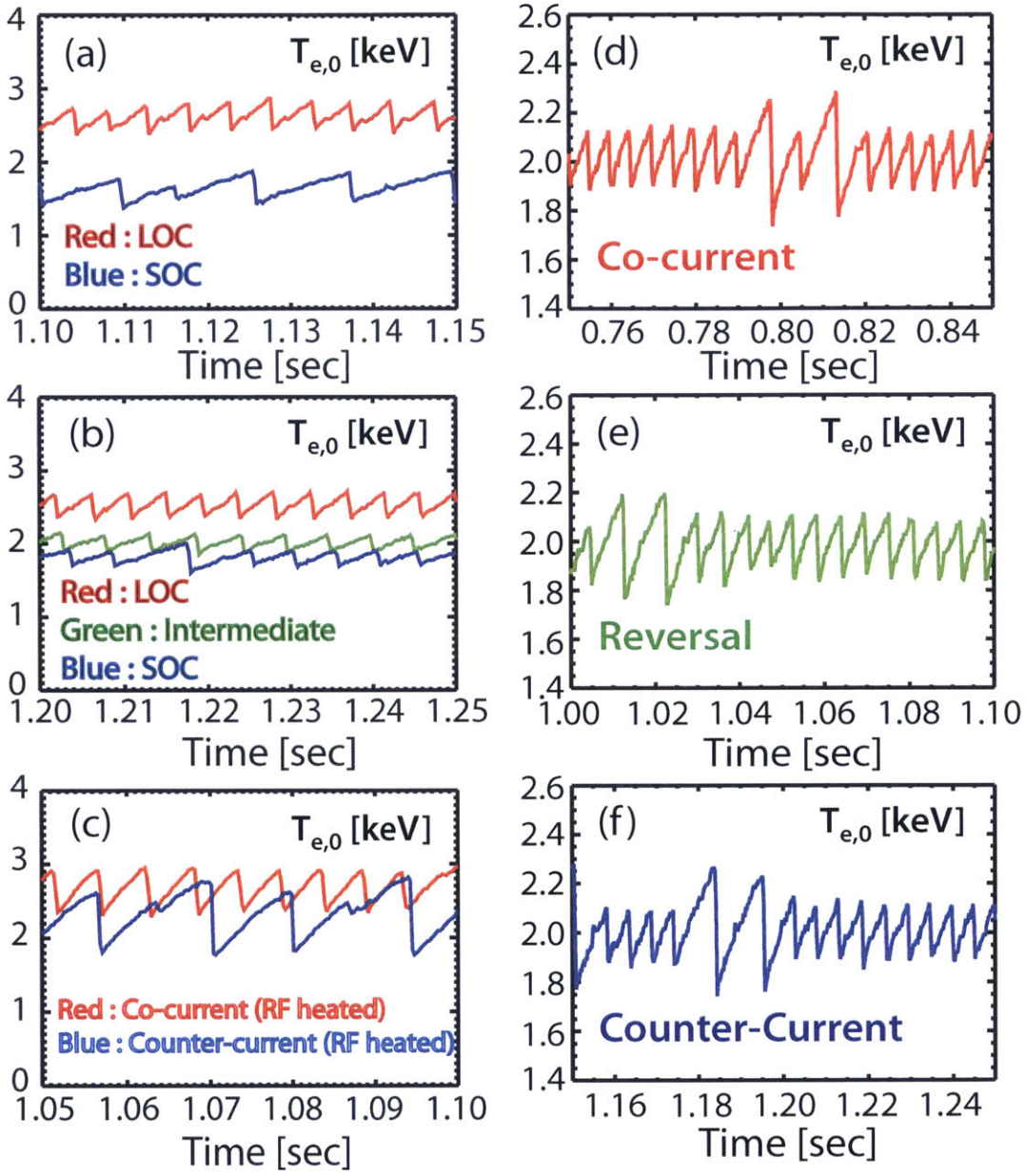

Figure 5-6: T_e near the magnetic axis measured by the ECE diagnostic for (a) two Ohmic discharges analyzed in section 4.5 (first set of Ohmic discharges in section 4.5) (b) the second set of Ohmic discharges in section 4.5 (c) A pair of RF heated discharges which rotate in opposite directions due to different density levels, analyzed in section 5.1.1. (d) Co-current phase (before rotation reversal) in the rotation reversal discharge analyzed in section 5.1.2. (e) Reversal phase (during rotation reversal) and (f) Counter-current phase (after rotation reversal) in the same discharge.

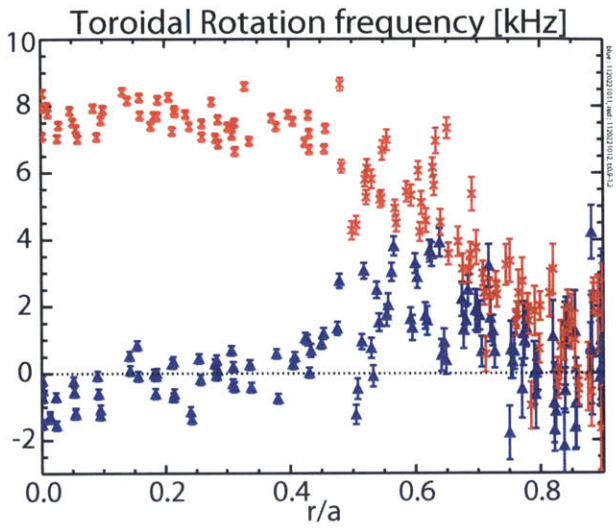

Figure 5-7: Toroidal rotation frequency profile of a pair of discharges with different average densities (red : lower density discharge (shot 1120221011, t:0.9-1.2s), blue : higher density discharge (shot 1120221011, t:0.9-1.2s)). Adapted from A. E. White et al, 2013, *Physics of Plasmas*, *20*, 056106, copyright 2014 American Institute of Physics.

discharges via power balance analysis (TRANSP), as explained in section 3.3. As shown in Fig. 5-9 (a), there is little to no change in electron heat flux (Q_e) between the two discharges. Ion heat flux (Q_i), which is shown in Fig. 5-9 (b), increases in the higher density discharge rotating in the counter-current direction compared to the lower density discharge rotating in the co-current direction. However, considering the estimated uncertainty of the heat fluxes ($\sim 30\%$), the changes in Q_i are within the uncertainty. Therefore, no significant changes in Q_i and Q_e were observed between the two discharges that have opposite toroidal rotation. This result is expected based on the small changes in the gradient scale lengths shown in Fig. 5-8.

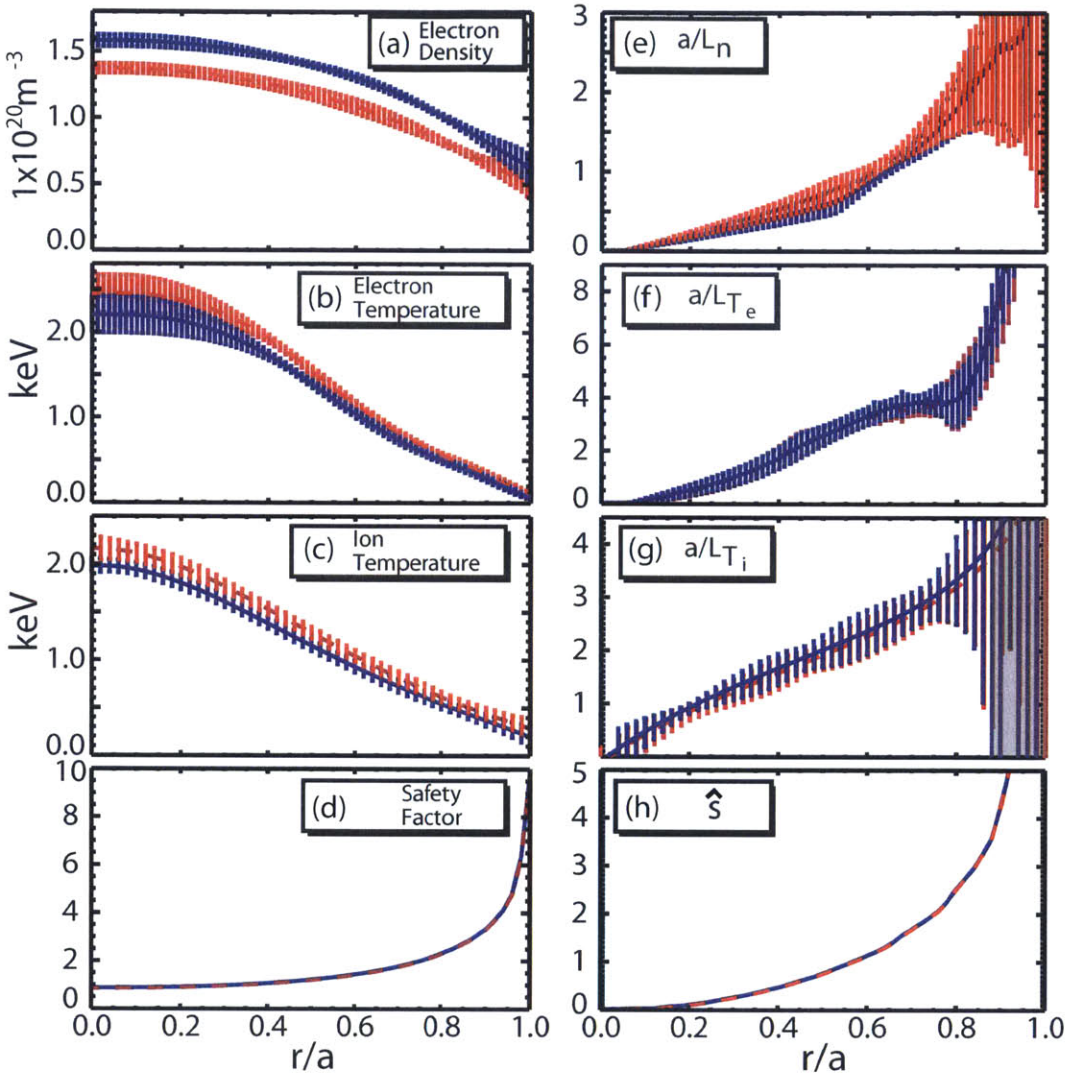

Figure 5-8: Profiles and their gradient scale lengths in the two RF heated discharges rotating in opposite directions due to different levels of average density (red dotted line : the lower density discharge rotating in the co-current direction (shot 1120221012, t:0.9-1.2s), blue : the higher density discharge rotating in the counter-current direction (shot 1120221011, t:0.9-1.2s)). Adapted from A. E. White et al, 2013, *Physics of Plasmas*, *20*, 056106, copyright 2014 American Institute of Physics.

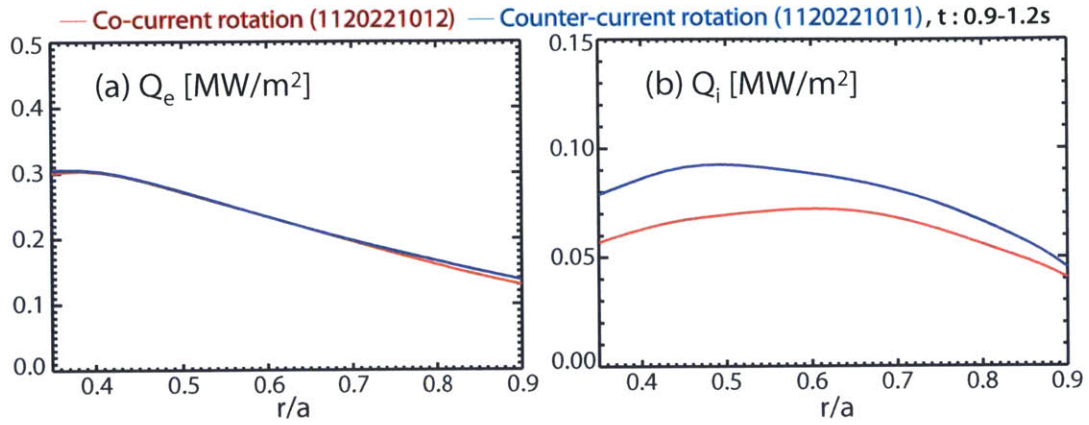

Figure 5-9: Experimental heat flux estimated from power balance analysis for the RF heated discharges rotating in opposite directions. (red : lower density discharge rotating in the co-current direction (shot 1120221012), blue : higher density discharge rotating in the counter-current direction (shot 1120221011)) (a) Electron heat flux (Q_e $[MW/m^2]$), (b) Ion heat flux (Q_i $[MW/m^2]$).

5.3 Gyrokinetic analysis for the RF heated discharges rotating in opposite directions with different densities

In this section, the changes in turbulence between the two RF discharges analyzed in section 5.2.2 are studied using gyrokinetic simulation, GYRO. We will first perform linear stability analysis using the experimental values for the two discharges. A more realistic picture will be studied with non-linear simulations.

5.3.1 Linear stability analysis

Linear stability analysis was performed for the two discharges analyzed in section 5.2.2 using the profiles in Fig. 5-8 without modification to investigate the changes in dominant turbulence mode across RF rotation reversals. An initial value solver in the GYRO code was used in this analysis to find the dominant turbulence mode, which has the highest growth rate, in each discharge. Only ion scale turbulence ($k_y\rho_S \leq 1.0$) was included in these simulations. Figure 5-10 shows the real frequency and the growth rate of the dominant mode in the two discharges at r/a=0.45, 0.60, 0.75 and

0.80. As explained in section 3.4, we can identify whether the dominant mode propagates in the electron diamagnetic direction (electron mode) or in the ion diamagnetic direction (ion mode) from Fig. 5-10 using the sign of the real frequency (positive - ion mode, negative - electron mode). We notice that the ion mode is dominant in both discharges for r/a $\leq$ 0.75, and that the dominant modes from the two different discharges are almost identical in this region. This result is consistent with the profile analysis results, which show little to no change in the gradient scale length. We also note that similar results were obtained from the linear simulations for the LOC and SOC discharges in the core region: no change in dominant mode between the LOC and SOC discharges at r/a=0.6. Fig. 5-10(d) shows that the electron mode is dominant for $k_y\rho_s < 0.5$ in the lower density discharge which rotates in the co-current direction, while the ion mode is still dominant in the higher density discharge rotating in the counter-current direction. However, the dominant mode changes to the ion mode at $k_y\rho_s = 0.5 - 0.6$ in the lower density discharge, implying that the electron mode is not robustly dominant. It is worth noting that similar features are observed in the linear runs for the LOC and SOC discharges at r/a$\sim$0.85 in section 4.4.1. In Ohmic discharges, the electron mode is dominant at r/a$\sim$0.85 in the LOC discharge (lower density), while ion mode is dominant in the SOC discharge (higher density). However, both electron and ion modes are comparable in both LOC and SOC discharges.

We investigated the characteristics of the dominant turbulence mode at r/a=0.6 and 0.8 in the RF heated discharges by observing the changes in the growth rate of the dominant mode with scan of a/L_{T_e} and a/L_{T_i}. Figure 5-11 shows the changes in the growth rate of the dominant mode with changes in a/L_{T_e} and a/L_{T_i} at r/a=0.6 and 0.8. A + sign in each contour in Fig. 5-11 indicates the experimental values of a/L_{T_e} and a/L_{T_i}. In this contour, the region where the growth rate of the dominant mode is sensitive to a/L_{T_e} is the TEM dominant region, and the region sensitive to a/L_{T_i} is the ITG dominant region. At r/a=0.6, experimental values in both plasmas are in the ITG dominant region as shown in Fig. 5-11(a) and (b). These two contours indicate that the ion modes observed in Fig. 5-10(a)-(c) are ITG-like turbulence. In the lower

density discharge (co-current rotation), we notice that the experimental values at r/a=0.8 are in the TEM dominant region, while the ITG mode is still dominant in the higher density discharge (counter-current rotation). However, it is inconclusive whether this result indicates a correlation between the rotation reversal and the linear mode transition from ITG to TEM at r/a=0.8. This is because experimental values in the lower density discharge at r/a=0.8 can be moved to the ITG dominant region within the uncertainties of the gradient scale lengths ($\sim$ 20%) (or the experimental values in the higher density discharge at r/a=0.8 can move to the TEM dominant region). Considering the error bars of a/L_{T_e} and a/L_{T_i}, identifying the dominant mode at r/a=0.6 is also inconclusive in both discharges. Thus, any transition in the linear mode is not clear, even when there are clear changes in the rotation profiles between the two discharges. These results are also consistent with the linear simulation results in the LOC and SOC discharges in Chapter 4, which show that it is hard to resolve the changes in the dominant turbulence mode within the uncertainty between the LOC and SOC discharges.

5.3.2 Non-linear simulations

In order to see a more realistic picture through gyrokinetic simulations, non-linear simulations were performed. We first looked at the heat transport at r/a=0.7 and 0.8 in the two discharges using local simulations. Although the basic setup in these simulations is explained in section 3.4, it is noteworthy that these simulations include all rotation relevant effects and exclude the electromagnetic turbulence because of low beta values of the discharges used in this study. Domain sizes of these simulations are $L_x \sim 100\rho_s$ and $L_y \sim 80\rho_s$, and 16 toroidal modes are used to include the ion scale turbulence, $k_y\rho_s < 1.3$.

We first should have heat the flux matched simulations for the "physical" base case, as explained in section 3.4. By adjusting input parameters within their uncertainties, similar to the process in section 4.4.3, we obtained ion heat flux (Q_i) matched simulations for both discharges in both locations (r/a=0.7 and 0.8), as shown in Fig. 5-12. However, electron heat flux (Q_e) was under-predicted in both discharges. Like in

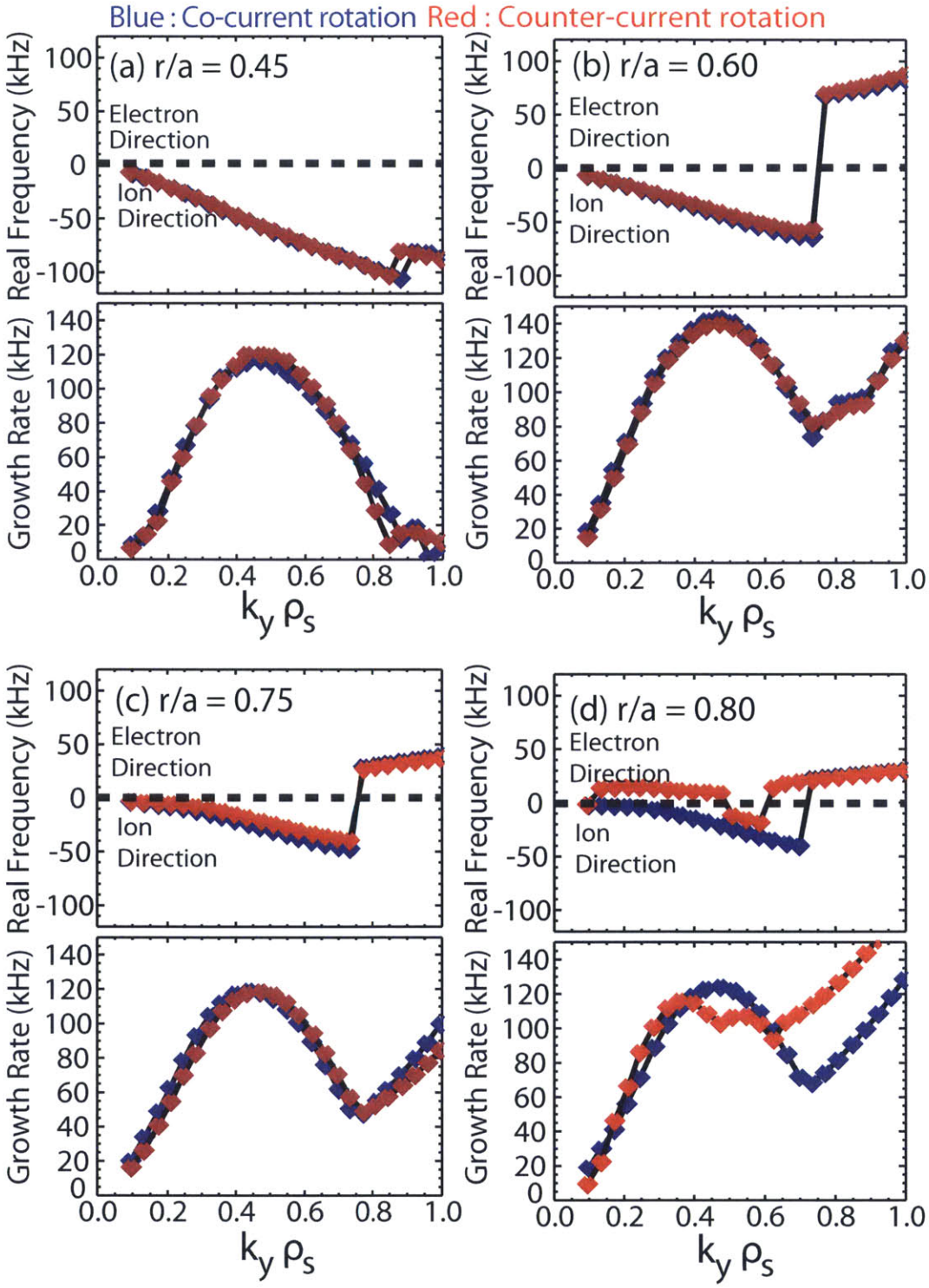

Figure 5-10: Linear stability analysis results of the two RF heated discharge rotating in opposite directions (red : lower density discharge rotating in the co-current direction (shot 1120221012), blue : higher density discharge rotating in the counter-current direction (shot 1120221011)) at (a) r/a=0.45, (b) r/a=0.60, (c) r/a=0.75 (d) r/a=0.8. A positive real frequency indicates a mode propagating in the electron diamagnetic direction, and a negative real frequency indicates the opposite case. Adapted from A. E. White et al, 2013, *Physics of Plasmas*, *20*, 056106, copyright 2014 American Institute of Physics.

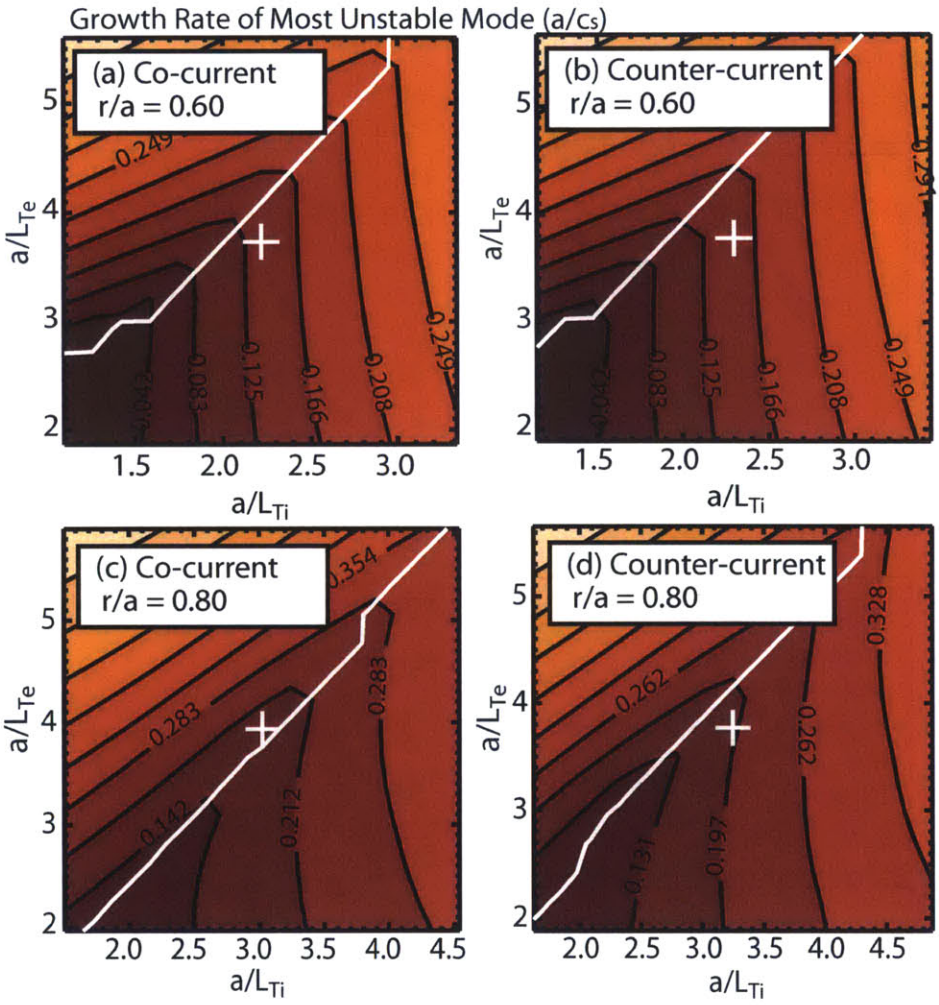

Figure 5-11: Contours of the growth rate of the most unstable mode with changes in a/L_{T_e} and a/L_{T_i} at r/a=0.6 in (a) the discharge rotating in the co-current direction and (b) the discharge rotating in the counter-current direction. At r/a=0.8 (c) the discharge rotating in the co-current direction and (d) the discharge rotating in the counter-current direction. The + mark indicates the experimental values. Adapted from A. E. White et al, 2013, *Physics of Plasmas*, *20*, 056106, copyright 2014 American Institute of Physics.

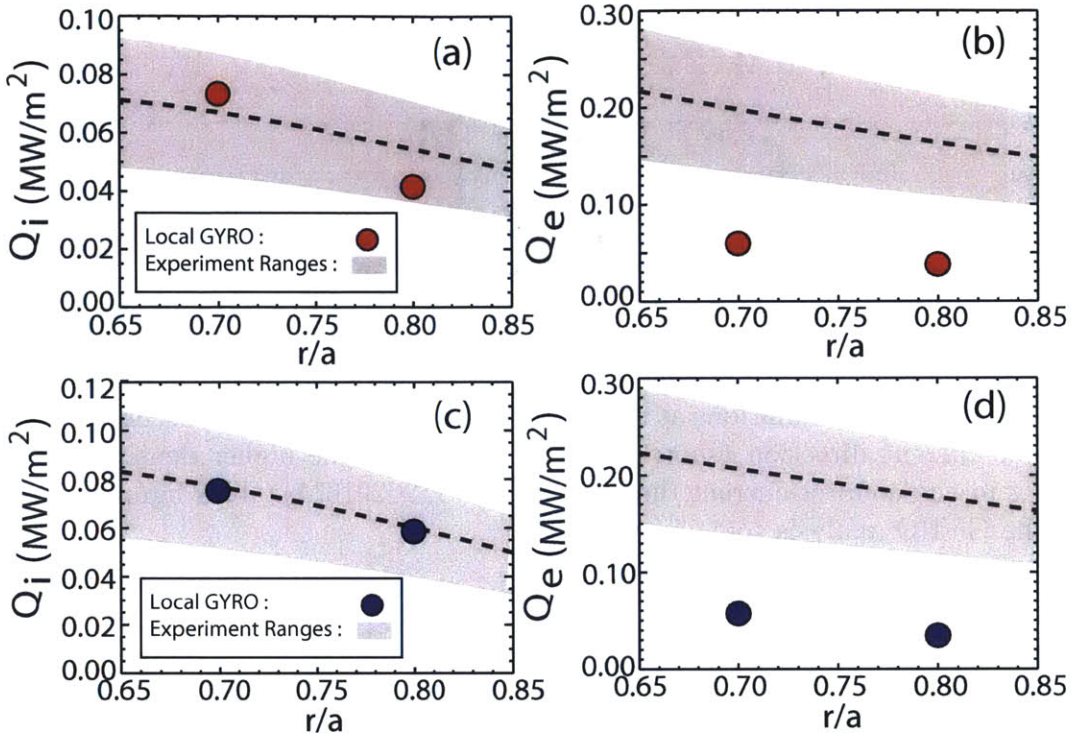

Figure 5-12: Comparison of the simulated heat fluxes from local nonlinaer runs at r/a=0.7 and 0.8 with the experimental heat fluxes of two RF heated discharge rotating in opposite directions. (a) Ion heat flux (Q_i) [MW/m^2] (b) electron heat flux (Q_e) [MW/m^2] for the lower density discharge rotating in the co-current direction, and (c) ion heat flux (Q_i) [MW/m^2] (d) electron heat flux (Q_e) [MW/m^2] for the higher density discharge rotating in the counter-current direction. The circles in the figure indicate the simulated heat flux values, and experimental heat flux with its uncertainty is shown as the black dashed line with the shaded area. Adapted from A. E. White et al, 2013, *Physics of Plasmas*, *20*, 056106, copyright 2014 American Institute of Physics.

Ohmic discharges, high k turbulence could be a reason for this under-prediction of electron heat flux. It is noteworthy that the simulated ion and electron heat flux levels are similar between the two discharges in both radial locations, which is consistent with the power balance analysis results in section 5.2.2.

The changes in the dominant mode in the nonlinear runs are first investigated. From the linear simulations, we did not observe clear changes in the dominant mode in $r/a \leq 0.8$ within the uncertainty of input parameters across the rotation reversal. Changes in the dominant mode in nonlinear runs are found from the power spectrum of fluctuating quantities per toroidal mode number, n, as shown Fig. 5-13. As men-

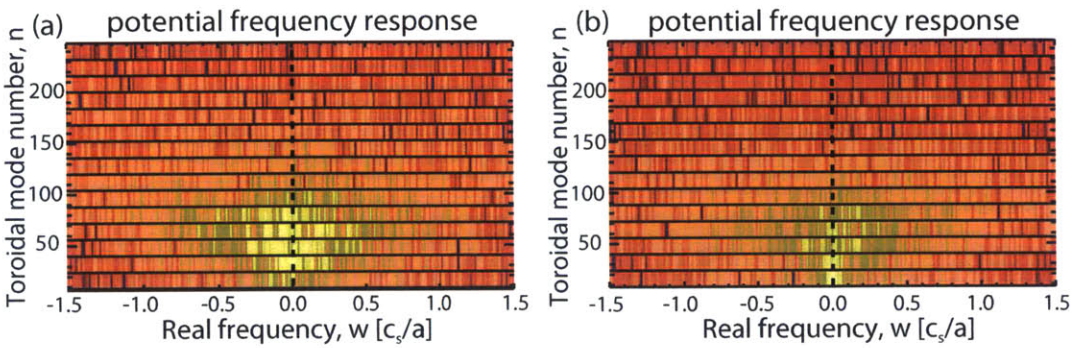

Figure 5-13: Power spectra of simulated potential fluctuations on the midplane from the local non linear simulations at r/a=0.8 for (a) the lower density discharge rotating in the co-current direction (shot:1120221012) and (b) the higher density discharge rotating in the counter-current direction (shot: 1120221011). This figure was made from the GYRO analysis tool, "vugyro".

tioned earlier, the electron and ion modes are determined from the sign of the real frequency (positive - ion, negative - electron). If one specific mode (either electron or ion) is dominant in the simulation, we will see the mode propagating more strongly on one side (either negative or positive) than the other side (either positive or negative) in real frequency space. Figure 5-13 shows the power spectrum of potential fluctuations on the midplane from the nonlinear runs at r/a=0.8 for the RF heated discharges. In both discharges, it is hard to identify the propagation direction of the dominant mode, indicating that electron and ion modes are comparable in both discharges. These results are consistent with the linear simulation results in Fig. 5-11, which show that the dominant mode is near the ITG/TEM boundary. Similarly, no dominant mode changes were observed at r/a=0.7. It is noteworthy that we found that a/L_{T_i} is the most sensitive input parameter in the nonlinear runs for both discharges, implying that the ITG mode is stronger than the TEM in these simulations, although TEM turbulence is not ignorable.

Global nonlinear simulations were performed deeper in the core region ($0.4 < r/a < 0.6$), where rotation reversal occurs between the two discharges. A simulation setup almost identical to that for the local runs is used for these global simulations. That is, ion scale turbulence ($k_y\rho_s < 1.3$) is modeled in these simulations with 16 toroidal modes with box size, $L_x \sim 100\rho_s$ and $L_y \sim 80\rho_s$. Within the uncertainties

of input parameters, it was found that GYRO can reproduce the experimental Q_i in both discharges, while Q_e was under-predicted in both discharges as shown in Fig. 5-14. It is noticeable that the simulated electron and ion heat flux levels are similar between the two discharges, consistent with the trend in experimental heat flux changes between two discharges as shown in section 5.2.2. As observed in the local simulations at r/a=0.7 and 0.8, we do not see changes in the dominant mode in the simulated turbulence in these simulations either. The under-prediction of Q_e in these runs may also indicate the importance of high k turbulence, which is not included in these simulations.

It is also of interest that GYRO does not over-estimate the ion heat flux in the core region for these RF heated discharges, while the simulated ion heat flux values in Ohmic plasmas are much higher than the experimental levels in the core region, as shown in section 4.3.2. It is worth noting that the linear simulations in Fig. 5-11 show that experimental values of the RF heated discharges are not far from the ITG/TEM boundary in both the core and near the edge region. In contrast, the experimental values of the Ohmic discharges at r/a=0.6 are in the ITG dominant region, far from the boundary. This may suggest that GYRO over-estimates the ion heat transport when the ITG mode is much stronger than the TEM. If this is true, the over-estimation of ion heat flux could be due to an incorrect estimation of other input parameters which modify the ITG drive strength, such as the main ion fraction or the ion temperature gradient. The main ion fraction, which is not well constrained in the experiment, may be a strong candidate, as suggested in [120]. It is also possible that GYRO misses some unknown physics related to ITG turbulence. Further study is required to resolve this discrepancy in the future.

The gyrokinetic model used in this study, which includes only electrostatic ion scale turbulence, do not show significant changes in simulated turbulence and heat transport between the two RF discharges which rotate in opposite directions at two different average density values. It is noteworthy that these simulation results are consistent with the gyrokinetic simulation results obtained from the LOC and SOC discharges rotating in opposite directions in Chapter 4. In other words, GYRO sug-

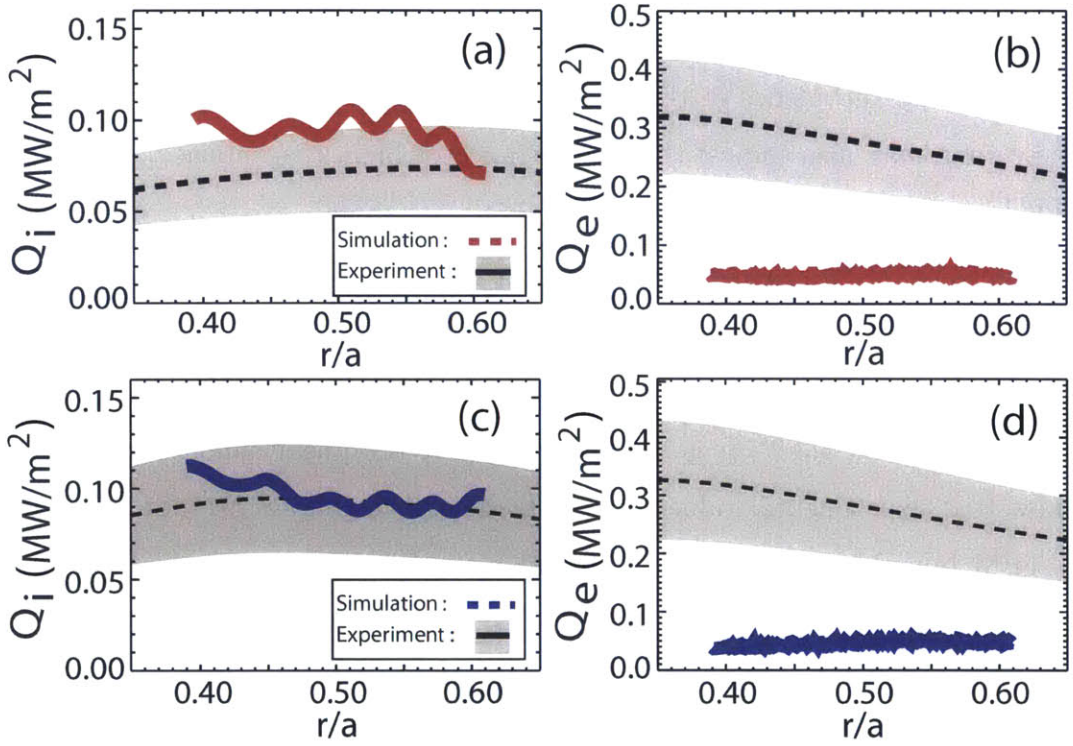

Figure 5-14: Comparison of the simulated heat fluxes from global nonlinear runs in $0.4 < r/a < 0.6$ with the experimental heat fluxes of two RF heated discharges rotating in opposite directions. (a) Ion heat flux (Q_i) [MW/m^2] (b) electron heat flux (Q_e) [MW/m^2] for the lower density discharge rotating in the co-current direction, and (c) ion heat flux (Q_i) [MW/m^2] (d) electron heat flux (Q_e) [MW/m^2] for the higher density discharge rotating in the counter-current direction. The thick solid lines in the figure indicate the simulated heat flux values, and experimental heat flux with its uncertainty is shown as the black dashed line with the shaded area. Adapted from A. E. White et al, 2013, *Physics of Plasmas*, *20*, 056106, copyright 2014 American Institute of Physics.

gests no changes in the dominant turbulence mode across the rotation reversal in either Ohmic or RF heated discharges.

5.4 Observation of profile self-similarity across rotation reversals

In Ohmic discharges, we observed a correlation between changes in edge n_e and T_e profiles and global confinement changes (or Ohmic confinement regimes) through self-similarity analysis, introduced in section 3.2.2. Since the change of the direction of core toroidal rotation was used as an indicator of Ohmic confinement regime in this study, it is of interest to investigate the self-similarity property in T_e and n_e profiles with different rotation phases.

We first studied the pair of RF discharges analyzed in section 5.3. As shown in Fig. 5-7, these two discharges rotate in opposite directions due to different average density values. Figure 5-15(a) and (b) show that the core T_e and n_e profiles are well fit by the exponential function in Eq. 3.14, and the edge data are below the exponential fitting lines, consistent with the results in section 4.5. It is shown in Fig. 5-15 (c) and (d) that the fit with a single exponential fitting parameter (λ_{T_e} and λ_{n_e}) works well in the core T_e and n_e profiles in both discharges. This indicates that the shape of the core n_e and T_e profiles changes little across the rotation reversal. The "1^{st} set" column of Table 5.1 also shows that λ_{T_e} varies little and λ_{n_e} varies within 15%. The changes in the edge profiles can be found in Fig. 5-15(e) and (f) and the "1^{st} set" column of Table 5.1. In T_e profiles, the T_e value at ρ=1.0, $T_{e,edge}$, decreases by about 25%, and the slope of the linear fit for the edge T_e profiles, μ_{T_e}, also decreases by around 10% in the discharge which has the higher density and rotates in the counter-current direction compared to the discharge which has the lower density and rotates in the co-current direction. These decreases will be linked to the 10% decrease in T_e (0.8), the T_e value from exponential fitting line at ρ=0.8. In n_e profiles, $n_{e,edge}$ and μ_{n_e} increase by about 25% and 35%, respectively, in the higher density discharge. These

		1^{st} set		2^{nd} set	
	Parameters	co-current	counter-current	co-current	counter-current
core T_e	λ_{T_e}	3.37	3.35	3.33	3.44
($\rho \leq \rho_{ped,T_e}$)	$T_e(0.8)$ [keV]	0.47	0.42	0.52	0.41
edge T_e	μ_{T_e} [keV]	2.08	1.82	2.24	1.70
($\rho \geq \rho_{ped,T_e}$)	$T_{e,edge}$ [keV]	0.08	0.06	0.06	0.05
	ρ_{ped,T_e}	0.85	0.80	0.77	0.75
core n_e	λ_{n_e}	1.06	0.94	1.05	0.75
($\rho \leq \rho_{ped,n_e}$)	$n_e(0.8)$ [$10^{20}m^{-3}$]	0.79	0.98	0.69	1.12
edge n_e	μ_{n_e} [$10^{20}m^{-3}$]	1.34	1.84	1.81	2.74
($\rho \geq \rho_{ped,n_e}$)	$n_{e,edge}$ [$10^{20}m^{-3}$]	0.48	0.60	0.27	0.49
	ρ_{ped,n_e}	0.70	0.78	0.75	0.76
	$P_e(0.8)$ [kPa]	5.94	6.59	5.74	7.35
	$\bar{n}_e$ [$10^{20}m^{-3}$]	1.0	1.2	0.9	1.4

Table 5.1: Parameters calculated from fitting and the average electron density ($\bar{n}_e$) in the two sets of RF heated discharges which rotate in opposite directions due to different average density levels (1^{st} set : shot 1120221012,011 t:0.9-1.2s, 2^{nd} set : shot 1120706019,018 t:0.8-1.3s). λ_{T_e} is an exponential fitting parameter for the core T_e profile, and μ_{T_e} is the slope of the linear fitting line applied to the edge T_e profile. $T_{e,edge}$ indicates the T_e value at $\rho = 1.0$ from the linear fitting line applied to the edge T_e profile. $\rho_{ped,Te}$ is the radial location which has the minimum difference between the exponential and linear fitting lines. The same definitions are applied to λ_{n_e}, μ_{n_e}, $n_{e,edge}$ and $\rho_{ped,ne}$ for n_e profiles.

increases will affect the approximately 25% increase in $n_e(0.8)$. A relatively larger increase in $n_e(0.8)$ ($\sim$ 25%) compared to the decrease in $T_e(0.8)$ ($\sim$ 10%) results in the increase of electron pressure at $\rho = 0.8$, $p_e(0.8)$, in the higher density discharge. Since core n_e and T_e profiles have a similar shape between the two discharges, the higher $p_e(0.8)$ value will indicate the higher pressure profile in the core region and better confinement.

The trend in the fitting parameters between these two discharges is consistent with the analysis results in section 4.5. In the LOC and SOC discharges, we observed an increase in μ_{n_e} and $n_{e,edge}$ with a decrease in μ_{T_e} and $T_{e,edge}$ as the average density value increases. A relatively larger increase in edge n_e profiles and $n_e(0.8)$ compared to a decrease in edge T_e profiles and $T_e(0.8)$ results in the increase in $p_e(0.8)$ in the SOC discharge. It is noticeable that the variations between the two discharges in this section are small compared to the Ohmic discharges analyzed in section 4.5, although the rotation reversal occurs clearly in both the Ohmic discharges in section

4.5 and the pair of RF heated discharges in this section. We must note that the variations in the average density between the two RF discharges are smaller than the variations in the Ohmic discharges in section 4.5. While the average density increases by more than 50% in the SOC discharges compared to the LOC discharges in section 4.5, the average density increases only 20% in the RF heated discharge rotating in the counter-current direction compared to the discharge rotating in the co-current direction.

In order to see the trend in the two RF heated discharges with larger variations in average density, self-similarity analysis was performed for discharges where we observed the reduction of T_e fluctuations in section 5.1.1. The average density varies by 50% between these two discharges ($\bar{n}_e = 0.9 \times 10^{20} m^{-3}$ (the discharge rotating in the co-current direction) and $1.4 \times 10^{20} m^{-3}$ (the discharge rotating in the counter-current direction)). Figure 5-16(a) and (c) shows that the shape of core T_e profiles remains similar across the rotation reversal. We also see that λ_{T_e} varies within 5% from the "2^{nd} set" column of Table 5.1. We find a similar shape of core n_e profiles between the two discharges in Fig. 5-16(b) and (d). Although the "2^{nd} set" column of Table 5.1 shows an approximately 30% decrease in λ_{n_e} in the higher density discharge rotating in the counter-current direction, it is hard to resolve whether or not this difference is meaningful due to the large uncertainty in the n_e data. Since a single λ_{n_e} value can be applied to fit the core n_e profiles in both discharges as shown in Fig. 5-16(d), we may be able to say that core n_e profiles retain a similar shape between the two discharges within the uncertainty of the data. It is noticeable from Fig. 5-16(e) and (f) that the variations in the edge n_e profiles between the two discharges are larger than those in the edge T_e profiles. Table 5.1 shows the decrease of μ_{T_e} and $T_{e,edge}$ by about 25% and 10%, respectively, in the discharge rotating in the counter-current direction (the higher density discharge). The $T_e(0.8)$ value also decreases by around 10% in the higher density discharge. In contrast, μ_{n_e} and $n_{e,edge}$ increase in the higher density discharge by about 50% and 80%, and $n_e(0.8)$ increases by around 60%. This relatively larger increase in $n_e(0.8)$ with the increase in density results in the larger $p_e(0.8)$ value ($\sim$ 30%) in the higher density discharge, which is connected

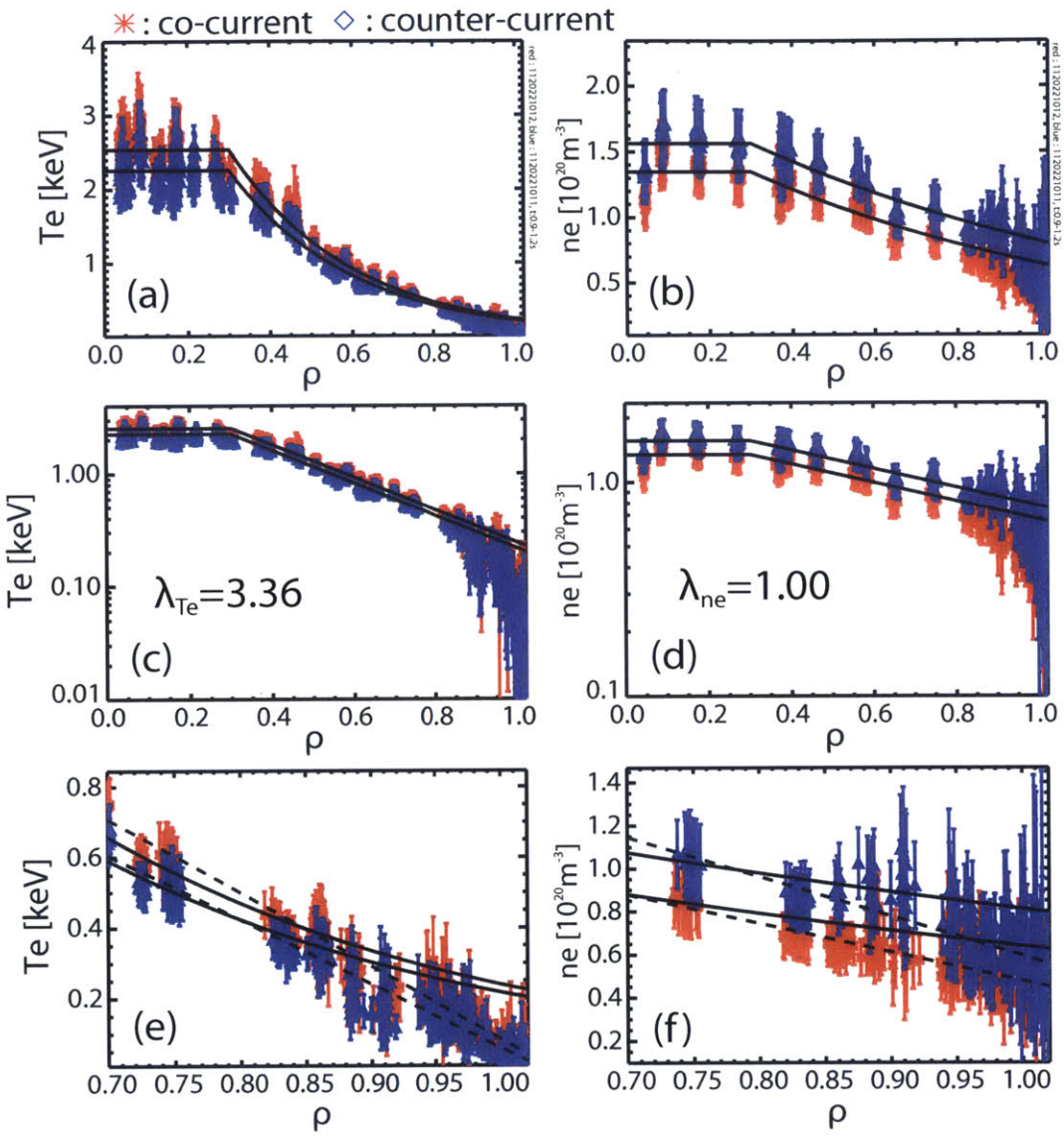

Figure 5-15: Profiles in the two RF heated discharges (red : the lower density discharge rotating in the co-current direction (shot 1120221012), blue : the higher density discharge rotating in the counter-current direction (shot 1120221011)) with the fitting lines (solid line : exponential fitting line for the core profile, dashed line : linear fitting line for the edge profile). (a) T_e profiles with the fitting lines in linear scale (b) n_e profiles with the fitting lines in linear scale (c) T_e profile with the fitting line with fixed λ_{T_e}(=3.36) in log scale (d) n_e profile with the fitting line with fixed λ_{n_e}(=1.00) in log scale (e) Edge T_e profiles with the fitting lines (e) Edge n_e profiles with the fitting lines.

to the better confinement. These analysis results show that larger variations in the average density are correlated with more significant changes in the edge n_e and T_e profiles.

It is also noteworthy that the two sets of RF heated discharges used in this section have similar discharge conditions except for the average density ($\bar{n}_e$). Table 5.1 shows the increase in $p_e(0.8)$ with the increase in $\bar{n}_e$ among these discharges. A similar trend was observed between the LOC and SOC discharges in section 4.5. This consistent trend may suggest that the LOC/SOC transition is not a special issue limited to Ohmic discharges. The physics of the LOC/SOC transition and Ohmic rotation reversals may be related to rotation reversals in RF heated discharges.

So far, we have observed consistent changes in n_e and T_e profiles with an increase in density (or across the rotation reversal due to the increase in the density). As shown in section 5.1.1, T_e fluctuations are also consistently reduced with the increase in density in both RF heated and Ohmic discharges. However, in section 5.1.2, it was shown that T_e fluctuations do not vary significantly with the different rotation phases in the rotation reversal discharge, where $\bar{n}_e$ varied slightly. It is of interest to compare T_e and n_e profiles at the three different phases of toroidal rotation (before/during/after core rotation reversal from co- to counter-current direction) in the same discharge. Figure 5-17(a) and (b) show that n_e and T_e profiles in the core region ($\rho \lesssim 0.8$), where rotation reverses, barely change before, during, and after the rotation reversal, while the core toroidal rotation changes from ~25km/s to ~-10km/s, which is consistent with the profile analysis results in section 5.2.2. Table 5.2 also shows that the λ_{T_e} and λ_{n_e} values are similar within 10% across the rotation reversal. Although the evident changes in the shape of edge profiles are not observed as shown in Fig. 5-17(c) and (d), Table 5.2 shows that $T_{e,edge}$ values decrease by more than 40% and μ_{n_e} increases by about a factor of two in the reversal and counter-current direction phase (during/after rotation reversal) compared to the co-current direction phase (before rotation reversal), while μ_{T_e} and $n_{e,edge}$ values remain similar to within 20% across the rotation reversal. Considering the scattered edge data, it is difficult to conclude whether or not the changes in the edge fitting parameters shown in Table 5.2 are

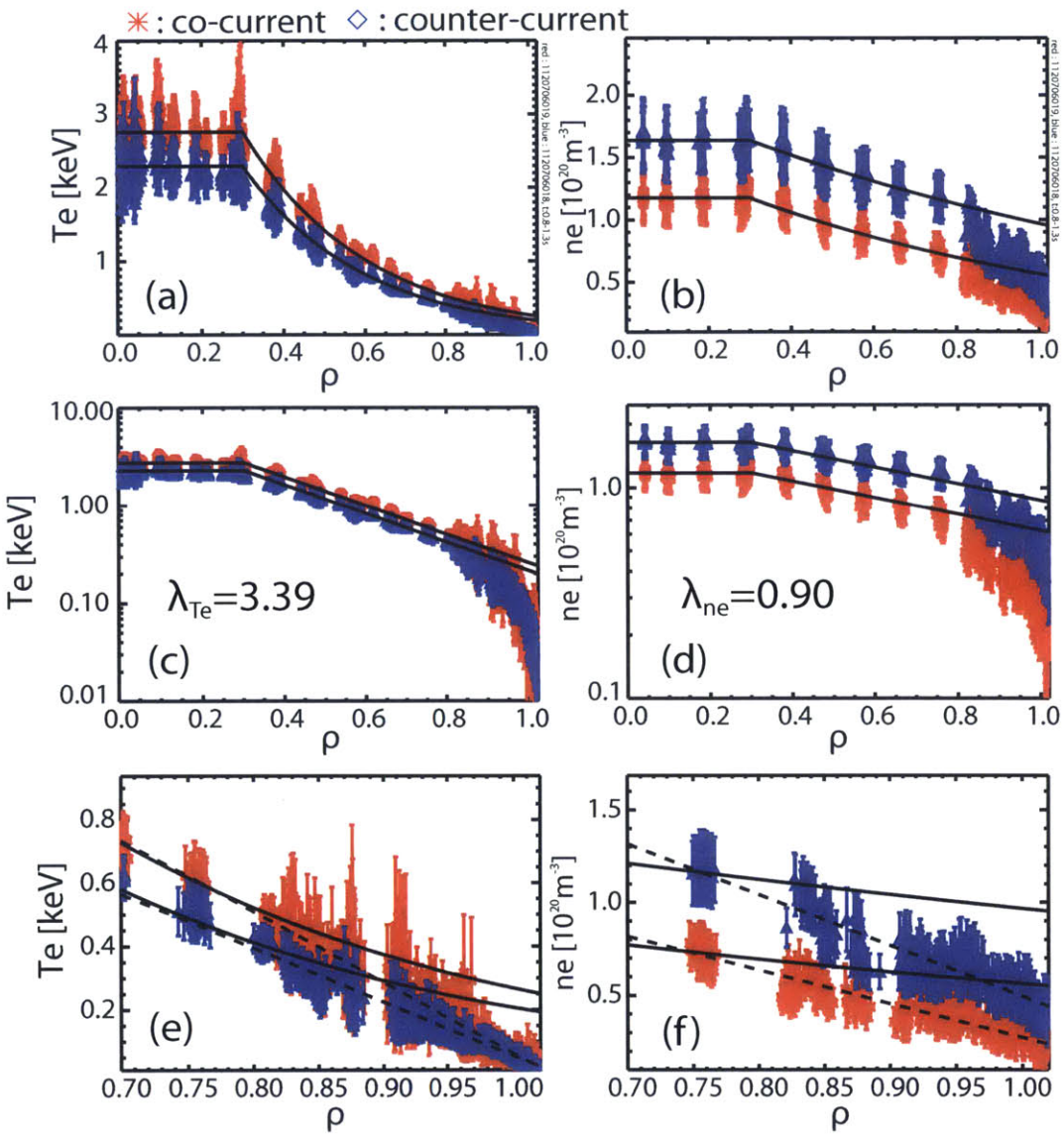

Figure 5-16: Profiles in the two RF heated discharges (red : the lower density discharge rotating in the co-current direction (shot 1120706019), blue : the higher density discharge rotating in the counter-current direction (shot 1120706018)) with the fitting lines (solid line : exponential fitting line for the core profile, dashed line : linear fitting line for the edge profile). (a) T_e profiles with the fitting lines in linear scale (b) n_e profiles with the fitting lines in linear scale (c) T_e profile with the fitting line with fixed λ_{T_e}(=3.36) in log scale (d) n_e profile with the fitting line with fixed λ_{n_e}(=1.00) in log scale (e) Edge T_e profiles with the fitting lines (e) Edge n_e profiles with the fitting lines.

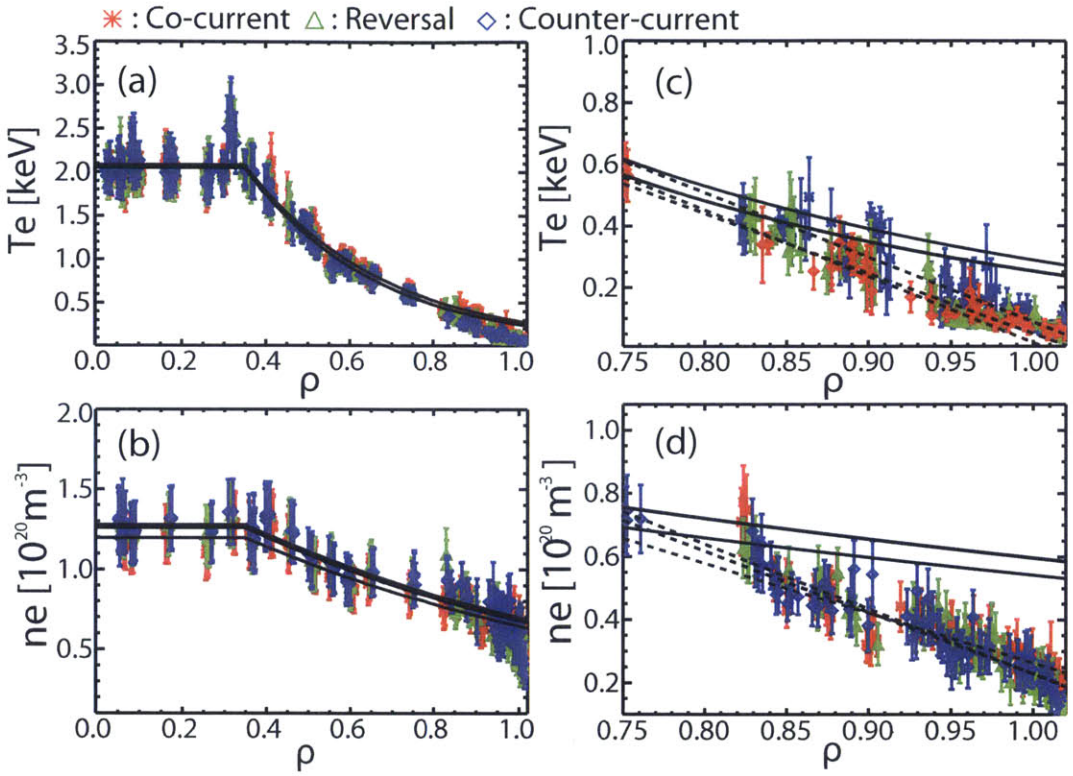

Figure 5-17: T_e and n_e profiles with different toroidal phases (red : co-current (before rotation reversal), green : reversal (during rotation reversal), blue : counter-current (after rotation reversal)) in the rotation reversal discharge in the second set of Ohmic discharges with the fitting lines (solid line : exponential fitting line for the core profile, dashed line : linear fitting line for the edge profile) (a) T_e profiles with the exponential fitting line (b) n_e profiles with the exponential fitting line (c) Edge T_e profiles with fitting lines (d) Edge n_e profiles with fitting lines.

meaningful. For example, we can obtain another possible fitting line for the edge n_e profile in the co-current phase (before reversal) with a small modification in the $n_{e,edge}$ value. The $n_{e,edge}$ value was a free parameter for the linear fit before. When we fixed the $n_{e,edge}$ value in the co-current phase to the level in the reversal phase, $0.53\times10^{20}m^{-3}$, the change in $n_{e,edge}$ is less than 20%, within the uncertainty. However, this change results in an increase in μ_{n_e} of about a factor of two, from 0.94 to 1.72. Since we observed that changes in edge profiles get larger with larger variations in the average density, it is more likely that the changes observed in Table 5.2 are due to a scatter in the edge data. However, further study is required to draw a more solid conclusion.

	Parameters	Co-current	Reversal	Counter-current
core T_e	λ_{T_e}	3.04	3.23	3.22
($\rho \leq \rho_{ped,T_e}$)	$T_e(0.8)$ [keV]	0.53	0.48	0.48
edge T_e	μ_{T_e} [keV]	2.10	2.15	1.94
($\rho \geq \rho_{ped,T_e}$)	$T_{e,edge}$ [keV]	0.09	0.02	0.05
	ρ_{ped,T_e}	0.71	0.72	0.73
core n_e	λ_{n_e}	0.94	0.95	0.92
($\rho \leq \rho_{ped,n_e}$)	$n_e(0.8)$ [$10^{20}m^{-3}$]	0.78	0.82	0.84
edge n_e	μ_{n_e} [$10^{20}m^{-3}$]	0.94 (1.72)	2.01	2.11
($\rho \geq \rho_{ped,n_e}$)	$n_{e,edge}$ [$10^{20}m^{-3}$]	0.62 (0.53)	0.53	0.57
	ρ_{ped,n_e}	0.92	0.88	0.91
	$P_e(0.8)$ [kPa]	6.61	6.30	6.45

Table 5.2: Parameters calculated from fitting with different rotation phases in the rotation reversal discharge analyzed in section 5.1.2 ((shot 1120626027, co-current phase (t:0.75-0.85s), reversal phase (t:1.0-1.1s), counter-current phase (t:1.15-1.25s)). λ_{T_e} is an exponential fitting parameter for the core T_e profile, and μ_{T_e} is the slope of the linear fitting line applied to the edge T_e profile. $T_{e,edge}$ indicates the T_e value at $\rho = 1.0$ from the linear fitting line applied to the edge T_e profile. $\rho_{ped,Te}$ is the radial location which has the minimum difference between the exponential and linear fitting lines. The same definitions are applied to $\lambda_{n_e}, \mu_{n_e}, n_{e,edge}$ and $\rho_{ped,ne}$ for n_e profiles. The values in the parenthesis in the μ_{n_e} and $n_{e,edge}$ rows in the co-current column are the values obtained when the $n_{e,edge}$ value is fixed to $0.53\times10^{20}m^{-3}$.

5.5 Discussion & Summary

The study in this chapter is motivated by the reduction of T_e fluctuations near the edge (r/a$\sim$0.85) in RF heated discharges rotating in opposite directions due to different average density levels, analogous to the trend observed across the LOC/SOC transition, as shown in Fig. 5-18. The correlation between momentum transport related to the rotation reversal and turbulence was suggested in the past [131]. In this chapter, we investigated the correlation between rotation reversal and the changes in turbulence and transport via analysis methods introduced in Chapter 3.

In the pair of RF heated discharges which have different density levels and rotate in opposite directions, we found several similarities with the LOC and SOC discharges analyzed in Chapter 4. First, T_e fluctuations near the edge were reduced across the rotation reversal in both Ohmic and RF heated discharges as shown in Fig. 5-18. Second, profile analysis shows no significant changes in the gradient scale lengths within the uncertainty between these two RF heated discharges. The higher density and lower temperature in the discharge rotating in the counter-current direction makes this discharge more collisional. Similar results were obtained from the LOC and SOC discharges as well. Third, we observed that the sawtooth signals have a longer period and become more irregular in the higher density discharge (co-current rotation) than in the lower density discharge (counter-current rotation) in both Ohmic and RF heated discharges. Fourth, gyrokinetic analysis suggests no changes in the dominant turbulence mode within the uncertainty across the rotation reversal in both Ohmic and RF heated discharge. In other words, we were not able to resolve the changes in the dominant mode between two discharges which rotate in opposite directions regardless of the plasma heating method, while the changes in core toroidal rotation are evident in both cases. Finally, self-similarity analysis shows consistent changes in edge n_e and T_e profiles across the rotation reversal in both RF and Ohmic heated discharges. All these similarities suggest the same physics can be applied in both RF and Ohmic heated discharges to explain the changes in T_e fluctuations near the edge and associated changes with the increase in density or across the rotation reversal.

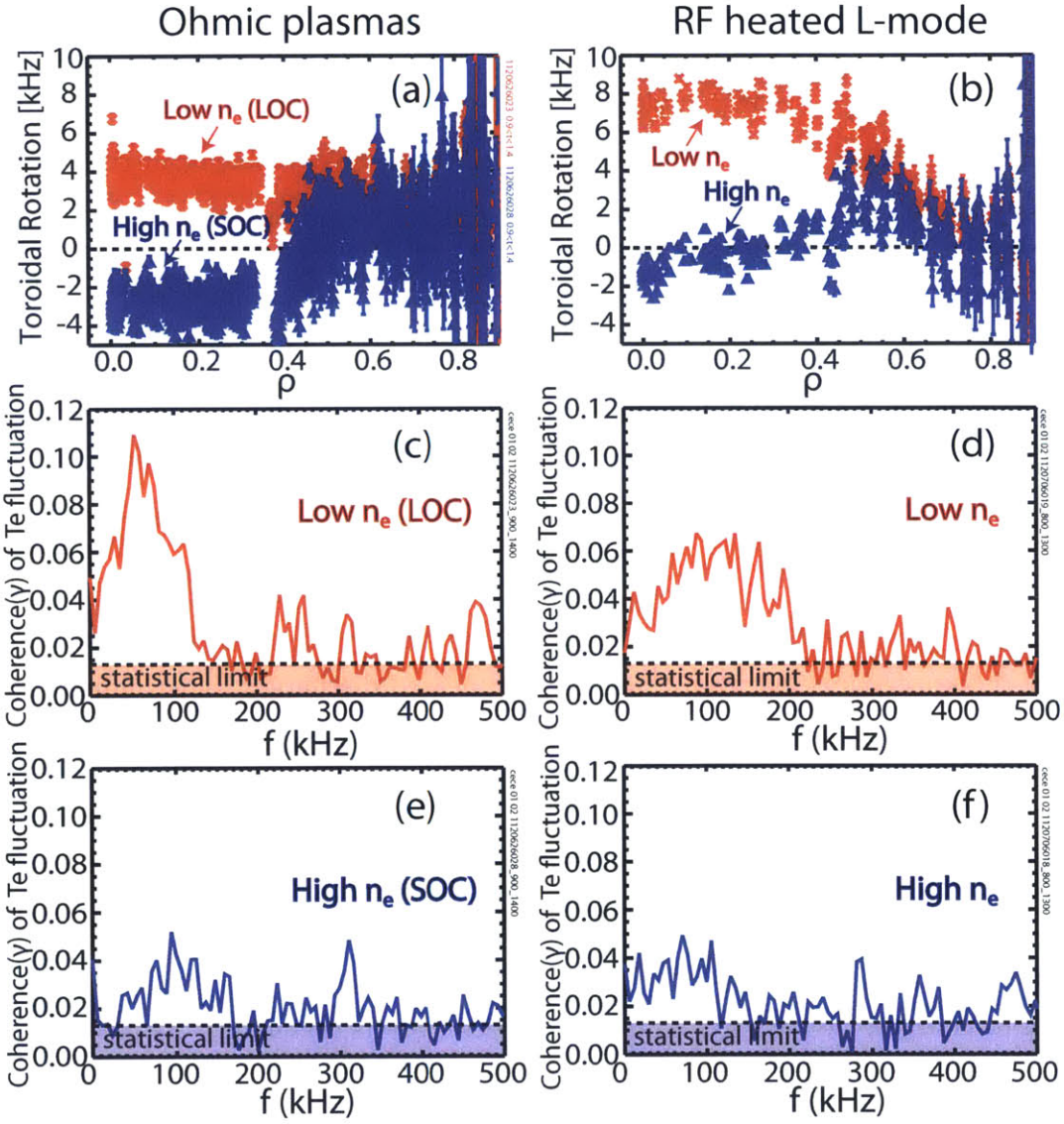

Figure 5-18: Changes in T_e fluctuations across rotation reversals in Ohmic and RF heated plasmas. Toroidal rotation profile with the change of electron density in (a) Ohmic plasmas, (b) RF heated L-mode plasmas. Coherence spectra of T_e fluctuations in (c) the low density Ohmic plasma (LOC plasma), (d) the low density RF heated L-mode plasma, (e) the high density Ohmic plasma (SOC plasma), (f) the high density RF heated L-mode plasma.

In the Ohmic and RF heated discharges, rotation reversal occurs when large variations in the average density, more than 50% (or large variations in the collisionality) are made. However, we must note that the rotation reversal can occur with smaller changes in the average density (e.g. less than 5%). It is therefore possible that the similarities between the Ohmic and RF heated discharges are related to the collisionality, not the rotation reversal. In order to see the effect of rotation reversal itself, without effects from collisionality, we investigated the changes in turbulence and profiles in one rotation reversal discharge (shot 1120626027), in which rotation reversal occurs with only slight changes in the average density (collisionality). No significant changes in T_e fluctuations near the edge and no change in sawtooth activity were found across the rotation reversal in the rotation reversal discharge. Self-similarity analysis showed that the profiles can change little within the uncertainty while the direction of core rotation reverses, but we cannot eliminate the possible correlation between the edge profile changes and the core rotation reversal.

Similar T_e fluctuations near the edge across the rotation reversal in the rotation reversal discharge suggest that T_e fluctuations near the edge region are not a direct cause (or effect) of the core rotation reversal. Instead, the increase in density or collisionality could explain both phenomena. In other words, the results in this chapter show a correlation between the collisionality and T_e fluctuations. However, it is still inconclusive whether the reduction in T_e fluctuations is due to the increase in collisionality or the changes in the gradient scale lengths, which have large uncertainties. We observed a consistent trend in the edge profiles with the increase in the average density in Ohmic and RF heated discharges through self-similarity analysis. This trend could be linked to the changes in the gradient scale lengths near the edge with the increase in density (or collisionality). Further study is required to clarify this possibility.

The absence of significant changes in edge T_e fluctuations with the different rotation phases in the rotation reversal discharge does not rule out a direct relation between turbulence deeper in the core and momentum transport. At this point, we do not know whether or not T_e fluctuations in the core region, near r/a=0.6, where

the rotation reversal occurs, are correlated with the rotation reversal. The gyrokinetic simulation results in the core region, which are the global simulation results deeper in the core region in this section and the local simulation results at r/a=0.6 in Chapter 4, suggests no significant changes in turbulence in the deep core region across the rotation reversal. In the future, we should confirm or refute these simulation predictions with experimental measurements.

It is noteworthy that "wing structure" in the Phase Contrast Imaging (PCI) measurements, mentioned in section 4.1.2, is observed only in the co-current rotation phase, and that this structure is disappeared in the counter-current rotation phase in the rotation reversal discharge with small changes in average density ($< 5\%$) [128, 129]. Thus, this structure is correlated with the rotation reversal, not the increase of density (or collisionality). It is inconclusive whether this structure comes from Doppler shift or changes in turbulence [175]. Nevertheless, this structure and the results in this chapter indicate that, in order to understand rotation reversals, we should classify the changes across rotation reversals into two categories: changes directly related to rotation reversals, which can be observed in the rotation reversal discharge, and changes related to collisionality, not directly connected to rotation reversals, not observed in the rotation reversal discharge.

Self-similarity analysis shows that the changes in the edge profiles and the boundary of the core profiles ($T_e(0.8)$ and $n_e(0.8)$) become more significant with larger variations in the average density. This result also suggests that the trend observed between the LOC and SOC discharges and RF heated discharges with rotation reversals is related to changes in the density, not directly related to the rotation reversal itself. Related to the negligible change in sawtooth activity across the rotation reversal in the rotation reversal discharge, it is worth noting that the relation of rotation to edge profile changes could be consistent with a related change of the sawtooth activity and a lower T_e profile due to a lower $T_e(0.8)$, leading to a flatter q profile with increasing q_o [142, 49]. Although the decrease in $T_{e,edge}$ was observed across the rotation reversal in the same discharge, with a similar slope of the linear fitting line for the edge T_e profiles, μ_{T_e}, this decrease does not change the core T_e profile signif-

icantly. Table 5.2 shows that $T_e(0.8)$ decreases by less than 10% across the rotation reversal, while we observed a 20-30% decrease across the LOC/SOC transition and the rotation reversal in the 2^{nd} set of RF heated discharges in Tables 4.5 and 5.1.

Although the observations in this chapter suggest no direct relation between rotation reversal and the changes in turbulence and radial pressure profiles, a rotation reversal is still well correlated with the LOC/SOC transition in C-Mod, as shown in Fig. 28 (the energy confinement time, τ_E vs electron density plot with rotation reversal) in [129]. The correlation between rotation reversal and global confinement changes in Ohmic discharges is still an open question. We must also note that electron heat flux is under-predicted in all non-linear simulations, which may suggest that the contribution of high k (electron scale) turbulence could be significant in the discharges analyzed in this section. Thus, a more complete picture for the relation between turbulence and rotation reversal may be found in simulations considering both electron and ion scale turbulence in the future.

Chapter 6

Energy transport in core plasma in high energy confinement regime: I-mode and H-mode

One of the purposes of turbulence measurements, including T_e fluctuations, will be to understand the correlation between changes in turbulence and the quality of confinement, and to figure out how to improve confinement. In validation study, turbulence measurements will be used to improve our ability to predict transport and overall plasma performance in the future device. In either perspective, the study of changes in turbulence across the low to the high energy or particle confinement regimes, such as I-mode and H-mode, is highly important. In DIII-D, it was shown that T_e fluctuations in the core region are reduced in H-mode compared to L-mode [145, 146]. It will be of interest to study the change in T_e fluctuations in high confinement regimes in C-Mod plasmas. As introduced in section 1.3.5, transport in another high energy confinement regime, I-mode which has H-mode energy confinement and L-mode particle confinement, has been actively studied in C-Mod. However, most studies focus on the edge and pedestal region [174, 82, 43], and the study of how the core plasma and edge plasma are coupled has not been explored in detail in high confinement regimes. In this chapter, we will first investigate the changes in T_e fluctuations inside the pedestal region (r/a<0.98) in the I-mode discharge compared to L-mode discharge

via CECE signal analysis, as explained in section 3.1. Then, the changes in the transport and turbulence characteristics across the L/I transition will be studied using analysis methods explained in section 3.2 and 3.3. We then present the self-similarity in the density and temperature profiles with confinement regimes (L/I/H-modes) via the self-similarity analysis introduced in section 3.4.

6.1 Changes in T_e fluctuations across L/I transition

In this section, we will investigate the changes in T_e fluctuations in the I-mode phase compared to the L-mode phase. We first describe the fluctuations in the steady L- and I-mode discharges. Since I-mode was obtained via the increase of external heating power (Ion Cyclotron Resonance Heating (ICRH) power) in this study, we should separate the effect of higher external power on the measured T_e fluctuations from the effect of changes in confinement regime. The relation between external heating power and T_e fluctuations will be studied by examining one C-Mod discharge with an input power scan.

6.1.1 Reduction of T_e fluctuations in steady I-mode discharges compared to steady L-mode discharges

We first observed the changes in T_e fluctuations near the edge (r/a$\sim$0.85) between L- and I-mode discharges (shot 1120917024, t:0.8-1.3s (L-mode), shot 1120917027, t:0.85-1.3s (I-mode)). Both plasmas were operated at toroidal magnetic field, B_t=5.5T in the co-current direction, plasma current, I_p=1.1MA, the average electron density, $\bar{n}_e$=1.2$\times 10^{20} m^{-3}$ in the Lower Single Null (LSN) configuration with R=0.67m, a=0.22m, elongation, κ=1.6, lower triangularity, δ_l=0.5, and upper triangularity, δ_u=0.25. The direction of B_t and I_p was set to have ion ∇B drift direction pointing away from the active x-point. The configuration of these discharge is called reversed field discharge in C-Mod from the direction of B_t and I_p, a counter-clockwise direction when we look down a tokamak. This configuration gives a wider operation

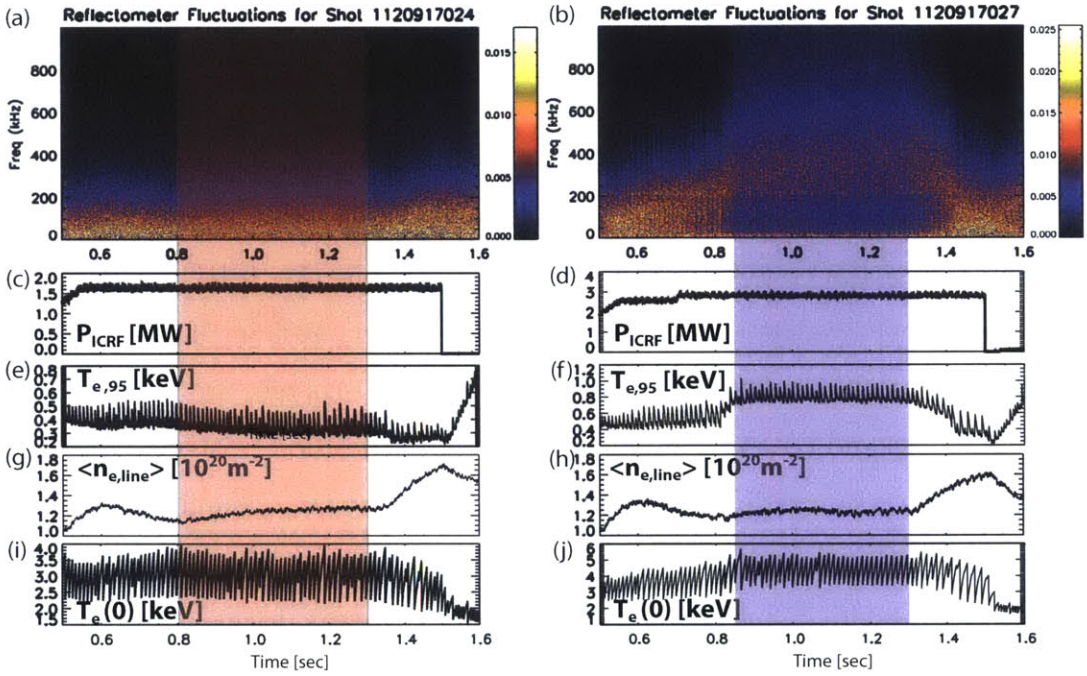

Figure 6-1: (a) and (b): Edge fluctuations measured by reflectometry in an L-mode discharge (shot 1120917024) and an I-mode discharge, respectively. In the same manner, (c) and (d): RF heating power [MW] for the L-mode and the I-mode, (e) and (f): T_e [keV] near the edge (r/a$\sim$ 0.94) in the L-mode and the I-mode, (g) and (h): central chord line averaged density [$10^{20}m^{-3}$] in the L-mode and the I-mode, (i) and (j): T_e [keV] on the magnetic axis in the L-mode and the I-mode. The CECE analysis was performed in the shaded regions.

window for I-mode by increasing the threshold heating power for the L/H transition [180]. The ICRF heating power, P_{ICRF} was varied to obtain the different confinement regimes: P_{ICRF}=1.6MW in the L-mode discharge and 2.8MW for the I-mode discharge. Figure 6-1 shows the time series data of these two discharges including the density fluctuations measured by reflectometry [46] near the edge (r/a$\sim$0.96-0.98). As shown in Fig. 6-1(a), the L-mode discharge has broadband n_e fluctuations up to 200kHz near the edge. In contrast, in the discharge that accessed the I-mode phase, broadband fluctuations are reduced as the WCM [180] appears in edge region, as shown in the shaded area in Fig. 6-1(b). Accessing I-mode can be also identified from the electron temperature near the edge (r/a$\sim$0.94), shown in Fig. 6-1(e) and (f). As the plasma accesses the I-mode phase, we notice the increases in electron temperature near the edge by almost a factor of two in Fig. 6-1(f). Figure 6-1(g) and (h) show that average electron density varies within 10% in the shaded region, in which CECE signal analysis was performed. Both discharges are sawtoothing, as seen in Fig. 6-1(i) and (j). Although the measurement position (r/a$\sim$0.85) is far from the sawtooth inversion radius (r/a$\sim$0.4), we observe the large amplitude heat pulse from the sawtooth activity near the edge in Fig. 6-1(e) and (f). The effect of this heat pulse to the CECE measurements should be a caveat in this study. However, large heat pulses were observed in both L- and I-mode discharges. Thus, we still can compare T_e fluctuations between these two discharges, although the heat pulse effect should be investigated in the future.

The changes in T_e fluctuations near the edge (r/a$\sim$0.85) between the L- and I-mode discharges are shown in Fig. 6-2. In this analysis, we filtered out the low frequency signals (f < 10kHz) to remove the parasitic noise explained in Appendix B. We notice the significant changes in T_e fluctuations in the I-mode discharge compared to the L-mode discharge. In the L-mode discharge, the broadband fluctuations up to 150kHz are resolved from both the coherence and cross phase spectra, as shown in Fig. 6-2(a) and (c), with fluctuation level about 1.0% (0-150kHz). In contrast, it is hard to resolve any fluctuations above the random noise in the I-mode discharge, shown in Fig. 6-2(b) and (d). We therefore conclude a more than 60% reduction in

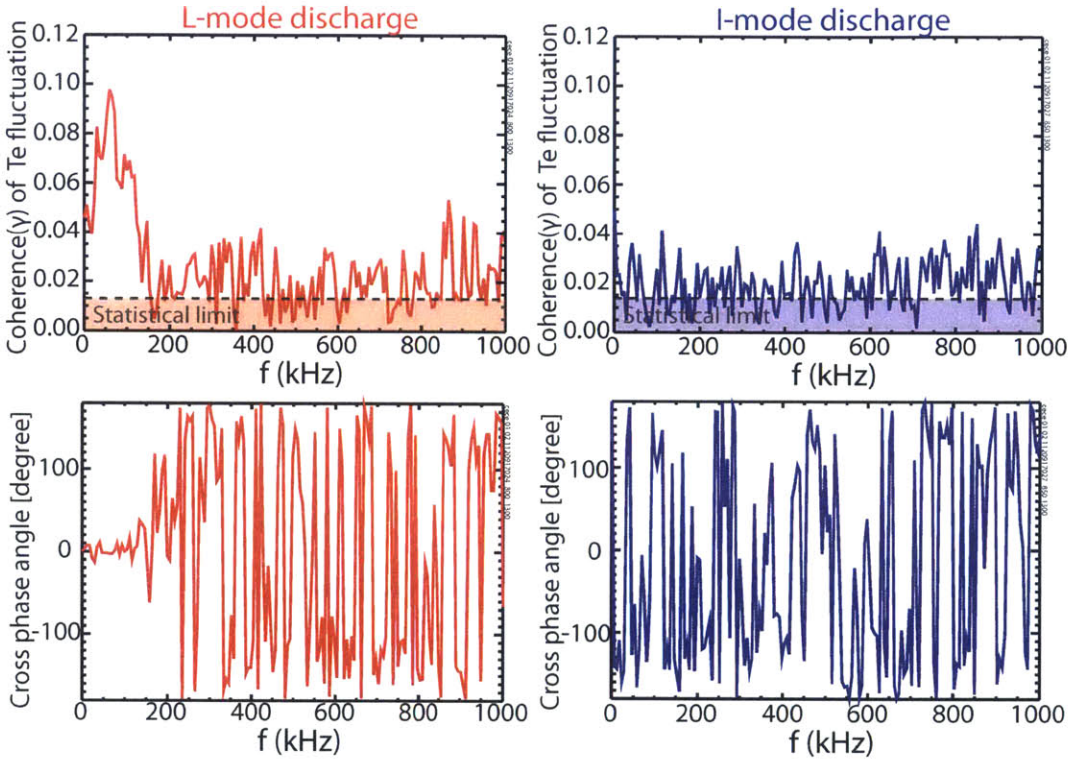

Figure 6-2: (a) Coherence (γ) of two CECE signals in an RF heated L-mode discharge (shot:1120917024). Horizontal dotted line indicates the statistical limit of coherence (b) Coherence (γ) of two CECE signals in an RF heated I-mode discharge (shot:1120917027) (c) the cross phase spectrum of two CECE signals in the L-mode discharge (d) the cross phase spectrum of two CECE signals in the I-mode discharge.

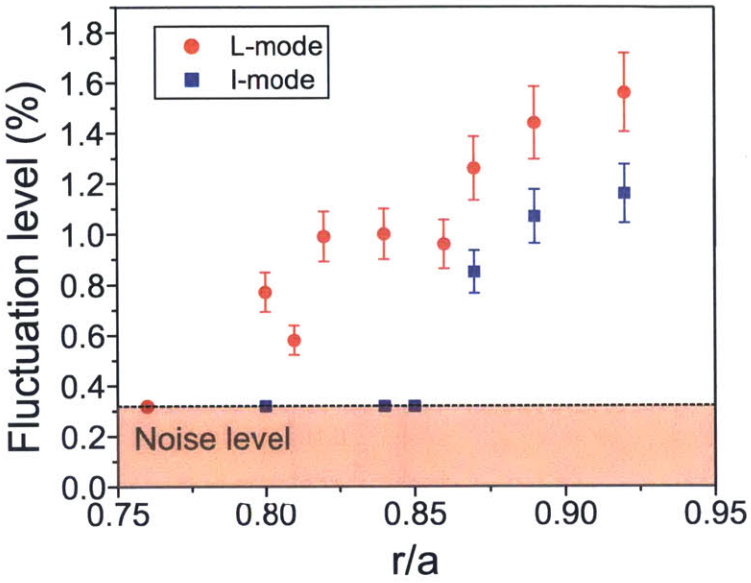

Figure 6-3: The change in T_e fluctuation profile between L-mode and I-mode discharges. The profile was obtained from the series of discharges with the scan of toroidal magnetic field (Adopted from M. Greenwald *et al*, Nucl. Fus. **53** 104004 (2013)).

T_e fluctuations near the edge (r/a$\sim$0.85) in the I-mode discharge compared to the L-mode discharge.

We then expand the measurement region of this comparison using the other CECE channels in identical discharges and in similar discharges with a slight change of toroidal magnetic field (5.4-5.5T), fixing the other discharge parameters. As a result, the T_e fluctuation profiles measured in the region, $0.75 < r/a < 0.95$, are shown in Fig. 6-3. In this figure, the fluctuation level is marked at the statistical limit (or the sensitivity level), given by Eq. 2.12, when no fluctuations were resolved from the coherence and cross phase spectra. We observe that T_e fluctuation levels decrease in I-mode plasmas compared to L-mode plasmas over the entire CECE accessible measurement region inside the pedestal ($0.8 \leq r/a < 0.95$). In both L- and I-mode plasmas, T_e fluctuations tend to decrease in the inner region, and no fluctuations above the noise level were found in $r/a \leq 0.85$ region in I-mode plasmas.

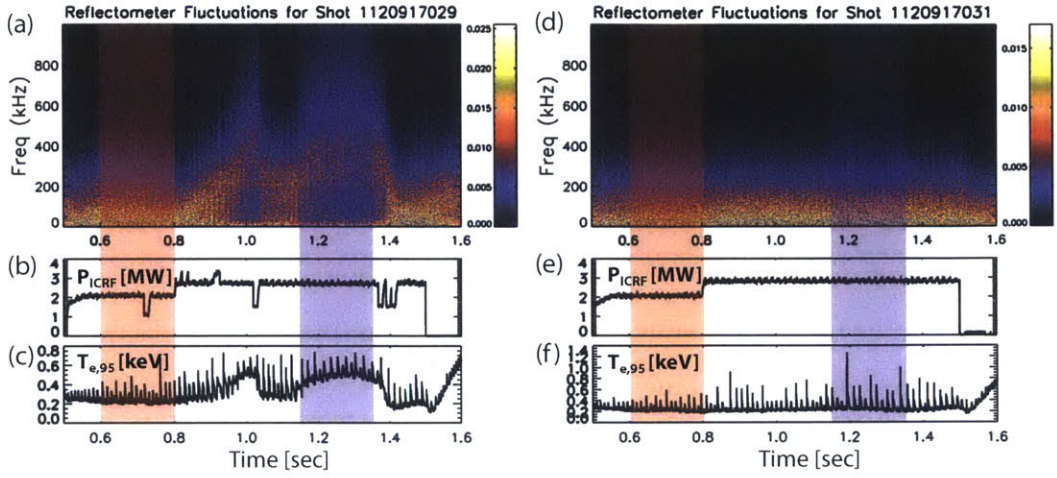

Figure 6-4: (a) Edge fluctuations of an L/I transition discharge (shot 1120917029) measured by reflectometry (b) RF heating power [MW] (c) T_e [keV] near the edge (r/a$\sim$0.98). (d) Edge fluctuations of an L-mode discharge (shot 1120917031), which has two different RF power phases, measured by reflectometry (e) RF heating power [MW] (f) T_e [keV] near the edge (r/a$\sim$0.98). Red shaded area indicates lower RF power phase. Both discharges are in the L-mode phase. Blue shaded area indicates higher RF power phase. The discharge shown in (a)-(c) is in the I-mode phase, while the discharge in (d)-(f) is in the L-mode phase.

6.1.2 Changes in T_e fluctuations in an L-mode with RF power scan

We must note that the I-mode regime was accessed by increasing the RF heating power (P_{ICRF}) in this study. It is possible that T_e fluctuations are correlated with the RF heating power, not with the confinement regime. In order to investigate this possibility, we compare T_e fluctuations in two discharges (shot 1120917029 and 1120917031). In one discharge (shot 1120917029), I-mode was accessed with the increase of the RF heating power from 2.0MW to 2.7MW. In the second discharge (shot 1120917031), the plasma remained in the L-mode discharge in spite of the increase of the RF heating power from 2.1MW to 2.8MW. By observing changes in T_e fluctuations with different RF power phases in these two discharges, we can study the relation between RF power and T_e fluctuations.

Figure 6-4 shows the time history of these two discharges including edge fluctua-

tions measured by reflectometry [46] at r/a$\sim$0.95-0.99. The L/I transition discharge is shown in Fig. 6-4(a)-(c). The L/I transition occurred around 0.95s after the RF power was increased at 0.8s. With the RF trip, the plasma went to the L-mode, and then back to I-mode from around 1.15s, and remained in the I-mode before another RF trip around 1.4s. I-mode can be identified from the WCM, shown in Fig. 6-4(a), and the increase of the T_e value near the edge (r/a$\sim$0.98) shown in Fig. 6-4(c). In another discharge which has a similar time trace in RF heating power, there is no change in the edge fluctuations and T_e value near the edge (r/a$\sim$0.98) in the whole time range shown in Figure 6-4(d)-(e). We must note that these two discharges have similar discharge conditions as follows: toroidal magnetic field, B_t=5.6T in the co-current direction, plasma current, I_p=1.1MA, average electron density, $\bar{n}_e$=1.3$\times 10^{20} m^{-3}$, in the Lower Single Null (LSN) configuration with R=0.67m, a=0.22m, elongation, κ=1.6, lower triangularity, δ_l=0.5, and upper triangularity, δ_u=0.25.

In order to investigate a correlation between RF power and T_e fluctuations, we compared T_e fluctuations with the different RF power phases, are shown in red and blue shaded areas in Fig. 6-4, in the L/I transition discharge (shot 1120917029) and the L-mode discharge, which has two RF power phases (shot 1120917031). In this analysis, a high pass filter (f>10kHz) was applied to eliminate noise. The CECE measurement position was r/a$\sim$0.9. Since the measurement position is further out than the other measurements shown in Chapter 4,5 and section 6.1 (r/a$\lesssim$0.85), we may need to consider the contribution of density fluctuations in the measurements as explained in section 3.1.2. However, high density and temperature values in these discharges cause the plasma to be optically thick (optical depth, $\tau > 4$) at the measurement position. The changes in T_e fluctuations in the L- and I-mode phases with different RF power are shown in Fig. 6-5. It is noticeable that T_e fluctuations were reduced in the I-mode, which has the higher RF power ($\sim$2.7MW), compared to the fluctuations in the L-mode, which has the lower RF power ($\sim$2.0MW). In the L-mode phase, we observed T_e fluctuations whose relative level is about 1.3% (0-160kHz). In contrast, it is hard to resolve any fluctuations in the I-mode phase shown in Fig. 6-5(b) and (d).

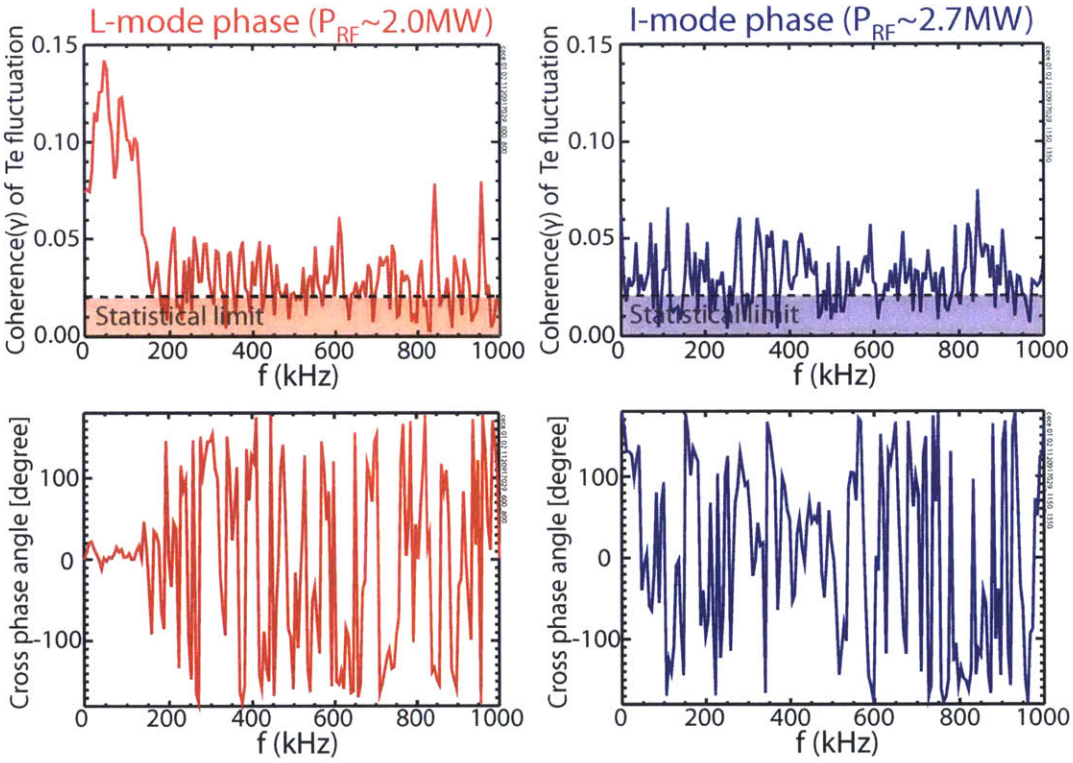

Figure 6-5: (a) Coherence (γ) of two CECE signals in the L-mode phase of one RF heated discharge (shot:1120917029). Horizontal dotted line indicates the statistical limit of coherence (b) Coherence (γ) of two CECE signals in the I-mode phase in the same discharge (c) the cross phase spectrum of two CECE signals in the L-mode phase (d) the cross phase spectrum of two CECE signals in the I-mode phase.

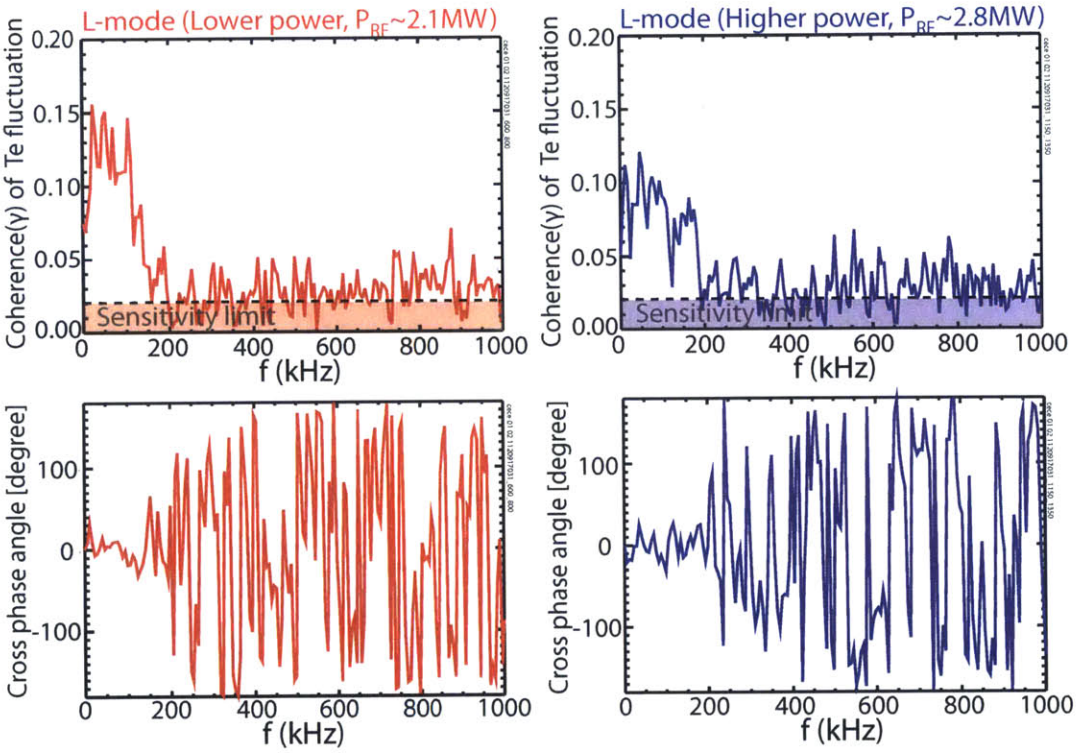

Figure 6-6: (a) Coherence (γ) of two CECE signals in the lower RF power L-mode phase of one RF heated discharge (shot:1120917031). Horizontal dotted line indicates the statistical limit of coherence (b) Coherence (γ) of two CECE signals in the higher RF power L-mode phase in the same discharge (c) the cross phase spectrum of two CECE signals in the lower RF power phase (d) the cross phase spectrum of two CECE signals in the higher RF power phase.

Figure 6-6 shows the changes in T_e fluctuations with RF power in the L-mode discharge. In this discharge, no significant changes in T_e fluctuations were found between two different RF power phases. In the lower power phase (P_{ICRF}=2.1MW), the relative fluctuation level is around 1.4% (0-200kHz), and the fluctuation level in the higher RF power phase (P_{ICRF}=2.8MW) is about 1.3% (0-290kHz). Thus, the two levels in different RF power phases are comparable and within the uncertainty of the measurements ($\sim$10%). This observation indicates that T_e fluctuations are not correlated with changes in RF heating power.

From the other CECE channels in the same discharges, we observed consistent reduction of T_e fluctuations in I-mode as shown in Fig. 6-7. Although the other CECE channels are further out than the channels used in Fig. 6-5 and 6-6, the lowest optical depth values at these measurements are around 2.0. The contribution of density fluctuations can vary the T_e fluctuation levels by at most 20% when the optical depth, τ, is 2 with 2% density fluctuations as shown in section 3.1.2. Nevertheless, this uncertainty will not change the main conclusion in Fig. 6-7; the reduction of T_e fluctuations across the L/I transition. These observations indicate that T_e fluctuations inside pedestal regime are reduced in I-mode plasmas compared to L-mode plasmas; not as a result of increased RF power, but due to changes in transport across the L/I transition. We note that these I-mode results are consistent with the observations in H-mode in DIII-D[145, 146]. These measurements and analysis results imply that reductions in core turbulence in I-mode (and maybe in H-mode) are related to the improvement in the energy confinement. In the following sections, we will investigate the changes in transport across the L/I transition using the analysis methods introduced in section 3.2-3.4.

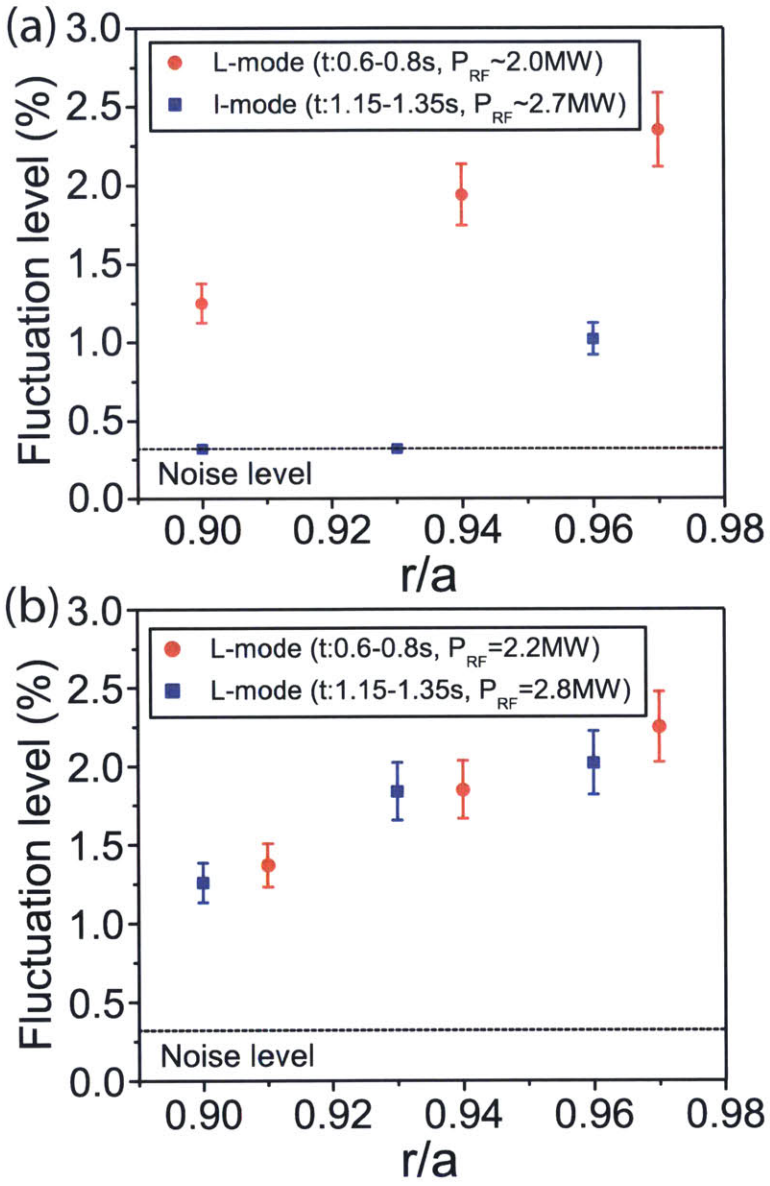

Figure 6-7: (a) The change in T_e fluctuations in the L/I transition discharge (shot 1120917029, t:0.6-0.8s (L-mode phase, P_{ICRF}=2.0MW) and t:1.15-1.35s (I-mode phase, P_{ICRF}=2.7MW)) (b) The change in T_e fluctuations in the L-mode discharge with RF power changes (shot 1120917031, t:0.6-0.8s (P_{ICRF}=2.1MW) and t:1.15-1.35s (P_{ICRF}=2.8MW))

6.2 Profile analysis & power balance analysis across the L/I transition

In order to investigate the changes in the profiles across the L/I transition, we performed profile analysis for the discharge where the L/I transition occurred (shot 1101209029). This discharge was run in Upper Single Null(USN) configuration with $B_t(0)$=5.7T, I_p=1.3MA and the following shape parameters, κ=1.7, δ_u=0.6, δ_l=0.3. Like the discharges in section 6.1, the ion ∇B drift direction was set to point away from the x-point. The direction of B_t and I_p in this discharge is clockwise, which is a normal field direction in C-Mod. The average electron density, $\bar{n}_e = 2.1 \times 10^{20} m^{-3}$, and there is a sawtoothing activity in this discharge with the inversion radius, r/a_{inv} ~0.45. Figure 6-8 shows the fluctuations measured by the reflectometry [46] channel near the edge (r/a~0.99) in this discharge. In the L-mode phase (t~0.7-0.87s), broadband fluctuations up to 200kHz were observed. The plasma accessed the I-mode phase, which can be identified by the Weakly Coherent Mode (WCM) [180] and the increase of the T_e value near the edge (r/a~0.99) at t~0.93-1.03s. More details about this discharge can be found in [83, 173].

The profile analysis was performed at one time slice in the L- and I-mode phases in the discharge described in the last paragraph (at t=0.836s (L-mode), t=0.938s (I-mode)). Figure 6-9 shows the profiles of electron density (n_e), electron temperature (T_e) and ion temperature (T_i) and their gradient scale lengths. From the profiles, we first notice that T_e and T_i increase in the I-mode phase compared to the L-mode phase, while n_e changes little across the L/I transition. In the gradient scale lengths, a/L_n and a/L_{T_e} do not vary outside the uncertainty ($\sim$ 20%), but a/L_{T_i} decreases in the I-mode phase outside the uncertainty (~30%) in r/a> 0.6. Since only one time slice was used in this analysis, the region inside sawtooth inversion radius, r/a_{inv}, will not be reliable in this study. We must note that this analysis was performed to obtain the radial profiles in $r/a \leq 0.8$. In other words, the region of interest in this analysis is $r/a \leq 0.8$. As explained in section 3.2.1, more careful analysis is required for the profiles in the outer region ($r/a > 0.8$, and it will be performed in

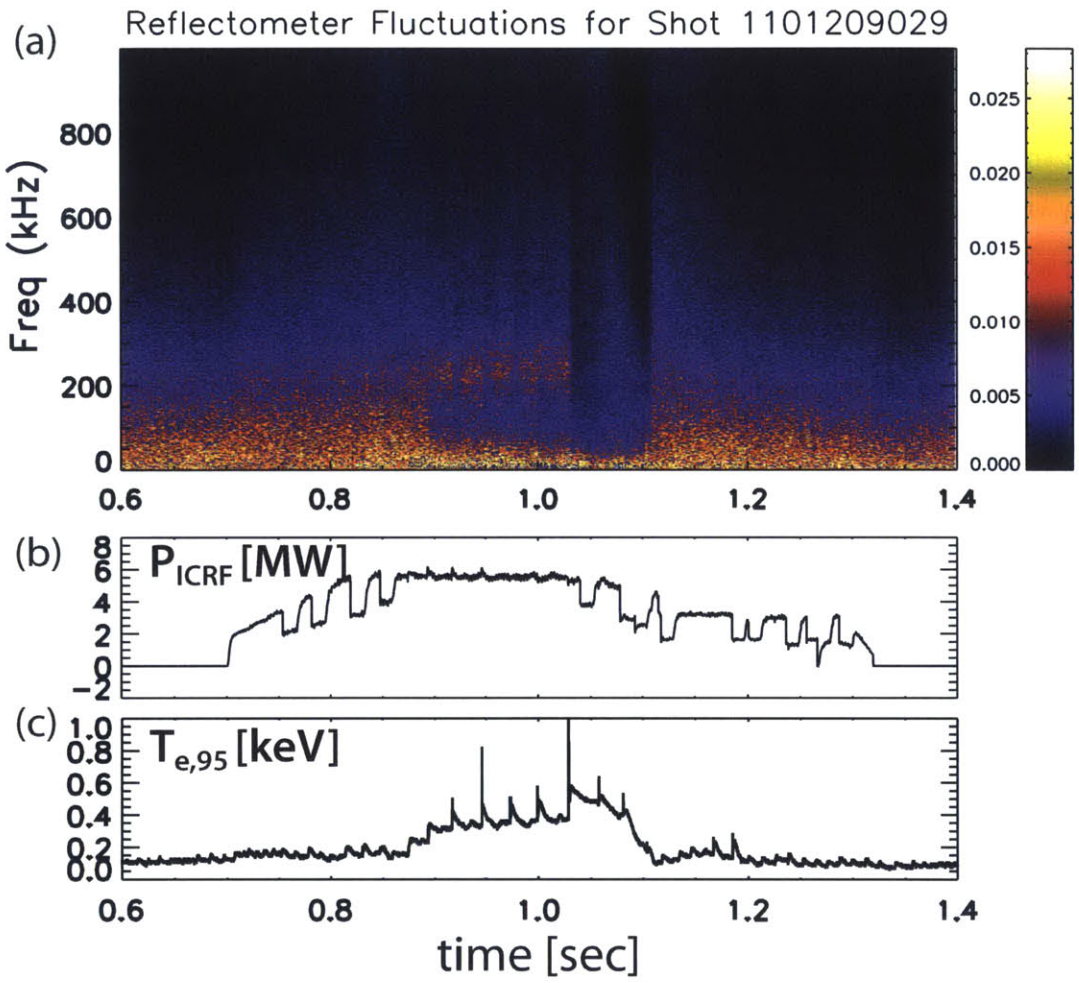

Figure 6-8: (a) Edge fluctuations of an L/I transition discharge (shot 1101209029) measured by reflectometry (b) RF heating power [MW] (c) T_e [keV] near the edge (r/a$\sim$0.99).

the future if it is necessary. The reliable region in the profiles shown in Fig. 6-9 is then $r/a_{inv} < r/a \leq 0.8$. We must note that the changes in profiles between L- and I-mode phases in this section refer to the changes in $r/a_{inv} < r/a \leq 0.8$.

We then performed the power balance analysis using the profiles shown in Fig. 6-9 to study the changes in the experimental heat transport across the L/I transition. The reliable region in the results from power balance analysis will also be $r/a_{inv} < r/a \leq 0.8$. As shown Fig. 6-10(a) and (b), electron heat diffusivity is reduced by about 50% in the I-mode phase compared to the L-mode phase, while ion heat diffusivity varies little between the two confinement regimes. Difffusivity, χ, is defined as $\chi = Q/n/\partial T/\partial r$. This result is consistent with the previous study in C-Mod [173], which shows a reduction of the one fluid effective heat diffusivity in I-mode compared to L-mode. Figure 6-10(c) shows that electron heat flux also decreases outside the uncertainty ($\sim$30%) in the I-mode phase compared to the L-mode phase. Consistent with Fig. 6-10(b), ion heat flux does not vary significantly across the L/I transition, as shown in Fig. 6-10(d).

From profile analysis and power balance analysis, we observed two changes in the I-mode heat transport compared to the L-mode. First, a/L_{T_i}, which drives ITG turbulence, decreases in the I-mode phase outside of r/a$\sim$0.6. Second, the electron heat transport was reduced in the I-mode phase, while the ion heat transport remains similar within the uncertainty. Both changes can be connected to the reduction of T_e fluctuations, discussed in section 6.1. The decrease of a/L_{T_i} will stabilize the ITG mode. It is therefore possible to explain the reduction of T_e fluctuations as the result of ITG mode suppression. The reduction of electron heat transport in the I-mode phase could also be related to the decrease in the measured T_e fluctuations across the L/I transition. The correlation between the linear ITG mode activity and the reduction of T_e fluctuations in the H-mode was shown in a previous study in DIII-D [146]. We will check this possibility through linear stability analysis in the next section.

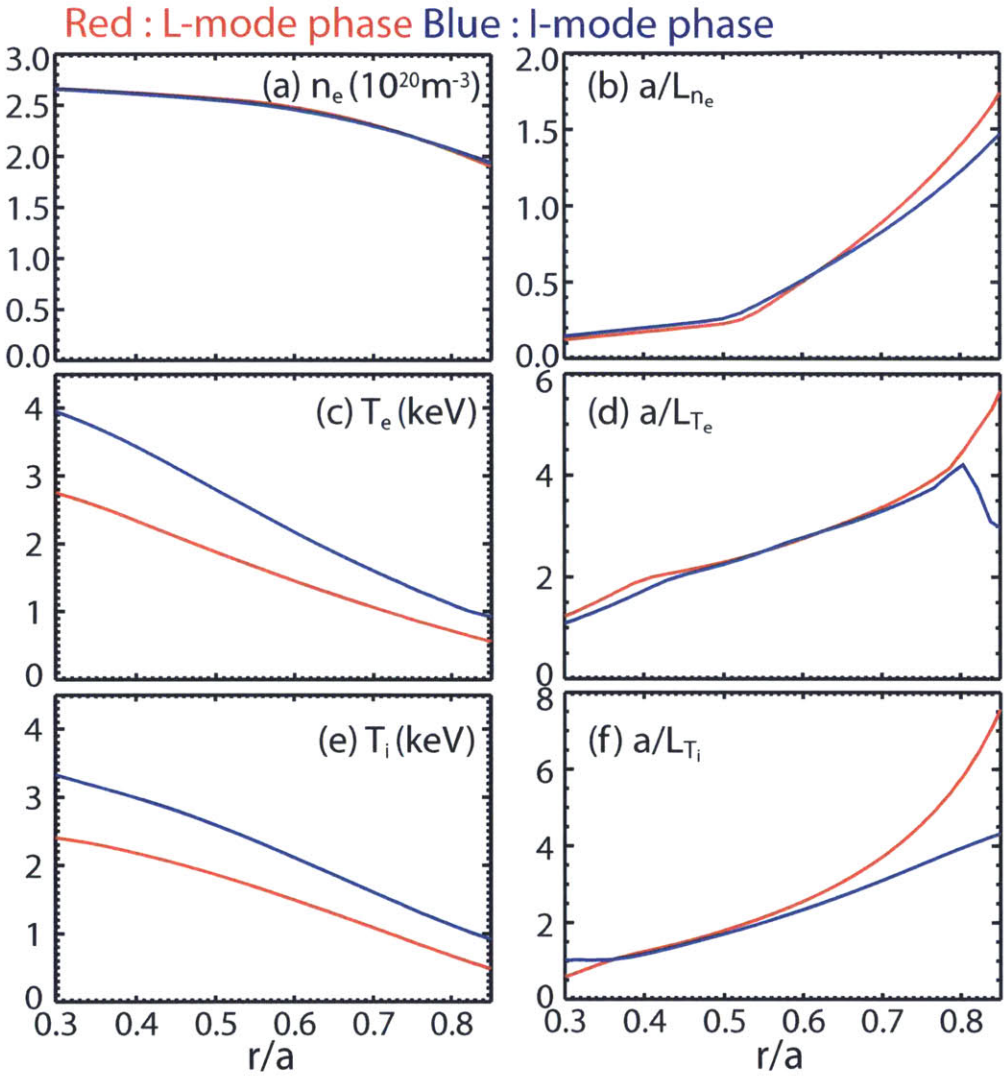

Figure 6-9: Profiles and their gradient scale lengths of two time slices at each confinement regime in one C-Mod discharge (shot 1101209029, t=0.836s for L-mode and t=0.938s for I-mode), Red : L-mode phase, Blue : I-mode phase. Adopted from A. E. White et al, 2014, *Physics of Plasmas*, submitted

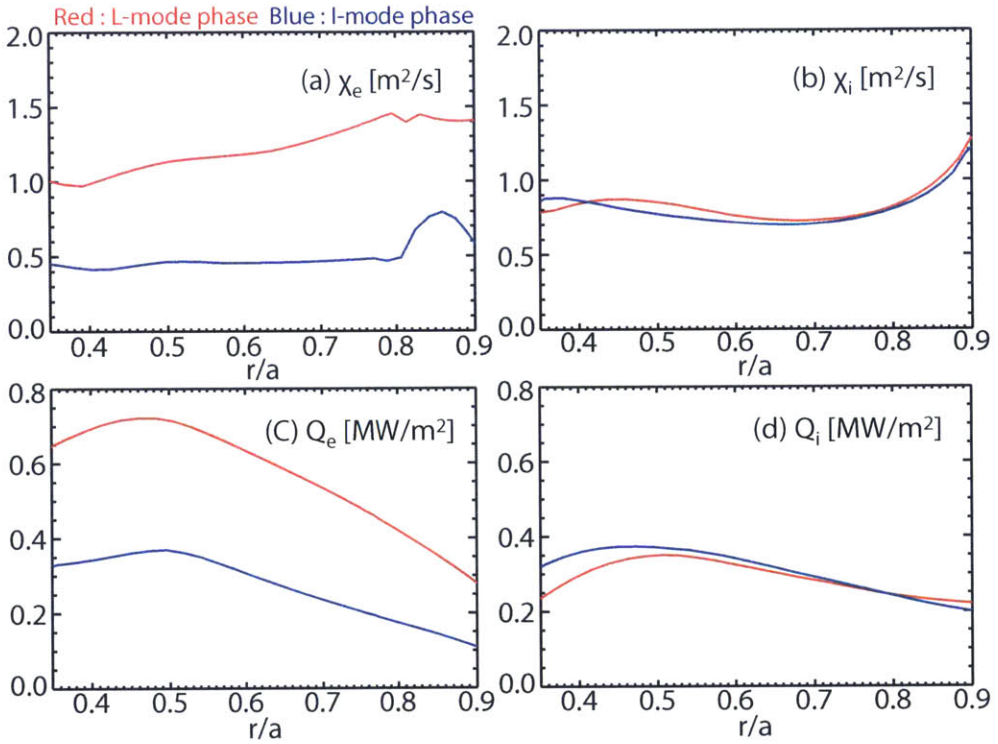

Figure 6-10: Heat diffusivity and flux for L- and I-mode phases in one C-Mod discharge (shot 1101209029) (red : L-mode phase (t=0.836s), blue : I-mode phase (t=0.938s)) (a) Electron heat diffusivity (χ_e $[m^2/s]$) (b) Ion heat diffusivity (χ_i $[m^2/s]$) (c) Electron heat flux (Q_e $[MW/m^2]$), (d) Ion heat flux (Q_i $[MW/m^2]$). A diffusivity, χ is defined as $\chi = Q/n/\partial T/\partial r$.

6.3 Linear stability analysis

In this section, we will investigate the reasons for the reduction of turbulence across the L/I transition via linear stability analysis at r/a=0.6 and 0.8. The profiles shown in Fig. 6-9 were used without modifications in this study. The initial value solver in the GYRO code was used in the linear simulations in this section to find the dominant mode, which has the fastest growth rate. These simulations consider only ion scale turbulence ($k_y\rho_s \leq 1.0$, where k_y is the poloidal wave number and ρ_s is the sound gyroradius of main ion, defined as $\rho_s = c_s/\Omega_{ci}$ with $c_s = \sqrt{T_e/m_i}$ and $\Omega_{ci} = eB/m_ic$), and gyrokinetic ions and driftkinetic electrons were used. In these simulations, a negative real frequency of the unstable mode indicates that this mode propagates in the ion diamagnetic direction (ion mode), and the positive real frequency implies the opposite case (electron mode), as explained in section 3.4.

Figure 6-11 shows the dominant modes in the L- and I-mode phases at r/a=0.6. We first notice that the ion mode is dominant in both L- and I-mode phases. It is also shown that the growth rate of the dominant mode in the I-mode phase is 20-30% lower than the growth rate in the L-mode phase. Considering the variations of the growth rate within the uncertainty of gradient scale lengths, shown in Fig. 6-13, this change may not be remarkable, and it would be reasonable to think that growth rates are comparable between two confinement phases at r/a=0.6. It is noteworthy that the $E \times B$ shearing rate, $\gamma_{E\times B}$, is at $\sim$ 25% of the level of the highest growth rate of the dominant mode in both L- and I-mode phases, as shown in Fig. 6-11.

We then move to the radial location of the linear simulations at r/a=0.8. The results are shown in Fig. 6-12. We note that the linear simulation results at r/a=0.8 are similar to the results at r/a=0.6. In both L- and I-mode phases, the ion modes are dominant, and the growth rates of the dominant modes in the two confinement phases are comparable. $\gamma_{E\times B}$ is about 15% of the maximum growth rate in the L-mode phase, and is about 25% of the maximum growth rate in the I-mode phase. Although the ratio of $\gamma_{E\times B}$ to the maximum growth rate increases in the I-mode phase compared to the L-mode phase, the changes are within the uncertainty and we

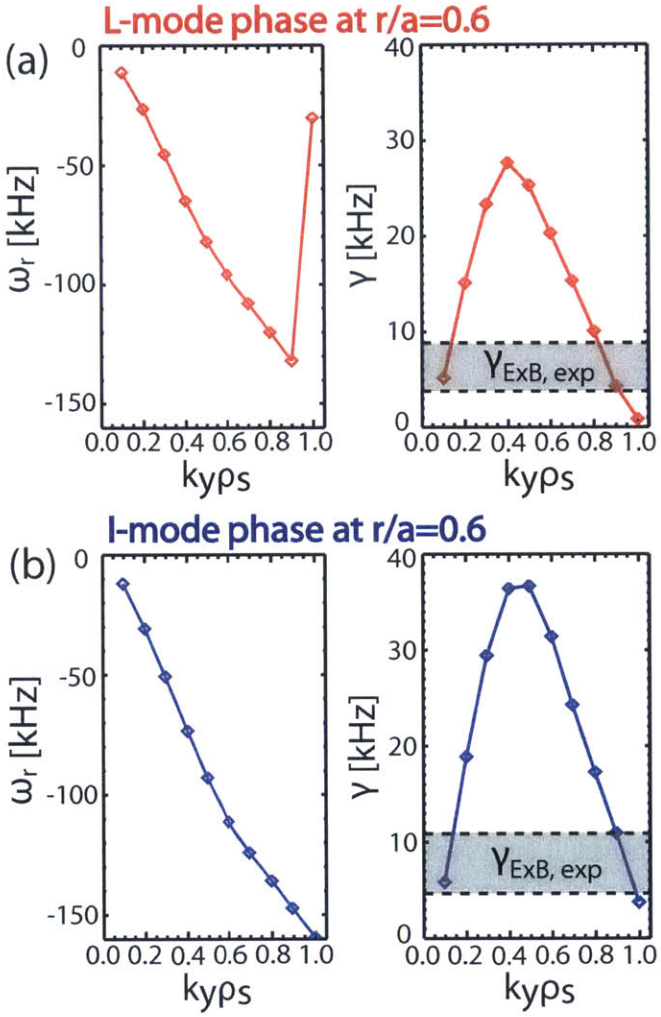

Figure 6-11: Linear stability analysis of (a) the L-mode phase and (b) I-mode phase at r/a=0.6 in one C-Mod discharge (shot 1101209029, t=0.836 (L-mode phase), t=0.938 (I-mode phase)). The left figures show the real frequency of the most unstable mode and the right figures show the growth rate of the unstable mode. The negative real frequency indicates the mode propagating in the ion diamagnetic direction. The shaded area indicates the experimental value of the $E \times B$ shearing rate, $\gamma_{E \times B}$, with 40% uncertainty.

do not observe the $E \times B$ shearing rate comparable to or higher than the maximum linear growth rate, at which point we can expect the suppression of the linear mode by $E \times B$ shearing. Thus, we do not observe the suppression of the dominant mode by $E \times B$ shearing in the I-mode phase in both r/a=0.6 and 0.8, inconsistent with the previous study of H-mode in DIII-D [146] and of I-mode in C-Mod [173]. This inconsistency may suggest that the suppression of turbulence by $E \times B$ shearing is not the main reason for the reduction of T_e fluctuations in the I-mode, or at least, it is not always correlated with the reduction of T_e fluctuations across the L/I transition.

We verified the dominant turbulence mode at r/a=0.6 and 0.8 through sensitivity analysis of the growth rate of the most unstable mode with changes in a/L_{T_e} and a/L_{T_i}. The results of this analysis are shown in Fig. 6-13. The + mark in Fig. 6-13 indicates the experimental values of a/L_{T_e} and a/L_{T_i}, and the extended + mark by the dotted line shows the estimated uncertainty (30% for a/L_{T_i} and 20% for a/L_{T_e}). If the extended + sign is in the region where the growth rate is sensitive to a/L_{T_i}, this result will indicate that the dominant mode is the ITG mode. In the opposite case, the dominant mode will be the TEM. If the extended + sign is near the boundary between these two regions, the TEM and ITG modes are comparable. Figure 6-13 shows that the extended + sign is in the ITG dominant region in both L- and I-mode phases in both locations, r/a=0.6 and 0.8. Thus, the dominant modes found in Fig. 6-11 and 6-12 are ITG mode, and we do not observe the changes in the dominant mode between the L- and I-mode phases in r/a=0.6 and 0.8.

Although we do not observe a correlation between the changes in the simulated turbulence and the reduction of T_e fluctuations across the L/I transition, we learned that $E \times B$ shearing may not be responsible for the reduction of T_e fluctuations in I-mode compared to L-mode. However, we must note that only linear stability analysis was performed in this section, and a more realistic picture should be obtained through non-linear simulations. The results or any conclusions from the linear simulations will be preliminary until nonlinear simulations are done in the future.

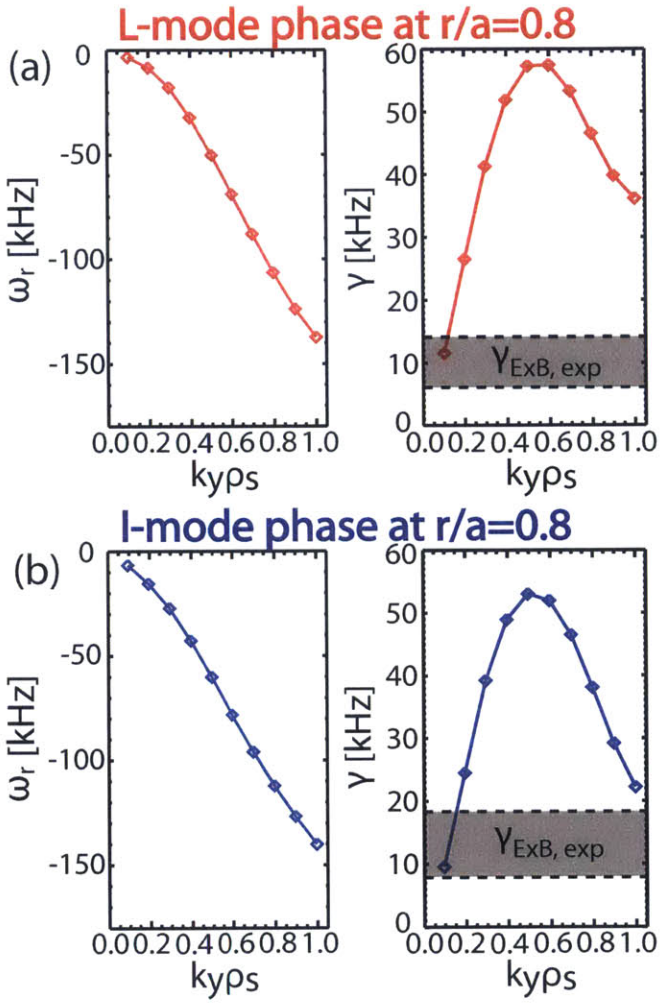

Figure 6-12: Linear stability analysis of (a) the L-mode phase and (b) I-mode phase at r/a=0.8 in one C-Mod discharge (shot 1101209029 t=0.836 (L-mode phase), t=0.938 (I-mode phase)). The left figures show the real frequency of the most unstable mode and the right figures show the growth rate of the unstable mode. The negative real frequency indicates the mode propagating in the ion diamagnetic direction. The shaded area indicates the experimental value of $E \times B$ shearing rate, $\gamma_{E \times B}$, with 40% uncertainty.

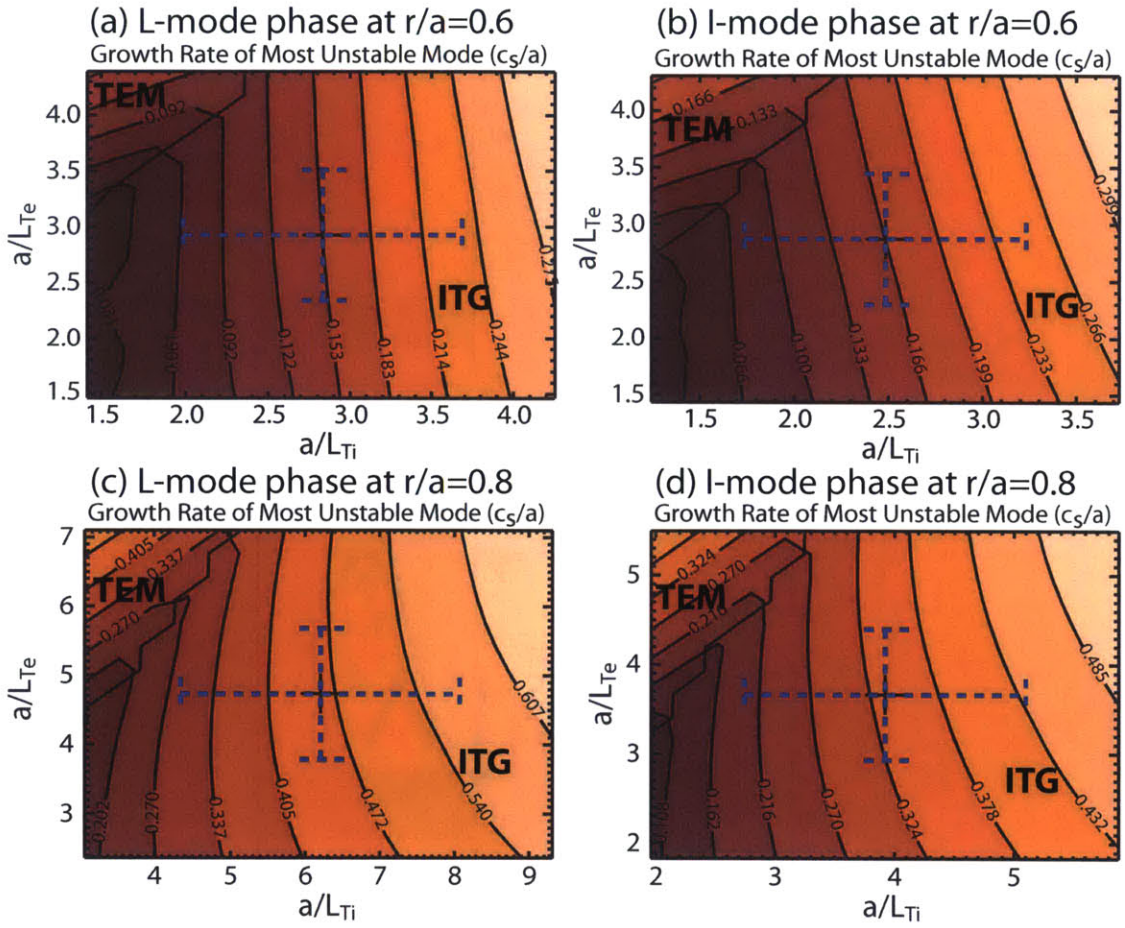

Figure 6-13: Contour of the growth rate of the most unstable mode with changes in a/L_{T_e} and a/L_{T_i} in the $k_y\rho_s$ range [0.1-0.75] in (a) the L-mode phase (shot 1101209029, t=0.836s) at r/a=0.6 and (b) the I-mode phase (shot 1101209029, t=0.938s) at r/a=0.6 (c) the L-mode phase at r/a=0.8 (d) the I-mode phase at r/a=0.8. The + mark indicates the experimental values, and the extended + sign by dotted line indicates the uncertainty.

6.4 Profile shape variations in high energy/particle confinement regime compared to low energy/particle confinement regime

In this section, we will explore the change of profile self-similarity with different confinement phases: L/I/H-modes. In one discharge (shot 1120824006), three different confinement phases were obtained. Table 6.1 shows the discharge conditions. This discharge was run in the Lower Single Null (LSN) configuration with toroidal magnetic field, B_t=5.5T, plasma current, I_p=1.0MA, and the following shape parameters: elongation, κ=1.6, upper triangularity, δ_u=0.3, lower triangularity, δ_l=0.5 with unfavorable ion ∇B drift direction, pointing away from the x-point. These parameters were constant regardless of confinement regime as shown in Table 6.1. We also notice the increase of the average electron density by about 40% in the H-mode phase compared to L- and I-modes, while the difference in the average electron density between L-mode and I-mode is about 5%. Figure 6-14(a) shows the n_e fluctuations measured by the reflectometry [46] channel near the edge (r/a$\sim$0.99) with different confinement phases, and Fig. 6-14(b)-(d) show the changes in RF heating power [MW], electron temperature on the magnetic axis, and electron temperature near the edge ($\rho \sim 0.9$). In this discharge, the plasma accessed the I-mode phase, which can be identified by appearance of the Weakly Coherent Mode (WCM) [180], between t$\sim$0.6-0.8s, in the edge region. From t$\sim$0.8s, the WCM disappeared and fluctuations were suppressed, which indicates the plasma went into the Edge Localized Mode (ELM)-free H-mode phase [63] until t$\sim$1.0s. At t$\sim$1.0s, the RF power was tripped, and the plasma went back into the L-mode phase. After RF power was recovered to the level at t=0.8s, L/I transition and back transition occurred repeatedly. As a result, we can see the WCM and broadband fluctuations up to 200kHz repeatedly as well. We determined the time range for the analysis in each confinement phase as the region which has steady on-axis T_e and T_e near the edge ($\rho \sim 0.9$), as represented by the shaded area in Fig. 6-14.

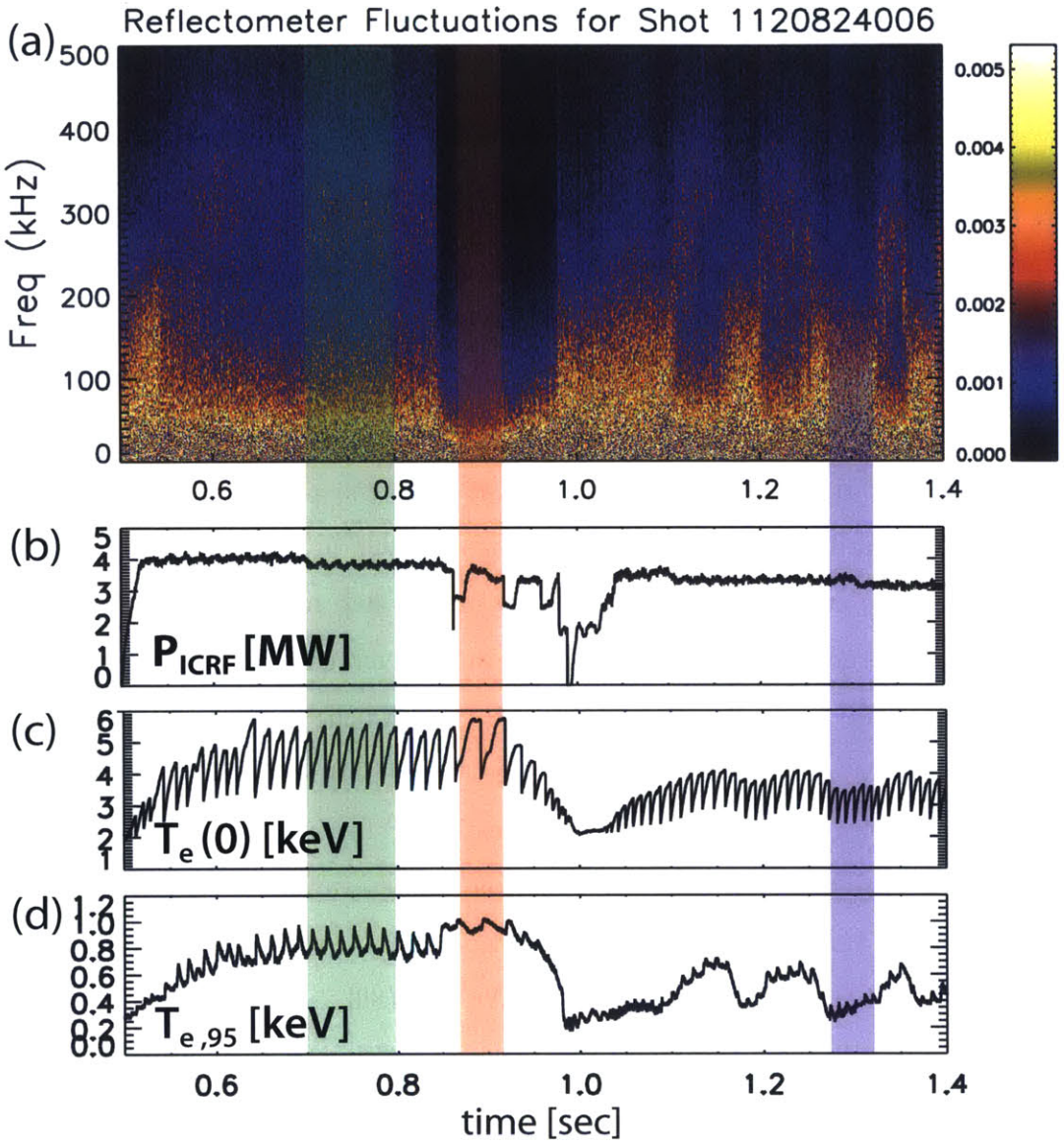

Figure 6-14: (a) Edge fluctuations of an L/I/H transition discharge measured by reflectometry (b) RF heating power (c) T_e on the magnetic axis (d) T_e near the edge (ρ ~0.9). The shaded regions indicate the different confinement phases used in the analysis (Blue : L-mode, Green : I-mode, Red : H-mode)

	L-mode	I-mode	H-mode
magnetic configuration	LSN	LSN	LSN
$B_t(0)$ [T]	5.5	5.5	5.5
I_p [MA]	1.0	1.0	1.0
$n_{e,avg}$ $[10^{20}m^{-3}]$	1.4	1.4	2.0
κ	1.6	1.6	1.6
δ_u	0.3	0.3	0.3
δ_l	0.5	0.5	0.5

Table 6.1: Discharge conditions of the three confinement phases (L-mode, I-mode and H-mode) in one RF heated discharge. Discharge conditions shown in this table are magnetic configuration (whether Lower Single Null (LSN) or Upper Single Null (USN) or double null configuration), magnetic field on the axis, $B_t(0)$ in Tesla, plasma current, I_p, in MA, average electron density, $n_{e,avg}$, in $10^{20}m^{-3}$, elongation, κ, upper triangularity, δ_u, and lower triangularity, δ_l. All shaping parameters (κ,δ_u and δ_l) are the values estimated at the separatrix.

We will first investigate the changes in the shape of the T_e profiles with different confinement phases (L/I/H-modes). Figure 6-15(a) shows T_e profiles with fitting lines in the whole radial region. In all three confinement phases, T_e data in the core region, at least $\rho > 0.5$, are well fit by exponential functions. In Fig. 6-15(b), we can see that T_e data normalized by $T_e(0.8)$ overlap in the ρ <0.8 region for L/I/H-modes, which indicates that the exponential fitting parameter, λ_{T_e}, does not change significantly across the L to I/H transition. Table 6.2 shows that λ_{T_e} varies by about 10% among L/I/H-modes. These results indicate that T_e profiles in the core region are self-similar across the L to I/H transition. At the same time, we note differences in T_e data in the edge region between the low energy confinement regime (L-mode) and the high energy confinement regimes (I/H-modes). In L-mode, edge T_e data are not on the exponential fit line as we observed in the Ohmic and RF heated L-mode discharges in Chapter 4 and 5, while edge T_e data in I/H-modes are well fit by the exponential fit line up to the top of the pedestal region. Thus, in this discharge, the radial region where self-similarity is valid extends to the top of the pedestal region in high energy confinement regimes such as I/H-modes. In other words, the value of $\rho_{ped,Te}$ increases in I- and H-modes compared to L-mode. Table 6.2 shows $\rho_{ped,Te}$ increases from 0.75 to 0.96 and 0.97 in I- and H-modes, respectively. From Fig. 6-15(c) and Table 6.2,

we also see that the slope of the linear fit, μ_{T_e}, increases by more than a factor of five in I/H-modes compared to L-mode, while the T_e value at $\rho = 1.0$ from the linear fit, $T_{e,edge}$, is similar in I-mode, and even smaller in H-mode compared to L-mode. These results may suggest that the increase of μ_{T_e} associated with ρ_{ped,T_e} correlates with the higher energy confinement.

In contrast to the T_e profiles, the shape of the core n_e profiles does change in H-mode. Figure 6-15(d) and Table 6.2 show that the exponential fitting parameter of core n_e profile, λ_{n_e}, decreases by about 50% in H-mode compared to L/I-modes, while the λ_{n_e} values between L- and I-modes are almost the same. Figure 6-15(e) shows that core n_e data normalized by $n_e(0.8)$ in L-mode overlap with the normalized core n_e values in I-mode, while the normalized data in H-mode are lower than L/I modes in the core region, which confirms the lower λ_{n_e} in H-mode compared to L/I-modes. The pedestal structure is shown clearly in the H-mode n_e profiles in Fig. 6-15(f). Figure 6-15(f) also shows that a linear fit works well in the pedestal region. The pedestal in the H-mode n_e profile results in the remarkable increase of the slope of the linear fit, μ_{n_e} and the increase of $n_e(0.8)$ by 60-80% in H-mode compared to L/I-modes as shown in both Fig. 6-15(f) and Table 6.2. If we assume that the edge n_e profile sets the boundary condition for the core n_e profile, the decrease of $n_{e,edge}$ by about 30% will not contribute to the increase of core n_e profile in H-mode, but the significant increase of μ_{n_e} in H-mode compared to L/I-modes will be the reason for the increase of the core n_e profile in H-mode. The increase of μ_{n_e} in the high particle confinement regime (H-mode) is analogous to the change in the edge T_e profile in high energy confinement regimes (I/H-modes) compared to L-mode. In other words, as we observed in T_e profiles, the increase of μ_{n_e} correlates with the increase of the core n_e profile and the improvement of particle confinement in H-mode.

We also notice the sixfold increase in μ_{n_e} in I-mode compared to L-mode from Fig. 6-15(f) and Table 6.2. However, the $n_e(0.8)$ value increases by about 10% in I-mode compared to L-mode and the scattered n_e data in L- and I-modes overlap each other in the whole radial region. The sixfold difference is therefore due to lack of accurate measurements. We also note that the increase of μ_{n_e} is not always observed

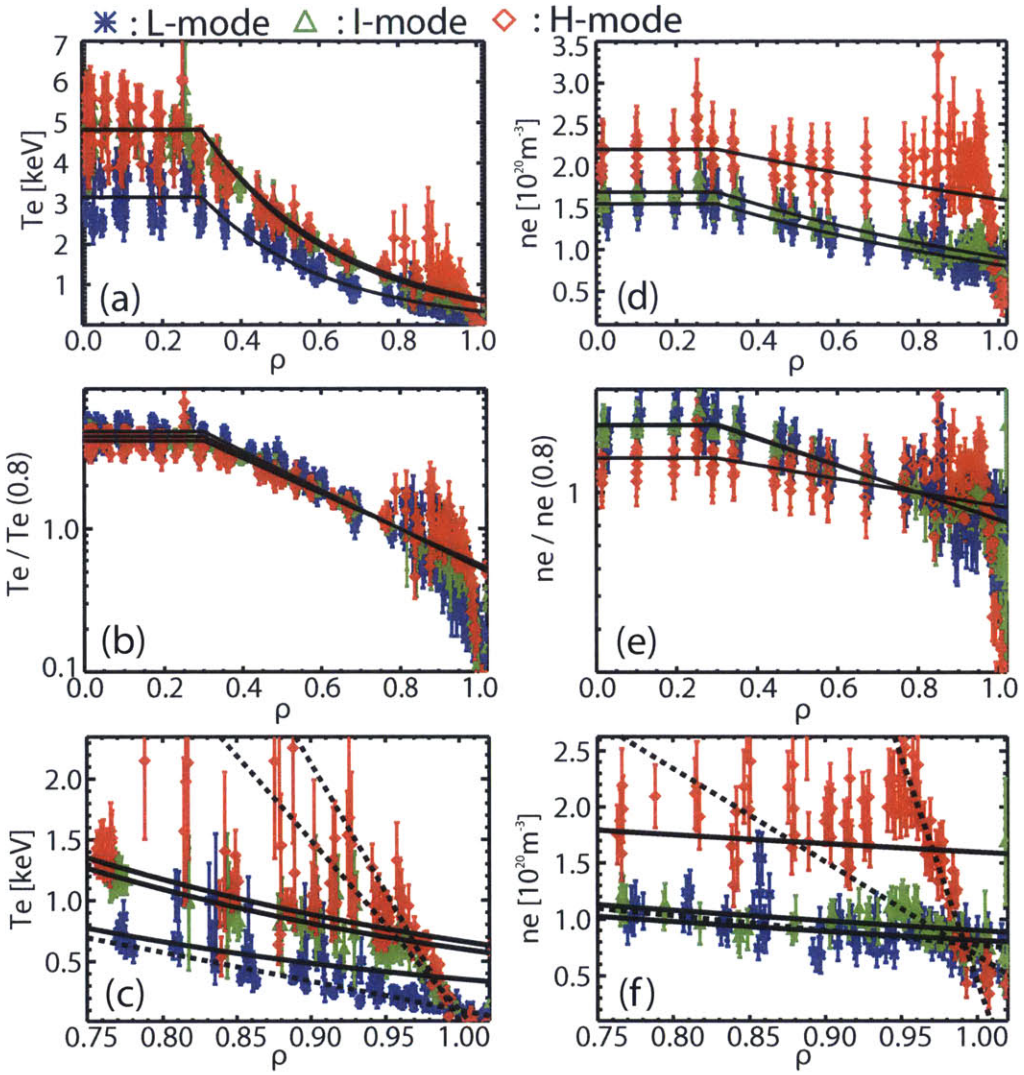

Figure 6-15: T_e profiles in L/I/H-modes (blue : L-mode, green : I-mode, red : H-mode) with the fitting lines (solid line : exponential fitting line for the core profile, dashed line : linear fitting line for the edge profile). (a) T_e profiles with the exponential fitting line in linear scale (b) The normalized T_e profiles by $T_e(0.8)$ with the exponential fitting line in log scale (c) Edge T_e profiles with the fitting lines (d) n_e profiles with the fitting lines in linear scale (e) The normalized n_e profiles by $n_e(0.8)$ with the exponential fitting line in log scale (f) Edge n_e profiles with the fitting lines.

	Parameters	L-mode	I-mode	H-mode
core T_e	λ_{T_e}	3.12	2.97	2.83
($\rho \leq \rho_{ped,T_e}$)	$T_e(0.8)$ [keV]	0.66	1.09	1.17
edge T_e	μ_{T_e} [keV]	2.38	13.93	21.21
($\rho \geq \rho_{ped,T_e}$)	$T_{e,edge}$ [keV]	0.1	0.1	0.01
	ρ_{ped,T_e}	0.75	0.96	0.97
core n_e	λ_{n_e}	0.92	0.90	0.46
($\rho \leq \rho_{ped,n_e}$)	$n_e(0.8)$ [$10^{20}m^{-3}$]	0.98	1.08	1.75
edge n_e	μ_{n_e} [$10^{20}m^{-3}$]	1.29	8.31	39.89
($\rho \geq \rho_{ped,n_e}$)	$n_{e,edge}$ [$10^{20}m^{-3}$]	0.77	0.68	0.46
	ρ_{ped,n_e}	0.92	0.97	0.97
	$P_e(0.8)$ [kPa]	10.35	18.84	32.76

Table 6.2: Parameters calculated from fitting with the different confinement phases (L/I/H-modes) in one discharge. λ_{T_e} is an exponential fitting parameter for the core T_e profile, and μ_{T_e} is the slope of the linear fitting line applied to the edge T_e profile. $T_{e,edge}$ indicates the T_e value at $\rho = 1.0$ from the linear fitting line applied to the edge T_e profile. $\rho_{ped,Te}$ is the radial location which has the minimum difference between the exponential and linear fitting line. The same definitions are applied to λ_{n_e}, μ_{n_e}, $n_{e,edge}$ and $\rho_{ped,ne}$ for n_e profiles.

across the L/I transition in other discharges. These observations may indicate that the changes in the edge n_e profile in I-mode compared to L-mode are inconclusive in this study and not remarkable compared to the change of both shape and amplitude of the n_e profile in H-mode.

The changes in the n_e profile in H-mode are associated with not only a higher slope of the linear fitting line in the edge region, μ_{n_e}, but also with the lower exponential fitting parameter in the core region, λ_{n_e}. Studies in the past have shown density peaking with lower collisionality [10, 60]. Using the definition of collisionality, $\nu_{eff} = 0.1 Z_{eff} < n_e > R/ < T_e >^2$, where <> indicates the volume averaged quantity, major radius, R, is in m and $< n_e >$ and $< T_e >$ are measured in $10^{19}m^{-3}$ and keV, respectively, Z_{eff} was set to 2.0, in [60], ν_{eff} ~0.81 and $n_e(0)/ < n_e > \sim$ 1.2 at the H-mode phase in this discharge. These values are qualitatively consistent with Fig. 2 in [60], which implies that the decrease of the exponential fitting parameter, λ_{n_e}, may also correlate with collisionality. Other previous studies also show that the shape of the n_e profile may vary with collisionality, external heating power or the dominant turbulence mode, while the gradient scale length of T_e profile varies

relatively less [11, 52, 160]. Understanding the change of the core n_e profile shape (or density peaking) will require more sophisticated analysis and data sorting such as comparison data with different collisionality or dominant turbulence mode obtained from gyrokinetic analysis as well as different particle confinement regimes, which are beyond the scope of this study.

6.5 Discussion & Summary

In this chapter, we presented the change in T_e fluctuations inside the pedestal region in I-mode compared to L-mode. The core T_e fluctuations in I-mode plasmas are reduced compared to the fluctuations in L-mode plasmas. From the comparison of T_e fluctuations in the L/I transition discharge with the L-mode discharge with an RF power scan, we can confirm that the change in T_e fluctuations is associated with the change in confinement regime, not the change in RF power. CECE measurements in I-mode plasmas imply that not only edge turbulence but also core turbulence in I-mode should be investigated to understand L/I transition physics.

The changes in T_e fluctuations in H-mode compared to L- or I-mode are not shown in this study. This is because we do not find an appropriate set of discharges which could be used for this comparison. The unstable density level in many H-mode plasmas in C-Mod or high density level near the cutoff of the CECE signals makes CECE measurements difficult in H-mode plasmas. Nevertheless, it is noteworthy that no strong T_e fluctuations were observed in C-Mod H-mode plasmas in the 2012 campaign. This may suggest that the T_e fluctuations are reduced in H-mode compare to L-mode. Dedicated experiments should be planned in the future to study the changes in T_e fluctuations across the L/H transition and also across the I/H transition.

In order to understand the reduction in T_e fluctuations across the L/I transition and the changes in core turbulence and transport, we investigated changes in profiles and experimental heat transport between L- and I-mode phases in one C-Mod discharge. It was observed that a/L_{T_i} was reduced in the I-mode phase compared to the L-mode, while a/L_{T_e} and a/L_n were remained at similar levels across the L/I

transition. Power balance analysis shows the reduction of electron heat transport in the I-mode phase with a similar level of ion heat transport. These observations can be linked to the reduction of T_e fluctuations in I-mode.

Linear stability analysis was performed at r/a=0.6 and 0.8 for the same discharge used in the profile analysis and power balance analysis. We do not observe any significant changes in the dominant mode across the L/I transition in either location. In both L- and I-mode phases, the ITG mode is dominant, and their growth rates are similar. Previous studies showed a correlation between the turbulence suppression by $E \times B$ shearing and the reduction of core turbulence in the high energy confinement regime (in I-mode [173] and in H-mode [146]). However, neither the increase of $E \times B$ shearing rate nor $E \times B$ shearing rate higher than or comparable with the maximum growth rate of the dominant mode is observed in this analysis. It is noteworthy that a different I-mode discharge (shot 1110215023) was used for linear stability analysis in [173] although the discharge used in this study (shot 1101209029) was discussed in [173]. We may need a larger data set to decide whether or not these discharges are outliers. Nevertheless, we can say that $E \times B$ shearing may not always be the reason for the reduction of turbulence and transport across the L/I transition. It is noteworthy that linear analysis is not enough to understand a role of $E \times B$ shearing. Further study using nonlinear analysis is therefore required.

We compared n_e and T_e profiles in different energy confinement regimes (L/I/H-modes) for one discharge. We showed that an exponential fit is valid and similar λ_{T_e} values are used in core T_e profiles regardless of confinement regime. However, the core region of the T_e profile, where an exponential fit is valid, extends outward radially towards the top of the pedestal region in I/H-modes in this discharge. Considering the pedestal as the region where the transport properties start to change from the core region, this observation supports the use of the term "pedestal" in L-mode discharges in [142]. This is because the core gradient scale length, one of the parameters related to transport behavior in the core region, starts to change near $\rho \sim 0.8$ in the L-mode T_e profile as it changes from the top of the pedestal in I/H-mode T_e profiles.

It was observed that the slope of the linear fitting for core T_e profiles, μ_{T_e}, increases

more than five times with comparable or lower $T_{e,edge}$ values in I/H-modes compared to L-mode, while λ_{T_e} in the core region varies by around 10% in all confinement regimes, implying that μ_{T_e} correlates with the improvement of energy confinement. We also observed a remarkable increase in μ_{n_e} in H-mode compared to L/I-modes. Although λ_{n_e} decreases in H-mode compared to L/I-modes, this decrease will cause lower particle confinement, indicating that the increase of μ_{n_e} correlates with the improvement of particle confinement as the increase of μ_{T_e} does with the improvement of energy confinement. This finding is consistent with previous studies, which show the correlation between the edge profile and global confinement [63, 62, 118].

However, self-similarity analysis also shows that the extension of the self-similar region in T_e profiles from $\rho \sim 0.8$ to the top of the pedestal is related to the improvement of global energy confinement. The next question will then be about the relation between extension of the self-similarity region and the increase of μ_{T_e}. Assuming the critical gradient model and causality between stiffness (in terms of local heat flux change with the gradient scale length) and self-similarity, it is possible to explain the extension of the self-similarity region as the result of the increase of T_e at $0.8< \rho <0.95$ with the higher value of μ_{T_e}. The low T_e in the edge region makes a/L_{T_e} higher than the critical gradient scale length, making the edge region non-stiff [56]. We also see the non-stiffness with low T_e as the decrease of gyro-Bohm power level, the saturated level of the conducted heat flux by turbulent transport. Since gyro-Bohm power is proportional to $T_e^{5/2}$ [48], the lower T_e in the edge region compared to the core region will result in the gyro-Bohm power being lower than the total conduction heat power in the edge region. Thus, the gradient will not be held constant by turbulent transport, but will vary with the total conducted heat flux, making the profile non-stiff. It is noteworthy that the extension of the self-similarity region was also observed in the L-mode discharges with different RF powers in ASDEX-U[138]. In [138], the self-similarity region extends radially outward as RF power increases. This can be explained by the increase of gyro-Bohm power with the increase of temperature. Figures 4 and 6 in [138] show that the gradient scale length of T_e increases abruptly as the value of T_e decreases below a certain value and electron heat trans-

port becomes non-stiff when a gradient scale length of T_e is above a certain point. Figure 1 in [48] also shows that the experimental temperature gradient scale length tends to separate from the critical gradient scale length, as experimental diffusivity is larger than gyro-Bohm diffusivity. Assuming electron heat transport at $0.8< \rho <0.95$ is non-stiff in L-mode, then the increase of μ_{T_e} will increase T_e and decrease a/L_{T_e} and increase gyro-Bohm heat flux, moving this region ($0.8< \rho <0.95$) from non-stiff to stiff. If the total conducted heat power is lower than the gyro-Bohm heat flux and the critical gradient scale length at $0.8< \rho <0.95$ is close to the critical gradient scale length at $\rho >0.8$, then the profile at $0.8< \rho <0.95$ will also show self-similarity. It is noteworthy that several assumptions are made in this explanation, and these assumptions should be proven in the future. We should note that it is also possible that the extension of the self-similarity region up to $\rho \sim 0.95$ with the fixed $T_{e,edge}$ results in the increase of μ_{T_e} or that these two changes do not have a cause-effect relationship. As suggested in [173], localized edge heating may elucidate the relation between the extension of self-similarity and the increase in μ_{T_e} across the L to I/H transition.

We must note that the previous study in ASDEX-U indicates that the extension of self-similarity region do not have to correlate with the confinement regime. Figure 26(a) in [142] also shows that the outer boundary of the self-similarity region, ρ_{ped}, varies from 0.65 to 0.9 in both T_e and n_e profiles. It will be of interest to investigate the extension of the self-similarity region with different discharge conditions in each confinement regime in the future. An exponential fit is also valid for core n_e profiles in all L/I/H-modes. However, the exponential fitting parameter for the core n_e profile, λ_{n_e}, decreases in H-mode compared to L/I-modes, and it is inconclusive whether the self-similarity region in n_e profiles extends radially outward in H-mode compared to L/I-modes. In addition, it is noteworthy that the self-similar n_e and T_e profiles observed in section 6.4 are consistent with the profile analysis results in section 6.2.

Although T_e fluctuation measurements in this chapter were not performed in the region where T_e profiles are self-similar in all confinement regimes (L/I/H-modes), it is worth noting that the reduction of turbulence in the high energy confinement regimes

(I/H-modes) compared to the low energy confinement regime (L-mode) occurs not only in the edge region but also in the core region, where T_e profiles are self-similar [145, 173]. These studies indicate that the global confinement change is associated with the change not only in the edge region but also in the core region. We may need to consider the relationship among the change of core turbulence, profile self-similarity in the core region and its extension, and the change in edge turbulence and edge profiles to understand the physics related to the change in global confinement.

Chapter 7

Conclusions & Future Work

This thesis work was motivated by anomalous transport in fusion plasmas, introduced in Chapter 1. In order to measure local T_e fluctuations, a new Correlation Electron Cyclotron Emission (CECE) diagnostic was designed and installed in C-Mod, as described in Chapter 2. In Chapter 3, we explained four analysis methods used to investigate the important transport topics in Alcator C-Mod plasmas in this thesis. They are CECE signal analysis, profile analysis, power balance transport analysis using the code, TRANSP [4], and gyrokinetic analysis through the gyrokinetic simulation code, GYRO [28]. It is noteworthy that two different profile analyses were introduced in this chapter. The first analysis method is fitting the profile using B-spline fitting to prepare the input profiles for TRANSP and GYRO. The second analysis method is self-similarity analysis to observe changes in the self-similarity property of the profiles. The second analysis method is adopted from [142]. In Chapter 4, Ohmic confinement transition physics were investigated and we performed a validation study of the gyrokinetic model for electrostatic ion scale turbulence in C-Mod Ohmic discharges. The correlation of rotation reversals and changes in transport was explored in Chapter 5. We also studied transport behavior changes across the low to high confinement regime transition in Chapter 6. This chapter presents conclusions drawn from Chapters 2-6 and future work inspired by this thesis.

7.1 Conclusions

7.1.1 Summary of T_e fluctuation measurements in Alcator C-Mod

Using constraints obtained from gyrokinetic simulations [176], a new CECE diagnostic was designed, built, and installed in C-Mod. Through upgrades in optics and electronics, we learned that the beam pattern of the CECE optics was one of the most important parameters in the CECE measurements. This result is consistent with the predictions from gyrokinetic simulation (GYRO) results [176], which showed that low poloidal resolution, determined by the beam pattern, was the reason for the null results in the past attempt [168]. High poloidal resolution in the CECE measurements in C-Mod would be related to its high magnetic field. As explained in Chapter 1, the turbulent eddy size for ion scale turbulence is on the order of the ion gyroradius, proportional to 1/B with magnetic field, B. This indicates smaller turbulent eddy size with higher magnetic field. Thus, the unique high magnetic field in C-Mod may make the CECE measurement difficult compared to other Tokamak experiments. Considering that next generation Tokamaks will have high magnetic fields similar to or higher than C-Mod [12, 107], these measurement results will be a good reference for T_e fluctuation measurements in the future Tokamak experiments.

This thesis also provides new experimental observations in each research topic studied in Chapters 4-6. In chapter 4, we found that T_e fluctuations near the edge region tend to decrease across the Ohmic confinement transition. In Chapter 5, we presented a reduction of T_e fluctuations across the rotation reversal in the RF heated discharge. This is consistent with the observations in Chapter 4, since rotation reversals occur across the Ohmic confinement transition. However, we found that T_e fluctuations are correlated with the increase of average density level, not with the rotation reversal directly. In Chapter 6, it was shown that T_e fluctuations decrease in the high confinement regime compared to the low confinement regime. The correlations between T_e fluctuations and these phenomena indicate that T_e fluctuations

are transport relevant. These measurements confirmed the importance of fluctuation measurements for fusion transport research.

7.1.2 Ohmic confinement transition physics and validation study of the gyrokinetic model

In Chapter 4, the Ohmic confinement transition (LOC/SOC transition) was studied using the four analysis methods introduced in Chapter 3. As mentioned in section 7.1.1, we found a reduction of T_e fluctuations near the edge region (r/a$\sim$0.85) across the LOC/SOC transition. Self-similarity analysis also showed that the changes in edge n_e and T_e profiles are correlated with the LOC/SOC transition. We also notice an increase in ion heat flux with no significant changes outside of the uncertainty in the electron heat transport in the SOC plasma compared to the LOC plasma in $r/a > 0.4$ from experimental power balance analysis using TRANSP. However, most of the turbulence relevant profiles, such as gradient scale length, are similar within the uncertainties, and gyrokinetic analysis via GYRO considering electrostatic ion scale turbulence suggests no linear mode transition across the Ohmic confinement transition.

The validation study of the electrostatic gyrokinetic model including ion scale turbulence was also performed for the LOC and SOC plasmas near the edge region (r/a$\sim$0.85) by comparing simulated heat fluxes and synthetic T_e fluctuations with the experiments. The existing synthetic CECE diagnostic was improved for the CECE diagnostic in C-Mod for this validation study, as explained in Chapter 3. We found that GYRO can reproduce ion heat flux and local T_e fluctuation levels and spectral shape within the uncertainties, while the simulated electron heat flux is underestimated outside of the uncertainties in both LOC and SOC discharges. It is noteworthy that ion heat transport will be mainly driven by ion scale turbulence and synthetic T_e fluctuations also come from the ion scale turbulence ($k_y\rho_s < 0.3$), while electron heat transport can be driven by both electron and ion scale turbulence. Thus, the validation results, matching both ion heat flux and synthetic T_e fluctuations with the

underestimated electron heat flux, suggest that the contribution of electron scale turbulence (ETG) may be significant near the edge region in C-Mod Ohmic discharges.

Although further study is required to elucidate the LOC/SOC transition physics from the results obtained in Chapter 4, we found that the conventional interpretation of the Ohmic confinement transition, which is that linear mode transition from TEM to ITG is responsible for this transition (LOC - TEM, SOC - ITG), should be revised. First, gyrokinetic analysis suggests no ITG/TEM transition across the Ohmic confinement transition. The validation study results also suggest the importance of ETG modes in C-Mod Ohmic discharges. Thus, instead of a simple linear picture, a more realistic picture should be considered for the LOC/SOC transition, which includes nonlinear interactions of turbulence modes including both ion and electron scale turbulence. We found a correlation between T_e fluctuations at r/a$\sim$0.85 and edge profile changes resolved from self-similarity analysis with the Ohmic confinement transition. In other words, changes in turbulence near the edge and edge radial pressure profiles are correlated with the global confinement transition. We must also note that the predominant interpretation, a simple linear picture of the Ohmic confinement transition, did not specify any local positions. In the future, it is worth studying which radial region is responsible for this global confinement transition in the Ohmic discharges. Further study is required to obtain a more realistic picture of the Ohmic confinement transition.

7.1.3 Rotation reversals in RF heated discharges

In C-Mod, it was observed that the toroidal rotation reverses with an increase in average density, and that the critical density of the Ohmic rotation reversal is well matched with the critical density of the Ohmic confinement transition [129]. The direction of core toroidal rotation was also used to determine the Ohmic confinement regime in this thesis. It is noteworthy that rotation reversals occur in RF heated L-mode discharges with a scan of average density as well [123, 175]. In Chapter 5, we found similarities between the pair of RF discharges rotating in opposite directions with different average density levels and the LOC and SOC discharges studied in

Chapter 4 via analysis methods explained in Chapter 3. We first presented a reduction of T_e fluctuations near the edge across rotation reversal in both Ohmic and RF heated discharges. Second, the gradient scale lengths of n_e, T_e, T_i profiles do not vary significantly across the rotation reversal. Third, we found that sawtooth signals tend to have a longer period and be more irregular across the rotation reversal. Fourth, there was no linear transition of the dominant turbulence mode across the rotation reversal in both Ohmic and RF heated discharges. Finally, we found that changes in edge n_e and T_e profiles are correlated with the rotation reversal in both Ohmic and RF discharges.

We must note that rotation reversal occurs with large variations in the average density (50%) in the Ohmic and RF heated discharges used for the comparison in the last paragraph. This large density difference causes the discharge with higher density level to be more collisional in both Ohmic and RF heated discharges. Thus, it is possible that the similarities observed in Ohmic and RF heated discharges are correlated with the collisionality, not the rotation reversal. In the rotation reversal discharge where the rotation reversal occurs with only a slight change in average density ($< 5\%$), we found no changes in either T_e fluctuations near the edge or sawtooth activity across the rotation reversal. The changes in edge profiles obtained from self-similarity analysis are inconclusive due to the large uncertainty of the data in this discharge, but it is evident that the changes in the edge region across the rotation reversal is not clear, while the rotation reversal is observed clearly in this discharge. These results indicate that the similarities found between Ohmic and RF heated discharges are not directly correlated with rotation reversal, but rather correlated with the collisionality. Nevertheless, we should note that rotation reversals are well correlated with the LOC/SOC transition in C-Mod. Further study is required to understand the relationship between rotation reversals and the LOC/SOC transition.

The similarities observed in the Ohmic and RF heated discharges in Chapter 5 indicate that similar changes in profile and turbulence will occur with a scan of density in fusion plasmas regardless of plasma heating method. In other words, the Ohmic confinement transition is not an issue limited to only Ohmic discharges. This

observation also suggests that the physics related to rotation reversals in RF heated discharges is related to the physics of the LOC/SOC transition and rotation reversals in Ohmic discharges.

7.1.4 Transport analyses in high confinement regime: I-mode and H-mode

This thesis showed that core T_e fluctuations inside the pedestal region were reduced across the transition from L-mode to I-mode. Previous work in DIII-D showed a reduction of core T_e fluctuations in H-mode compared to L-mode [146]. As explained in Chapter 1, I-mode is a high energy confinement regime, but not a high particle confinement regime, while H-mode is a high energy and particle confinement regime. Thus, the previous study in DIII-D [146], which showed a reduction of core T_e fluctuations across the L/H transition, and the T_e fluctuation measurements in I-mode in this thesis suggest that core T_e fluctuations are reduced in high energy confinement regimes compared to low energy confinement regimes. I-mode was accessed by increasing the external RF heating power in the discharges with CECE measurements in this study. To separate the correlation of T_e fluctuations with the confinement regime and with the external heating power, we observed the changes in T_e fluctuations in an L-mode discharge with a scan of external heating power. No significant changes in T_e fluctuations outside the uncertainties were found in this discharge, which indicates that core T_e fluctuations are correlated with the energy confinement regime, not external heating power.

From one C-Mod discharge with an L/I transition, we found a reduction in a/L_{T_i} and electron heat transport in the I-mode phase from profile analysis via B-spline fitting on the data of density and temperature, and also from power balance analysis using TRANSP. However, linear stability analysis using GYRO shows no significant changes in dominant turbulence mode between the L- and the I-mode phases. Further study is required to understand the reduction of T_e fluctuations across the L/I transition.

Self-similarity analysis for one C-Mod discharge with an L/I/H transition showed that the shape of core T_e profiles does not vary with confinement regime (L/I/H-modes), but the self-similar region, where an exponential fit is valid, is extended outward radially towards the top of the pedestal region in high energy confinement regimes (I- and H-modes). This result supports the existence of the "L-mode pedestal" used in [142]. In high confinement regimes, a pedestal region is considered to be the region where the transport properties in the core region start to change. In L-mode, the gradient scale length, which is one of the important parameters related to turbulent transport, starts to change around $\rho \sim 0.8$, where ρ is the square root of the normalized plasma volume, while the gradient scale length of the core profile changes abruptly from the top of pedestal region in high energy confinement regimes. Thus, the edge region, where the linear fit is valid, in L-mode could be termed the "L-mode pedestal."

This analysis also shows that the pedestal region of n_e and T_e profiles in I- and H-modes are well fit by a linear fit as this form works well in the edge L-mode profiles ($\rho \gtrsim 0.8$). We may be able to quantify the pedestal structure in both low and high confinement regimes using the linear fit in the future instead of using the modified tanh fit [65], which is more conventional. It is also noteworthy that this analysis showed that the changes in the edge region associated with the pedestal are correlated with global particle/energy confinement.

7.2 Future work

7.2.1 Improvements in the CECE measurements and analysis

Extension of the T_e fluctuation measurement region

Although we observed a correlation of T_e fluctuations with the Ohmic confinement transition, rotation reversal, and the transition from the low to the high confinement regime, all T_e fluctuation measurements are limited in $r/a \gtrsim 0.75$ in this thesis. This is because the CECE optical system is optimized for measurements near the edge

region (r/a=0.8-0.9). This limitation results in a caveat in the CECE measurements in Ohmic plasmas due to marginal optical depth values, as explained in Chapter 4. Deeper core measurements are also required to draw more solid conclusion. In Chapter 4, we raised the possibility of a correlation between local turbulence changes near the edge and global confinement. However, it is inconclusive whether the reduction of T_e fluctuations across the Ohmic confinement transition occur locally, near the edge region, or globally, in the whole radial region. In Chapter 5, it was shown that T_e fluctuations near the edge are not correlated with the core toroidal reversal. However, we should be cautious to draw a conclusion about the relationship between T_e fluctuations and core rotation reversal until we study the correlation between T_e fluctuations in the core region, where rotation reversals occur ($r/a \lesssim 0.6$), and rotation reversals. Thus, T_e fluctuation measurements deeper in the core region will be useful for further study related to this thesis.

Improvements in the CECE signal analysis

We should note that T_e fluctuation levels in this thesis were obtained by integrating the cross power spectral density in the frequency range where coherent fluctuations are observed. We used the following criteria to determine the frequency range of the turbulent T_e fluctuations. First, the signal should be larger than the statistical level of coherence [17]. Second, the cross phase should be smaller than $\pi/2$ and it should not be fluctuating randomly. Since the two CECE signals used for the correlation analysis come from largely overlapped emission volume, the criteria used here will be reasonable and conservatively correct. However, when we use a CECE diagnostic for other purposes such as the correlation length measurements, they will not be valid. Two signals used in the correlation length measurements may not have an overlapped emission volume, but may rather be separated within the correlation length of the turbulence. Consequently, it is possible to have coherent fluctuations between two CECE signals with a cross phase angle larger than $\pi/2$ in the correlation length measurements. We must note that cross phase signals will not fluctuate randomly even in this case. In this study, the randomness of the cross phase spectrum was

determined "by eye." For future measurements, we should have quantitative criteria to determine the randomness of cross phase signals.

Correlation length and phase angle measurements

In this thesis work, the CECE diagnostic was used to measure only T_e fluctuation levels. We should note that the CECE diagnostic can be used to measure other transport relevant quantities. For example, radial correlation length of T_e fluctuations can be measured by scanning a radial distance with the two channels used for the measurements or by comparing the fluctuation levels obtained from the correlation between one specific channel and other channels which have different radial distances from this channel. It would also be possible to measure the phase angle between electron density fluctuations and electron temperature fluctuations, as performed in the previous study in DIII-D [177] if reflectometry and CECE in C-Mod share the same optical system. Obtaining various fluctuating quantities relevant to turbulent transport will be helpful not only in understanding the transport physics but also in validating the gyrokinetic model.

7.2.2 Reduction of uncertainty in GYRO input parameters

We did not obtain a clear conclusion concerning the correlation between changes in T_e fluctuations and changes in turbulence from the gyrokinetic analysis using GYRO performed in this thesis. In Chapter 4, it is difficult to reproduce the reduction of T_e fluctuations across the LOC/SOC transition in nonlinear GYRO runs due to the large variations in the synthetic T_e fluctuations within the uncertainty of input parameters, especially the gradient scale lengths of profiles (a/L_{T_i}, a/L_{T_e}, and a/L_n) and main ion fraction. When we attempted to interpret T_e fluctuation measurements via gyrokinetic analysis in Chapter 4-6, the changes obtained from gyrokinetic simulations between the discharges that have large difference in the measured T_e fluctuations were usually not meaningful within the uncertainties of the GYRO input parameters.

There are two possible ways to explain these results. First, the uncertainty we

have is too large to obtain (or resolve) meaningful results from GYRO. It is also possible that the gyrokinetic model we used (electrostatic ion scale turbulence) does not have enough physics to interpret changes in T_e fluctuation measurements in C-Mod. To check these possibilities, we need to reduce the uncertainty of GYRO input parameters in the future. Discharges which are steady for longer ($\geq 0.5s$) than the discharge in this study will be helpful in reducing the uncertainty of the profiles of n_e, T_e, and T_i by time averaging. A method which can estimate the main ion fraction more accurately should be developed in the future as well.

7.2.3 Caveats in the self-similarity analysis

We should note that the self-similarity analysis in this thesis has caveats, which should be resolved in the future. First, we note that the linear fit for the edge profiles shown in this thesis does not prove or disprove that the edge region has a constant gradient since it is difficult to resolve the gradient values accurately in the edge region due to the large uncertainty of the measured n_e and T_e data. Nevertheless, the results obtained from the self-similarity analysis in this study show that the linear fit can be applied to the edge region within the uncertainties and that the changes in the edge region with different confinement regimes can be quantified by the linear fit. Second, the exponential fitting parameters for T_e and n_e profiles, λ_{T_e} and λ_{n_e}, have uncertainties of approximately 20-25% due to the uncertainty in core T_e and n_e data. Thus, self-similar core profiles observed in this study do not refer to profiles with the exact same shape, but refer to profiles which have similar shape and whose differences cannot be resolved within the uncertainty of the data. We may need to consider shifting the plasma slightly to obtain better spatial resolution and more accurate gradients of n_e and T_e profiles with smaller uncertainty, as performed in [142, 138]. Dedicated experiments to remove the ambiguities in this study due to large uncertainty should be planned in the future.

7.2.4 Future work in the gyrokinetic analysis

Numerical issues in the GYRO simulations

In Chapter 4, when the synthetic T_e fluctuation spectra are compared with the measured spectra, we observed a spurious peak near 30kHz in the synthetic spectra in both LOC and SOC runs, as shown in Fig. 4-26(c) and (d). This peak in the SOC run was mitigated to a reasonable level by changing the numerical setup for the collision calculation, modifying the order of radial basis functions of the collision operator, ORD_RBF, from 3 to 5. This implies that the peak in the synthetic spectra is a numerical issue related to the collision calculation. Although the LOC run with the modified ORD_RBF value was not performed in this study, we expect the suppression of the peak near 30kHz with the change in ORD_RBF value in the LOC run as well. However, it should be confirmed in the future. It is noteworthy that $Q_i(k_y)$ spectra had a strange peak in low k_y region ($k_y\rho_S < 0.1$) in both LOC and SOC runs, as mentioned in section 4.4.2 and that this peak was also mitigated by changing ORD_RBF from 3 to 5. Thus, the peak in $Q_i(k_y)$ spectrum is also related to collisions. It is noted that the collision calculation in GYRO must be improved for a high collisionality regime such as in the pedestal region and near the edge region where GYRO was performed in Chapter 4 [16]. Thus, it is worth trying in the future to perform another gyrokinetic simulation with the collision operator optimized for high collisionality regime (CGYRO [16]) in order to see whether or not these peaks come from the collision issue and to obtain more accurate gyrokinetic analysis results.

Multi-scale gyrokinetic simulation

In both Chapters 4 and 5, nonlinear GYRO runs including only ion scale turbulence under-predicted electron heat transport, which suggests a non-negligible contribution of electron scale turbulence (ETG) to heat transport. Since it is known that electron scale turbulence nonlinearly interacts with ion scale turbulence [77], the gyrokinetic analysis results, including the simulated ion heat flux and synthetic T_e fluctuations, matched with the experiments, as well as the simulated electron heat flux, obtained

in this thesis should be revised in the future through multi scale simulations, which include both electron and ion scale turbulence. We also should build a high-k scattering system on C-Mod to measure electron scale density fluctuations to provide a new constraint on thes simulations. While quite difficult, it could be possible to measure electron scale electron temperature fluctuations. Such a measurement would likely not use a radiometer, but perhaps a scattering technique could be developed.

GYRO validation procedure

In nonlinear gyrokinetic analysis using GYRO in Chapter 4, we first found heat flux matched simulations. We then compared synthetic T_e fluctuations and performed the sensitivity analysis from these flux matched runs. We observed that synthetic T_e fluctuations differ by only 10% between LOC and SOC runs in the ion heat flux matched simulations, while the measured T_e fluctuations were reduced by 40% in the SOC run compared to the LOC run. Since T_e fluctuations are more closely related to electron heat flux, and GYRO including only ion scale turbulence underpredicted electron heat flux in both LOC and SOC runs, these simulations may not be optimized for the comparison of T_e fluctuations. It will be of interest to see whether the validation results are similar or different when we find a T_e fluctuation matched simulation first, then compare the simulated heat fluxes with the experimental levels.

Further analysis using GYRO

In this thesis, changes in the turbulence simulated by GYRO between two discharges, which are in different confinement regimes or rotate in opposite directions, were studied by comparing the changes in the dominant mode in linear GYRO runs or the propagating direction of the simulated turbulence in non-linear GYRO runs. We also compared the simulated fluctuating quantities and synthetic T_e fluctuations between these discharges. We must note that changes in turbulent transport can be studied by observing other quantities as well. For example, we can obtain a phase angle between fluctuations of density and potential, and fluctuations of temperature and potential from GYRO simulations. As mentioned in section 1.2.1, these phase angles also affect

turbulent particle and heat fluxes. Thus, studying the changes in these phase angles will clarify the changes in the simulated turbulence. Stiffness is another quantity we can study using GYRO simulations in the future. Here, stiffness refers to the ratio of diffusivity (or heat flux) to the difference between the temperature gradient scale length and its critical gradient scale length. It is possible that the stiffness can change without significant changes in the dominant mode in linear runs, as shown in [172]. Thus, it is worth attempting to check the stiffness to determine the changes in the simulated turbulence.

Part I

Appendices

Appendix A

In-vessel mirror alignment procedure

This chapter presents the alignment procedure for the in-vessel mirrors used in the CECE (Correlation Electron Cyclotron Emission) measurements. The alignment procedure consists of two parts: the pre-alignment of the in-vessel mirrors (flat and parabolic mirrors) in the canister and laser pointers used in this alignment in the laboratory, and the installation and alignment of the mirror canister inside vessel. Since the beam pattern is an important parameter in the CECE measurements in C-Mod, we must minimize any anomalous effects on the beam pattern due to misalignment of the mirror. In this study, we used laser pointers to align the in-vessel mirrors and their canister. Although the CECE measurements were successful in the 2012 campaign, the alignment procedure for the in-vessel mirrors was not perfect, and should be improved. The purpose of this chapter is to record what was done for the alignment to improve this procedure in the future.

A.1 Pre-alignments of in-vessel mirrors in the laboratory

Before installing the in-vessel mirrors in the C-Mod Tokamak, we should align the mirrors in the canister, and also align the laser pointers, which will be used for the alignment in the cell. The diagram for this pre-alignment is shown in Fig. A-1.

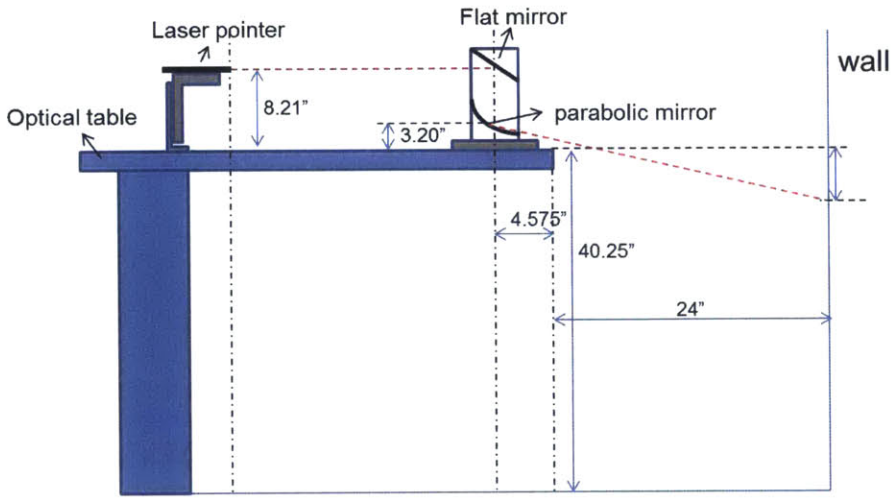

Figure A-1: Block diagram of the set-up for the pre-alignment.

In order to align the in-vessel mirrors, we first should align the laser pointer used to align them. We will call this laser the green laser pointer. The alignment procedure of this laser pointer is as follows:

1. Place the green laser pointer on the xyz stage.

2. Using a ruler as a collimator, check whether or not the laser beam's path is straight. First, place the ruler just in front of laser and check the height and position, as shown in Fig. A-2.

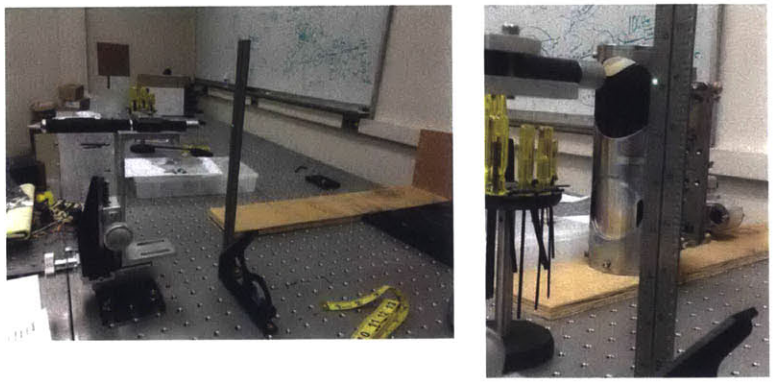

Figure A-2: The setup for the alignment of the laser pointer will be used to align in-vessel mirrors in the canister.

3. Place the ruler away from the laser parallel to the side of the optical table from its original position, and check whether or not the laser hits the same spot

4. By adjusting the position of xyz stage and laser, ensure that the laser hits the

same spot to align the laser beam with the optical table.

5. Iterate procedure 2-4 until laser is aligned.

6. After the alignment is done, mark the spot where the beam hit the wall.

We will then align the in-vessel mirrors using the aligned laser pointer in the following steps:

1. Draw a vertical line on the wall from the marked spot where the aligned laser beam hit the wall.

2. Attach the co-centric target on the flat and parabolic mirror and adjust the canister so that the laser hits the center of the target.

3. Changing the height of the laser pointer, align the position of the canister so that the laser hits the vertical center line of the target.

4. Remove the target on the mirror, and check the laser on the wall. If the laser does not hit the vertical line on the wall, adjust the parabolic mirror, and iterate procedures 2-4 until the laser hits the vertical line. Figure A-3 shows procedures 3 and 4.

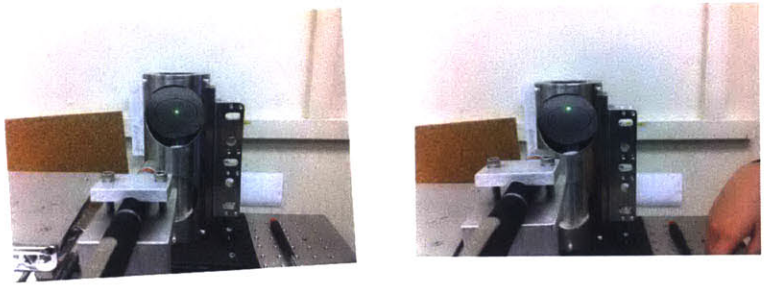

Figure A-3: Procedures 3-4 in the in-vessel mirror alignment in the laboratory.

5. Finally, if the laser hits the vertical line, fix the position of the parabolic mirror.

For the alignment of the mirror canister, four laser pointers in the rack were used. These laser pointers should be aligned first. We aligned the laser pointers in the rack as follows:

1. Using optical mounts or blocks, place the laser pointer rack parallel to the one side of optical table.

2. Place the target right in front of the rack, and mark where the laser beams from the rack hit the target.

3. Move the laser rack away from the target (∼1m) and place the laser pointer rack parallel to the same side of optical table. Separate it from the aligned side the same distance as that between the rack and the side of table in procedure 1.

4. Check where the beams hit the target and if the beams hit a different position to the spot in 3, then adjust the direction of the lasers using the knots in the rack to align the laser. Iterating procedures 1-4 may be required to align the lasers in the rack.

The alignment of the laser pointers in the rack is shown in Fig. A-4.

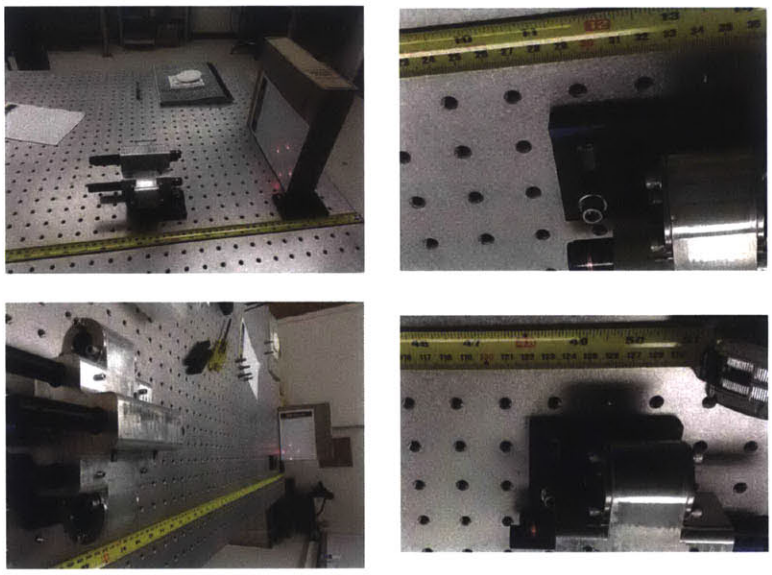

Figure A-4: Procedures 2-3 in the alignment of the laser pointers in the rack.

A.2 Alignment of the canister for in-vessel mirrors in the vessel

In the laboratory, we aligned four laser pointers in the rack and in-vessel mirrors in the canister. We should then install the canister in the vessel, and align it using the laser pointers in the rack. The canister will be installed on the outer wall, but the outer wall surface is not flat, and the position from the outer wall is not accurate. Thus, we must correct the position after we install the canister. It is also noteworthy that the canister should be aligned toroidally as well as radially and vertically. The

procedure of the installation and alignment of the canister in the vessel is as follows:

1. Calculate the expected path of the laser beam and the position of the beam on the inner wall based on the target location of the canister in the vessel.

2. Make the inner wall target, and place it at the calculated position on the inner wall.

3. Place the laser pointer rack in front of A port in the C-Mod Tokamak.

4. Install the canister at the target location in the vessel, and turn on the laser pointers. The diagram of this alignment set-up is shown in Fig. A-5.

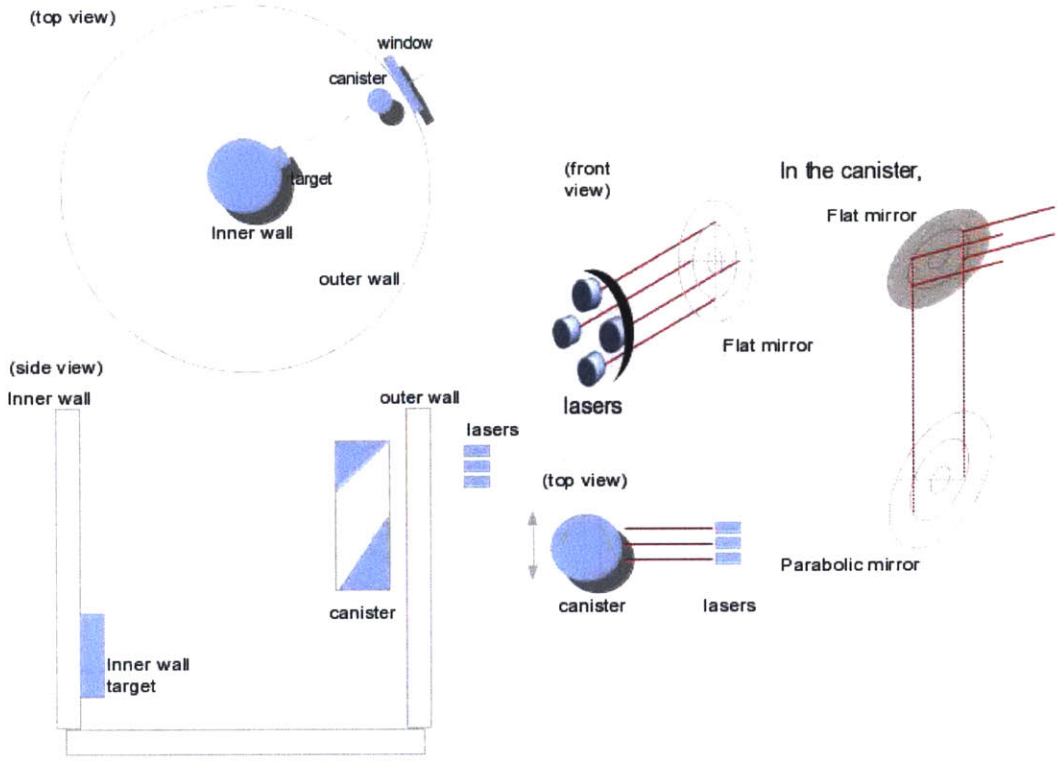

Figure A-5: The diagram for the canister alignment set-up.

5. Align the canister by adjusting its position toroidally, vertically and radially until all lasers hit the target, as shown in Fig. A-6(a). Figure A-6(b) shows the laser beams hitting on the inner wall target after the alignment is done.

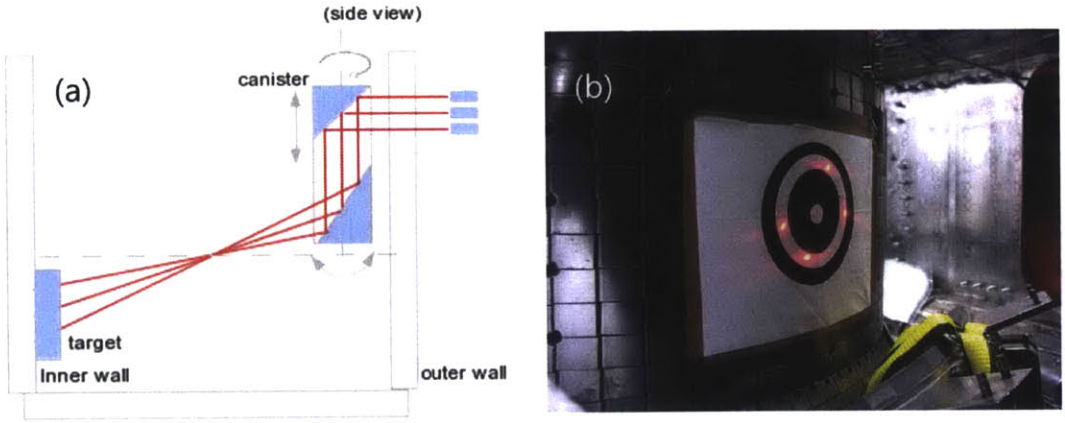

Figure A-6: (a) The diagram describing the canister alignment (b) The result of the alignment, laser beams hitting the inner wall target, after the alignment is done in 2012.

6. Measure the final position of the canister following the measurement list shown in Fig. A-7.

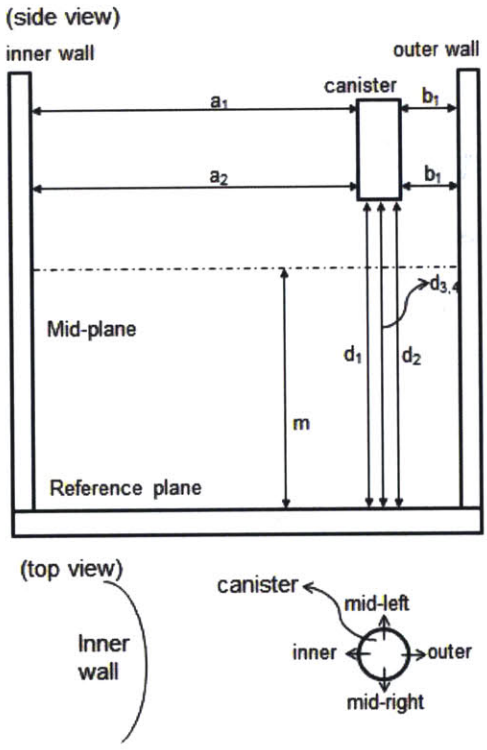

Measurement List

Measurement	Distance [cm]
The distance between the inner upper side of canister and the inner wall (a_1)	
The distance between the inner lower side of canister and the inner wall (a_2)	
The distance between the outer upper side of canister and the outer wall (b_1)	
The distance between the outer lower side of canister and the outer wall (b_2)	
The distance between reference plane and the bottom inner side of canister (d_1)	
The distance between reference plane and the bottom outer side of canister (d_2)	
The distance between reference plane and the bottom mid-left side of canister (d_3)	
The distance between reference plane and the bottom mid-right side of canister (d_4)	
The distance between mid-plane and the reference (m)	

Figure A-7: The measurement list to record the position of the canister after the alignment is finished.

Appendix B

Parasitic noise in the CECE measurements

Separate from the thermal noise (which is intrinsic to radiometer measurements), there may also be noise from the radiometer electronics that can possibly mask true temperature fluctuations. In this section, the parasitic noise observed in the CECE measurements is reported.

B.1 High frequency noise due to impedance mismatching

As mentioned in section 2.1.2 and 3.1.2, the intrinsic thermal noise is dominant in the fluctuations measured by the radiometer. Since thermal noise is not dependent on frequency, i.e. a white noise, the auto power spectrum of the CECE signal should be nearly flat. However, high frequency noise ($f = 1000 - 1500$kHz) was observed in the auto power spectrum of the CECE signal at the initial phase of the CECE diagnostic, February, 2012.

Figure B-1(a) shows the auto power spectrums of CECE Ch1 in one C-Mod discharge (shot : 1120221012). The blue line shows the auto power spectrum when the discharge is not fully developed yet (t:0.0-0.05 sec), and the red line shows the

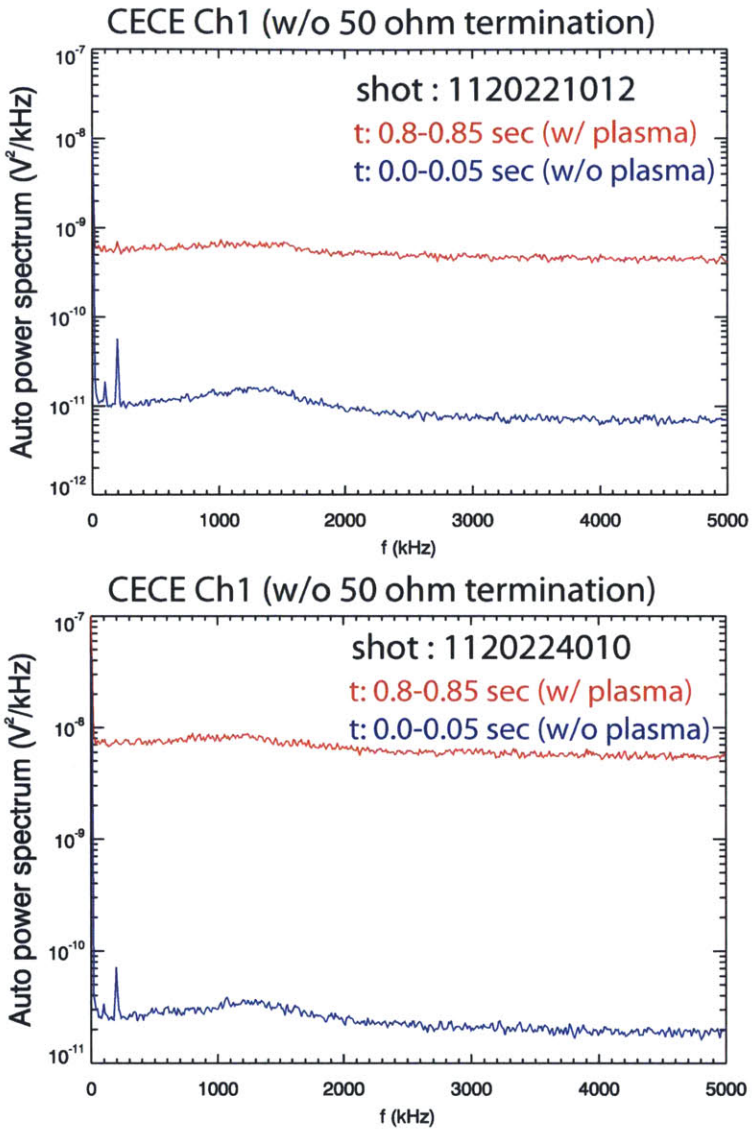

Figure B-1: Auto power spectra of CECE Ch1 in (a) shot 1120221012 and (b) shot 1120224010. The red line indicates the auto power spectrum when the plasma is fully developed (t:0.8-0.85sec), and the blue line indicates the spectrum before the plasma is fully developed.

spectrum after the plasma is fully developed. We can see that the amplitude of the red line, which is the auto power when plasma is fully developed, is almost 1000 times higher than the blue line, which is the auto power when the plasma is not fully developed yet. In the blue line, a peak near 100 and 200kHz and a bump near 1000-1500kHz were observed. Since the amplitude of the blue line is three order of magnitude smaller than the red line, we do not need to remove all of this noise. However, the noise near 1000-1500kHz can be also found in the red line, which indicates that this noise gets larger together with the amplitude of real signal. Since this noise was observed in the auto power spectrum in which thermal noise is dominant, and turbulent electron temperature fluctuations are much smaller than the thermal noise, the observed noise can mask real electron temperature fluctuations. Figure B-1(b) shows the auto power spectrum of the same CECE channel (Ch1) in another C-Mod discharge on a different run day (shot : 1120224010). Since the same noise is observed, this noise was not generated by the operating condition related to one specific discharge.

Figure B-2(a) shows the auto power spectrum of CECE Ch2 in the same discharges used in Fig. B-1(a). We can see a similar structure, which is a bump near $f = 1000 - 1500$kHz. This indicates that this noise does not result from a problem in one specific channel. We observed a similar structure in the rest of the channels as well. Fortunately, we found the origin of this noise. It was identified by adding a 50 ohm termination between the video amplifier and the digitizer. More details about the hardware used in the receiver are discussed in section 2.3.2. It is shown that adding the 50 ohm termination removes the noise near $f = 1000 - 1500$kHz in Fig. B-2(b). This indicates that impedance matching is helpful for minimizing the observed noise. It is well known that mismatched impedance between input and output load results in reflected power, generating noise. The input impedance of the digitizer is 5k ohms, while the output impedance of the video amplifier is around 50 ohms. (In the specification, the output impedance of the video amplifier is equal to or larger than 50 ohms, but the data in the test sheet tested only the case when the impedance of the output load is 50 ohms.) After we observed that 50 ohm termination was also

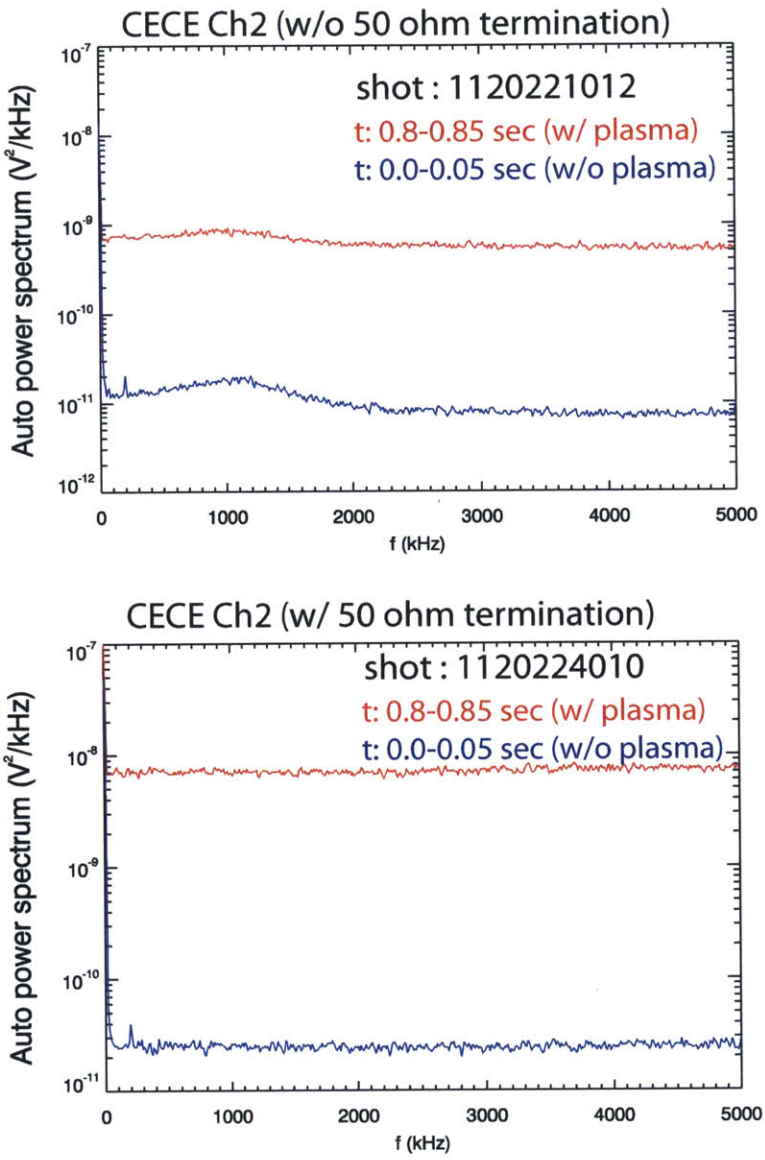

Figure B-2: Auto power spectra of CECE Ch2 in (a) shot 1120221012 and (b) shot 1120224010. The red line indicates the auto power spectrum when the plasma is fully developed (t:0.8-0.85sec), and the blue line indicates the spectrum before the plasma is fully developed. The number of points in each sub data set is 1024.

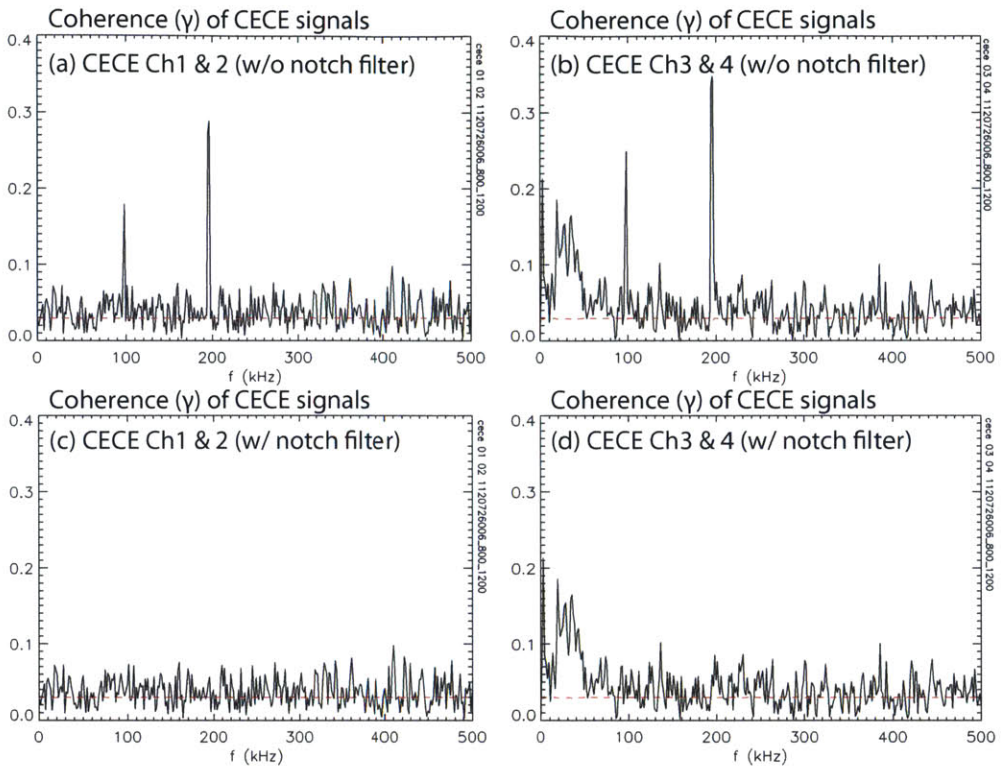

Figure B-3: Coherence (γ) spectra of CECE signals in one C-Mod discharge (shot 1120726006, t : 0.8-1.2s) (a) CECE Ch1 and 2 w/o notch filter (b) CECE Ch3 and 4 w/o notch filter (c) CECE Ch1 and 2 w/ notch filter (d) CECE Ch3 and 4 w/ notch filter. The number of points in each ensemble is 4096 to resolve the coherent peaks more evidently.

effective in eliminating the noise near $f = 1000 - 1500$kHz in other channels, 50 ohm termination was added to all CECE channels between the video amplifier and the digitizer, and all fluctuation measurements were performed with 50 ohm termination.

B.2 Coherent peaks from electronics at $f \simeq$100 and 200kHz

Coherent peaks near 100 and 200 kHz from the old IF box in fluctuation measurements were observed. One example is shown in Fig. B-3(a) and (b). In Fig. B-3, 4096 points were included in one sub data set in the ensemble averaging, which is four times larger than the number of points usually used in most analysis (=1024) in this study, to

identify this coherent peak clearly. We note that there are no evident fluctuations in Fig. B-3(a), while broadband fluctuations were observed in Fig. B-3(b). Not only in this discharge but also in most measurements, these peaks are observed regardless of existence of broadband fluctuations. Interestingly, we do not observe these coherent peaks in the new IF box, indicating that this noise was generated by the electronics, not real fluctuations. We do not know the origin of this noise, but it is easy to identify. In the analysis, we applied a notch filter to remove these peaks [112]. Figure B-3(c) and (d) shows the coherence spectrum after applying the notch filter. In the analysis, this notch filter is routinely applied.

B.3 Low frequency noise in f <10kHz

As shown Fig. 2-18, the low frequency CECE signal ($\lesssim$10kHz) is filtered out by a passive high pass filter connected to the video amplifier. However, for some discharges, we observed a coherent signal near the DC range ($f \simeq$ 0kHz). Fig. B-4 shows an example. In both figures, we see the coherent peak at very low frequency ($f \simeq$0kHz). This noise was observed in both IF boxes. The origin of this low frequency noise is unknown. One relevant observation is that we did not observe this noise in the filters whose center frequency is 4 and 4.25GHz with 200MHz bandwidth, while this noise was observed in other filters, including YIG filters, but we must study this noise more closely.

If we want to compare fluctuations on the same run day and the CECE signals in all discharges have this low frequency noise, we may be able to minimize the contamination from the electronic noise by applying a digital high pass filter during post-processing. In this case, it may be possible to find a trend of electron temperature fluctuations among discharges with different discharge conditions that we intend to change. However, for a broader data base from several different run days, this noise can make it hard to find a trend among the fluctuation data if the CECE signals have the low frequency noise on some run days but do not have it on the other run days. This is the case in section 4.1.3.

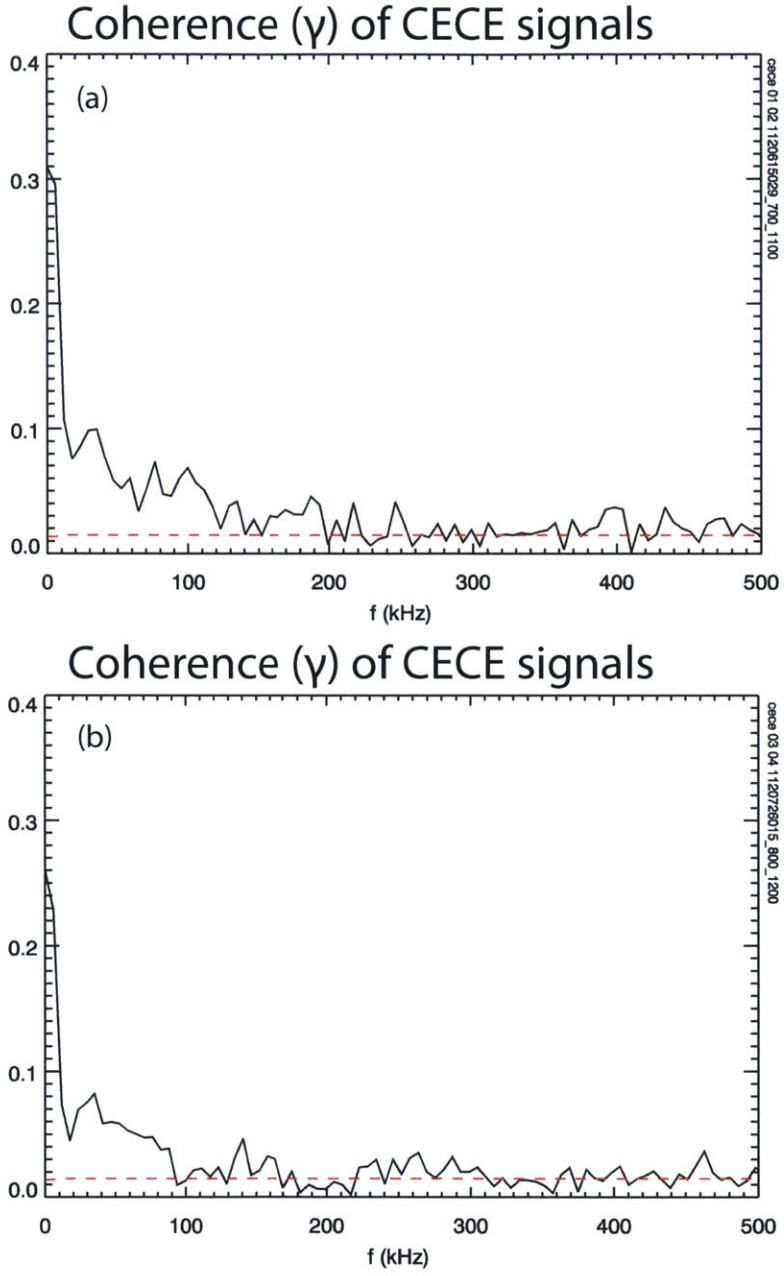

Figure B-4: Coherence (γ) of two CECE signals (a) between Ch1 and Ch2 (Shot : 1120615029, time : 0.7-1.1 sec) (b) between Ch3 and Ch4 (Shot : 1120726015, time : 0.8-1.2 sec).

In order to resolve the trend of electron temperature fluctuations near the edge in Ohmic discharges with the critical density for rotation reversal, we collected data in all Ohmic discharges in the C-Mod 2012 campaign. For some discharges, as shown in Fig. B-4, we observed the low frequency noise, but the other discharges do not have this noise. Including the discharges which have the low frequency noise makes it hard to identify the trend of electron temperature fluctuations in Ohmic discharges. Figure B-5 shows the changes in the electron temperature fluctuations in r/a=0.83-0.87 including all discharges regardless of low frequency noise. The blue points indicate the discharges which have low frequency noise. As shown in Fig. B-5, it is hard to resolve the trends clearly when the blue points are included. We must note that high pass filtering ($f > 10$kHz) [112] was applied to the blue points in Fig. B-5. This is because the electron temperature fluctuation levels from the discharge with this low frequency noise tend to be higher than the levels from the discharges without this noise. Although the origin of this low frequency peak is unknown, it is evident that this is the noise from the response curve of the high pass filter we used. It is noteworthy that the reduction of electron temperature fluctuations with the increase in density is observed among discharges on the same run day. We then decided to exclude the data points obtained from the discharges which have the low frequency noise in section 4.1.3 to resolve the trend in electron temperature fluctuations near the edge in Ohmic discharges. Table B.1 shows the list of discharges and CECE channels excluded in Fig. 4-5. The low frequency noise was also observed in the discharges used in section 6.1. In this case, all discharges in section 6.1 were performed on the same run day, and we observed the low frequency noise in most discharges. Thus, it is possible to resolve the trend of electron temperature fluctuations among these discharges. Digital high pass filtering ($f > 10$kHz) [112] was used in the analysis in section 6.1 to minimize the effect from the low frequency noise in the measured electron temperature fluctuation level.

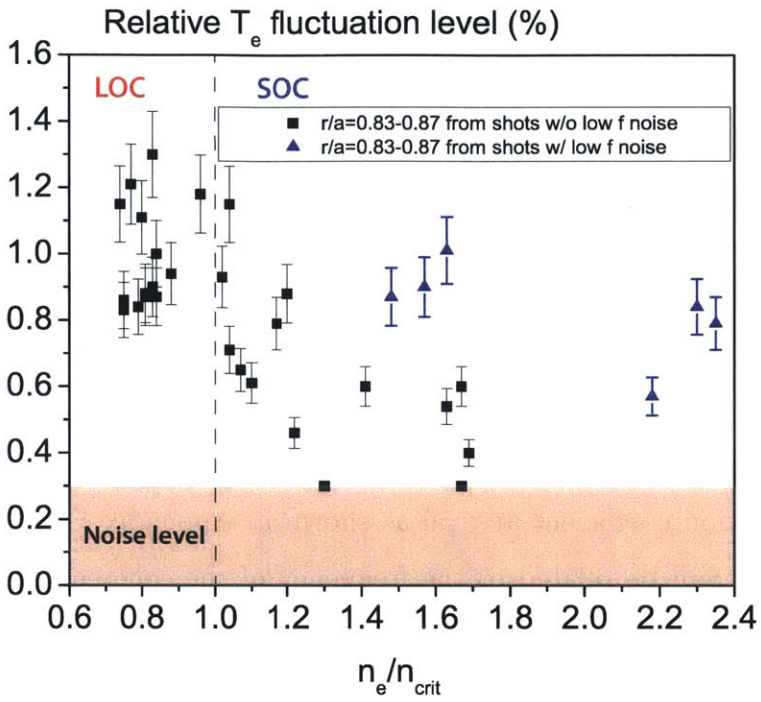

Figure B-5: Relative T_e fluctuation levels with $n_{e,avg}/n_{crit}$ at r/a=0.83-0.87 in the C-Mod Ohmic discharges including the discharges which have low frequency noise (blue points). For the signals contaminated by low frequency noise, high pass filtering ($f > 10$kHz) was applied, while a high pass filter was not applied to black points, which are from the discharges without this noise. n_{crit} is the critical density for toroidal rotation reversal in the core region, defined as $n_{crit} = 2.8I_p/B^{0.6}$ with n_{crit} in $10^{20}m^{-3}$, on axis toroidal magnetic field, B, in T and I_p in MA. The toroidal rotation reversal in the core region is indicative of the transition from the LOC to SOC according to [129]

Shot	Time (sec)	CECE chs
1120726009	0.8-1.2	Ch3 and 4
1120726014	0.8-1.2	Ch3 and 4
1120726015	0.8-1.2	Ch3 and 4
1120726016	0.8-1.2	Ch3 and 4
1120926025	0.8-1.3	Ch3 and 4
1120926026	0.9-1.4	Ch3 and 4

Table B.1: The list of discharges and CECE channels in which we observed the low frequency noise in Ohmic discharges, which are blue points in Fig. B-5.

B.4 Negatively coherent noise

As mentioned in section 3.1.1, fluctuation levels can be calculated from either the cross power spectrum or the cross correlation coefficient. However, we observed a sharp dip in the correlation curve. Figure B-6 shows an example. In this discharge (shot 1120720016, t: 0.8-1.4 sec), we observed broadband fluctuations in the 0-150kHz range as shown in the coherence spectrum (Fig. B-6(a)) and the cross phase spectrum (Fig. B-6(b)). In the cross correlation coefficient curve (Fig. B-6(c)), the sharp dip was observed near lag time, τ=0. This noise is critical when we calculate the fluctuation level from the cross coefficient curve since the fluctuation level is proportional to the cross correlation coefficient at τ=0 as shown in Appendix E. The width of the correlation curve will be related to the frequency of the coherent fluctuations. The width of the curve will be comparable to the inverse of the highest frequency of the coherent fluctuations as observed in section 2.4.3. The width of the dip is around $1\mu s$, which corresponds to the value near the applied video bandwidth (1MHz) as shown in Fig. B-6. We also see that the negative dip is added to the structure which has broader width. If we ignore the dip in this broad structure, the correlation time (width) of this structure is around $5\mu s$, which corresponds to 200kHz, close to the highest frequency of the observed broadband fluctuations in Fig. B-6(a) and (b). This may indicate that the correlation curve is affected by the high frequency (near 1MHz) parasitic noise, which are negatively correlated with one another.

In order to verify this speculation, the correlation curves from the same signal in Fig. B-6 with different video bandwidth, B_{vid}, values are compared in Fig. B-7. We see that the amplitude of the dip decreases as B_{vid} decreases from 1MHz to 0.5MHz, and it disappears when B_{vid}=0.3MHz. It is also noteworthy that the width of the dip when B_{vid}=0.5MHz is broader than the width when B_{vid}=1MHz as shown in Fig. B-7(a) and (b). This may suggest that the mitigation of the dip in Fig. B-7(b) results from filtering of high frequency noise which is negatively coherent. It is inconclusive whether the negatively coherent noise is spread throughout the whole frequency range or the amplitude of this noise is higher in the high frequency range (> 500kHz). In

either case, it is evident that lower B_{vid} is desirable not only to improve the sensitivity of the radiometer, given in Eq. 2.12, but also to avoid or minimize the effect of this noise.

However, lowering the B_{vid} value limits the measurable fluctuations. In other words, the lowest B_{vid} value will be limited by the frequency range of the measured fluctuations. We observed that the fluctuations are spread near 500kHz in high energy confinement regimes such as I-mode in Chapter 6. In contrast, we do not need to decrease B_{vid} values to minimize the effect of this negatively coherent noise when we use the cross power spectrum to resolve the electron temperature fluctuations. This is because the effect of this noise will be minimized when we integrate the cross power spectrum in the determined frequency range for the observed fluctuations. For this reason, the fluctuation level was calculated from the cross power spectrum rather than the cross correlation coefficient at τ=0.

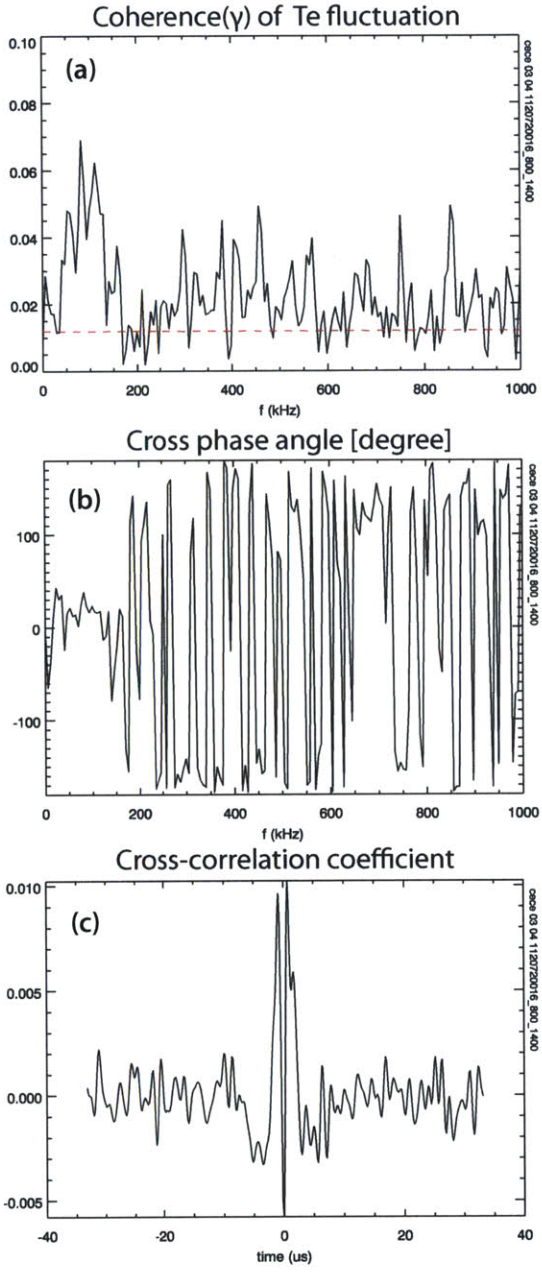

Figure B-6: (a) Coherence (b) cross phase spectrum (c) cross correlation curve of two CECE signals in one C-Mod discharge (shot 1120720016, t:0.8-1.4 sec) with IF bandwidth, B_{IF}=200MHz and video bandwidth, B_{vid}=1MHz.

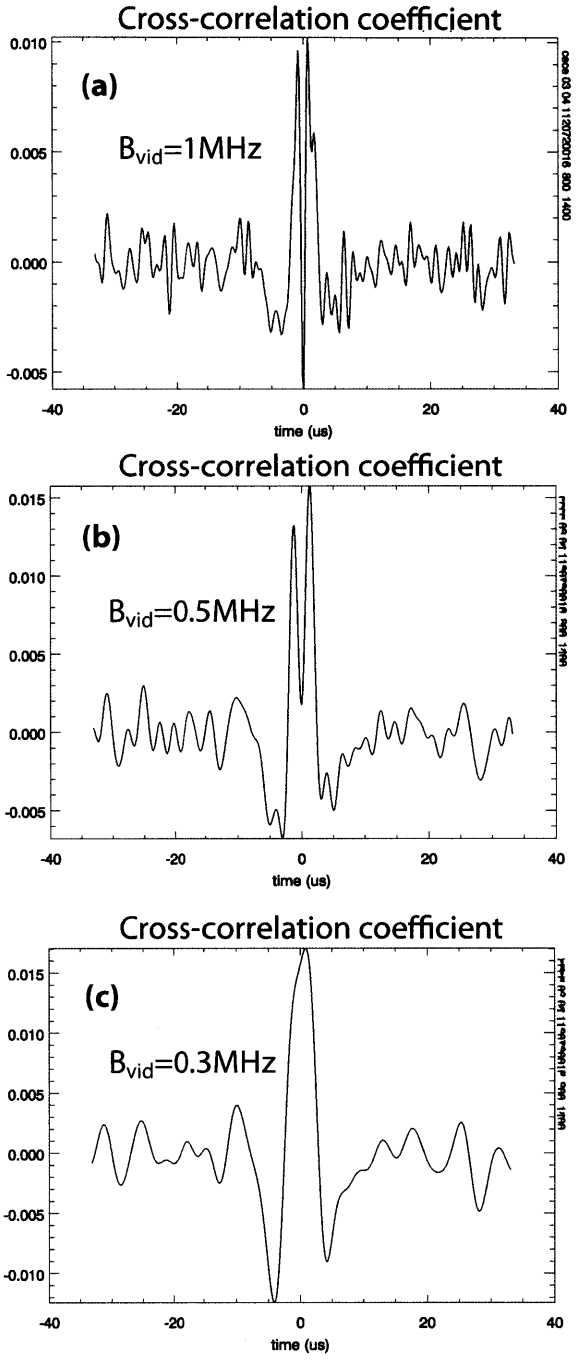

Figure B-7: Cross correlation curve of two signals used in Fig. B-6 with a different video bandwidth, B_{vid}. (a) B_{vid}=1MHz (b) B_{vid}=0.5MHz (c) B_{vid}=0.3MHz.

Appendix C

System noise temperature estimation

This section will describe the simple estimation of the noise temperature of the CECE receiver using the Y-factor method. As mentioned in Chapter 2, the sensitivity of the ECE radiometer is determined by its system temperature. The Y-factor, Y, is defined as the ratio of the noise level of the DUT (Device Under Test) with a noise source to that without a noise source.

$$Y = \frac{N^{ON}}{N^{OFF}} \tag{C.1}$$

with the noise level with noise source, N^{ON}, and the noise level without, or turning off, the noise source, N^{OFF}.

As shown in Eq. 2.6, the noise level is proportional to the noise temperature. Then, the Y-factor, Y, can be written in terms of the noise temperature in the following way:

$$Y = \frac{N^{ON}}{N^{OFF}} = \frac{T_s^{ON} + T_{sys}}{T_s^{OFF} + T_{sys}} \tag{C.2}$$

where T_s^{ON} and T_s^{OFF} are the noise source temperature when the source is turned on and off, respectively. T_{sys} indicates the system noise temperature.

We then express T_{sys} in terms of Y factor as follows:

$$T_{sys} = \frac{T_s^{ON} - YT_s^{OFF}}{Y - 1} \tag{C.3}$$

	Ch1	Ch2	Ch3	Ch4
N_{off} [mV]	-82	-81	-85	-84
N_{on} [mV]	-1120	-1040	-1080	-1000
Y factor	13.7	12.8	12.7	11.9
T_sys [eV]	0.04	0.05	0.05	0.05

Table C.1: The system temperature estimated from Y-factor method from the test results in section 2.4.1.

In the test using the Y-factor method, a calibrated noise source is used. In other words, we usually know T_s^{ON}. The noise source temperature when the source is off, T_s^{OFF}, is usually assumed to be room temperature (~290K). Thus, once we measure the Y-factor, the ratio of the noise levels turning on and off the noise source, the system noise temperature will be estimated from Eq. C.3. More detailed analysis related to the Y-factor method, including error analysis for T_{sys} measurements, can be found in [110].

As mentioned in Chapter 2, a calibrated noise source manufactured by HP (346B) was used for the system noise temperature estimation. The noise source temperature can be obtained given the Excess Noise Ratio (ENR) at each frequency, which is defined as,

$$ENR[dB] = 10\log_1 0[(T_s^{ON} - T_s^{OFF})/T_o] \simeq 10\log_1 0[T_s^{ON}/T_o - 1] \qquad (C.4)$$

This approximation was used based on the assumption that $T_s^{OFF} \simeq T_o \simeq$290K.

We can then apply the Y-factor method to the results obtained from the IF section test (IF section response (or gain) test) performed in section 2.4.1. As mentioned in section 2.4.1, T_s^{ON} ~0.86-0.87eV (10026-10100K) at the frequency range used in this test (8-8.5GHz) from the given ENR of the noise source. Using the test results shown in Table 2.3, the Y-factor and system noise temperature are obtained as shown in Table C.1.

In this test, the system temperature is extremely small, less than 1eV. This may

be because of large amplification. We checked the system temperature in various combinations of amplifiers and attenuators, and the estimated system temperature value was less than 10eV, which is acceptable for T_e measurements, where T_e is in the hundreds of eV to keV range.

Appendix D

Estimation of calibration factor of the CECE diagnostic from the laboratory test

In this section, the calibration factor will be estimated from laboratory tests using a noise source (346B by HP), as performed in section 2.4.1. To be specific, we will use the results shown in Table 2.3. We first need to know the input power of the square law detector. From the gain of the video amplifier in each channel and the response curve of the detector, which can be found in the manual [9], it is possible to estimate the input power of the detector. Table D.1 shows the measured voltage gain of the video amplifier in each channel.

In Table D.1, both the input and output amplitudes were measured by an oscilloscope. While output voltage amplitudes were stable, the input voltage amplitude fluctuated by around 30%. Thus, the measured gain will also have around 30% un-

	Ch1	Ch2	Ch3	Ch4
Input amplitude $[mV_{pp}]$	12.4	12.4	12.2	12.0
Output amplitude$[V_{pp}]$	7.12	6.60	3.20	4.82
Gain	574	532	262	402

Table D.1: The gain of amplitude of the video amplifier in each channel. Input signal (sine wave with $f = 1$MHz) is generated by a function generator (33210A by Agilent).

	Ch1	Ch2	Ch3	Ch4
Voltage gain [mV]	1038	959	995	916
Gain of video amp.	574	532	262	402
Output amplitude after detector [mV]	1.8	1.8	3.8	2.3

Table D.2: The estimated amplitude of output signal after the square law detector.

certainty. From the measured voltage gain values in the response test written in Table D.1 (Ch1 : 1038 mV, Ch2 : 959 mV, Ch3 : 995mV, Ch4 : 916 mV), we can estimate the output voltage amplitude after the detector as shown in Table D.2. Then, using the response curve given in the manual [9], shown as Fig. D-1, the estimated input powers are as follows :∼-23dBm (Ch1 and 2), ∼-18dBm (Ch3) and ∼-20dBm (Ch4). Since we have only a graph in log scale, this estimation is not accurate. Considering 30% uncertainty in the estimated gain of the video amplifiers and the rough estimation of input power from the graph, we will give ±2dB uncertainty in the estimated input power. We did not include background noise power here. This is because the input power from the noise source is the value we know correctly, and ±2dB uncertainty will cover the input power contribution from the background noise power.

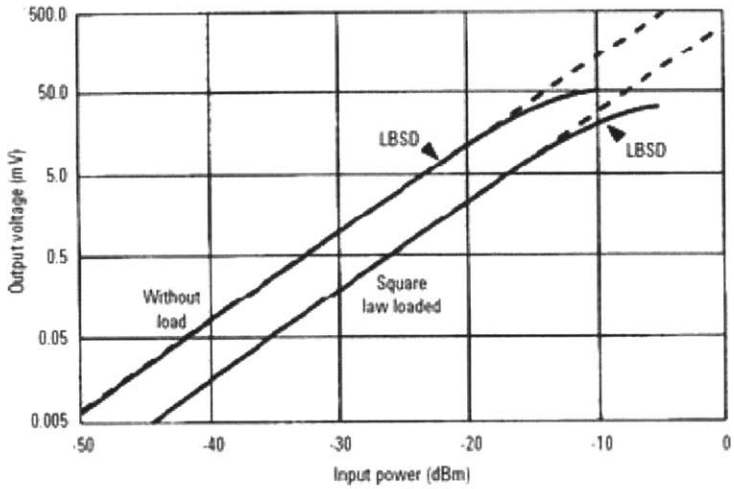

Figure D-1: The response curve of a square law detector (8472B by Agilent), which is taken in [9].

Using the estimation performed so far and Fig. 2-16, we can generate the response

curve of the detector in each channel. The vertical axis of Fig. 2-16 is converted by using the gain of video amplifiers from the response in voltage to the amplitude of the output signal after the detector. The horizontal axis of Fig. 2-16 will be replaced with the estimated input power. The response curve of each detector is shown in Fig. D-2.

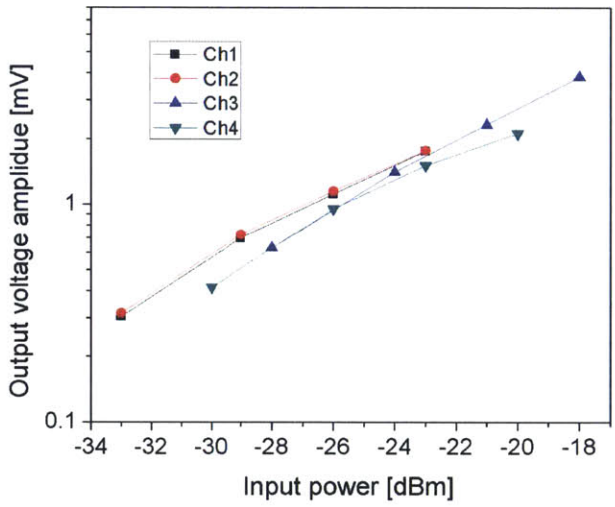

Figure D-2: The estimated response curve of the square law detector (8472B by Agilent) in each channel.

Since we know the input power of the noise source (-78.5dBm at 8GHz with 100MHz bandwidth) and the gain from the two amplifiers (total 72dB, 33dB from the 1^{st} amplifier and 39dB from the 2^{nd} amplifier), we can estimate the loss in each channel. For Ch1, the loss from the noise source to the detector will be about 16.5dB (-78.5+72-loss$\simeq$-23dBm). In the same way, the estimated loss of the rest of the channels will be 16.5dB (Ch2), 11.5dB (Ch3) and 13.5dB (Ch4). Since the same components used in the CECE measurement for the calibration are used in this test except for the additional attenuator and longer SMA cable, the loss from the 1^{st} amplifier to the detector can be estimated. Considering the 16dB attenuator used in the calibration, and that the additional loss from the longer cable is around 5dB, the loss from 1^{st} amplifier to the square law detector in Ch 1 will be 37.5dB (=16.5+16+5). In the same way, the loss in the other channels will be 37.5dB (Ch2), 32.5dB (Ch3) and

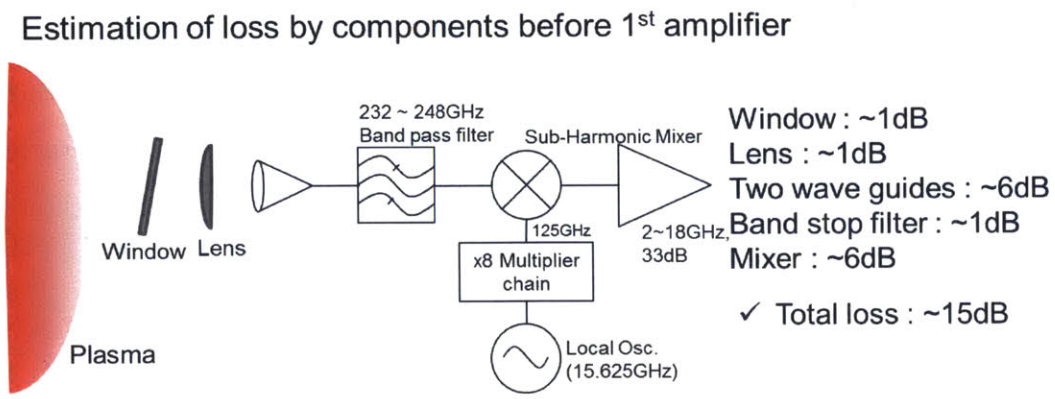

Figure D-3: The estimation of loss in RF section (front end) before 1^{st} amplifier.

34.5dB (Ch4). The estimated losses from the plasma to the 1^{st} amplifier are about 15dB as shown in Fig. D-3.

Now, we know the losses from the plasma to the square law detector, which are 52.5dB (Ch1 and 2), 47.5dB (Ch3) and 49.5dB (Ch4). When the plasma temperature is 1keV, the detected power with IF bandwidth B_{IF}=100MHz is about -47dBm. Then, the input power right before the square law detector in Ch1 is -47 dBm+72dB (from amplifiers)-52.5dB=-27.5dBm. In the same way, the input power in the other channels will be -27.5dBm (Ch2), -22.5dBm (Ch3), -24.5dBm (Ch4). Considering ±2dB uncertainty, the estimated output voltage amplitude of Ch1 from the estimated response curve in Fig. D-2 is 0.9mV (0.7-1.2mV from ± 2dB uncertainty). In the same way, we can get 0.9mV (0.7-1.2mV), 1.8mV (1.3-2.5mV) and 1.2mV (0.9-1.6mV) for Ch2, Ch3 and Ch4, respectively. Finally, the amplitude of a signal after a video amplifier will be the estimated output voltage multiplied by the gain of the video amplifier. They are 0.52V (0.40-0.69V), 0.48V (0.37-0.64V), 0.47V (0.34-0.66V) and 0.48V (0.36-0.64V) for Ch1, Ch2, Ch3 and Ch4, respectively. Since these results are the estimated values when the plasma temperature is 1keV, the calibration factor [keV/V] will be 1.9keV/V($\simeq$1keV/0.52V) (1.5-2.5keV/V) , 2.1keV/V (1.6-2.7keV/V) , 2.1keV/V (1.5-2.9keV/V) and 2.1keV/V (1.6-2.8keV/V) for Ch1, Ch2, Ch3 and Ch4, respectively. The results of the estimation in each step are shown in Table D.3. The estimated calibration factors agree with the measured calibration factors in section 2.4.2 within the uncertainty.

	Ch1	Ch2	Ch3	Ch4
Loss from 1^{st} amp. to the detector [dB]	16.5 (14.5-18.5)	16.5 (14.5-18.5)	11.5 (9.5-13.5)	13.5 (11.5-15.5)
Estimated output amplitude after the detector when T_e=1keV [mV]	0.9 (0.7-1.2)	0.9 (0.7-1.2)	1.8 (1.3-2.5)	1.2 (0.9-1.6)
Estimated output amplitude after the video amp when T_e=1keV [V]	0.52 (0.40-0.69)	0.48 (0.37-0.64)	0.47 (0.34-0.66)	0.48 (0.36-0.64)
Calibration factor [keV/V]	1.9 (1.5-2.5)	2.1 (1.6-2.7)	2.1 (1.5-2.9)	2.1 (1.6-2.8)

Table D.3: The estimated values of loss, output amplitude and the calibration factor of CECE channels. The loss from the plasma to the 1^{st} amplifier is estimated as 15dB.

Appendix E

Derivation of the T_e fluctuation levels from the CECE measurements

E.1 Derivation of T_e fluctuation levels using the cross correlation coefficient

We can think of the CECE signal as having two parts, which are the mean or steady part, $\bar{x}$ and the fluctuation part, $\tilde{x}$. If two signals have common electron temperature fluctuations and do not have any correlated noise, the fluctuation part will consist of two parts, which are thermal noise, N_{th}, and common electron temperature fluctuations, $\tilde{T}_e$. Removing the steady part of each signal, the fluctuation part of each signal will be,

$$\tilde{x} = N_{th,x} + \tilde{T}_e/c_x \tag{E.1}$$

$$\tilde{y} = N_{th,y} + \tilde{T}_e/c_y \tag{E.2}$$

where c_x and c_y are the calibration factor of each signal.

Assuming thermal noise is not correlated, from Eq. 3.2 and 3.3, R_{xx}, R_{yy} at $\tau = 0$ are,

$$R_{xx}(0) = N_{th,x}^2 + \tilde{T}_e^2/c_x^2 \tag{E.3}$$

$$R_{yy}(0) = N_{th,y}^2 + \tilde{T}_e^2/c_y^2 \tag{E.4}$$

Thermal noise may be uncorrelated with each other if the two signals have disjoint frequency bands. Through cross correlation, thermal noise can be eliminated and common electron temperature fluctuations will be revealed. Then, from Eq. 3.4, R_{xy} is,

$$R_{xy}(0) = \tilde{T}_e^2/(c_x c_y) \tag{E.5}$$

Using Eq. E.3-E.5, the cross correlation coefficient when lag time is zero, $C_{xy}(0)$, will be,

$$C_{xy}(0) = \frac{\tilde{T}_e^2/(c_x c_y)}{\sqrt{(N_{th,x}^2 + \tilde{T}_e^2/c_x^2)(N_{th,y}^2 + \tilde{T}_e^2/c_y^2)}} \tag{E.6}$$

The thermal noise level of the radiometry is given by [15],

$$N_{th,x}^2 = \frac{2B_{vid}}{B_{IF}}\bar{x}^2 = \frac{2B_{vid}}{B_{IF}}T_e^2/c_x^2 \tag{E.7}$$

$$N_{th,y}^2 = \frac{2B_{vid}}{B_{IF}}\bar{y}^2 = \frac{2B_{vid}}{B_{IF}}T_e^2/c_y^2 \tag{E.8}$$

For the CECE diagnostic in this study (B_{vid}=0.5MHz,B_{IF}=200MHz), the thermal noise level is $\sim 7\%$ of the mean value of the signal. Considering temperature fluctuations are $\sim 1\%$, we can ignore the contribution of electron temperature fluctuations in auto correlation functions (R_{xx}, R_{yy}).

$$R_{xx}(0) = N_{th,x}^2 + \tilde{T}_e^2/c_x^2 \simeq N_{th,x}^2 = \frac{2B_{vid}}{B_{IF}}T_e^2/c_x^2 \tag{E.9}$$

$$R_{yy}(0) = N_{th,y}^2 + \tilde{T}_e^2/c_y^2 \simeq N_{th,y}^2 = \frac{2B_{vid}}{B_{IF}}T_e^2/c_y^2 \tag{E.10}$$

Using Eq. E.9 and E.10, $C_{xy}(0)$ will be,

$$C_{xy}(0) = \frac{\tilde{T}_e^2/(c_x c_y)}{\sqrt{(\frac{2B_{vid}}{B_{IF}}T_e^2/c_x^2)(\frac{2B_{vid}}{B_{IF}}T_e^2/c_y^2)}} = \frac{B_{IF}\tilde{T}_e^2}{2B_{vid}T_e^2} \tag{E.11}$$

Thus, the relative fluctuation level($\tilde{T}_e/T_e$) is,

$$\frac{\tilde{T}_e}{T_e} = \sqrt{\frac{2B_{vid}}{B_{IF}} C_{xy}(0)} \tag{E.12}$$

E.2 Derivation of the T_e fluctuation levels using the cross spectral density function

We can also obtain the relative fluctuation level ($\tilde{T}_e/T_e$) by integrating the cross spectral power density, $G_{xy}(f)$. The root mean square (RMS) fluctuation amplitude of the CECE signal can be obtained by integrating the cross spectral power density in the frequency range in which broadband fluctuations are observed [37]. For uncalibrated signals, the RMS fluctuation amplitude will be proportional to the integral of the cross spectral power density.

E.2.1 Derivation for continuous data

When we have data in the continuous time domain, x(t), the Fourier transformed quantity, $X(f)$ is defined as

$$X(f) = \int_0^\infty x(t) e^{-j2\pi ft} \mathrm{d}t \tag{E.13}$$

Since the measurement time is finite, there will be a total time length, T in the measurements, and we can define the Fourier transformed quantity during a finite time period as follows:

$$X_T(f) = \int_0^T x(t) e^{-j2\pi ft} \mathrm{d}t \tag{E.14}$$

The spectral density function can be calculated from $X_T(f)$. The autospectral density function (one sided), $G_{xx}(f)$ is defined as,

$$G_{xx}(f) = \frac{2}{n_d T_{ens}} \sum_{k=1}^{n_d} |X_{Tens}(f)|^2 \tag{E.15}$$

where T_{ens} is a time length of a sub data set, and n_d is the number of sub data sets. Thus, $T = T_{ens} n_d$. In addition, $G_{xx}(f)$ is defined as only the positive frequency range.

In the same manner, we can define a cross spectral density function, $G_{xy}(f)$. When we have two data sets, x(t) and y(t), the cross spectral density function, $G_{xy}(f)$ is defined as,

$$G_{xy}(f) = \frac{2}{n_d T_{ens}} \sum_{k=1}^{n_d} |X^*_{T_{ens}}(f) Y_{T_{ens}}(f)| \tag{E.16}$$

where $X^*_{T_{ens}}(f)$ is the complex conjugate of $X_{T_{ens}}(f)$.

From Eq. E.15 and E.16, we know that spectral density is a time averaged Fourier transformed value. Thus, we can obtain time averaged fluctuations from the spectral density functions. For CECE measurements, fluctuations were obtained through the cross correlation technique. Thus, we can quantify the fluctuations from the cross spectral density function, G_{xy}. Although measured CECE signals are uncalibrated, they are proportional to the temperature and its fluctuations. Thus, temperature fluctuations can be calculated as follows:

$$\tilde{T_e}^2 = c_x c_y \int_0^\infty G_{xy}(f) \mathrm{d}f \tag{E.17}$$

where C_x and C_y are calibration factor for data set, x(t) and y(t).

In most cases, fluctuations are observed in a finite frequency range, which is from f_1 to f_2. In that case, temperature fluctuations, $\tilde{T_e}$ will be,

$$\tilde{T_e}^2 = c_x c_y \int_{f_1}^{f_2} G_{xy}(f) \mathrm{d}f \tag{E.18}$$

In order to obtain the relative fluctuation level, $\frac{\tilde{T_e}}{\bar{T_e}}$ in an uncalibrated signal, we should find the mean temperature, $\bar{T_e}$, from the signal. According to Parseval's Theorem, the sum of the square of a time series of data is the same as the sum of the square of the Fourier transformed data. When the measured time range is from t_1 to

t_2 and the total measuring time is T, Parseval's Theorem can be written as below.

$$\int_{t_1}^{t_2} |x(t)|^2 \mathrm{d}t = \int_{-\infty}^{\infty} |X_T(f)|^2 \mathrm{d}f \tag{E.19}$$

The variance for the data is defined as follows:

$$Var[x(t)] = \frac{1}{T}\int_{t_1}^{t_2} |x(t) - \bar{x}(t)|^2 \mathrm{d}t = \frac{1}{T}\int_{t_1}^{t_2} |\tilde{x}(t)|^2 \mathrm{d}t \tag{E.20}$$

where $\bar{x}(t)$ is the average value of x(t), and $\tilde{x}(t)$ is the fluctuating part. Thus, x(t) can be represented as $x(t) = \bar{x}(t) + \tilde{x}(t)$.

It is known that the variance of data from the radiometer is related to the bandwidths of the radiometer. It is given that,

$$Var[x(t)] = \frac{2B_{vid}}{B_{IF}}\bar{x}(t)^2 \tag{E.21}$$

where B_{vid} is a video bandwidth, and B_{IF} is an IF (Intermediate Frequency) bandwidth.

Using Eq. E.21 and Parseval's Theorem, we can obtain the information of the mean value from the Fourier transformed quantity. Assuming that we treat only the fluctuating component for the Fourier transform ,i.e. $\bar{x}(t) = 0$, variance can be represented as follows:

$$Var[x(t)] = \frac{1}{T}\int_{t_1}^{t_2} |\tilde{x}(t)|^2 \mathrm{d}t = \frac{2}{T}\int_{0}^{\infty} |X_T(f)|^2 \mathrm{d}f \tag{E.22}$$

Then, $\bar{x}(t)$ can be obtained as below:

$$\bar{x}(t)^2 = \frac{B_{IF}}{2B_{vid}}\frac{2}{T}\int_{0}^{\infty} |X_T(f)|^2 \mathrm{d}f \tag{E.23}$$

Mean temperature in CECE measurements can be obtained using a calibration factor in the above equation:

$$\bar{T_e}^2 = c_x^2 \frac{B_{IF}}{2B_{vid}}\frac{2}{T}\int_{0}^{\infty} |X_T(f)|^2 \mathrm{d}f \tag{E.24}$$

In CECE measurements, two data sets are required. Assuming that the temperature values from the two data sets are the same, the relative fluctuation level will be represented as follows:

$$\bar{T_e}^2 = c_x c_y \frac{B_{IF}}{2B_{vid}} \frac{2}{T} [\int_0^\infty |X_T(f)|^2 \mathrm{d}f \int_0^\infty |Y_T(f)|^2 \mathrm{d}f]^{0.5} \tag{E.25}$$

$$\frac{\tilde{T_e}^2}{\bar{T_e}^2} = \frac{c_x c_y \int_{f_1}^{f_2} G_{xy}(f) \mathrm{d}f}{c_x c_y \frac{B_{IF}}{2B_{vid}} \frac{2}{T} [\int_0^\infty |X_T(f)|^2 \mathrm{d}f \int_0^\infty |Y_T(f)|^2 \mathrm{d}f]^{0.5}} \tag{E.26}$$

$$\frac{\tilde{T_e}}{\bar{T_e}} = \{\frac{2B_{vid} T \int_{f_1}^{f_2} G_{xy}(f) \mathrm{d}f}{2B_{IF} [\int_0^\infty |X_T(f)|^2 \mathrm{d}f \int_0^\infty |Y_T(f)|^2 \mathrm{d}f]^{0.5}}\}^{0.5} \tag{E.27}$$

E.2.2 Derivation for discrete data

For real measurements, we will obtain digitized data. Thus, the integral in the previous section will be represented by summing each data point. First of all, the Fourier transformed quantity, $X_T(f)$ will be,

$$X_T(f) = \int_0^T x(t) e^{-j2\pi ft} \mathrm{d}t = \triangle t \sum_{k=0}^{N-1} x(t) e^{-j2\pi fn\triangle t} \tag{E.28}$$

where N is the number of data points in the time range of interest and $\triangle t$ is the separation time between two adjacent data points. Discrete data points also give discrete frequency values such as $f_k = \frac{k}{T}$. Using this discrete frequency value and $T = N\triangle t$, the above equation can be changed as follows:

$$X_T(f_k) = \triangle t \sum_{k=0}^{N-1} x(t) e^{-j\frac{2\pi kn}{N}} \tag{E.29}$$

It is noteworthy that FFT does not give the same value as the above, since the sampling rate is not considered in the FFT process. The quantity from FFT is the following:

$$X_k = \frac{X_T(f_k)}{\triangle t} = \sum_{k=0}^{N-1} x(t) e^{-j\frac{2\pi kn}{N}} \tag{E.30}$$

Using the definition of $X_T(f_k)$ and X_k, the spectral density value can be defined

as below:

$$G_{xx}(f_{ens,k}) = \frac{2}{n_d T_{ens}} \sum_{n=1}^{n_d} |X_{T_{ens},n}(f_k)|^2 = \frac{2}{n_d N_{ens} \triangle t} \sum_{n=1}^{n_d} |X_{k_{ens},n} \triangle t|^2 = \frac{2\triangle t}{n_d N_{ens}} \sum_{k=1}^{n_d} |X_{k_{ens},n}|^2 \tag{E.31}$$

$$G_{xy}(f_{ens,k}) = \frac{2\triangle t}{n_d N_{ens}} \sum_{n=1}^{n_d} |X^*_{k_{ens},n} Y_{k_{ens},n}| \tag{E.32}$$

where N_{ens} is the number of data points in one subset, and $X_{k_{ens}}$ is the FFT value from one data subset. It was also assumed that x(t) and y(t) have the same sampling rate.

Parseval's Theorem also should be changed as follows:

$$\int_{t_1}^{t_2} |x(t)|^2 \mathrm{d}t = \int_{-\infty}^{\infty} |X_T(f)|^2 \mathrm{d}f \rightarrow \sum_{n=1}^{N} |x(k_n \triangle t)|^2 \triangle t = \sum_{k=0}^{N-1} |X_T(f_k)|^2 \triangle f \tag{E.33}$$

Then, using the previous definitions,

$$\sum_{n=1}^{N} |x(k_n \triangle t)|^2 = \sum_{k=0}^{N-1} |X_T(f_k)|^2 \frac{\triangle f}{\triangle t} = \sum_{k=0}^{N-1} |X_k|^2 \triangle f \triangle t = \frac{1}{N} \sum_{k=0}^{N-1} |X_k|^2 \tag{E.34}$$

Since the variance in the discrete data will be,

$$Var[x(t)] = \frac{1}{T} \int_{t_1}^{t_2} |\tilde{x}(t)|^2 \mathrm{d}t = \frac{1}{N \triangle t} \sum_{k=0}^{N-1} |\tilde{x}(t)|^2 \triangle t = \frac{1}{N} \sum_{k=0}^{N-1} |\tilde{x}(t)|^2 \tag{E.35}$$

For data with zero mean value, i.e. $\tilde{x}(t) = x(t)$, Parseval's theorem can be written as follows:

$$Var[x(t)] = \sum_{k=0}^{N-1} \frac{|X_k|^2}{N^2} \tag{E.36}$$

Following Eq. E.21-E.24, a mean temperature can be expressed as the following:

$$\bar{T_e}^2 = c_x c_y \frac{B_{IF}}{2B_{vid}} [\sum_{k=0}^{N-1} \frac{|X_k|^2}{N^2} \sum_{k=0}^{N-1} \frac{|Y_k|^2}{N^2}]^{0.5} \tag{E.37}$$

In order to calculate the fluctuation, we must consider the integral of the cross spectral density:

$$\int_{f_1}^{f_2} G_{xy}(f)\mathrm{d}f = \sum_{k=i_1}^{i_2} G_{xy}(f_{ens,k})\triangle f_{ens} \tag{E.38}$$

where i_1 and i_2 are the index numbers corresponding to f_1 and f_2, and $\triangle f_{ens}$ is the frequency resolution bandwidth used in the ensemble averaging, defined as $\triangle f_{ens} = \frac{1}{T_{ens}}$. Thus, $\triangle f_{ens} = n_d \triangle f$. Then, the temperature fluctuation will be,

$$\tilde{T_e}^2 = C_x C_y \int_{f_1}^{f_2} G_{xy}(f)\mathrm{d}f = C_x C_y \sum_{k=i_1}^{i_2} G_{xy}(f_{ens,k})\triangle f_{ens} \tag{E.39}$$

Finally, the fluctuation level will be,

$$\frac{\tilde{T_e}^2}{\bar{T_e}^2} = \frac{\sum_{k=i_1}^{i_2} G_{xy}(f_{ens,k})\triangle f_{ens}}{\frac{B_{IF}}{2B_{vid}}[\sum_{k=0}^{N-1}\frac{|X_k|^2}{N^2}\sum_{k=0}^{N-1}\frac{|Y_k|^2}{N^2}]^{0.5}} \tag{E.40}$$

$$\frac{\tilde{T_e}}{\bar{T_e}} = \{\frac{2B_{vid}\sum_{k=i_1}^{i_2} G_{xy}(f_{ens,k})\triangle f_{ens}}{B_{IF}[\sum_{k=0}^{N-1}\frac{|X_k|^2}{N^2}\sum_{k=0}^{N-1}\frac{|Y_k|^2}{N^2}]^{0.5}}\}^{0.5} \tag{E.41}$$

E.2.3 Application in IDL

In order to use Eq. E.41, we need to check the definition and real output value of the FFT from the software we are using. Here, IDL is used. In IDL help, the definition of the FFT value in IDL is,

$$X_{k,IDL} = \frac{1}{N}\sum_{k=0}^{N-1} x(t)e^{-j2\pi fn\triangle t} = \frac{1}{N}X_k \tag{E.42}$$

If the above definition is correct, Parseval's theorem will be,

$$Var[x(t)] = \sum_{k=0}^{N-1}\frac{|X_k|^2}{N^2} = \sum_{k=0}^{N-1}|X_{k,IDL}|^2 \tag{E.43}$$

We can check the above equation using data from CECE. For shot 1120626023, t:0.8-0.9s, the variance of Ch1 is 0.0704. The sum of $|X_{k,IDL}|^2$ is exactly same, 0.0704.

Thus, we can check both Parseval's Theorem and the definition of FFT in IDL. In this FFT, no window functions or overlapping processes were applied. An FFT with hanning window, 50% overlapping and ensemble averaging was also tried, to remove noise and obtain a more correct FFT value. The sum of FFT values in this case is 0.0701. The value is slightly decreased because random noise is removed and side lobe leakage is minimized, but the result is within 1% in this case. Thus, we can use either way to calculate the auto power spectrum value to obtain information about mean temperature. To save computation time and obtain a more correct value, the latter method is more desirable.

Considering the FFT definition in IDL, the spectral density value will be,

$$G_{xx}(f_{ens,k}) = \frac{2\triangle t}{n_d N_{ens}} \sum_{n=1}^{n_d} |X_{k_{ens},n}|^2 = \frac{2\triangle t N_{ens}}{n_d} \sum_{n=1}^{n_d} |X_{k_{ens},IDL,n}|^2 \tag{E.44}$$

$$G_{xy}(f_{ens,k}) = \frac{2\triangle t}{n_d N_{ens}} \sum_{n=1}^{n_d} |X^*_{k_{ens},n} Y_{k_{ens},n}| = \frac{2\triangle t N_{ens}}{n_d} \sum_{n=1}^{n_d} |X^*_{k_{ens},IDL,n} Y_{k_{ens},IDL,n}| \tag{E.45}$$

Then, the fluctuation level will be,

$$\frac{\tilde{T}_e}{\bar{T}_e} = \{\frac{2B_{vid}\triangle f_{ens} \sum_{k_{ens}=i_1}^{i_2} \frac{2\triangle t N_{ens}}{n_d} \sum_{n=1}^{n_d} |X^*_{k_{ens},IDL,n} Y_{k_{ens},IDL,n}|}{B_{IF}[\sum_{k=0}^{N-1} |X_{k,IDL}|^2 \sum_{k=0}^{N-1} |Y_{k,IDL}|^2]^{0.5}}\}^{0.5} \tag{E.46}$$

Using $\triangle f_{ens} = \frac{1}{N_{ens}\triangle t}$,

$$\frac{\tilde{T}_e}{\bar{T}_e} = \{\frac{2B_{vid} \sum_{k_{ens}=i_1}^{i_2} \frac{2}{n_d} \sum_{n=1}^{n_d} |X^*_{k_{ens},IDL,n} Y_{k_{ens},IDL,n}|}{B_{IF}[\sum_{k=0}^{N-1} |X_{k,IDL}|^2 \sum_{k=0}^{N-1} |Y_{k,IDL}|^2]^{0.5}}\}^{0.5} \tag{E.47}$$

When we use ensemble averaging for the calculation of auto power, the equation will be as follows.

$$\frac{\tilde{T}_e}{\bar{T}_e} = \{\frac{2B_{vid} \sum_{k_{ens}=i_1}^{i_2} \frac{2}{n_d} \sum_{n=1}^{n_d} |X^*_{k_{ens},IDL,n} Y_{k_{ens},IDL,n}|}{B_{IF}[\sum_{k_{ens}=0}^{N/n_d-1} \frac{1}{n_d} \sum_{n=1}^{n_d} |X_{k_{ens},IDL,n}|^2 \sum_{k_{ens}=0}^{N/n_d-1} \frac{1}{n_d} \sum_{n=1}^{n_d} |Y_{k_{ens},IDL,n}|^2]^{0.5}}\}^{0.5} \tag{E.48}$$

Appendix F

Preparation of GYRO input files for C-Mod Ohmic discharges

This section presents the profile analysis, including the error analysis, performed for the input profiles and parameters used in the power balance analysis using the code, TRANSP, and the gyrokinetic analysis using the code, GYRO, such as density and temperature profiles. Concerning error analysis, the uncertainty for each measured data point can be estimated by the diagnostician. However, not only raw data itself but also gradients in the profiles are important input parameters in the gyrokinetic simulations. The proper gradient value and its uncertainty should be estimated by the simulation-runner so that the uncertainty from input profiles is clarified and the validation study can be done properly.

The parameters related to impurities such as Z_{eff} and dilution fraction may also be important parameters in the gyrokinetic simulations. Z_{eff} can affect the transport due to TEM since the collisionality, which affects the trapped particle's activity, is a function of Z_{eff}. Higher dilution fraction will decrease the transport due to the ITG mode by a dilution of main ions and the modification of the mode-particle resonance [104]. Thus, we should know the correct values of Z_{eff} and dilution fraction before gyrokinetic simulation.

The turbulence measurements we used for the GYRO validation study in this study are the electron temperature fluctuations measured by Correlation ECE (CECE).

CECE measures the time averaged electron temperature fluctuations during a stationary time period. However, the gyrokinetic simulation is performed at one time slice. It is possible to run several times at different time slices in the stationary time period, but it would be too expensive. Instead of running several time slices, the average profiles and parameters will be used in the simulation. The deviation of the profile or parameter from the averaged value during the stationary time period will be considered to be the uncertainty of the input profile or parameter. For discharges of interest here (shot 1120626023, 1120626028), the stationary time period is 0.9-1.4s.

F.1 Profile analysis for electron temperature and density

As mentioned in Chapter 3, we used fiTS, the fitting tool used in C-Mod, to obtain the radial profiles of electron density (n_e) and the electron temperature (T_e). The radial profiles at each time slice are usually obtained from fiTS with the default setup, but if the fitting line is not physical, we fix a fitting line by removing outliers or adjusting fitting parameters. Time-averaged profiles are used in this study, and the uncertainty of n_e and T_e profiles and their radial gradients are estimated from the standard deviation of the time averaging. Figure F-1 shows the profiles at each time slice and the time-averaged profile for n_e and T_e in one C-Mod discharge used in this study (shot 1120626023, t:0.9-1.4s). The most relevant parameter from the n_e and T_e profiles in the gyrokinetic simulations are the scale length normalized by minor radius, a, a/L_{n_e} and a/L_{T_e} for n_e and T_e profiles, respectively. For a certain profile, X, its gradient scale length normalized by minor radius, a/L_X, is defined as $a/L_X = a/X \mid dX/dr \mid$. Both a/L_{n_e} and a/L_{T_e} are calculated from the averaged n_e and T_e profiles and their gradient values among the fitted profiles, and its error is estimated via the error propagation technique as follows:

$$(\frac{\sigma_{a/L_{n_e}}}{a/L_{n_e}})^2 = (\frac{\sigma_{n_e}}{n_e})^2 + (\frac{\sigma_{dn_e/dr}}{dn_e/dr})^2 + (\frac{\sigma_a}{a})^2 \tag{F.1}$$

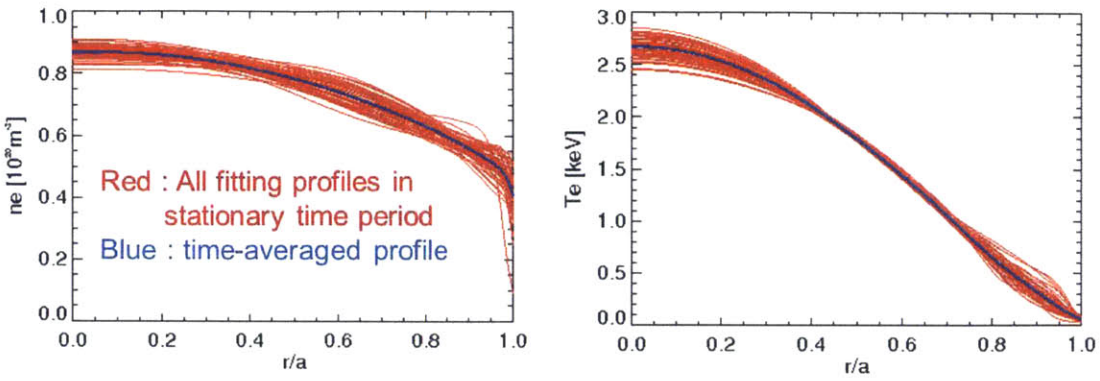

Figure F-1: The n_e and T_e profiles fitted by fiTS for one C-Mod discharge (shot 1120626023, t:0.9-1.4s). The red line indicates the fitted profiles at each time slice in the stationary time period, and the blue line indicates the time-averaged profile.

$$(\frac{\sigma_{a/L_{T_e}}}{a/L_{T_e}})^2 = (\frac{\sigma_{T_e}}{T_e})^2 + (\frac{\sigma_{dT_e/dr}}{dT_e/dr})^2 + (\frac{\sigma_a}{a})^2 \tag{F.2}$$

F.2 Ion temperature profile analysis

In Alcator C-Mod, the ion temperature (T_i) profile is measured by high resolution x-ray spectroscopy (HIREX) [87, 122]. It is known that there is an offset in the T_i profile measured by HIREX due to hardware issue. Edge T_i profile where r/a$\geq\sim$ 0.87 can be obtained by charge exchange recombination spectroscopy (CXRS) [103]. In order to obtain the proper T_i profile, it is required to estimate the proper offset and to determine the proper gradient and its error through fitting or other methods.

F.2.1 Determination of the offset in the T_i profile measured by HIREX

There are several ways to determine the proper offset for the T_i profile from HIREX. We can use the T_e profile near the edge where $T_e \sim T_i$ because of the frequent collisions between electrons and ions, or the T_i profile from CXRS can be used as well. Using these methods, the offset value will be determined mainly by the T_i or T_e values near the edge. Moreover, if the T_i profile from CXRS is reliable, it may be better to

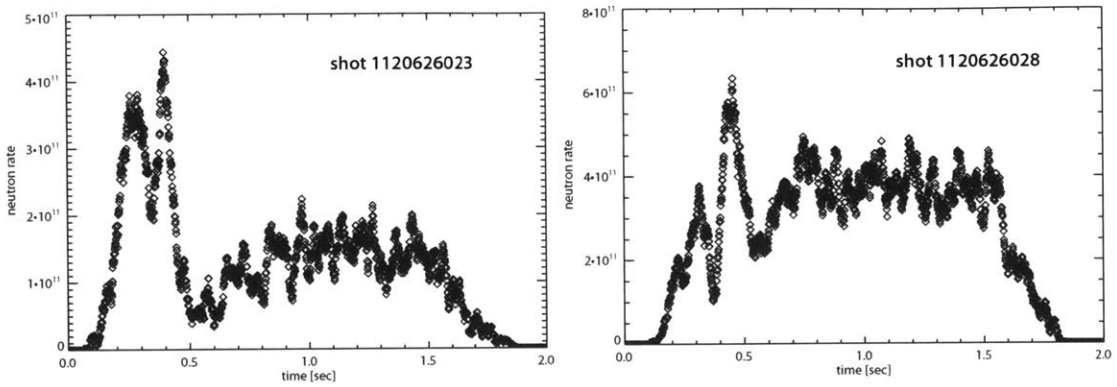

Figure F-2: The measured neutron rate for shot 1120626023 and shot 1120626028.

use CXRS data to make the T_i profile instead of using it for the offset estimation. Another method of offset estimation is to compare the calculated neutron rate from the T_i profile measured by HIREX with the measured neutron rate by the neutron detector [14]. Since most neutrons will be generated in the core, this method will be affected by the T_i value in the core. Once the proper offset value is estimated from the neutron rate, then the raw data profile can be generated from core T_i data from HIREX with proper offset and edge T_i data from CXRS. Since the latter method gives constraints on both the core and edge regions, the uncertainty in the T_i profile can be minimized. Thus, the latter method was used in this thesis.

In order to determine the proper offset, two discharges studied in section 4.2-4.4 (shot 1120626023, 1120626028) were used. Both discharges have a stationary period for a long enough time (~0.5sec) to estimate the measured error from the variance in the stationary period. Figure F-2 shows the measured neutron rate in each shot. The error in the neutron measurement was determined by the standard deviation of the measured neutron rate in the stationary period (0.9-1.4sec). In the neutron rate calculation, the Bosch-Hale parameterization for the d(d,n)He^3 reaction [81] was used for the $< \sigma v >$ value and the plasma volume for each flux surface was calculated from EFIT. The dilution fraction, f_I is also an important parameter in this calculation, which is defined as $f_I = \Sigma Z_{I,i} n_{I,i}/n_e$ where $Z_{I,i}$ is the charge state of the i^{th} impurity in the plasma and $n_{I,i}$ is the density of the i^{th} impurity. $f_I = 0.11 - 0.23$ is used for shot 1120626023 and $f_I = 0.027 - 0.063$ is used for shot 1120626028

(Please see section F.4.1 for details about the estimation of the dilution fraction). The maximum/minimum allowable offset value was determined by finding the offset value which matches the calculated neutron rate to the averaged measured neutron rate in the stationary period plus or minus the standard deviation of the neutron rate in this period when the smallest/largest f_I value is used. Figure F-3(a) and (b) show the calculated neutron rate with the measured rate. For shot 1120626023, the allowable offset values are 0.014-0.173 keV and for shot 1120626028, they are 0.099-0.168 keV. HIREX data with offset is compared with CXRS data in Figure F-3(c) and (d). We can see that HIREX data is reasonably matched with CXRS data within the error in the offset range. Since the offset in the T_i profile is due to the hardware problem, this value will not be changed based on specific shot conditions. Thus, it is proper to set the allowable offset range which satisfies the neutron rate comparison for both shots. For these two discharges, the proper range is 0.1-0.169keV. In other words, the proper offset value is $\sim$0.134keV$\pm$0.035keV.

F.2.2 Determination of input profile

Although the measured T_i values are reliable within the uncertainty, it is difficult to determine the gradient from just the measured value. This is because the measured amplitude can be changed within the error, and it will change the gradient more widely than the error of the amplitude. Moreover, we cannot generate the profile by just connecting the measured data points. This is because the measured profile sometimes has a structure that gives very low or high gradient value. This structure, or significantly high/low gradients in the profile is not allowed physically since low gradient in the T_i profile will decrease turbulent transport, increasing confinement and local T_i value and its gradient and the opposite phenomena will occur for the high gradient case. Thus, the profile will have a stiff gradient at each radial position and it will be smoothed without any odd points. Nevertheless, we should figure out the correct and proper profile based on the measured raw data points and their errors. Fitting including consideration of error, such as weighting or picking random data within the error, will be one of the best ways to obtain the proper profile, since

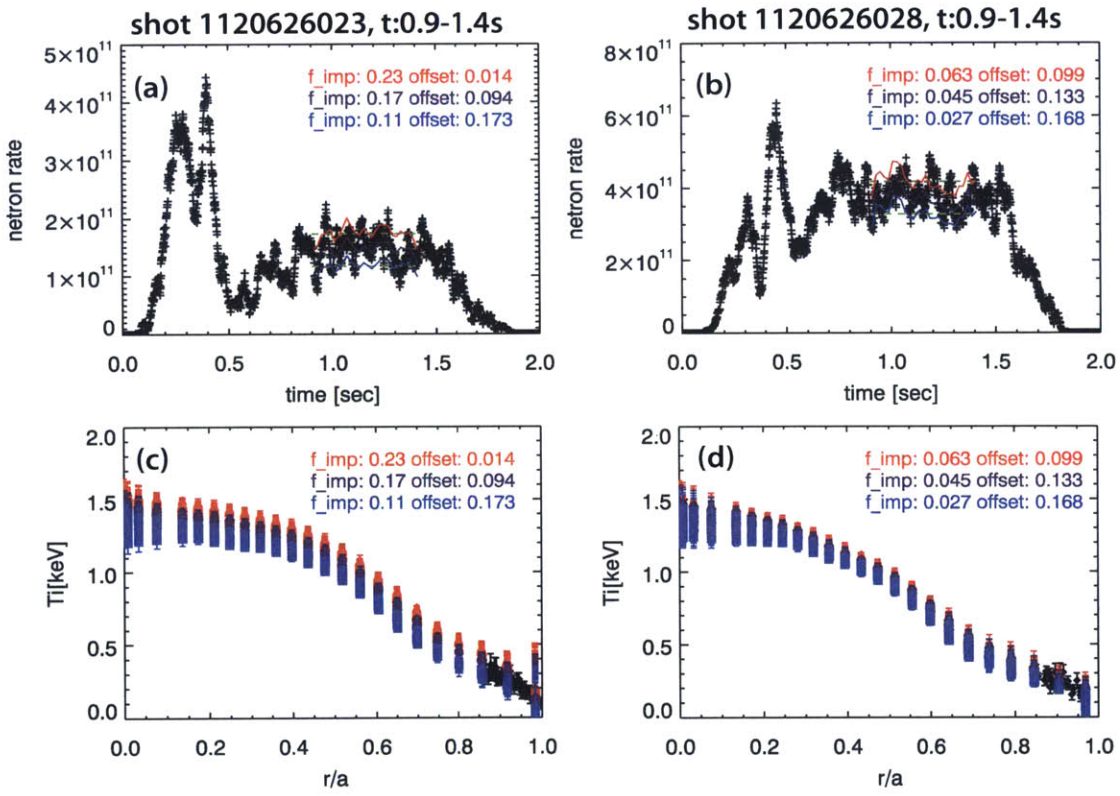

Figure F-3: The comparison of measured neutron rate with the calculated neutron rate from the given dilution fraction and the offset of the HIREX T_i data for (a) shot 1120626023 and (b) shot 1120626028. The comparison of HIREX T_i data with the given offset with CXRS data for (c) shot 1120626023 and (d) shot 1120626028.

the fitting will give a profile without unreasonable structure in most cases and can generate the error and a reasonable value for the gradient. B-spline fitting is used in this analysis.

The errors for both T_i data from HIREX and CXRS have already been estimated by diagnosticians. However, the error for HIREX measurements is estimated from photon statistics, which gives an unreasonably small error value. In order to estimate the proper error value, errors from two different sources are added. First, the error from the asymmetry between T_i profiles from lower and higher fields are added. We can assume that the profile in the higher field side is the same as the one in the lower field side, but the measured values are not the exactly same and this difference can be considered as an error in the measurement or analysis. It is also possible that the T_i profile depends on the poloidal angle. However, we assume that the T_i profile does not depend on the poloidal angle. Thus, this asymmetry may be considered as error in both cases. We may also consider the variation in the stationary period as error. Assuming that the plasma is steady during some period, the T_i value should also be steady. Thus, the standard variation of T_i during the stationary period may be used as the random error. For the HIREX T_i data, these three errors are added through the standard error propagation technique. The error in T_i for CXRS, which comes from CXRS data processing (to be specific, it comes from the Doppler broadening width estimation), is estimated by the diagnostician. Error from asymmetry between the lower and higher field side is not available for CXRS data and the number of time points during the stationary period is insufficient to estimate the error. Although only one error source is considered for CXRS data, the error amplitude is comparable to the error of the HIREX data. The HIREX T_i data also have error from the offset. However, the error from the offset is different from the errors from other sources. Unlike random error, the error from the offset will not change the gradient of the T_i profile and it will change the T_i value at all radial points at the same time. Thus, this error should be treated separately.

As mentioned before, the combined T_i data set from HIREX and CXRS will be the most appropriate way to minimize the error from the offset. In the combined T_i data

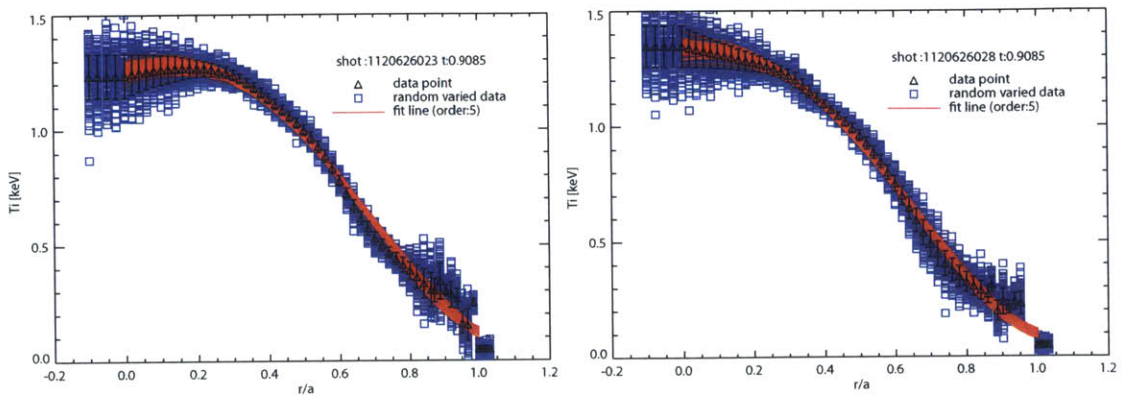

Figure F-4: Example of the fitting using the randomly picked data from the measured data points within the error at t:0.9s for shot 1120626023 and 1120626028. Black triangle points show the raw data points and points for fitting constraints with the error bar. The blue squares indicate the randomly selected data points from the black triangle points. Random data picked 100 times. Red line indicates the fitting line using 5^{th} order B-spline fitting.

set, HIREX data are used in r/a≤0.86, and CXRS data are used in the outer region (0.87≤r/a≤1.0). In the fitting process, two constraints are used. The first constraint is for the T_i gradient on the magnetic axis(r/a=0). Physically, the gradient of the T_i profile should be zero at r/a=0. In order to make the gradient of T_i on the magnetic axis zero, 4 more data points whose value is $T_i(0)$ are added in -0.1≤r/a≤0.0 at each time slice in the stationary period. The error for these additional points is the same as the error of $T_i(0)$. The second constraint is for a negative gradient near r/a=1.0. Higher order (≥5) B-spline fitting sometimes gives a positive gradient near the edge. A positive gradient is not physically allowed. To prevent this, 4 data points are added in 1.0≤r/a≤1.03 at each time slice. Since ions and electrons will be well coupled through collisions near the edge, $T_i \sim T_e$ is expected. Thus, $T_i \sim T_e$ might not be a bad assumption at the edge. From this assumption, these 4 data points have the same amplitude as the T_e (r/a=1.0) at each time slice. The error for those points is also the same as the error of T_e (r/a=1.0) at each time slice. In addition, it should be mentioned that CXRS data points are interpolated on the HIREX time slice and the reference radial position to facilitate the time averaging of the fitted line.

In order to estimate the error of the fitted profile and its gradient, a T_i data point in each radial region is randomly selected within the error. It is noteworthy that

this random process was set to have a Gaussian distribution whose mean value is the data value and the standard deviation is the error of the each data point so that the random error can be taken account of by this random picking process. With the given offset value (0.135keV) for the HIREX data, the T_i data were selected randomly and the line is fitted on the randomly selected data set. 100 fitted profiles were made at each time slice from the repeated random picking process and fitting. The mean value of the profile and its error are estimated from averaging these fitted profiles and their standard deviation in the averaging. Since several time slices in the stationary time period are considered in the simulation and only the profile at one time slice will be considered in the gyrokinetic simulation as the input profile, all the fitted profiles at each time slice are included in the averaging. Figure F-4 shows an example of this process for shots 1120626023 and 028 at a certain time slice. The uncertainty from the offset can be included only in the T_i profile through error propagation. To be specific, the error of the T_i profile, σ_{T_i} will be,

$$\sigma_{T_i}^2 = \sigma_{random}^2 + \sigma_{offset}^2 \tag{F.3}$$

where σ_{random} is the random error and σ_{offset} is the error of the offset.

Finally, the most relevant parameter from the T_i profile in gyrokinetic simulation will be a/L_{T_i}. In the same manner used for the a/L_{n_e} and a/L_{T_e} estimations, this parameter is calculated from the average T_i and its gradient value among the fitted profiles, and its error is estimated by error propagation. The error of $a/L_{T_i}, \sigma_{a/L_{T_i}}$, is,

$$(\frac{\sigma_{a/L_{T_i}}}{a/L_{T_i}})^2 = (\frac{\sigma_{T_i}}{T_i})^2 + (\frac{\sigma_{dT_i/dr}}{dT_i/dr})^2 + (\frac{\sigma_a}{a})^2 \tag{F.4}$$

The proper fitting order should be also determined. Here, the reduced chi square, χ_{red}^2, is used to determine the proper order of fit. χ_{red}^2 is defined as,

$$\chi_{red}^2 = \frac{\chi^2}{\nu} = \frac{1}{\nu}\sum \frac{(X_{fit} - X_{data})^2}{\sigma^2} \tag{F.5}$$

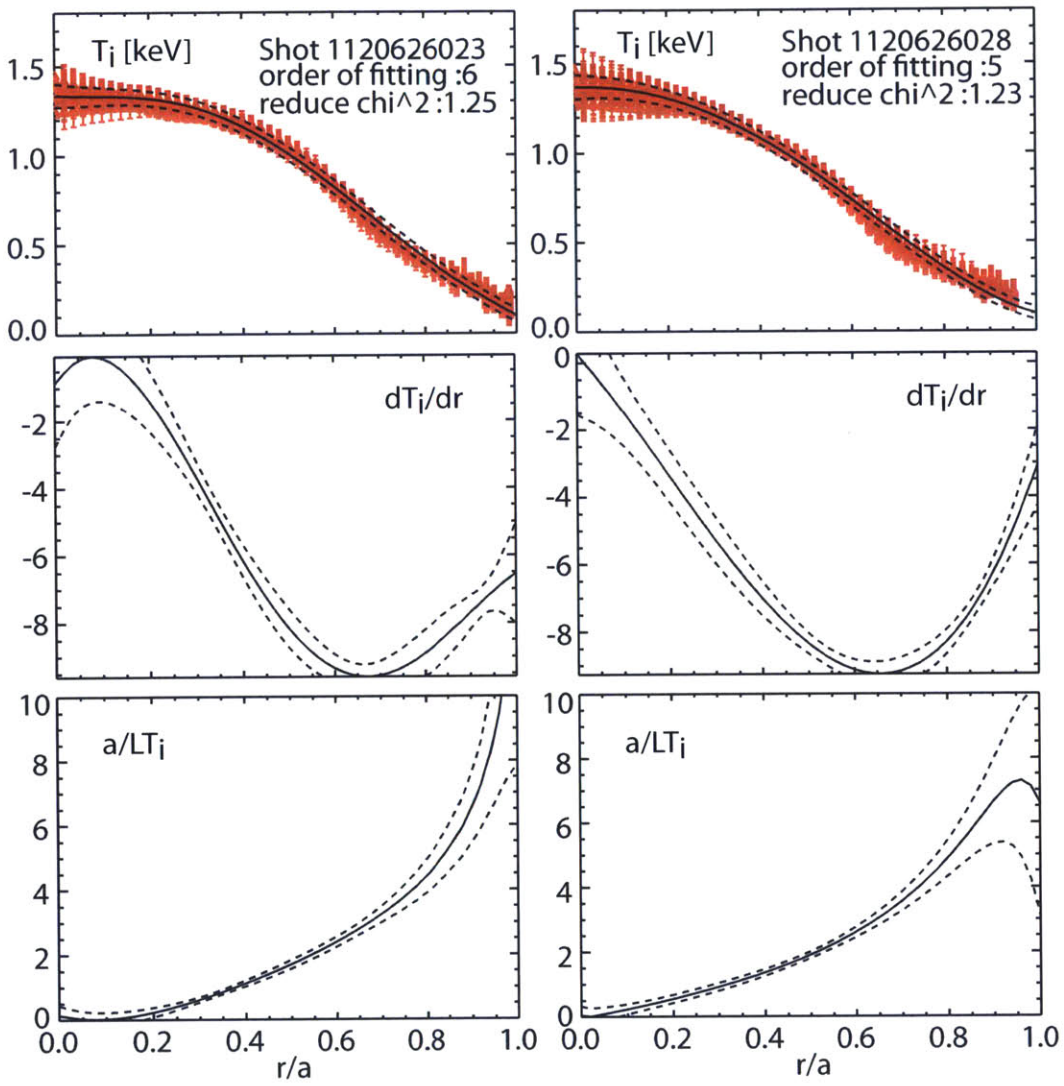

Figure F-5: Fitting results based on the data at each time slice during the stationary period (0.9-1.4s) for shot 1120626023 and 1120626028. With the given offset (0.135keV), the profile was determined as the average profile among the fitted profiles from each time slice. The dotted lines indicate the error of the profiles. The solid line is the mean value of the profiles.

fitting order	shot 1120626023 (t:0.9-1.4s)	shot 1120626028 (t:0.9-1.4s)
4^{th} order	2.33	1.96
5^{th} order	1.36	1.23
6^{th} order	1.25	1.78

Table F.1: The value of χ^2_{red} depending on the fitting order and the manner of treating the data (fitting based on the whole data set or on the data at each time slice and the average the value from each time slice) when the HIREX offset value is 0.099-0.169keV.

Where ν is the degree of freedom, which is given by N-m-1 with N, the number of observations (the number of data points used in this calculation) and m is the number of fitting parameters.

The χ^2_{red} indicates the quality of the fitting. $\chi^2_{red} > 1$ indicates that the fitting does not capture the data well and $\chi^2_{red} < 1$ indicates overfitting. $\chi^2_{red} = 1$ is the well fitted case. Thus, we can determine the proper order of fitting from χ^2_{red}. In other words, we can pick the order which gives χ^2_{red} closest to 1.

Table F.1 shows the χ^2_{red} value depending on the fitting order for shot 1120626023 and 1120626028. As shown in the table, 6^{th} order fit brings the closest χ^2_{red} to 1 for shot 1120626023, and 5^{th} order gives the closest χ^2_{red} to 1 for shot 1120626028. Thus, 6^{th} order and 5^{th} order will be used for shot 1120626023 and 1120626028, respectively. Figure F-5 shows the T_i, dT_i/dr and a/L_{T_i} profiles for those two shots, which are fit based on the data points at each time slice with the selected fitting order.

F.3 Toroidal velocity profile analysis

In this section, we present how the profiles of the toroidal velocity (V_t) are obtained. The toroidal velocity is measured by high resolution imaging x-ray spectroscopy (HIREX) and charge exchange spectroscopy (CXRS) in this study. As mentioned in Chapter 3, the toroidal velocity measured by HIREX has a large uncertainty in the edge region. For the Ohmic discharges used in the gyrokinetic analysis in Chapter 4, the region of interest is r/a$\sim$0.85. To constrain the edge V_t profile, we used a CXRS diagnostic. For these Ohmic discharges, only He-like Ar (Ar^{16+}) was used

for the HIREX measurements due to the low temperature in the Ohmic discharges. CXRS measures the velocity of B^{5+}. As mentioned in Chapter 3, toroidal velocities of impurities are well coupled. We can therefore generate V_t profiles by combining the data from these two diagnostics.

For the Ohmic discharges used in Chapter 4, the reliable region of the CXRS measurements is $0.85 < r/a < 0.9$. From the HIREX and CXRS measurements, we may have a correct V_t value at r/a$\sim$0.85. However, the absence of a constraint for the V_t profiles in r/a$>$ 0.9 results in a large uncertainty in the radial gradient of the V_t profile, which will be important for the $E \times B$ shearing rate estimation. As applied for T_i profiles, B-spline fitting is applied to obtain the radial profile. Instead of finding the correct order of B-spline fitting, we used three different orders of B-spline fitting (order 4-6) to obtain the V_t profile. Since the gradient of the edge region will vary with the order of the fitting, as shown in Fig. F-6, we may be able to consider the large uncertainty in the gradient of V_t at the edge region by including fitting profiles with different fitting orders. The V_t profile and its gradient values are obtained from time averaging of the fitted profiles at each time slice and at each fitting order. The uncertainties of the V_t profile and its gradient were estimated from the standard deviation in the averaging. The V_t profiles for the C-Mod LOC and SOC discharges used in Chapter 4, obtained as the result of this profile analysis, are shown in Fig. F-7.

F.4 The estimation of Z_{eff} and dilution

F.4.1 Estimation of Z_{eff} and its error

The Z_{eff} value can be obtained from either spectroscopic measurements or a conductivity calculation. The spectroscopic measurements use the bremsstrahlung radiation whose intensity is proportional to $n_e^2 Z_{eff}$ [85]. We can also estimate Z_{eff} from neoclassical conductivity. In this estimation, the plasma current is calculated as a function of Z_{eff} from neoclassical conductivity with measured quantities such as loop voltage, electron density and temperature, and equilibrium analysis from EFIT. Comparing

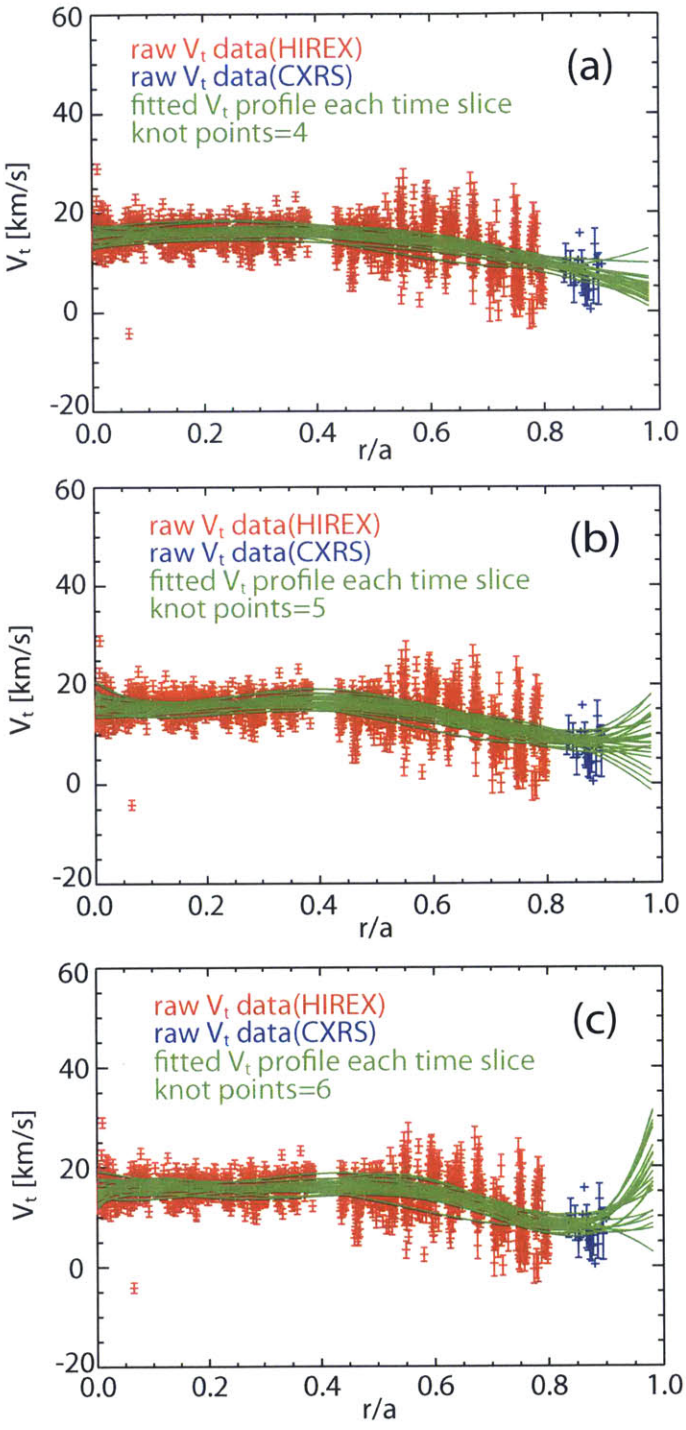

Figure F-6: The results of the fitted toroidal velocity (V_t) profile with raw data measured by HIREX (red) and CXRS (blue) for one C-Mod discharge (shot 1120626023, t:0.9-1.4s) with different orders of B-spline fitting. (a) 4^{th} order (b) 5^{th} order (c) 6^{th} order. The green lines represent the fitted V_t profiles at each time slice.

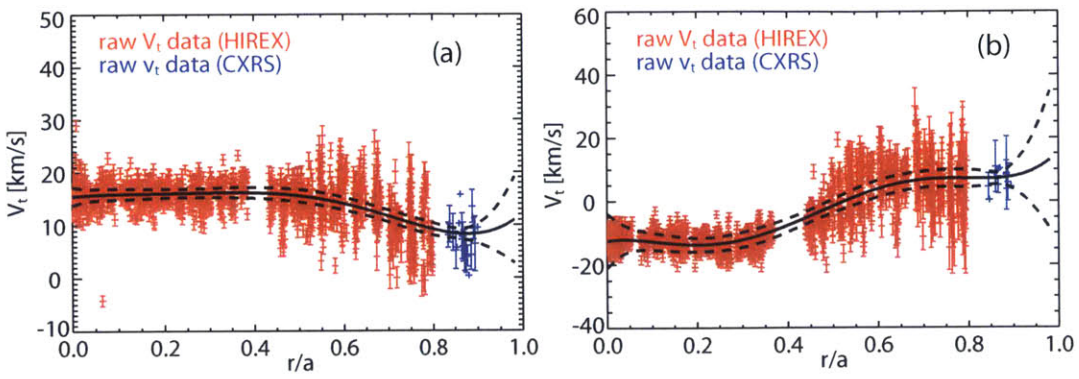

Figure F-7: The fitted toroidal velocity (V_t) profiles with the raw data measured by HIREX (red) and CXRS (blue) for (a) the LOC discharge (shot 1120626023, t:0.9-1.4s) and (b) the SOC discharge (shot 1120626028, t:0.9-1.4s). The solid black line indicates the V_t profile obtained as a result of profile analysis, and the dotted black line shows the uncertainty of the V_t profile.

the calculated plasma current with the plasma current measured by a Rogowski coil, we can find the Z_{eff} value which matches the calculated plasma current to the measured one. As shown in Figure F-8, Z_{eff} values from these two different methods are well matched in H-mode plasmas, but there is a discrepancy between the two values in Ohmic plasmas in C-Mod. Z_{eff} from bremsstrahlung radiation is usually higher than Z_{eff} from neoclassical conductivity. One possible explanation for the discrepancy is background radiation in the bremsstrahlung radiation measurements. Although it is still inconclusive which method gives a correct Z_{eff} value, we do not have any serious issues with the neoclassical calculation so far. Thus, the Z_{eff} value from the neoclassical calculation will be used in this analysis.

There are several error sources in the neoclassical calculation. First, the error in the measured profiles such as n_e and T_e can be propagated in the neoclassical calculation. Since it is hard to calculate the neoclassical conductivity analytically, we cannot apply the error propagation technique to determine the error of Z_{eff} due to the measurement error. Instead, the change in the calculated Z_{eff} value with T_e and n_e profiles with addition or subtraction of their errors is considered to be the error due to n_e and T_e measurements. The error in Z_{eff} due to the error in T_e measurements is estimated as the change of Z_{eff} value when $T_e + / - \sigma(T_e)$ is applied. The error from n_e measurements is estimated in the same way.

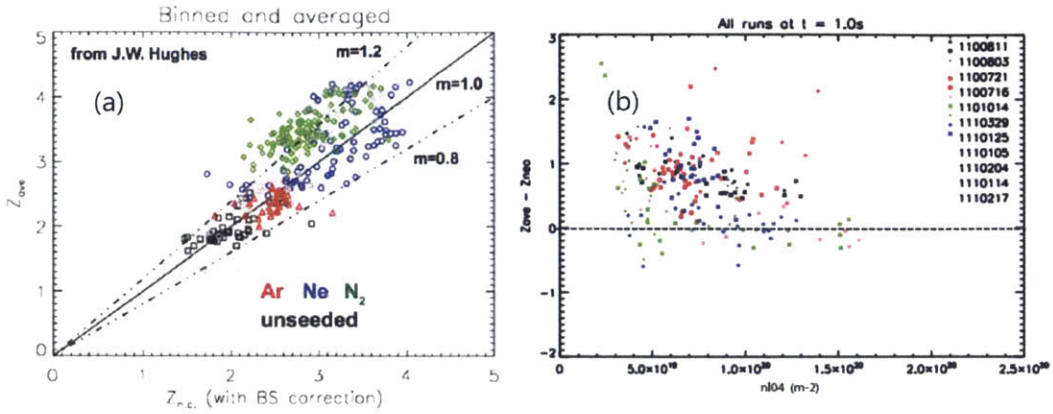

Figure F-8: Z_{ave} refers to the Z_{eff} value measured from bremsstrahlung radiation, and Z_{neo} refers to the Z_{eff} value calculated from neoclassical conductivity (a) The comparison of Z_{ave} with Z_{neo} in H-mode plasmas in C-Mod. They are well matched within 20% (b) The difference of Z_{ave} with Z_{neo} in Ohmic plasmas. The difference between two values grows with lower density, and it was known that low plasma current increase the discrepancy in low density Ohmic plasmas in C-Mod.

There will be also the error in measurements from magnetic diagnostics and from the equilibrium analysis from EFIT. One way to estimate the error from both magnetics and EFIT is to compare the measured plasma current with the calculated plasma current from EFIT. This plasma current is calculated from the poloidal B field in the equilibrium and constrained by the magnetics measurements. The discrepancy between the calculated and measured plasma currents may result from the error of the magnetics or EFIT analysis. We can consider the difference in Z_{eff} value depending on which plasma current value to be the propagated error in the neoclassical Z_{eff} value calculation due to the error in the magnetics and EFIT analysis. The Z_{eff} value was calculated using two different plasma current values. The difference of the maximum and minimum Z_{eff} from this calculation was set to range. This is because these two different plasma currents may be considered to be one of possible plasma current values we could pick. The range of Z_{eff} due to the different I_p values is converted to the error, σ, using the formula in [108].

Another error source is the conductivity (or resistivity) calculation. The neoclassical conductivity was calculated from Sauter's formula [143] with the approximated trapped fraction defined as $\epsilon^{0.5}$, where ϵ is the local inverse aspect ratio. First, we

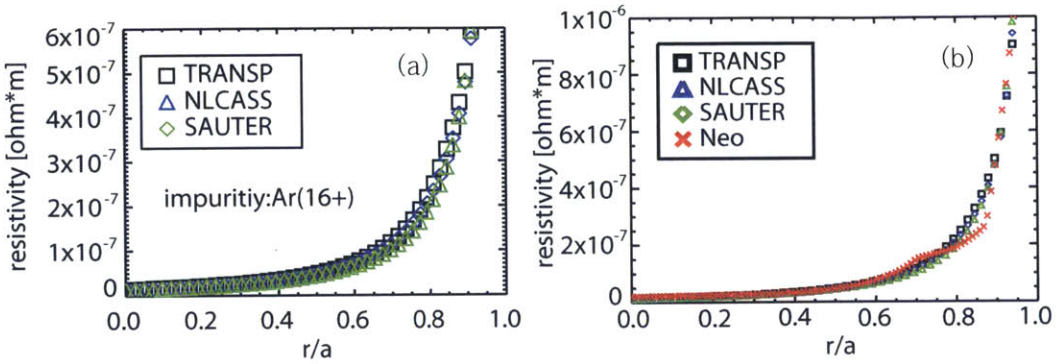

Figure F-9: (a) The resistivity value from three different models are compared. TRANSP indicates the TRANSP default model [71]. NCLASS indicates the resistivity value from NCLASS code. Sauter indicates Sauter's model. The resistivity value is for shot 1120626023, Z_{eff}=2.52 and only Ar is used for impurity with the fraction consistent with Z_{eff} (b) The comparison of resistivity from models calculated from TRANSP with the one from Sauter's formula with the approximated trapped fraction ($\epsilon^{0.5}$). Neo indicates the resistivity with the approximated trapped fraction.

must show that Sauter's formula gives the correct conductivity (or resistivity) value by comparing another formula or model. Using TRANSP, we compared the resistivity value from Sauter's formula with two different resistivity values from another formula [71], which is default model in TRANSP, and NCLASS model [76]. It is noteworthy that the trapped fraction will be estimated correctly via TRANSP unlike the calculation for Z_{eff}. Figure F-9(a) shows the result for shot 1120626023 when Z_{eff}=2.52 and Ar is used for the impurity with impurity fraction consistent with the Z_{eff} value. As shown in the figure, they are very similar to each other. For shot 1120626028, the result was the same. Thus, we believe that Sauter's formula gives a reasonable conductivity (resistivity) value. We must also verify the error of the calculated resistivity value due to the use of an approximated trapped fraction. As shown in Fig. F-9(b), the resistivity value is significantly different in the outer region, which has larger trapped fraction. In the neoclassical Z_{eff} calculation, conductivity (or resistivity) is used to obtain the current density, j from Ohm's law, $j = \sigma E$. Plasma current is then calculated from area integral of the current density. Thus, we can track how the error of conductivity (or resistivity) will propagate in the Z_{eff} calculation. I_p is calculated as follows:

$$I_p = \int jdA = \sum j_i dA_i = \sum \sigma_i E dA_i \tag{F.6}$$

with electric field, E.

Since we know the difference between the resistivity value with the approximated trapped fraction and the one with the correct trapped fraction, we can calculate the difference in I_p due to the difference in resistivity. The fractional difference of I_p, ϵ_{I_p}, due to the different resistivity values will be,

$$\epsilon_{I_p} = \frac{[\sum(\sigma_{i,sauter} - \sigma_{i,neo})EdA_i)^2]^{1/2}}{[\sum(\sigma_{i,neo})EdA_i)} = \frac{[\sum(\sigma_{i,sauter} - \sigma_{i,neo})dA_i)^2]^{1/2}}{[\sum(\sigma_{i,neo})dA_i)} \tag{F.7}$$

where $\sigma_{i,sauter}$ is the conductivity calculated from TRANSP using Sauter's formula and $\sigma_{i,neo}$ is also conductivity from Sauter's formula but with the approximated trapped fraction ($\epsilon^{0.5}$) is used. ϵ_{I_p} is $\sim$0.03 for both shot 1120626023 and shot 1120626028. Now, the change in Z_{eff} due to the error in the resistivity model can be evaluated by calculating the Z_{eff} value with $I_p \times (1 \pm \epsilon_{I_p})$. Using the same method used in calculating the error due to EFIT and magnetic measurements, we can find the range from the maximum and minimum value of these trials and convert it to the error, σ.

Finally, the variation of Z_{eff} during the stationary period is considered to be another error source. Using the errors from different error sources, the error of the calculated Z_{eff} can be calculated through error propagation. That is, the error of Z_{eff}, $\sigma(Z_{eff})$, will be,

$$\begin{aligned}(\frac{\sigma(Z_{eff})}{Z_{eff}})^2 =& (\frac{\sigma(Z_{eff,n_e})}{Z_{eff,n_e}})^2 + (\frac{\sigma(Z_{eff,T_e})}{Z_{eff,T_e}})^2 + (\frac{\sigma(Z_{eff,mag})}{Z_{eff,mag}})^2 \\ &+ (\frac{\sigma(Z_{eff,model})}{Z_{eff,model}})^2 + (\frac{\sigma(Z_{eff,st})}{Z_{eff,st}})^2\end{aligned} \tag{F.8}$$

where mag indicates error from magnetics and EFIT, model indicates the error from the resistivity model and st indicates the error from the assumption of a stationary period. The value in the denominator for each error term is the mean value of the

shot	time (sec)	$\epsilon_{Z_{eff,n_e}}$	$\epsilon_{Z_{eff,T_e}}$	$\epsilon_{Z_{eff,mag}}$	$\epsilon_{Z_{eff,model}}$	$\epsilon_{Z_{eff,st}}$	$\epsilon_{Z_{eff}}$	Z_{eff}(± error)
1120626023	0.9-1.4	0.0041	0.12	0.016	0.056	0.055	0.14	2.53±0.36
1120626028	0.9-1.4	0.0052	0.10	0.020	0.061	0.052	0.13	1.48±0.20

Table F.2: The fraction error from each error source for the shot 1120626023 and 1120626028

different Z_{eff} values depending on the input parameters of interest. For example, Z_{eff,n_e} is the mean Z_{eff} value among the different n_e profiles, which are n_e and $n_e \pm \sigma(n_e)$ and $\sigma(Z_{eff,n_e})$ is the standard deviation of these trials.

Using this method, the Z_{eff} value and its error for the shots of interest are calculated. The results are shown in Table F.2, 2.50±0.34 for shot 1120626023 and 1.45±0.17 for shot 1120626028.

F.4.2 Estimation of the dilution fraction and its error

Unfortunately, we do not have a good way to estimate or measure the dilution fraction in C-Mod plasmas. However, one way we can try is to use impurity line radiation. Assuming collisional reactions are dominant compared to spontaneous ones, brightness of the measured line radiation, I_{imp}, is approximated as the product of the electron density and the impurity density, and the sigma-v factor, i.e., $I_{imp} \sim n_e n_{imp} < \sigma v >$. Since sigma-v factor is a function of temperature, for plasmas whose temperature is similar, $\frac{I_{imp}}{n_{e,line}^2} \propto \frac{n_{imp}}{n_e}$. Since spectroscopy measures the line integrated brightness, the line integrated electron density, $n_{e,line}$, is used. Among Ohmic discharges of interest to this analysis, the above assumption is acceptable. Once we know the calibration factor, C_I, which satisfies $\frac{n_{imp}}{n_e} = C_I \frac{I_{imp}}{n_{e,line}^2}$, the impurity fraction can be estimated from the brightness. Using $Z_{eff} = 1 + \sum f_i Z_i(Z_i - 1) = 1 + \sum C_{I,i} \frac{I_{imp,i}}{n_{e,line}^2} Z_i(Z_i - 1)$, the Z_{eff} can be used to find the calibration factor. If we know the correct Z_{eff} value and the major impurities in the plasma, the equation for the calibration factor can be solved. For m impurities and n shots, we will have a matrix problem, XC=Z where X is an m×n matrix with $X_{i,j} = \frac{I_{imp,j}}{n_{e,line,i}^2} Z_{i,j}(Z_{i,j} - 1)$, C is an n×1 matrix and C_j is the calibration factor of the j^{th} impurity. Z is the m×1 matrix with $Z_i = Z_{eff,i} - 1$.

In this analysis, 8 shots and 6 impurities are considered in the matrix problem.

shot	time (sec)	Z_{eff}(± error)	explanation
1120131030	1.2-1.3	2.24(±0.56)	F burst
1120217021	0.6-1.4	1.04(±0.21)	Intrinsic only
1120224033	1.0-1.3	3.71(±1.02)	Moly burst
1120203019	1.1-1.4	1.84(±0.28)	Ar burst
1120203027	0.9-1.1	2.15(±0.33)	N burst
1120214002	0.7-1.0	1.04(±0.19)	Moly burst
1120626023	0.9-1.4	2.53(±0.47)	LOC discharge
1120626028	0.9-1.4	1.48(±0.25)	SOC discharge

Table F.3: The shots used in the calibration factor estimation. The Z_{eff} value was calculated from neoclassical conductivity and the n_e and T_e profiles from quickfit were used. The error of Z_{eff} was estimated using Eq F.8.

	B	N	O	F	Ar	Mo
Calibration factor	0.073	0.23	1.20	0.041	0.0043	0.00082

Table F.4: The calibration factor of each impurity (B, N, O, F, Ar, Mo).

shot	time(sec)	f_B	f_N	f_O	f_F	f_{Ar}	f_{Mo}	dilution	$Z_{eff,input}$	$Z_{eff,output}$
1120131030	1.2-1.3	0.0025	0.0021	0.012	0.0023	0.0010	1.36e-5	0.16	2.24	2.24
1120217021	0.6-1.4	0.0005	0.0003	0.0009	2.73e-5	1.22e-6	2.44e-7	0.012	1.04	1.08
1120224033	1.0-1.3	0.0036	0.0061	0.021	0.0004	0.0003	0.0010	0.27	3.71	3.71
1120203019	1.1-1.4	0.0006	0.0009	0.0028	7.44e-5	0.0026	1.91e-6	0.074	1.84	1.85
1120203027	0.9-1.1	0.0003	0.023	0.0026	3.58e-5	0.0001	1.31e-6	0.18	2.15	2.15
1120214002	0.7-1.0	0.0007	6.25e-5	0.0003	1.19e-5	1.25e-6	3.84e-7	0.0063	1.04	1.03
1120626023	0.9-1.4	0.0014	0.0052	0.011	0.0003	0.0023	1.12e-5	0.18	2.53	2.54
1120626028	0.9-1.4	0.0006	0.0014	0.003	6.48e-5	0.0008	2.24e-6	0.047	1.48	1.42

Table F.5: The fraction of each impurity and dilution from the calibration factor in table F.4. The Z_{eff} value from the calibration factors is also included, which is similar to the value calculated from neoclassical conductivity.

These 8 shots are 6 Ohmic discharges which have an impurity burst and 2 Ohmic plasmas of particular. Table F.3 shows details about the 8 shots used here. The 6 impurities considered here are B,N,O,F,Ar and Mo. The calibration factor was determined as the value which gives the least squares error, and the dilution fraction was estimated from the calibration factor. Table F.4 shows the calculated calibration factor for each impurity. Using these calibration factors, the dilution fraction and the fraction of each impurity were obtained as shown in Table F.5. These values are the average values during t:0.9-1.4s. One way to determine whether or not this estimation is correct is to compare the boron fraction (n_B/n_e) from the calibration factor and the brightness of line radiation with the boron fraction from CXRS measurements. From the CXRS measurements, the boron fraction was 0.0008 for shot 1120626023 (t:0.9-1.4s) and 0.0006 for shot 1120626028(t:0.9-1.4s). As shown by Table F.5, the boron fraction from the calibration factors(0.0014 for shot 1120626023 and 0.0006 for shot 1120626028) is similar to the value from the CXRS measurements. Although this result does not guarantee that the estimation in this section is correct, the consistent boron fraction supports the calculation that the calculated dilution fraction is reasonable.

The error of the dilution fraction can be estimated using a covariance matrix [135]. We can estimate the error propagated from the error in Z_{eff} through a covariance matrix. The error in Z_{eff} estimated in the previous section was used to construct the covariance matrix. We can also include the error of the line integrated electron density, which is defined as 5% of the measured value through error propagation. The error in the brightness measurements is not included at this point. The dilution fractions including error are 0.175$\pm$0.085 for shot 1120626023 and 0.047$\pm$0.027 for shot 1120626028 during t:0.9-1.4s. Under the assumption of a stationary time period, the error of dilution is the averaged value among the error at each time slice during 0.9-1.4s.

Appendix G

Non-adiabatic electron response in T_e fluctuations

A first order electron velocity distribution function perturbed by turbulence has two parts, as shown in Eq. G.1.

$$f_e(\vec{v}) = \frac{e\phi}{T_e} f_{Me} + h(\vec{v}) \tag{G.1}$$

where f_{Me} is a Maxwellian distribution function for electrons and ϕ is the turbulent electrostatic potential.

The first term on the right hand side in Eq. G.1 represents an adiabatic (or a Boltzmann) electron response, and the second term shows a non-adiabatic electron response. The electron energy and density fluctuations will be defined as Eq. G.2 and Eq. G.3, respectively.

$$\tilde{E} = \int \frac{1}{2} m_e \vec{v}^2 f_e(\vec{v}) \mathrm{d}\vec{v} \tag{G.2}$$

$$\tilde{n}_e = \int f_e(\vec{v}) \mathrm{d}\vec{v} \tag{G.3}$$

In the first order approximation, electron temperature fluctuations can be ex-

tracted from electron energy fluctuations as shown in Eq. G.4-G.6.

$$E + \tilde{E} = \frac{3}{2}(n_e + \tilde{n}_e)(T_e + \tilde{T}_e) \tag{G.4}$$

where E, n_e and T_e are quantities in the equilibrium state, and $E = \frac{3}{2}n_e T_e$.

$$\tilde{E} \sim \frac{3}{2}(\tilde{n}_e T_e + \tilde{T}_e n_e) = \frac{3}{2}n_e T_e(\frac{\tilde{n}_e}{n_e} + \frac{\tilde{T}_e}{T_e}) \tag{G.5}$$

$$\frac{\tilde{T}_e}{T_e} \sim \frac{2}{3}\frac{\tilde{E}}{n_e T_e} - \frac{\tilde{n}_e}{n_e} \tag{G.6}$$

T_e fluctuations can then be calculated from the definitions of $\tilde{E}$ and $\tilde{n}_e$. The first and second terms in Eq. G.6 will be calculated as Eq. G.7 and Eq. G.8, respectively.

$$\begin{aligned}
\frac{2}{3}\frac{\tilde{E}}{n_e T_e} &= \frac{2}{3n_e T_e}\int \frac{1}{2}m_e\vec{v}^2 f_e(\vec{v})\mathrm{d}\vec{v} \\
&= \frac{2}{3n_e T_e}\int \frac{1}{2}m_e\vec{v}^2[\frac{e\phi}{T_e}f_{Me} + h(\vec{v})]\mathrm{d}\vec{v} \\
&= \frac{e\phi}{T_e} + \frac{2}{3n_e T_e}\int \frac{1}{2}m_e\vec{v}^2 h(\vec{v})\mathrm{d}\vec{v}
\end{aligned} \tag{G.7}$$

$$\begin{aligned}
\frac{\tilde{n}_e}{n_e} &= \frac{1}{n_e}\int f_e(\vec{v})\mathrm{d}\vec{v} \\
&= \frac{1}{n_e}\int [\frac{e\phi}{T_e}f_{Me} + h(\vec{v})]\mathrm{d}\vec{v} \\
&= \frac{e\phi}{T_e} + \frac{1}{n_e}\int h(\vec{v})\mathrm{d}\vec{v}
\end{aligned} \tag{G.8}$$

Using the results in Eq. G.7 and G.8, the T_e fluctuation level is represented as Eq. G.9

$$\begin{aligned}
\frac{\tilde{T}_e}{T_e} &= \{\frac{e\phi}{T_e} + \frac{2}{3n_e T_e}\int \frac{1}{2}m_e\vec{v}^2 h(\vec{v})\mathrm{d}\vec{v}\} - \{\frac{e\phi}{T_e} + \frac{1}{n_e}\int h(\vec{v})\mathrm{d}\vec{v}\} \\
&= \frac{2}{3n_e T_e}\int \frac{1}{2}m_e\vec{v}^2 h(\vec{v})\mathrm{d}\vec{v} - \frac{1}{n_e}\int h(\vec{v})\mathrm{d}\vec{v}
\end{aligned} \tag{G.9}$$

As shown in Eq. G.9, the non-adiabatic electron response is dominant in T_e fluctuations.

Appendix H

Error estimation of experimental heat flux via error propagation in C-Mod Ohmic discharges

This section presents error analysis for the experimental heat flux values via power balance analysis using TRANSP in the C-Mod Ohmic discharges used in section 4.2-4.4. As shown in Eq. 3.20, the heat flux values are determined from the conduction and convection power loss in the power balance equation. Thus, we should first estimate the uncertainty of the convection and conduction power losses. The convection power loss is determined by the measured density and temperature profiles and the radial velocity calculated in TRANSP. The conduction power loss is obtained from the power balance equation. To be specific, all terms in the power balance equation except for conduction power loss are obtained from experimental data or modeling, and then we calculate the conduction power loss in the power balance equation.

From Eq. 3.15 and 3.16, the electron conduction power loss, $\nabla \cdot \vec{q}_{e,cond}$, is given by,

$$\nabla \cdot \vec{q}_{e,cond} = P_{OH} + P_{ext,e} - P_{ion} - P_{rad} - q_{ie} - \frac{3}{2}\frac{\partial}{\partial t}(n_e T_e) - \nabla \cdot (\frac{3}{2} n_e T_e \vec{v}_e) - n_e T_e \cdot \nabla(\vec{v}_e) \tag{H.1}$$

with Ohmic power, P_{OH}, external heating power absorbed by electrons, $P_{ext,e}$, power loss due to ionization of a neutral, P_{ion}, radiation power loss, P_{rad}, and power loss by transfer to ions through coulomb collisions, q_{ie}. $\frac{3}{2}\frac{\partial}{\partial t}(n_e T_e)$ represents the change in electron energy, $\nabla \cdot (\frac{3}{2} n_e T_e \vec{v}_e)$ indicates the convection power loss ($\nabla \cdot \vec{q}_{e,conv}$), and $-n_e T_e \cdot \nabla(\vec{v}_e)$ denotes the compression power ($P_{e,comp}$).

In the same manner, ion conduction power loss, $\nabla \cdot \vec{q}_{i,cond}$, can be obtained from Eq. 3.17.

$$\nabla \cdot \vec{q}_{i,cond} = P_{ext,i} + q_{ie} - P_{CX} - \frac{3}{2}\frac{\partial}{\partial t}(n_i T_i) - \nabla \cdot (\frac{3}{2} n_i T_i \vec{v}_i) - n_i T_i \cdot \nabla(\vec{v}_i) \quad \text{(H.2)}$$

with the power loss due to charge exchange with neutrals, P_{CX}.

Under the assumption that the terms on the right hand side in each equation are not correlated, the uncertainty of the conduction power loss, $\sigma_{\nabla \cdot \vec{q}_{e,cond}}$ and $\sigma_{\nabla \cdot \vec{q}_{i,cond}}$, will be,

$$\sigma^2_{\nabla \cdot \vec{q}_{e,cond}} = \sigma^2_{P_{OH}} + \sigma^2_{P_{ext,e}} + \sigma^2_{P_{ion}} + \sigma^2_{P_{rad}} + \sigma^2_{q_{ie}} + \sigma^2_{\frac{3}{2}\frac{\partial}{\partial t}(n_e T_e)} + \sigma^2_{\nabla \cdot P_{e,conv}} + \sigma^2_{P_{e,comp}} \quad \text{(H.3)}$$

$$\sigma^2_{\nabla \cdot \vec{q}_{i,cond}} = \sigma^2_{P_{ext,i}} + \sigma^2_{P_{CX}} + \sigma^2_{q_{ie}} + \sigma^2_{\frac{3}{2}\frac{\partial}{\partial t}(n_i T_i)} + \sigma^2_{\nabla \cdot P_{i,conv}} + \sigma^2_{P_{i,comp}} \quad \text{(H.4)}$$

There is no external heating in Ohmic discharges. That is, $P_{ext,e}$=$P_{ext,i}$=0 in this analysis. We can also simplify Eq. H.3 and H.4 by comparing the amplitude of terms in the power balance equations. Figure H-1 shows the radial profile of each term in the electron and ion power balance equations for the C-Mod Ohmic discharges (LOC and SOC discharges) used in section 4.2-4.4. It is shown that the ion conduction power loss is determined mainly by q_{ie} in r/a< 0.9 in both LOC and SOC discharges and that P_{OH}, P_{rad}, and q_{ie} are dominant in the electron power balance equation in r/a< 0.9 in both discharges. Although it was not shown in the power balance

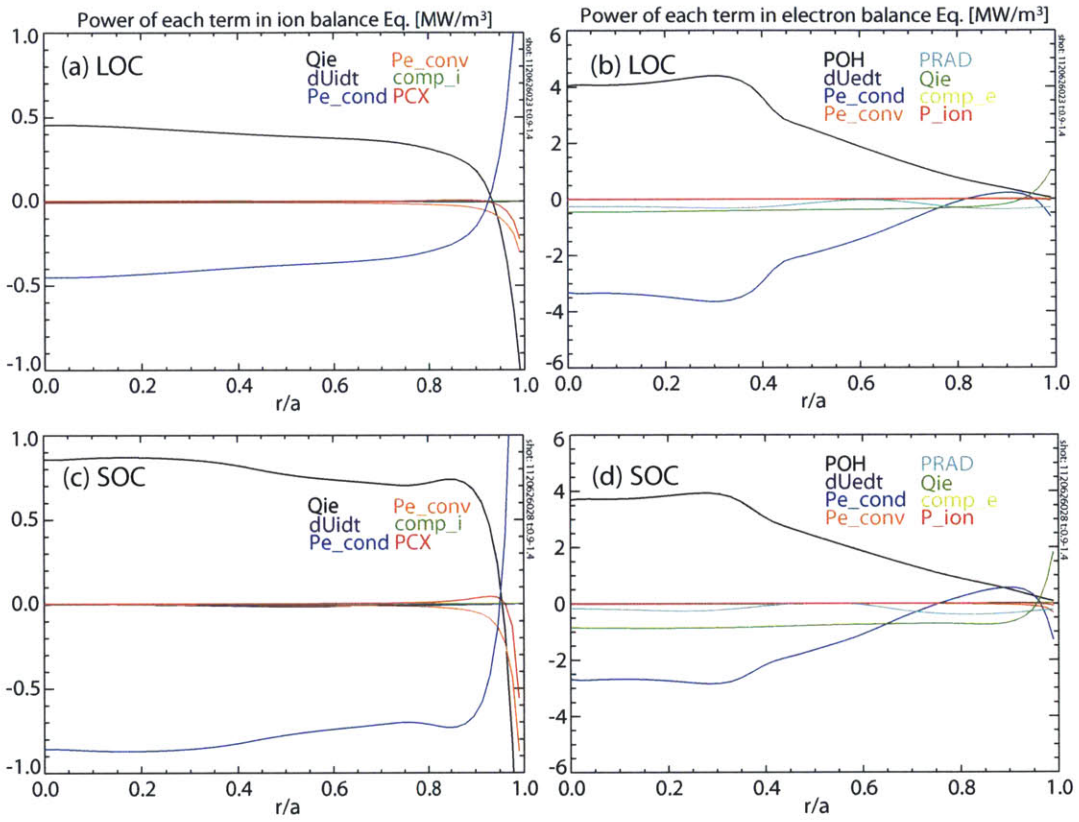

Figure H-1: The power of each term $[MW/m^3]$ in the (a) ion and (b) electron power balance equations in the LOC discharge (shot : 1120626023, t: 0.9-1.4s), and the power of each term $[MW/m^3]$ in the (c) ion and (d) electron power balance equations in the SOC discharge (shot : 1120626028, t: 0.9-1.4s). Energy gain has a positive sign and loss is presented by a negative sign. In the ion power balance figures ((a) and (c)), black : the power transferred from electrons to ions by collisions, q_{ie}, purple : the rate of change of ion energy, blue : ion conduction power loss, orange : ion convective power loss, green : ion compressional power, red : power loss due to charge exchange. In the electron power balance figures ((b) and (d)), black : Ohmic heating power, purple : the rate of change of electron energy, blue : electron conduction power loss, red : electron convective power less, light blue : power loss due to radiation, green : q_{ie}, yellow : electron compression power, red : power loss due to ionization.

equations, heat flux values will also vary depending on Z_{eff} values. The uncertainty due to the error in Z_{eff} should be also estimated. We will include the uncertainty due to the error in Z_{eff}, $\sigma_{\nabla\cdot\vec{q}_{cond},Z_{eff}}$, in the uncertainty of the conduction heat flux. The uncertainty of ion and electron conduction power loss in r/a< 0.9 for the LOC and SOC discharges is then approximately given by,

$$\sigma^2_{\nabla\cdot\vec{q}_{e,cond}} \sim \sigma^2_{P_{OH}} + \sigma^2_{P_{rad}} + \sigma^2_{q_{ie}} + \sigma^2_{\nabla\cdot\vec{q}_{e,cond},Z_{eff}} \tag{H.5}$$

$$\sigma^2_{\nabla\cdot\vec{q}_{i,cond}} \sim \sigma^2_{q_{ie}} + \sigma_{\nabla\cdot\vec{q}_{i,cond},Z_{eff}} \tag{H.6}$$

It is noteworthy that the heat flux is calculated from not only the conduction power loss but also convection power loss, as shown in Eq. 3.20. That is, the divergence of the heat flux equals the power loss due to both conduction and convection, $\nabla\cdot\vec{q} = \nabla\cdot\vec{q}_{cond} + \nabla\cdot\vec{q}_{conv}$. Thus, we must evaluate the uncertainty of the convection power loss. However, convection power loss is near zero in both electron and ion power balance equations in both LOC and SOC discharges, as shown in Fig. H-1. We can therefore ignore the uncertainty of the convection power loss, i.e., $\sigma_{\nabla\cdot\vec{q}} \sim \sigma_{\nabla\cdot\vec{q}_{cond}}$.

We must then evaluate the uncertainty of P_{OH}, P_{rad}, and q_{ie} and the uncertainty due to the error in the Z_{eff} estimation to calculate the uncertainties of the electron and ion conduction power losses. First, P_{OH} is defined as $P_{OH}(r) = j^2(r)/\sigma(r)$, where j(r) is the current density profile and $\sigma(r)$ is the conductivity. The neoclassical conductivity was used in this study. Since neoclassical conductivity is too complicated to estimate the error analytically, the uncertainty of P_{OH} was estimated from the standard deviation of P_{OH} in the stationary time period. Second, P_{rad} was measured by bolometry [14]. According to the diagnostician responsible for this measurement, the uncertainty of P_{rad} was set to 10%. Third, the uncertainty of q_{ie} was estimated through error propagation. From the definition of q_{ie} in section 3.3 ($q_{ie} = \frac{3m_e}{m_i}\frac{n_e}{\tau_e}[Z](T_e - T_i)$), $q_{ie} \propto n_e^2 T_e^{-3/2}(T_e - T_i)$ since the electron collision time, $\tau_e \propto n_e^{-1}T_e^{3/2}$. Then, assuming these three terms are not correlated, the uncertainty of q_{ie}, $\sigma_{q_{ie}}$, will be,

$$(\frac{\sigma_{q_{ie}}}{q_{ie}})^2 = (\frac{\sigma_{n_e}}{n_e})^2 + (\frac{3}{2}\frac{\sigma_{T_e}}{T_e})^2 + (\frac{\sigma_{T_e-T_i}}{T_e - T_i})^2 \tag{H.7}$$

with $\sigma^2_{T_e-T_i} = \sigma^2_{T_e} + \sigma^2_{T_i}$.

We then calculate $\sigma_{q_{ie}}$ from the uncertainties of n_e, T_e, and T_i estimated in Appendix F.

It is difficult to estimate the effect of Z_{eff} on the conduction power loss analytically. In this study, we ran two TRANSP runs for each LOC and SOC discharge with $Z_{eff} \pm \sigma_{Z_{eff}}$. The estimated uncertainty of Z_{eff} in Appendix F is used as $\sigma_{Z_{eff}}$. We then have a range of electron/ion conduction power losses by varying Z_{eff} within its uncertainty. Then, using the conversion formula from range to standard deviation, $\sigma_{\nabla\cdot\vec{q}_{e,cond},Z_{eff}}$ and $\sigma_{\nabla\cdot\vec{q}_{i,cond},Z_{eff}}$ were estimated.

So far, we have estimated the uncertainty of the conduction power loss, approximately the uncertainty of the power loss due to conduction and convection ($\nabla \cdot \vec{q}$), by using the estimated uncertainties on the right hand side in Eq. H.5 and H.6. As shown in Eq. 3.20, the heat flux value at a certain radial point, r_o, is obtained by integrating $\nabla \cdot \vec{q}$ from r=0 to r_o. Since each radial position is deeply correlated, we cannot estimate the uncertainty of the heat flux by randomly varying $\nabla \cdot \vec{q}$ weighted by its uncertainty. Instead, the uncertainty of the electron and ion heat fluxes were estimated from the range of each heat flux value within the uncertainty of $\nabla \cdot \vec{q}$. In other words, the range of each heat flux was obtained by varying $\nabla \cdot \vec{q}$ by its uncertainty ($\nabla \cdot \vec{q} \pm \sigma_{\nabla\cdot\vec{q}}$). This range was then converted to the standard deviation using the conversion formula in [108]. In addition, the uncertainty of heat diffusivity was obtained via error propagation. The heat diffusivity, χ, is defined as $\chi = \frac{q_{cond}}{n\frac{\partial T}{\partial r}}$. Assuming that the three terms on the right hand side in the definition of χ are not correlated, the uncertainty of the heat diffusivity, σ_χ will be,

$$\sigma^2_\chi = \sigma^2_{q_{cond}} + \sigma^2_n + \sigma^2_{\partial T/\partial r} \tag{H.8}$$

The estimated uncertainties of electron and ion heat fluxes and diffusivities were used in Chapter 4, as shown in Fig. 4-8.

In this study, we assume that there is no correlation among the quantities used in the error propagation, which will not always be true. In the future, we should consider the correlation among the quantities when we apply the error propagation technique.

Appendix I

Details of gyrokinetic analysis performed for C-Mod Ohmic plasmas at r/a$\sim$0.85

I.1 Development of GYRO simulation base case for C-Mod Ohmic plasmas at r/a$\sim$0.85

I.1.1 Convergence study in velocity space at r/a=0.6

We first performed a convergence study of the local gyrokinetic simulations for an Ohmic discharge (shot 1120626028 at r/a=0.6, TRANSP ID: 88249). The parameters varied in this test are as follows: the number of trapped/passing pitch angles (TRAP_GRID, PASS_GRID), the number of grid points in the poloidal direction along a particle orbit (ORBIT_GRID), the number of finite elements used to discretize Maxwell's equations (BLEND_GRID), and the number of energy grid points (ENERGY_GRID). More information about these input parameters can be found in [28, 2]. The base case for this test was set from the recommendation in [2] and previous GYRO settings in C-Mod (TRAP_GRID=PASS_GRID=4, ORBIT_GRID=BLEND_GRID=6, ENERGY_GRID=8). We then varied these pa-

	PASS/TRAP_GRID	ORBIT/BLEND_GRID	ENERGY_GRID
Base case	4	6	8
Test run 1	4	6	12
Test run 2	6	9	8
Test run 3	6	6	6

Table I.1: The numerical setup for velocity space in GYRO runs used in the convergence test for the Ohmic discharge used in this thesis at r/a=0.6.

	Ion heat flux [MW/m^2]	Electron heat flux [MW/m^2]
Base case	0.41 ± 0.076	0.19 ± 0.034
Test run 1	0.41 ± 0.086	0.20 ± 0.037
Test run 2	0.43 ± 0.10	0.20 ± 0.044
Test run 3	0.45 ± 0.084	0.21 ± 0.038

Table I.2: The time averaged heat flux values of the runs used in the convergence test for the Ohmic discharge used in section 4.2-4.4 (averaging time : 400-820 [a/c_s].

rameters by 50%. The numerical setup for velocity space used in these runs are shown in Table I.1.

Table I.2 shows the electron and ion heat fluxes of these runs. For all these runs, heat flux values are obtained by time averaging in the stationary time period more than 400 [a/c_s]. The uncertainty of the heat fluxes is estimated from the standard variation of the time averaging. As shown in Table I.2, both ion and electron heat flux values vary less than 10% although input parameters relevant to the numerical setup in the velocity space varies by about 50%. In other words, the simulated heat fluxes converge with the resolutions in velocity space. This indicates that the numerical setup in the base case is enough for these GYRO runs, and that we can keep the resolution of the base run for other runs using the discharges that have similar conditions. We used the numerical setup from the base run in the GYRO runs for Ohmic discharges at r/a=0.6 and ~0.85 in this thesis.

I.1.2 Numerically well resolved simulation for C-Mod Ohmic plasmas at r/a~0.85

First trial using the numerical setup used for the run at r/a=0.6

Figure I-1 shows the results of the first gyrokinetic simulation trial for the plasma in SOC regime (shot 1120626028) at r/a ~0.85. In the first trial, we used the simulation setup used for the runs at r/a=0.6, where radial domain size, L_x is $\sim 81.0\rho_s$, poloidal domain size, L_y is $\sim 68.0\rho_s$ and the highest $k_y\rho_s$ is ~ 1.0. Figure I-1(b) shows ion heat flux spectrum on $k_y\rho_s(Q_i(k_y)$ spectrum). This spectrum is the time averaged spectrum while the turbulence is saturated in the simulation. As shown in Fig. I-1(b), the peak of the $Q_i(k_y)$ spectrum is at the lowest $k_y\rho_s$. As explained in section 3.4, the peak at the lowest $k_y\rho_s$ in the $Q_i(k_y)$ spectrum indicates that this simulation is not well resolved numerically. If the peak in the $Q_i(k_y)$ spectrum is at the lowest $k_y\rho_s$, the poloidal resolution (resolution of $k_y\rho_s$) of this simulation will be considered insufficiently to resolve all important turbulence in the simulation. When we have a peak in the low $k_y\rho_s$ region, it will therefore be required to separate this peak from the lowest $k_y\rho_s$ mode by increasing the poloidal resolution. Thus, finer poloidal resolution is required for the case shown in Fig. I-1(b), and finer poloidal resolution required larger poloidal box size. In addition, a square shaped domain is desirable to avoid numerical instabilities. Thus, the radial box size should be increased together with the poloidal box size.

Figure I-1(d) shows the $Q_e(k_y)$ spectrum, which is also a time averaged spectrum while turbulence is saturated in the simulation. The same criteria used for the $Q_i(k_y)$ spectrum can be applied. Although the peak in the $Q_e(k_y)$ spectrum is not at the lowest $k_y\rho_s$, electron heat flux from the highest $k_y\rho_s$ mode is not negligible compared to the peak value. As mentioned above, this indicates that the simulation may not capture all important turbulence modes. In this case, we must increase the maximum $k_y\rho_S$ value included in the simulation. The value at highest $k_y\rho_s$ is about half of the peak value in Figure I-1 (d). It should be at most 10-20% of the peak value. Thus, the simulation needs to include higher $k_y\rho_s$ modes higher than 1.0.

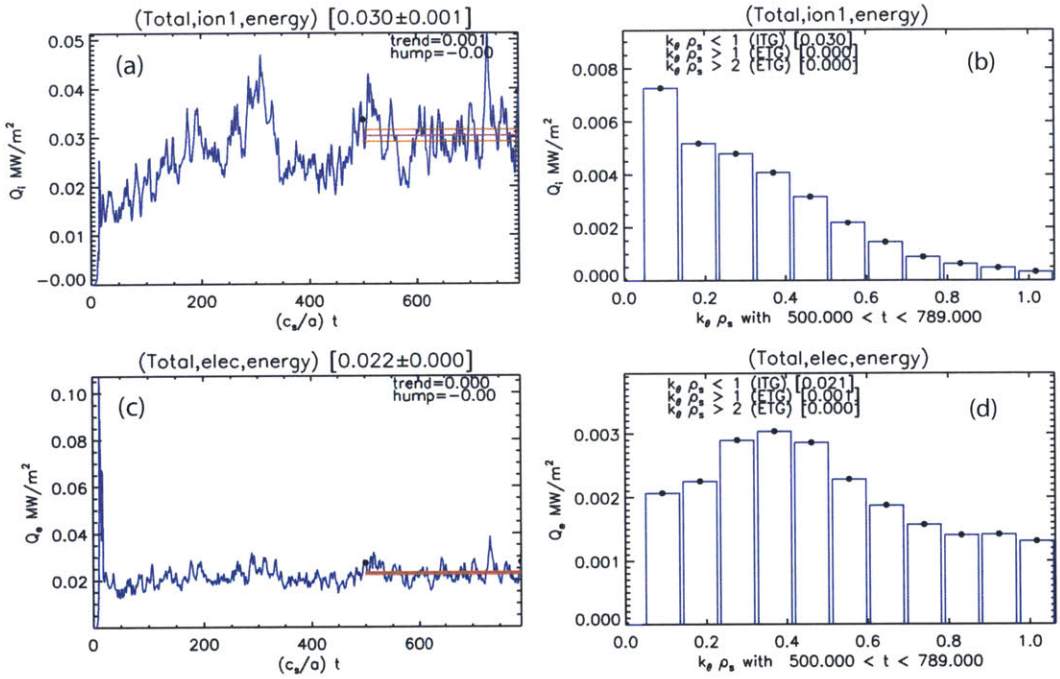

Figure I-1: Results from the first trial for the SOC plasma (1120626028). Radial domain size, L_x is $\sim 81.0\rho_s$, poloidal domain size, L_y is $\sim 68.0\rho_s$ and the highest $k_y\rho_s$ is ~ 1.0. (a) Ion heat flux, Q_i, depending on simulation time, $Q_i(t)$ (b) Time-averaged Q_i spectrum on $k_y\rho_s$, $Q_i(k_y)$ spectrum (averaging time : 500-789 [a/c_s]) (c) Electron heat flux, $Q_e(t)$ plot (d) Time-averaged $Q_e(k_y)$ spectrum (averaging time : 500-789 [a/c_s]).

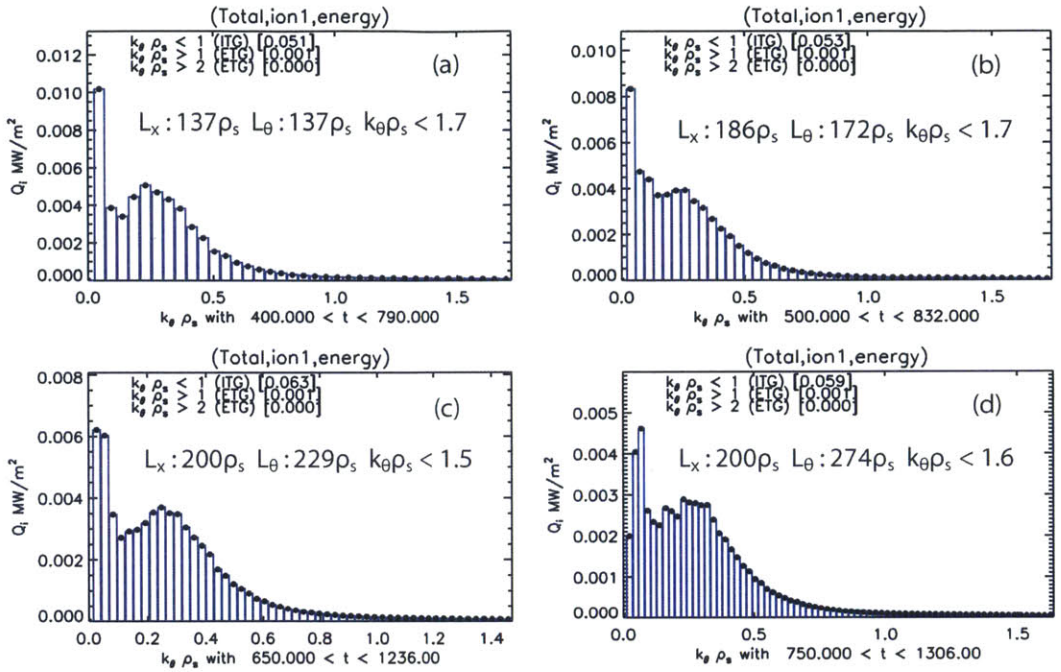

Figure I-2: Time-averaged $Q_i(k_y)$ spectrum with the increase in box size for the SOC plasma (shot 1120626028) (a) L_x : $137.0\rho_s$, L_y : $137.0\rho_s$, $k_y\rho_s < 1.7$ averaging time : 400-790 [a/c_s] (b) L_x : $186.0\rho_s$, L_y : $172.0\rho_s$, $k_y\rho_s < 1.7$ averaging time : 500-832 [a/c_s] (c) L_x : $200.0\rho_s$, L_y : $229.0\rho_s$, $k_y\rho_s < 1.5$ averaging time : 850-1236 [a/c_s] (d) L_x : $200.0\rho_s$, L_y : $274.0\rho_s$, $k_y\rho_s < 1.6$ averaging time : 750-1306 [a/c_s].

Numerically well resolved simulations with large domain size

First, the poloidal domain size was increased to resolve the peak at the lowest $k_y\rho_s$ in the $Q_i(k_y)$ spectrum for the SOC discharge (shot 1120626028). The highest $k_y\rho_s$ was fixed near 1.5-1.7. With this $k_y\rho_s$ range, the value at the highest $k_y\rho_s$ in the Q_e spectrum is 10-20% of the peak value. Figure I-2 shows the change in the $Q_i(k_y)$ spectrum with the change in domain size. You can see that the simulation is resolved numerically when the poloidal box size is $274\rho_s$. A similar box size scan was performed for an LOC plasma (shot 1120626023), and Fig. I-3 shows the results. For the LOC plasma, a well-resolved simulation is obtained when the poloidal box size is $\sim 180\rho_s$. It is noteworthy that we still have the structure in the low k_y region ($k_y\rho_s < 0.1$) in the well-resolved simulation for both LOC and SOC runs. Due to this low k_y mode, a large box size is required for both LOC and SOC plasmas.

Although a large domain size ($\sim$180-270 ρ_s) resolves all poloidal modes, this large

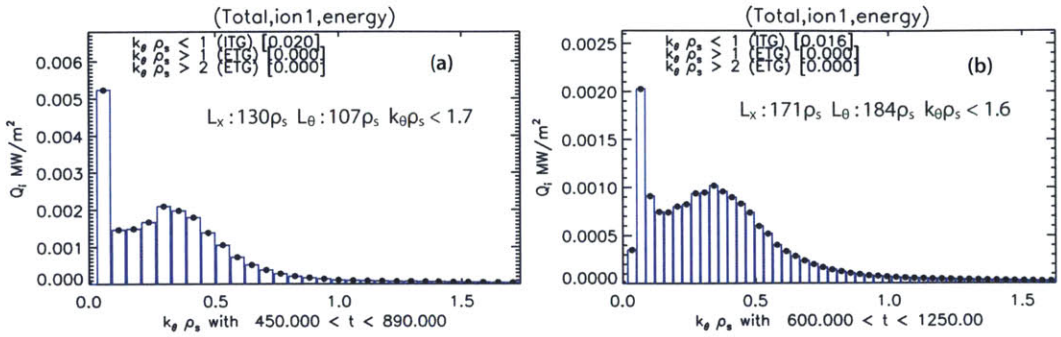

Figure I-3: Time-averaged $Q_i(k_y)$ spectrum with the increase in box size for an LOC plasma (shot 1120626023) (a) L_x : $130.0\rho_s$, L_y : $107.0\rho_s$, $k_y\rho_s < 1.7$ averaging time : 450-890 [a/c_s] (b) L_x : $171.0\rho_s$, L_y : $184.0\rho_s$, $k_y\rho_s < 1.6$ averaging time : 600-1250 [a/c_s].

domain will violate the gyrokinetic ordering. As explained in section 1.2.3, in gyrokinetics, the velocity distribution function, which is the solution of the Fokker-Planck equation, is separated into two parts, the ensemble-averaged part and the turbulent part. It is assumed that the variation of the turbulent part (or the wavelength of the unstable mode) is close to the gyroradius and the variation of the ensemble-averaged part is close to the machine size (∼a). The variation of the turbulent part is therefore much smaller than the equilibrium part's variation. With the separation of the ensemble-averaged part and the turbulent part, gyrokinetic simulation solves the drift kinetic and gyrokinetic equations for the first order ensemble-averaged part and the turbulent part, respectively. As the box size increases, the longer wavelength modes are included and it will threaten this fundamental assumption in gyrokinetics. In the LOC and SOC runs performed here, the sound gyroradius of the main ion (deuterium), ρ_s is ∼0.03cm. When the poloidal domain size is ∼180 ρ_s, the longest poloidal wavelength of the mode in this simulation is about 6cm. Considering that the minor radius of C-Mod is about 20cm, this simulation will violate gyrokinetic ordering and its result will not be meaningful. For physically meaningful simulations, the longest poloidal wavelength which can be resolved in the simulation will be at most 20% of the equilibrium length scale, and if we set the minor radius of the plasma to the equilibrium length scale, the largest domain size should be shorter than $150\rho_s$ at r/a∼0.85 in the LOC and SOC runs. In addition, one complete run with the

large domain size takes about 200-300k CPU hours and physically 3-5 days including queue waiting time, which is intractable for a sensitivity scan considering both physical hours and the assigned CPU hours. Considering both physics and computing time, the domain size of these simulations should therefore be reduced and it should be at most $\sim 130\rho_s \times \sim 130\rho_s$. However, as shown above, in both LOC and SOC runs, we cannot have numerically resolved simulations with L_y $\sim$130-140ρ_s. The low k_y peak should be investigated to solve this issue.

Convergence study for the $k_y\rho_s$ range

Before we investigate the peak in the low k_y region ($k_y\rho_s < 0.1$), we must justify the maximum value of $k_y\rho_s$ included in the simulation (max. $k_y\rho_s \sim 1.5 - 1.7$). In order to justify the range of $k_y\rho_s$, we performed the run for the LOC discharge with the same domain size used for Fig. I-3, but with a larger maximum $k_y\rho_s$ value, from 1.6 to 2.4. Table I.3 and Fig. I-4 show the comparison of the simulated heat flux and the synthetic T_e fluctuations. In this test, a Gaussian shape point spread function (PSF) was used for the synthetic T_e fluctuations with $1/e^2$ diameter in the radial direction, l_R=1.0cm, and $1/e^2$ diameter in the poloidal direction, l_Z=0.64cm. High pass filtering was also applied to the synthetic T_e fluctuations. As shown in Table I.3, both heat fluxes and synthetic T_e fluctuations are varied within their uncertainties in spite of the increases in $k_y\rho_s$ by about 50%. Figure. I-4 also shows that the spectral shapes of $Q(k_y)$ and synthetic T_e fluctuations are not different. Thus, the simulation results converge with the maximum $k_y\rho_s$ value, which indicates that the $k_y\rho_s$ range set in the last section ($k_y\rho_s < 1.6 - 1.7$) is enough for the gyrokinetic simulations for the LOC discharge at r/a=$\sim$0.85. We will assume that the $k_y\rho_s$ range for the dominant turbulence mode does not vary significantly, so that the same range can be applied to the SOC discharge.

Investigation of low k_y peak in the well resolved runs

At this point, one important question will be whether this low k_y mode is physically real or artificial due to any numerical issues or one or some of the uncertain input

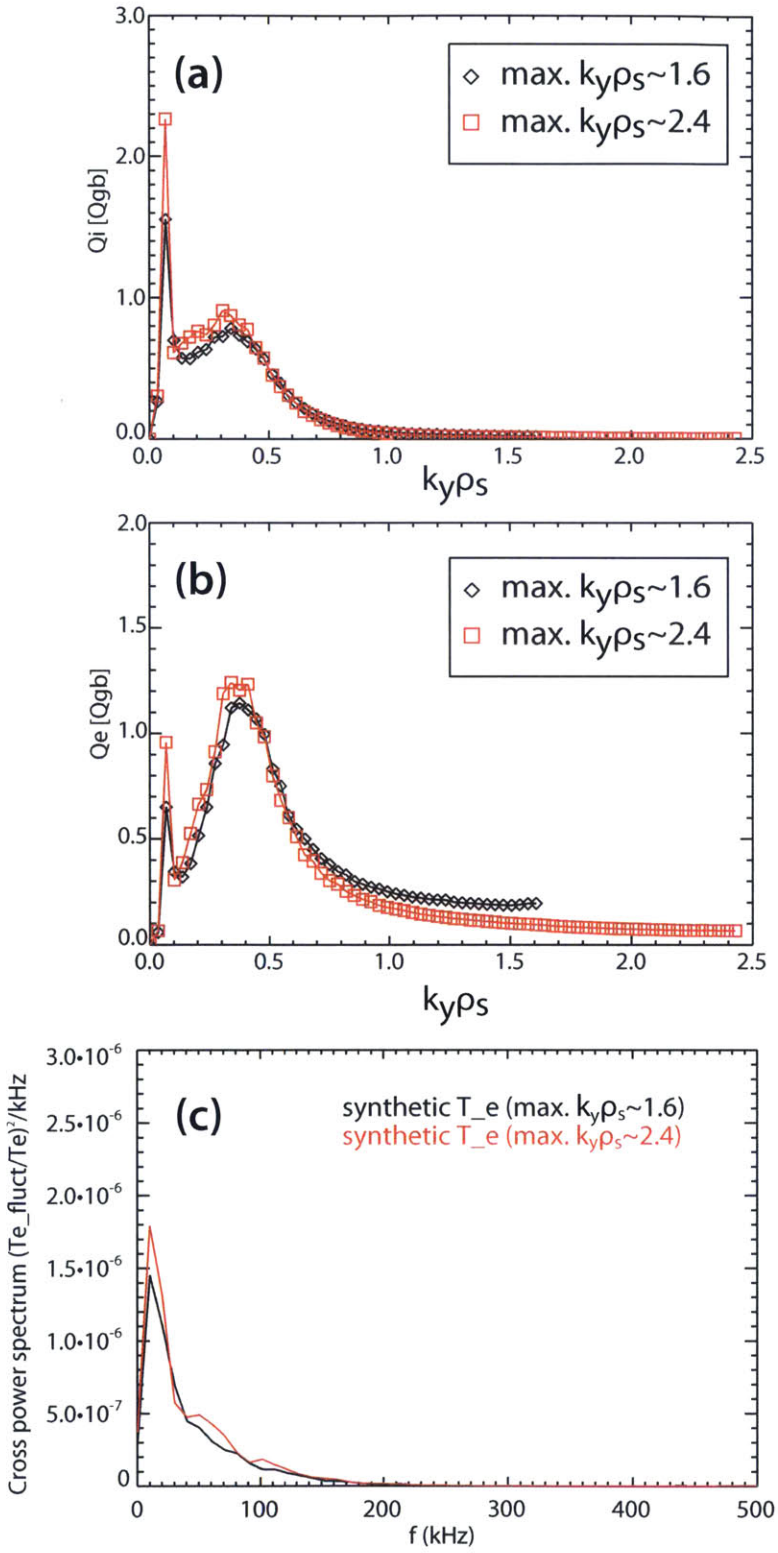

Figure I-4: (a) Time-averaged $Q_i(k_y)$ spectrum with changes in the maximum (b) Time-averaged $Q_e(k_y)$ spectrum (c) Synthetic T_e fluctuation measurements for the GYRO runs used in Table I.3.

	Ion heat flux [MW/m^2]	Electron heat flux [MW/m^2]	Synthetic T_e fluctuation level [%]
Run with max. $k_y\rho_s$ ~1.6	0.019 ± 0.0017	0.027 ± 0.0021	0.77 ± 0.054
Run with max. $k_y\rho_s$ ~2.4	0.021 ± 0.0020	0.028 ± 0.0020	0.84 ± 0.059

Table I.3: The time averaged heat flux values and synthetic T_e fluctuations of the runs with $L_x \sim 171\rho_s$, $L_y \sim 184\rho_s$. These two runs have different $k_y\rho_s$ ranges, with maximum $k_y\rho_s$ value, 1.6 and 2.4, respectively. For synthetic T_e fluctuations, a Gaussian shape point spread function was used in both radial and poloidal directions with $1/e^2$ diameter in the radial direction, l_R=1.0cm, and in the poloidal direction, l_Z=0.64cm. Averaging time range : 600-1250 $[a/c_s]$ for the run with max. $k_y\rho_s$ ~1.6, 800-1280 $[a/c_s]$ for the run with max. $k_y\rho_s$ ~2.4.

parameters such as E×B shearing rate. Shearing rates in these runs are $0.017 \pm 0.015[c_s/a]$ and $0.0015 \pm 0.022[c_s/a]$ for the LOC and SOC runs, respectively. These values are much lower than the nominal value of the E×B shearing rate (~0.05 $[c_s/a]$). It is noteworthy that the error of the E×B shearing rate is about 100% for the LOC run and more than 100% for the SOC run due to the quality of the rotation data at r/a~0.85. If the E×B shearing rate used in this simulation is lower than the real experimental value, which we do not know exactly, it is possible that the low E×B shearing rate cannot suppress the low k_y mode, which has a long poloidal wavelength, while this mode is suppressed in the real experiment.

In order to study this possibility, an E×B shearing rate scan within its error is performed for the well-resolved LOC and SOC simulations. Figure I-5 and Figure I-6 show the results of LOC and SOC runs, respectively. In the LOC runs, the results show that the low k_y peak is sensitive to the E×B shearing rate, and with the highest E×B shearing rate within the error, this peak is almost suppressed. It is also noteworthy that while the low k_y peak changes more than an order of magnitude with the change in E×B shearing rate within the uncertainty, the flux in the $k_y\rho_s > 0.1$ region varies within 20-30%. Especially when the E×B shearing rate is increased, the change in flux in the $k_y\rho_s > 0.1$ region is about 10%. A larger decrease in the $k_y\rho_s < 0.1$ region compared to $k_y\rho_s > 0.1$ is also observed in SOC runs. Thus, it is possible that an E×B shearing rate lower than the experimental value results in the low k_y peak, which can be suppressed in real experiments.

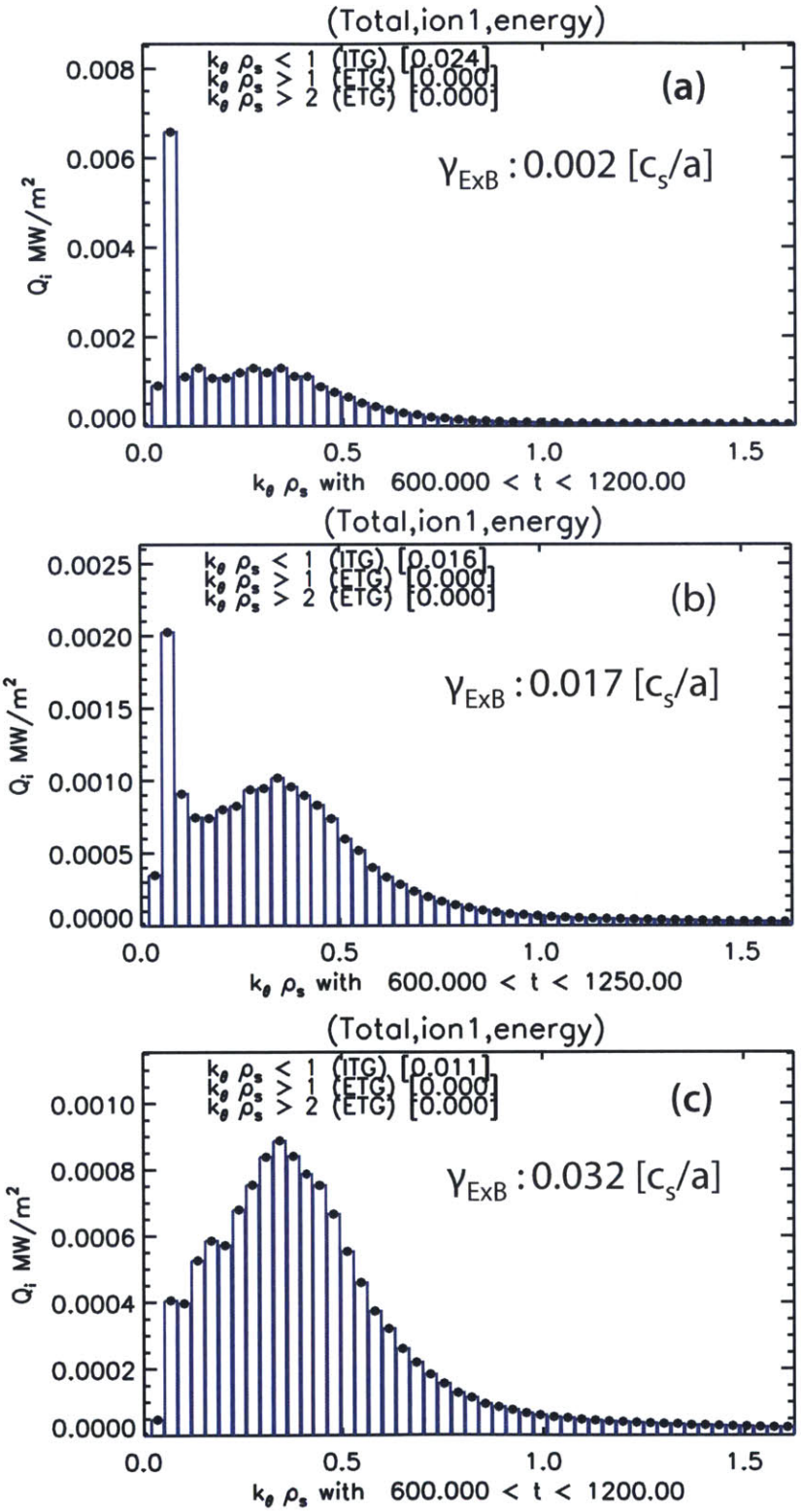

Figure I-5: Time-averaged $Q_i(k_y)$ spectrum with the change in E×B shearing rate, $\gamma_{E\times B}$, within the uncertainty in the LOC plasma (shot 1120626023) with L_x : $171.0\rho_s$, L_y : $184.0\rho_s$, $k_y\rho_s < 1.6$ (a) $\gamma_{E\times B} = 0.002[c_s/a]$ (b) $\gamma_{E\times B} = 0.017[c_s/a]$ (c) $\gamma_{E\times B} = 0.032[c_s/a]$

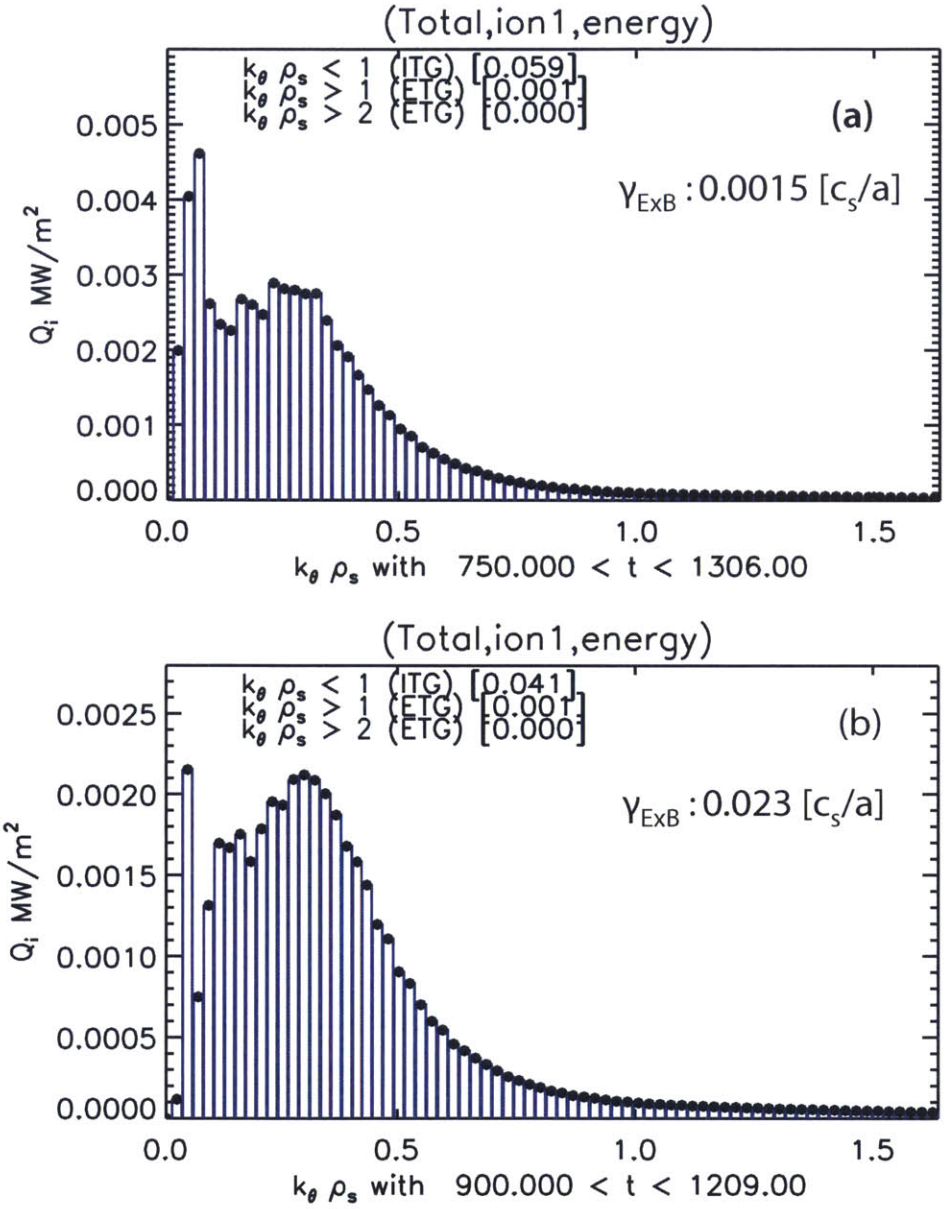

Figure I-6: Time-averaged $Q_i(k_y)$ spectrum with the change in E×B shearing rate, $\gamma_{E\times B}$, within the uncertainty in the SOC plasma (shot 1120626028) with L_x : $200.0\rho_s$, L_y : $274.0\rho_s$, $k_y\rho_s < 1.6$ (a) $\gamma_{E\times B} = 0.0015[c_s/a]$ (b) $\gamma_{E\times B} = 0.023[c_s/a]$

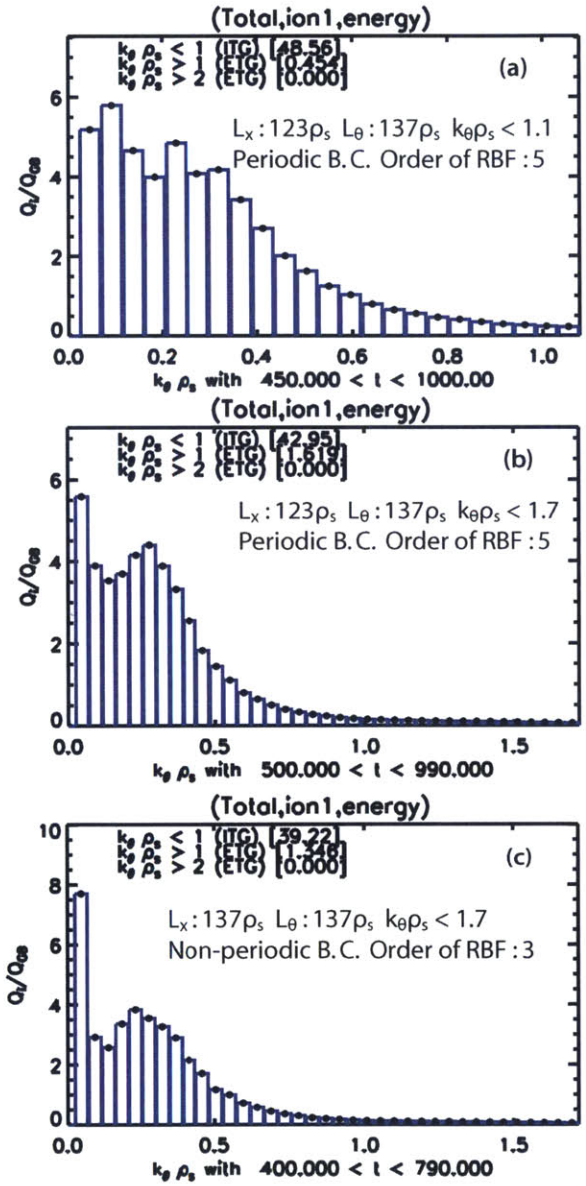

Figure I-7: Time-averaged $Q_i(k_y)$ spectrum with the order of radial base function for an SOC plasma (shot 1120626028). The heat flux is normalized by the gyro-Bohm flux, Q_{gb} ~$1.32\times10^{-3} MW/m^2$. (a) L_x : $123.4\rho_s$, L_y : $137.1\rho_s$, $k_y\rho_s < 1.1$ averaging time : 450-1000 [a/c_s] with periodic boundary conditions and 5th order radial basis function (b) L_x : $123.4\rho_s$, L_y : $137.1\rho_s$, $k_y\rho_s < 1.7$ averaging time : 500-990 [a/c_s] with periodic boundary conditions and 5th order radial basis function (c) L_x : $137.0\rho_s$, L_y : $137.0\rho_s$, $k_y\rho_s < 1.7$ averaging time : 400-790 [a/c_s] with non-periodic boundary conditions and 3rd order radial basis function.

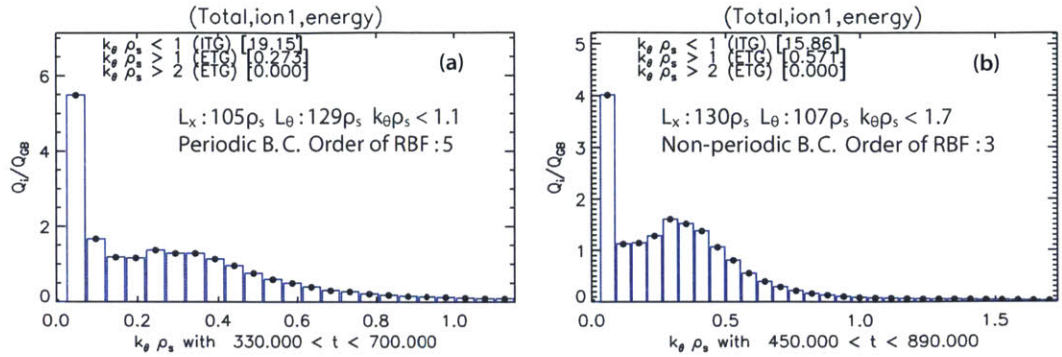

Figure I-8: Time-averaged $Q_i(k_y)$ spectrum with the order of radial base function for LOC plasma (shot 1120626023). The heat flux is normalized by gyro-Bohm flux, $Q_{gb} \sim 1.30 \times 10^{-3} MW/m^2$. (a) L_x : $104.6\rho_s$, L_y : $128.5\rho_s$, $k_y\rho_s < 1.1$ averaging time : 330-700 [a/c_s] with periodic boundary condition and 5th order radial basis function (b) L_x : $130.0\rho_s$, L_y : $107.0\rho_s$, $k_y\rho_s < 1.7$ averaging time : 450-890 [a/c_s] with periodic boundary condition and 3rd order radial basis function.

At r/a$\sim$0.85, the plasma becomes more collisional than in the core. In GYRO simulation, there may be an issue in the accuracy of the collision calculations in highly collisional regime [2]. This possibility should therefore be investigated. The accuracy of the collision frequency can be improved by increasing the order of the radial basis function used to evaluate the collision operator in GYRO. In normal GYRO simulations, 3rd order is used. Figure I-7(a) and (b) show the results of simulation with a 5th order radial basis function for the SOC plasma, which is more collisional than the LOC plasma. In the simulations with a 5th order radial basis function, periodic boundary conditions were used, i.e., E$\times B$ shearing effects are not included. Figure I-7 (c) shows the run with similar box size to Fig. I-7 (a) and (b) but with non-periodic boundary conditions and a 3rd order radial basis function. As shown in the figures, the low k_y peak is mitigated in runs with a 5th order radial basis function although Fig. I-7 (b) still has a peak at the lowest k_y. This mitigation implies that this mode might be artificial and is related to a numerical issue. However, we did not see the mitigation of the low k_y mode in the LOC plasma as shown in Fig. I-8. Thus, the collision issue might contribute to this mode partially and the origin of this mode is still inconclusive.

The poloidal wavelength of the low k_y peak in the well-resolved LOC and SOC

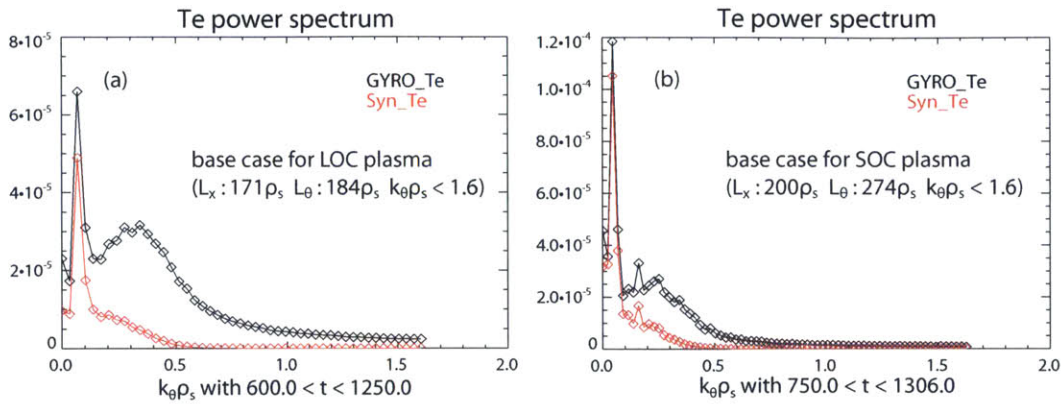

Figure I-9: T_e fluctuation auto power spectrum from the well resolved simulations. The black line shows the power spectrum without consideration of the resolution of CECE and the red line shows the synthetic auto power spectrum. (a) LOC (L_x : $171.0\rho_s$, L_y : $184.0\rho_s$, $k_y\rho_s < 1.6$) (b) SOC (L_x : $200.0\rho_s$, L_y : $274.0\rho_s$, $k_y\rho_s < 1.6$).

runs is about 3-4cm. Figure I-9 shows the $T_e(k_y)$ power spectrum at the CECE measurement position for the numerically well-resolved LOC and SOC run. The black line indicates the GYRO T_e power spectrum without consideration of the finite resolution of CECE measurements and the red line indicates T_e power spectrum with the consideration of the finite resolution of the measurements. As shown in the figure, most modes in the high k_y region are suppressed due to the poloidal resolution of the CECE diagnostic, estimated as $k_y\rho_s < 0.3$ from Gaussian beam calculations. We can also see that the low k_y peak has the largest T_e fluctuation value among the modes which have non-zero poloidal wavelength ($k_y > 0$) and the portion of the low k_y peak becomes larger when poloidal resolution of the CECE diagnostic is considered. In the experiments, the important parameter in T_e fluctuation measurements in C-Mod was the poloidal resolution [167, 176, 153]. If this mode existed with an amplitude similar to the simulation result in the real experiments, the poloidal resolution in the measurements would be less important than the real measurements. In that case, T_e fluctuations could have been measured in the past attempts in 2004.

	Q_i [MW/m^2]	Q_e [MW/m^2]	$Q_i(k_y\rho_s < 0.1)$ [MW/m^2]	$Q_e(k_y\rho_s < 0.1)$ [MW/m^2]	$\frac{Q_i(k_y\rho_s<0.1)}{Q_i}$	$\frac{Q_e(k_y\rho_s<0.1)}{Q_e}$
Base case	0.019 (±0.0019)	0.027 (±0.0021)	0.0026	0.00093	0.137	0.034
$a/L_{T_e} + \sigma_{a/L_{T_e}}$	0.013 (±0.0010)	0.036 (±0.0023)	0.0015	0.0006	0.115	0.017
$a/L_{T_e} - \sigma_{a/L_{T_e}}$	0.039 (±0.0049)	0.028 (±0.0031)	0.0076	0.0023	0.195	0.082
$a/L_{T_i} + \sigma_{a/L_{T_i}}$	0.035 (±0.0042)	0.035 (±0.0032)	0.0045	0.0016	0.129	0.046
$a/L_{T_i} - \sigma_{a/L_{T_i}}$	0.011 (±0.00097)	0.025 (±0.0019)	0.0012	0.00046	0.109	0.018
$a/L_n + \sigma_{a/L_n}$	0.012 (±0.0012)	0.027 (±0.0031)	0.00031	0.00011	0.026	0.004
$a/L_n - \sigma_{a/L_n}$	0.026 (±0.0023)	0.028 (±0.0022)	0.0042	0.0014	0.162	0.050
$\gamma_{E\times B} + \sigma_{\gamma_{E\times B}}$	0.014 (±0.0011)	0.025 (±0.0021)	0.00045	0.00016	0.032	0.006
$\gamma_{E\times B} - \sigma_{\gamma_{E\times B}}$	0.028 (±0.0047)	0.031 (±0.0035)	0.0084	0.0033	0.300	0.106
$\nu_{ei} + \sigma_{\nu_{ei}}$	0.021 (±0.0019)	0.026 (±0.0020)	0.0037	0.0012	0.176	0.046
$\nu_{ei} - \sigma_{\nu_{ei}}$	0.023 (±0.0026)	0.030 (±0.0031)	0.0029	0.0010	0.126	0.033
$n_D/n_e + \sigma_{n_D/n_e}$	0.028 (±0.0023)	0.031 (±0.0022)	0.0048	0.0016	0.171	0.052
$n_D/n_e - \sigma_{n_D/n_e}$	0.014 (±0.0012)	0.025 (±0.0021)	0.0020	0.00075	0.143	0.030

Table I.4: Sensitivity analysis of the LOC plasma with low k_y mode, L_x : $171.0\rho_s$, L_y : $184.0\rho_s$, $k_y\rho_s < 1.6$. Experimental values and n_D/n_e=0.82 are used in the base case.

Resolved runs with the suppression of the low k_y mode in a reasonable small box size

Considering the simulation results so far, it is likely that the low k_y peak is not physically real mode, but is instead artificial. Although simulation results show that a low E×B shearing rate and inaccurate collision calculations can enhance the low k_y peak, the origin of this mode is still inconclusive. However, it is not possible to obtain physically meaningful simulations with this low k_y peak. If it is possible, this mode should be suppressed within the uncertainty of input parameters to use these simulations for validation and the study of relevant physics. Sensitivity analysis for the low k_y peak in the LOC plasma was performed within the uncertainty of input parameters. As shown in Table I.4, the low k_y peak is suppressed by an increase in the E×B shearing rate and a decrease in a/L_n. As mentioned before, the E×B shearing rate in both LOC and SOC runs has a large uncertainty and a lower value than the nominal value. Thus, the E×B shearing rate should be adjusted first to suppress the low k_y mode. From Fig. I-10, the LOC plasma could have a well-resolved simulation with the highest E×B shearing rate within the uncertainty in a domain size (L_x : $130.8\rho_s$, L_y : $107.1\rho_s$) smaller than the resolved run with the experimental E×B shearing rate. For the SOC plasma, the E×B shearing rate is not sufficient for the

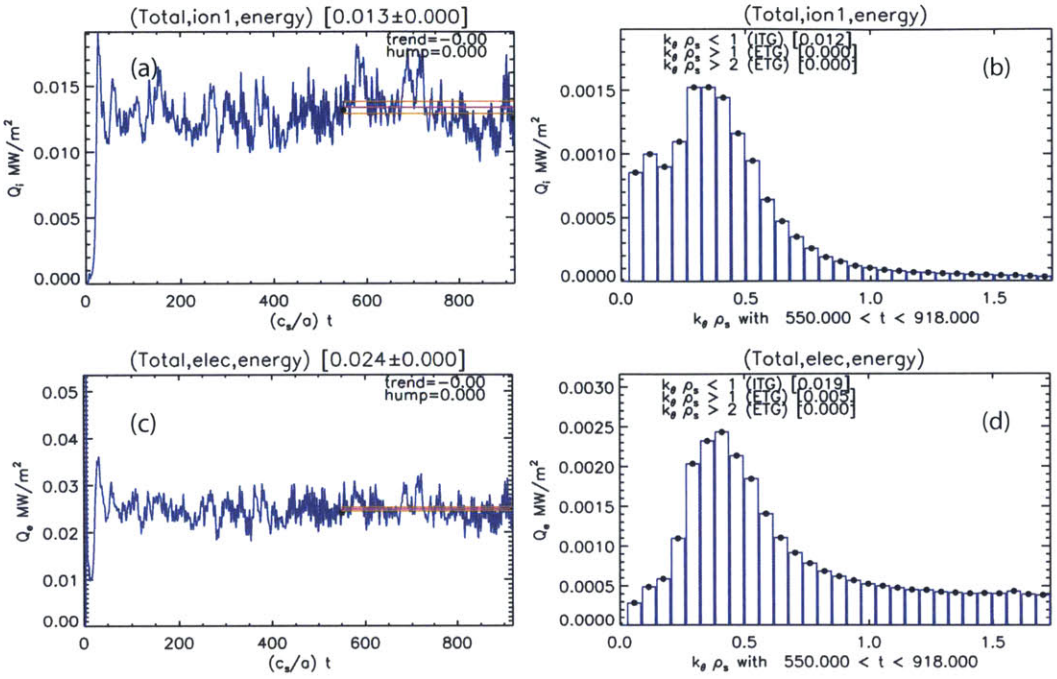

Figure I-10: Results of the LOC plasma with a high shearing rate, ($\gamma_{E\times B} = 0.032[c_s/a]$) and smaller domain size compared to the resolved simulation. (radial domain size, L_x is $\sim 130.0\rho_s$, poloidal domain size, L_y is $\sim 107.0\rho_s$ and the highest $k_y\rho_s$ is ~ 1.7) (a) $Q_i(t)$ (b) $Q_i(k_y)$ spectrum (averaging time : 550-918 [a/c_s]) (c) $Q_e(t)$ (d) $Q_e(k_y)$ spectrum (averaging time : 550-918 [a/c_s]).

resolved simulation in smaller domain size (L_x : $114.3\rho_s$, L_y : $130.9\rho_s$) and a/L_n should also be adjusted within the uncertainty to suppress the low k_y peak. Figure I-11 shows the resolved SOC run in the smaller domain size. The study through GYRO runs for the C-Mod LOC and SOC discharges at r/a$\sim$0.85 will start from these two runs since both runs are numerically resolved in a reasonable box size by suppressing the low k_y peak within the uncertainty of input parameters.

I.2 Error analysis of the synthetic T_e fluctuation level

In order to estimate the uncertainty of the synthetic T_e fluctuation level, three error sources were considered. They are the uncertainty of the distance between two channels, the uncertainty of the radial broadening width, and the random error of the cross power spectrum. Here, we estimated the uncertainty of the synthetic T_e fluctuation level for the specific case of the local gyrokinetic analysis for the C-Mod Ohmic

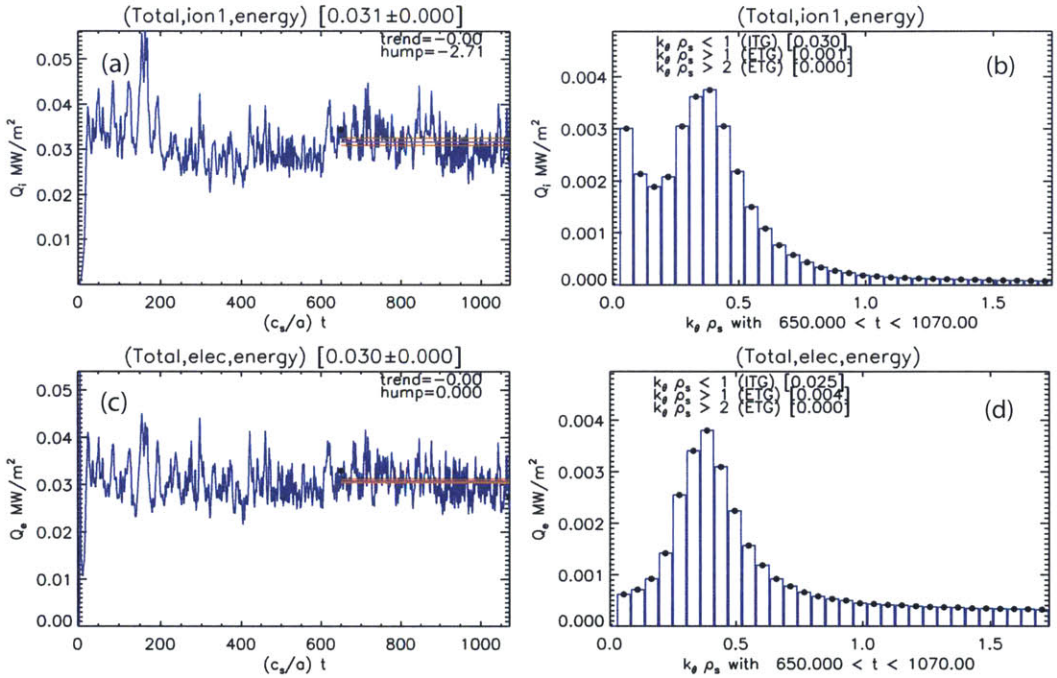

Figure I-11: Results of the SOC plasma with a high shearing rate and a high a/L_n within their uncertainties ($\gamma_{E\times B} = 0.023[c_s/a]$, a/$L_n$=1.87) and a smaller domain size compared to the resolved simulation. (radial domain size, L_x is $\sim 130.9\rho_s$, poloidal domain size, L_y is $\sim 114.3\rho_s$ and the highest $k_y\rho_s$ is ~ 1.7) (a) $Q_i(t)$ (b) $Q_i(k_y)$ spectrum (averaging time : 650-1070 [a/c_s]) (c) $Q_e(t)$ (d) $Q_e(k_y)$ spectrum (averaging time : 650-1070 [a/c_s]).

	Measured I_p [kA]	Estimated I_p [kA]	Fractional error
LOC (shot 1120626023)	897.8	914.5	~0.02
SOC (shot 1120626028)	897.5	915.6	~0.02

Table I.5: The comparison of the plasma current measured by the rogowski coil with the plasma current estimated by equilibrium solver, EFIT for the LOC and SOC discharges (shot 1120626023 (LOC), shot 1120626028 (SOC)). Both values are time averaged during the stationary time period (t:0.9-1.4s).

discharges near the edge, which was treated in Chapter 4. For the discharges used in the local GYRO simulation in Chapter 4 (shot 1120626023 (LOC), shot 1120626028 (SOC)), we used two CECE channels whose center frequencies were 241.5GHz and 242GHz, with a 200MHz bandwidth, for the T_e fluctuation measurements. Although error analysis is explained for a certain type of discharge in this section, similar analysis can be done for other cases as well.

First, the uncertainty of the distance between the two channels is estimated from the uncertainty of the radial position of each channel. We can estimate the uncertainty of radial position by considering the uncertainty of the poloidal magnetic field (B_p). As explained in Chapter 2, the toroidal magnetic field is well defined in a Tokamak. The poloidal magnetic field is estimated via the equilibrium solver, EFIT [96] in this study. One way to check the uncertainty of the poloidal magnetic field estimated from EFIT is by comparing the plasma current measured by the rogowski coil with the plasma current by EFIT. Table I.5 shows the difference between the two plasma current values for the LOC and SOC discharges used in the local gyrokinetic analysis in this thesis. It is shown that there is a 2% difference in the estimated plasma current value compared to the measured plasma current value in both discharges. Although we cannot say which region has a larger error compared to other regions in the plasma, we can roughly say that the estimated poloidal magnetic field has about 2% uncertainty.

We then calculate the range of the radial position of each channel (CH1 and CH2) used in the CECE measurements by varying poloidal magnetic field within 2%, that is $0.98\times B_{p,EFIT}$-$1.02\times B_{p,EFIT}$. The ranges of the radial position of two channels are shown in Table I.6. Assuming that three radial positions, $B_p = B_{p,EFIT}, 0.98 \times$

	R [cm] for CH1	R [cm] for CH2
LOC (shot 1120626023)	84.7-84.8	84.8-84.9
SOC (shot 1120626028)	84.6-84.7	84.8-84.9

Table I.6: The range of the radial position of two CECE channels (CH1 : a CECE channel with center frequency 242GHz with 200MHz bandwidth, CH2 : a CECE channel with center frequency 241.5GHz with 200MHz bandwidth) when the poloidal magnetic field is varied 2% from the estimated value from EFIT. The radial position is estimated from the center frequency, and this value is not mapped on mid-plane. That is, this value indicates the radial position of each channel, which are above midplane (~7cm).

$B_{p,EFIT}$, $1.02 \times B_{p,EFIT}$ are random points, the conversion formula from range to standard deviation [108] can be used. The estimated uncertainty of the radial position is about 0.07cm for both CECE channels. The radial distance between the two channels, dx, is defined as, dx=$|R_{CH1} - R_{CH2}|$. Assuming the radial position of the two channels are not correlated, the uncertainty of dx can be estimated through error propagation as shown in Eq. I.1,

$$\sigma_{dx}^2 = \sigma_{R,CH1}^2 + \sigma_{R,CH2}^2 \tag{I.1}$$

The estimated σ_{dx} is about 0.1cm. The estimated dx value from the center frequency of two channels is about 0.2cm. Thus, dx=0.2±0.1 cm in this case.

Second, there will be an uncertainty in the estimation of the radial broadening width. Since the radial broadening width is calculated numerically, as shown in section 2.3.3, it is difficult to find its uncertainty analytically. Nevertheless, a rough estimate is still possible from the uncertainty of the estimated radiation emissivity, $I(\nu, s)$ with frequency, ν, and location, s. For the second harmonic measurements, the absorption coefficient, $\alpha(\nu), \sim n_e T_e \phi(\nu)$, with shape function, $\phi(\nu)$. The optical depth, $\tau, \sim n_e T_e$ with the tenuous plasma approximation. The definition of these quantities can be found in section 2.3.3. When the plasma is optically thick and the angle of the radiation from the magnetic field is $\pi/2$, we can find the emissivity of the radiation, $I(\nu, s)$, as given by,

$$I(\nu, s) = C_I n_e T_e^{-3/2} \exp(-\frac{C_T}{T_e} - C_\tau n_e T_e) \tag{I.2}$$

where C_I and C_τ are constants, and functions of electron mass, charge, and vacuum permittivity. C_T is defined as, $C_T = \frac{m_e c^2}{2}(1 - (\frac{1}{2}\frac{\omega}{\Omega})^2)$.

We can estimate the uncertainty of $I(\nu, s), \sigma_I$, by considering the uncertainty of n_e and T_e (σ_{n_e} and σ_{T_e}) through error propagation in the following:

$$\sigma_I^2 = (\frac{\partial I}{\partial n_e}\sigma_{n_e})^2 + (\frac{\partial I}{\partial T_e}\sigma_{T_e})^2 \tag{I.3}$$

where $\frac{\partial I}{\partial n_e} = \frac{I}{n_e} - C_\tau T_e I$, and $\frac{\partial I}{\partial T_e} = -\frac{3}{2}\frac{I}{T_e} - C_\tau n_e I + \frac{C_\tau}{T_e^2}$.

It is noteworthy that CECE measures the EC radiation in a certain frequency range, not at one specific frequency. We summed 11 emissivity curves within the measured frequency range to consider the bandwidth of the measurements in section 2.2.3. The uncertainty of the measured emissivity curve can be also estimated by propagating the uncertainty of the 11 emissivity curves. In other words, the uncertainty of the emissivity curve at each radial location can be estimated by propagating the uncertainties of the 11 emissivity curves at the same location. In this estimation, it was assumed that the uncertainties of each emissivity curve are perfectly correlated since the 11 emissivity curves are significantly overlapped, as shown in Fig. 2-13. We now have the estimated intensity profile of the measured EC radiation, and its uncertainty. We then randomly generate the intensity profile 100 times by varying each point in the emissivity curve weighted by its uncertainty, and estimated the radial broadening width of each randomly generated intensity profile. The uncertainty of the radial broadening width is determined from the standard deviation of the radial broadening width of the randomly generated intensity profiles. For both LOC and SOC discharges, the fractional uncertainty of the radial broadening width estimated by this method is around 5%.

The random error of the cross power spectrum, which can be obtained from [17] is another error source we can consider. As mentioned in section 3.4, the synthetic fluctuation level is calculated by integrating the synthetic cross power spectrum in a

	$l_R = l_{R,exp}$, dx=dx_{exp}	$l_R = l_{R,exp} + \sigma_{l_R}$, dx=$dx_{exp} + \sigma_{dx}$	$l_R = l_{R,exp} - \sigma_{l_R}$, dx=$dx_{exp} - \sigma_{dx}$
LOC (shot 1120626023)	0.83±0.01%	0.78±0.01%	0.87±0.01%
SOC (shot 1120626028)	0.80±0.01%	0.74±0.01%	0.86±0.01%

Table I.7: The changes in the synthetic T_e fluctuation level with changes in the radial distance between two CECE channels, dx, and the radial width of the CECE channel, l_R, within their uncertainties for the Q_i matched LOC/SOC runs obtained in Chapter 4. The poloidal width of the channel is fixed as 0.64cm, $l_Z = 0.64$cm.

frequency range we set. In order to estimate the uncertainty from the random error of the cross power spectrum, we generated 100 cross power spectra by randomly varying the data points in the spectrum obtained from the synthetic CECE diagnostic weighted by its uncertainty, and calculate the fluctuation level from each spectrum. From the standard deviation of the fluctuation levels obtained from the randomly generated one hundred cross power spectra, we obtained the uncertainty of the synthetic fluctuation level. However, the uncertainty due to the random error in the cross power spectrum is fairly small, around 1% or less than 1%.

In order to estimate the propagated uncertainty due to the errors in the radial distance between two CECE channels and in the estimated radial broadening width, we first obtain the range of fluctuation levels within these uncertainties. That is, we observed the changes in the fluctuation level with two extreme cases, which will give the highest fluctuation level with the shortest distance between two channels and the smallest radial broadening width ($1/e^2$ diameter in the radial direction) within the estimated uncertainty, and the lowest fluctuation level with the longest radial distance and the largest radial broadening width value. Table I.7 shows the changes in the synthetic T_e fluctuation level with the changes in the radial distance between two channels, dx, and the radial broadening width, l_R for the Q_i matched LOC and SOC runs. Although these points are not randomly selected, a rough estimate for the uncertainty can be obtained through the conversion formula from range to standard deviation [108]. As a result, the fractional uncertainty of the synthetic T_e fluctuation level is about 7% for the LOC run, and about 9% for the SOC run. These fractional uncertainties were used in this study. However, we should note that this estimation is crude, and we do not consider the uncertainty from the poloidal beam

width estimation. The error analysis for the synthetic T_e fluctuation level should be improved in the future.

I.3 Estimation of uncertainties of rotation relevant parameters and collision frequency in GYRO

This section will describe the uncertainty estimation for rotation relevant parameters, such as rotation frequency, ω_o, $E \times B$ shearing rate, $\gamma_{E\times B}$, and collision frequency, ν_e, in the GYRO runs for the C-Mod Ohmic discharges used in section 4.2-4.4. We must note that we estimate the uncertainties of ω_o and $\gamma_{E\times B}$ calculated in GYRO based on the radial electric field, E_r, value estimated in TRANSP.

A rotation frequency, ω_o, in GYRO is defined as,

$$\omega_o = \frac{cE_r}{RB_p} \tag{I.4}$$

with major radius at each location, R, and poloidal magnetic field, B_p.

As described in Eq. 4.1, we can separate E_r into three components: $E_{r,tor}$, determined by the toroidal velocity (V_t) and poloidal magnetic field (B_p), $E_{r,pol}$, determined by the poloidal velocity (V_p) and toroidal magnetic field (B_t), and $E_{r,dia}$, determined by the diamagnetic effect (∇p_i), with $p_i = n_i T_i$. That is, $E_r = E_{r,tor} + E_{r,pol} + E_{r,dia}$. Consequently, ω_o can be expressed with the same three components as E_r ($\omega_o = \omega_{o,tor} + \omega_{o,pol} + \omega_{o,dia}$). Assuming that these three components of ω_o are uncorrelated, the uncertainty of ω_o, σ_{ω_o} will be,

$$\sigma^2_{\omega_o} = \sigma^2_{\omega_{o,tor}} + \sigma^2_{\omega_{o,pol}} + \sigma^2_{\omega_{o,dia}} \tag{I.5}$$

As shown in Fig. 4-25, $E_{r,dia}$ is negligible compared to $E_{r,tor}$ and $E_{r,pol}$. Thus, $\omega_{o,dia}$ and its uncertainty will be also ignorable. Thus,

$$\sigma^2_{\omega_o} \simeq \sigma^2_{\omega_{o,tor}} + \sigma^2_{\omega_{o,pol}} \tag{I.6}$$

For $\sigma_{\omega_{o,tor}}$, its uncertainty comes from uncertainties of B_p, R, and V_t. As shown in Appendix I.2, the estimated uncertainty of B_p was small ($\sim 2\%$), and the uncertainty of R is only 0.1cm, which is less than 1% of the R value (> 67 cm). Comparing the uncertainty of V_t ($\geq 10\%$), these two uncertainties are ignorable. Then, using error propagation, $\sigma_{\omega_{o,tor}}$ will be,

$$\frac{\sigma_{\omega_{o,tor}}}{|\omega_{o,tor}|} \simeq \frac{\sigma_{V_t}}{|V_t|} \tag{I.7}$$

Using the uncertainty of V_t estimated in Appendix F, $\sigma_{\omega_{o,tor}}$ was obtained in this study. $\sigma_{\omega_{o,pol}}$ is also mainly determined by the uncertainty of V_p since B_t is well known in the experiment, and the uncertainties of B_p and R are small. As explained in section 4.4.6, V_p was estimated from the neoclassical calculation, and it is difficult to estimate the uncertainty of this value. We estimate the uncertainty of $\omega_{o,pol}$ from the standard deviation of time averaging in the stationary time period of the Ohmic discharges used in section 4.2-4.4. From the estimated $\sigma_{\omega_{o,tor}}$ and $\sigma_{\omega_{o,pol}}$, the uncertainty of ω_o was calculated via Eq. I.6.

$\gamma_{E\times B}$ in GYRO is defined as,

$$\gamma_{E\times B} = -\frac{r}{q}\frac{\partial \omega_o}{\partial r} = -\frac{r}{q}\frac{\partial}{\partial r}[\frac{cE_r}{RB_p}] = \gamma_{E\times B,1} + \gamma_{E\times B,1} \tag{I.8}$$

where r is the minor radius at each location, and q is the safety factor. $\gamma_{E\times B,1}$ and $\gamma_{E\times B,2}$ are,

$$\gamma_{E\times B,1} = -\frac{r}{q}[\frac{1}{RB_p}\frac{\partial cE_r}{\partial r}] \tag{I.9}$$

$$\gamma_{E\times B,2} = -\frac{r}{q}[cE_r(-\frac{1}{(RB_p)^2}\{R\frac{\partial B_p}{\partial r} + B_p\frac{\partial R}{\partial r}\})] \tag{I.10}$$

In the same manner used for ω_o, $\gamma_{E\times B,1}$ and $\gamma_{E\times B,2}$ can be also separated as follows:

$$\gamma_{E\times B,i} = \gamma_{E\times B,i,tor} + \gamma_{E\times B,i,pol} + \gamma_{E\times B,i,dia} \tag{I.11}$$

where i=1,2.

Assuming $\gamma_{E\times B,1}$ and $\gamma_{E\times B,2}$ are uncorrelated, the uncertainty of $\gamma_{E\times B}$, $\sigma_{\gamma_{E\times B}}$, will be,

$$\sigma^2_{\gamma_{E\times B}} = \sigma^2_{\gamma_{E\times B,1}} + \sigma^2_{\gamma_{E\times B,2}} \tag{I.12}$$

As discussed in the σ_{ω_o} estimation, the uncertainties of the positions (r and R) and the magnetic fields (B_p and B_t) are ignorable. Thus, the uncertainty of the safety factor, q, which is a function of the positions and magnetic fields, is also ignorable. From the almost flat radial profile of $E_{r,dia}$ shown in Fig. 4-25, we will ignore the uncertainties from the diamagnetic terms ($\sigma_{\gamma_{E\times B,1,dia}}$ and $\sigma_{\gamma_{E\times B,2,dia}}$). $\gamma_{E\times B,1,tor}$ is proportional to $\frac{\partial E_{r,tor}}{\partial r}$. Using $\frac{\partial E_{r,tor}}{\partial r} \propto \frac{\partial V_t}{\partial r}$, the uncertainty of $\gamma_{E\times B,1,tor}$, $\sigma_{\gamma_{E\times B,1,tor}}$ is,

$$\frac{\sigma_{\gamma_{E\times B,1,tor}}}{|\gamma_{E\times B,1,tor}|} \simeq \frac{\sigma_{\frac{\partial E_{r,tor}}{\partial r}}}{|\frac{\partial E_{r,tor}}{\partial r}|} \simeq \frac{\sigma_{\frac{\partial V_t}{\partial r}}}{|\frac{\partial V_t}{\partial r}|} \tag{I.13}$$

$\sigma_{\gamma_{E\times B,1,tor}}$ is then estimated using the uncertainty of the radial gradient of V_t, obtained in Appendix F.

In the same manner, the uncertainty of $\gamma_{E\times B,2,tor}$ can be obtained from the uncertainty of V_t, estimated in Appendix F, as follows:

$$\frac{\sigma_{\gamma_{E\times B,2,tor}}}{|\gamma_{E\times B,2,tor}|} \simeq \frac{\sigma_{E_{r,tor}}}{|E_{r,tor}|} \simeq \frac{\sigma_{V_t}}{|V_t|} \tag{I.14}$$

The uncertainties of $\gamma_{E\times B,1,pol}$ and $\gamma_{E\times B,2,pol}$ are obtained from the standard deviation of the time averaging in the stationary time period. We then calculate the uncertainties of $\gamma_{E\times B,1}$ and $\gamma_{E\times B,2}$, and finally, the uncertainty of $\gamma_{E\times B}$ was obtained through Eq. I.11 and I.12. The estimated uncertainty was used in Chapter 4 and section I.1.

The uncertainty of the collision frequency, ν_e, used in GYRO was also estimated using the error propagation technique. ν_e is given in GYRO as follows:

$$\nu_e(\epsilon_e) = \frac{\nu_{ee}}{\epsilon_e^{3/2}}[Z_{eff} + H(\epsilon_e^{0.5})] \tag{I.15}$$

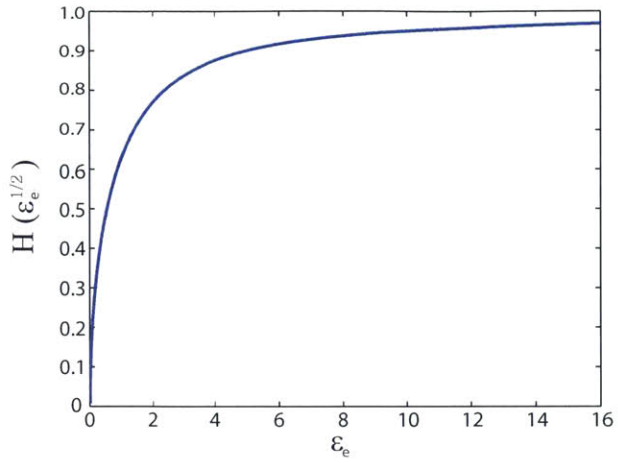

Figure I-12: The value of the H-function used in the collision frequency in GYRO with the normalized electron density, ϵ_e.

with the normalized electron energy, $\epsilon_e = \frac{E_e}{T_e} = \frac{m_e v^2}{2T_e}$ and electron-electron collision frequency, ν_{ee}. H-function is defined as,

$$H(x) = \frac{e^{-x^2}}{\pi^{0.5}x} + (1 - \frac{1}{2x^2})erf(x) \tag{I.16}$$

As shown in Fig. I-12, the H-function has a value between 0 and 1. We can roughly estimate the average H-function value is around 0.5. Since Z_{eff} values in the Ohmic discharges used in section 4.2-4.4 are three to five times larger than the average H-function value (~0.5), we will ignore the uncertainty of the H-function in ν_e. Using that ν_{ee} is proportional to $n_e T_e^{-3/2}$ and that ν_e is proportional to $\frac{\nu_{ee} Z_{eff}}{\epsilon_e^{3/2}}$, we notice that ν_e is proportional to $n_e Z_{eff}$ ($\nu_e \propto n_e Z_{eff}$). Ignoring the correlation between Z_{eff} and n_e, the uncertainty of ν_e can be estimated as follows:

$$\frac{\sigma_{\nu_e}{}^2}{\nu_e} \simeq \frac{\sigma_{n_e}{}^2}{n_e} + \frac{\sigma_{Z_{eff}}{}^2}{Z_{eff}} \tag{I.17}$$

We can then estimate the uncertainty of ν_e from the uncertainty of n_e and Z_{eff}, estimated in Appendix F. For both LOC and SOC discharges, the uncertainty of Z_{eff} was dominant, and the fractional uncertainty of ν_e is around 20% for both LOC and SOC discharges.

Appendix J

Global gyrokinetic simulations for C-Mod Ohmic plasmas near the edge

In Chapter 4, we used the GYRO runs at the local flux surface to investigate the changes in turbulence between the LOC and SOC discharges. This section will present global simulation results, which include profile variations in the simulation domain, for the same discharges. The global simulations were performed in r/a=[0.7-0.9] and study the changes in transport and T_e fluctuations in global simulations compared to the local simulations.

J.1 Motivation

There are three motivations for the gyrokineitc analysis using global runs. First, in the local runs near the edge (r/a$\sim$0.85), we found a large amplitude peak in the low k_y region ($k_y\rho_s < 0.1$) of the $Q_i(k_y)$ spectrum in both LOC and SOC discharges. A huge domain size ($L \gtrsim 200\rho_s$) was required to resolve this peak, and this domain size threatens the basic gyrokinetic ordering, as explained in Appendix I. Moreover, this peak may not exist in the real experiment. We observed that its amplitude varies with changes in the collision calculation setup and that a very low $E \times B$ shearing rate compared to its nominal value ($0.05[c_s/a]$) in these discharges may result in this peak. Although we do not know the origin of this peak, we should suppress it to

obtain a numerically resolved simulation with a reasonable box size. This peak was suppressed by changing input parameters (a/L_n and $\gamma_{E\times B}$) within their uncertainties. We should check whether or not this peak is observed in the global runs as well in order to investigate the origin of this peak and to justify the approach used for the local runs near the edge.

Second, the estimated radial broadening width of the CECE measurements is about 1cm, as shown in Chapter 2. In terms of r/a, the CECE relevant region is $r/a \sim 0.8-0.87$. We must note that the CECE measurement region is radially broad, not just one point, and that input parameters vary in the CECE measurement region, as shown in Fig. J-1. We must compare the heat fluxes and synthetic T_e fluctuations with variation of input parameters, including gradient scale lengths, with the results in the local simulations.

Third, as mentioned in Chapter 4, GYRO over-predicts Q_i deeper in the core region ($r/a < 0.8$) in Ohmic discharges [99, 120]. If turbulence in $r/a < 0.8$ affects significantly the turbulence in $r/a > 0.8$, the validation study performed in Chapter 4 would not be valid. We must identify whether turbulence near r/a ~ 0.85 is driven by locally or affected by the turbulence in more unstable region or the region which has high transport level (deeper in core region).

J.2 Simulation setup & convergence test

The basic setup for the global simulations near the edge is the same as explained in section 3.4. We used gyrokinetic ions and driftkinetic electrons, and 128 grid points were set in velocity space with 8 energies, 8 pitch angles and 2 signs of velocity. Only ion scale turbulence ($k_y\rho_s \lesssim 1.5$) was considered in both LOC and SOC runs. As mentioned at the beginning of this section, the radial domain was set to r/a=[0.7,0.9]. Domain size was set to radial box size, $L_x, \sim 110 - 120\rho_s$ by poloidal box size, $L_y, \sim 100\rho_s$ with radial spacing, $\Delta r \sim 0.2\rho_s$. It is noteworthy that two input parameters are modified to avoid numerical instability in the global runs in this study. First, radial grid spacing was set to be proportional to the local value of ρ_s/a

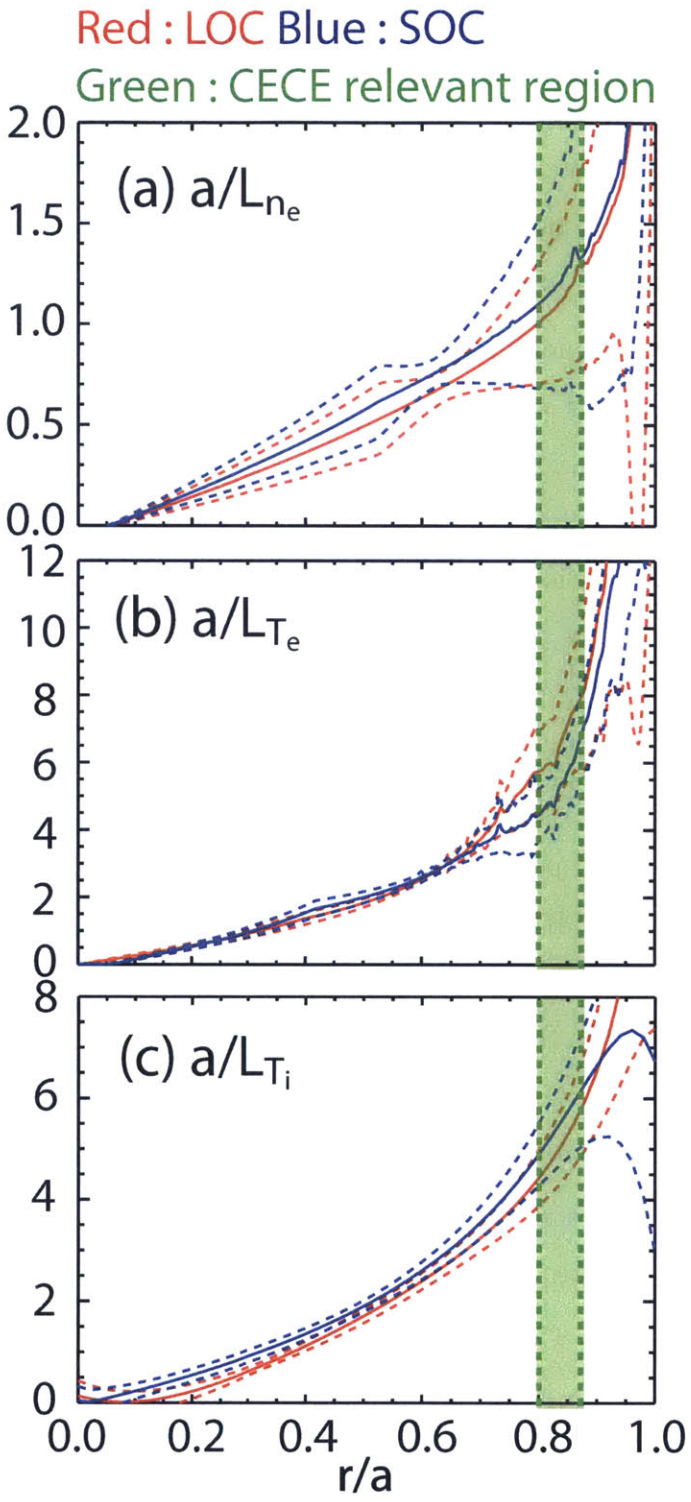

Figure J-1: The radial profiles of gradient scale lengths with the CECE relevant (or measurement) region (Green shaded region) for two C-Mod Ohmic discharges used in section 4.2-4.4 (Red : LOC plasma (shot 1120626023, t:0.9-1.4s), blue : SOC plasma (shot 1120626028, t:0.9-1.4s)). (a) a/L_{n_e} (b) a/L_{T_e} (c) a/L_{T_i}.

(NONUNIFORM_GRID_FLAG=1.0 in GYRO input file). In the local simulation, the radial grid spacing was set to be uniform. Second, the source annihilation rate is increased in the global runs. The source is used to avoid numerical instability from the non-periodic boundary condition in GYRO [28, 3]. The source annihilation rate was set to 1.0 $[c_s/a]$ in the global runs (NU_SOURCE=1.0 in GYRO input file). This value was set to 0.1 $[c_s/a]$ in the local runs.

The simulation setup including the domain size, maximum $k_y\rho_s$, and the grids in velocity space was justified via the convergence study. The convergence study for the global simulations was performed using the Q_i matched runs for the LOC and the SOC discharges, which will be discussed in section J.4. In this convergence study, we set the Q_i matched simulation as the base run, and then varied the following input parameters: poloidal box size, L_y, maximum $k_y\rho_s$ value included in the simulation, the number of trapped/passing pitch angles (TRAP_GRID, PASS_GRID), the number of grid points in the poloidal direction along a particle orbit, the number of finite elements used to discretize Maxwell's equations (ORBIT_GRID and BLEND_GRID), the number of energy grid points and the location of the largest energy grid point in terms of T_e (ENERGY_GRID and ENERGY_MAX). The radial box size, L_x, was fixed in this test to prevent changes in turbulence due to newly included flux surfaces with a larger L_x. For the SOC runs, the order of the radial basis function for the collision operator, ORD_RBF, was set to 5.0. The reason for this will be explained in the next section. The simulation setups for the runs used in the convergence study for the LOC and SOC discharges are shown in Table J.1 and J.2, respectively.

We checked the changes in ion and electron heat fluxes among these runs, but not synthetic T_e fluctuations. Compared to the local simulations, in global simulations it is required to run much longer to implement the synthetic CECE diagnostic. In the local simulations, we could use five to six pairs of the synthetic signals in the simulation domain since the same input parameters are used in the whole simulation domain in the local run, which is helpful to reduce random error. However, the input parameters vary at each point in the global simulations. Thus, we can apply only one pair of the synthetic diagnostics at the same location with measurements in the

	L_y $[\rho_s]$	Max. $k_y\rho_s$	PASS & TRAP_GRID	ORBIT & BLEND_GRID	ENERGY_GRID (ENERGY_MAX $[T_e]$)	Δr $[\rho_s]$
Base case	96.0	1.5	4	7	8 (5.0)	0.2
Test run 1	128.0	1.5	4	7	8 (5.0)	0.2
Test run 2	96.0	2.0	4	7	8 (5.0)	0.2
Test run 3	96.0	1.5	6	7	8 (5.0)	0.2
Test run 4	96.0	1.5	5	10	8 (5.0)	0.2
Test run 5	96.0	1.5	4	7	12 (7.0)	0.2
Test run 6	96.0	1.5	4	7	8 (5.0)	0.1

Table J.1: The numerical setup for the global runs used in the convergence test for the LOC discharge used in section 4.2-4.4. L_x was set to 107.8 ρ_s in all runs in this table.

	L_y $[\rho_s]$	Max. $k_y\rho_s$	PASS & TRAP_GRID	ORBIT & BLEND_GRID	ENERGY_GRID (ENERGY_MAX $[T_e]$)	Δr $[\rho_s]$
Base case	97.2	1.5	4	7	8 (5.0)	0.2
Test run 1	126.4	1.5	4	7	8 (5.0)	0.2
Test run 2	97.2	2.0	4	7	8 (5.0)	0.2
Test run 3	97.2	1.5	6	7	8 (5.0)	0.2
Test run 4	97.2	1.5	4	10	8 (5.0)	0.2
Test run 5	97.2	1.5	4	7	12 (7.0)	0.2
Test run 6	97.2	1.5	4	7	8 (5.0)	0.15

Table J.2: The numerical setup for the global runs used in the convergence test for the SOC discharge used in section 4.2-4.4. L_x was set to 117.0 ρ_s in all runs in this table.

	Averaging time $[a/c_s]$	Ion heat flux $[MW/m^2]$	Electron heat flux $[MW/m^2]$
Base case	300-600	0.030 ± 0.0051	0.041 ± 0.0050
Test run 1	300-600	0.028 ± 0.0036	0.041 ± 0.0053
Test run 2	200-600	0.025 ± 0.0045	0.037 ± 0.0055
Test run 3	400-1000	0.029 ± 0.0046	0.040 ± 0.0055
Test run 4	300-600	0.025 ± 0.0032	0.040 ± 0.0044
Test run 5	350-600	0.029 ± 0.0031	0.044 ± 0.0045
Test run 6	200-500	0.028 ± 0.0046	0.037 ± 0.0057

Table J.3: The time and spatially averaged heat flux values of the runs used in the convergence test for the LOC discharge used in section 4.2-4.4.

	Averaging time $[a/c_s]$	Ion heat flux $[MW/m^2]$	Electron heat flux $[MW/m^2]$
Base case	250-600	0.058 ± 0.0086	0.041 ± 0.0057
Test run 1	200-600	0.064 ± 0.0096	0.044 ± 0.0063
Test run 2	330-600	0.064 ± 0.016	0.045 ± 0.010
Test run 3	300-800	0.062 ± 0.011	0.041 ± 0.0061
Test run 4	300-600	0.061 ± 0.0099	0.042 ± 0.0065
Test run 5	300-600	0.069 ± 0.010	0.049 ± 0.0067
Test run 6	220-560	0.066 ± 0.013	0.044 ± 0.0077

Table J.4: The time and spatially averaged heat flux values of the runs used in the convergence test for the SOC discharge used in section 4.2-4.4.

global simulations, and a longer run time is required to have a similar level of random error as obtained in the local simulations. Since each global simulation in this test is expensive, we were not able to run long enough to apply the synthetic diagnostic. Nevertheless, comparing ion and electron heat fluxes may be enough for this purpose since synthetic T_e fluctuations tend to vary with the electron heat flux. Table J.3 and J.4 show the changes in the ion and electron heat fluxes among LOC and SOC runs used in this convergence test, respectively. The heat flux values in these tables are obtained from time and spatial averaging, and their uncertainty was obtained from the standard deviation from the averaging. We notice that the heat flux values are similar within their uncertainties among the runs in this convergence test, which indicates that the average heat flux values converge with the initial simulation setup. Thus, it is acceptable to keep the simulation set-up in the base run for other runs in this section.

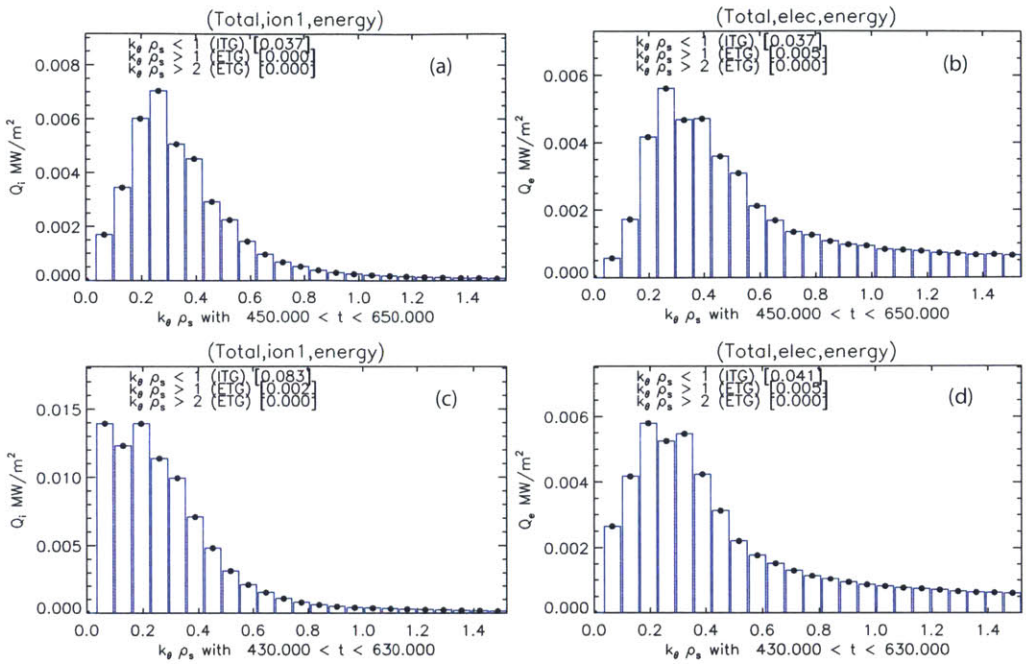

Figure J-2: (a) $Q_i(k_y)$ and (b) $Q_e(k_y)$ spectra obtained from the LOC global run with the experimental profiles. (c) $Q_i(k_y)$ and (d) $Q_e(k_y)$ spectra obtained from the SOC global run with the experimental profiles.

J.3 Global simulation results with experimental profiles

We first performed the global runs with experimental profiles without any modifications. From these runs, we can check whether the low k_y peak is also observed in the global runs or this peak is observed only in the local runs. We will also gather information on how to obtain the heat flux matched global simulations from the runs with experimental profiles. Figure J-2 shows the $Q_i(k_y)$ and $Q_e(k_y)$ spectra in the LOC and SOC runs with the experimental profiles. We first note that there is no huge peak in the low k_y region in the $Q_i(k_y)$ spectra in both runs. Thus, the low k_y peak is an issue limited to the local runs, and probably not physically meaningful.

However, we notice that the Q_i at the lowest k_y value is still the highest in the $Q_i(k_y)$ spectrum in the SOC run, as shown in Figure J-2(c), although it is not huge

compared to the modes in other wavenumbers. Since the SOC plasma is collisional, we checked the issue related to the collision calculation by changing the order of the radial basis function for the collision operator (ORD_RBF) from 3 to 5. With ORD_RBF=5, the Q_i at the lowest k_y value is reduced, but the heat flux values are similar within 10%, as shown in Fig. J-3. Instead of modifying input parameters or increasing domain size to reduce the Q_i at the lowest k_y value, we will set ORD_RBF=5 for the numerically resolved simulations for the SOC discharge.

Figure J-4 shows the comparison of the simulated Q_i and Q_e with the experimental values estimated from power balance analysis using TRANSP. In both LOC and SOC runs, Q_i is over-estimated in $r/a < 0.8$, and under-estimated in $r/a > 0.85$, while Q_e is under-estimated in the whole simulation domain. It is noteworthy that the under-prediction of both Q_i and Q_e at r/a$\sim$0.85 is consistent with the local simulation results. We compared the heat flux values of these global simulations with the heat flux values in the local simulations with the same input profiles at r/a=0.8 and at the CECE cold resonance position (r/a$\sim$0.85). Table J.5 and J.6 show this comparison. The heat flux values of the global simulations are the values at r/a=0.8 and $\sim$0.85. We notice that the differences in heat flux values between the global and local simulations are within their uncertainties in most cases. (In the LOC runs, the differences in ion heat flux at r/a$\sim$0.85 and electron heat flux at r/a=0.8 are slightly outside of their uncertainties.) In any case, significant differences were not observed. As mentioned in section 3.4, it is expected that local simulation results are similar to the global simulation results when $\rho_*(= \rho_s/a)$ values are small ($\lesssim 0.002$) [29]. Thus, this result is consistent with the expected results from small $\rho_*(= \rho_s/a)$ values (0.0014-0.0019) in the local runs used in this comparison. This comparison result also suggests that the over-estimated heat flux deeper in the core region may not significantly affect the results near the edge.

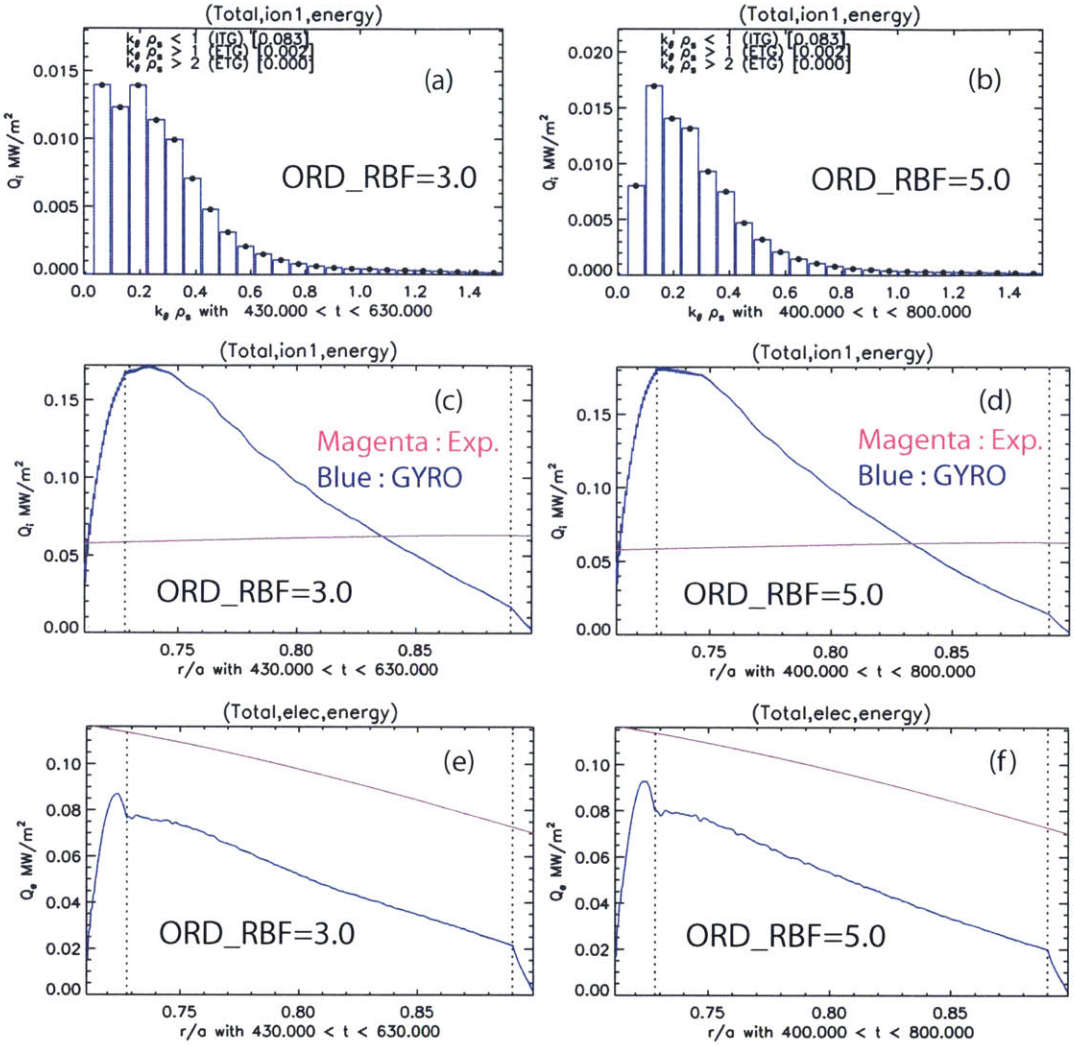

Figure J-3: $Q_i(k_y)$ spectrum in the SOC run with experimental profiles with (a) ORD_RBF=3.0 and (b) ORD_RBF=5.0. Comparison of the experimental Q_i with the simulated Q_i in the SOC runs with the experimental profiles with (c) ORD_RBF=3.0 and (d) ORD_RBF=5.0. Comparison of the experimental Q_e with the simulated Q_e in the SOC runs with the experimental profiles with (c) ORD_RBF=3.0 and (d) ORD_RBF=5.0.

	r/a=0.8		r/a∼0.85	
	local	global	local	global
Ion heat flux [MW/m^2]	0.054 ± 0.0075	0.045 ± 0.0061	0.025 ± 0.0031	0.017 ± 0.0022
Electron heat flux [MW/m^2]	0.061 ± 0.0083	0.047 ± 0.0054	0.030 ± 0.0033	0.029 ± 0.0033

Table J.5: Comparison of heat flux values between global and local simulations at r/a=0.8 and the CECE cold resonance position (r/a∼0.85) for the LOC discharge used in section 4.2-4.4. The experimental profiles without any modifications are used in both simulations.

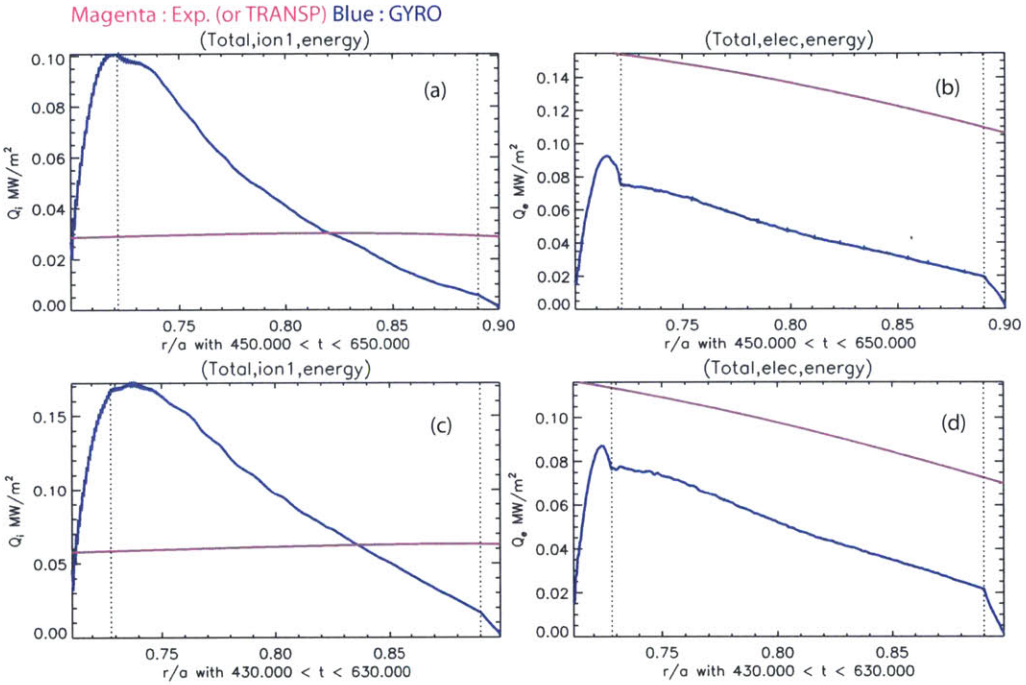

Figure J-4: The comparison of the simulated heat fluxes from global simulations using experimental profiles with the experimental heat fluxes via power balance analysis using TRANSP. (a) Ion heat flux (b) Electron heat flux in the LOC discharge used in section 4.2-4.4. (c) Ion heat flux (d) Electron heat flux in the SOC discharge used in section 4.2-4.4.

	r/a=0.8		r/a~0.85	
	local	global	local	global
Ion heat flux [MW/m^2]	0.12 ± 0.022	0.10 ± 0.022	0.055 ± 0.0072	0.043 ± 0.0093
Electron heat flux [MW/m^2]	0.068 ± 0.012	0.053 ± 0.010	0.035 ± 0.0043	0.032 ± 0.0061

Table J.6: Comparison of heat flux values between global and local simulations at r/a=0.8 and the CECE cold resonance position (r/a~0.85) for the SOC discharge used in section 4.2-4.4. The experimental profiles without any modifications are used in both simulations.

J.4 The comparison of simulation results between local and global Q_i matched simulations

In order to investigate changes in the synthetic T_e fluctuations compared to the results in the local runs, we will first obtain ion heat flux (Q_i) matched simulations, and the synthetic T_e fluctuations in the Q_i matched global simulations will be compared with the synthetic fluctuations in the Q_i matched local simulations. The main purpose of this comparison is to investigate the changes in synthetic T_e fluctuations due to profile variations in the point spread function (PSF), which was introduced in section 3.4. Thus, we will suppress the higher Q_i in $r/a < 0.8$, and try to match Q_i in the CECE relevant region (r/a=[0.8-0.87]). We also ran these simulations for long enough (> 2500 [a/c_s]) to obtain synthetic T_e fluctuations with small random error.

In the Q_i matched simulations, we varied a/L_{T_i} within the uncertainty in the CECE relevant region, but outside the CECE relevant region, a/L_{T_i} was modified outside its uncertainty to match Q_i, as shown in Fig. J-5. Figure J-6 shows that the simulated Q_i in the global simulations with the modified T_i profiles in Fig. J-5 are matched with the experimental level in most radial regions as well as the CECE relevant region within the uncertainty.

We then compared the results of these global Q_i matched simulations with the results from local Q_i matched simulations. Table J.7 shows the comparison of the heat flux and synthetic T_e fluctuation levels between local and global Q_i matched simulations. The heat flux values in the global runs are the simulated values at the same location where the local runs were performed. We note that the differences in the heat flux values and the synthetic T_e fluctuation levels between local and global Q_i matched runs are less than their uncertainties. The synthetic fluctuation spectra of local and global Q_i matched runs are shown in Fig. J-7. We see no significant changes in the spectral shape between local and global simulations. Both spectra are less Doppler shifted than the measured spectrum. As expected from the similar fluctuation levels in Table J.7, the amplitudes of these spectra are also similar in both local and global simulations. This may indicate that the profile variations within the

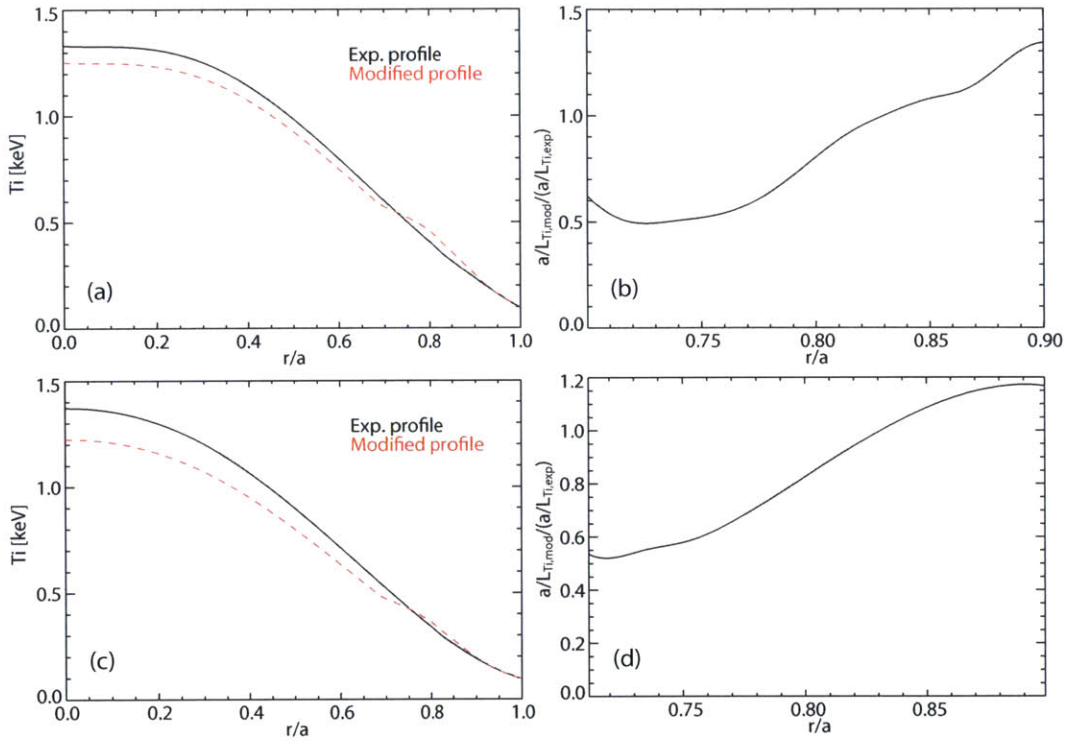

Figure J-5: (a) The comparison of the modified T_i profile for the Q_i matched simulation with the experimental T_i profile in the LOC discharge used in section 4.2-4.2. (b) The fractional changes in the modified a/L_{T_i} in the Q_i matched simulation compared to the experimental a/L_{T_i} in the LOC discharge. (c) The comparison of the modified T_i profile for the Q_i matched simulation with the experimental T_i profile in the SOC discharge used in section 4.2-4.2. (b) The fractional changes in the modified a/L_{T_i} in the Q_i matched simulation compared to the experimental a/L_{T_i} in the SOC discharge.

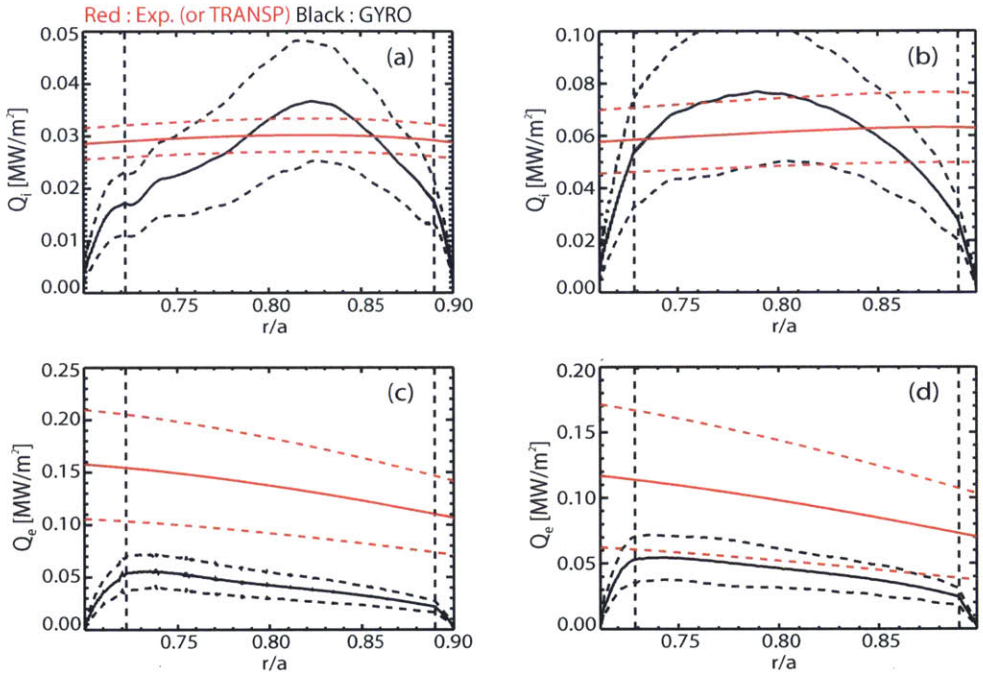

Figure J-6: The comparison of the simulated ion heat flux (black) in the simulations with the T_i profile in Fig. J-5 with the experimental level (red) in the (a) LOC and (b) SOC discharges used in section 4.2-4.2. The comparison of the simulated electron heat flux (black) in the simulations with the T_i profile in Fig. J-5 with the experimental level (red) in the (c) LOC and (d) SOC discharge used section 4.2-4.2. The dotted lines indicate the uncertainty, estimated from the standard deviation of the time averaging. The vertical dotted line indicates the boundary between the real simulation domain and the buffer region.

	Ion heat flux $[MW/m^2]$	Electron heat flux $[MW/m^2]$	Synthetic T_e fluctuation level [%]
Local Q_i matched LOC run	0.026 ± 0.0032	0.031 ± 0.0036	0.86 ± 0.06
Global Q_i matched LOC run	0.030 ± 0.0089	0.031 ± 0.0089	0.76 ± 0.05
Local Q_i matched SOC run	0.053 ± 0.0085	0.041 ± 0.0065	0.82 ± 0.07
Global Q_i matched SOC run	0.057 ± 0.018	0.036 ± 0.012	0.72 ± 0.06

Table J.7: The comparison of the time averaged heat flux values and synthetic T_e fluctuations between local and global Q_i matched simulations. The heat flux values in the global simulations are the values at the location where local simulations were performed (r/a$\sim$0.85).

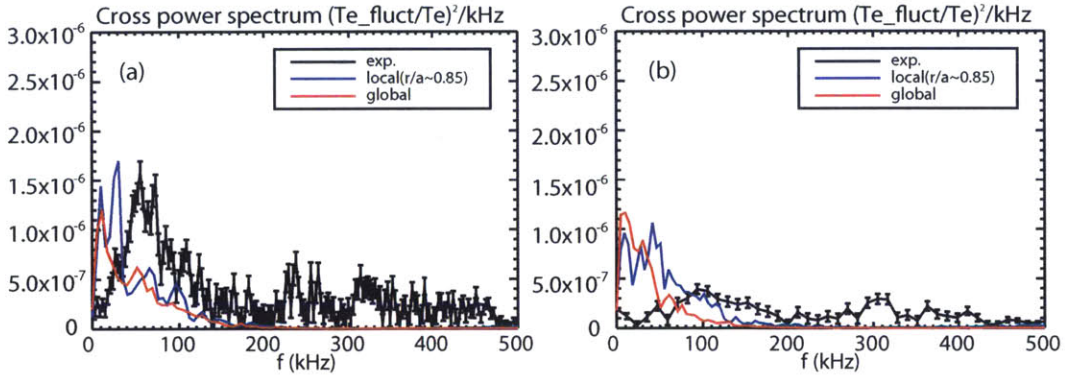

Figure J-7: The comparison of the synthetic T_e fluctuations in local (blue) and global (red) Q_i matched simulations in the (a) LOC and (b) SOC discharges used in section 4.2-4.4. The measured T_e fluctuations (black) are also plotted.

PSF (or the CECE emission volume) do not significantly affect the synthetic T_e fluctuations.

J.5 Investigation of the effect of changes in the inner radial region on the outer region

In this section, we will study the changes in the outer radial region in the global simulations (r/a$>$ 0.8), where the CECE measurements are relevant, when we modify the input parameter in the inner radial region (r/a$<$ 0.8). To be specific, we will increase a/L_{T_i}, the most sensitive input parameter in the local runs, by 20% in r/a$<$ 0.75 from the T_i profiles used in the Q_i matched simulations. We then observe the changes in the heat fluxes and synthetic T_e fluctuations. Figure J-8 shows the changes

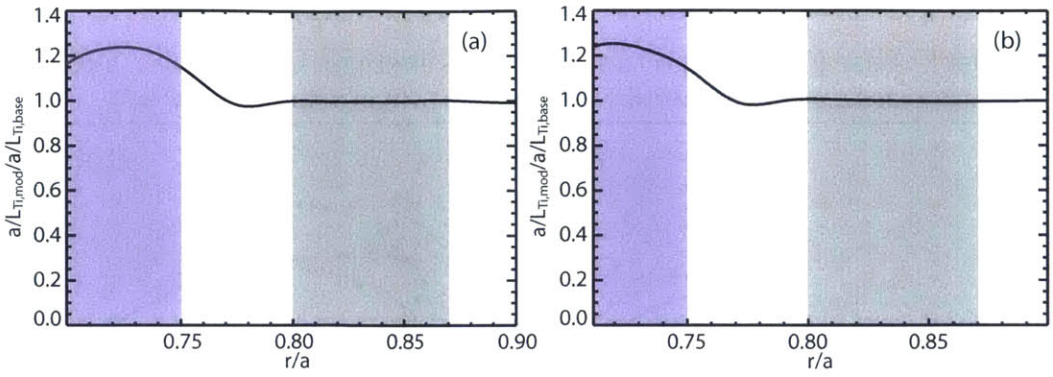

Figure J-8: The fractional changes in a/L_{T_i} in the runs used in this section from the Q_i matched simulations. (a) The run for the LOC discharge (b) the run for the SOC discharge. The black shaded area indicates the CECE relevant region, and the red shaded area indicates the region where a/L_{T_i} is increased by about 20%.

in a/L_{T_i} in the runs used in this section compared to a/L_{T_i} in the Q_i matched runs. It is difficult to increase a/L_{T_i} step-wise from a certain point. Instead, as shown in Fig. J-8, a/L_{T_i} increases gradually from r/a ~ 0.76, and increases in a/L_{T_i} are about 20% in r/a< 0.75 in both LOC and SOC runs.

We first see the changes in ion heat fluxes from Fig. J-9(a) and (b). We notice the shape of the simulated Q_i profile changes in the r/a< 0.75 region in both LOC and SOC runs. Although the changes in Q_i with an approximately 20% increase in a/L_{T_i} in $r/a < 0.75$ are within the uncertainty, it is clearly shown that the changes in a/L_{T_i} modifies the Q_i profile shape and its amplitude in $r/a < 0.75$ in both runs, which suggest that Q_i is driven by local parameters. However, there was no significant changes ($\leq 10\%$) in the amplitude of Q_e and its profile shape, as shown in Fig. J-9(c) and (d). Synthetic T_e fluctuations, shown in Fig. J-9(f) and (g), increase with the changes in a/L_{T_i} in $r/a < 0.75$ in both LOC and SOC runs. In the LOC run, the changes are outside the uncertainty, and the changes are marginally less than the uncertainty in the SOC run. In both cases, the changes in synthetic T_e fluctuations are larger than the changes in Q_e. Further study is required to understand why only the Q_i profile changes its shape while the Q_e profile retains a similar shape with the increase in a/L_{T_i} in $r/a < 0.75$, and to understand the relatively larger changes in synthetic T_e fluctuations compared to changes in Q_e.

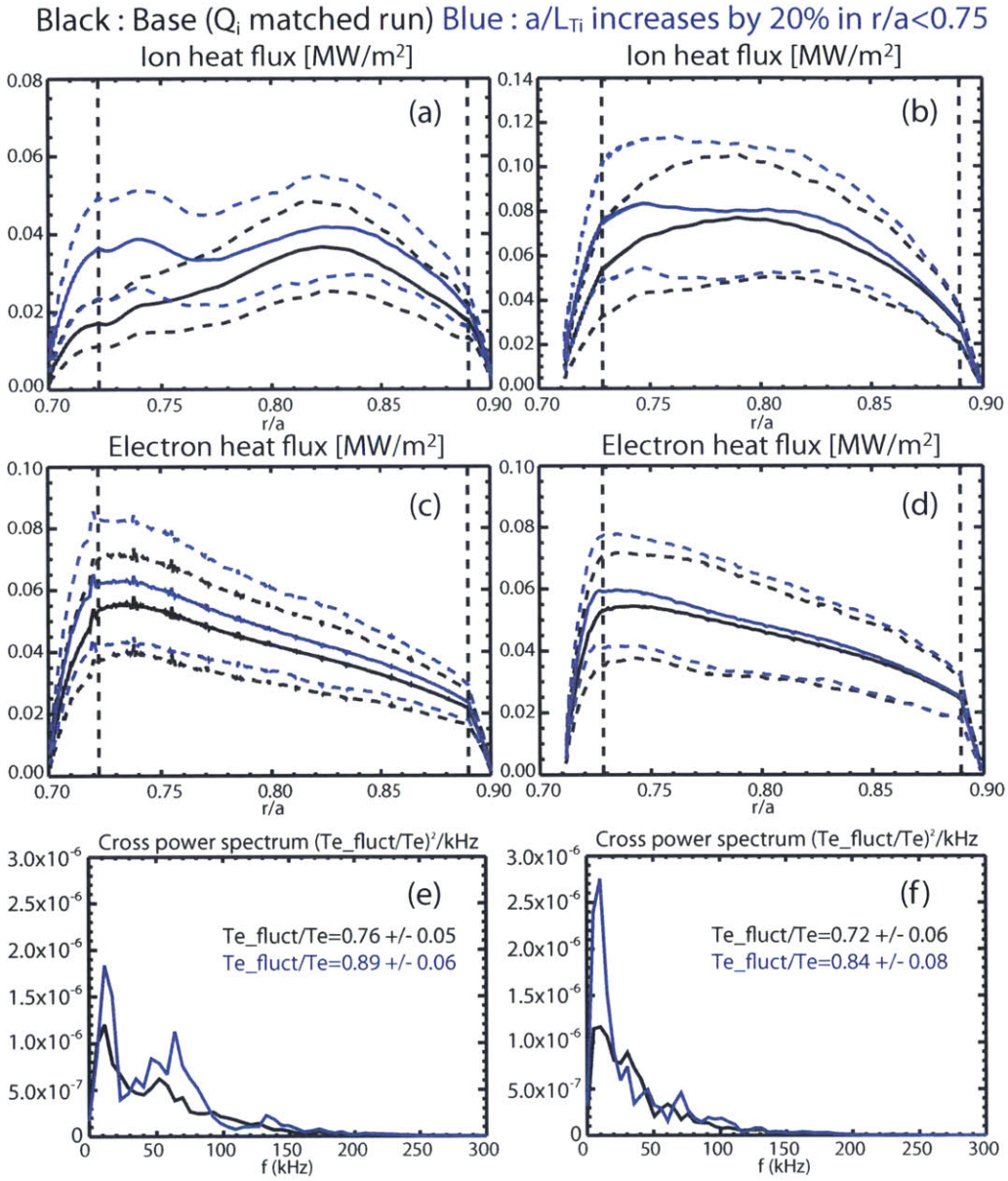

Figure J-9: The comparison of ion heat flux between the Q_i matched simulation (black) and the run with the 20% increase of a/L_{T_i} in $r/a < 0.75$ from the T_i profile used in the Q_i matched run for (a) the LOC discharge and (b) the SOC discharge. The comparison of electron heat flux between the same local and global simulations in (c) the LOC case and (d) the SOC case. The comparison of synthetic T_e fluctuations between the same local and global simulations in (e) the LOC case and (f) the SOC case. The dotted line indicates the uncertainty, which is the standard deviation of the time averaging, and the vertical dotted line indicates the boundary between the real simulation domain and the buffer region.

J.6 Summary

In this section, we compared the global simulation results with the local simulation results used in section 4.4. We found that the low k_y peak, which was observed in the local simulations, was not observed or was not significant in the global simulations, which suggests that this peak is not physically meaningful, and may be related to a numerical issue in the local simulations. The profile variations in the CECE emission volume or point spread function (PSF) used for synthetic T_e fluctuations do not significantly affect the synthetic T_e fluctuation results. However, we found that increasing a/L_{T_i} by 20% in $r/a < 0.75$ affects synthetic T_e fluctuations in $r/a > 0.8$. This global effect should be investigated more in the future.

Appendix K

Lists of C-Mod shots and codes used in the thesis

K.1 List of C-Mod shots used in this thesis

Chapter 2

section 2.4.2

Discharges on run day 1120210, 1120214, 1120216, 1120217

shot 1120221014

Chapter 3

section 3.1.2

shot 1120502021

Chapter 4

section 4.1-4.4

shot 1120626023, 1120626028

Shots used in Fig. 4-5 are shown in Table K.1.

section 4.5

shot 1120620027, 1120620028, 1120626023, 1120626027, 1120626028

Chapter 5

section 5.1, 5.4

shot 1120706018, 1120706019, 1120626027

shot (time)	CECE channel	Frequency range [kHz] for $\tilde{T}_e/T_e$ level
1120626023 (0.9-1.4s)	'01' & '02'	0-170
1120626028 (0.9-1.4s)	'01' & '02'	70-170
1120627001 (0.8-1.2s)	'01' & '02'	0-80
1120627002 (0.8-1.1s)	'01' & '02'	0-95
1120627009 (0.9-1.2s)	'01' & '02'	0-60
1120627011 (0.8-1.1s)	'01' & '02'	0-60
1120627012 (0.8-1.2s)	'01' & '02'	0-80
1120627013 (0.8-1.1s)	'01' & '02'	0-40
1120720019 (0.9-1.4s)	'03' & '04'	0-235
1120720020 (0.8-1.3s)	'03' & '04'	no fluct.
1120720021 (0.8-1.3s)	'03' & '04'	no fluct.
1120726001 (0.8-1.2s)	'03' & '04'	0-100
1120726003 (1.2-1.5s)	'03' & '04'	0-120
1120726004 (0.8-1.2s)	'03' & '04'	0-90
1120726005 (0.8-1.2s)	'03' & '04'	0-100
1120726007 (0.8-1.2s)	'03' & '04'	0-100
1120809017 (0.7-1.0s)	'03' & '04'	0-110
1120919011 (0.8-1.3s)	'15' & '16'	0-180
1120919012 (0.9-1.2s)	'15' & '16'	0-135
1120919013 (0.8-1.3s)	'01' & '02'	0-100
1120919014 (0.8-1.3s)	'01' & '02'	0-100
1120919015 (0.9-1.2s)	'01' & '02'	5-100
1120919016 (1.0-1.4s)	'01' & '02'	0-100
1120919018 (1.0-1.4s)	'01' & '02'	0-80
1120926032 (1.0-1.3s)	'01' & '02'	40-190
1120926033 (0.8-1.1s)	'01' & '02'	5-160
1120926034 (0.9-1.4s)	'01' & '02'	0-90

Table K.1: List of shots used in Fig. 4-5. The CECE channel and frequency range used for $\tilde{T}_e/T_e$ level are also presented. "no fluct." indicates that there were no fluctuations which could be resolved.

shot (time)	CECE channel	Frequency range [kHz] for $\tilde{T}_e/T_e$ level
1120917023 (0.8-1.3s)	'01' & '02'	no fluct.
1120917023 (0.8-1.3s)	'03' & '04'	250-500
1120917023 (0.8-1.3s)	'15' & '16'	no fluct.
1120917024 (0.8-1.3s)	'01' & '02'	0-150
1120917024 (0.8-1.3s)	'03' & '04'	0-200
1120917024 (0.8-1.3s)	'15' & '16'	0-150
1120917025 (0.8-1.3s)	'01' & '02'	no fluct.
1120917025 (0.8-1.3s)	'03' & '04'	0-200
1120917025 (0.8-1.3s)	'15' & '16'	0-200
1120917026 (0.8-1.3s)	'01' & '02'	0-130
1120917026 (0.8-1.3s)	'03' & '04'	0-170
1120917026 (0.8-1.3s)	'15' & '16'	0-150
1120917027 (0.85-1.3s)	'01' & '02'	no fluct.
1120917027 (0.85-1.3s)	'03' & '04'	200-550
1120917027 (0.85-1.3s)	'15' & '16'	250-580

Table K.2: List of shots used in Fig. 6-3. The CECE channel and frequency range used for $\tilde{T}_e/T_e$ level are also presented. "no fluct." indicates that there were no fluctuations which could be resolved.

section 5.2, 5.3

shot 1120221011, 1120221012

Chapter 6

section 6.1.1

Shots used in Fig. 6-3 are shown in Table K.2.

section 6.1.2

shot 1120917029, 1120917031

section 6.2-6.3

shot 1101209029

section 6.4.

shot 1120824006

K.2 List of codes used in this thesis

In C-Mod cluster

Calculation of the CECE measurement postion and optical depth

/home/sck83/idl/CECE/shot_condtion_v8.pro

Calculation of the T_e fluctuation level and its spectrum

/home/sck83/idl/CECE/rxy_cmod_cece_anne_bias.pro

Codes used for profile analysis

/home/sck83/transp/sources_nathan/load_ti_profile_ck_7_2_2.pro

/home/sck83/transp/sources_nathan/load_rot_lint_cxrs_2_2.pro

/home/sck83/idl/CECE/plot_fits_v4.pro

/home/sck83/idl/CECE/qprofile_v5.pro

The error analysis of experimental heat fluxes

/home/sck83/idl/CECE/transp_power_6.pro

Synthetic CECE diagnostic

/home/sck83/idl/GYRO/syncece_local_combine_v2.pro

Codes used for self-similarity analysis

/home/sck83/idl/CECE/check_stiffness_v6_edge_v3.pro

/home/sck83/idl/CECE/edge_scan_stiffness_v3.pro

Code used to prepare GYRO simulations

/home/sck83/GYRO/gyro_input_tools_ck.pro

In LOKI cluster

Linear simulation analysis and preparation

/home/sck83/gacode/gyro/sim/make_stability_4.pro

Linear simulation for Eigen value solver

/home/sck83/gacode/gyro/sim/eigen_find_ck_v2.pro

Nonlinear heat flux check

/home/sck83/gacode/gyro/vugyro/gyro_analysis_flux.pro

RMS fluctuation level from nonlinear runs

/home/sck83/gacode/gyro/vugyro/gyro_analysis_rms_fluct.pro

power spectrum of the simulated fluctuations in (n,w) space

/home/sck83/gacode/gyro/vugyro/gyro_analysis_temp_n.pro

Bibliography

[1] Fits manual, http://www.psfc.mit.edu/research/alcator/cmodwiki/images/d/d3/fitsusersman August 2010.

[2] Gyro web page, https://fusion.gat.com/theory/gyrousermanual, 2013.

[3] Gyro technical manual, https://fusion.gat.com/theory/gyrodoc, 2014.

[4] Transp homepage, http://w3.pppl.gov/transp/, November 2014.

[5] Webpage for profiles_gen utility, https://fusion.gat.com/theory/profiles_gen, November 2014.

[6] Webpage for trxpl, http://w3.pppl.gov/ntcc/trxplib/, November 2014.

[7] Ian G Abel. *Multiscale gyrokinetics for rotating tokamak plasmas.* PhD thesis, University of Oxford, 2013.

[8] J. C. Adam, W. M. Tang, and P. H. Rutherford. Destabilization of the trapped-electron mode by magnetic curvature drift resonances. *Physics of Fluids (1958-1988)*, 19(4):561–566, 1976.

[9] Agilent Technologies. *Agilent 423B, 8470B, 8472B, 8473B/C Low Barrier Schottky Diode Detectors data sheet*, 2011.

[10] C. Angioni, L. Carraro, T. Dannert, N. Dubuit, R. Dux, C. Fuchs, X. Garbet, L. Garzotti, C. Giroud, R. Guirlet, et al. Particle and impurity transport in the Axial Symmetric Divertor Experiment Upgrade and the Joint European Torus, experimental observations and theoretical understanding. *Physics of Plasmas (1994-present)*, 14(5):055905, 2007.

[11] C. Angioni, A. G. Peeters, F. Ryter, F. Jenko, G. D. Conway, T. Dannert, H. U. Fahrbach, M. Reich, W. Suttrop, and ASDEX Upgrade team. Relationship between density peaking, particle thermodiffusion, ohmic confinement and microinstabilities in ASDEX Upgrade L-mode plasmas. *Physics of Plasmas*, 12:040701, 2005.

[12] R. Aymar, P. Barabaschi, and Y. Shimomura. The ITER design. *Plasma physics and controlled fusion*, 44(5):519, 2002.

[13] L. Bai, X. M. Qiu, L. Huang, and X. M. Song. A possible hybrid dissipative trapped electron ion temperature gradient mode. *Physics of Plasmas (1994-present)*, 3(8):3004–3012, 1996.

[14] N. P. Basse, A. Dominguez, E. M. Edlund, C. L. Fiore, R. S. Granetz, A. E. Hubbard, J. W. Hughes, I. H. Hutchinson, J. H. Irby, B. LaBombard, L. Lin, Y. Lin, B. Lipschultz, J. E. Liptac, E. S. Marmar, D. A. Mossessian, R. R. Parker, M. Porkolab, J. E. Rice, J. A. Snipes, V. Tang, J. L. Terry, S. M. Wolfe, S. J. Wukitch, K. Zhurovich, R. V. Bravenec, P. E. Phillips, W. L. Rowan, G. J. Kramer, G. Schilling, S. D. Scott, and S. J. Zweben. Diagnostic systems on Alcator C-Mod. *Fusion Science and Technology*, 51:476, 2007.

[15] G. Bekefi. *Radiation Processes in Plasmas.* John Wiley and Sons, NY, 1966.

[16] E. A. Belli and J. Candy. Gyrokinetics with advanced collision operators. In *56th Annual Meeting of the APS Division of Plasma Physics, Abstract: NP8.00026 (2014) Vol. 59, number 15.*

[17] J. S. Bendat and A. G. Piersol. *Random Data: Analysis and Measurement Procedures.* John Wiley and Sons, NY, 1986.

[18] M. Bornatici, R. Cano, O. De Barbieri, and F. Engelmann. Electron cyclotron emission and absorption in fusion plasmas. *Nuclear Fusion*, 23(9):1153, 1983.

[19] G. Bracco and K. Thomsen. Analysis of a global energy confinement database for JET ohmic plasmas. *Nuclear Fusion*, 37:759, 1997.

[20] Marco Brambilla. Numerical simulation of ion cyclotron waves in tokamak plasmas. *Plasma Physics and Controlled Fusion*, 41(1):1, 1999.

[21] R. V. Bravenec, K. W. Gentle, P. E. Phillips, T. R. Price, W. L. Rowan, K. Empson, W. L. Hodge, C. Klepper, T. P. Kochanski, D. M. Patterson, J. Proter, and B. Richards. Confinement time scaling in TEXT. *Plasma Physics and Controlled Fusion*, 27:1335, 1985.

[22] R. V. Bravenec and W. M. Nevins. System for simulating fluctuation diagnostics for application to turbulence computations. *Review of scientific instruments*, 77(1):015101, 2006.

[23] R. V. Bravenec and A. J. Wootton. Effects of limited spatial resolution on fluctuation measurements. *Review of scientific instruments*, 66(1):802–805, 1995.

[24] A. J. Brizard and T. S. Hahm. Foundations of nonlinear gyrokinetic theory. *Reviews of modern physics*, 79(2):421, 2007.

[25] D. L. Brower, W. A. Peebles, S. K. Kim, N. C. Luhmann Jr., W. M. Tang, and P. E. Phillips. Observation of a high-density ion mode in tokamak microturbulence. *Physical Review Letter*, 59:48, 1987.

[26] K. H. Burrell. Effects of E× B velocity shear and magnetic shear on turbulence and transport in magnetic confinement devices. *Physics of Plasmas (1994-present)*, 4(5):1499–1518, 1997.

[27] Stephen Butterworth. On the theory of filter amplifiers. *Wireless Engineer*, 7:536–541, 1930.

[28] J. Candy and R. E. Waltz. An Eulerian gyrokinetic-Maxwell solver. *Journal of Computational Physics*, 186:545, 2003.

[29] J. Candy, R. E. Waltz, and W. Dorland. The local limit of global gyrokinetic simulations. *Physics of Plasmas*, 11(5):L25, 2004.

[30] P. J. Catto, W. M. Tang, and D. E. Baldwin. Generalized gyrokinetics. *Plasma Physics*, 23(7):639, 1981.

[31] R. Chatterjee, P. E. Phillips, J. Heard, C. Watts, R. Gandy, and A. Hubbard. High resolution ECE radiometer for electron temperature profile and fluctuation measurements on Alcator C-Mod. *Fusion engineering and design*, 53(1):113–121, 2001.

[32] F. F. Chen. *Introduction to plasma physics and controlled fusion.* Springer, 1984.

[33] Yang Chen and Scott E Parker. Electromagnetic gyrokinetic δf particle-in-cell turbulence simulation with realistic equilibrium profiles and geometry. *Journal of Computational Physics*, 220(2):839–855, 2007.

[34] M. Chilenski, M. Greenwald, Y. Marzouk, N. Howard, A. White, J. Rice, and J. Walk. Improved profile fitting and quantification of uncertainty in experimental measurements of impurity transport coefficients using Gaussian process regression. *Nuclear fusion (accepted)*, 2014.

[35] C. Chrystal, K. H. Burrell, B. A. Grierson, R. J. Groebner, and D. H. Kaplan. Calculation of impurity poloidal rotation from measured poloidal asymmetries in the toroidal rotation of a tokamak plasma. *Review of Scientific Instruments*, 83(10):10D501, 2012.

[36] G. Cima. Thermal, nonthermal, and simulated fluctuations of tokamak electron cyclotron radiation. *Review of Scientific Instruments*, 63(10):4630–4632, 1992.

[37] G. Cima, R. V. Bravenec, A. J. Wootton, T. D. Rempel, R. F. Gandy, and C. Watts. Core temperature fluctuations and related heat transport in the Texas Experimental TokamakUpgrade. *Physics of Plasmas*, 2:720, 1995.

[38] J. Citrin, F. Jenko, P. Mantica, D. Told, C. Bourdelle, R. Dumont, J. Garcia, J. W. Haverkort, GMD. Hogeweij, Thomas Johnson, et al. Ion temperature profile stiffness: non-linear gyrokinetic simulations and comparison with experiment. *Nuclear Fusion*, 54(2):023008, 2014.

[39] Jonathan Citrin, F. Jenko, P. Mantica, D. Told, C. Bourdelle, J. Garcia, J. W. Haverkort, GMD. Hogeweij, Thomas Johnson, and M. J. Pueschel. Nonlinear stabilization of tokamak microturbulence by fast ions. *Physical review letters*, 111(15):155001, 2013.

[40] J. W. Connor and H. R. Wilson. Survey of theories of anomalous transport. *Plasma Physics and Controlled Fusion*, 36(5):719, 1994.

[41] B. Coppi. Nonclassical Trasport and the "Principle of profile Consistency". *Comm. Plasma physics and controlled fusion*, 5(10):261, 1980.

[42] J. G. Cordey, ITPA H mode Database Working Group, ITPA Pedestal Database Working Group, et al. A two-term model of the confinement in Elmy H-modes using the global confinement and pedestal databases. *Nuclear Fusion*, 43(8):670, 2003.

[43] I. Cziegler and et al. Fluctuating zonal flows in the I-mode regime in alcator c-moda). *Physics of Plasmas*, 20(5):055904, 2013.

[44] Robert Henry Dicke. The measurement of thermal radiation at microwave frequencies. *Review of Scientific Instruments*, 17(7):268–275, 1946.

[45] A. M. Dimits, G. Bateman, M. A. Beer, B. I. Cohen, W. Dorland, G. W. Hammett, C. Kim, J. E. Kinsey, M. Kotschenreuther, A. H. Kritz, et al. Comparisons and physics basis of tokamak transport models and turbulence simulations. *Physics of Plasmas (1994-present)*, 7(3):969–983, 2000.

[46] A. Dominguez. *Study of density fluctuations and particle transport at the edge of I-mode plasmas.* PhD thesis, MIT, 2012.

[47] W. Dorland, F. Jenko, M. Kotschenreuther, and B. N. Rogers. Electron temperature gradient turbulence. *Physical Review Letters*, 85(26):5579, 2000.

[48] W. Dorland, M. Kotschenreuther, M. A. Beer, G. W. Hammett, R. E. Waltz, R. R. Dominguez, P. M. Valanju, JWH. Miner, J. Q. Dong, W. Horton, et al. Comparisons of nonlinear toroidal turbulence simulations with experiment. *Institute for Fuion Studies, University of Texas, Austin IFR*, 677, 1994.

[49] B. P. Duval, A. Bortolon, A. Karpushov, R. A. Pitts, A. Pochelon, O. Sauter, A. Scarabosio, G. Turri, TCV Team, et al. Spontaneous L-mode plasma rotation scaling in the TCV tokamak. *Physics of Plasmas (1994-present)*, 15(5):056113, 2008.

[50] D. R. Ernst, P. T. Bonoli, P. J. Catto, W. Dorland, C. L. Fiore, R. S. Granetz, M. Greenwald, A. E. Hubbard, M. Porkolab, M. H. Redi, et al. Role of trapped electron mode turbulence in internal transport barrier control in the Alcator C-Mod Tokamak. *Physics of Plasmas (1994-present)*, 11(5):2637–2648, 2004.

[51] B. Esposito, M. Marinucci, G. Bracco, C. Castaldo, V. Cocilovo, E. Giovannozzi, M. Leigheb, G. Monari, S. Nowak, C. Sozzi, O. Tudisco, R. Cesario, D. Frigione, C. Gormezano, G. Granucci, L. Panaccione, V. Pericoli-Ridolfini, L. Pieroni, FTU, and ECRH teams. Transport analysis of ohmic, L-mode and improved confinement discharges in FTU. *Plasma Physics and Controlled Fusion*, 46:1793, 2004.

[52] Catherine L Fiore, Darin Richard Ernst, John E Rice, Kirill Zhurovich, N. Basse, P. T. Bonoli, M. J. Greenwald, Earl S Marmar, and Stephen J Wukitch. Internal transport barriers in Alcator C-Mod. *Fusion science and technology*, 51(3):303–316, 2007.

[53] J. Friedberg. *Plasma Physics and Fusion Energy.* Cambridge University Press, 2007.

[54] E. A. Frieman and Lie Chen. Nonlinear gyrokinetic equations for lowfrequency electromagnetic waves in general plasma equilibria. *Physics of Fluids*, 25:502, 1982.

[55] X. Garbet, Y. Idomura, L. Villard, and T. H. Watanabe. Gyrokinetic simulations of turbulent transport. *Nuclear Fusion*, 50(4):043002, 2010.

[56] X. Garbet, P. Mantica, F. Ryter, G. Cordey, F. Imbeaux, C. Sozzi, A. Manini, E. Asp, V. Parail, R. Wolf, et al. Profile stiffness and global confinement. *Plasma physics and controlled fusion*, 46(9):1351, 2004.

[57] X. Garbet, J. Payan, C. Laviron, P. Devynck, S. K. Saha, H. Capes, X. P. Chen, J. P. Coulon, C. Gil, G. R. Harris, T. Hutter, and A. L. Pecquet. Turbulence and energy confinement in Tore Supra ohmic discharges. *Nuclear Fusion*, 32:2147, 1992.

[58] P. F. Goldsmith. *Gaussian Beam Quasioptical Propagation and Applications.* The Institute of Electrical and Electronics Engineers, Inc., NY, 1998.

[59] R. J. Goldston, D. C. McCune, H. H. Towner, S. L. Davis, R. J. Hawryluk, and G. L. Schmidt. New techniques for calculating heat and particle source rates due to neutral beam injection in axisymmetric tokamaks. *Journal of Computational Physics*, 43:61, 1981.

[60] M. Greenwald, C. Angioni, J. W. Hughes, J. Terry, and H. Weisen. Density profile peaking in low collisionality H-modes: comparison of Alcator C-Mod data to ASDEX Upgrade/JET scalings. *Nuclear Fusion*, 47(9):L26, 2007.

[61] Martin Greenwald. Verification and validation for magnetic fusiona). *Physics of Plasmas (1994-present)*, 17(5):058101, 2010.

[62] Martin Greenwald, N. Basse, Paul Bonoli, R. Bravenec, E. Edlund, D. Ernst, C. Fiore, R. Granetz, A. Hubbard, J. Hughes, et al. Confinement and transport research in Alcator C-Mod. *Fusion science and technology*, 51(3):266–287, 2007.

[63] Martin Greenwald, R. L. Boivin, F. Bombarda, P. T. Bonoli, C. L. Fiore, D. Garnier, J. A. Goetz, S. N. Golovato, M. A. Graf, R. S. Granetz, et al. H mode confinement in Alcator C-Mod. *Nuclear Fusion*, 37(6):793, 1997.

[64] B. A. Grierson, K. H. Burrell, W. W. Heidbrink, M. J. Lanctot, N. A. Pablant, and W. M. Solomon. Measurements of the deuterium ion toroidal rotation in the DIII-D tokamak and comparison to neoclassical theory. *Physics of Plasmas (1994-present)*, 19(5):056107, 2012.

[65] R. J. Groebner and T. N. Carlstrom. Critical edge parameters for H-mode transition in DIII-D. *Plasma physics and controlled fusion*, 40(5):673, 1998.

[66] T. S. Hahm, W. W. Lee, and A. Brizard. Nonlinear gyrokinetic theory for finitebeta plasmas. *Physics of Fluids*, 31:1940, 1988.

[67] H. J. Hartfuss, T. Geist, and M. Hirsch. Heterodyne methods in millimetre wave plasma diagnostics with applications to ECE, interferometry and reflectometry. *Plasma Physics and Controlled Fusion*, 39(11):1693, 1997.

[68] R. J. Hawryluk et al. An empirical approach to tokamak transport. *Physics of plasmas close to thermonuclear conditions*, 1:19–46, 1980.

[69] P. Helander and D. J. Sigmar. *Collisional transport in magnetized plasmas*. Cambridge University Press, Cambridge, UK, 2005.

[70] J. C. Hillesheim, J. C. DeBoo, W. A. Peebles, T. A. Carter, G. Wang, T. L. Rhodes, L. Schmitz, G. R. McKee, Z. Yan, G. M. Staebler, et al. Experimental characterization of multiscale and multifield turbulence as a critical gradient threshold is surpassed in the DIII-D tokamak. *Physics of Plasmas (1994-present)*, 20(5):056115, 2013.

[71] S. P. Hirshman, R. J. Hawryluk, and B. Birge. Neoclassical conductivity of a tokamak plasma. *Nuclear Fusion*, 17(3), 1977.

[72] C. Holland, L. Schmitz, T. L. Rhodes, W. A. Peebles, J. C. Hillesheim, G. Wang, L. Zeng, E. J. Doyle, S. P. Smith, R. Prater, et al. Advances in validating gyrokinetic turbulence models against l-and h-mode plasmas a). *Physics of Plasmas (1994-present)*, 18(5):056113, 2011.

[73] C. Holland, A. E. White, G. R. McKee, M. W. Shafer, J. Candy, R. E. Waltz, L. Schmitz, and G. R. Tynan. Implementation and application of two synthetic diagnostics for validating simulations of core tokamak turbulence. *Physics of Plasmas (1994-present)*, 16(5):052301, 2009.

[74] W Horton. Drift waves and transport. *Reviews of Modern Physics*, 71(3):735, 1999.

[75] Wendell Horton. Nonlinear drift waves and transport in magnetized plasma. *Physics Reports*, 192(1):1–177, 1990.

[76] W. A. Houlberg, K. C. Shaing, S. P. Hirshman, and M. C. Zarnstorff. Bootstrap current and neoclassical transport in tokamaks of arbitrary collisionality and aspect ratio. *Physics of Plasmas (1994-present)*, 4(9):3230–3242, 1997.

[77] N. T. Howard, C. Holland, A. E. White, M. Greenwald, and J. Candy. Synergistic cross-scale coupling of turbulence in a tokamak plasma. *Physics of Plasmas (1994-present)*, 21(11):112510, 2014.

[78] N. T. Howard, A. E. White, M. Greenwald, M. L. Reinke, J. Walk, C. Holland, J. Candy, and T. Görler. Investigation of the transport shortfall in Alcator C-Mod L-mode plasmas. *Physics of Plasmas (1994-present)*, 20(3):032510, 2013.

[79] N. T. Howard, A. E. White, and C. Sung. Measurement of Electron Temperature Fluctuations Using a Tunable Correlation Electron Cyclotron Emission System on Alcator C-Mod. *Review of Scientific Instruments*, 85(11):11D811, 2014.

[80] T. C. Hsu. *The submillimeter Wave Electron Cyclotron Emission Diagnostic for the Alcator C-Mod Tokamak.* PhD thesis, MIT, 1993.

[81] Joseph Donald Huba. NRL plasma formulary. Technical report, Naval Research Laboratory, 2006.

[82] A. E. Hubbard and et al. Edge energy transport barrier and turbulence in the I-mode regime on Alcator C-Mod. *Physics of Plasmas*, 18(5):056115, 2011.

[83] A. E. Hubbard, D. G. Whyte, R. M. Churchill, A. Dominguez, J. W. Hughes, Y. Ma, E. S. Marmar, Y. Lin, M. L. Reinke, and A. E. White. Threshold conditions for transitions to I-mode and H-mode with unfavourable ion grad B drift direction. *Nuclear Fusion*, 52(11):114009, 2012.

[84] J. W. Hughes, D. A. Mossessian, K. Zhurovich, M. DeMaria, K. Jensen, and A. Hubbard. Thomson scattering upgrades on Alcator C-Mod. *Review of Scientific Instruments*, 74:1667, 2003.

[85] I. H. Hutchinson. *Principles of Plasma Diagnostics.* Cambridge University Press, UK, 2002.

[86] Y. Idomura, M. Wakatani, and S. Tokuda. Gyrokinetic theory of slab electron temperature gradient mode in negative shear tokamaks. *Physics of Plasmas (1994-present)*, 7(6):2456–2468, 2000.

[87] A. Ince-Cushman, J. E. Rice, M. Bitter, M. L. Reinke, K. W. Hill, M. F. Gu, E. Eikenberry, Ch. Broennimann, S. Scott, Y. Podpaly, S. G. Lee, and E. S. Marmar. Spatially resolved high resolution x-ray spectroscopy for magnetically confined fusion plasmas. *Review of Scientific Instruments*, 79:10E302, 2008.

[88] J. H. Irby, E. S. Marmar, E. Seviilano, and S. M. Wolfe. Two-color interferometer system for Alcator C-Mod. *Review of Scientific Instruments*, 59:1568, 1988.

[89] F. Jenko, W. Dorland, and G. W. Hammett. Critical gradient formula for toroidal electron temperature gradient modes. *Physics of Plasmas*, 8(9):4096, 2001.

[90] F. Jenko, W. Dorland, M. Kotschenreuther, and B. N. Rogersa. Electron temperature gradient driven turbulence. *Physics of Plasmas*, 7(5):1904, 2000.

[91] Eun jin Kim and P. H. Diamond. Zonal Flows and Transient Dynamics of the L-H Transition. *Physical review letters*, 90(18):185006, 2003.

[92] B. B. Kadomtsev and O. P. Pogutse. Plasma instability due to particle trapping in a toroidal geometry. *Sov. Phys. JETP*, 24:1172, 1967.

[93] B. B. Kadomtsev and O. P. Pogutse. Trapped particles in toroidal magnetic systems. *Nuclear Fusion*, 11(1):67, 1971.

[94] Eugene F Knott, John Shaeffer, and Michael Tuley. *Radar cross section*. SciTech Publishing, 2004.

[95] Martin David Kruskal and R. M. Kulsrud. Equilibrium of a magnetically confined plasma in a toroid. *Physics of Fluids (1958-1988)*, 1(4):265–274, 1958.

[96] L. L. Lao, H. St. John, R. D. Stambaugh, A. G. Kellman, and W. Pfeiffer. Reconstruction of current profile parameters and plasma shapes in tokamaks. *Nuclear fusion*, 25(11):1611, 1985.

[97] John D Lawson. Some criteria for a power producing thermonuclear reactor. *Proceedings of the Physical Society. Section B*, 70(1):6, 1957.

[98] L. Lin, E. M. Edlund, M. Porkolab, Y. Lin, and S. J. Wukitch. Vertical localization of phase contrast imaging diagnostic in Alcator C-Mod. *Review of Scientific Instruments*, 77:10E918, 2006.

[99] L. Lin, M. Porkolab, E. M. Edmund, M. Greenwald, N. Tsujii, J. Candy, R. E. Waltz, and D. R. Mikkelsen. Studies of turbulence and transport in Alcator C-Mod ohmic plasmas with phase contrast imaging and comparisons with gyrokinetic simulations. *Plasma Physics and Controlled Fusion*, 51:065006, 2009.

[100] P. Mantica, G. Gorini, F. Imbeaux, J. Kinsey, Y. Sarazin, R. Budny, I. Coffey, R. Dux, X. Garbet, L. Garzotti, et al. Perturbative transport experiments in JET low or reverse magnetic shear plasmas. *Plasma physics and controlled fusion*, 44(10):2185, 2002.

[101] Paola Mantica, D. Strintzi, T. Tala, C. Giroud, T. Johnson, H. Leggate, E. Lerche, T. Loarer, A. G. Peeters, A. Salmi, et al. Experimental study of the ion critical-gradient length and stiffness level and the impact of rotation in the JET tokamak. *Physical review letters*, 102(17):175002, 2009.

[102] E. S. Marmar and Alcator C-Mod Group. The Alcator C-Mod program. *Fusion Science and Technology*, 51:261, 2007.

[103] R. M. McDermott, B. Lipschultz, J. W. Hughes, P. J. Catto, A. E. Hubbard, I. H. Hutchinson, R. S. Granetz, M. Greenwald, B. LaBombard, K. Marr, et al. Edge radial electric field structure and its connections to H-mode confinement in Alcator C]-Mod plasmas. *Physics of Plasmas (1994-present)*, 16(5):056103, 2009.

[104] Stefano Migliuolo. Ion temperature gradient modes and impurities in toroidal shaped plasmas. *Nuclear fusion*, 33(1):3, 1993.

[105] D. R. Mikkelsen, H. Shirai, H. Urano, T. Takizuka, Y. Kamada, T. Hatae, Y. Koide, N. Asakura, T. Fujita, T. Fukuda, et al. Stiff temperature profiles in JT-60U ELMy H-mode plasmas. *Nuclear fusion*, 43(1):30, 2003.

[106] R. L. Miller, M. S. Chu, J. M. Greene, Y. R. Lin-Liu, and R. E. Waltz. Non-circular, finite aspect ratio, local equilibrium model. *Physics of Plasmas (1994-present)*, 5(4):973–978, 1998.

[107] Farrokh Najmabadi, A. Abdou, L. Bromberg, T. Brown, V. C. Chan, M. C. Chu, F. Dahlgren, L. El-Guebaly, P. Heitzenroeder, D. Henderson, et al. The ARIES-AT advanced tokamak, advanced technology fusion power plant. *Fusion Engineering and Design*, 80(1):3–23, 2006.

[108] M. G. Natrella. *Experimental statistics*. Dover Books on Mathematics, 2005.

[109] W. M. Nevins, J. Candy, S. Cowley, T. Dannert, A. Dimits, W. Dorland, C. Estrada-Mila, G. W. Hammett, F. Jenko, M. J. Pueschel, et al. Characterizing electron temperature gradient turbulence via numerical simulation. *Physics of Plasmas (1994-present)*, 13(12):122306, 2006.

[110] Application Note. 57-2: Noise Figure Measurement Accuracy-The Y-Factor Method. *Agilent Technologies, Palo Alto, California, USA*, page 31, 2000.

[111] Harry Nyquist. Thermal agitation of electric charge in conductors. *Physical review*, 32(1):110–113, 1928.

[112] C. Y. M. Oi. Studies of Electron Temperature Fluctuations in the Core of Alcator C-Mod Plasmas via Correlation Electron Cyclotron Emission. Master's thesis, MIT, 2013.

[113] J. P. H. E. Ongena, M. Evrard, and D. McCune. Numerical transport codes. *Fusion Science And Technology*, 45(2T):371–379, 2004.

[114] T. H. Osborne, N. H. Brooks, K. H. Burrell, T. N. Carlstrom, R. J. Groebner, W. Howl, A. G. Kellman, L. L. Lao, T. S. Taylor, D. N. Hill, et al. Observation of the H-mode in ohmically heated divertor discharges on DIII-D. *Nuclear Fusion*, 30(10):2023, 1990.

[115] P. J. O'Shea, A. E. Hubbard, and the Alcator C-Mod Group. Nine channel polychromator for fast Te measurements on Alcator C-Mod. *Proc. 9th Joint Workshop on ECE and ECRH (BorregoSprings, USA, 1995) ed. J. LOHR (World Scientific, Singapore, 1995)*, page 7, 1995.

[116] R. R. Parker, M. Greenwald, S. C. Luchhardt, E. S. Marmar, M. Porkolab, and S. M. Wolfe. Progress in tokamak research at MIT. *Nuclear Fusion*, 25:1127, 1985.

[117] C. C. Petty, M. R. Wade, J. E. Kinsey, R. J. Groebner, T. C. Luce, and G. M. Staebler. Dependence of heat and particle transport on the ratio of the ion and electron temperatures. *Physical review letters*, 83(18):3661, 1999.

[118] C. S. Pitcher, A. H. Boozer, H. Murmann, J. Schweinzer, W. Suttrop, H. Salzmann, ASDEX Upgrade Team, and NBI Group. The relation of edge confinement to global confinement in ASDEX Upgrade (Axially Symmetric Divertor Experiment). *Physics of Plasmas (1994-present)*, 4(7):2577–2583, 1997.

[119] M. Planck. *The Theory of Heat Radiation.* John Wiley and Sons, NY, 1959.

[120] M. Porkolab, J. Dorris, P. Ennever, C. Fiore, M. Greenwald, A. Hubbard, Y. Ma, E. Marmar, Y. Podpaly, M. L. Reinke, et al. Transport and turbulence studies in the linear ohmic confinement regime in Alcator C-Mod. *Plasma Physics and Controlled Fusion*, 54(12):124029, 2012.

[121] M. Porkolab, J. C. Rost, N. Basse, J. Dorris, E. Edlund, L. Lin, Y. Lin, and S. J. Wukitch. Phase contrast imaging of waves and instabilities in high temperature magnetized fusion plasmas. *IEEE Transactions on Plasma Science*, 34:229, 2006.

[122] M. L. Reinke, Y. A. Podpaly, M. Bitter, I. H. Hutchinson, J. E. Rice, L. Delgado-Aparicio, C. Gao, M. Greenwald, K. Hill, N. T. Howard, A. Hubbard, J. W. Hughes, N. Pablant, A. E. White, and S. M. Wolfe. X-ray imaging crystal spectroscopy for use in plasma transport research. *Review of Scientific Instruments*, 83:113504, 2012.

[123] M. L. Reinke, J. E. Rice, A. E. White, M. Greenwald, N. T. Howard, P. Ennever, C. Gao, A. E. Hubbard, and J. W. Hughes. Density sensitivity of intrinsic rotation profiles in ion cyclotron range of frequency-heated L-mode plasmas. *Plasma Physics and Controlled Fusion*, 55(1):012001, 2013.

[124] T. D. Rempel, R. F. Gandy, and A. J. Wootton. Density fluctuation effects on electron cyclotron emission correlation measurements in optically gray plasmas. *Review of Scientific Instruments*, 65:2044, 1994.

[125] C. L. Rettig, T. L. Rhodes, J. N. Leboeuf, W. A. Peebles, E. J. Doyle, G. M. Staebler, K. H. Burrell, and R. A. Moyer. Search for the ion temperature gradient mode in a tokamak plasma and comparison with theoretical predictions. *Physics of Plasmas*, 8:2232, 2001.

[126] T. L. Rhodes, C. Holland, S. P. Smith, A. E. White, K. H. Burrell, J. Candy, J. C. DeBoo, E. J. Doyle, J. C. Hillesheim, J. E. Kinsey, et al. L-mode validation studies of gyrokinetic turbulence simulations via multiscale and multifield turbulence measurements on the diii-d tokamak. *Nuclear Fusion*, 51(6):063022, 2011.

[127] T. L. Rhodes, W. A. Peebles, X. Nguyen, J. C. Hillesheim, L. Schmitz, A. E. White, and G. Wang. Quasioptical design of integrated Doppler backscattering and correlation electron cyclotron emission systems on the DIII-D tokamak. *Review of Scientific Instruments*, 81(10):10D912, 2010.

[128] J. E. Rice, I. Cziegler, P. H. Diamond, B. P. Duval, Y. A. Podpaly, M. L. Reinke, P. C. Ennever, M. J. Greenwald, J. W. Hughes, Y. Ma, E. S. Marmar, M. Porkolab, N. Tsujii, and S. M. Wolfe. Rotation Reversal Bifurcation and Energy Confinement Saturation in Tokamak Ohmic L-Mode Plasmas. *Physics Review Letter*, 107:265001, 2011.

[129] J. E. Rice, B. P. Duval, M. L. Reinke, Y. A. Podpaly, A. Bortolon, R. M. Churchill, I. Cziegler, P. H. Diamond, A. Dominguez, P. C. Ennever, C. L. Fiore, R. S. Granetz, M. J. Greenwald, A. E. Hubbard, J. W. Hughes, J. H. Irby, Y. Ma, E. S. Marmar, R. M. McDermott, M. Porkolab, N. Tsujii, and S. M. Wolfe. Observation of core toroidal rotation reversals in Alcator C-Mod ohmic L-mode plasmas. *Nuclear Fusion*, 51:083005, 2011.

[130] J. E. Rice, C. Gao, M. L. Reinke, P. H. Diamond, N. T. Howard, H. J. Sun, I. Cziegler, A. E. Hubbard, Y. A. Podpaly, W. L. Rowan, J. L. Terry, M. A. Chilenski, L. Delgado-Aparicio, P. C. Ennever, D. Ernst, M. J. Greenwald, J. W. Hughes, Y. Ma, E. S. Marmar, M. Porkolab, A. E. White, and S. M. Wolfe. Non-local heat transport, rotation reversals and up/down impurity density asymmetries in Alcator C-Mod ohmic L-mode plasmas. *Nuclear Fusion*, 53:033004, 2013.

[131] J. E. Rice, M. J. Greenwald, Y. A. Podpaly, M. L. Reinke, P. H. Diamond, J. W. Hughes, N. T. Howard, Y. Ma, I. Cziegler, B. P. Duval, P. C. Ennever, D. Ernst, C. L. Fiore, C. Gao, J. H. Irby, E. S. Marmar, M. Porkolab, N. Tsujii, and S. M. Wolfe. Ohmic energy confinement saturation and core toroidal rotation reversal in Alcator C-Mod plasmas. *Physics of Plasmas*, 19:056106, 2012.

[132] J. E. Rice, J. W. Hughes, P. H. Diamond, Y. Kosuga, Y. A. Podpaly, M. L. Reinke, M. J. Greenwald, ÖD. Gürcan, T. S. Hahm, A. E. Hubbard, et al. Edge Temperature Gradient as Intrinsic Rotation Drive in Alcator C-Mod Tokamak Plasmas. *Physical review letters*, 106(21):215001, 2011.

[133] J. E. Rice, A. Ince-Cushman, L-G Eriksson, Y. Sakamoto, A. Scarabosio, A. Bortolon, K. H. Burrell, Duval B. P, C. Fenzi-Bonizec, M. J. Greenwald, et al. Inter-machine comparison of intrinsic toroidal rotation in tokamaks. *Nuclear Fusion*, 47(11):1618, 2007.

[134] John E Rice, P. T. Bonoli, J. A. Goetz, M. J. Greenwald, I. H. Hutchinson, E. S. Marmar, M. Porkolab, S. M. Wolfe, S. J. Wukitch, and C. S. Chang. Central impurity toroidal rotation in ICRF heated Alcator C-Mod plasmas. *Nuclear Fusion*, 39(9):1175, 1999.

[135] P. H. Richter. Estimating errors in least-squares fitting. *TDA Progress Report*, pages 42–122, 1995.

[136] F. Romanelli and S. Briguglio. Toroidal semicollisional microinstabilities and anomalous electron and ion transport. *Physics of Fluids B: Plasma Physics (1989-1993)*, 2(4):754–763, 1990.

[137] F. Ryter, C. Angioni, M. Beurskens, S. Cirant, G. T. Hoang, et al. Experimental studies of electron transport. *Plasma physics and controlled fusion*, 43(12A):A323, 2001.

[138] F. Ryter, F. Imbeaux, F. Leuterer, H-U. Fahrbach, W. Suttrop, and ASDEX Upgrade Team. Experimental characterization of the electron heat transport in low-density ASDEX Upgrade plasmas. *Physical review letters*, 86(24):5498, 2001.

[139] F. Ryter, F. Leuterer, G. Pereverzev, H-U. Fahrbach, J. Stober, W. Suttrop, and ASDEX Upgrade Team. Experimental evidence for gradient length-driven electron transport in tokamaks. *Physical review letters*, 86(11):2325, 2001.

[140] S. Sattler and H. J. Hartfuss. Intensity interferometry for measurement of electron temperature fluctuations in fusion plasmas. *Plasma physics and controlled fusion*, 35(9):1285, 1993.

[141] S. Sattler and H. J. Hartfuss. Experimental evidence for electron temperature fluctuations in the core plasma of the $W7 - AS$ stellarator. *Physical review letters*, 72(5):653, 1994.

[142] O. Sauter, S. Brunner, D. Kim, G. Merlo, R. Behn, Y. Camenen, S. Coda, B. P. Duval, L. Federspiel, T. P. Goodman, et al. On the non-stiffness of edge transport in L-mode tokamak plasmas. *Physics of Plasmas (1994-present)*, 21(5):055906, 2014.

[143] Olivier Sauter, Clemente Angioni, and Y. R. Lin-Liu. Neoclassical conductivity and bootstrap current formulas for general axisymmetric equilibria and arbitrary collisionality regime. *Physics of Plasmas (1994-present)*, 6(7):2834–2839, 1999.

[144] J. M. Schachter. *Local Transport Analysis for the Alcator C-Mod Tokamak.* PhD thesis, MIT, 1997.

[145] L. Schmitz, A. E. White, T. A. Carter, W. A. Peebles, T. L. Rhodes, K. H. Burrell, W. Solomon, and G. M. Staebler. Observation of Reduced Electron-Temperature Fluctuations in the Core of H-Mode Plasmas. *Physical review letters*, 100(3):035002, 2008.

[146] L. Schmitz, A. E. White, G. Wang, J. C. DeBoo, G. R. McKEE, J. C. Hillesheim, W. A. Peebles, T. L. Rhodes, T. A. Carter, E. D. Doyle, et al. Observation of reduced core electron temperature fluctuations and intermediate wavenumber density fluctuations in h-mode plasmas. *Nuclear Fusion*, 49(9):095004, 2009.

[147] J. A. Snipes, R. S. Granetz, M. Greenwald, O. J. W. F. Kardaun, A. Kus, F. Ryter, U. Stroth, J. Kollermeyer, S. J. Fielding, M. Valovic, et al. H mode power threshold database for ITER. *Nuclear Fusion*, 36(9):1217, 1996.

[148] Joseph Allan Snipes, R. S. Granetz, M. Greenwald, I. H. Hutchinson, D. Garnier, J. A. Goetz, S. N. Golovato, A. Hubbard, J. H. Irby, B. LaBombard, et al. First ohmic H modes in Alcator C-Mod. *Nuclear fusion*, 34(7):1039, 1994.

[149] W. M. Solomon, K. H. Burrell, R. Andre, L. R. Baylor, R. Budny, P. Gohil, R. J. Groebner, C. T. Holcomb, W. A. Houlberg, and M. R. Wade. Experimental test of the neoclassical theory of impurity poloidal rotation in tokamaks. *Physics of Plasmas (1994-present)*, 13(5):056116, 2006.

[150] Hideo Sugama and W. Horton. Nonlinear electromagnetic gyrokinetic equation for plasmas with large mean flows. *Physics of Plasmas (1994-present)*, 5(7):2560–2573, 1998.

[151] C. Sung, A. E. White O. Sauter, C. Gao, M. Greenwald, N. T. Howard, A. E. Hubbard, J. Hughes, M. Reinke, J. Rice, and J. Walk. Study of profile shape variations with confinement regimes in Alcator C-Mod discharges. *Physics of Plasmas (1994-present), submitted.*

[152] C. Sung, A. E. White, N. T. Howard, D. Mikkelsen, J. Irby, R. Leccacorvi, R. Vieira, C. Y. Oi, J. E. Rice, et al. Correlation ECE diagnostic in Alcator C-Mod. In *18th Joint Workshop on Electron Cyclotron Emission.*

[153] C. Sung, A. E. White, N. T. Howard, C. Y. Oi, J. E. Rice, C. Gao, P. Ennever, M. Porkolab, F. Parra, D. Mikkelsen, et al. Changes in core electron temperature fluctuations across the ohmic energy confinement transition in Alcator C-Mod plasmas. *Nuclear Fusion*, 53(8):083010, 2013.

[154] C. Sung, A. E. White, J. H. Irby, R. Leccacorvi, R. Vieira, C. Y. Oi, W. A. Peebles, and X. Nguyen. Design of a correlation electron cyclotron emission diagnostic for Alcator C-Mod. *Review of Scientific Instruments*, 83:10E311, 2012.

[155] R. J. Taylor, M. L. Brown, B. D. Fried, H. Grote, J. R. Liberati, G. J. Morales, P. Pribyl, D. Darrow, and M. Ono. H-mode behavior induced by cross-field currents in a tokamak. *Physical review letters*, 63(21):2365, 1989.

[156] P. W. Terry, M. Greenwald, J-N Leboeuf, G. R. McKee, D. R. Mikkelsen, W. M. Nevins, D. E. Newman, Stotler D. P, US Transport Task Force, et al. Validation in fusion research: Towards guidelines and best practices. *Physics of Plasmas (1994-present)*, 15(6):062503, 2008.

[157] P. W. Terry and W. Horton. Drift wave turbulence in a low-order k space. *Physics of Fluids (1958-1988)*, 26(1):106–112, 1983.

[158] C. E. Thomas and R. F. Gandy. Autocorrelation and crossed sightline correlation of ECE for measurement of electron temperature and density fluctuations on ATF and TEXT. *Review of Scientific Instruments*, 61:3570, 1990.

[159] G. R. Tynan, A. Fujisawa, and G. McKee. A review of experimental drift turbulence studies. *Plasma Physics and Controlled Fusion*, 51(11):113001, 2009.

[160] Dávid Wágner, Emiliano Fable, Andreas Pitzschke, Olivier Sauter, Henri Weisen, et al. Understanding the core density profile in TCV H-mode plasmas. *Plasma Physics and Controlled Fusion*, 54(8):085018, 2012.

[161] F Wagner. A quarter-century of H-mode studies. *Plasma Physics and Controlled Fusion*, 49(12B):B1, 2007.

[162] F. Wagner, G. Becker, K. Behringer, D. Campbell, A. Eberhagen, W. Engelhardt, G. Fussmann, O. Gehre, J. Gernhardt, G. v. Gierke, et al. Regime of improved confinement and high beta in neutral-beam-heated divertor discharges of the ASDEX tokamak. *Physical Review Letters*, 49(19):1408, 1982.

[163] F. Wagner and U. Stroth. Transport in toroidal device-the experimentalist's view. *Plasma Physics and Controlled Fusion*, 35:1321, 1993.

[164] J. R. Walk, J. W. Hughes, A. E. Hubbard, J. L. Terry, D. G. Whyte, A. E. White, S-G. Baek, M. L. Reinke, C. Theiler, R. M. Churchill, et al. Edge-localized mode avoidance and pedestal structure in I-mode plasmas. *Physics of Plasmas (1994-present)*, 21(5):056103, 2014.

[165] R. L. Watterson, R. E. Slusher, and M. Surko. Low frequency density fluctuations in a tokamak plasma. *Physics of Fluids*, 28:2857, 1985.

[166] C. Watts. A review of ECE correlation radiometry techniques for detection of core electron temperature fluctuations. *Fusion Science and Technology*, 52:176, 2007.

[167] Christopher Watts, H. J. Hartfuss, and M. Häse. Comparison of different methods of electron cyclotron emission-correlation radiometry for the measurement of temperature fluctuations in the plasma core. *Review of scientific instruments*, 75(10):3177–3184, 2004.

[168] Christopher Watts, Yongkyoon In, John Heard, Perry Phillips, Alan Lynn, Amanda Hubbard, and Rex Gandy. Upper limit on turbulent electron temperature fluctuations in the core of Alcator C-Mod. *Nuclear fusion*, 44(9):987, 2004.

[169] J. Weiland, E. Asp, X. Garbet, P. Mantica, V. Parail, P. Thomas, W. Suttrop, T. Tala, et al. Effects of temperature ratio on JET transport in hot ion and hot electron regimes. *Plasma physics and controlled fusion*, 47(3):441, 2005.

[170] Jan Weiland. *Collective Modes in Inhomogeneous Plasmas: Kinetic and Advanced Fluid Theory.* IOP Publishing, 2000.

[171] J. Wesson. *Tokamaks.* Clarendon Press-Oxford, 2004.

[172] A. E. White. Reduction of core turbulence and transport in I-mode and comparisons with nonlinear gyrokinetic simulations. In *56th Annual Meeting of the APS Division of Plasma Physics, Abstract: NI1.00001 (2014) Vol. 59, number 15.*

[173] A. E. White, M. Barnes, A. Dominguez, M. Greenwald, N. T. Howard, A. E. Hubbard, J. W. Hughes, D. R. Mikkelsen, F. I. Parra, M. L. Reinke, et al. Reduction of Core Turbulence in I-mode Plasmas on Alcator C-Mod. *Nuclear Fusion*, 54:083019, 2014.

[174] A. E. White and et al. Electron temperature fluctuations associated with the weakly coherent mode in the edge of I-mode plasmas. *Nuclear Fusion*, 51(11):113005, 2011.

[175] A. E. White, N. T. Howard, M. Greenwald, M. L. Reinke, C. Sung, S. Baek, M. Barnes, J. Candy, A. Dominguez, D. Ernst, et al. Multi-channel transport experiments at Alcator C-Mod and comparison with gyrokinetic simulations. *Physics of Plasmas (1994-present)*, 20(5):056106, 2013.

[176] A. E. White, N. T. Howard, D. R. Mikkelsen, M. Greenwald, J. Candy, and R. E. Waltz. Feasibility study for a correlation electron cyclotron emission turbulence diagnostic based on nonlinear gyrokinetic simulations. *Plasma Physics and Controlled Fusion*, 53(11):115003, 2011.

[177] A. E. White, W. A. Peebles, T. L. Rhodes, C. H. Holland, G. Wang, L. Schimitz, T. A. Carter, J. C. Hillesheim, E. J. Doyle, L. Zeng, G. R. McKee, G. M. Staebler, R. E. Waltz, J. C. DeBoo, C. C. Petty, and K. H. Burrell. Measurements of the cross-phase angle between density and electron temperature fluctuations and comparison with gyrokinetic simulations. *Physics of Plasmas*, 17:056103, 2010.

[178] A. E. White, L. Schmitz, W. A. Peebles, T. A. Carter, T. L. Rhodes, E. J. Doyle, P. A. Gourdain, J. C. Hillesheim, G. Wang, C. Holland, et al. A correlation

electron cyclotron emission diagnostic and the importance of multifield fluctuation measurements for testing nonlinear gyrokinetic turbulence simulations. *Review of Scientific Instruments*, 79:103505, 2008.

[179] A. E. White, L. Schmitz, W. A. Peebles, T. L. Rhodes, T. A. Carter, G. R. McKee, M. W. Shafer, G. M. Staebler, K. H. Burrell, J. C. DeBoo, and R. Prater. Simultaneous measurement of core electron temperature and density fluctuations during electron cyclotron heating on DIII-D. *Physics of Plasmas*, 17:020701, 2010.

[180] D. G. Whyte, A. E. Hubbard, J. W. Hughes, B. Lipschultz, J. E. Rice, E. S. Marmar, M. Greenwald, I. Cziegler, A. Dominguez, T. Golfinopoulos, et al. I-mode: an H-mode energy confinement regime with L-mode particle transport in Alcator C-Mod. *Nuclear Fusion*, 50(10):105005, 2010.

[181] John C Wright, P. T. Bonoli, Marco Brambilla, Fernando Meo, Eduardo DâĂŹAzevedo, Donald B Batchelor, E. F. Jaeger, Leslie A Berry, C. K. Phillips, and Alexandre Pletzer. Full wave simulations of fast wave mode conversion and lower hybrid wave propagation in tokamaks. *Physics of Plasmas (1994-present)*, 11(5):2473–2479, 2004.

[182] P. H. Diamond Y. B. Kim and R. J. Groebner. Neoclassical poloidal and toroidal rotation in tokamaks. *Physics of Fluids B: Plasma Physics (1989-1993)*, 3(8):2050–2060, 1991.

[183] L-J Zheng, M. Kotschenreuther, and M. S. Chu. Rotational stabilization of resistive wall modes by the shear alfvén resonance. *Physical review letters*, 95(25):255003, 2005.